'REDUCTION OF TITANIUM DIOXIDE PHOTOACTIVITY'

ROBERT WILLIAM HARRISON

SCHOOL OF CHEMICAL ENGINEERING AND ADVANCED MATERIALS, BEDSON BUILDING, UNIVERSITY OF NEWCASTLE UPON TYNE, NEWCASTLE UPON TYNE.

2001-2004

A THESIS SUBMITTED TO THE UNIVERSITY OF NEWCASTLE UPON TYNE FOR THE DEGREE OF DOCTOR OF PHILOSOPHY.

Abstract:

Titanium dioxide, "titania" is used for a wide range of everyday applications, such as in sunblocks, paints, paper, and some plastics. For these uses it is necessary to reduce the photoactivity of the titania for either product quality or consumer safety. Titanium dioxide also finds application in the field of photocatalysis for pollution abatement, and in this instance a high photoactivity is desirable.

This thesis describes the development and characterisation of two main strategies intended to reduce titania photoactivity: the addition of iron dopants to suppress the number of surface radicals (Chapters 3 and 4), and the addition of an organic coating to the titania to scavenge the radicals (Chapters 5 and 6). The titania was iron doped in two ways, either only on the surface, or in the lattice and on the surface (shown by Electron Paramagnetic Resonance "EPR" spectra). The effect of several novel organic coatings on the photoactivity was tested: a phosphate, an organophosphate based coating and an organosilane. Two types of titanium dioxide were modified, a rutile sample used in commercial sunblocks and Degussa P25, a titania commonly used in research.

The efficiencies of these strategies were tested by several methods to determine the effect of solution medium on the photoactivity. A new technique of 2-nitrophenol degradation was developed to measured photoactivity in aqueous solutions and compared with the well characterised technique of 2-propanol oxidation. In addition, a test based on salicylic acid degradation was developed and shown to measure the photoactivity by direct hole oxidation.

Infra red spectroscopy and surface area determination were used to analyse how the coatings formed on the titania surface. IR spectra show that the headgroups bond to the surface and so the coatings are hydrophobic. Careful analysis showed that organosilanes form on the surface as crosslinked polymers.

Lastly, work on 4-nitrophenol degradation carried out under my guidance complements earlier work on 2-nitrophenol degradation to show that UV absorption by the solution affects the measured kinetics of photocatalytic degradation.

Declaration.

This thesis records work performed initially in the Department of Chemistry and subsequently the School of Chemical Engineering and Advanced Materials at the University of Newcastle Upon Tyne, Newcastle Upon Tyne, NE1 7RU between October 2001 and September 2004. Except where explicitly stated, this work is believed to be by the author and original. Extracts from this work have been published and presented in the following scientific journals and conferences; a copy of published work is given in Appendices 1 to 3 at the rear of the thesis:

R. W. Harrison.

I. T. A. Egerton; P. A. Christensen; R. W. Harrison; J. W. Wang, *J. Applied. Electro*, **2005**, *35*, 799.

II. A. L. Attwood; D. M. Murphy; J. L. Edwards; T. A. Egerton; R. W. Harrison, Res. Chem. Intermed, 2003, 29, 449.

III. T. A. Egerton. '*UV absorption by nitrophenol: implications for design of photocatalytic and photoelectrocatalytic reactors*' in '*Proceedings of TiO_2-9 and AOT-10*' San-Diego, USA, 2004.

IV. Verbal and poster presentation at '*Young Chemist Conference*', Torino, Italy 2004.

V. Poster presentation at '*Eighth Conference on TiO_2 Photocatalysis: Fundamentals & Applications*' Montréal, Canada, 2003

Acknowledgements.

I would like to take this opportunity to thank all the people who have helped and supported me throughout the duration of study at Newcastle. Firstly, my supervisors Dr. Terry. A. Egerton and Dr. Paul. A. Christensen, for their continual help and encouragement, both during the course of my study and the compiling of this thesis. I would also like to thank all the members of the PAC/TAE research group and department of Chemistry both past and present for making this project especially fulfilling.

I would like to thank the industrial sponsors, Uniqema ICI for the considerable support and impetus that they have offered throughout this research, and in particular, Dr. Lorna. Kessell, and Dr. I. Tooley.

The staff of the glassblowing and mechanical workshops for their advice and for the construction of apparatus.

I would also like to acknowledge the financial support from the Engineering and Physical Research Council (EPSRC) for the duration of my study.

Lastly I would like to thank my parents and all my family for their support and faith, and Jodi for her encouragement and patience.

'Tis all a Chequer-board of Nights and Days
Where Destiny with Men for Pieces plays:
Hither and thither moves, and mates, and slays,
And one by one back in the Closet lays.

'*The Rubaiyat*'
Omar Khayyam.
Scientist, mathematician,
astronomer, philosopher,
and Poet.

TABLE OF CONTENTS.

1. INTRODUCTION.

1.1. Background to titanium dioxide.

The practical and potential applications of pigmentary and nano-sized Titanium dioxide are vast - it is in widespread use in paints, plastics, sunscreens/cosmetics, finishings/coatings, and in printing and paper products [1-7]. The end use determines whether pigmentary or nanosized grade particulate titanium dioxide is utilised. For these applications a surface coating is typically applied to control the dispersion and optical properties and to minimise the inherent photoactivity. In addition there has been considerable research into the use of titanium dioxide as a photocatalyst for environmental remediation, although currently this technique is not widely commercially viable [8,9], and for 'self cleaning' windows or buildings [10,11]. Global demand for titanium dioxide exceeds 4 million metric tonnes and is estimated to be rising at 3 % per annum [12].

Titanium dioxide naturally occurs in three crystalline forms: anatase, rutile and brookite [13] – of which only the former two find application and are produced commercially (although Brookite may be produced in the laboratory by heating amorphous TiO_2 prepared from titanium alkoxides) [14]. Rutile (from the Latin 'rutilus') is the major ore of titanium dioxide and was discovered in 1803 by Werner in Spain. Anatase (earlier named octahedrite) was named by R. J. Hauy in 1801 from the Greek word 'anatasis' meaning extension, due to its longer vertical axis than rutile. Brookite was named in honour of H. J. Brooke and discovered by A. Levy in 1825 at Snowden, England. Anatase and brookite transform to the rutile phase with heating as this is the most thermodynamically stable phase – the anatase to rutile transition is at approximately 700°C [14]. Both anatase and rutile have a tetragonal structure (Figure 1.i) with the TiO_6 octahedra sharing four edges, and two edges and two corners respectively. The physical properties of anatase and rutile are collected in Table 1.i. The rutile form has a more closely packed structure with the bridge oxygen's more displaced towards each other than in anatase, giving a more closely packed dense structure. This structural feature gives rise to a greater chemical stability, greater hardness, higher specific gravity, and higher refractive index – hence its common use as an opacifier.

Electronically, anatase and rutile are broad band gap semiconductors (filled valence band and empty conduction band) with characteristic band gaps for pure crystals of roughly 3.20 eV and 3.05 eV respectively – requiring photons of wavelength ≤ 383nm and 403nm respectively to promote valence band electrons. Excited electrons, and the consequent valence band holes are free to migrate within the crystal giving rise to electrical conductivity - the electrons having the greater contribution [13] and also leads to photochemical properties (see below).

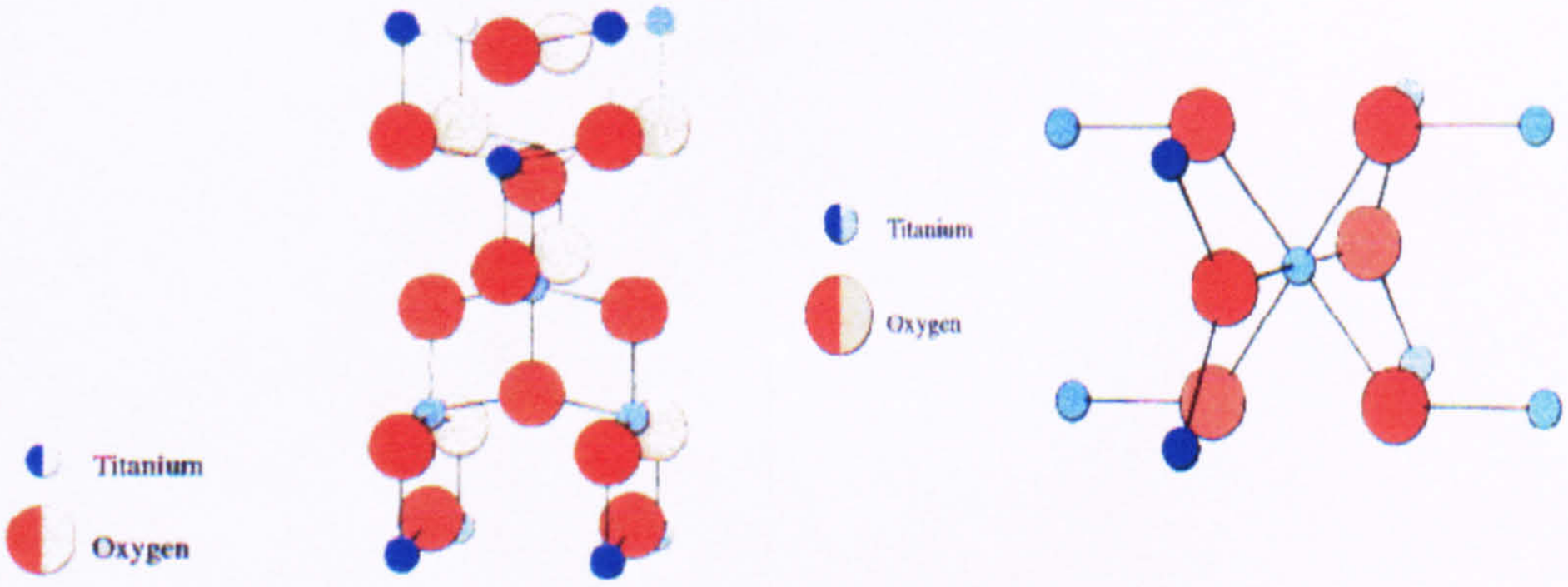

Figure 1.i. Crystal structures of a) anatase and b) rutile titanium dioxide.

Property	Anatase	Rutile
Crystal structure	Tetragonal	Tetragonal
Number Ti/unit cell	4	2
Lattice parameters (pm)	a = b = 378.45 c = 951.43	a = b = 459.37 c = 295.87
Ti-O distance (pm)	2 at 191.00 4 at 195.00	2 at 198.80 4 at 194.40
Bond angle O-Ti-O	90°, 81.21°, 98.79°	90°, 78.1°, 101.9°
Density	3.90 g cm^{-3}	4.25 g cm^{-3}
Refractive index	2.55	2.70
Hardness (Mohs' scale)	5.5-6	7-7.5

Table 1.i. Compiled crystal parameters and physiochemical data for anatase and rutile titanium dioxide [14,15].

1.2. Surface structure of titanium dioxide.

The existence of hydroxyl groups on the surface of titanium dioxide is well documented from infrared spectroscopy data, which in principle arise from adsorption of water with the surface planes to satisfy the vacancy saturation [16] i.e. water is chemisorbed at co-ordinately unsaturated Ti^{4+} sites and dissociates to give hydroxyl groups [16,17]. Adsorption isotherms for a variety of ions suggest that the surface is only partially hydroxylated (~50 %) [18].

The surface of titanium dioxide is composed of different crystal planes; for rutile the (100), (101), and (110) planes, with the latter accounting for ~ 60 % of the surface. The dissociative chemisorption of a water molecule on a bare metal results in the transfer of a proton to the surface oxide ion (forming OH) leaving OH on the titanium ion. For both the prevalent rutile (110) and anatase (001) planes, this results in two types of hydroxyl groups, one having monodentate attachment to a single Ti site, the other bridging two Ti sites (the rutile (110) plane is pictured below in Figure 1.ii). Jones and Hockey [19] considered that the (101) and (100) planes could not permit the dissociative chemisorption of water in a similar manner as this would result in two OH per titanium ion for which there is insufficient space and thus water is adsorbed molecularly on these faces.

The amphoteric nature of the titanium dioxide surface resulting from dissociative water adsorption has been comprehensively demonstrated for rutile and anatase. The bridged bidentate hydroxyl group is strongly polarised by two Ti^{4+} cations and is acidic, and the monodentate hydroxyl group is basic. The acid groups react with amines, whereas anions (e.g. $H_2PO_4^-$) can exchange with the basic hydroxyls [20]. Herman et al [20] found for P25 that at pH 6.6 (the isoelectric point) fluoride ions exchange with the basic groups, and at pH 4.6 with all the hydroxyl groups.

Metal chelate formation with the titanium dioxide surface has been demonstrated to be possible for several anatase and rutile samples using hydroxyquinoline, salicylic anhydride, and acetylacetone [21]. Since chelate formation is not possible if there is only one co-ordination site available, this data suggests that each basic hydroxyl group is associated with an anion vacancy on the same Ti^{4+}.

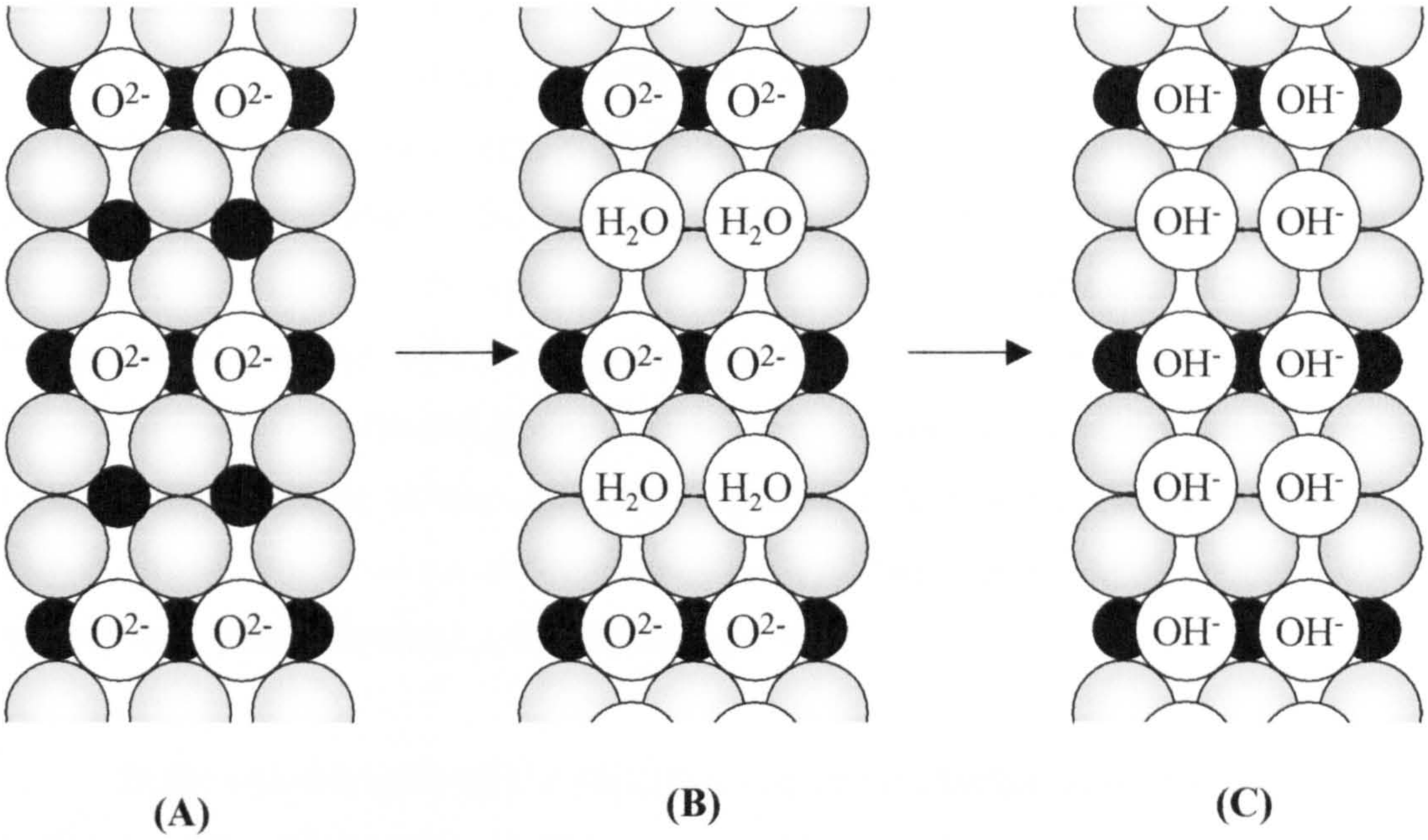

Figure 1.ii. Illustration of the dissociative adsorption of water on the rutile (110) face. (A) cleaved plane prior to adsorption; (B) adsorbed molecular water; (C) after water dissociation to give hydroxyl groups (note the two different hydroxyl group environments)

1.3. Manufacture of titanium dioxide.

Pigmentary titanium dioxide is commercially manufactured by either the 'Chloride' or 'Sulphate' process followed by finishing and coating. The decision to use one process above the other is base on a combination of factors such as the availability of raw materials, freight and waste disposal costs. The Chloride process is more common and in general less environmentally destructive, a considerable advantage given that the titanium dioxide industry has received unfavourable and special attention from environmental regulatory agencies in Western Europe and the United States [14] although there has been advances in environmental standards in the Sulphate process [22]. However, the Sulphate process does present the advantage that both titanium dioxide polymorphs and titanium chemicals may be produced in one process.

In the sulphate process [12,14,23], ilmenite ore is reacted with sulphuric acid to form titanium and iron sulphates. Unreacted ore (<5%) is removed by settling and

filtration, and most iron sulphates removed by crystallisation and filtration. Controlled heating and hydrolysis initiates precipitation of finely divided 'pulp' titanium dioxide. The initial precipitate is microcrystalline anatase with seeded nuclei added either prior or during calcination to control the crystal growth and ultimate crystal form of the product. The precipitation is followed by leaching, filtration, and washing to reduce any remaining iron impurity to typically < 300 ppm. Inorganic salts are added to control crystallisation and the pulp calcined at high temperature in the region of 900°C to 1000°C. Finally, the cooled titanium dioxide is milled and typically finished with a coating. The sulphate process generates significant co-products, which for economic and environmental reasons are separated and further reacted to form products for agricultural, water treatment, and construction uses.

In the chloride process [12,14,23] impure rutile titanium dioxide ore is converted to titanium tetrachloride by carbothermal chlorination at high temperature. The titanium tetrachloride is oxidised by air in the gas phase, with aluminium chloride added to induce rutile crystal growth; in the absence of this additive an anatase/rutile mixture is produced. The hot gas stream is carefully cooled and the product filtered and slurried. The chlorine gas is recycled to the original chlorination stage and the pigment taken for finishing and coating.

In addition to the common commercial production methods there are numerous laboratory scale methods for the production of titanium dioxide particles, coated films and electrodes [24-33]. The exact preparation methods are crucial in determining the final crystal morphology, particle size and shape, and the ultimate physiochemical and photophysical properties. The samples studied in the present work were made either by hydrolysis of aqueous solutions of $TiCl_4$ (Sample A) [34], or by flame hydrolysis in the gas phase (P25).

1.4. Optical properties of titanium dioxide.

Undoped titanium dioxide does not absorb visible light and thus the optical properties in the visible region are primarily determined by the scattering of visible light by the particles [35-37]. For end uses such as paints, a high opacity is desired and thus a high scattering in the visible region, and to this end large pigmentary sized particles are used. Conversely, for end uses such as sunscreens it is important that there be minimum

scattering in the visible region so that the applied cream does not appear white, and to this end ultrafine nanosized titanium dioxide is used. Figure 1.iii shows typical curves for the optical properties for these two sizes of titanium dioxide.

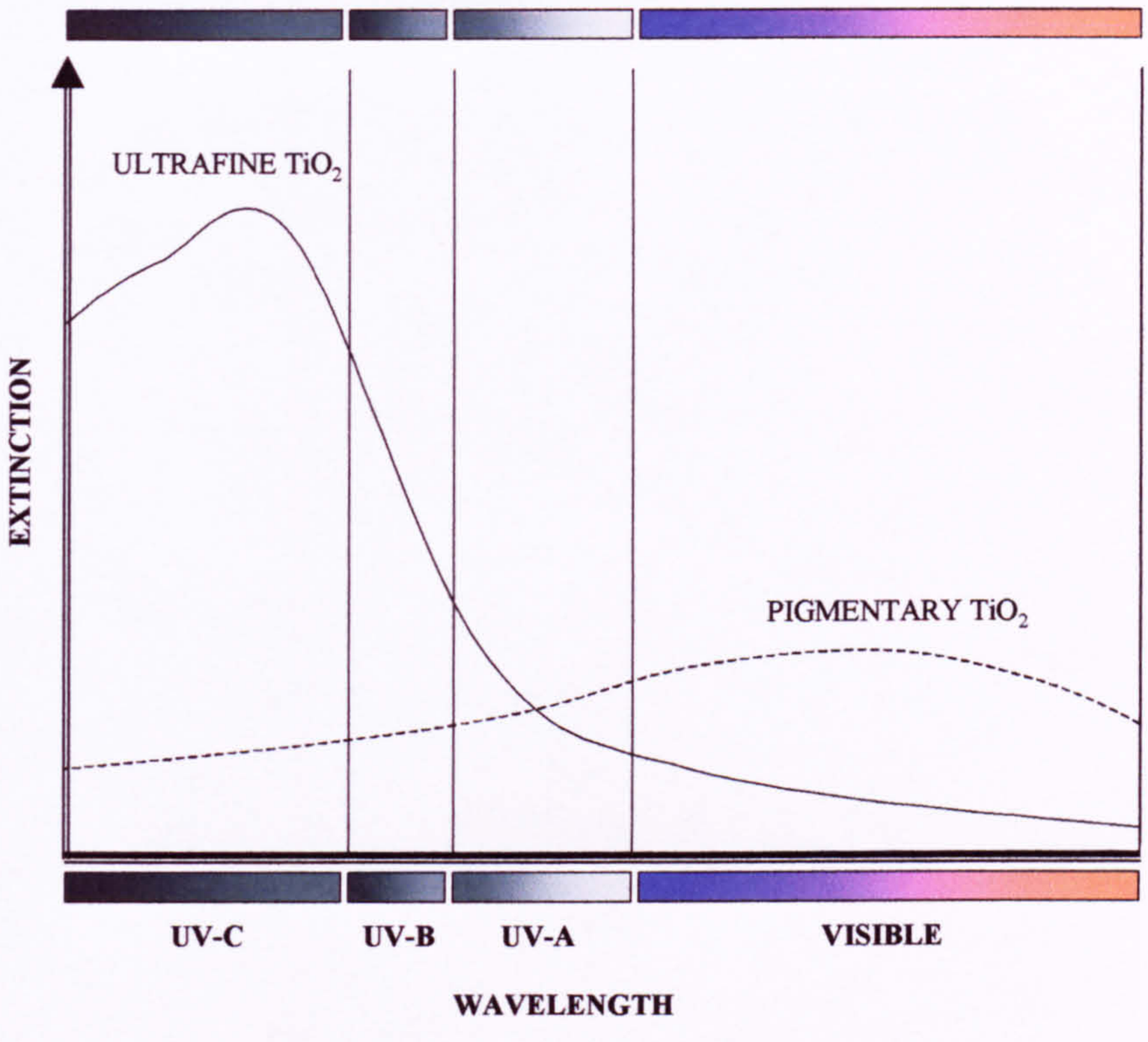

Figure 1.iii. Optical properties arising from the combination of scattering and absorption of ultrafine (~ 50 nm) and pigmentary (~ 220 nm) sized titanium dioxide [35].

It also necessarily follows that any coating, finishing or processing must maintain or aid the effective dispersion of the titanium dioxide and prevent agglomeration to unsuitable particle sizes consistent with the end use [35-37].

The optical properties can be modelled using a number of theories dependant on the particle size. *Rayleigh theory* [38] is used for small particles where the particle diameter is less than the wavelength of the incident radiation. The intensity of scattered light is modelled by $1/\lambda^4$ (where λ is the wavelength of incident light) i.e. small particles more efficiently scatter light of short wavelength. For larger particles, *Mie theory* [14] is used, which considers the phase shift of the radiation as it passes through the large particles. As the model assumes that particles do not interact this model works best for dilute systems with fewer particles. The Mie theory reduces to *Fraunhofer theory* [39]

for particles much greater than the wavelength where the radiation diffracted external to the particle is more dominant than that diffracted internally. Lastly, *Kubelka-Munk theory* [14,40] relates the scattering and absorption coefficients to opacity for pigmented films. This theory has been successfully applied to sunscreens and paints despite the fact that the coefficients need be determined experimentally.

Modelling the optical properties is even more difficult as the titanium dioxide also absorbs radiation of suitable low wavelength (as discussed below). Thus, at wavelengths above those absorbed, incident light is scattered for pigmentary sized particles and modelled by Mie theory, whilst only a small fraction is scattered for ultrafine particles. Despite the difficulties, the importance of the optical properties of titanium dioxide ensures that this area receives considerable attention.

1.5. Titanium dioxide as a photocatalyst.

Unless suitably minimised, the inherent photocatalysis by titanium dioxide typically presents a serious problem in the end use application. For example, high photoactivity can lead to low weatherability paints as the titanium dioxide filler catalyses the solar destruction of organic binders and other ingredients [1,2,7]. For cosmetic applications, in addition to this problem, which may lead to undesirable optical properties through the degradation of the organic medium, there is at least a theoretical or perceived health risk of damage to the skin by carcinoma formation [41,42,43] from titanium dioxide photocatalysis. A detailed study has shown that titanium dioxide efficiently degrades rheological modifiers in sunscreens [44]. As mentioned above a coating is typically applied to ideally eliminate, or a least minimise this effect. Alternatively, the photochemical properties of titanium dioxide can be utilised for environmental remediation for detoxification/disinfection or general cleaning, to photocatalytically degrade chemicals or biological organisms [12,45]. Considerable research effort has focused on the use of titanium dioxide as a catalyst for the photoproduction of ammonia as an alternative to the Haber process, although yields remain too low for current commercialisation [46]. In either case a thorough understanding of the theory of semiconductor photocatalysis is required to successfully study titanium dioxide for these applications. The substantial research in these areas is reflected in the increasing quantity of publications both in the general field of titanium dioxide and in photocatalytic uses for this material [12].

1.5.1. Semiconductors and Band theory.

Molecular orbital theory dictates then when two atoms are brought together to form a molecule, orbitals of similar energy overlap and form a bonding and antibonding orbital. For three atoms, there are three molecular orbitals; a bonding, an antibonding, and a non-bonding level energetically in between. It follows that when there are N atomic orbitals, N molecular orbitals are formed and overlap in energy covering a band of finite width. When N is infinitely large, then the difference between neighbouring energy levels approaches an infinitely small value, but the band still possesses a finite width. In the case of solids, each atom can take part in bonding, which is spread throughout the structure [47]. A band can be thought of as consisting of N different molecular orbitals, the lowest energy orbital is fully bonding, and the highest fully antibonding. A band made up of contributions from s-orbitals is called an 's-band', and a band made up of p-orbitals a 'p-band'. If the atomic p-orbitals in the p-band are of higher energy than the s-orbitals in the s-band then the p-band will be higher, and if the energy difference between the two are large enough then an energy gap with no orbitals will lie between the bands, termed the 'band gap'. Figure 1.iv illustrates energy band diagrams for a metal, a semiconductor, and an insulator. Although commonly used this latter term is not absolute and is dependent on the extent of the band gap.

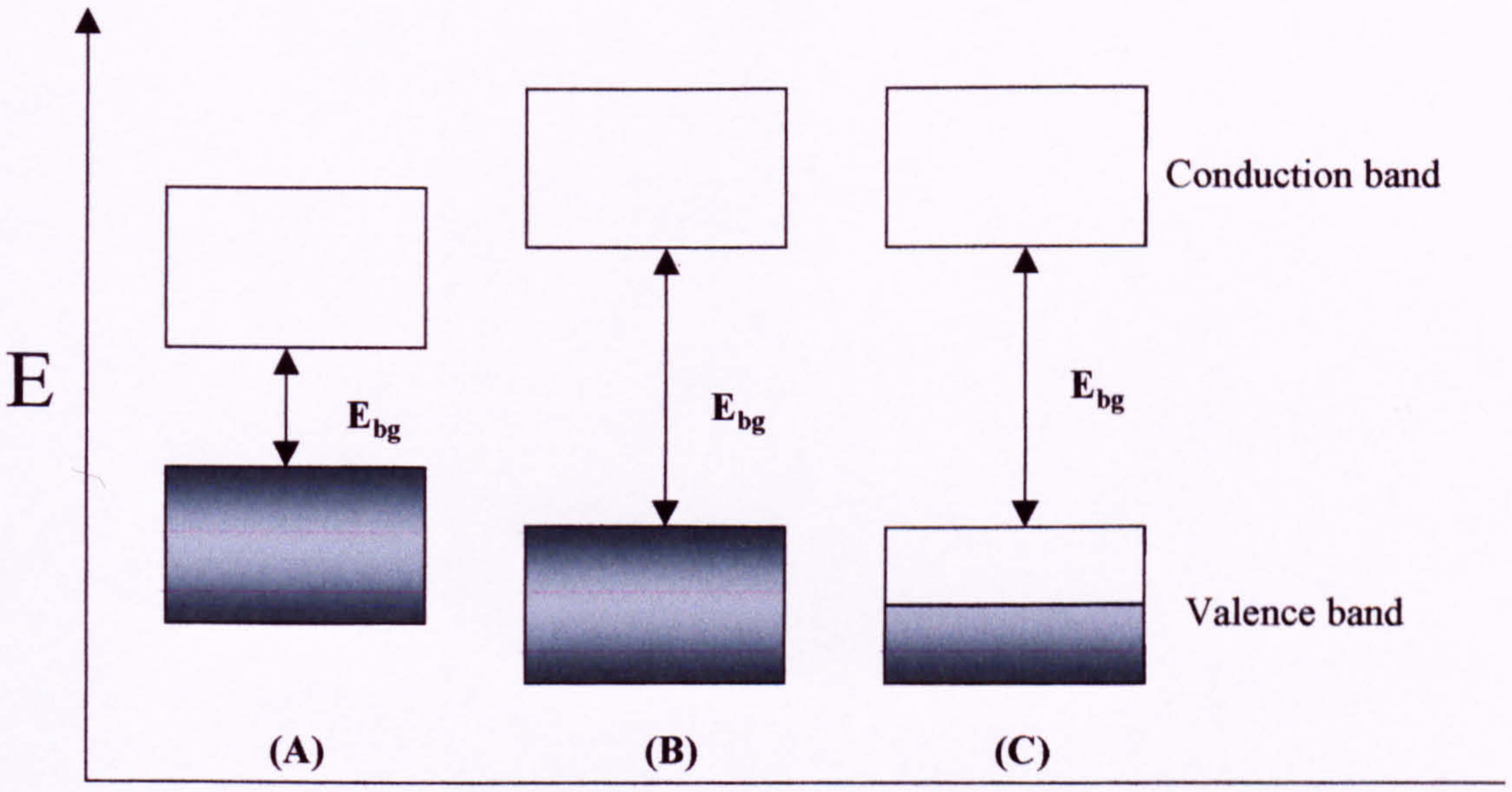

Figure 1.iv. Illustration of energy diagrams for a semiconductor (A), an insulator (B) and a metal (C).

For a solid formed from atoms such as alkali metals, which only contribute one electron then at absolute zero only the lower half of the band will be filled i.e. ½ N and the highest occupied molecular orbital (HOMO) is termed the 'Fermi level' and in this case the solid is a metal (C). Unlike the case for a semiconductor or insulator, there are energy levels very close in energy to the Fermi level (as the Fermi level does not lie within the bandgap). It thus requires very little energy to excite the uppermost electrons into the energy levels in the top half of the band where they are mobile and give rise to electrical conductivity.

For metals, there is no sharp distinction between the occupied and unoccupied energy levels above absolute zero, and the population (P) of the levels can be given by the Fermi-Dirac distribution (Equation 1.1):

$$P = \frac{1}{e^{(E-E_F)/kT} + 1} \qquad [1.1]$$

Where P is the orbital population, E_F the Fermi energy (the energy for which P=1/2), K the Boltzmann constant (1.3807×10^{-23} JK^{-1}), and T the temperature (K). For energies well above the Fermi energy then the denominator can be neglected and this approximates to, with the population resembling a Boltzmann distribution:

$$P \sim - e^{(E-EF)/kT} \qquad [1.2]$$

Alternatively, if each atom provides two electrons, the 2N electrons fill the N orbitals of the lowest band. At absolute zero, the Fermi energy lies above the valence band, and there is a gap before the next band begins. In this case the material is a semiconductor (A) and electrons can be promoted to the empty 'conduction' band (upper) from the full 'valence' band (lower) by energy higher than the band gap leaving a positive hole in the valence band. The electron and the hole are mobile and give rise to electrical conductivity - the major contribution from the conduction band electron. If the band gap is large then very few electrons will be promoted and the conductivity will be low and the solid termed an insulator (B), although as mentioned above there is no absolute distinction between an insulator and a semiconductor. For rutile titanium dioxide which is termed a broad-band semiconductor, the conduction band is

unpopulated at room temperature and has a population of only ~ 0.015% at 2000K which is only just below the melting point of 2100K [14,15].

1.5.2. Photoexcitation of electrons in semiconductors.

Alternatively, if the semiconductor absorbs photons of energy greater than the band gap (Figure 1.v) then electrons are excited from the valence band to the conduction band, leaving a positive hole in the valence band to maintain electroneutrality. The hole and electron are mobile and either recombine and release heat, or migrate to the surface where they may participate in surface redox reactions [12,45].

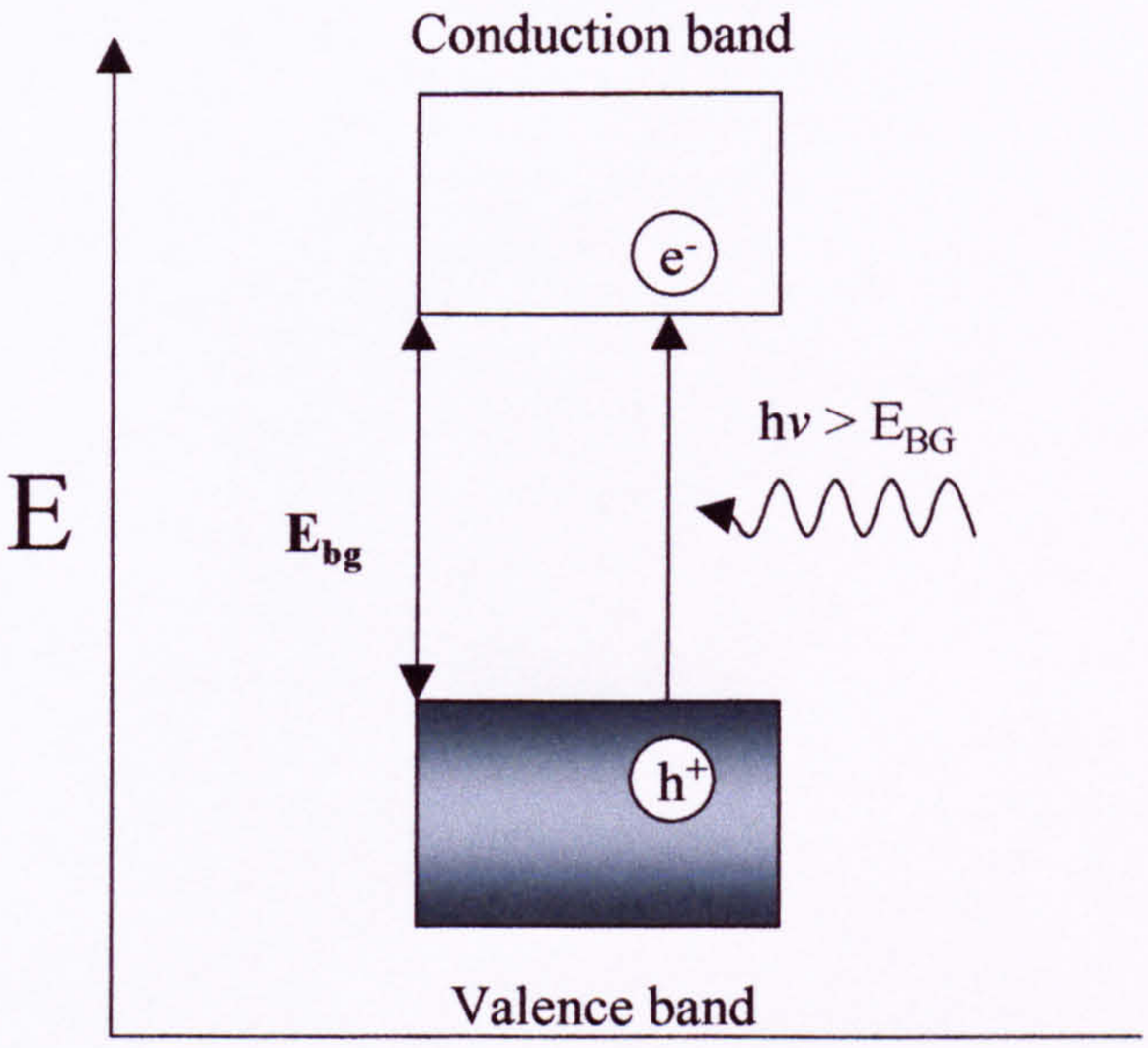

Figure 1.v. Photoexcitation of an electron from the semiconductor valence band to the conduction band, leaving a positive hole in the valence band.

The valence band of titanium dioxide is composed of the 2p oxygen electrons, and the conduction band the titanium 3d electrons. The band gap energy (E_{BG}) is 3.2 eV and 3.02 eV for the anatase and rutile morphologies respectively, requiring photons of wavelength less than 384 nm and 410 nm (i.e. ultraviolet light) to excite electrons across the band gap [48,49,50]. Figure 1.vi shows the band gap of titanium dioxide compared with that for several other commonly used semiconductors.

The energy level at the top of the valence band determines the oxidising ability of the holes and the energy level at the bottom of the conduction band the reducing ability of the electrons. The energy levels are termed flat band potentials (V_{FB}). Thermodynamically, the valence band holes can *oxidise* adsorbed couples photochemically if they have *more negative* redox potentials than the V_{FB} of the valence band. Similarly, the conduction band electrons can *reduce* adsorbed couples if they are *more positive* than the V_{FB} of the conduction band.

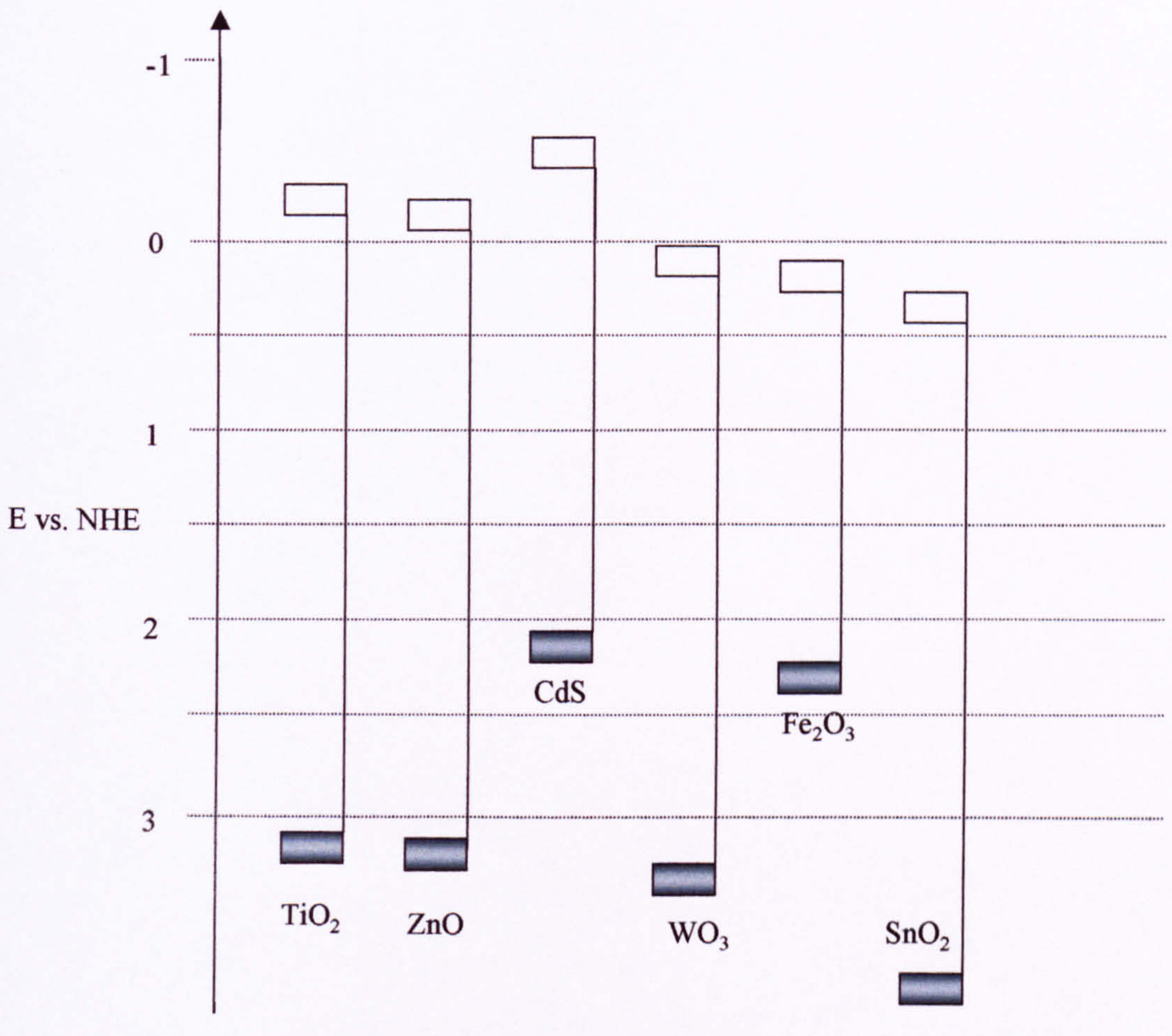

Figure 1.vi. Comparison of the position of the valence band (Grey), conduction band (White) and band gap of several semiconductors with that for titanium dioxide (anatase). Energies vs. standard normal-hydrogen electrode. Adapted from [49,50].

Energy levels can be introduced into the band gap of titanium by heating in a reductive atmosphere, such as hydrogen, altering the lattice structure and giving rise to oxygen vacancies and titanium interstitial sites energetically just below the conduction band [51]. These sites can donate electrons to the conduction band by thermal excitation.

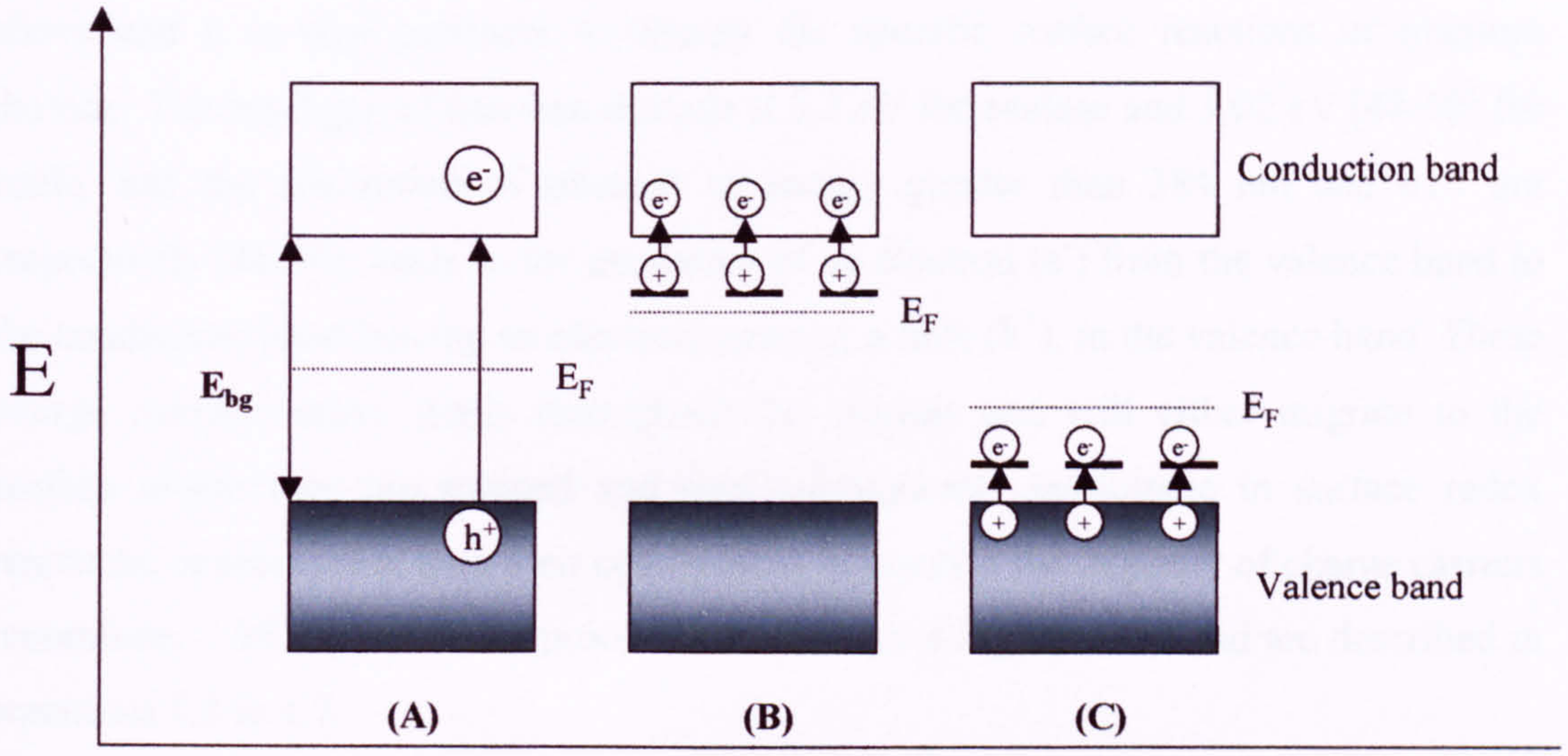

Figure 1.vii. Illustration of an intrinsic semiconductor (A), a n-type semiconductor (B) and a p-type semiconductor (C).

Alternatively localised energy levels may be introduced into the band gap by doping with other elements such as nitrogen or carbon [52-55], although more commonly with transition metal ions [12]. An electron donor dopant with a filled energy level close to the conduction band may donate electrons into the titanium dioxide conduction band by thermal excitation and the doped titanium dioxide is termed an 'n-type' semiconductor as *negative* charge carriers carry the conductivity. Niobium is an n-type dopant as it can readily lose five electrons but only four can be accommodated in the conduction band. For a 'p-type' semiconductor, an electron accepting dopant with a empty energy level just above the valence band accepts thermally excited electrons donated from the valence band to this level leaving positively charge holes. The remaining electrons may move freely; as the conductivity is caused by an electron deficiency in the valence band (*positive* holes) the doped titanium dioxide is a 'p-type' semiconductor. For n-type semiconductors the Fermi level (where P = 1/2) is shifted

closer to the conduction band, and for a p-type semiconductor the opposite occurs with the Fermi level shifted closer to the valence band. These effects are illustrated in Figure 1.vii, above. Introducing dopants may also affect the photoactivity as explained later.

1.5.3. Mechanism for titanium dioxide photocatalysis.

The fundamental origins of semiconductor photocatalysis have been discussed above and it is now pertinent to discuss the specific surface reactions of titanium dioxide. The band gap of titanium dioxide is 3.2 eV for anatase and 3.02 eV [48-50] for rutile, and the absorption of photons of energy greater than 384 nm and 410 nm respectively [48-50], leads to the excitation of an electron (e^-) from the valence band to the conduction band leaving an electron vacancy, a hole (h^+), in the valence band. These *charge carriers* move freely throughout the crystals and will either migrate to the surface where they are trapped and may subsequently participate in surface redox reactions, or recombine with their counterpart. In practice the majority of charge carriers recombine, > 95% [45]. These processes are shown in Figure 1.viii and are described in equations 1.3 to 1.7.

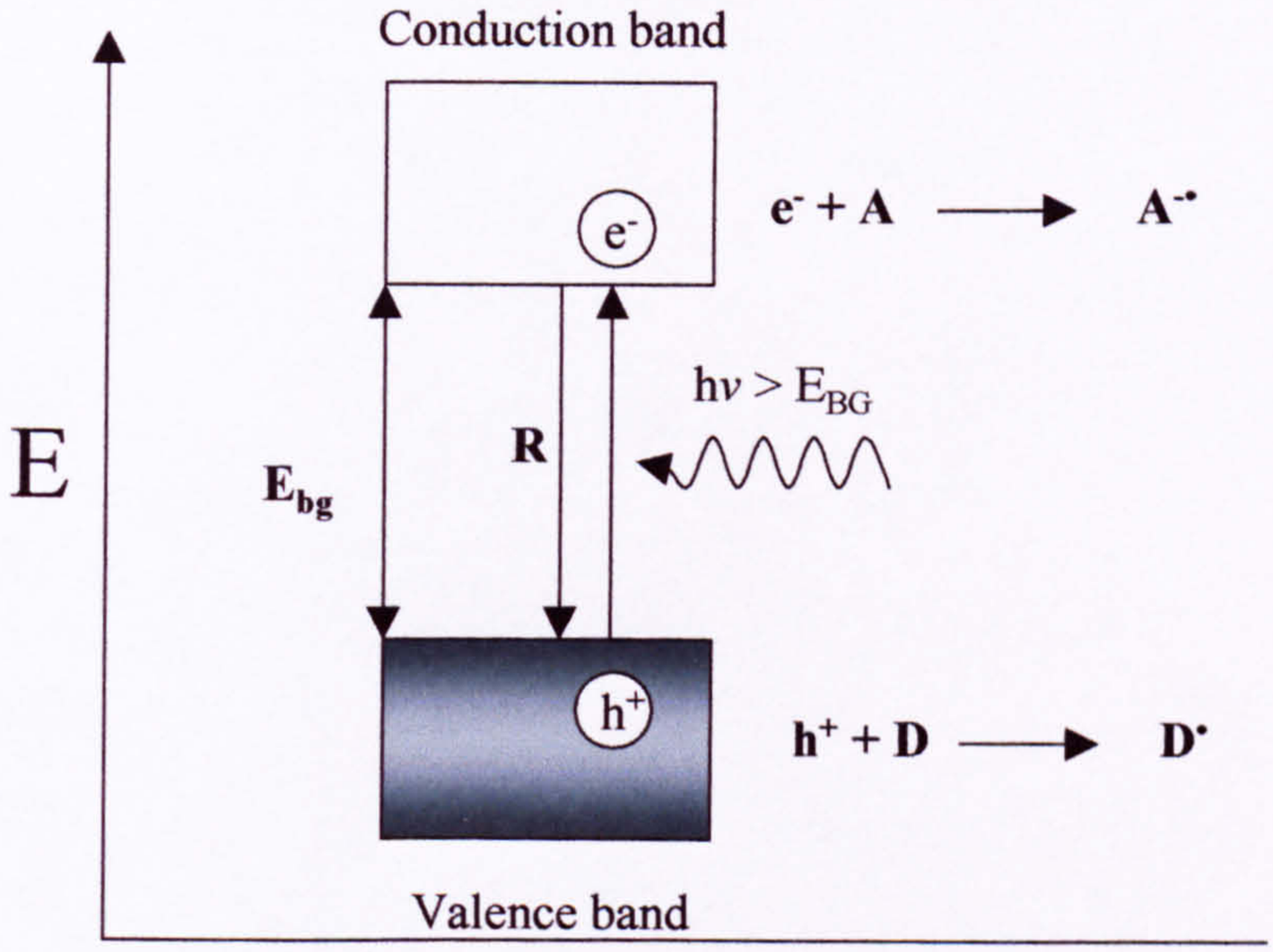

Figure 1.viii. Illustration of the fundamental and primary surface steps in titanium dioxide photocatalysis. 'A' is an adsorbed electron acceptor, and 'D' an electron donor. 'R' represents the recombination of the electron (e^-) and hole (h^+).

Absorption of a photon of energy greater than the titania bandgap (E_{BG}) leads to the generation of mobile charge carriers, an electron (e^-) in the conduction band and a hole (h^+) in the valence band:

$$TiO_2 + hv \rightarrow TiO_2 (h^+_{vb} - e^-_{cb}) \quad [1.3]$$

These charge carriers either migrate to the surface or recombine in the lattice (Equation 1.4):

$$TiO_2 (h^+_{vb} - e^-_{cb}) \rightarrow TiO_2 + \text{Thermal energy} \quad [1.4]$$

If they reach the surface the hole is typically trapped by an adsorbed hydroxyl (or adsorbed water) as the titanium dioxide surface has been shown to be hydroxylated [19,56,57], while Ti^{IV} traps the electron [58]:

$$h^+_{vb} + >Ti^{IV}\text{-}OH \rightarrow (>Ti^{IV}\text{-}OH^{\bullet})^+ \quad [1.5]$$

$$e^-_{cb} + >Ti^{IV}\text{-}OH \rightarrow (>Ti^{III}\text{-}OH) \quad [1.6]$$

The formation of hydroxyl radicals has been inferred from Electron Spin Resonance (ESR) studies using spin traps [59-61]. The importance of the hydroxyl radical in the oxidation of liquid 2-propanol was stressed in a deuteration study by Cunningham et al [62]. Some authors [63,64] have also suggested that the hole may be trapped in a subsurface site:

$$h^+_{vb} + Ti^{IV}\text{-}O^{2-}\text{-}Ti^{IV} \rightarrow (Ti^{IV}\text{-}O^{\bullet-}\text{-}Ti^{IV}) \quad [1.7]$$

Once the charge carriers are trapped at the surface, interfacial charge transfer can occur with electron donors (D) and accepters (A); except in deaerated systems the acceptor is typically O_2 (leading to reactive oxygen species). Interfacial charge transfer can only occur by Equation 1.10 under certain circumstances i.e. when the electron donor molecule is strongly adsorbed [65].

$$(>Ti^{IV}\text{-}OH^{\bullet})^+ + D \rightarrow >Ti^{IV}\text{-}OH + D^{\bullet} \quad [1.8]$$

$$(>Ti^{III}\text{-}OH) + A \rightarrow >Ti^{IV}\text{-}OH + A^{\bullet-} \quad [1.9]$$

$$(Ti^{IV}\text{-}O^{\bullet-}\text{-}Ti^{IV}) + D \rightarrow Ti^{IV}\text{-}O^{2-}\text{-}Ti^{IV} + D^{\bullet} \quad [1.10]$$

Or surface recombination can occur, either by direct quantum tunnelling of the two charge carriers trapped on the surface (Equation 1.11) or by recombination with newly formed charge carriers from subsequently photoexcited electrons:

$$(>Ti^{IV}\text{-}OH^{\bullet})^{+} + (>Ti^{III}\text{-}OH) \rightarrow 2\,(>Ti^{IV}\text{-}OH) \quad \textbf{[1.11]}$$

$$h^{+}_{vb} + (>Ti^{III}\text{-}OH) \rightarrow >Ti^{IV}\text{-}OH \quad \textbf{[1.12]}$$

$$e^{-}_{cb} + (>Ti^{IV}\text{-}OH^{\bullet})^{+} \rightarrow >Ti^{IV}\text{-}OH \quad \textbf{[1.13]}$$

Direct interfacial charge transfer to an electron donor only occurs when the organic molecule is strongly adsorbed, usually by forming an inner sphere complex with the surface [65]. It has been suggested that salicylic acid, catechol, formic acid and other similar molecules [65-67] are oxidised directly by holes rather than through a hydroxyl mediated mechanism (Equation 1.8). The degradation of 4-chlorophenol has been studied by radiological studies and found to proceed partly be direct hole oxidation [68]. The exact route may well depend on the reaction conditions as found for salicylic acid [65].

In addition to oxidation through one of these mechanisms, the organic may be oxidised by other oxygen radicals formed from the reduction of adsorbed oxygen in its role as an electron acceptor (see also equation 1.9):

$$(>Ti^{III}\text{-}OH) + O_2 \rightarrow >Ti^{IV}\text{-}OH + O_2^{\bullet-} \quad \textbf{[1.14]}$$

This superoxide species may proceed to form additional hydroxyl radicals through hydrogen peroxide as an intermediate [69]. Hydrogen peroxide may also be formed as a termination reaction of two hydroxyl radicals [69]. Decomposition to active oxidising reactants may well play a role in the oxidation process. Active oxygen species that have been proposed as reaction intermediates including mononuclear oxygen anion (O^{-}), superoxide (O_2^{-}), ozonide (O_3^{-}), hydroperoxy (HO_2^{-}), alkylperoxy (ROO^{-}), or singlet oxygen ($^1O_2$) [70]. Certainly, the study of active oxygen intermediates in photocatalysis has and continues to receive considerable attention. The precise intermediates are beyond the interest of the current study and readers are directed to

studies such as that by Murphy et al [70] and references contained within, which found that the intermediates were dependant on the type of titanium dioxide and hydration.

1.5.4. Factors influencing the efficiency of titanium dioxide photocatalysis.

The study of factors affecting the rate of titanium dioxide photocatalysis has been the focus of considerable research effort. The major factors are the crystal morphology [71], particle size [72,73], and dopants [12], although such factors as hydroxyl group density have also been found to influence photoactivity, a higher amount of hydroxyl groups favouring photoactivity as these act as hole traps [74]. Recently the dispersion of the titanium dioxide has also been found to significantly affect the measured photoactivity [75].

1.5.4.1. Titanium dioxide crystal morphology.

The crystal morphology affects the photocatalytic ability of the titanium dioxide for several reasons. The first, most obvious reason is that the band positions and band gap are different for the rutile and anatase polymorphs (see Figure 1.ix). While the valence bands are at roughly the same energy levels, the conduction band of anatase is ~ 0.2 eV more negative than for rutile, and thus conduction band electrons in anatase have a greater reduction potential [12] and this could enhance the photoadsorption of oxygen. In addition, the shorter band gap of rutile leads to greater light utilisation, even slightly infringing into the visible region of the spectrum, the effect of this dependant on the output of the radiation source.

It has also been suggested that the faster rate of recombination for rutile is significant. This is considered to be due to the lower charge separation caused by the lower oxygen adsorption in rutile [71] and hence a lower rate of electron trapping (equation 1.14) and when alternative electron acceptors are available, rutile can be of a similar photoactivity to anatase.

Degussa P25, the commercially available titanium dioxide, ~ 80% anatase/20% rutile, used in this study, shows rather unique photoactivity as it has been shown to be more photoactive than similar mixtures of titanium dioxide, or either of the pure phases [71]. Several authors suggested that the synergistic nature between anatase and rutile at interfaces acts to reduce charge recombination in anatase. An ESR study suggests it

may be more complex, with charge transfer also occurring from rutile to anatase, extending photoactivity to higher wavelengths [76,77].

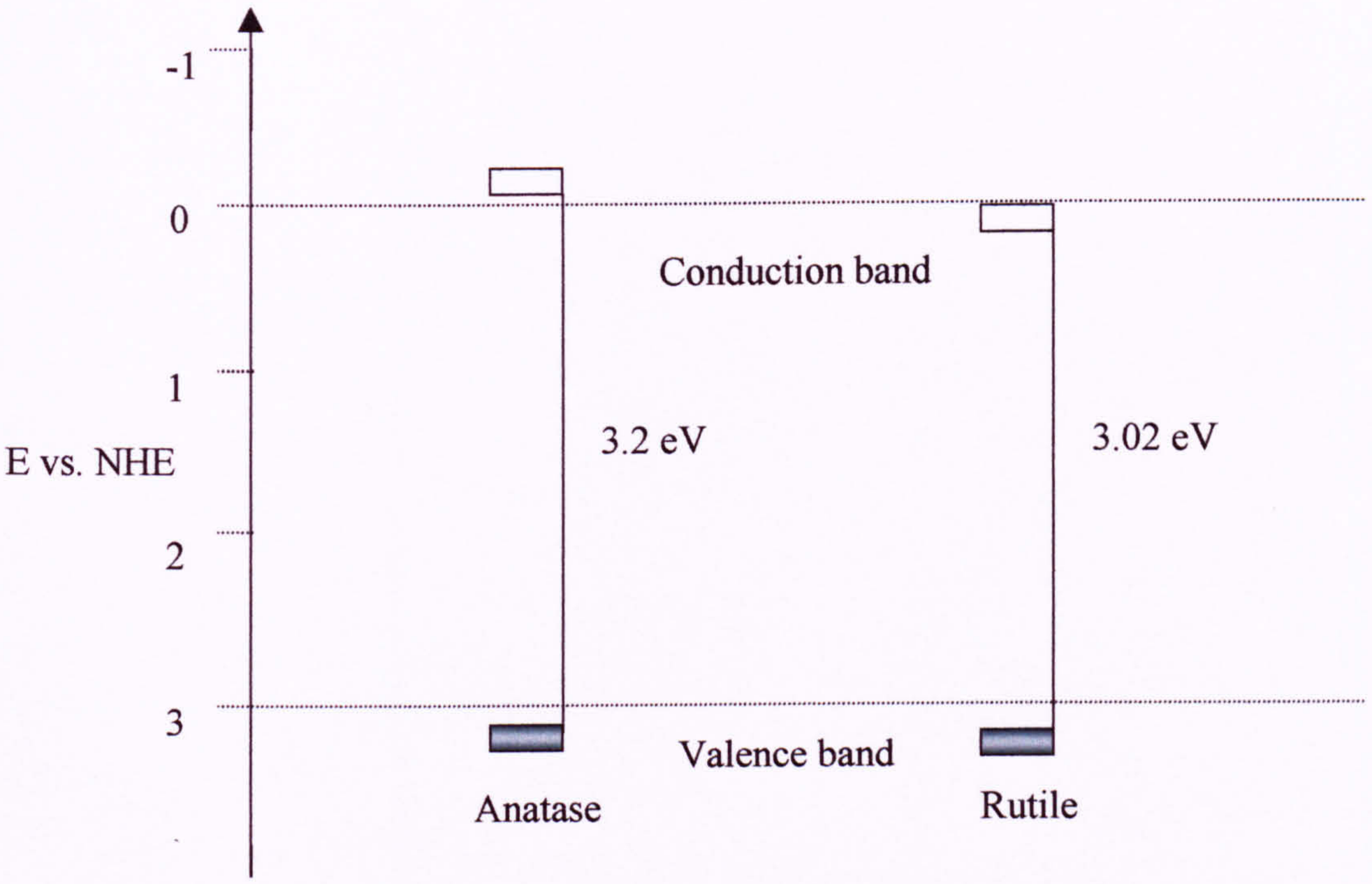

Figure 1.ix. Energy levels of the conduction and valence bands for anatase and rutile titanium dioxide [12,49,50].

1.5.4.2. Particle size/surface area.

Ying et al [72] studied the effect of particle size on the photoactivity of anatase, and concluded that this was a major determining factor. The authors attributed the results to the charge carrier recombination and interfacial charge transfer rates. For very large particles, volume recombination is a dominant factor, most electron-hole pairs recombining before reaching the surface, and thus a reduction in particle size results in an increase in photoactivity. However, for very small particles, the high surface recombination rates offset and exceed the photoactivity gains from lower bulk recombination. Thus, there is an optimum particle size for high photoactivity, 11nm in that study. The results were consistent with an earlier study by Serpone et al [78] examining the effect of particle size on the charge carrier lifetimes and a study by Yeung et al who found an optimum primary particle size of 7 nm for the gas phase

oxidation of trichloroethylene [73]. The nanosized titanium dioxide used in the current study has a crystal size of ~ 10nm (Sample A) or ~ 30nm for Degussa P25 [79].

1.5.4.3. The role of dopants.

Considerable research effort has focused on improving the photoactivity of titanium dioxide by doping with other elements such as nitrogen or carbon [52-55], although more commonly with transition metal ions [12]. A main aim has been to improve the utilisation of the incident radiation. As undoped titanium dioxide only absorbs UV light the fraction of usable solar radiation is small, the incorporation of dopants, and especially transition metal dopants, can extend the absorption significantly into the visible region by introducing localised energy levels into the bandgap [80].

However, it is now generally accepted that the dominant effect of doping titanium dioxide with transition metal dopants is to alter the rates of electron – hole recombination and charge transfer reactions by charge trapping [80]. For example Choi et al [80] studied the energetics of charge trapping by transient absorption spectroscopy for 3-4 nm sized anatase doped with a range of transition metals and dopant concentrations and concluded that the observed photoactivity could be explained by reference to the lifetime of electron-hole pairs. The authors also stressed the role of transition metals in mediating the surface electron transfer processes.

It nevertheless remains difficult to predict the role of transition metal dopants on the photoactivity. Karakitsou and Verikios [81] concluded that doping titanium dioxide with cations with higher valence than IV, n-type doping, (W^{6+}, Ta^{5+}, Nb^{5+}) gave enhanced rates for water cleavage. This agrees with results presented by Park et al [74] who reported that high valence dopants (Mo^{5+}, W^{6+}, Nb^{5+}) gave an enhanced photoactivity and those of lower valence than IV (Fe^{3+}, Co^{2+}, Ni^{2+}) a reduced photoactivity. However, Mu et al [82] found that doping anatase with trivalent (Ga^{3+}, Cr^{3+}) and pentavalent (Sb^{5+}, V^{5+}) gave reduced rates. Doping with transition metal ions has variously been shown to increase the rate in some cases and decrease the rate in different studies [46]. The level of dopant has been found to affect the photoactivity by a variety of authors [46], with lower concentrations tending to give higher photoactivity than higher concentrations. In general, an optimum concentration was found [80,84-87], shown to be dependant on the titanium dioxide crystal size by Zhang et al [85].

A likely explanation for such contradictory results is that the final photoactivity of doped titanium dioxide is determined by a plethora of factors relating to doping in addition to those relevant for undoped samples. The location and identity of the dopant, with consequent effects on the recombination, has been shown to be important [80], but structural changes caused by the doping procedure have also been identified as affecting the photoactivity - in particular, changes in the crystal size and surface area, light absorption, lattice defects, extent of hydroxylation, and the ability to adsorb the substrate [88]. In particular, Karvinen [89] studied the effect of low levels of transition metals on the crystal properties and found that the identity and concentration of the dopant significantly affected the final surface area, crystal size and morphology.

From this literature review the conclusion is that the general trend for transition metal doping is difficult to predict. A tentative conclusion is that low levels of transition metal doping give enhanced photoactivity when compared with lower levels of doping, and there is typically an optimum dopant concentration as found by several authors [80,84-87]. An extensive review of literature for iron doped titanium dioxide, with which this study is primarily concerned, is presented in Chapter 4.

1.5.4.4. Degree of dispersion of the titanium dioxide.

A recent study by Egerton and Tooley [75] found that the rate of liquid phase 2-propanol oxidation was affected by the degree of titanium dioxide dispersion for three titanium dioxide samples. For a fixed loading, the titanium dioxide was milled in a small scale sand mill to break up aggregates and flocculates of individual crystals which are present in dispersions. Rather than increase the rate of reaction due to an increase in available surface area, milling was found to significantly decrease the measured photoactivity.

By measurement of the transmission of light into the slurry (a technique called optical density determination), the authors observed that milling the titanium dioxide resulted in the UV light being absorbed in a shorter pathlength i.e. the incident photons are being absorbed by a smaller number of crystals; say 1/F of the original number. As a consequence, each crystal absorbs a greater fraction of the UV. However, as each crystal is a nanoreactor, and as it had been demonstrated that due to the dominance of recombination the rate is proportional to the square root of intensity, the rate does not

scale linearly but rather by $F^{-0.5}$ i.e. the reduction in pathlength gives a lower rate of reaction.

The authors developed a quantitative model based on this theory; with the necessary assumptions that the scattering and absorption coefficients roughly parallel each other (a reasonable assumption from data published by Tunstall [90]), and that the rate of generation of charge carriers is equally efficient for all wavelengths. The authors found that this simple model qualitatively predicts the changes in photoactivity that occur with reduced pathlength caused by milling.

The authors stated that it is likely that the catalyst dispersion would affect the measured optics, and hence measured photoactivity, in all semiconductor photocatalysis reactions. These results gain added poignancy given that the processing during modification of titanium dioxide would likely affect the degree of agglomeration and thus the measured photoactivity.

1.6. Deviations from band theory.

Band theory has been extensively used with success for the photocatalytic reactions of semiconductors. As discussed above, the valence band is composed of the 2p energy levels of the oxygen, and the conduction band the 3d electrons from titanium. The oxidation potential for valence band holes is taken to be the energy level at the top of the valence band, and the reduction potential of conduction band electrons the energy level at the bottom of the conduction band.

However, there is now a substantial body of evidence suggesting that this may be too simplistic an approach [91-94]. The assumption from classical band theory is that regardless of the initial energy states that the charge carriers occupy, there is efficient communication between the different sub-band states and consequently they quickly relax to the edge of their respective bands. In terms of time scale this means that the time for relaxation is shorter than the lifetime of the charge carriers and thus the diffusion coefficient, diffusion length and recombination are constant, and there would be no dependence on the initial spectral energy providing that it is above the band gap, except at the edge of intrinsic absorption where the absorption coefficient varies with wavelength.

Serpone and co-workers [91] examined the spectral dependence of phenol and 4-chlorophenol photodegradation by Degussa P25 and concluded that the photonic efficiencies and quantum yields demonstrated a well resolved fine band structures i.e. the rates of reaction were dependant on the wavelength of illumination, even at energies higher than the bandgap. The authors observed that that the energy relaxation time may be longer than the lifetime of free charge carriers. This possibility arises if elastic collisions dominate inelastic as a major pathway for electron/phonon interactions in the particle as this pathway leads to the establishment of equilibrium when energy relaxation has not occurred and a greater population of higher energy charge electrons. An additional cause arises if communication is poor between different states for example in nanosized particles where the number of elementary units, and hence energy states composing a band is likely to be relatively low. In such cases the lifetimes, the mobility, and diffusion length, and hence the surface concentration, of photogenerated charge carriers are dependant on the energy/wavelength of the initial photon. Thus the rate of phenol and 4-chlorophenol is dependant on the energy of the incident photon. An additional finding was that the selectivity of different intermediates was also dependant on the wavelength due to the spectral difference in population of different electronic states. Spectral dependence has also been observed for other semiconductors [92].

1.7. Modification of titanium dioxide by coatings.

Typically the final steps of titanium dioxide manufacture involve the application of a coating to control the final surface properties of the powder. Specifically, coatings are applied to control the dispersion and photocatalytic properties. A wide range of inorganic and organic coatings have been investigated with particular emphasis on varieties of silica and alumina, most commonly hydrous oxides [95-97]. For titanium dioxide alumina coatings are applied to control the dispersion, while the photocatalysis is minimised by silica coatings [95], although these may adversely affect the light scattering properties [98]. Typically, coating levels are optimised for light scattering properties or for the minimisation of photocatalysis dependant on the end use [95]. Coatings can also be applied to control the electrical properties, especially minimisation of static, and for novel optical effects [99].

The most common means of coating are by precipitation of the coating components from the aqueous phase onto the particle surface. Alternatively, the coating

may be formed in the vapour phase by Chemical Vapour Deposition (CVD). This method is particularly useful for the treatment of particles formed in the vapour phase as this simplifies processing [95]. The precursors (typically inorganic chlorides) are introduced into the vapour phase downstream from the titanium dioxide and probably deposit on formed particles [95].

1.7.1. Silica and silica-alumina coatings.

The most widely applicable means of applying a silica coating is Iller's dense silica method [100], which has been demonstrated to reduce the photoactivity of titanium dioxide. The coating mechanism is broadly understood and involves the careful control of pH during the reaction in order that a coating is formed rather than a discrete colloids or gels. The first step is probably the adsorption of silicate onto the titanium dioxide surface with this providing a surface for which subsequent coating occurs. The main step is the formation and deposition of $Si(OH)_4$ onto the titanium dioxide. The pH is carefully controlled as this species reversibly polymerises to form stable silica particles. Optimised conditions enable the coating to grow at the expense of discrete silica particles by Oswald ripening; this dictates that surfaces with a small curvature (large particles) grow at the expense of those with a high curvature (small silica particles in this case). The dense silica coating occurs as a result of molecular deposition of $Si(OH)_4$ as shown in Figure 1.x:

Figure 1.x. Illustration of the molecular deposition of silica on a metal (M) oxide surface, such as titanium dioxide.

Silica-alumina coatings can be optimised to provide good dispersive properties in addition to minimum photoactivity. The deposition mechanism of these coatings is different to that for dense silica [95]; the first stage is probably the adsorption of polysilicate anions, with a complex alumina-silica species forming on the surface with acidification. In an exhaustive study, Howard and Parfitt [101] concluded that the solubility of aluminium hydroxide probably controls the precipitation of aluminium.

Tooley and Egerton [102] compared the photocatalytic properties and absorption of 'infrared active' nitrogen for silica and alumina coated nanosized rutile. At certain highly energetic sites on the titanium dioxide, adsorbed nitrogen is rendered infra-red active. It was found that these sites were selectively coated by silica, such that the intensity of the infrared active nitrogen was significantly reduced at low coating levels. The selective coating of these sites at low silica loadings coincided with a significant reduction in photoactivity measured by 2-propanol oxidation. The reduction in the intensity of the IR active sites with increased coating directly correlated with photoactivity. Thus it was concluded that specific sites on the surface were disproportionately responsible for photoactivity, and that these sites are selectively coated by silica. A further finding was that the alumina coatings did not selectively coat these areas and the reduction in photoactivity was not significantly reduced at low coating levels confirming that alumina coatings are not particularly effective at minimising photoactivity.

1.7.2. Silane coatings.

There are several patents for silane and siloxane coated titanium dioxide and other fillers, utilising a variety of silane materials, with the intention of minimising the photoactivity [103-108]. Silanes are also highly useful as they can be easily functionalised, indeed a wide variety of functionised silanes are commercially available, and thus in addition to minimising photoactivity may be used to control the particles dispersion through functionisation of the organic tail relevant to the intended media. Alkane organic tails are suitable for oil media, whereas alkane tails containing for example nitrate groups would be suitable for dispersion in aqueous media.

This functionality also ensures that silanes are also highly useful as 'anchors' for other molecules i.e. the surface is coated silane in order to be receptive to another molecule. A high degree of ordering is possible, and several published works describe the formation of Self Assembled Monolayers (SEM's) on metals and crystalline metal oxides [109,110].

Typically, silane coatings are achieved in the vapour phase by Chemical Vapour Deposition (CVD) or in the liquid phase [111-114]. In either case the presence of surface water has been shown to be crucial to the deposition of the silane [113-114]. For

titanium dioxide (and also silica) the initial reaction step in the silane hydrolysation converting the silane to the corresponding silanol. The generic deposition mechanism involves the exchange of surface hydroxyl groups for the silanol [115-116], and this is the rate determining step, Figure 1.xi.

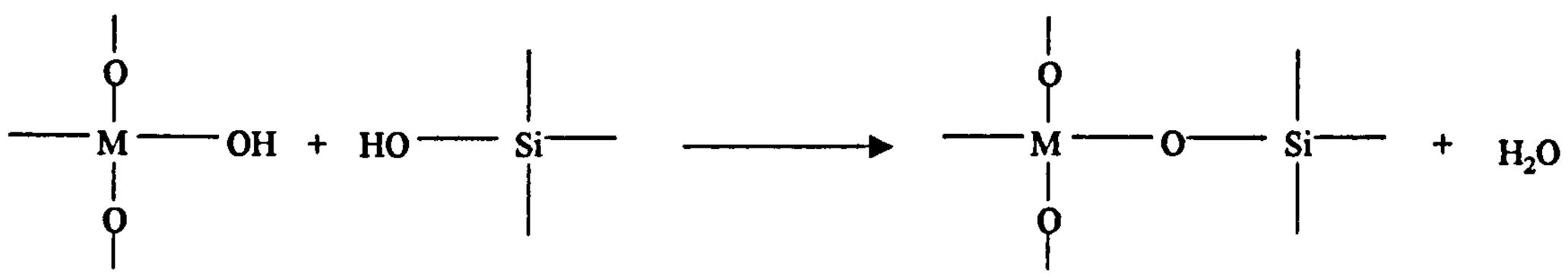

Figure 1.xi. Mechanism for silanol reaction with surface hydroxyl groups.

Tri-silanols (arising from suitable precursors such as trimethoxysilanes) tend to crosslink to form siloxanes rather than forming multiple links with the metal oxide surface i.e. lateral reactions dominate for silanes capable of crosslinking [117].

Importantly, it has been found for a range of silane coated titanium dioxide electrodes, the coating was found to be stable during the photooxidation of water i.e. the coating was not degraded during photocatalysis. It should be noted that this was determined by monitoring the Si peak by X-Ray Photoelectron Spectroscopy (XPS), and it is the Ti-O-Si moiety that has been found to be stable rather than the entire silane molecule [118].

1.7.3. Phosphate and phosphate derived coatings.

There is considerable published work describing phosphate adsorption to titanium dioxide [119-123], and several patents describe coatings, which incorporate phosphate, most likely to control the dispersive properties [124-126]. There are also several papers describing the adsorption of organophosphates [127-131] usually as Self Assembled Monolayers (SEM's). There is however considerably more published work for organophosphonates [132,133], especially for SEM's as most probably as these materials are more widely commercially available.

As coatings, organophosphates share many of the desirable properties of silanes, such as the high availability of functionalised derivatives, and thus may be used for

anchors or for the functionalisation of the titanium dioxide surface. Unlike silanes, phosphate, organophosphates, and organophosphonates do not tend to crosslink and thus multiple bonding with the titanium dioxide surface is possible, with mono-, bi- and tridentate adsorption suggested as bonding modes [119-123]. In a similar fashion to silanes, these materials have been shown to bond to the titanium dioxide surface by exchange with hydroxyl groups [119-123].

Phosphates and polyphosphates are typically added as an ingredient in final products to enhance titanium dioxide dispersion [124-126]. However, coating the titanium dioxide with phosphate has several potential advantages: having the phosphate associated with the titanium dioxide at an early stage would aid further processing (such as milling), the coating is at a constant and known level and should not be affected by changes in pH of the end product, and the specific coating method may reduce photoactivity more effectively than simple adsorption from solution.

For the present study a phosphate ester (formula $[H_{33}C16PO4]^{2-}[K_2]^{2+}$) was chosen to investigate the effect on the photoactivity of titanium dioxide by coating with an organophosphate. This material goes by the trade name Arlatone Map 160K, INCI nomenclature Potassium Cetyl Phosphate and was kindly made available by Uniqema ICI. It is a water soluble long chain organic phosphate ester and is generally used as a co-emulsifier i.e. it enhances the stability of emulsions and thicken creams and lotions. It is suitable for use in dermatological and personal care products in the cosmetics industry as it is completely non-irritating to skin [134].

1.8. The characterisation of uncoated and coated nanosized powders.

The characterisation of coated nanosized powders presents a significant challenge. Most importantly, it is necessary to determine that a coating has been achieved rather than a physical mixture of the uncoated titanium dioxide with a separate precipitate of the coating material. Through utilisation of several techniques it would ideally be possible to build a complete picture of the coating; whether the coating is patchy, whether it only coats part of the titanium dioxide surface, or whether a coherent 'shell' or 'skin' is formed, encapsulating the particle. In practice it is more difficult to gain information about nano-sized titanium dioxide than for pigmentary grade material.

Described below is a selection of the common techniques used to characterise coated powders such as surface area determination and electron microscopy. Also described are several techniques used in this study to characterise the coated, doped, and unmodified titania; such as photoactivity tests, and Electron Paramagnetic Resonance (EPR). The techniques described are by no means exhaustive as there is a huge range of methods available depending on the nature of the samples and the information sought.

1.8.1. Photoactivity tests.

Simple tests for titanium dioxide photoactivity typically utilise a probe molecule, the oxidation or reduction of which may easily be followed. In following sections below, the techniques following the oxidation of 2-propanol, 2-nitrophenol, and salicylic acid are described. In addition to these tests, there are a plethora of probe molecules that have been used to measure either reduction or oxidation reactions [12,45]. For example, a commonly used test for the reduction pathway in industrial circles is 'photogreying' whereby the concentration of surface Ti^{3+} is measured; Ti^{3+} results from surface trapped electrons formed by equation 1.6 above - detection is relatively simple as this species has a characteristic grey colour. Other common tests include phenol and $CHCl_3$ for oxidative processes, or CCl_4 and methyl viologen for the reductive processes [64,86,135].

1.8.1.1. 2-Propanol oxidation (IPA)

Bickley, Munera, and Stone [136] studied the photoadsorption and photocatalysis of isopropanol vapour on powdered rutile. The primary oxidation product was found to be acetone, although they noted that this may be slowly oxidised to formic acid. They proposed that the primary oxidants were hydroxyl radicals ($OH_s^{\bullet}$) formed from the trapping of holes by surface hydroxyl ions, and superoxide (O_2^-), formed by the trapping of photoelectrons by adsorbed oxygen - studied by the same authors in a previous paper [137]. This led to two possible reaction schemes involving either proton or hydrogen atom transfer from the isopropanol. They stressed that the rate of oxidation was dependent on the efficient photoadsorption of oxygen.

Cundall, Rudham, and Salim [138] studied the photocatalytic oxidation of liquid isopropanol by both rutile and anatase. They suggested that this reaction was similar to the gas phase oxidation studied by Stone *et al* (above). They reported a

similar quantum yield, and concluded that titanium dioxide, oxygen, and UV were required for the oxidation to acetone. The rate of acetone formation was directly proportional to the incident light intensity. Crucially, the study proposes mechanisms that consider the role of hydroxyl radicals and superoxide. The following mechanism was proposed for oxidation in the presence of oxygen:

$$h^+ + OH^-_s \longrightarrow OH^\bullet_s \quad [1.15]$$

$$e^- + O_2 \longrightarrow O_2^-{}_{(ads)} \quad [1.16]$$

The hydroxyl radical reacts with isopropanol, and the superoxide abstracts a proton from H_2O (most probably adsorbed on the surface) to give the perhydroxyl radical ($HO_2^\bullet$). The proton transfer to O_2^- from H_2O (Equation 1.18) is favoured over proton transfer from isopropanol due to the lower pK_a of H_2O.

$$OH^\bullet_s + Me_2CHOH \longrightarrow Me_2COH^\bullet + H_2O \quad [1.17]$$

$$O_2^-{}_{(ads)} + H_2O \longrightarrow OH^-_s + HO_2^\bullet \quad [1.18]$$

The formation of the acetone product can then occur in three ways:

$$Me_2COH^\bullet + HO_2^\bullet \longrightarrow Me_2CO + H_2O_2 \quad [1.19]$$

$$Me_2COH^\bullet + O_2 \longrightarrow Me_2CO + HO_2^\bullet \quad [1.20]$$

$$2Me_2COH^\bullet \longrightarrow Me_2CO + Me_2CHOH \quad [1.21]$$

Hydrogen peroxide may be formed from reaction between two perhydroxyl radicals:

$$2HO_2^\bullet \longrightarrow H_2O_2 + O_2 \quad [1.22]$$

They proposed that the hydrogen peroxide formed in reaction [1.19] or [1.22] does not participate further unless decomposed by reaction with an additional photoelectron to form two hydroxyl radicals:

$$h^+ + e^- + H_2O_2 + OH^- \longrightarrow 2OH^\bullet + OH^- \quad [1.23]$$

The authors also studied the effect of the mole fraction of propanol by varying the addition of water to the reaction mixture and found a parabolic relationship with a maximum at about 0.3-0.4 mole fraction of isopropanol. They attributed this to opposing effects whereby reaction [1.18] is enhanced and [1.17] inhibited.

Egerton and King [139] examined the effect of UV intensity on the rate of degradation of liquid isopropanol using pigmentary rutile TiO_2. These authors also considered that the primary oxidants are the hydroxyl radical and perhydroxyl radical formed by reactions [1.15], and the combination of [1.16] and [1.18] respectively - although only one of these processes was thought to be rate limiting. The rate of acetone formation was found to be proportional to the square root of the incident light intensity except at very low intensities where it is directly proportional to light intensity. The discrepancy between this result and that of Cundall *et al* (above) was attributed to the greater range of study in the Egerton and King study. The following model was proposed in which the rate of recombination of the photogenerated holes and electrons is the rate limiting step:

$$TiO_2 + h\nu \xrightarrow{k_1} h^+ + e^- \qquad [1.24]$$

$$h^+ + e^- \xrightarrow{k_2} heat \qquad [1.25]$$

$$h^+ + OH^-_s \xrightarrow{k_3} OH\bullet_{ads} \qquad [1.26]$$

If I = light intensity and k_1 is the TiO_2 absorption coefficient then:

$$\text{Rate of formation of holes} = k_1.I \qquad [1.27]$$

If h is the concentration of holes and if we assume that h = e then:

$$\text{Rate of bimolecular recombination} = k_2.h^2 \qquad [1.28]$$

$$\text{Rate of acetone formation} = k_3.h \qquad [1.29]$$

The steady state concentration of holes (*dh/dt*) is therefore made up of a positive contribution from equation [1.27] and negative contributions from [1.28] and [1.29] as follows:

$$\frac{dh}{dt} = 0 = k_1 I - k_2 h^2 - k_3 h \qquad [1.30]$$

At high light intensity, a large number of holes and electrons will be formed and hence $k_2h^2 >> k_3h$.

Thus, equation [1.30] approximates to:

$$\frac{dh}{dt} = 0 = k_1 I - k_2 h^2 \qquad [1.31]$$

Solving for h gives: $$h = \left(\frac{k_1.I}{k_2}\right)^{1/2} \quad [1.32]$$

Rate of acetone formation $= k_3.h = \left(\frac{k_3^2.k_1}{k_2}\right)^{1/2} I^{1/2} = K.I^{1/2}$ [1.33]

Therefore, at high intensity the rate of acetone formation is proportional to $I^{1/2}$ and the quantum yield will be low. At very low light intensity, the recombination term, $k_2.h^2$, is small and hence:

Rate of acetone formation = $k_3.h = k_1.I$ [1.34]

i.e. at very low light intensity the rate of acetone formation is directly proportional to I, and since the rate of recombination is low the quantum efficiency will be high.

Irick [140] studied the oxidation of liquid isopropanol to acetone as a simple test for the photoactivity of various types of titanium dioxide and other pigments. There was no detailed discussion of the mechanism, but the author compared isopropanol oxidation with photoactivity tests for polymeric media and concluded that it is a reliable test for photoactivity.

The studies described above all used pigmentary grade titanium dioxide. Tooley [141] studied the photooxidation of liquid isopropanol as a simple test to differentiate between coated *ultrafine* TiO_2. Particular emphasis was placed on the degree of dispersion of the titanium dioxide. A model was proposed that accounted for the differences in photoactivity when there were changes in the amount of titanium dioxide particles absorbing a particular number of photons. With regard to the photooxidation mechanism the results of the study broadly agreed with the studies discussed above. Similar to the Egerton and King study, the rate of oxidation was found to be proportional to $I^{1/2}$. For the P25 titanium dioxide (also used in our present study) and zinc oxide samples the result of varying the mole fraction of isopropanol is similar to the Cundall *et al* study (above). However, in contrast to this there was a steady increase in the rate of reaction as the mole fraction of isopropanol was

increased for photocatalysis using the ultrafine rutile sample (analogous to the Sample A used in the present study).

By comparison of the relative rates of isopropanol oxidation the author concluded that this was a reliable test for the photoactivity of coated ultrafine rutile titanium dioxide. A similar test was therefore used in the present study to determine the photoactivity of coated/treated ultrafine rutile and P25 titanium dioxide.

1.8.1.2. 2-nitrophenol degradation (NP).

Nitrophenols are commonly found in aquatic waste streams as a result of the production of herbicides, pesticides and synthetic dyes [142] and in particular, nitrophenol isomers are a major contaminant in aqueous effluent from the large-scale production of aniline by reduction of nitrobenzene [143]. They are classified among the priority toxic pollutants by the US Environmental Protection Agency (EPA) [144] and as such, a large amount of work has focused on the degradation of these species [145-148]. Among this research, the photocatalytic degradation of nitrophenol isomers using titanium dioxide has received much attention due to the ability to reduce pollutant concentration to the parts per billion (PPB) range, and that in theory sunlight may be used to activate the reaction. This research has even reached the pilot plant stage of development.

The aqueous phase kinetics of 2-nitrophenol photocatalytic degradation been studied extensively [145-147]. It is now widely accepted that the degradation requires UV, oxygen, and titanium dioxide - although a small amount of photolysis can occur with just UV. First order kinetics are followed, and the pseudo rate constant decreases with increased initial concentration. This has been attributed to Langmuir-Hinshelwood kinetics [149-150]. However, in the present study it is suggested that this is better explained as a consequence of increased absorption of UV by the nitrophenol [151]. While the reaction is thought to proceed mainly by a hydroxyl mediated process, the precise reaction mechanism is not fully understood.

Tanaka, Luesaiwong and Hisanaga [152] studied the photocatalysed degradation of several nitrophenol isomers (including 2-nitrophenol) using Fujititan Co TP-2. For 2-nitrophenol degradation, 2-nitrohydroquinone and catechol, in a ratio of approximately 5:1, were the only aromatic intermediates detected. The authors

suggested that these intermediates were formed by hydroxylation of the ring by hydroxyl radicals, and by implication that addition at the 4- position was predominant. Further hydroxylation of the ring yielded a complex mixture of organic acids, which where themselves oxidised to formic and acetic acids and thence to CO_2. NO_3^- was the major nitro mineralisation product followed by NO_2^-, and NH_4^+, although the ratio of NH_4^+: NO_3^- was greater than for 4-nitrophenol due to the preferred hydroxyl addition at the 4- position. Since NH_4^+ is unlikely to be formed from reduction of NO_3^-, and by consideration that the nitro group is not substituted until relatively late in the reaction, the authors suggested that NH_4^+ was formed from the reduction of nitrated aliphatics.

Pelizzetti *et al* [153] studied the photocatalysed degradation of several mononitrophenol isomers (including 2-nitrophenol), and monoaminophenols using Degussa P25 in acidic solution. For nitrophenols they found the relative quantities of evolved inorganic nitrogen to be independent of the isomer. They considered the initial oxidative substitution of the nitro group to give rise to NO_2^-, which was then oxidised in solution to NO_3^+. In contrast to Tanaka *et al* (above) they hypothesised a parallel reductive degradation route in which the nitro group was reduced *before* ring opening - this species giving rise to the observed NH_4^+ via the corresponding aminophenol. The hypothesised oxidation mechanism is as follows:

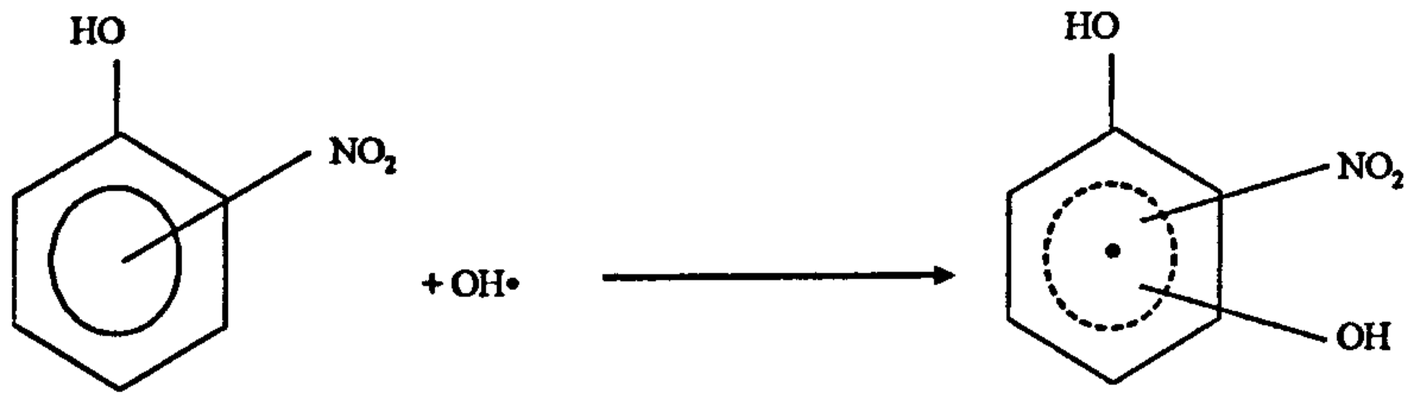

[1.35]

The hydroxyl group can eliminate a hydrogen atom at the 4- ring position to give nitrohydroquinone, equation [1.36], or the 2- ring position to give catechol, equation [1.37]:

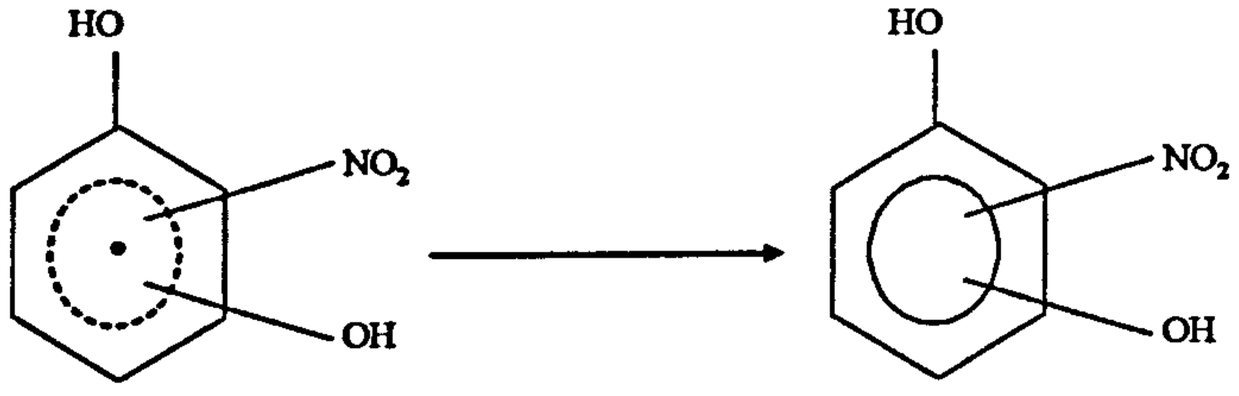

[1.36]

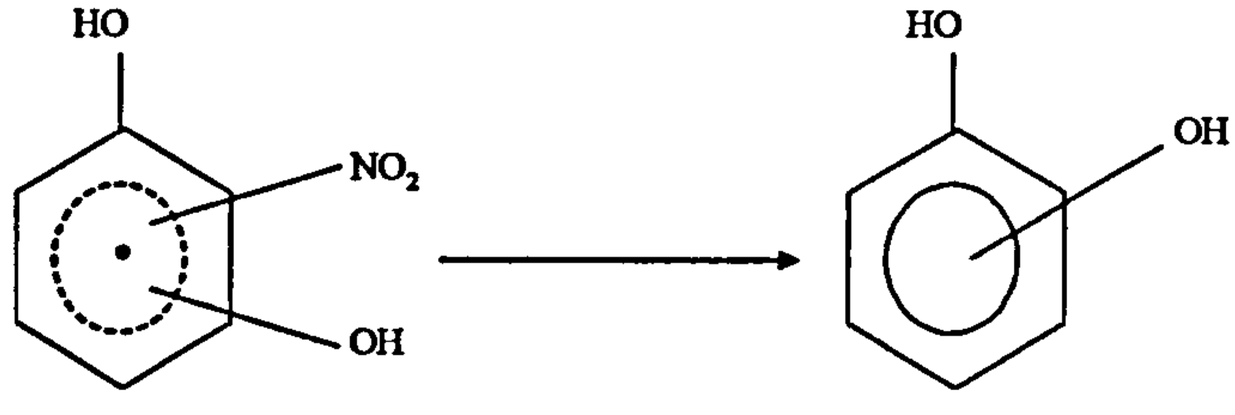

[1.37]

The nitrohydroquinone and catechol can then be further oxidised leading to ring opening and eventually CO_2, NO_2^- and NO_3^-.

In parallel with this oxidation mechanism, the following reductive mechanism was proposed, whereby aminophenol is formed, equation [1.38]:

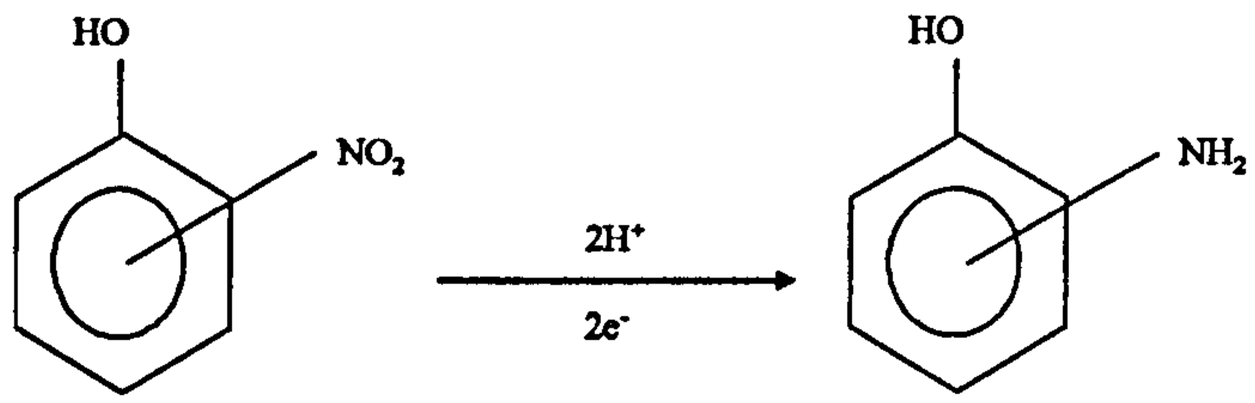

[1.38]

The ring can then be oxidised by hydroxyl radicals:

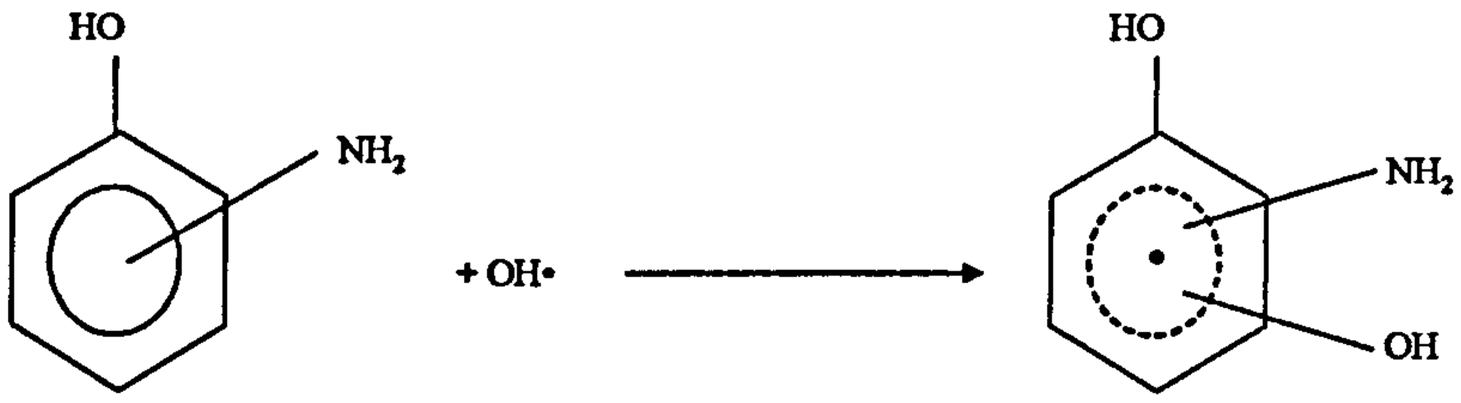

[1.39]

The hydroxyl group can eliminate a hydrogen atom at the 4- ring position to give aminohydroquinone, equation [1.40], or a tautomeric quinonoid compound [1.41]:

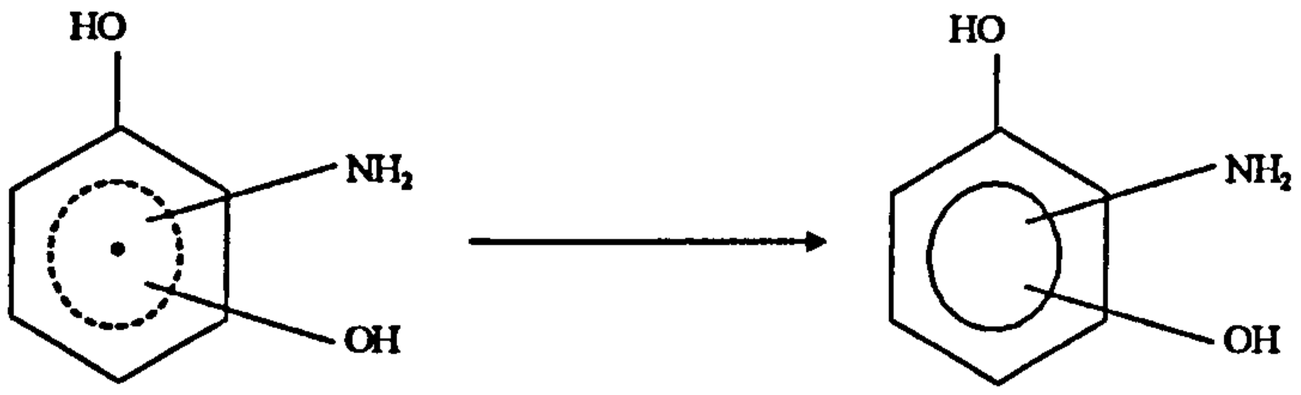

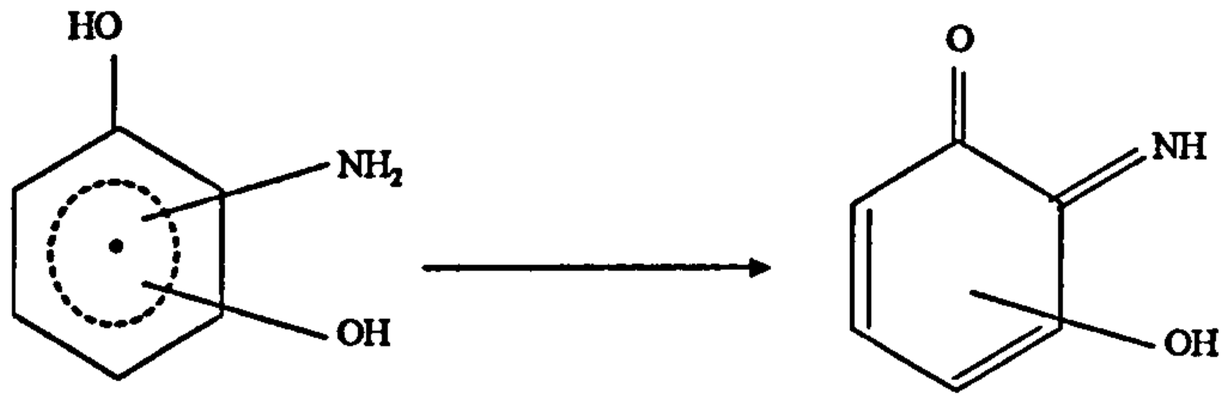

[1.40]

[1.41]

quinonoid, which can be reduced back by electrons:

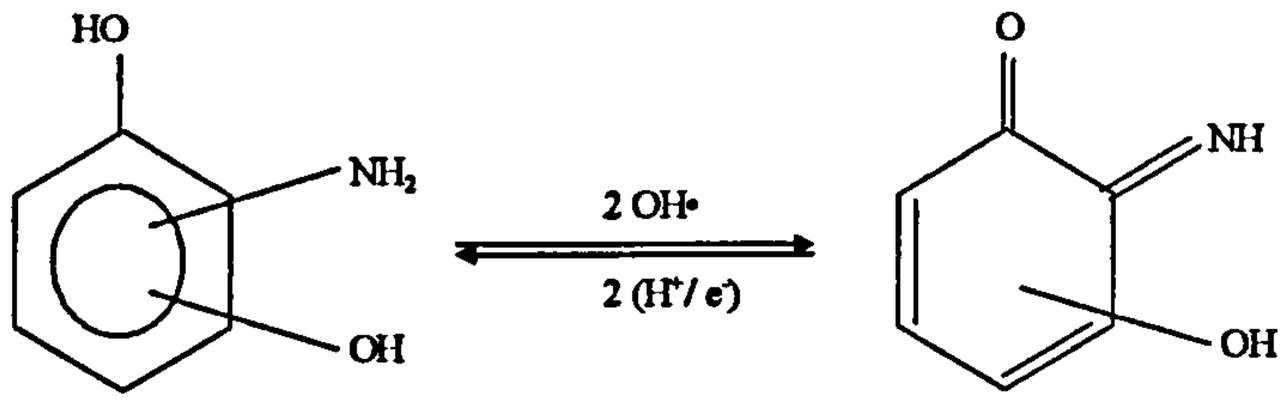

[1.42]

The aminohydroquinone formed by equation [1.40] can be further oxidised leading to ring opening to give aliphatic amino compounds, and finally CO_2 and NH_4^+. The quinonoid can be hydrolysed to give the same products.

In parallel with the above aminophenol ring oxidation mechanism of equations [1.39] to [1.42], the aminophenol formed in reaction [1.38] can undergo oxidation of the amino group:

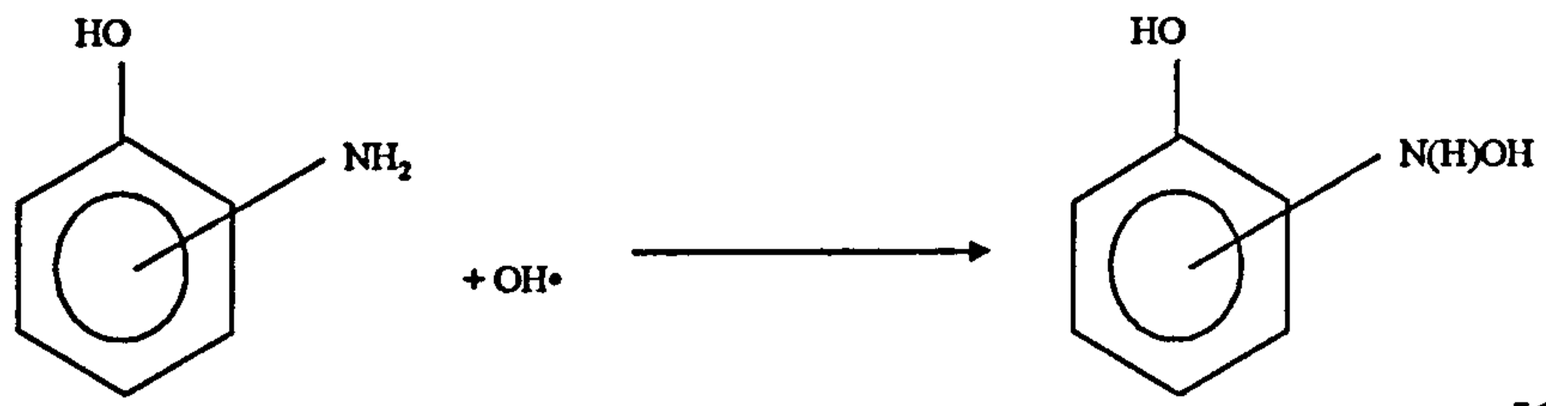

[1.43]

This compound can then undergo further oxidation reactions to give the CO_2, NO_2^- and NO_3^- mineralisation products.

Paola *et al* [154] studied the photocatalysed degradation of 2-nitrophenol, 3-nitrophenol and 4-nitrophenol using Degussa P25 in unbuffered solution. Similar to the studies above the main intermediates for 2-nitrophenol were found to be 2-nitrocatechol (named 3-nitrocatechol) and 2-nitrohydroquinone. The authors

suggested that these intermediates were formed when the initially formed unstable oxidation intermediates, the dihydroxynitrocyclohexadienyl radicals (see equation [1.35] above), disproportionate:

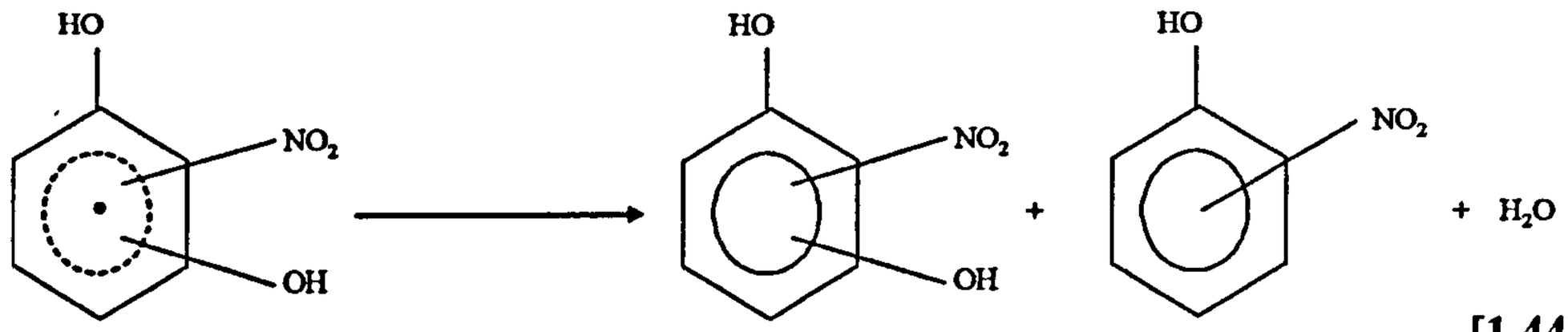

[1.44]

2-nitrocatechol could also be formed by the trapping of the cyclohexadienyl radical by oxygen to form $HO_2^{\bullet}$:

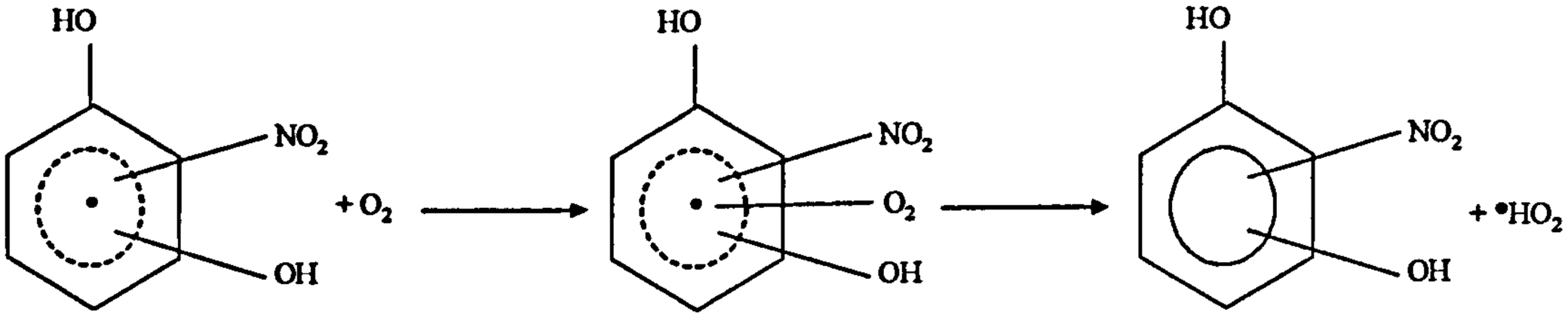

[1.45]

The authors considered that for 4-nitrophenol the nitro group could be eliminated to form the detected hydroquinone either through a $HOC_6H_4O^{\bullet}$ or the $HOC_6H_4(O)(NO_2)^{\bullet}$ radical. Analogous intermediates are suggested for 2-nitrophenol (and 3-nirophenol) but were not investigated. Significantly, the authors suggest that the reaction between the hydroxyl radicals and nitrophenol mainly occurs in solution, most probably close to the surface. They state that adsorption of nitrophenol would alter the electronic charge and hence the expected intermediates would be different from those found. Indeed, the intermediates found are the same as those found by Alif and Boule [155] from the homogeneous solution phase phototransformation of nitrophenols using excited nitrite and nitrate ions.

1.8.1.3. Salicylic acid degradation (SA).

Tunesi and Anderson [65] studied the photocatalytic degradation mechanism of salicylic acid (and also that of benzoic acid, phenol and chlorophenol) using suspended titanium dioxide membranes, and the role that chemisorption plays in determining the reaction pathway. Two possible initial steps were hypothesised:

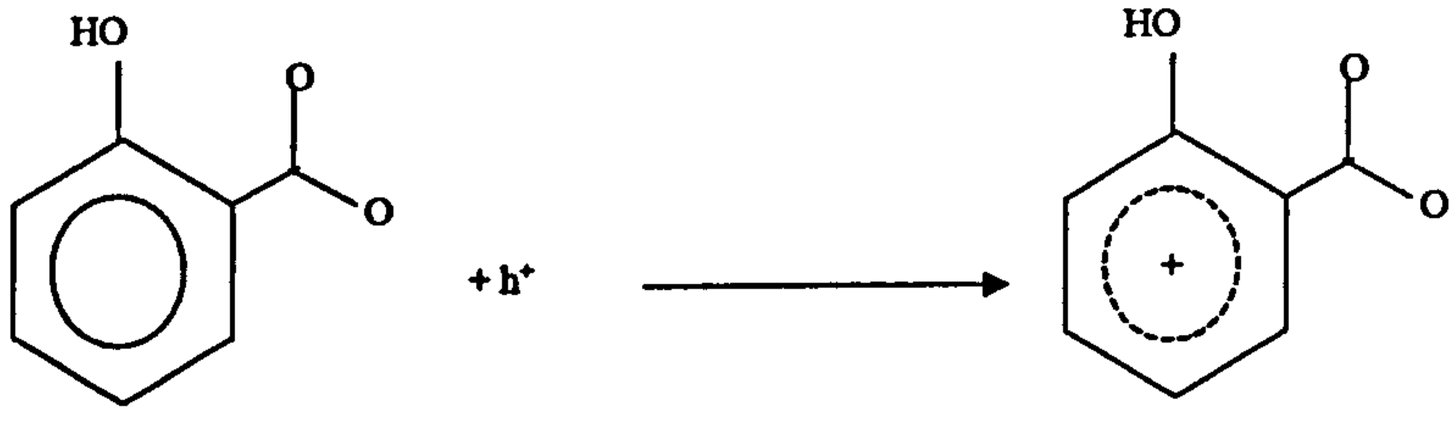

[1.46]

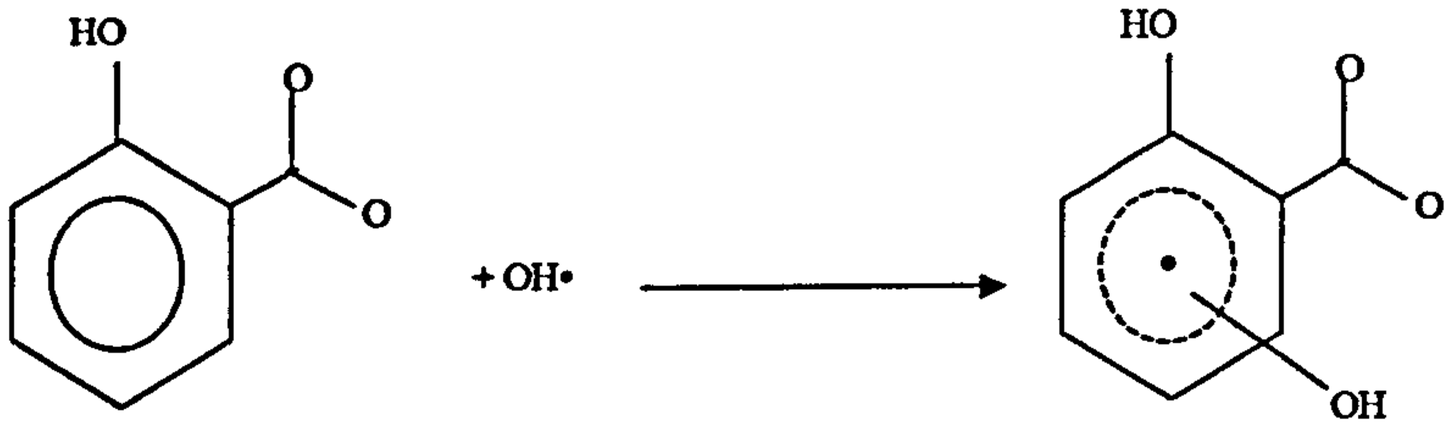

[1.47]

With regard to salicylic acid, they studied the effect of pH at two initial concentrations on the adsorptive properties and the rate of photocatalysed degradation with and without methanol. They found that adsorption is favoured at low pH (~4) and that the Freundlich isotherm best fitted the adsorption data indicating a continuous distribution of adsorption sites. They postulated that the salicylic acid adsorbs preferentially at sites of high Lewis acidity to form a chelate structure with the titanium atom at the centre of the surface bond, similar to surface complexes observed by Tejedor-Tejedor *et al* [156] for salicylate adsorbed on geothite (Figure 1.xii).

At the lower salicylic acid concentration (40μM) the rate of degradation increased at lower pH values, while for the high concentration (80μM) the rate of degradation increased at high pH values (~9). The addition of methanol to scavenge hydroxyl radicals at high pH lowered the rate of salicylic acid degradation, whilst at low pH (~4) there was little change.

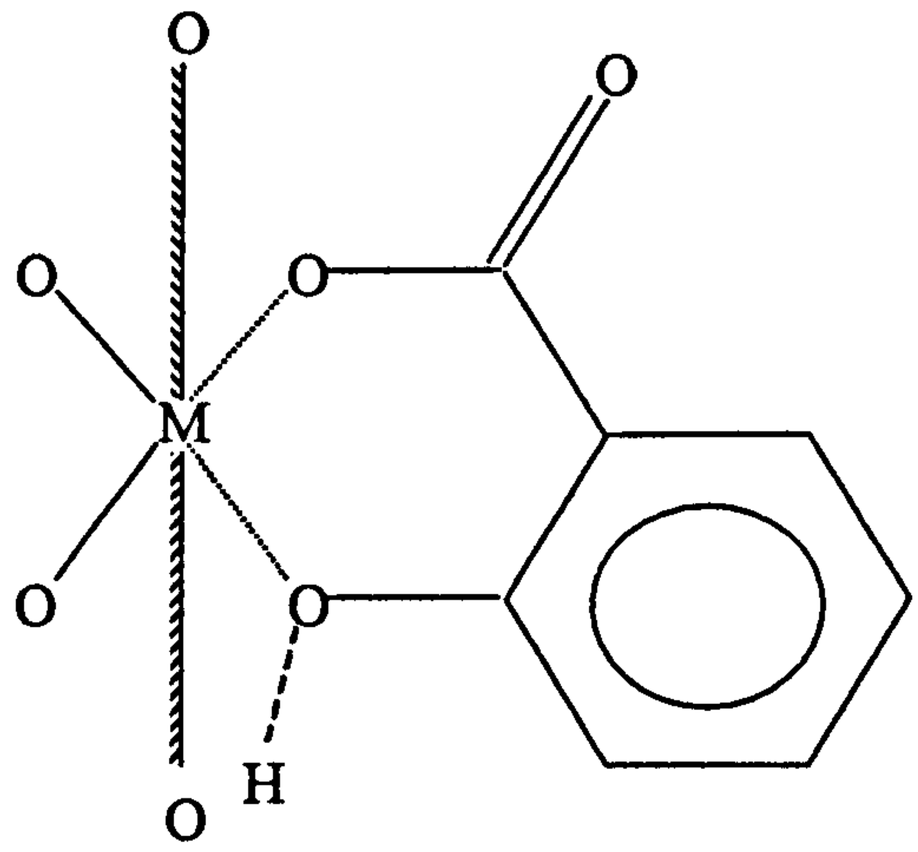

Fig 1.xii. Proposed surface complex between salicylic acid and titanium dioxide.

On the basis of these experimental results and by consideration of a mechanistic review, they concluded that at low pH (4) the degradation was primarily by direct hole oxidation (equation [1.46]), and primarily by hydroxyl mediated degradation at high pH (equation [1.47]). At low pH, the titanium hydroxide bond is positively charged and therefore good salicylate adsorption occurs through the strongly electron donating oxygen atoms of the phenol and carboxylic substituents. This bond would likely have a high covalent character with interaction between the salicylate and the O(2p) valence band orbitals, and thus the salicylate could be oxidised directly by holes formed in this band.

Increasing the pH reduces adsorption and electrostatic repulsion thus reduces electron transfer as distance increases. Hydroxyl radicals diffusing through the double layer, favouring conditions of high salicylic acid concentration, would therefore degrade the salicylic acid. A theoretical study by Turchi and Ollis [157] concluded that for a generic titanium dioxide photocatalytic reaction, hydroxyl radicals may diffuse ($\sim 10^{-6}$ m) from the particle surface.

Vione, Picatonotto, and Carlotti [158] studied the effect of adding 1,3-butanediol and benzoic acid on the rate of photocatalytic degradation of phenol and salicylic acid using uncoated TiO_2 and alumina coated TiO_2. They found that the addition of the alcohol significantly reduced the rate of phenol degradation, but that

even in excess had practically no effect on the rate of salicylic acid degradation. Conversely, the addition of benzoic acid inhibited the salicylic acid degradation, with only a limited inhibition of the phenol degradation rate. The authors concluded that phenol, in a similar manner to alcohols, undergoes degradation mainly by hydroxyl radicals, but that salicylic acid is oxidised directly by surface holes as described by Tunesi and Anderson. Benzoic acid was degraded mainly by direct holes in a similar manner to salicylic acid, but not to the same extent, with a lesser degradation by a hydroxyl mediated mechanism.

In a later paper [159], the same authors used salicylic acid and phenol degradation to test the photoactivity of several coated, and one uncoated, rutile titanium dioxide pigments. They compared the photoactivity of the different pigments for phenol degradation and noted that coatings significantly reduced the reaction rate, but that for salicylic acid degradation the coatings did not reduce the rate. This was attributed to the different degradation mechanisms of the two organics; predominately hydroxyl mediated for phenol and direct hole oxidation for salicylic acid. The poor ability of the coatings to inhibit the degradation of salicylic acid was most likely caused by the use of a single model molecule to test the photoactivity of pigments during development. They concluded that ideally the effectiveness of coatings to reduce the photoactivity of TiO_2 pigments should be tested by a model molecule that degrades by a hydroxyl mechanism such as phenol or an alcohol, and by a molecule that is degraded by an electron transfer mechanism such as salicylic acid.

1.8.2. Surface area determination by gravimetric adsorption.

During development of both pigmentary and fine particle [95] solids, one of the most common and simplest ways of characterisation is surface area determination. This is principally by adsorption of a gas or vapour (the *adsorptive*, or *adsorbate* when attached to the solid *adsorbent*) by either volumetric methods or gravimetry. In the former, the flow rate of gas entering and exiting the system is monitored and the rate of gas uptake onto the sample is the difference between the two. When integrated this gives the fractional coverage at any stage. In the latter, the sample is suspended from a spring balance in an enclosed system and exposed to a gas or vapour at a given pressure. As adsorption occurs, the vapour pressure drops and the mass of the sample increases. The amount of gas adsorbed at a given pressure can thus be determined by

the increase in mass. Adsorption occurs by either physical or chemical forces acting between the solid and vapour molecules – termed *physisorption* or *chemisorption* respectively.

1.8.2.1 Physisorption – physical adsorption.

Physisorption is brought about by either attractive van der Waals or London dispersive forces acting between the adsorbate and the solid adsorbent, and is analogous to the forces that bring about condensation. Van der Waals forces arise from induced dipole-dipole interactions, while dispersive forces arise from rapid fluctuation of electron density within an adsorbent molecule inducing an electrical moment in a near neighbour. Short-range repulsive forces also arise from the interpenetrating electron clouds of the two atoms. These have been modelled by London [160] and later workers using quantum mechanical perturbation theory [161].

The enthalpy of physisorption is weak and usually in the range of –20 to -40 kJ mol^{-1}, and may be measured by determined by calorimetrically measuring the increase in temperature of a sample of known heat capacity. This energy is not sufficiently high so as to lead to bond breaking and thus a physisorbed molecule retains its original identity but may be distorted by the surface [47]. Note that the adsorption is always exothermic due to the decrease in entropy from the adsorbate (ΔS is negative), and thus ΔH must be negative if the process is to proceed spontaneously (ΔG negative) according to standard thermodynamics, equation [1.48]. Since ΔS is negative also means that adsorption is favoured at low temperatures (thus minimising the positive $T\Delta S$ term).

$$\Delta G = \Delta H - T\Delta S \qquad [1.48]$$

1.8.2.2 Chemisorption – chemical adsorption.

In chemisorption the adsorptive forms a chemical bond (usually covalent) to the adsorbent. This type of adsorption is more surface specific than physical adsorption and molecules tent to adsorb to sites that maximise their coordination number to the adsorbent, and the demand of unsatisfied vacancies can lead to a molecule being torn apart into two or more fragments on the surface. The enthalpy of chemisorption is much greater than physisorption, with typical values of the magnitude of -200 kJ mol^{-1} comparable to bulk chemical reactions. With the

exception of special cases chemisorption must be exothermic since the adsorbate loses translational energy upon adsorption and thus ΔS is negative as in physisorption. One exception is the endothermic adsorption of H_2 onto glass. The molecule dissociates into two H atoms and the translational movement (and hence the entropy) is greater than gaseous hydrogen.

In the past, the principal test of differentiating between physisorption and chemisorption was the enthalpy of adsorption. Values less negative than -25 kJ mol^{-1} were taken to imply physisorption, while values more negative than -40 kJ mol^{-1} implied chemisorption. More recently, spectroscopic methods are used to identify surface species and thus identify whether physisorption or chemisorption has taken place.

1.8.2.3 Characterisation of adsorption isotherms.

During adsorption the adsorbate is in dynamic equilibrium with the adsorptive - that is molecules from the gas phase adsorb and then desorb after a period of time. The fractional coverage of the surface (θ) is thus dependant on the pressure of the adsorptive gas. The dependence of θ on the pressure at a fixed temperature is fixed temperature is called an *adsorption isotherm*. Alternatively, the adsorption data can be expressed as the variation of θ with temperature at a fixed pressure (*adsorption isobar*), or the variation of temperature with adsorptive pressure at a fixed fractional coverage (*adsorption isothere)*.

1.8.2.3.1 Langmuir Isotherm.

Type I isotherms, where adsorption rises rapidly at low relative adsorptive pressures, and levels out gradually as monolayer coverage is reached (typically at partial pressures of approximately 0.5), are analysed by Langmuir linearisation. The Langmuir model has three simplifying assumptions [162]:

1) The surface is considered to be energetically uniform, and that all adsorption sites are equivalent.
2) Adsorption is limited to monolayer coverage.
3) Adsorbed molecules do not interact with each other, i.e. the adsorption is independent of surface coverage.

The Langmuir equation is given by:

$$\frac{P}{n} = \frac{P}{n_m} + \frac{1}{K.n_m} \qquad [1.49]$$

Where P = The Pressure of the adsorbate.

n = The equilibrium amount of adsorbate adsorbed per unit mass of adsorbent at pressure P ($mmol.g^{-1}$)

n_m = The amount of adsorbate required for complete monolayer coverage of the adsorbent ($mmol.g^{-1}$)

K = The coefficient of adsorption, dependant on temperature and specific to each adsorbate/adsorbent system.

Thus, a plot of P/n against P is a linear plot (of the type y = mx +c), with a gradient of $1/n_m$ and intercept $1/Kn_m$. The molecular dimensions of nitrogen are taken to be 0.162 nm^2 assuming that molecules are hexagonally close packed spheres. Thus, with the information from equation 1.49, the specific surface area can be determined from Equation 1.50:

$$S = n_m.A_m.L \qquad [1.50]$$

Where S = The specific surface area ($m^2.g^{-1}$)

A_m = The average area occupied by one molecule of the adsorbate at monolayer coverage (m^2).

L = Avogadro's constant, 6.0221367×10^{23} (mol^{-1})

n_m = The amount of adsorbate required for complete monolayer coverage of the adsorbent ($mol.g^{-1}$)

While the Langmuir isotherm remains useful for determining surface areas for Type I isotherms, the inherent basic assumptions result in limitations in the application of the relationship. There have been reported variations in the calculated values of n_m for low and high pressure ranges – probably arising from the approximation that all sites are energetically uniform. In practice high energetic sites are filled first, and at higher pressures those with lower energy will be filled.

1.8.2.3.2 Brunauer-Emmett-Teller (BET) Isotherm.

The BET is an extension of the Langmuir model accounting for multiplayer formation in the adsorption process [163]. The model uses the assumptions of the Langmuir model, primarily the postulate that the rate of adsorption is equal to the rate of desorption. The initial monolayer formed from the Langmuir equation is assumed to act as a substrate for further absorption, with the energy of adsorption equal to that of liquefaction. Specifically, the assumptions of the BET model are:

1) The adsorbent is a regular array of energetically equal sites, with a constant enthalpy of adsorption, ΔH_A.
2) Adsorption is localised to these sites.
3) There are no interactions between adsorbed molecules.
4) Multiplayer formation proceeds to an infinite level.
5) The enthalpy of adsorption for the second layer and subsequent multiplayer is constant, and equal to the enthalpy of liquefaction, ΔH_L.
6) Adsorption and desorption can only occur on or from exposed sites.

The BET model is given by Equation 1.51 and is often used for Type II and Type IV isotherms.

$$\frac{P}{n\,(P^O - P)} = \frac{1}{n_m.C} + \frac{(C-1)}{n_m.C} \cdot \frac{P}{P^O} \qquad [1.51]$$

Where: P = Pressure of the adsorbate (Pa).

P^O = Saturation vapour pressure of the adsorbate (Pa) at the reaction temperature.

n = the uptake of adsorbate at a pressure, P ($mol.g^{-1}$)

n_m = The amount of adsorbate required for complete monolayer coverage of the adsorbent ($mol.g^{-1}$)

C = Constant dimensionless quantity, related to the adsorption energy of the first layer. Given by equation 1.52.

$$C = \exp\left[\frac{\Delta H_A - \Delta H_L}{RT}\right] \qquad [1.52]$$

Where: ΔH_A = The enthalpy of adsorption for the first layer ($J.mol^{-1}$)

ΔH_L = The enthalpy of adsorption for the second and subsequent layers ($J.mol^{-1}$).

Thus a plot of $P / n(p^O-p)$ against p / p° is linear with a gradient of $(C-1)/(n_mC)$ and an intercept of $1/(n_mC)$. The monolayer capacity (n_m) and C can thus be determined. The surface area can then be calculated using equation 1.50 as for the Langmuir model. Due to the assumptions upon which it is base, the BET model is only considered to be effective over the pressure range $P/P^O = 0.05 - 0.35$ [163]. Below this range the model fails due to the adsorbent surface energetic heterogeneity, above this range due to adsorbate-adsorbate interactions. A comprehensive description of BET theory is given by Gregg and Singh [163].

1.8.3. Infrared spectroscopy.

Infrared (IR) spectroscopy is a useful tool for the characterisation of coated powders. Through identification of the appropriate bonds and by determination of their character, it is possible to study the interaction of the coating with the particle surface, and the interaction of neighbouring molecules in the coating e.g. chain ordering [164-166]. Although in practice this can be difficult depending on the coating/particle system at hand, it potentially allows the practitioner to visualise the coated surface and infer a significant amount of information.

Infrared spectra arise from molecular vibrations within the molecule when it is subjected to radiation of an appropriate energy to induce these transitions; typically the energy is expressed as wavenumbers (cm^{-1}). Radiation is extracted from an IR beam and absorption bands appear at the appropriate frequencies for the vibrational transitions [167]. For gas phase molecules, fine structure from simultaneous rotational excitation of the molecule is often observed whereas in liquid spectra the rotational transitions are often lost due to collisions between molecules [47].

The IR induced vibrations can be separated into three categories; bond stretching, bond bending, and torsional motions [90]. The type of vibration, the masses of the atoms concerned, and the strength of the bond between them (given by the force constant), determines the vibrational frequencies. It is theoretically possible to calculate the frequencies when these quantities are known, though in practice this is difficult for complex systems.

For vibrations to be infrared active, the transition must change the electric dipole moment [47], and molecules where this is not the case are generally infrared inactive. Examples include homonuclear diatoms such as nitrogen (N_2), where the dipole remains zero regardless of the distance between the two atoms.

1.8.3.1. Application to adsorbed species.

Infrared spectroscopy may be used to study both chemically and physically adsorbed molecules on surfaces [168,169]. In the former case, it is the loss of rotational freedom, and a change in symmetry that is observed. Strong surface force fields may also render changes in frequency, and 'activate' previously inactive transitions, for example nitrogen adsorbed on titanium dioxide, zinc oxide and zeolites can be IR active [102]. In the latter case of chemical adsorption, the formation of new chemical species can be characterised by IR spectroscopy. Also, the disappearance of surface species upon coating may give valuable information on bonding modes. Several IR techniques are commonly used to study adsorbed species, some of which are described below.

Transmittance IR spectroscopy is perhaps the simplest; the sample, as a thin disc or film is placed directly in the IR beam and the spectra measured. This method does however suffer from two disadvantages; firstly the strong adsorption and scattering of IR by the solid [170]. To minimise this, high area finely divided particles are used to increase the concentration of the adsorbate and decrease scattering by the particles by reducing the size below the wavelength of the IR radiation. Secondly, the samples need to be pressed or deposited as a thin film, which may change the physical properties. Despite these disadvantages, quality consistent results have been obtained by this method and its popularity remains high.

Diffuse Reflectance Infrared spectroscopy (DRIFTS) has several advantages over transmission IR. Loose unpressed powders can be used, reducing the physical stress exerted on the sample, and as the method requires scattering samples, the spectra do not show energy loss at high wavenumbers associated with transmission spectra. This technique works by directing the IR through the sample using a special DRIFTS accessory. The specular reflectance (directly reflected radiation) from the interaction of the beam with the sample is separated from the useful detected diffuse reflectance (which passes through the sample) by a beam splitter. The main disadvantages are that the diffuse reflectance approaches zero where the absorbivity of the sample is high, and the lack of reproducible quantification caused by different loadings of sample between each experiment. Therefore, difference spectra are difficult to measure accurately and DRIFTS spectra are often referenced to a non-adsorbing powdered background sample, usually KBr, and presented in Kubelka-Munk format [40]. The sample spectrum can be obtained in a pure powder form or diluted with a mixture of KBr. The Kubelka-Munk format is given by equation 1.53.

$$KM = (1-R)^2 / (2R) \qquad [1.53]$$

Where: R = The reflectance spectrum, given by R = S/B

S = The sample spectrum.

B = The background spectrum.

A potential problem arises if R is greater than 1, occurring if the sample spectrum has a higher reflectance in parts of the spectrum than the reference (KBr) spectrum.

1.8.3.2. Fourier Transform Infrared Spectroscopy (FTIR).

FTIR is now almost universally used in spectrometers as it has greater sensitivity and signal to noise ratio than traditional dispersive spectrometers. At the centre of the technique is the Michelson interferometer, for separating a composite signal into individual frequencies. The beam from a sample is split into two and a pathlength difference introduced between them. When the two signals recombine there is a phase difference between them, and depending on the extra pathlength that one beam has taken, they interfere either constructively or destructively, and as the

pathlength is altered, the detected signal oscillates as the two components interfere. The interferometer coverts the presence of a particular component into an intensity variation which is then detected by the spectrometer. The total intensity detected is a sum of all the oscillating intensities of a large number of wavenumbers. Using a Fourier transform step, the intensity signal is converted to an absorbance spectrum. The advantages of this technique, as opposed to dispersive instruments mostly arise from the detection of all the radiation.

1.8.4. X-Ray Diffraction (XRD).

X-Ray diffraction is a valuable tool for examining the crystal structure of particles. However, it is of limited use for examining coatings, as even for potentially suitable inorganic materials e.g. silica, alumina or ferrous oxides, these are typically amorphous. The XRD pattern for anatase and rutile polymorphs of titanium dioxide are easily distinguishable and this technique is used in the current study to examine the crystal composition of samples. Briefly, this technique works as follows:

Atoms in a crystalline structure can be considered to be a reflective plane for x-rays. A crystal has several atomic planes and so an incident X-Ray beam is reflected in several directions, and by analysis of the angular direction and relative intensities of the reflected beams, the position of all the atoms in the unit cell may be determined. By comparison with a library of positions and relative intensities the sample can be identified. The Bragg equation (1.54) is the fundamental relationship of crystal structure determination [171]:

$$\lambda = 2d \sin\theta \qquad [1.54]$$

Where: d = The distance between atoms.

θ = The angle of reflection.

The crystal size can be determined from XRD peaks by use of the Debye-Sherrer equation:

$$B = (k.\lambda)/(L.\cos\theta) \qquad [1.55]$$

Where: B = The line broadening at half the maximum intensity.

L = The diameter of crystal particles.

λ = The wavelength of the incident X-Ray source.

θ = The position of the peak maximum.

k = A constant dependant on crystalline shape (usually taken as 0.9)

1.8.5. Electron Paramagnetic Resonance (EPR).

EPR and Electron Spin Resonance are fundamentally the same technique, with the difference being largely in the nomenclature. 'EPR' is label used to denote the technique when dealing with paramagnetic metals, and 'ESR' when dealing with organic radicals. ESR/EPR spectroscopy has two major applications in the field of titanium dioxide characterisation. Firstly, for the detection of photocatalytic reaction intermediates in-situ; several ESR studies have probed this aspect, occasionally by use of spin traps such as DMPO, [70] with considerable success.

The second application is in the specific area of doped titanium dioxide where EPR can both detect and give important information on paramagnetic species for example, Fe^{3+}, Cr^{3+} and V^{5+} [172,173]. Undoped, pure, titanium dioxide is infrared inactive as it does not possess unpaired electrons, although the reduced form, Ti^{3+} surface sites have characteristic signals [70].

For the specific case of Fe^{3+}, dopants on the surface possess different symmetry to dopants located substitutionally within the titanium dioxide lattice and thus show different spectra. These systems have been thoroughly investigated, both theoretically and experimentally, and thus bands can be unambiguously assigned to one of the two species, and the dopant position within the lattice determined [172].

1.8.6. Electron Microscopy.

Arguably the most useful method for assessing the coating quality on particles, Electron Microscopy allows the particle and coating to be effectively visualised [95]. Transmission Electron Microscopy (TEM) can be used to detect changes in the uniformity and texture of a coating and identify the formation of bulk precipitates if the coating has been unsuccessful. Electron microscopy suffers from two major disadvantages. Primarily, the technique has statistically poor reproducibility as relatively few particles are examined e.g. one gram of pigmentary titanium dioxide particles contains approximately 10^{14} crystals, and it is improbable that more than a few hundred are examined. This problem is even more acute for nanosized crystals.

Secondly, transmission microscopy measures thought he particles and averages thicknesses, which may vary over the depth dimension. Despite these considerable limitations, this technique remains a primary method for assessing coating quality.

1.8.7. Electrophoresis and Point of Zero Charge (PZC) measurements.

The point of zero charge of titanium dioxide can be used to determine if a coating has been formed. The point of zero charge, the pH at which the charge on the particle is neutral, for uncoated titanium dioxide is typically ~ 6. At a solution pH below this value, the surface is positively charged as it attracts protons from the medium, while at pH values above this value the surface is negatively charged. The application of a coating, such as silica, on titanium dioxide reduces the pzc and thus determination of the PZC can be used to infer a successful coating. Adsorbed anions, such as phosphate, have also been shown [174] to dramatically reduce the pzc, in this case to ~ 2.

1.8.8. X-Ray Photoelectron Spectroscopy (XPS).

X-Ray Photoelectron Spectroscopy (XPS), also termed ESCA measures the energy of electrons ejected from a solid by bombardment with incident X-Ray photons. The energy of the ejected electron is characteristic of the element from which it is ejected [47]. As the electrons that penetrate into the bulk material cannot escape to be detected, this technique at first appears ideally suited to the study of coated materials, with surface sensitivity typically two orders of magnitude higher than bulk. However, XPS at typical coating levels this technique cannot usually differentiate between an even coating that encapsulates a particle and one that is twice as thick but covers only half the surface. It nevertheless is a useful technique for monitoring bulk changes, and also finds use for examining the oxidation states of doped metals [74].

1.9. Research background and objectives.

The aims of the present study were to investigate the effect of modification of titanium dioxide nanoparticles on the photoactivity, and to this end:

1) To investigate the effect of doping with iron on the photoactivity. Particularly, the effect of location i.e. whether the Fe is substituted within the titanium dioxide crystal or is on the surface.

2) To investigate the effect of different coatings on the photoactivity. Specifically coatings of: a) hydrophobic silane, b) a phosphate ester (Arlatone Map 160K), and c) a hydrophilic phosphate coating.
3) To develop an aqueous phase photoactivity test for these samples and to compare this test with the existing photoactivity test – 2-propanol oxidation.
4) To use these photoactivity tests to investigate the effect of low coating levels in order to test whether activity is associated with specific sites on the TiO2

The present study examines two nanosized titanium dioxide samples; Firstly, Sample A, a pure rutile, prepared by aqueous hydrolysis of titanium tetrachloride following a method used by Uniqema. Relatively little work has been done on high area rutile samples. Much more work has been done on Degussa P25, a commercially available photocatalytic material mainly composed of anatase, and commonly used as a standard [45]. – because the aim in such studies has been to maximize photocatalytic activity. Although the aim in the current study has been to minimise photoactivity, the comparison with Degussa P25 provide a useful link to the main body of literature. The first type of titanium dioxide is similar to that used in the sunscreen industry and thus the results may be industrially important. Studying these two materials also enables a direct comparison of the effects of coating and doping on rutile and a mainly anatase material.

Also, it has been shown by other authors [76,77,175] that Sample A has 'active sites' i.e. that certain areas of the surface are responsible for the majority of the photoactivity and that these sites are selectively coated by the dense silica method. It is useful to examine if the coating materials used in the present study have similar effects. Several authors have speculated that Degussa P25 has 'active sites', most probably at anatase/rutile interfaces, and it is useful to examine whether coatings will selectively deposit on these sites in an analogous manner to Sample A.

1.10. References.

1. G. Kaempf; W. Papenroth; R. Holm; A. G. Bayer, *J. Paint. Tech.* **1974**, *46*, 56.
2. T. I. Browbridge; J. R. Brand, *Surface coatings Australia*: Magazine, Sept **1990**.
3. J. Braford; G. E. Maud; M. L. Demosthenous, (To Tioxide Group Services LTD): EU Patent number EP0753546A2 (**1996**).
4. A. Guez; C. Steiner, (To Millennium Inorganic Chemicals): US patent number 6200375B1 (**1999**).
5. B. G. Park; S. J. Knowland; B. R. Flutter, (To Oxonica LTD): Int Patent number WO2004058209 (**2004**).
6. M. A. Claridge; P. L. Cowe, (To ICI Group LTD): UK Patent number 1336292 (**1970**).
7. W. F. Sullivan, *Prog. Org. Coatings*, **1972**, *1*, 157.
8. I. K, Konstantinou; T. A. Albani, *Appl Catal*, **2003**, *43*, 319.
9. J. M. Hermann; C. Guillard; P. Pichat, *Catal. Today*, **1993**, *17*, 7.
10. R. Wang; K. Hashimoto; A. Fujishima; M. Chikuni; E. Kojima; A. Kitamura; M. Shimohigoshi; T. Watanabe, *Nature*, **1997**, *388*, 431.
11. E. Kojima; M. Chikuni; A, Fujishima; M. Hayakawa; K. Hashimoto; A. Kitamura; M. Machida; K. Norimoto; T. Watanabe, (To Toto LTD): EU patent number EP0869156, (**1998**).
12. O. Carp; C. L. Huisman; A. Reller, *Prog. Sol. State. Chem.* **2004**, *32*, 33.
13. F. A. Cotton; G. Wilkenson, Advanced Inorganic Chemistry, 5th Edition, Wily-Interscience, Chichester, (**1988**).
14. T. A. Egerton, Titanium Compounds, Kirk-Othmer Encyclopaedia of Chemical Technology, 4th Ed, John Wiley and Sons, (**1977**).
15. F. A. Grant, *Rev. Mod. Phys.* **1959**, *31*, 646.
16. G. D. Parfitt, *Prog. Surf. Membrane. Sci*, **1976**, *11*, 181 and references therein.
17. H. P. Boehm, Chemical Identification of Surface Groups, Academic Press, New York and London, (**1996**), Vol 16.
18. R. E. Day; G. D. Parfitt, *Trans. Faraday. Soc*, **1971**, *63*, 708.
19. P. Jones; J. A. Hockey, *Trans. Faraday. Soc*, **1971**, *67*, 2679.
20. J. M. Hermann; U. Kaluza; H. P. Boehm, *Anorg. Allgem. Chemie*, **1970**, *372*, 308.
21. H. P. Boehm, *Discuss. Faraday. Soc*, **1971**, *52*, 264.

22. R. Thompson, *Industrial Inorganic Chemicals: Production and uses*, The Royal Society of Chemistry, **1995**.
23. Tioxide Group Ltd, *Titanium Dioxide Pigments Manufacture and General Properties*, **1996**.
24. G. H. Zhang; L. Gao;J. K. Guo, *Nanostruct. Mater*, **1999**, *11*, 1293.
25. S. Banerjee; S. S. Wong, *Nano Lett*, **2002**, *2*, 195.
26. L. Gao; Q. Zhang, *Scripta. Mater*. **2001**, *44*, 1195
27. Z. Xu; J, Shang; C. Liu; C. Kang; H. Gao; Y. Du, *Mat. Sci. Eng. B*, **1999**, *56*, 211.
28. U. Gesenhues, *Chem. Eng. Tech*. **2001**, *24*, 685.
29. A. Sclafani; L. Palmisano; M. Sciavello, *J. Phys. Chem*. **1990**, *94*, 829.
30. A. Yasumori; K. Ishizu; S. Hayashi; K. Okada, *J. Mater. Chem*. **1998**, *8*, 2521.
31. P. Stefchev. V. Blaskov; M. Machkova; P. Vitanov; V. Kozhukharov, *Int. J. Inorg. Mat* **2001**, *3*, 531.
32. Q. Huang; L. Gao, *Chem. Lett*. **2003**, *32*, 638.
33. T. Kasuga; M. Hiramatsu; A. Hoson; T. Sekino; K. Niihara. *Adv. Mater*, **1999**, *11*, 1307.
34. G. P. Dransfield; S. Cutter; P. L. Lyth, (To Uniqema ICI Ltd): Int Patent number WO02/00797A1 (**2002**).
35. J. L. Robb; L. A. Simpson; D. F. Tunstall, *Drug. Cos. Ind*, **1994**, *154*, 32.
36. L. A. Simpson, *Measuring opacity*, Tioxide Plc **1988**.
37. M. R. Hornby, *The particle size measurement of Titanium Dioxide Pigments*, Tioxide Group Ltd, **1989**.
38. Lord Rayleigh, *Philos. Mag*, **1871**, *41*, 447.
39. T. Allen, Particle. Size. Measurement, 4th Ed, Chapman and Hall, London, **(1990)**.
40. H. S. Shah; D. G. Adroja; D. B. Vaidya, *Indian. J. Pure. Appl. Phys*. **1993**, *31*, 560.
41. R. G. Molen; H. M. H. Hurks; C. Out-Luiting; F. Spies; J. M. Van't Noordede; H. K. Koerten; A. M. Mommaas, *J. Phochem. Photobiol B*, **1998**, *44*, 143.
42. A. S. Dussert; E. Gooris; J. Hemmerle, *Int. J. Cos. Sci*, **1997**, *19*, 119.
43. T. Uchino; H. Tokunaga; M. Ando; H. Utsumi, *Toxicology in Vitro*, **2002**, *16*, 629.

44. V. Rossatto; T. Picatonotto; D. Vione; M. E. Carlotti, *J. Disp. Sci. Tech*, **2003**, *24*, 259.
45. A. Mills; S. Le-Hunte, *J. Photochem. Photobiol. A*, **1997**, *108*, 1 and references contained therein.
46. M. I. Litter; J. A. Navio, *J. Photochem. Photobiol. A*, **1996**, *98*, 171 and references contained therein.
47. P. W. Atkins, Physical Chemistry, 5th Ed, Oxford University Press, Oxford, 1994.
48. V. P. S. Judin, *Chem. Britt*, **1993**, 503.
49. N. Serpone, *Sol. Energy. Mat. Sol. Cells*, **1995**, *38*, 369.
50. M. Gratzel, *Nature*, **2001**, *414*, 338.
51. H. Liu; H. T. Ma; X. Z. Li; W. Z. Li; M. Wu; X. H. Bao, *Chemosphere*, **2003**, *50*, 39.
52. C. D. Valentin; G. Pacchioni; A. Selloni; S. Livraghi; E. Giamello, *J. Phys. Chem. Lett*, **2005**, *109*, 11414.
53. O. Diwald; T. L. Thompson; T. Zubkov; E. G. Goralski; S. D. Walck; J. T. Yates, *J. Phys. Chem* B **2004**.
54. H. Wang; J. P. Lewis, *J. Phys. Condens. Mater* **2005**, *17*, L209.
55. S. Sato; R. Nakamura; S. Abe, *Appl. Cat B*, **2005**, *284*, 131.
56. D. J. C. Yates; *J. Phys. Chem*, **1961**, *18*, 746.
57. P. Jackson; G. D. Parfitt, *Trans. Faraday. Soc*, **1971**, *67*, 2469.
58. J. Moser; M. Gratzel; R. Galley, *Helv. Chim. Acta*, **1987**, *70*, 1596.
59. H. M. Swartz; K. J. Liu; T. Walczak; T. Panz; M. Kobayashi; W. Zavadoski, *J. Cosmet. Sci*, **1998**, *49*, 125.
60. G. Riegel; J. R. Bolton *J. Phys. Chem*, **1995**, *99*, 4215.
61. C. D. Jaeger; A. J. Bard, *J. Phys. Chem*, **1979**, *83*, 3146.
62. J. Cunningham; S. Srijaranai, *J. Photocehm. Photobiol A*, **1988**, *43*, 329.
63. O. Legrini; E. Oliveros; A. M. Barun, *Chem. Rev*, **1993**, *93*, 671.
64. M. R. Hoffmann; S. T. Martin; W. Choi; D. W. Bahnermann, *Chem. Rev*, **1995**, *95*, 69.
65. S. Tunesi; M. Anderson, *J. Phys. Chem*, **1991**, *95*, 3399.
66. R. Rodriguez; M. A. Blesa; A. E. Regazzoni, *J. Colloid. Interface. Sci*, **1996**, *177*, 122.

67. T. L. Vallarreal; R. Gomez; M. Neumann-Spillart; N. Alonso-Vante; P. Salvador, *J. Phys. Chem*, **2004**, *108*, 15172.
68. S. Goldstein; G. Czapski; J. Rabani, *J. Phys. Chem*, **1994**, *98*, 6586.
69. M. Ulmann; N. R. Tacconi; J. Augustynski, *J. Phys. Chem*, **1986**, *90*, 5623.
70. A. L. Attwood; D. M. Murphy; J. L. Edwards; T. A. Egerton; R. W. Harrison, *Res. Chem. Intermed*, **2003**, *29*, 449 and references therein.
71. B. Sun; P. G. Smirniotis, *Cat. Today*, **2003**, *88*, 49.
72. C. C. Wang; Z. Zhang; J. Y. Ying, *Nanostructred Mat.* **1997**, *9*, 583.
73. A. J. Maira; K. L. Yeung; C. Y. Lee; P. L. Yue; C. K. Chan, *J. Catal*, **2000**, *192*, 185.
74. S. E. Park; H. Joo; J. W. Kang, *Sol. Energy. Mat. Sol. Cells*, **2004**, *83*, 39.
75. T. A. Egerton and I. R. Tooley, *J. Phys. Chem B*, **2004**, *98*, 5066.
76. R. I. Bickley; T. Gonzalez-Carreno; J. S. Less; L. Palmisano; R. J. D. Tilley, *J. Solid. State. Chem.* **1991**, *92*, 178.
77. D. C. Hurm; A. G. Agrios; K. A. Gray; R. Rajh; M. C. Thurnauer, *J. Phys. Chem B*, **2003**, *107*, 4545.
78. N. Serpone; D. Lawless; R. Khairlutdinov; E. Pellizetti, *J. Phys. Chem*, **1995**, *99*, 16655.
79. Degussa P25 data sheet.
80. W. Choi; A. Termin; M. R. Hoffmann, *J. Phys. Chem.* **1994**, *98*, 13669.
81. K. E. Karakitsou; X. E. Verikios, *J. Phys. Chem*, **1993**, *97*, 1184.
82. W. Mu; J. M. Herrmann; P. Pichat, *Cat. Lett*, **1989**, *3*, 73.
83. J. Yang; D. Li; Z. Zhang; Q. Li; H. Wang, *J. Photochem. Photobiol A*, **2000**, *137*, 197.
84. J. Zhu; W. Zheng; B. He; J. Zhang; M. Anpo, *J. Mol. Cat A*, **2004**, *216*, 35.
85. Z. Zhang; C. C. Wang; R. Zakaria; J. Y. Ying, *J. Phys. Chem. B*, **1998**, *102*, 10871.
86. J. A. Navio; F. J. Marchena; M. Rocel; M. A. De La Rosa, *J. Photochem. Photobiol A*, **1991**, *55*, 319.
87. X. Li; P. Yue; C. Kutal, *New. J. Chem*, **2003**, *27*, 1264.
88. K. Wilke; H. D. Breuer, *J. photochem. Photobiol. A.* **1999**, *121*, 49.
89. S. Karvinen, *Solid state Sci*, **2003**, *5*, 811.
90. D. F. Tunstall, *J. Cosmet. Sci*, **2000**, *51*, 303.
91. A. Emeline; A. Salinarno; N. Serpone, *J. Phys. Chem B*, **2000**, *104*, 11202.

92. A. Emeline; G. N.Kuzmin; D. Purevdorj; V. K. Ryabchuck; N. Serpone, *J. Phys. Chem B*, **2000**, *104*, 2989.

93. M. A. Grela; A. J. Colussi, *J. Phys. Chem B*, **1999**, *103*, 2614.

94. A. V. Emeline; V K. Ryabchuck, N. Serpone, *J. Phys. Chem. B*, **1999**, *103*, 1316.

95. T. A. Egerton, *Kona Powder and Particle*, **1998**, *16*, 46 and reference therein.

96. U. Gensehues, *J. Colloid. Interface. Sci*, **1994**, *168*, 428.

97. P. Mulvaney; L. M. Liz-Marzan; M. Giersig; T. Ung, *J. Mater. Sci*, **2000**, *10*, 1259.

98. D. R. Lide; Handbook of Chemistry and Physics, 71st Edition, CRC Press Inc, **1990**.

99. K. H. Haas; S. Amberg-Schwab; K. Rose, *Thin Sol. Films*, **1999**, *351*, 198.

100. R. K. Iller, *The Chemistry of Silica*, John Wiley and Sons, New York, US, **1979**.

101. P. B. Howard; G. D. Parfitt, *Croat. Chem. Acta*, **1977**, *50*, 15.

102. T. A. Egerton; I. R. Tooley, *J. Mater. Chem*, **2002**, *12*, 1111.

103. M. Kazuyuki; F. Masahiro; Y. Masaaki; Y. Akira (To Shinetsu Co JP): EU Patent number EP0902069. (**1999**).

104. G. R. Davidson; M. J. Goldsworthy; M. I. James (To Proctor and Gamble US): UK Patent number 2300629 (**1995**).

105. P. A. Tooley; P. M. Neidenzu; A. H. Reid (To EI Du Pont US): Int Patent number WO 95/23193 (**1995**).

106. J. N. Birmingham; D. A. Holtzen; J. F. Hunt; R. S. Jenkins; P.D. Spohn; J. T. Walnock (To EI Du Pont US): Int Patent number WO 95/23417 (**1995**).

107. P. M. Niedenzu; S. M. Herkimer; R. L. Chaney (To EI Du Pont US): Int Patent number WO 95/23194 (**1995**).

108. M. A. Mitchinick; A. J. O'Lenick (To Sunsmart Inc, Silatech Inc): US Patent number 5,756,788 (**1998**).

109. A. Ulman, *Chem. Rev*, **1996**, *96*, 1533 and references therein.

110. A. Y. Fadeev; R. Helmy; S. Marcinko, *Langmuir*, **2002**, *18*, 7521.

111. W. Hertl, *J. Phys. Chem.* **1968**, *72*, 1248

112. W. Hertl, *J. Phys. Chem*, **1968**, *72*, 3993.

113. C. P. Tripp, *Langmuir*, **1995**, *11*, 1215.

114. D. W. Britt; V. Hlady, *Langmuir*, **1999**, *15*, 1770.

115. C. P. Tripp; P. Kazmaier; M. L. Hair, *Langmuir*, **1996**, *12*, 6404.

116. H. O. Finklee; R. Vithanage, *J. Phys. Chem.* **1982**, *86*, 3621.

117. R. Helmy; A. Y. Fadeez, *Langmuir*, **2002**, *18*, 8924.

118. H. O. Finklea; R. W. Murray, *J. Phys. Chem*, **1979**, *83*, 353.

119. K. I. Hadjiivanov; D. G. Klissurski; A. A. Davydov, *J. Catal*, **1989**, *116*, 498.

120. S. K. Samantaray; K. Parida, *Appl. Cat A*, **2001**, *220*, 9.

121. S. K. Samantaray; K. Parida, *J. Mol. Cat A*, **2001**, *176*, 151.

122. W. Gong, *Int. J. Miner. Process*, **2001**, *63*, 147.

123. P. A. Connor; A. J. McQuillen, *Langmuir*, **1999**, *15*, 2916.

124. P. B. Howard; B. Barnard; D. Unwin, (To Tioxide Group PLC UK): UK Patent number 2115394 (**1982**).

125. B. Barnard; W. T. Laverick (To Tioxide Group LTD UK): US Patent number 4239548 (**1980**).

126. F. Takashi; Y. Kazuo; K. Tsuneo (To Toho Titanium Co LTD JP): JP Patent number 11222442 (**1999**).

127. H. Ando; M. Nakahra; M. Yamamoto; K. Itoh, *Langmuir*, **1996**, *12*, 6399.

128. M. Suzuki; A. Fujishima; T. Miyazaki; H. Hiramatsu; H. Ando; M. Nakahara; M. Yamamoto; K. Itoh, *J. Biomed. Mater. Res.* **1997**, 252.

129. M. B. Mitchell; V. N. Sheeinker; E. A. Mintz, *J. Phys. Chem. B*, **1997**, *101*, 11192.

130. M. K. Templeton; W. H. Wein berg, *J. Am. Chem. Soc*, **1985**, *107*, 97.

131. B. Aurian-Blajeni; M. M. Boucher, *Langmuir*, **1989**, *5*, 170.

132. W. Gao; L. Dickensen; C. Grozinger; F. G. Morin; L. Reven, *Langmuir*, **1996**, *12*, 6429.

133. C. S. Kim; R. J. Lad; Carl. P. Tripp, *Sensors. Actuators*. **2001**, *76*, 442.

134. Catalogue: *Solaveil ICI*, **2005**.

135. C. Diaper, *Internal Technical Report*, Tioxide Specialities. 1995.

136. R. I. Bickley, C. Munera, and F. S. Stone, *J. Catal*, **1973**, *31*, 398.

137. R. I. Bickley; F. S. Stone, *J. Catal*, **1973**, *31*, 389.

138. R. B. Cundall; R. Rudham; M. S. Salim, *J. Chm. Soc. Faradat. Trans*, **1976**, *72*, 1642.

139. T. A. Egerton; C. J. King, *J. Oil. Col. Chem. Soc.* **1979**, *62*, 386.

140. G. Irick, *J. Appl. Polymer. Sci*, **1972**, *16*, 2387.

141. I. R. Tooley, PhD Thesis, University of Newcastle Upon Tyne, Newcastle Upon Tyne, NE1 7RU, (**2002**).

142. Dieckmann, M.S; Gray, K.A, *Water Res*, **1996**, *30*, 1169.

143. McMurray, J, Organic Chemistry, 4th Ed, Brooks Cole Publishing Co, **1996.**

144. http://www.EPA.com.

145. V. Augugliarno, L. Palmisano, M. Schiavello and A. Sclafani, *Appl. Catal.* **1991**, *69*, 323.

146. R. Andreozzi, V. Caprio, A. Insola, G. Longo and V. Tufano, *J. Chem. Tech. Biotechnol.* **2000**, *75*, 131

147. N. San, A. Hatipoglu, G. Kocturk and Z. Cinar, *J. Photochem. Photobiol. A:Chem.* **2002**, *146*, 189.

148. R. W. Harrison, MPhil Thesis, University of Newcastle Upon Tyne, Newcastle Upon Tyne, NE1 7RU, **(2001)**.

149. K. H. Wang, Y.H. Hsieh and L.J. Chen, *J. Haz. Mater.* **1998**, *59*, 251.

150. D. Chen and A.K. Ray, *Wat. Res.* **1998**, *32*, 3223.

151. T. A. Egerton; P. A. Christensen; R. W. Harrison; J. W. Wang, *J. Applied. Electro*, **2005**, *35*, 799

152. Tanaka, K; Luesiwong, W; Hisanga, T, *J. Mol. Cat A*, **1997**, *122*, 67.

153. Maurino, V; Minero, C; Pelizetti, E; Piccinini, P; Serpone, N; Hidaka, H, *J. Photochem .Photobiol A: Chem*, **1997**, *109*, 171.

154. Paola *et al*, *Journal of Photochem Photobiol A*, 55, 207.

155. Alif ; Boule *J. Photochem .Photobiol A*, 59, 357.

156. G. Sposito, *The Surface Chemistry of Soil*, Oxford University Press: London, **1984**.

157. C. S. Turchi; D. F. Ollis, *J. Catal*, **1990**, *122*, 178.

158. D. Vione, T. Picatonotto, and M. E. Carlotti, *J. Disp. Sci. Tech.* **2002**, *23*, 845.

159. D. Vione, T. Picatonotto, and M. E. Carlotti, *J. Cosmet. Sci.* **2003**, *54*, 513.

160. F. London, Z. Physik, **1930**, *63*, 245.

161. D. M. Young; A. D. Crowell, Physical Adsorption of Gases, Butterworths, London, **(1962)**.

162. I. Langmuir, *J. Am. Chem. Soc*, **1916**, *38*, 2221.

163. S. J. Gregg; K. S. W. Singh, Adsorption, Surface Area and Porosity, 2nd Ed, Academic Press, London, **(1982)**.

164. R. G. Snider, *J. Chem. Phys*, **1967**, *47*, 1316.

165. A. H. M. Sondag; M. C. Raas, *J. Chem. Phys*, **1989**, *91*, 4926.

166. S. R. Cohen; R. Naaman; J. Sagiv, *J. Chem. Phys*, **1986**, *90*, 3054.

167. C. N. Banwell; E. M. McCash, Fundamentals of Molecular Spectroscopy, 4th Ed, McGraw-Hill book company, London, (**1994**).

168. Y. Sakata; N. Kinoshita; K. Domen; T. Onishi, *J. Chem. Soc. Faraday Trans* 1, **1987**, *83*, 2765.

169. T. A. Egerton; N. Sheppard, *J. Chem. Soc. Faraday Trans 1*, **1974**, *64*, 1357.

170. L. H. Little, Infrared Spectra of Adsorbed Species, Academic Press, London and New York, (**1966**).

171. B. D. Cullidy, Elements of X-Ray Diffraction, 2nd Ed, Addison-Wesley Publishing Co Inc, (**1978**).

172. T. A. Egerton; E. Harris; E. J. Lawson; B. Mile; C. C. Rowlands, *Phys. Chem. Chem. Phys*, **2001**, *3*, 497.

173. T. A. Egerton; E. Harris; E. J. Lawson; B. Mile; C. C. Rowlands, *Phys. Chem. Chem. Phys*, **2000**, *2*, 3275.

174. B. P. Nelson; R. Candal; R. M. Corn; M. A. Anderson, *Langmuir*, **2000**, *16*, 6094.

175. A. G. Agrios; K. A. Gray; E. Weitz, *Langmuir*, **2003**, *19*, 1402.

2. SAMPLE PREPARATION AND EXPERIMENTAL TECHNIQUES.

This chapter describes the preparation of the home prepared titania (Sample A) and the methods used to modify this and the commercially available Degussa P25 (P25), together with the experimental techniques used to analyse the samples. The photoactivity was measured using three model compounds: 2-propanol oxidation, 2-nitrophenol degradation, and salicylic acid degradation. The samples were also characterised using gravimetric adsorption, Fourier Transform infra red spectroscopy (FTIR), optical density measurements, and x-ray diffraction (XRD). The iron treated samples were also characterised by electron paramagnetic resonance (EPR). Preliminary work to determine typical experimental conditions for 2-propanol oxidation (IPA) and 2-nitrophenol degradation (NP) is also described.

2.1. SAMPLE PREPARATION METHOD.

Two main types of titanium dioxide were used in this work. Sample A is a home prepared high area rutile prepared by aqueous hydrolysis of dilute titanium tetrachloride according to the following reaction:

$$TiCl_4 + H_2O \rightleftharpoons TiOCl_2 + 2HCl \quad [2.1]$$

$$TiCl_4 + 4NaOH \longrightarrow Ti(OH)_4 + 4NaCl \quad [2.2]$$

$$Ti(OH)_4 \longrightarrow TiO_2 + 2H_2O \quad [2.3]$$

Property	Sample A	Degussa P25
Physical state	White powder	White powder
Composition (%)	>99.9% rutile	~ 80% anatase, ~ 20% rutile
BET surface area ($m^2 g^{-1}$)	133	55
Average 1^o particle size (nm)	9.5	~ 30
pH in aqueous solution	9-10	3-4

Table 2.i: Physical properties of sample A and Degussa P25.

Details of the preparation method are given below (2.1.2). The other titania studied was the commercially available Degussa P25. This material is made using a vapour phase method of flame hydrolysis of titanium tetrachloride. Physical properties for these samples are summarised in Table 2.i. Samples C, D, F, H, and J are modified versions of sample A, and samples E, G, I, K, L are modified versions of P25.

2.1.1 Preparation reagents.

Titanium tetrachloride solution was supplied by Millennium Chemicals at a concentration of 400 g dm^{-3} (Fe < 30 ppm). Sodium hydroxide pellets (99%) and sodium hydroxide solution (99.8%) were supplied by BDH. Iron acetate (99.99%), hydrochloric acid (37%), methanol (99.9%), octadecyl-trimethoxy-silane (ODTMOS) (90%), sodium hydrogen phosphate (99%), sodium acetate (99%) were supplied by Aldrich. Arlatone Map 160K (AM160K), a phosphate ester, was kindly supplied by the industrial sponsors, Uniqema; this material is described elsewhere (Section 1.7.3).

2.1.2. Preparation of Sample A.

The method used for the preparation of 200 g of Sample A, and the final slurry is approximately 80 g dm^{-3} is given below. The reaction vessel is shown in Figure 2.i.

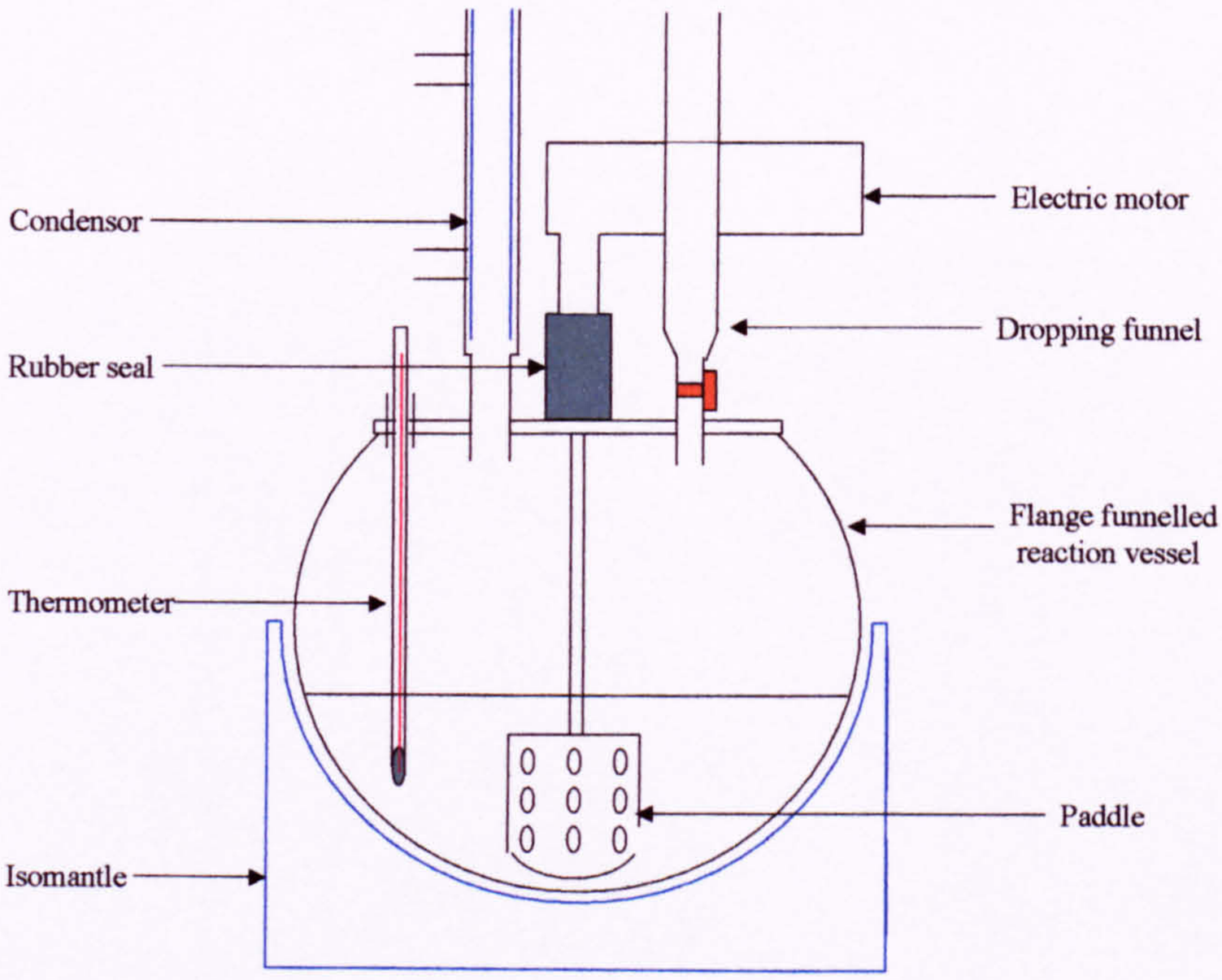

Fig 2.i: Reaction vessel to prepare Sample A.

A solution of NaOH was made at a concentration of 187.5g dm^{-3} by dissolving 282.7g NaOH pellets in 1514 ml demineralised water and allowed to cool before placing in the flange funnelled reaction vessel (FFRV). Titanium tetrachloride (500ml) was added dropwise to the NaOH over 30 minutes with stirring to precipitate TiO_2. The slurry was then heated to 82°C and maintained at this temperature for 120 minutes to encourage crystallisation. After allowing cooling to room temperature the slurry was neutralised with 339 ml of NaOH (187.5 g dm^{-3}).

2.1.2.1. Filtration method and washing.

A 125 ml portion of the slurry was filtered using a Buckner funnel and two filter papers (Whatman®), Grade 6 (slow filter, fine) on the bottom and grade 542 (coarse) on top - the remainder of the slurry was retained for treatment/coating. This gave a final mass of approximately 10 g of Sample A for analysis. The filter cake was then washed on the filter by displacement washing with Millipore water (1000 ml) and then reslurried in a further 100 ml. This was repeated until a conductivity of less than 500 μS was achieved. Finally the cake was dried at 110°C overnight, ground with pestle and mortar and sieved to < 212 μm.

2.1.3. Preparation of iron treated TiO_2 by coprecipitation (Samples C).

A series of iron treated analogous of Sample A in the range 0.001 atm% to 5 atm% were prepared by coprecipitation of iron acetate and titanium tetrachloride. The preparation apparatus is similar to that for the preparation of Sample A (Fig 2.i), with the exception that an additional dropping funnel was required for the iron acetate.

All aspects of the method are as for preparation of Sample A (2.1), except that aqueous iron acetate solution (500ml) of the appropriate concentration for the target doping level was added dropwise to the NaOH over 30 minutes during the addition of the titanium tetrachloride.

2.1.3.1. Filtration method and washing.

The iron treated TiO_2 was filtered using a Buckner funnel with an identical arrangement of filter paper to that detailed in 2.2.1 for Sample A. The filter cake was washed on the funnel with twice the volume of Millipore water as the original slurry, reslurried at a loading of approximately 100 g dm^{-3}, and filtered again - this was

repeated until a conductivity of less than 500 μS was achieved. The cake was then washed with 30 ml of acetone to displace the remaining water. Finally the cake was dried at 110°C overnight, ground with pestle and mortar and sieved to < 212 μm.

2.1.4. Preparation of iron treated TiO_2 by precipitation (Samples D and E).

A series of iron treated versions of Samples A and P25 in the range 0.001 atm% to 5 atm% was prepared by precipitation of iron acetate. This preparation was performed with the TiO_2 as a slurry. For Sample A, the existing slurry was diluted to a total volume of 1500 ml (10.7 g dm^{-3}). For P25, 16 g TiO_2 was slurried by addition of 1500 ml to give the same loading. The reaction apparatus is shown in Figure 2.ii.

Sodium hydroxide (3 mol dm^{-3}) was added to 16 g of TiO_2 as a 10.7 g dm^{-3} slurry in Millipore water to increase the pH of the slurry to 10. Iron acetate solution (500 ml), of the appropriate concentration to give the desired level of treatment was added dropwise over 60 minutes with stirring at 120 rpm, and the slurry left to stir for a further 60 minutes. The slurry was then filtered, washed and dried as described above in section 2.3.1.

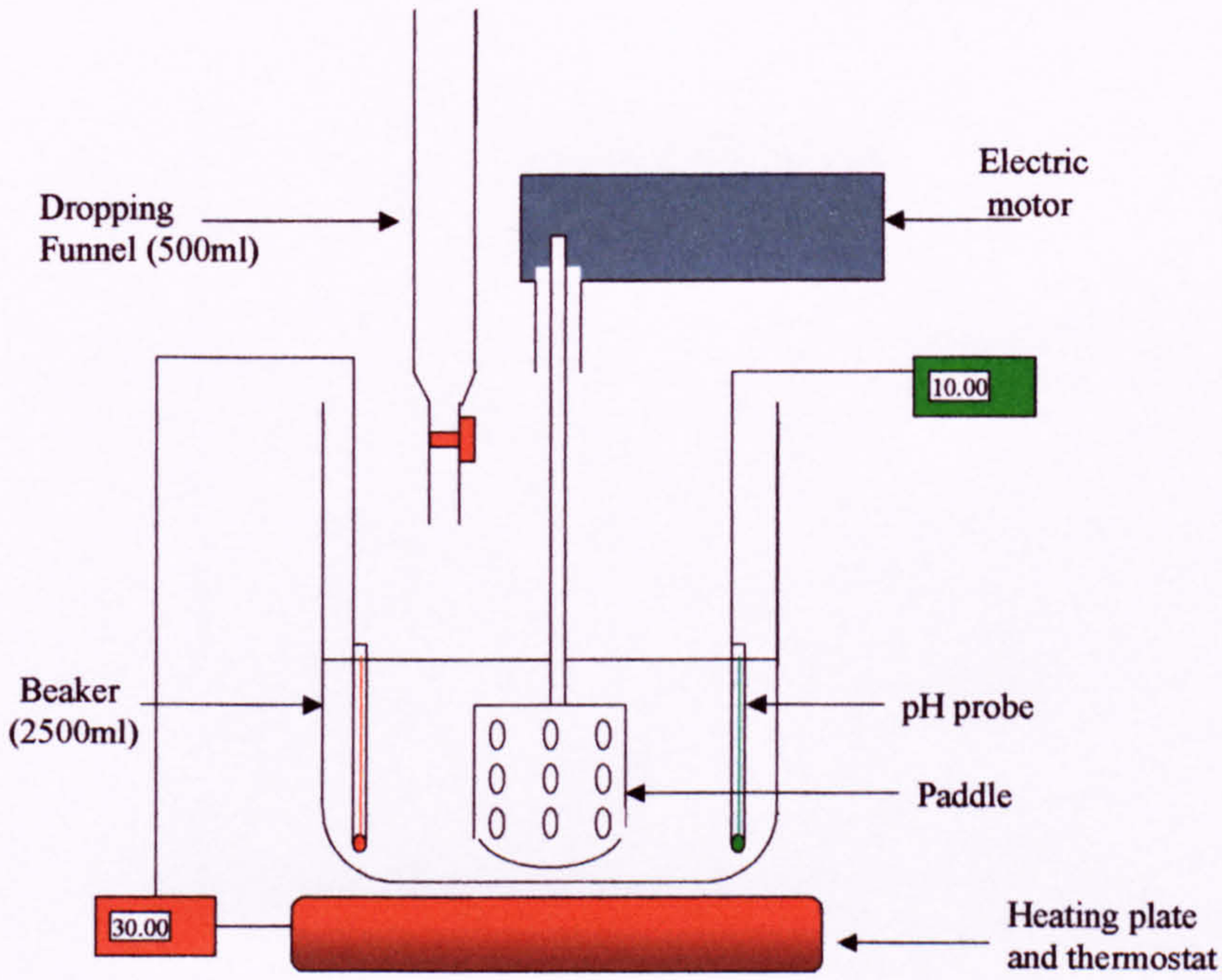

Fig 2.ii: Reaction apparatus for the preparation of iron treated TiO_2 by precipitation

2.1.5. Preparation of Arlatone Map 160K coated TiO_2 (Samples F and G).

Arlatone Map 160K is a phosphate ester kindly supplied by Uniqema ICI, more fully described in Section 1.7.3. A series of Arlatone Map 160K (AM160K) coated versions of Sample A and P25 at a coating level of 10% to 100% (as a proportion of surface area) was prepared. The reaction apparatus is shown in Figure 2.ii.

The appropriate mass of AM160K required for the target coating level was dissolved in 1000 ml Millipore water in a 2.5 dm^{-3} glass beaker by heating on a thermostat controlled hot plate to 75°C – the pH at this stage was 6.3. TiO_2 slurry (200 ml, 50 g dm^{-3}) also at 75°C and with pH altered to 6.3 was added to the AM160K solution with stirring at 120 rpm. The slurry was then allowed to cool gradually to room temperature (the AM160K precipitates at ~55°C). The slurry was then neutralised to pH 6.5-7 using hydrochloric acid (3 mol dm^{-3}).

2.1.5.1. Filtration method and washing.

The AM160K coated TiO_2 was filtered using a Buckner funnel with an identical arrangement of filter paper to that detailed in 2.2.1 for Sample A. The filter cake was washed on the funnel with 1000 ml Millipore water, then reslurried at a loading of approximately 100 g dm^{-3} and filtered again. This was repeated until a conductivity of less than 500 μS was achieved. Finally the cake was dried at 110°C overnight, ground with pestle and mortar and sieved to < 212 μm.

2.1.6. Preparation of Octadecyl-trimethoxy-silane coated TiO_2 (Samples H and I).

Octadecyl-trimethoxy-silane (ODTMOS) coated versions of Sample A and P25 at two different coating levels of up to 100% (as a proportion of surface area) were prepared. The reaction apparatus is shown in Figure 2.ii above.

A solution of 90:10 Methanol/Water (100ml) with a few drops of acetic acid was mixed with the appropriate amount of ODTMOS to form a monolayer coating (8.5ml for Sample A, 3.3 ml for P25), for 30 mins to allow hydrolysis to occur. This solution was added to a slurry of TiO_2 (10.7 gpl, 1500 ml) at a pH ~10 over 30 mins and allowed to mix for a further 30 minutes. A 500 ml sample was taken and neutralised to pH 6.5-7 (Samples H_i and I_i). The remainder was allowed to mix for a further 240 minutes, then

neutralised to pH 6.5-7 (Sample H_{ii} and I_{ii}). The aim being to achieve two different coating levels, the second greater than the first.

2.1.6.1 Filtration method and washing.

The ODTMOS coated TiO_2 was filtered using a Buckner funnel with an identical arrangement of filter paper to that detailed in 2.2.1 for Sample A. The filter cake was washed on the funnel with twice the amount of Millipore water as the original slurry – i.e. 1000 ml for samples H_i and I_i, 2000 ml for samples H_{ii} and I_{ii}, then reslurried at a loading of approximately 100 g dm^{-3} and filtered. This was repeated until a conductivity of less than 500 µS was achieved. Finally the cake was dried at 110°C overnight, ground with pestle and mortar and sieved to < 212 µm.

2.1.7. Preparation of phosphate coated TiO_2 (Samples J and K).

Phosphate coated versions of Sample A and P25 from sodium hydrogen phosphate ($[Na^+_2][PO_4H]^{2-}$) were prepared at a coating level of 10% to 100% (as a proportion of surface area). The reaction apparatus is shown in Figure 2.ii.

The appropriate mass of sodium hydrogen phosphate for the target coating level was dissolved in 1200 ml of a TiO_2/Millipore water slurry at a loading of 8.3 g dm^{-3} (10g) in a 2.5 dm^{-3} glass beaker and stirred at 120 rpm. The pH of the slurry was altered to 4.0 with hydrochloric acid (3 mol dm^{-3}). The temperature of the slurry was increased to 60°C (at approximately 1°C min^{-1}) and held at this temperature for 120 minutes. The slurry was then allowed to cool gradually to room temperature and neutralised to pH 6.5-7 using sodium hydroxide solution (0.5 mol dm^{-3}). The filtration method for the phosphate coated TiO_2 is identical to that for the AM160K coated TiO_2 above (section 2.1.5.1).

2.1.8. Preparation of acetate coated TiO_2 (Sample L).

This section details the preparation of acetate coated versions of P25 using sodium acetate at a level of 25% (as a proportion of surface area). The reaction apparatus is shown in Figure 2.ii.

The appropriate mass of sodium acetate for the target coating level was dissolved in 1200 ml of a TiO_2/Millipore water slurry at a loading of 8.3 g dm^{-3} (10g) in

a 2.5 dm^{-3} glass beaker and stirred at 120 rpm. The temperature of the slurry was increased to 80°C (at approximately 1°C min^{-1}) and held at this temperature for 120 minutes. The slurry was then allowed to cool gradually to room temperature and neutralised to pH 6.5-7 using sodium hydroxide solution (0.5 mol dm^{-3}). The filtration method for the acetate coated TiO_2 is identical to that for the AM160K coated TiO_2 above (section 2.1.5.1).

2.1.9 Table of samples.

The following table summarises the samples used for this study.

Identifier	Base TiO_2	Treatment	Morphology
A	High area Rutile	None	Rutile 99%+
B	Degussa P25	None	~ 80% anatase, ~ 20% rutile
C	Sample A	Coprecipitated iron acetate Range 0.001at% - 5at%	Rutile 99%+
D	Sample A	Precipitated iron acetate Range 0.001at% - 5at%	Rutile 99%+
E	Degussa P25	Precipitated iron acetate Range 0.001at% - 5at%	~ 80% anatase, ~ 20% rutile
F	Sample A	AM160K surface coating Range 10% - 100%	Rutile 99%+
G	Degussa P25	AM160K surface coating Range 10% - 100%	~ 80% anatase, ~ 20% rutile
H	Sample A	ODTMOS surface coating H_i = 31% and H_{ii} 64%	Rutile 99%+
I	Degussa P25	ODTMOS surface coating I_i 41% and I_{ii} 84%	~ 80% anatase, ~ 20% rutile
J	Sample A	Phosphate surface coating Range 5% - 100%	Rutile 99%+
K	Degussa P25	Phosphate surface coating Range 10% - 100%	~ 80% anatase, ~ 20% rutile
L	Degussa P25	Acetate surface coating 25%	~ 80% anatase, ~ 20% rutile

2.2. EXPERIMENTAL TECHNIQUES.

2.2.1. 2-Propanol oxidation (IPA).

Typically, the photoactivity of treated and untreated samples was determined by measuring the concentration of acetone formed during illumination of a slurry of 0.4g titanium dioxide in 50 ml isopropanol. The photoreactor and light source for this reaction is shown below (Figures 2.iiia and b).

The photoreactor was illuminated from below by two Philips PL-L 36W 09 actinic lamps. A pyrex filter and a heat filter of 10 ml of water were fitted into the illumination port to eliminate radiation below 300 nm and reduce heating respectively. The spectral distribution, measured at 10 nm intervals using a Spex 740A Radiometer, for the filtered light source is shown in Figure 2.iv. The temperature throughout the reaction was controlled at 303K using a heat jacket fitted around the reaction vessel.

Prior to illumination, a 30 minute equilibration time was allowed for the reaction temperature to stabilise and for the lamp to reach full intensity. During this period the slurry was continuously stirred and sparged with a continuous flow of air. Subsequently, irradiation was begun and the dispersion was continuously stirred whilst a flow of air was slowly bled across the top of the suspension. Samples (2ml) of the reaction mixture were withdrawn by a hypodermic syringe through a sampling port fitted with a septum cap both immediately prior to illumination after 15 minutes, 30 minutes and then in 30 minute intervals for typically a total time of 150 minutes. The titanium dioxide was removed using a 2μm PTFE syringe filter. A previously prepared internal standard (50μl), see below, was added to 1ml of the filtered reaction mixture and a 2μl sample injected into the GC for analysis.

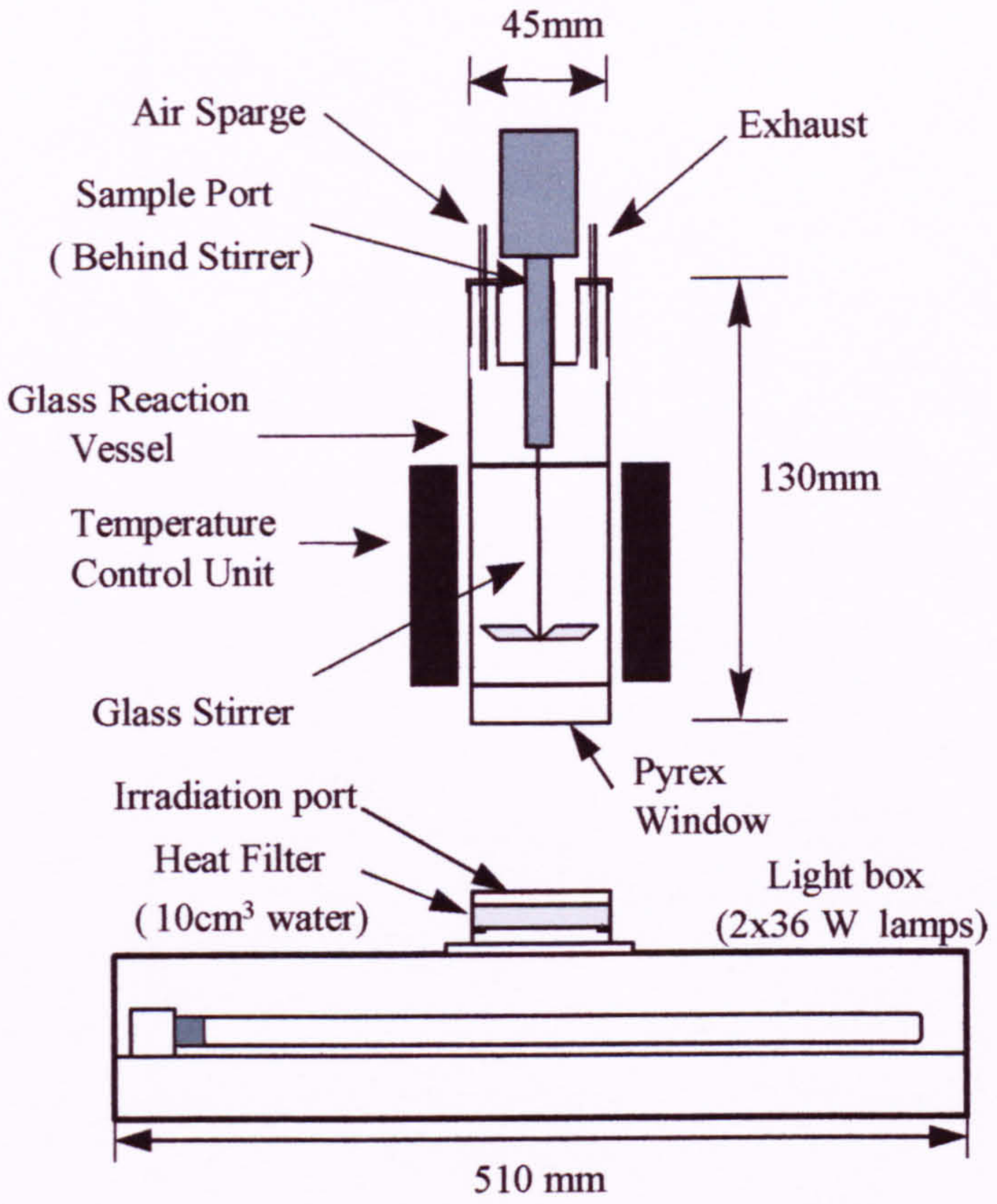

Fig 2.iiia. Photoreactor and light source for isopropanol oxidation (Landscape view).

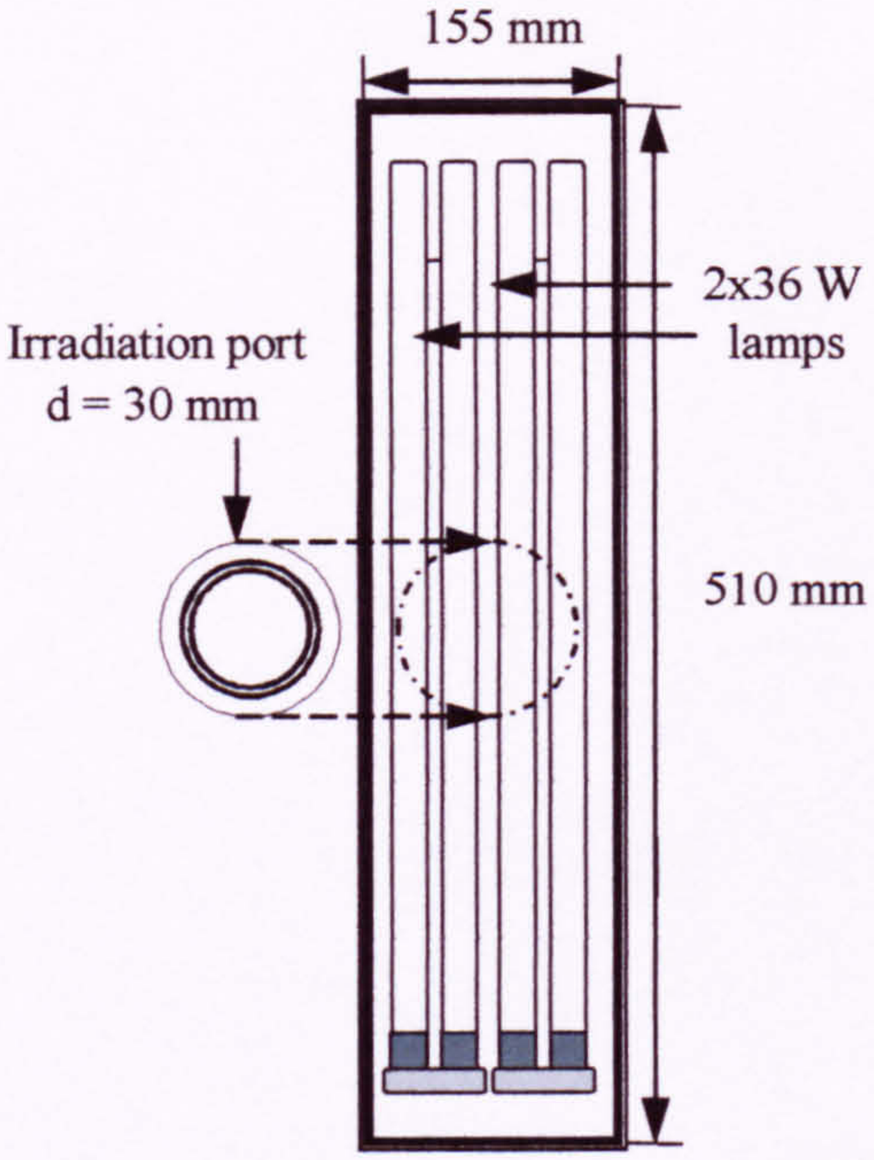

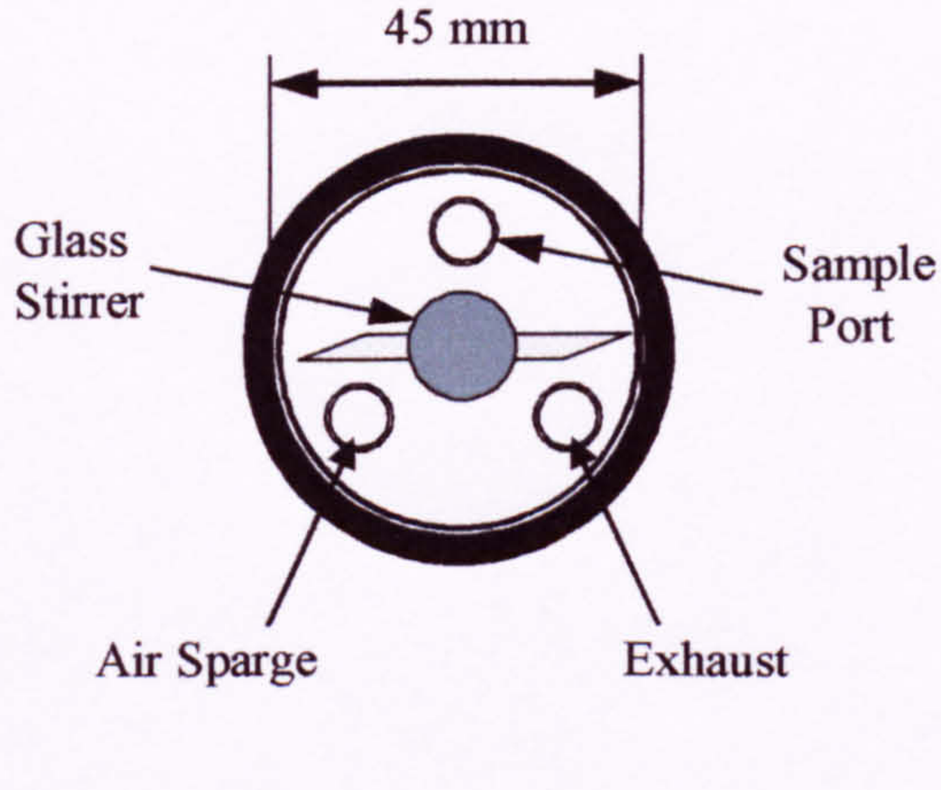

Fig 2.iii.b. Plan view of photoreactor and light source.

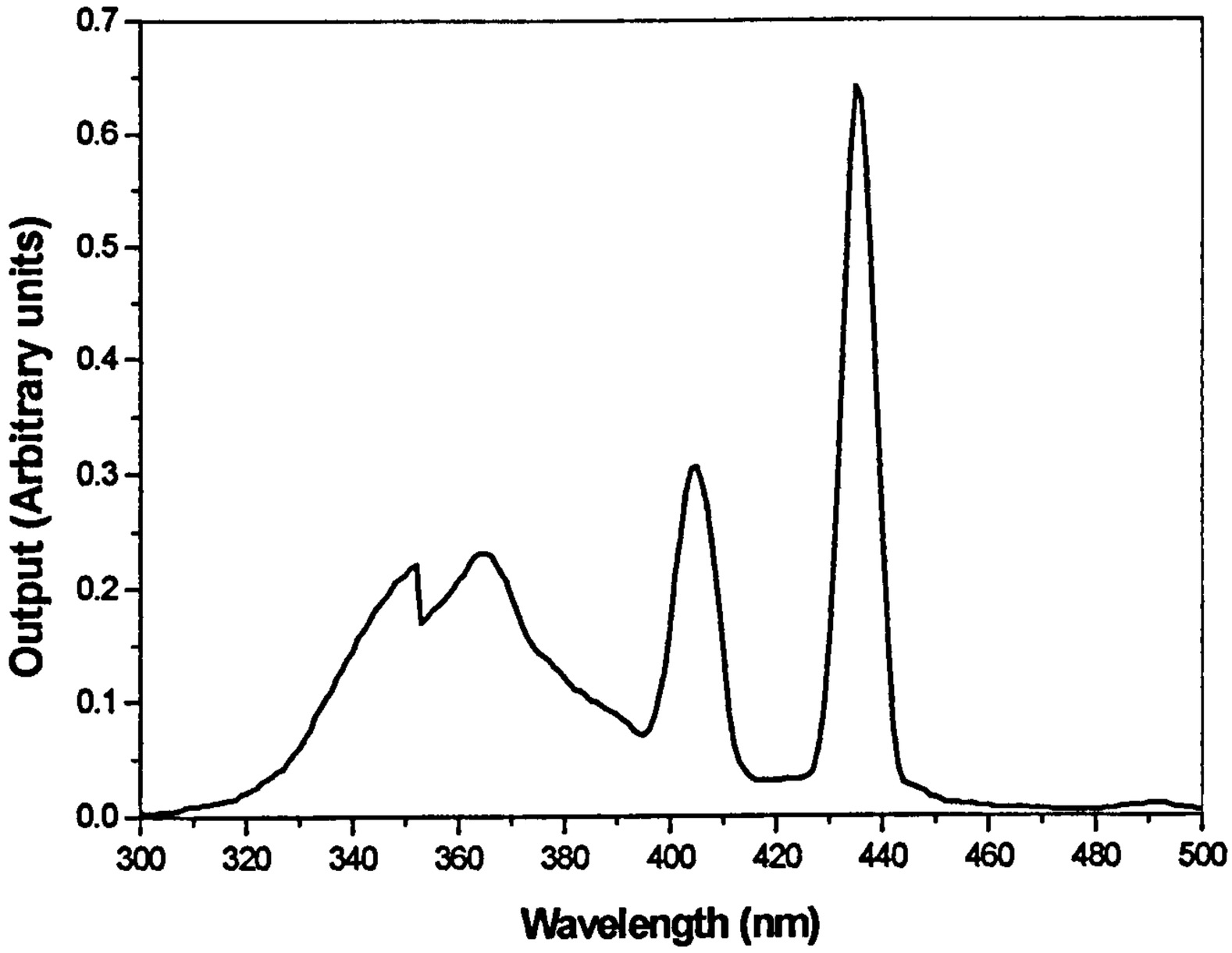

Fig 2.iv. Spectral output of the Philips PL-L 36W 09 actinic lamps.

2.2.1.1 Analysis for acetone concentration by Gas Chromatography (GC).

An Ai Cambridge GC94 Gas Chromatograph fitted with a Chromosorb wax 60/80 mesh column and flame ionisation detector (FID) was used to analyse acetone concentration. The column temperature was held at 70^0C, the inlet and detector temperature at 95^0C. The carrier gas was nitrogen flowing at 30 ml min^{-1} to give a column pressure of 4 psi. The FID gases, hydrogen and air, were at a pressure of 4 psi and 2 psi respectively. Typically an amplifier Gain of 1 was used or Gain 10 when acetone concentration was especially low.

The GC was calibrated by determination of the acetone/ether ratio when 50µl of internal standard (typically 200µl of diethyl ether in 25ml of isopropanol) was added to an acetone/isopropanol mixture (1ml) of known acetone concentrations between 5.45×10^{-4} and 1.09×10^{-2} mol dm^{-3}. For GC operation at Gain 10 an internal standard of 20µl of diethyl ether in 25ml of isopropanol was used. Linear calibration plots for these two Gain sensitivities with slopes of 1.18×10^{-2} mol dm^{-3}

($R^2 = 0.999$) for Gain 1, and 1.32 x10^{-3} mol dm^{-3} ($R^2 = 0.999$) for Gain 10 for these conditions are shown below (Figure 2.v).

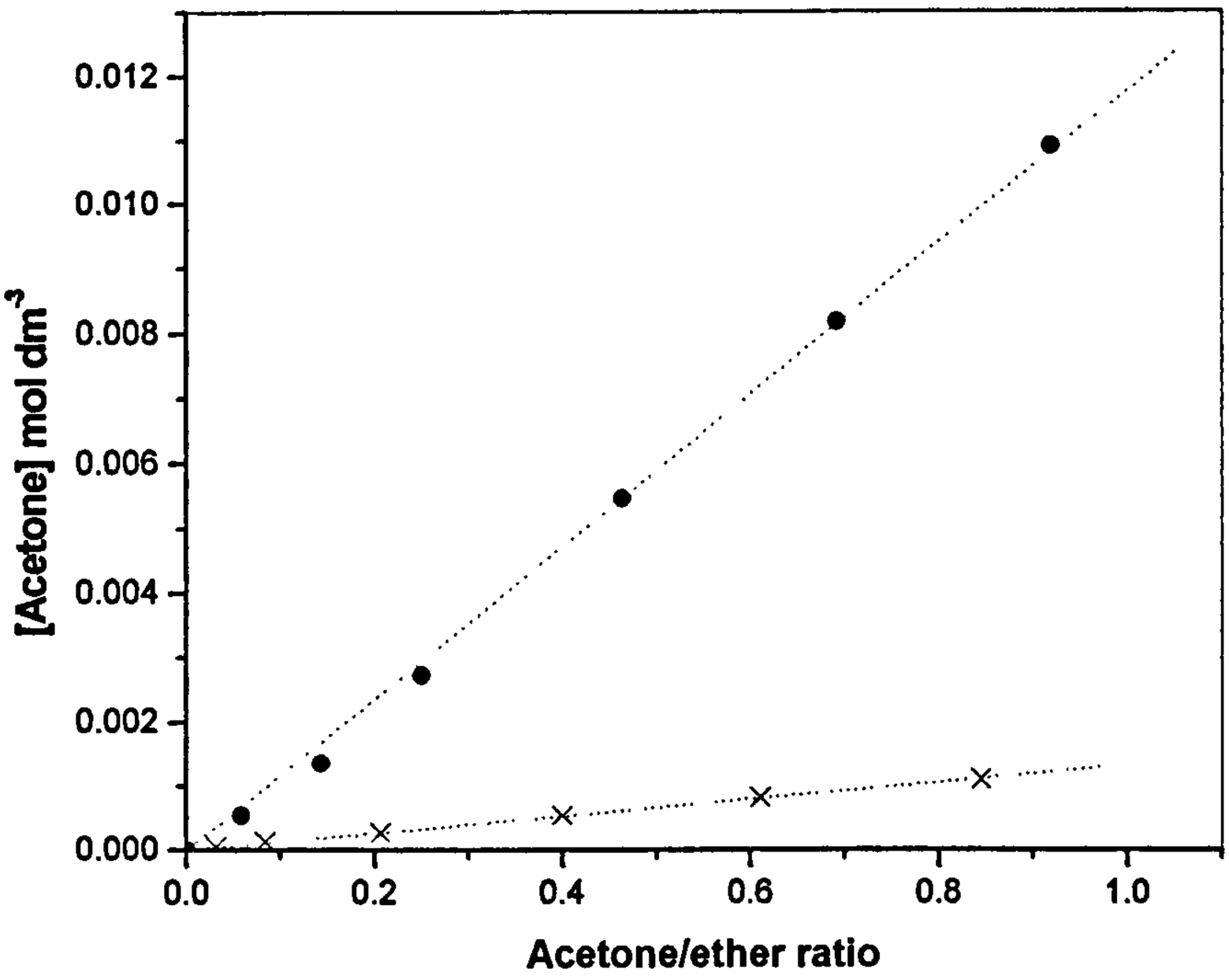

Fig 2.v. Calibration plot for the calculation of acetone concentration from the acetone/ether ratio. • Gain 1 (Gradient = 1.09 x 10^{-2} mol dm^{-3}); x Gain 10 (Gradient = 1.32 x10^{-3} mol dm^{-3})

2.2.1.2. Sample milling procedure.

Egerton and Tooley [1] varied the degree of dispersion of the titanium dioxide particles in the slurry by milling the samples to reduce aggregation and found that this affects the rate of oxidation of isopropanol. Therefore, in this study samples are typically compared when they have been milled for 30 minutes in a small-scale sand mill (Figure 2.vi).

Typically 0.4g of titanium dioxide was milled in 40ml of isopropanol using 50g of soda glass ballotini (Grade 11 Jenkins Scientific Ltd, sieved 180-212μm) and agitated in the mill at 900 rpm. The agitated glass ballotini break up the aggregates of titanium dioxide particles by collision. These relatively mild conditions have been chosen in order to minimise the formation of bulk defects reported by Heller *et al* [2] when the samples

were milled for protracted periods of time using alumina grinding materials. After milling, typically for 30 minutes, the isopropanol/titanium dioxide slurry was decanted, and the ballotini washed with isopropanol to a total volume of 50ml. The isopropanol oxidation was then carried out as described above.

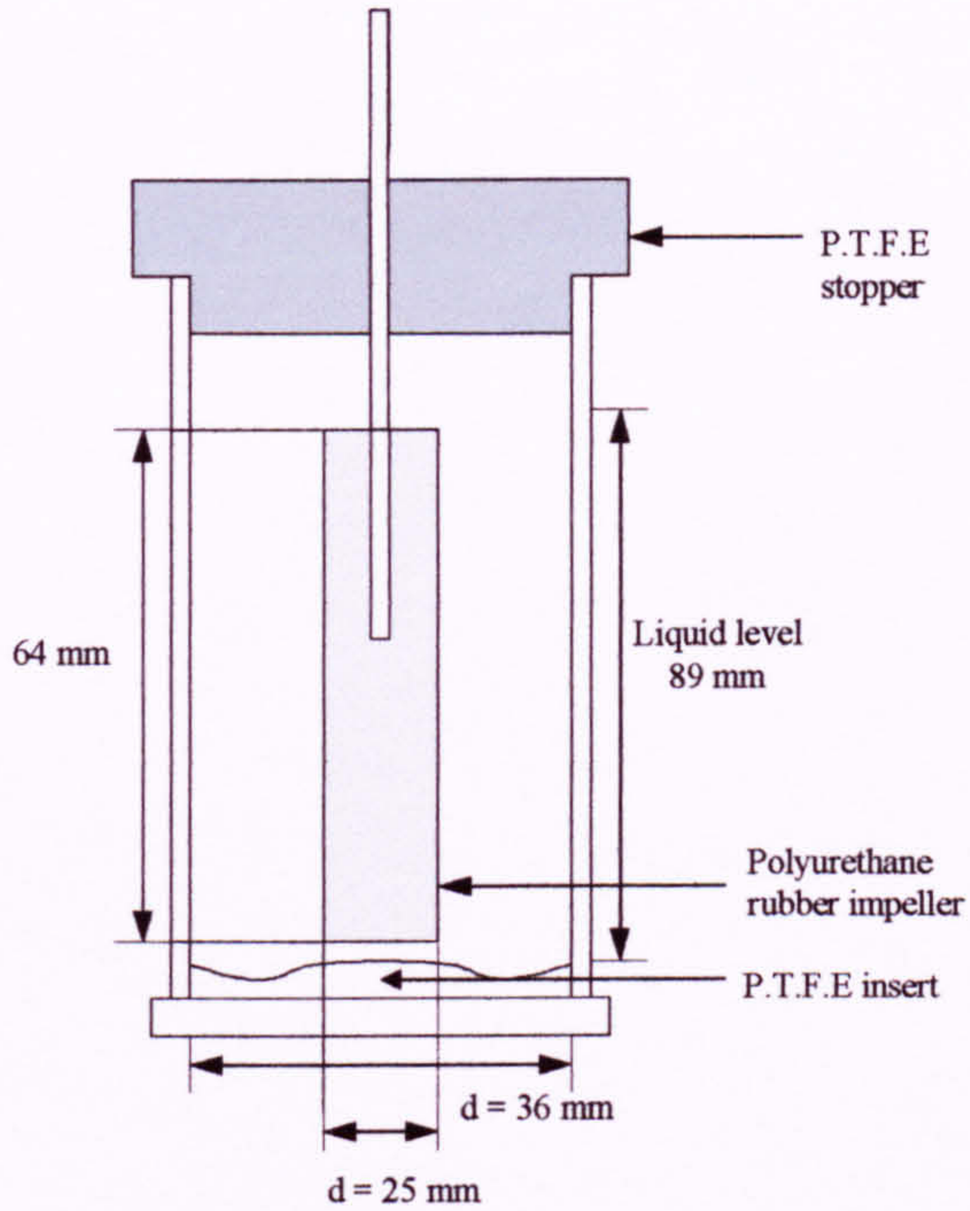

Fig 2.vi. Small sand mill used for milling titanium dioxide.

2.2.2. 2-nitrophenol degradation (NP).

Typically, the photoactivity of treated and untreated samples was determined by illumination of a slurry of 0.1g titanium dioxide in 50 ml 0.2mM 2-nitrophenol. The concentration of nitrophenol was measured rather than that of the products since several intermediates were expected to be formed based on literature reviewed in the introduction (section 1.8.1.2). The same photoreactor and light source was used for this reaction as for the isopropanol oxidation shown above (Figure 2.iiia and b), with the exception that oxygen rather than an air sparge was used. Typically, titanium dioxide samples were not typically milled for reasons described below in the Section 2.3.2.2.

UV only blanks were performed in the absence of TiO_2 to determine if 2-nitrophenol solutions were subject to photolysis under irradiation by the light sources

used. Prior to irradiation the lamp was allowed to reach full intensity by switching on for 30 mins. 50ml nitrophenol were irradiated for 150 mins with a continuous oxygen flow over the solution. 2ml samples were taken using a syringe every 30 mins. They were then injected into the HPLC for analysis (see below).

Preliminary adsorption experiments were performed to determine the time taken for the slurry to reach equilibrium to ensure that photodegradation experiments were performed at equilibrium concentration. Solutions of 50ml nitrophenol and 0.1g TiO_2 were stirred in the dark for 150 mins with a continuous oxygen flow over the slurry. In all cases, equilibrium was reached within 150 mins - the time taken was noted and used as below. The titanium dioxide was removed using a 2μm PTFE syringe filter and the nitrophenol solution was then injected into the HPLC for analysis.

Prior to illumination, solutions of 50ml nitrophenol and 0.1g TiO_2 were stirred in the dark for an appropriate time for equilibrium to be reached, for the reaction temperature to stabilise, and for the lamp to reach full intensity. During this period the slurry was sparged with a continuous flow of oxygen. Subsequently, irradiation was begun and the dispersion was continuously stirred whilst a flow of oxygen was slowly bled across the top of the suspension. Samples (2ml) of the reaction mixture were withdrawn by a hypodermic syringe through a sampling port fitted with a septum cap both immediately prior to illumination after 30 minutes, 60 minutes and then in 60 minute intervals for typically 240 minutes. The titanium dioxide was removed using a 2μm PTFE syringe filter, and the nitrophenol solution was then injected into the HPLC for analysis.

2.2.2.1 Analysis for 2-nitrophenol concentration by High Performance Liquid Chromatography (HPLC).

The degradation of nitrophenols was followed using HPLC to monitor the decrease in nitrophenol concentration. The HPLC analyser (Dionex model UVD170S HPLC) was fitted with a C_{18} reverse phase column (polar components have shorter elution time), and a UV detector. A degassed carrier solution of 40:60 v/v methanol/Millipore water with approximately 1ml of acetic acid was used and the flow rate set at 1ml min^{-1}. UV detection wavelengths were set at 210nm, 245nm, 275nm, and

410nm. Samples of 50µl were manually injected into the valve using glass syringe. A calibration plot was constructed for 2-nitrophenol over a concentration range at a wavelength of 210nm (Figure 2.vii). The signal observed was found to correspond to the appropriate concentration.

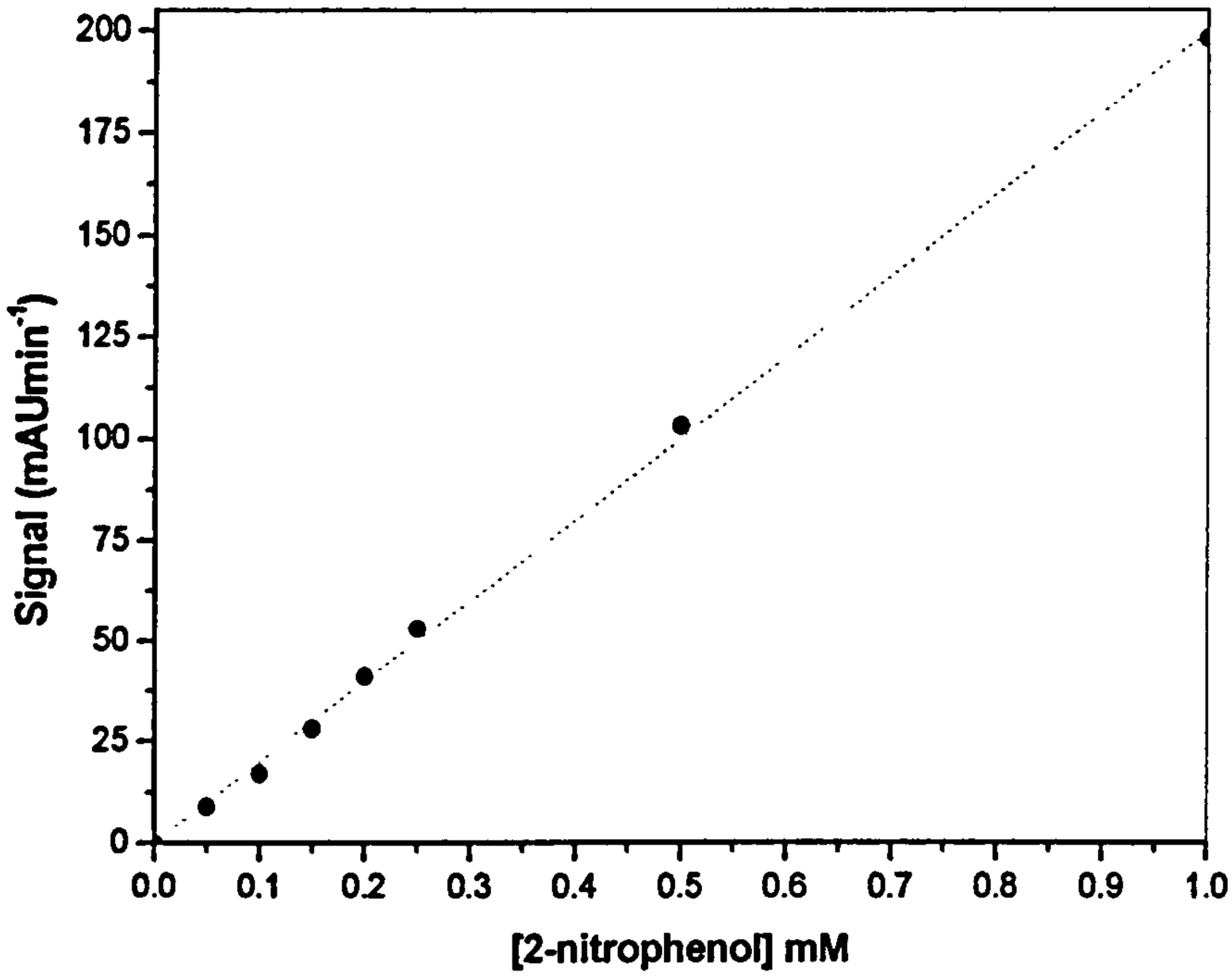

Fig 2.vii. HPLC calibration plot for 2-nitrophenol.

2.2.2.2. Sample milling procedure.

As with 2-propanol oxidation above, the effect of milling was investigated (see section 2.3.2.2) and on the basis of these results, the samples were not typically milled. For the initial investigation and for those samples that were milled the procedure is now described.

The samples were milled in the same small-scale sand mill described above (Figure 2.vi). Typically 0.1g of titanium dioxide was milled in 40ml of deionised water using 50g of soda glass ballotini (Grade 11 Jenkins Scientific Ltd, sieved 180-212µm) and agitated in the mill at 900 rpm. After milling, the water/titanium dioxide slurry was decanted, and the ballotini washed with additional deionised water to a total volume of 45ml. 5ml of 2-nitrophenol (2mM) was then added so that the 2-nitrophenol

concentration and the total volume of solution were the same as for the unmilled technique. The nitrophenol degradation was then carried out as described above.

2.2.3. Salicylic acid degradation.

Typically, the photoactivity of treated and untreated samples was determined by illumination of a slurry of 0.1g titanium dioxide in 50 ml 0.36mM salicylic acid at either pH 4 or pH 10 – altered using HCl and NaOH respectively. In a similar manner to 2-nitrophenol above, the concentration of salicylic acid was measured rather than that of the products. The same photoreactor and light source was used for this reaction as for the isopropanol oxidation shown above (Figures 2.iiia and b), with the exception that oxygen rather than an air sparge was used. Titanium dioxide samples were typically unmilled for reasons described elsewhere (see Chapter 3).

UV only blanks were performed in the absence of TiO_2 to determine if salicylic acid solutions were subject to photolysis under irradiation by the light sources used. Prior to irradiation the lamp was allowed to reach full intensity by switching on for 30 mins. 50ml salicylic acid at the appropriate pH was irradiated for 150 mins with a continuous oxygen flow over the solution. 2ml samples were taken using a syringe every 30 mins. They were then injected into the HPLC for analysis (see below).

Preliminary adsorption experiments were performed to determine the time taken for the slurry to reach equilibrium to ensure that photodegradation experiments were performed at equilibrium concentration. Solutions of 50ml salicylic acid and 0.1g TiO_2 at the appropriate pH were stirred in the dark for 150 mins with a continuous oxygen flow over the slurry. In all cases, equilibrium was reached within 150 mins - the time taken was noted and used as below. The titanium dioxide was removed using a 2μm PTFE syringe filter and the salicylic acid solution was then injected into the HPLC for analysis.

Prior to illumination, solutions of 50ml salicylic acid and 0.1g TiO_2 at the appropriate pH were stirred in the dark for an appropriate time for equilibrium to be reached, for the reaction temperature to stabilise, and for the lamp to reach full intensity. In all cases for sample A and modified versions of A, equilibrium was reached within 90 minutes, for P25 within 30 minutes - during this period the slurry was sparged with a

continuous flow of oxygen. Subsequently, irradiation was begun and the dispersion was continuously stirred whilst a flow of oxygen was slowly bled across the top of the suspension. Samples (2ml) of the reaction mixture were withdrawn by a hypodermic syringe through a sampling port fitted with a septum cap both immediately prior to illumination after 30 minutes and then in 30 minute intervals for typically 150 minutes. The titanium dioxide was removed using a 2μm PTFE syringe filter, and the salicylic acid solution was then injected into the HPLC for analysis.

2.2.3.1. Analysis for salicylic acid concentration by High Performance Liquid Chromatography (HPLC).

The degradation of salicylic acid was followed using HPLC to monitor the decrease in salicylic acid concentration. The HPLC analyser (Dionex model UVD170S HPLC) was fitted with a C_{18} reverse phase column (polar components have shorter elution time), and a UV detector. A degassed carrier solution of 50:50 v/v acetonitrile/Millipore water with pH adjusted to approximately 2 using phosphoric acid was used and the flow rate set at 1ml min^{-1}. UV detection wavelengths were set at 201nm, 234nm, 299nm, and 350nm. Samples of 50μl were manually injected into the valve using glass syringe.

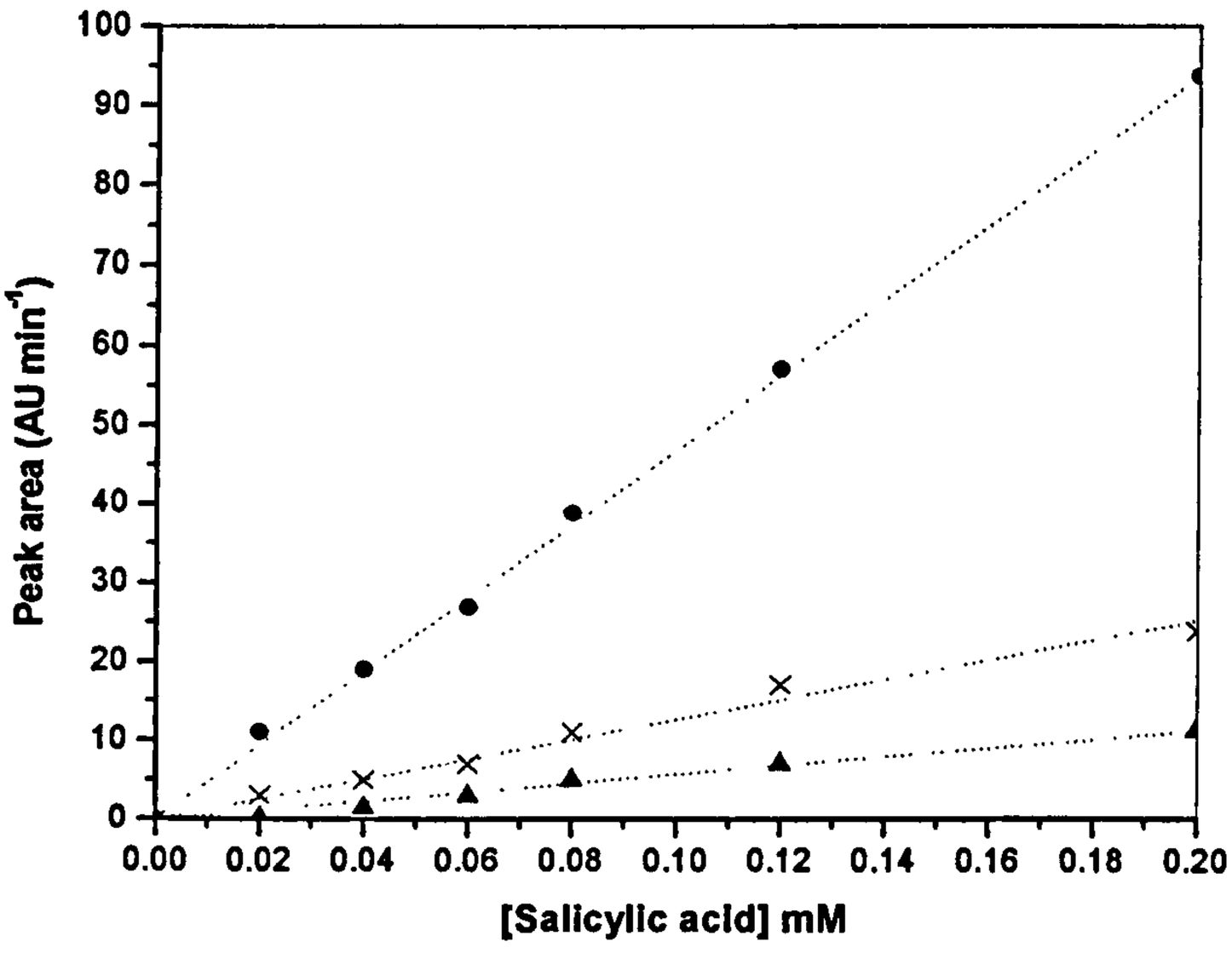

Fig 2.viii. HPLC calibration plot for salicylic acid; ● 201 nm; x 234 nm; ▲ 299 nm.

A calibration plot was constructed for salicylic acid over a concentration range at wavelengths of 201nm, 234nm and 299 nm (Figure 2.viii). The signal observed was found to correspond to the appropriate concentration; R^2 values of 0.998, 0.996, and 0.988 were achieved. The most sensitive wavelength of 201nm was typically used for calculation of the concentration.

2.2.3.2. Sample milling procedure.

As with 2-propanol oxidation and 2-nitrophenol degradation above, the effect of milling was investigated (see Chapter 3) and on the basis of these results, the samples were not typically milled. For the initial investigation and for those samples that were milled the procedure is now described.

The samples were milled in the same small-scale sand mill described above (Figure 2.vi). Typically 0.1g of titanium dioxide was milled in 40ml of deionised water using 50g of soda glass ballotini (Grade 11 Jenkins Scientific Ltd, sieved 180-212μm) and agitated in the mill at 900 rpm. After milling, the water/titanium dioxide slurry was decanted, and the ballotini washed with additional deionised water to a total volume of 45ml. 5ml of salicylic acid solution (3.6mM) was then added so that the salicylic acid concentration and the total volume of solution were the same as for the unmilled technique. The salicylic acid degradation was then carried out as described above.

2.2.4. Surface area determination by gravimetric adsorption.

The surface area of treated and untreated samples was determined by physisorption of N_2 at 77 K onto the degassed titania – the quantity of adsorbed N_2 being determined by gravimetric analysis. The surface areas were calculated using BET theory (explained fully in section 1.8.2.3.2). A schematic of the M°bain gravimetric adsorption rig kindly made available by Professor K. M. Thomas for this experiment is shown below in Figure 2.ix.

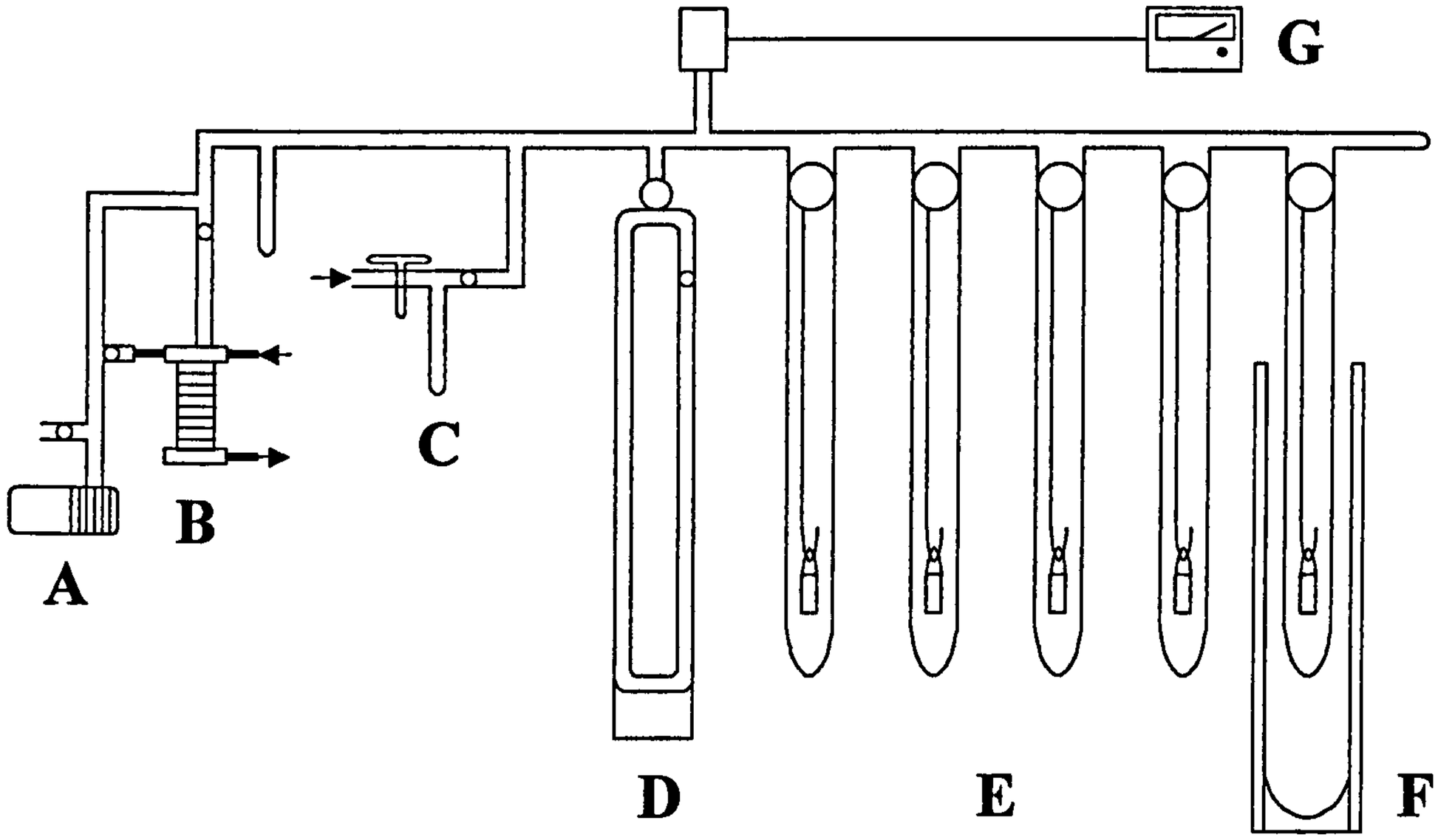

Fig 2.ix. M^{c}bain gravimetric adsorption rig. A: Rotary pump; B: Diffusion pump; C: Nitrogen inlet; D: Mercury manometer; E: Sample buckets and hangdowns; F: Vacuum dewar; G: Pirani gauge.

A known mass of sample (approx 200 mg) was placed in an aluminium bucket, suspended on a silica hangdown from a silica glass spring, and the spring extension measured using a cathetometer. This was compared to the spring extension without the sample to give the *calibration constant* for the spring i.e. the extension length per unit mass according to the equation 2.4. This procedure is repeated for each of the samples in turn.

$$\frac{\text{(extension with sample – extension without sample) (cm)}}{\text{Sample mass (g)}} \qquad \textbf{[2.4]}$$

The system was placed under a vacuum of approximately 4×10^{-2} mbar using the rotary and diffusion pumps in combination and the samples outgassed by heating under vacuum for 3 hours using isomantles set at 200°C. After allowing the samples to slowly cool to room temperature they were further cooled to 77K by addition of liquid nitrogen to vacuum dewars which were placed around the glass tubing (see Figure 2.ix. F). The samples are maintained at this temperature for the duration of the experiment. The spring extension is measured at this point ($P_{N2} = 0$) to determine the extension for the outgassed titania with no adsorbed nitrogen gas.

Nitrogen gas was introduced in typically 6-8 pressure steps over the $P/P_0 = 0.05$ to 0.35 range (~38 mmHg to 266 mmHg). After each addition 50 minutes is allowed for adsorptive-adsorbent equilibration, and the spring extensions measured using a cathetometer. The uptake of nitrogen adsorbed after equilibration of each pressure step was calculated in $mmol.g^{-1}$ and the surface area calculated by the BET method using $\sigma_{N2} = 0.162\ nm^2$ described in Section 1.8.2.3.2.

2.2.5 Fourier Transform Infra Red Spectroscopy (FTIR).

Coated and doped samples were analysed by FTIR to determine the nature of the surface species. In general samples were analysed as pressed discs by transmission spectroscopy as this was found to be sufficiently sensitive to detect changes in the titania surface groups after coating. For selected samples, in particular where the carboxyl region is of interest, transmission spectra were not judged to be sufficiently discerning and the alternative technique of Diffuse Reflectance Infra Red Spectroscopy (DRIFTS) was used. For both techniques a Bio-Rad FTS-40 Pro infrared spectrometer was used.

2.2.5.1 Transmission spectra.

The KBr background sample was prepared by pressing powdered KBr (200 mg) at 8 tonnes in a pump press for approximately 30 seconds to give a solid disc of 20 mm diameter and ~ 2-3 mm thickness. The KBr disc thus prepared was placed in the sample holder so that the IR beam passed directly through the sample. A single beam spectrum was recorded at room temperature with 100 scans and a resolution of 4 cm^{-1} between 800 – 4000 cm^{-1} using the Bio-Rad Infra Red Spectrometer. The sample discs were composed of KBr (200 mg) and a small amount of sample (typically 5 mg) and prepared as for the KBr background. Single beam spectra were recorded at room temperature with 100 scans and a resolution of 4 cm^{-1} between 800 – 4000 cm^{-1} and referenced to the single beam KBr background spectrum.

Liquids (i.e. Silanes) were analysed by transmission spectroscopy by depositing a thin layer of the sample between two calcium fluoride windows and placing the cell so that the IR beam passes directly through the sample. Single beam spectra were recorded at room temperature with 100 scans and a resolution of 4 cm^{-1} between 800 – 4000 cm^{-1} and referenced to a single beam background spectrum of the cell without sample.

2.2.5.2 Diffuse Reflectance Infra Red Spectroscopy (DRIFTS).

DRIFTS spectra were recorded using the Spectra-Tech DRIFTS assembly placed in the Bio-Rad FTS-40 Pro infrared spectrometer as shown in Figure 2.x.

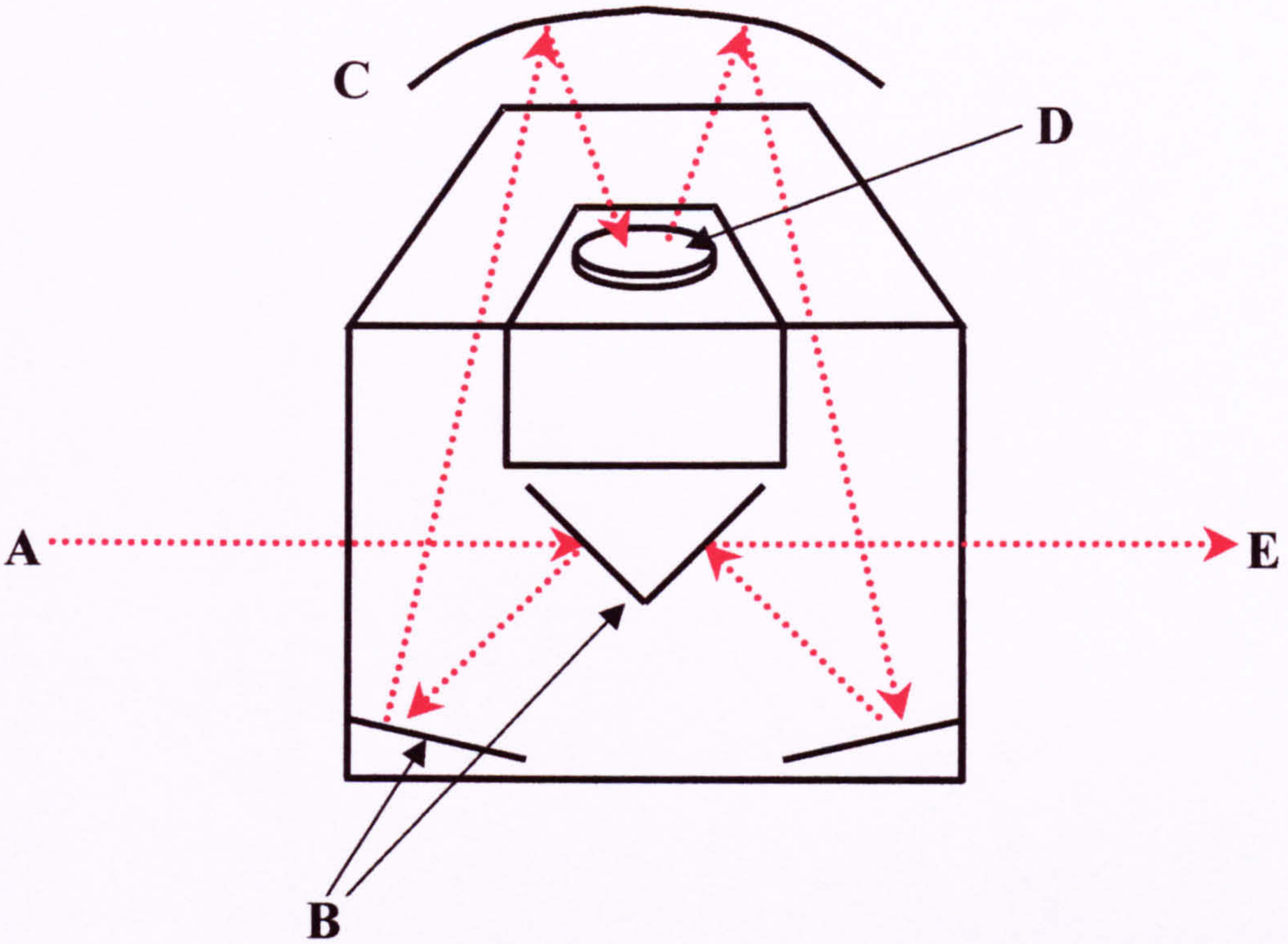

Fig 2.x. Spectra Tech DRIFTS assembly showing A: Incident IR; B: Alignment mirrors; C: Concave mirror; D: Sample cup; E: IR throughput.

Prior to the sample acquisition a small polished mirror attachment was placed in the sample cup holder and the maximum IR throughput (typically 4.5-5.5 V) achieved by adjustment of the alignment mirrors in series. KBr was placed in the sample cup (D) and excess powder brushed away so that the sample cup was full and the sample surface level. A single beam spectrum was recorded at room temperature with 100 scans and a resolution of 4 cm^{-1} between 800 – 4000 cm^{-1} using the Bio-Rad Infra Red Spectrometer. Samples were analysed by placing them in the sample cup as for KBr, with Kubelka-Munk spectra recorded at room temperature with 100 scans, a resolution of 4 cm^{-1} between 800 – 4000 cm^{-1} and referenced to the single beam KBr background spectrum.

2.2.6. Optical density (OD) measurements.

Samples were characterised by measurement of the UV/VIS spectra from 200nm to 700nm of a titania /2-propanol slurry at a sample loading of 0.4 g dm^{-3} using a 1mm far UV quartz cell in a Shimadzu UV/Vis spectrometer. Typically samples were milled for 30 minutes, the method for which is described above in section 2.2.1.2 with the exception that slurry is decanted, and the ballotini washed with isopropanol, to a total volume of 100ml, rather than 50ml, to ensure that all of the sample has been washed from the ballotini. The samples were then diluted to the required loading.

2.2.7. Powder X-Ray Diffraction (XRD).

Powder diffractograms were recorded using a Philip's X'Pert powder diffractometer system (Cu radiation, $\lambda = 0.154$ nm), scanning speed 0.03° 2θ s^{-1} and a 1 second step time between 20 – 75°. Crystal sizes were calculated from the Scherrer equation using the 2θ = 27.5° peak for rutile and 2θ = 25.4° peak for anatase. See Section 1.8.4. for relevant equations.

2.2.8. Electron Paramagnetic Resonance (EPR).

Approximately 0.2g of sample was placed in a 5mm od Spectrosil tubes, and the tube inserted into the cavity of the EPR spectrometer. Prior to recording the spectra, the Iris and the detector bias were tuned to critically couple the Microwave Bridge with the cavity. Samples were measured at room temperature between 500G - 5500G at a microwave frequency of 9.38 GHz, and with 10-15 accumulation scans.

2.3. Preliminary work to determine experimental conditions.

This section describes the preliminary work to determine appropriate conditions for the 2-propanol oxidation (IPA) and 2-nitrophenol degradation (NP) photoactivity tests using unmodified titania. In these experiments the reproducibility, and the effect of titania loading and sample milling time on measured photoactivity, was determined. The development of the aqueous salicylic acid degradation photoactivity test is shown in Chapter 3 (Section 3.10.2) with the results for this technique when used to analyse iron doped titania.

2.3.1. 2-propanol oxidation (IPA).

2.3.1.1. Effect of titania loading on the rate of acetone formation.

Separate oxidation experiments were performed as described in section 2.2.1. The samples were milled for 30 minutes prior to oxidation, and the initial titania loading was varied between 0.5 g dm^{-3} and 16 g dm^{-3} (i.e. between 0.025g and 0.8g in 50 ml of isopropanol). The rate of acetone formation (taken from the gradients of straight line plots of acetone formation against time) against titania loading for Sample A and P25 is shown in Figure 2.xi.

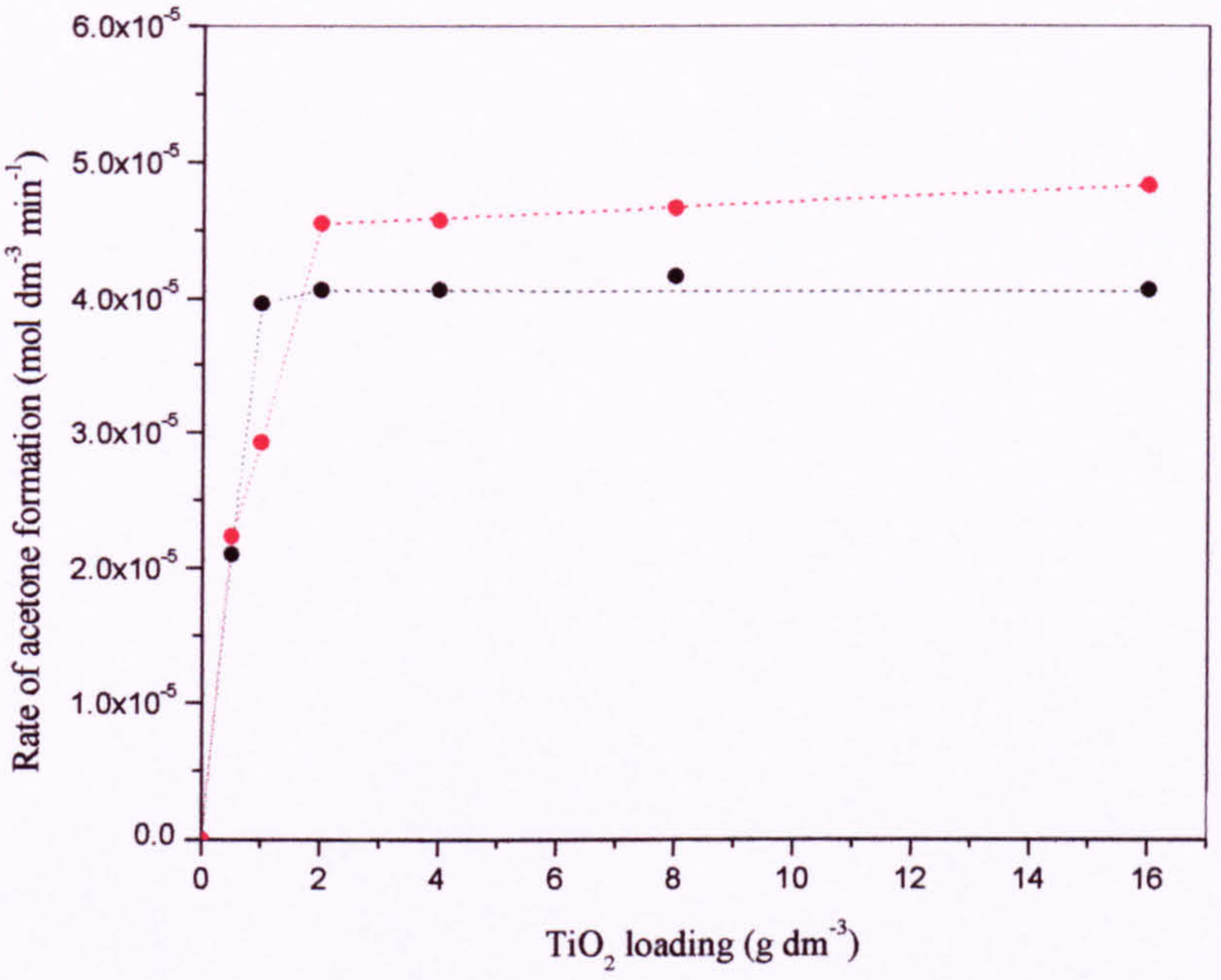

Fig 2.xi. Rates of acetone formation against titania loading for Sample A (---) and P25 (---).

As can be seen from figure 2.xi, the rates of acetone formation increase at low titania loadings for both Sample A and P25 then plateau at 1 to 2 g dm^{-1} – reasonably consistent with results by Tooley [3] for unmilled samples of the same titania. Given that the rate of reaction is relatively insensitive to titania loading between 2 - 16 g dm^{-1}, a point mid-way on the plateau of 8 g dm^{-1} (0.4 g in 50 ml isopropanol) was chosen as the typical loading for this technique.

2.3.1.2. Effect of milling time on the rate of acetone formation.

Separate oxidation experiments were performed as described in section 2.2.1 with the typical titania loading of 8 g dm^{-3}, and the milling-time of the samples varied between 0 minutes (i.e. unmilled) and 60 minutes. The normalised rate constant for acetone formation against sample mill time for Sample A and P25 is shown in Figure 2.xii.

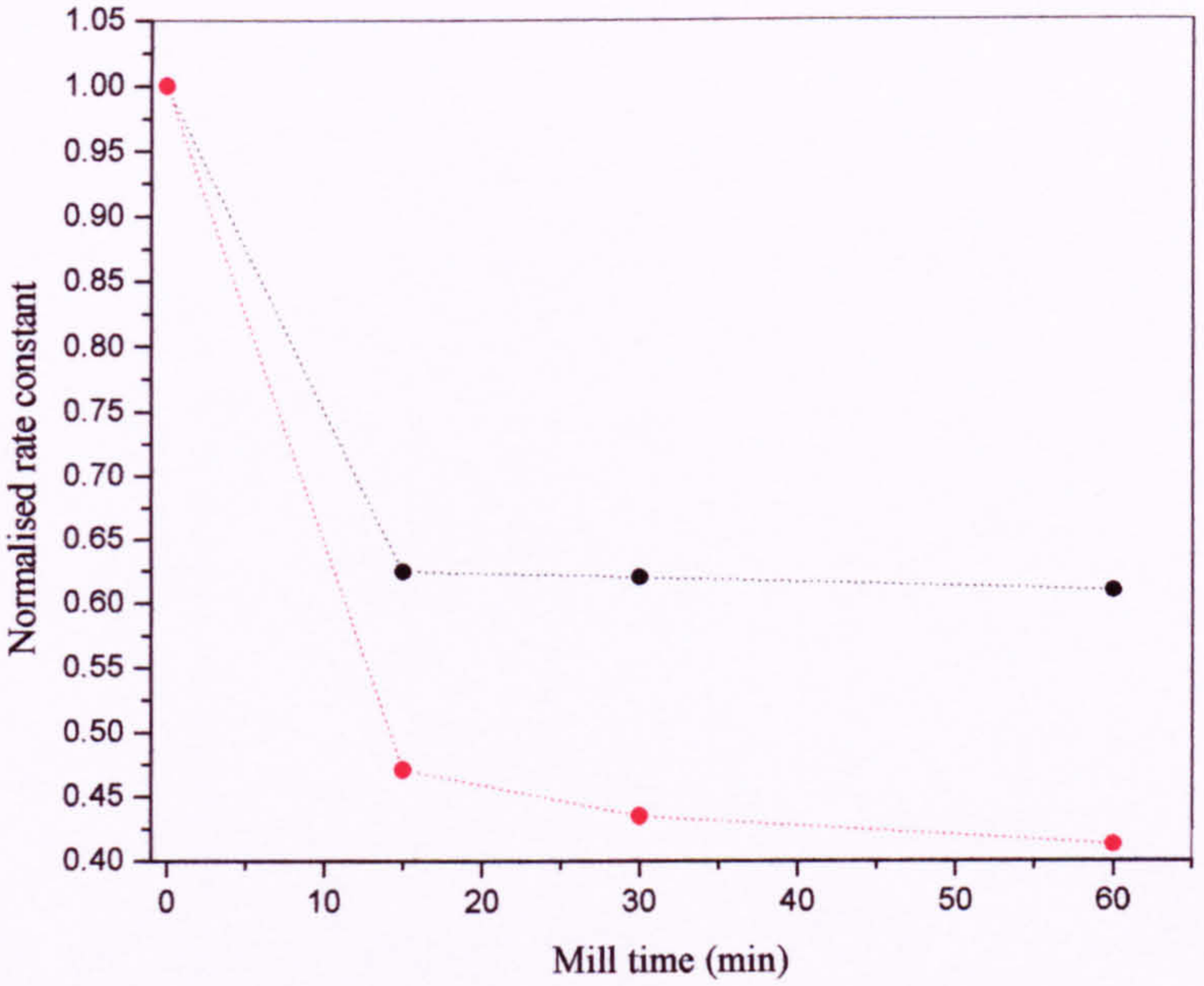

Fig 2.xii. Normalised rate constant for acetone formation against sample mill time for Sample A (---) and P25 (---).

The measured rate constant for acetone formation decreases sharply up to 15 minutes milling, with longer milling times giving at most marginal further decreases for both Sample A and P25 i.e. after 15 minutes milling the rate constant is relatively insensitive to milling time. In view of these results, a milling time of 30 minutes was chosen as the typical milling time for this technique. The dispersion theory explaining the decrease in measured photoactivity with milling is explained in section 1.5.4.4.

2.3.1.3. Reproducibility measurements.

Three separate oxidation experiments were performed (as described in section 2. 2.1) to determine the experimental reproducibility of this technique. On the basis of the results above (sections 2.3.1.1 and 2.3.1.2), the typical loading of 0.4g in 50 ml of

isopropanol (8g dm^{-3}) was used and the samples milled for 30 minutes. Plots of acetone concentration against time for Sample A are shown in Figure 2.xiii.

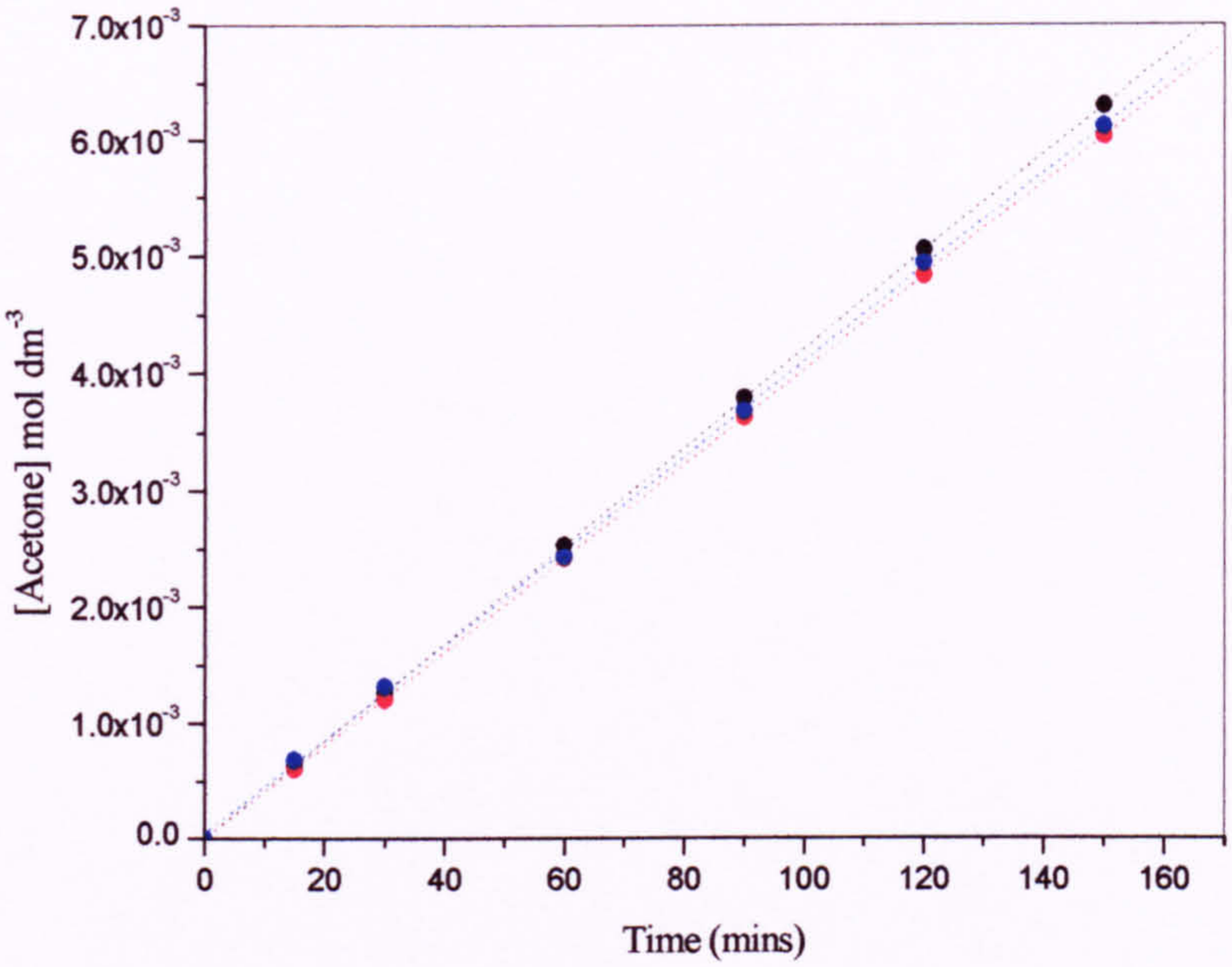

Fig 2.xiii. Acetone concentration against time for unmodified Sample A, 8g dm^{-3}, milled for 30 minutes. Three separate repeats.

The rate constants for acetone formation (gradients of the three straight line plots) for the three separate oxidation experiments show good reproducibility and are all within 2.5% of the mean. On the basis of these results an error of $\pm$ 5% reproducibility is ascribed to this technique.

2.3.2. 2-nitrophenol degradation (NP).

Although there are some instances in the literature of its application in this manner e.g. [4], 2-nitrophenol degradation is a relatively rare technique for determining titania photoactivity compared with isopropanol oxidation. This method was chosen as a suitable technique due to the wealth of published knowledge available through the study of nitrophenol degradation for environmental abatement [5-17] and also because of previous study by the author [18].

2.3.2.1 Effect of titania loading on the rate constant for nitrophenol degradation.

Separate degradation experiments were performed as described in section 2.2.2. The samples were unmilled, and the titania loading varied between 0.5 – 4 g dm^{-3} (i.e. 0.025 to 0.2 g in 50 ml 2-nitrophenol) to determine the effect of loading on the rate constant. Plots of rate constant against loading for unmilled Sample A and P25 are shown in Figure 2.xiv.

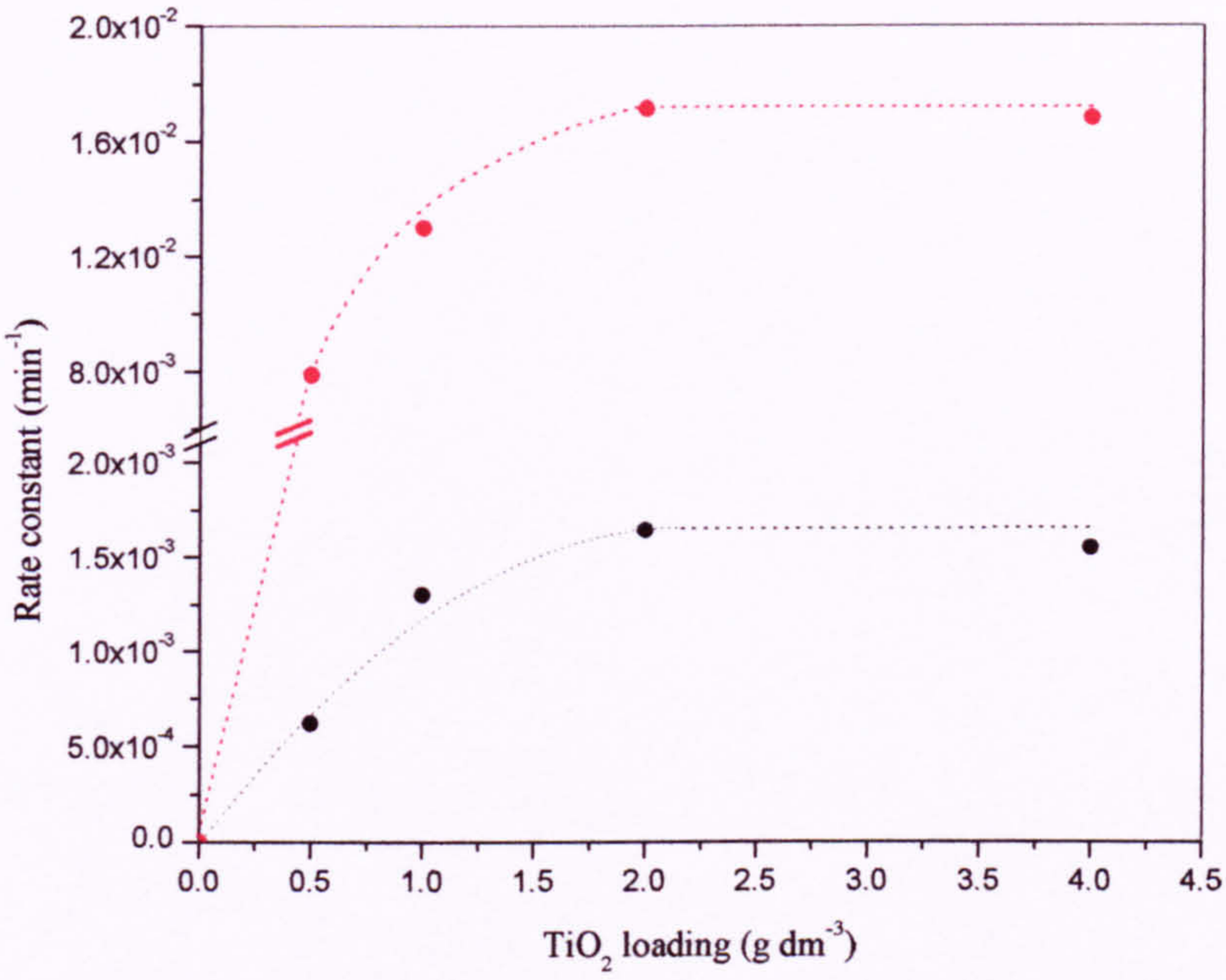

Fig 2.xiv. Rate constant for 2-nitrophenol degradation with titania loading for Sample A (---) and P25 (---).

For both Sample A and P25, the rate constant rises with loading over the 0-2 g dm^{-3} range and is then relatively insensitive to further increases. In view of this result a typical loading of 2 g dm^{-3} (0.1g in 50 ml nitrophenol) was chosen for this technique.

2.3.2.2. Effect of milling time on the rate constant for nitrophenol degradation.

Separate degradation experiments were performed as described in section 2.2.2 with the typical titania loading of 2 g dm^{-3} (1g in 50 ml 2-nitrophenol), and the milling time varied between 0 minutes (unmilled) and 60 minutes milling. The normalised rate constant for 2-nitrophenol degradation against milling time for Sample A and P25 is shown in Figure 2.xv.

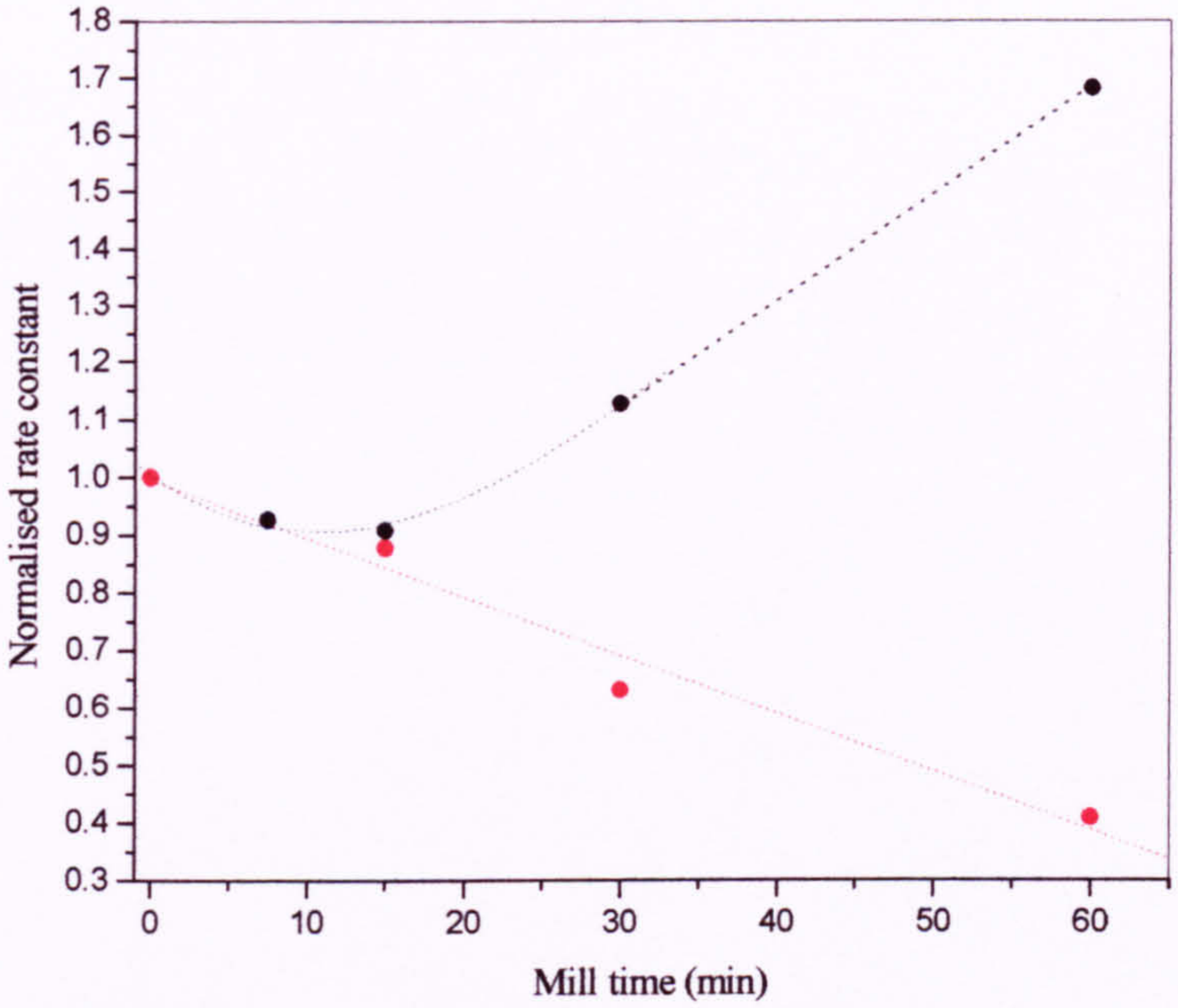

Fig 2.xv. Normalised rate constant for 2-nitrophenol degradation against sample milling time for Sample A (---) and P25 (---).

The effect of milling the titania on the measured rate constants for 2-nitrophenol degradation is different for Sample A and P25. For P25, the rate constant decreases roughly linearly with milling time and does not reach a plateau, as in the case of the analogous IPA experiments, indicating that agglomerates continue to be broken up over the milling times studied.

For Sample A, short milling times (up to 15 minutes) lead to a moderate reduction in the measured rate constant, with longer times leading to an *increase* in the rate of 2-nitrophenol degradation - in contrast to the analogous case of isopropanol oxidation that shows a reduction in rate until a plateau is reached. One possible explanation for this behaviour is that in aqueous solutions Sample A is very highly agglomerated (it rapidly settles unless stirred), and that the break up of these agglomerates leads to an increase in the number of titania photoreactors available. By contrast, in an isopropanol medium, the titania is less agglomerated and the break up of these agglomerates by milling does not lead to an increase in the number of photoreactors, instead decreasing the reaction rate due to an increase in the recombination rate caused by reduced UV penetration. See Section 1.5.4.4 for a full

explanation of the 'dispersion theory'. A full study of these unusual results was not undertaken due to time constraints, and due to the uncertain causes of this milling effects samples were not typically milled in the application of this technique.

2.3.2.3. Reproducibility measurements.

As the rate constants for reaction are of a different magnitude for the two types of titania, three separate degradation experiments were performed for both Sample A and P25 to determine the experimental reproducibly of this technique. The samples were unmilled and typical titania loadings of 2 g dm^{-3} were used on the basis of the results above (sections 2.3.2.1 and 2.3.2.2). Plots of ln C/Co against time for the three repeats are shown in Figure 2.xvi and Figure 2.xvii for Sample A and P25 respectively.

For both Sample A and P25 there is reasonable reproducibility between the three separate repeats with all rate constants within 5% of the mean. On the basis of these results a $\pm$10% error is assigned to this technique for analysis of both types of titania. Note that in the case of P25, the rate constants are calculated for ln C/Co values between 0 and –2, i.e. up to ~ 90% 2-nitrophenol degradation. Beyond this there is significant deviation from linearity, which has been attributed to a reduction in UV absorption by the 2-nitrophenol resulting in a greater fraction absorbed by the titania [17, 18].

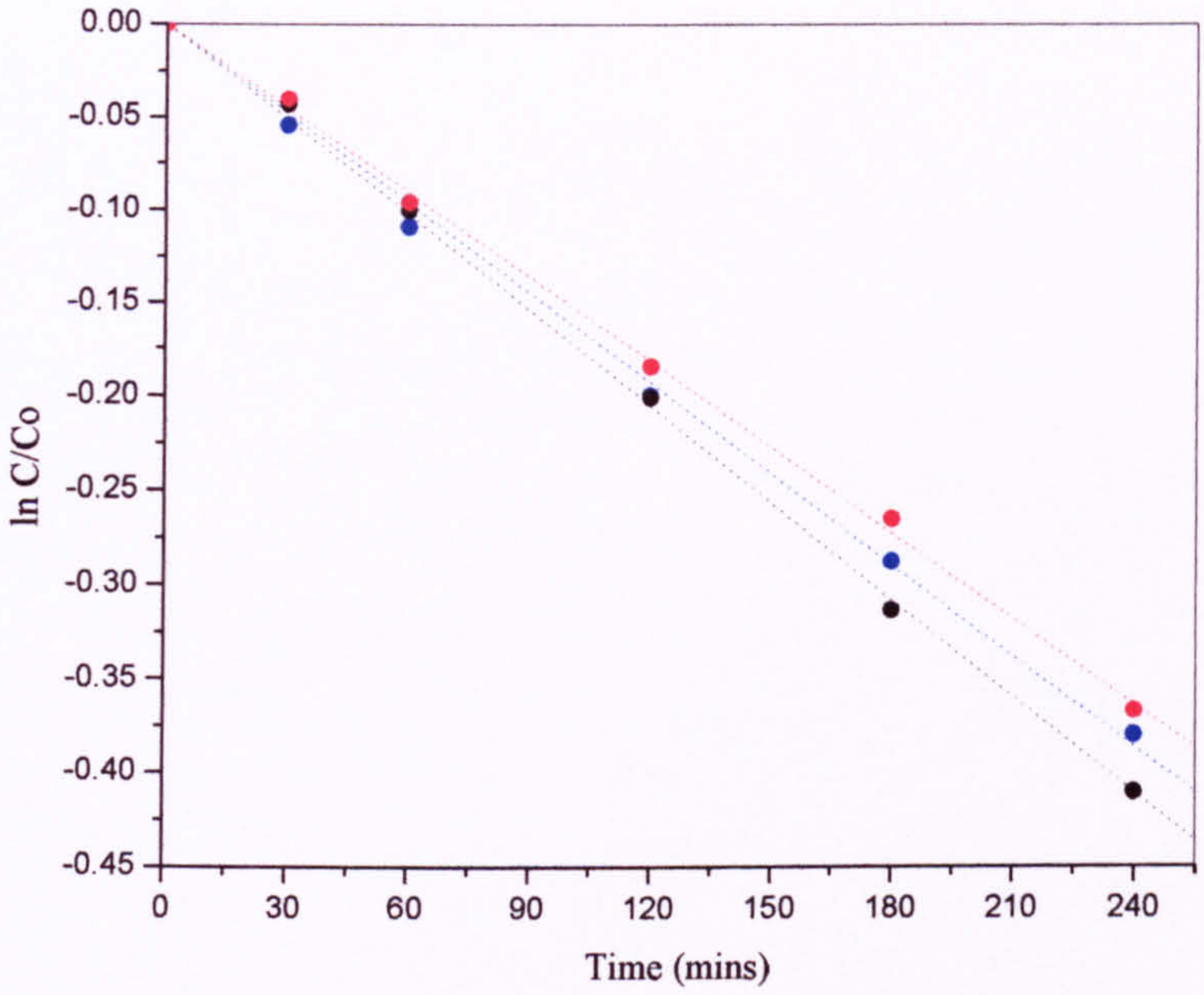

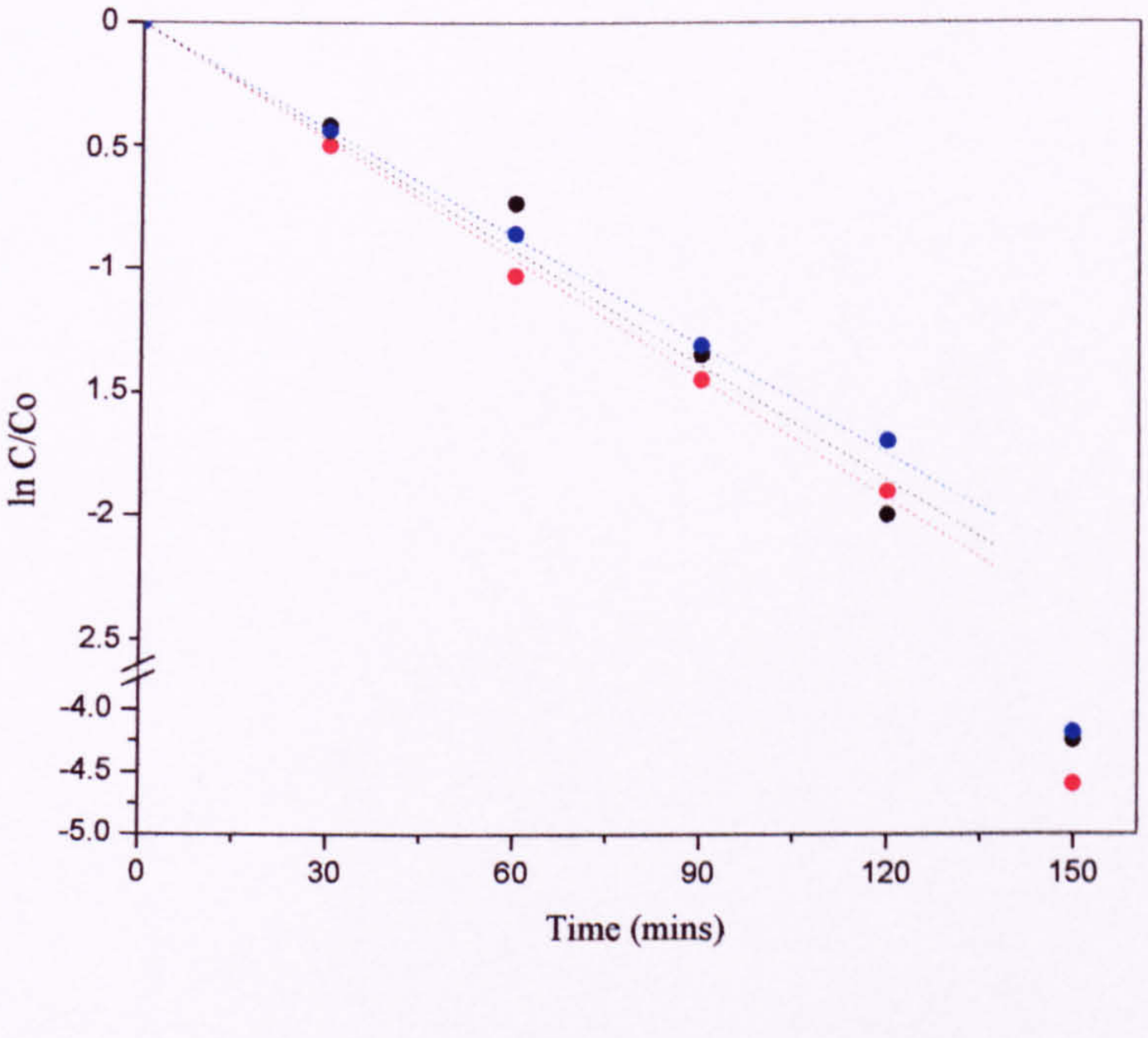

Figure 2.xvi and 2.xvii. ln C/Co against time for three repeats of Sample A (top) and P25 (lower); titania loading 8 g dm^{-3}, unmilled.

2.3.3. Conclusions – preliminary work to determine experimental conditions.

The main conclusions of this preliminary work are:-

1. For isopropanol oxidation (IPA) for both loading and milling experiments a plateau was reached. A typical loading of 8 g dm^{-3} and a milling time of 30 minutes lie on the plateau and were chosen for use of the technique. Reproducibility was $\pm$5%.
2. For nitrophenol 2-degradation (NP), a plateau was reached for the loading experiments and a loading of 2 g dm^{-3} was chosen. Due to the unusual effect of milling on the rate constant, samples were typically analysed unmilled by this technique. Reproducibility was reasonable at $\pm$10%.

2.4. Appendices.

A2.1. Sample coating level calculation.

Sample calculation for coating Sample A with a quantity of Arlatone Map 160K (AM160K) sufficient to cover 25% of the surface (Sample A 25% AM160K). The cross sectional area of AM160K (M_r = 398 $g.mol^{-1}$) is taken to be 0.3 nm^2 (assuming the molecule bonds to the titania surface linearly through the phosphate headgroup i.e. $\sigma[AM160K] \approx \sigma[PO_4^{3-}]$) and the surface area of Sample A 130 $m^2.g^{-1}$.

Therefore 1 molecule AM160K occupies 3×10^{-19} m^2

Therefore 1 mole AM160K occupies $(3 \times 10^{-19}\ m^2).(N_A) = 1.8 \times 10^5\ m^2$.

For a 25% coverage on 1g TiO_2: $(0.25) \times (130\ m^2)/(1.8 \times 10^5\ m^2.mol^{-1})$

$= 1.81 \times 10^{-4}$ moles.

= 0.0719 g are required to coat 25% of the surface area of 1g Sample A.

or four times this quantity to form a monolayer (100%) coating (0.288g).

i.e. a monolayer requires a 29% by mass coating.

2.5. References.

1. T. A .Egerton and I. R. Tooley, *J. Phys. Chem B*, **2004**, *98*, 5066.
2. A. Heller; Y. Degani; D. W. Johnson; P. K. Gallagher, *J. Phys. Chem*, **1987**, *91*, 5987.
3. I. R. Tooley, PhD Thesis, University of Newcastle Upon Tyne, Newcastle Upon Tyne, NE1 7RU, **(2002)**.
4. L. Palmisano; S. Sciavello, A. Sclafani; C. Martin; I. Martin; V. Rives, *Cat. Lett*, **1994**, *24*, 303.
5. T. A. Egerton, 'UV absorption by nitrophenol: implications for design of photocatalytic and photoelectrocatalytic reactors'. In *Proceedings of TiO_2-9 and AOT-10*, San Diego, **2005**.
6. K. Tenaka; W. Luesaiwong; T. Hisanaga, *J. Mol. Cat*, **1997**, *122*, 67.
7. K. Wang; Y. Hsieh; L. Chen, *J. Haz. Mat*, **1998**, *59*, 251.
8. M. Ksibi; A. Zemzemi; R. Boukchina, *J. Photochem. Photobiol A*, **2003**, *159*, 61.
9. V. Augugliarno; M. J. Lopez-Munoz; L. Palmisano; J. Soria, *Applied Cat A*, **1993**, *101*, 7.
10. V. Augugliarno; L. Palmisano; M. Schiavello; A. Sclafani; L. Marchese; G. Martra; F. Miano, *Applied Cat*, **1991**, *69*, 323.
11. D. Chen; A.K. Ray, *Wat. Res*, **1998**, *32*, 3223.
12. R. Andreozzi; V. Caprio; A. Insola; G. Longo; V. Tufano, *J. Chem. Tech. Biotech*, **2000**, *75*, 131.
13. N. San; A. Hatipoglu; G. Kocturk; Z. Cinar, *J. Photochem. Photobiol A*, **2002**, *146*, 189.
14. J. Lea; A. A. Adesina, *J. Chem. Tech. Biotech*, **2001**, *76*, 803.
15. V. Maurino; C. Minero; E. Pelizzetti; P. Piccinini; N. Serpone; H. Hidaka, *J. Photochem. Photobiol A*, **1997**, *109*, 171.
16. D. Chen; A. K. Ray, *Applied Cat B*, **1999**, *23*, 143.
17. T. A. Egerton; P.A. Christensen; R. W. Harrison; J. W. Wang, *J. Appl. Electrochem*, **2005**, *35*, 799.
18. R. W. Harrison, MPhil Thesis, University of Newcastle Upon Tyne, Newcastle Upon Tyne, NE1 7RU, **(2001)**.

3. IRON DOPING OF TIO2.

This chapter describes the analysis of iron doped titanium dioxide. The effect of lattice doping Sample A by coprecipitation and surface doping by precipitation was examined while Degussa P25 was surface treated by the precipitation method only - the procedures are described in section 2.1.3 and 2.1.4 for coprecipitation and precipitation respectively. Samples are referred to by the TiO_2 type (Sample A, or P25) followed by the method (Coprecipitation, C, or precipitation, P) and then the level expressed as an atom percentage. For example, "A/C/0.1%" refers to Sample A bulk doped with 0.1% iron by coprecipitation. Coating levels are expressed as a percentage of the amount of coating required to cover the entire titania surface. For example, "P25/66%/acetate" refers to a sample of P25 coated with a quantity of acetate to cover 66% of the titania surface. Also described is the development of a new test to determine the rate of degradation of a model compound by direct electron transfer, rather than hydroxyl mediated oxidation as in the case of isopropanol or 2-nitrophenol, together with the results of this test to determine the photoactivity of the surface and lattice iron doped Sample A.

3.1. Introduction.

There is a significant body of published work on the effect of iron doping on titanium dioxide [1]. The majority of these studies deal either with large pigmentary sized particles or with anatase; where the samples are doped to improve the photoactivity, whereas relatively little work has been done on high area rutile samples. The comparison of the high area rutile with Degussa P25 provides a useful link to the main body of literature. A flaw in some of these studies is that high temperature calcination alters the crystal morphology, size, and surface area, which will affect changes in the photoactivity and in addition, different conclusions were reached dependent on the method for measuring photoactivity. Karvinen [2] found significant changes in the crystal properties of titanium dioxide by doping with several transition metals (including iron). In the present study, the doping method was careful chosen to minimise these changes and thus represents a consistent examination of the effect of iron doping on the titanium dioxide photoactivity measured by several methods.

3.2. Effect of surface iron doping on photoactivity measured by IPA.

Isopropanol oxidation was used to determine the photoactivity of surface iron doped Sample A and P25 as explained in section 2.2.1, and for these oxidation experiments a typical titania concentration of 8 g dm^{-3} was used. Plots of acetone concentration against time for unmilled samples of Sample A and P25 doped with increasing amounts of iron are shown in Figure 3.i and 3.ii respectively. The acetone concentrations for unmilled, undoped samples are shown for comparison.

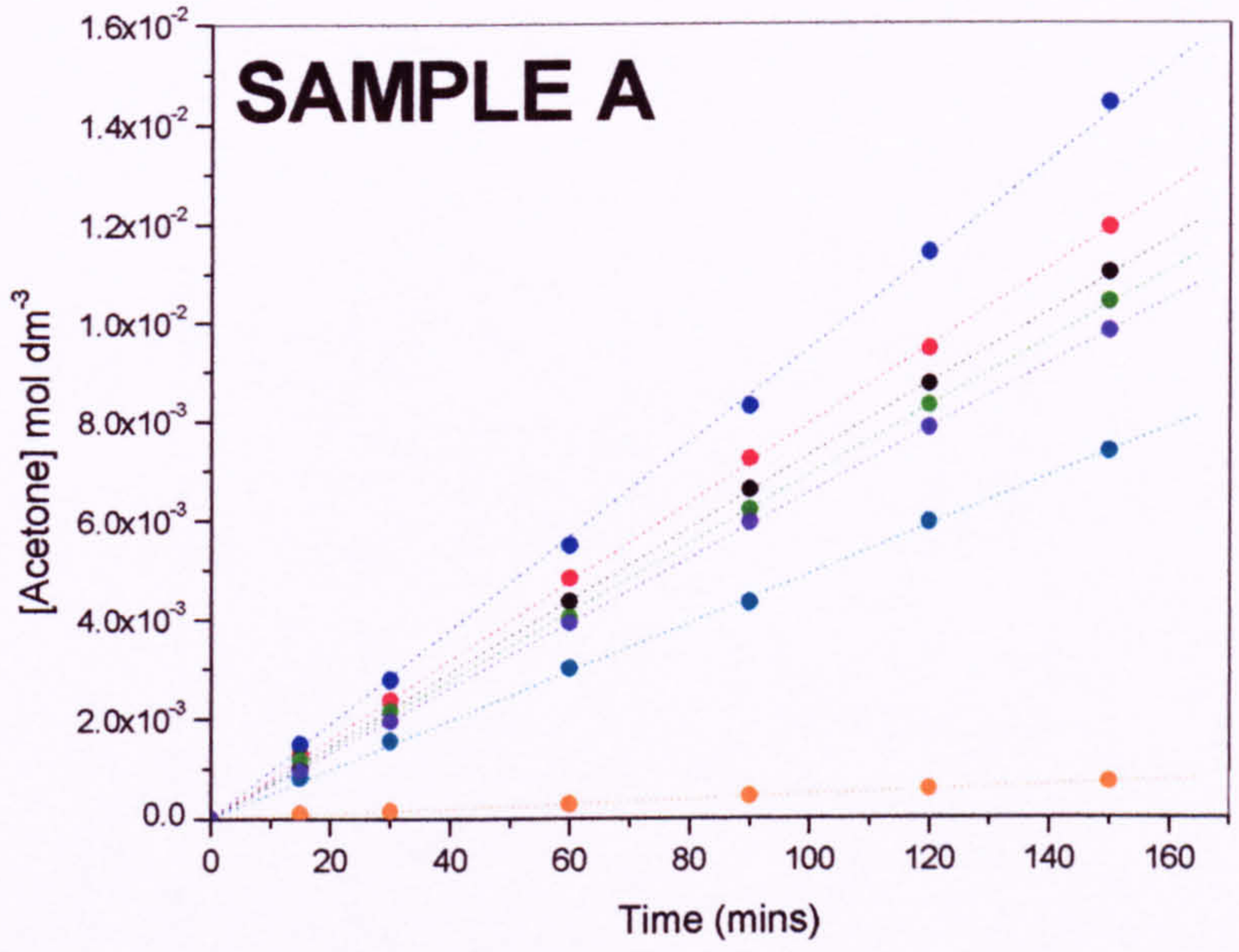

Fig 3.i. Acetone concentration against time for surface iron treatment by precipitation for Sample A. --- 0.001%; --- 0.005%; --- 0.01%; --- 0.1%; --- 1%; --- 5%; --- Untreated sample.

The rates of acetone formation against treatment level (log scale) for surface iron doped samples are shown in Figure 3.iii. The rate constant for undoped samples is shown for comparison (horizontal lines). The reproducibility for this technique is within $^{+}5\%$.

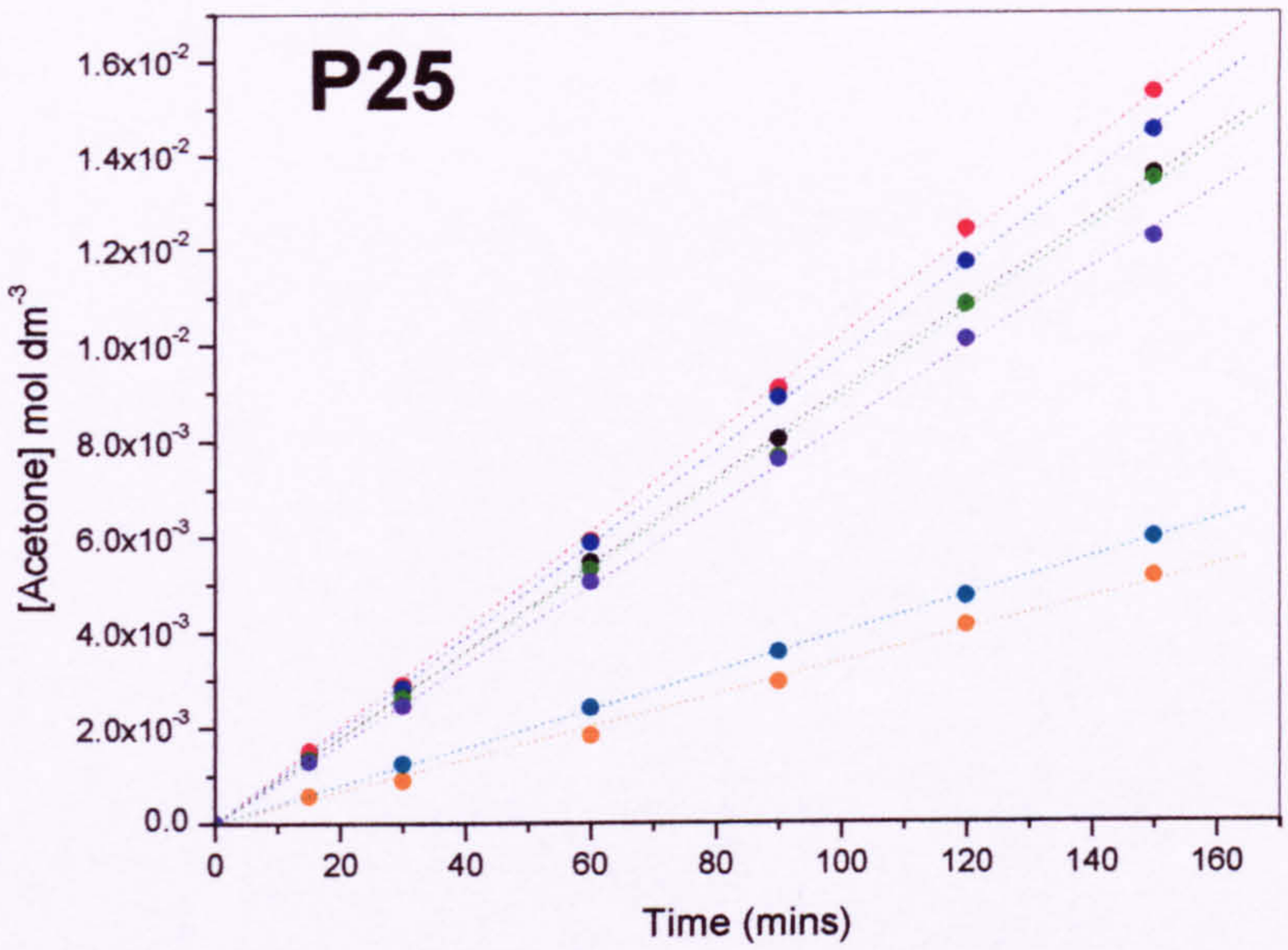

Fig 3.ii. Acetone concentration against time for surface iron treatment by precipitation for P25. --- 0.001%; --- 0.005%; --- 0.01%; --- 0.1%; --- 1%; --- 5%; --- Untreated sample.

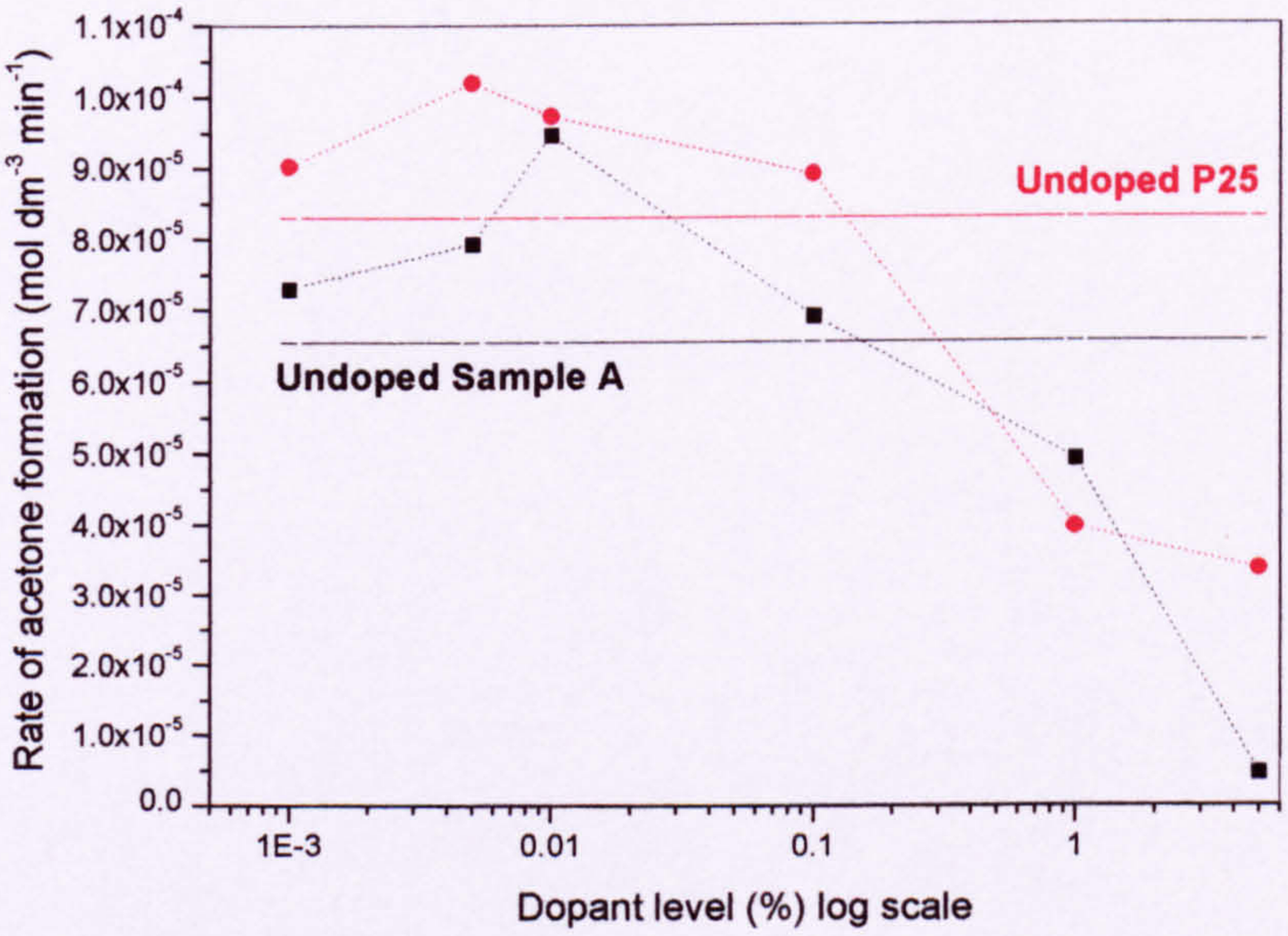

Fig 3.iii. Rates of acetone formation for unmilled surface iron doped samples. --- Sample A; --- P25. Horizontal lines (undoped samples).

As can be seen from Fig 3.iii, the effect of surface doping both Sample A and P25 is to increase the photoactivity at low levels of iron i.e. between 0.001% and 0.1% and to decrease the photoactivity at higher levels. Whilst this trend would be expected (see discussion, section 4.2) it could be argued that an increase in the photoactivity could be caused by particle agglomeration during the doping procedure. An increase in particle agglomeration results in increased penetration of light into the slurry and thus a higher measured photoactivity as the UV is absorbed by a higher number of titania particles, suppressing charge recombination [3]. To preclude this possibility, the same oxidation experiments were repeated with the titania samples milled for 30 minutes prior to oxidation to break up the agglomerates and give a similar state of dispersion, and thus a similar penetration of UV, for the uncoated and coated samples - this argument is explained more fully in section 1.5.4.4. Plots of acetone concentration against time for milled surface doped Sample A are shown in Fig 3.iv.

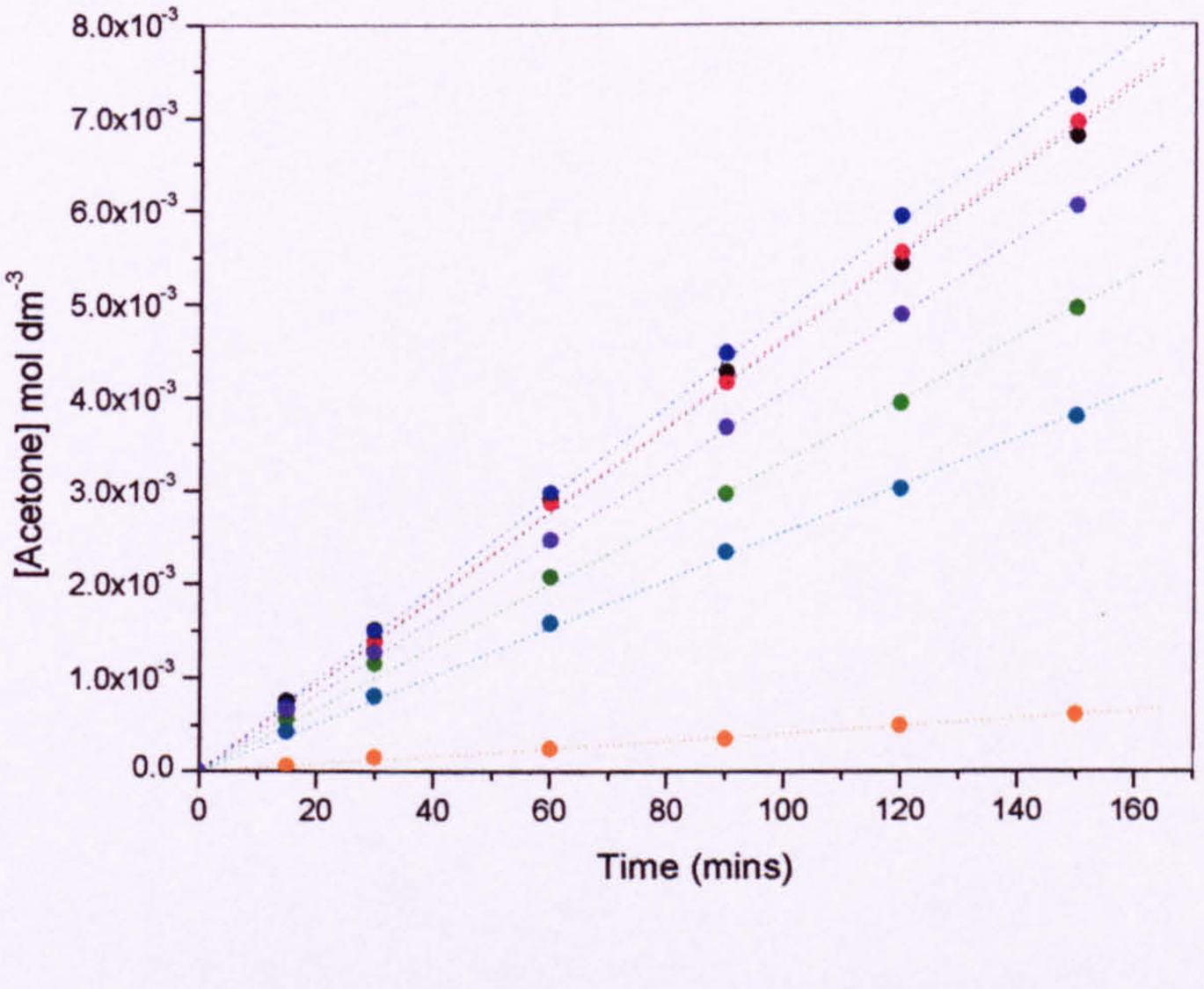

Fig 3.iv Acetone concentration against time for surface iron doping by precipitation for milled Sample A. --- 0.001%; --- 0.005%; --- 0.01%; --- 0.1%; --- 1%; --- 5%; --- Untreated sample.

Rates of acetone formation against treatment level for surface iron doped Sample A and P25 are shown in Figure 3.v with the rate constants for undoped samples that have been similarly milled shown as horizontal lines for comparison.

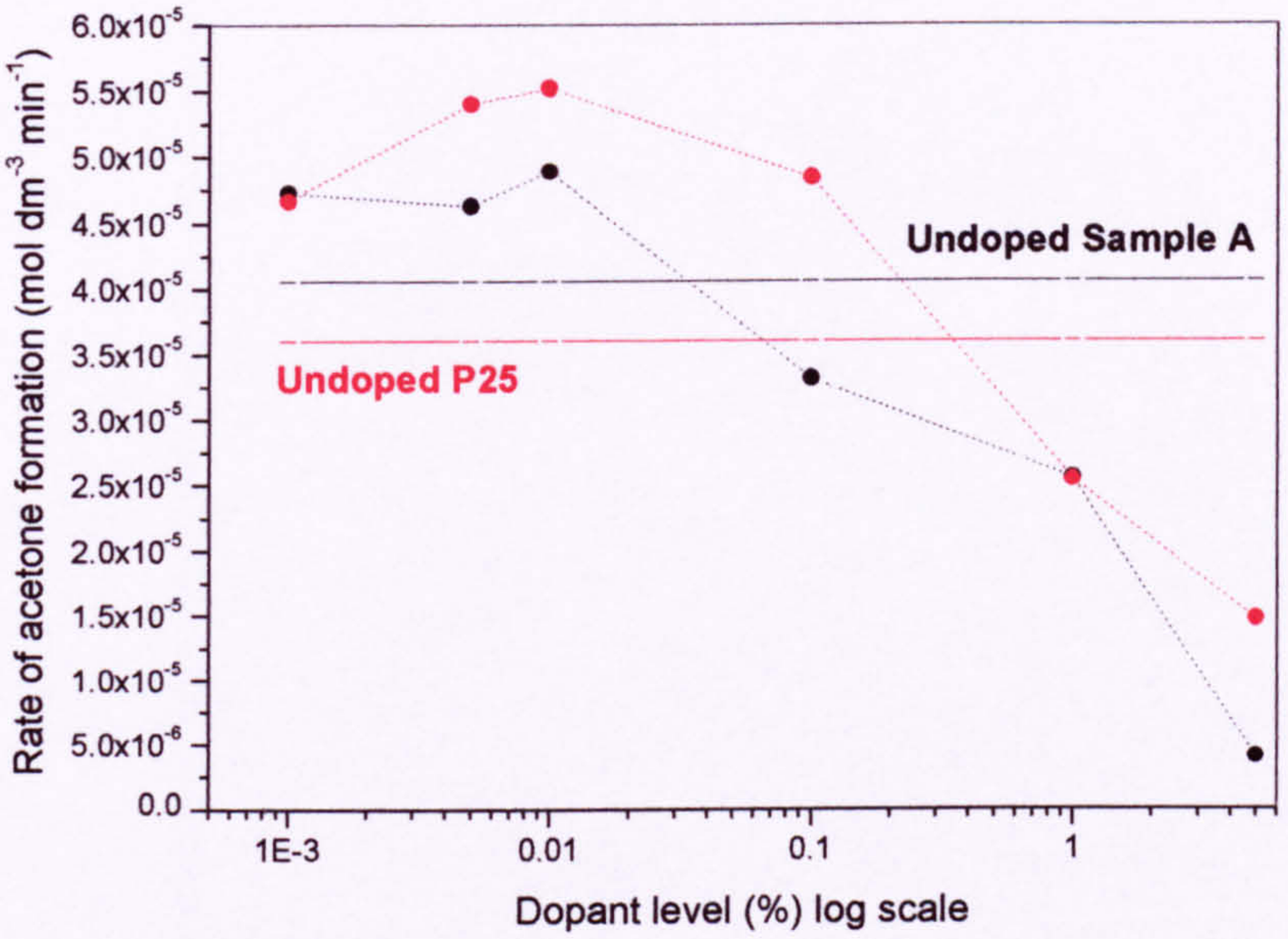

Fig 3.v. Rates of acetone formation for unmilled surface iron doped samples. --- Sample A; --- P25. Horizontal lines represent undoped samples.

As can be seen by comparing Fig 3.v with Fig 3.iii the effect of milling was to lower the photoactivity for all the samples by breaking up the agglomerates as explained above. However, the same overall trends for the effect of surface iron doping are seen as for the unmilled samples i.e. at low levels of doping the photoactivity is enhanced and at higher levels reduced. It can therefore be concluded that any agglomeration caused by the iron treatment does not significantly affect the photoactivity. Although agglomeration does not affect this general trend, the photoactivity of iron doped Sample A is reduced relative to the undoped sample by milling indicating that it does have an effect on the relative photoactivities i.e. while milling reduces the observed photoactivity for all samples, the photoactivity of the iron doped samples is reduced by a relatively greater degree.

3.3. Effect of surface iron doping on photoactivity measured by NP.

In order to compare the effect of surface iron doping on the photoactivity in IPA with the photoactivity measured in a totally different aqueous, surface iron doped Sample A and P25 were tested for photoactivity by nitrophenol degradation as explained in section 2.2.2, and for these experiments the typical titania concentration of 2 g dm^{-3} was used. Plots of ln C/Co against time for unmilled samples of Sample A and P25 are shown in Figure 3.vi and 3.vii respectively. The comparable plots for unmilled samples are shown for comparison. The measured rate constants for nitrophenol degradation with P25 are of the order of ten times greater than with Sample A.

The rate constants for nitrophenol degradation against dopant level (log scale) for surface iron doped samples of sample A (left hand scale) and P25 (right hand scale) are shown in Figure 3.viii. The rate constant for undoped samples is shown for comparison (horizontal lines). The reproducibility for this technique is within $^{+}$5%.

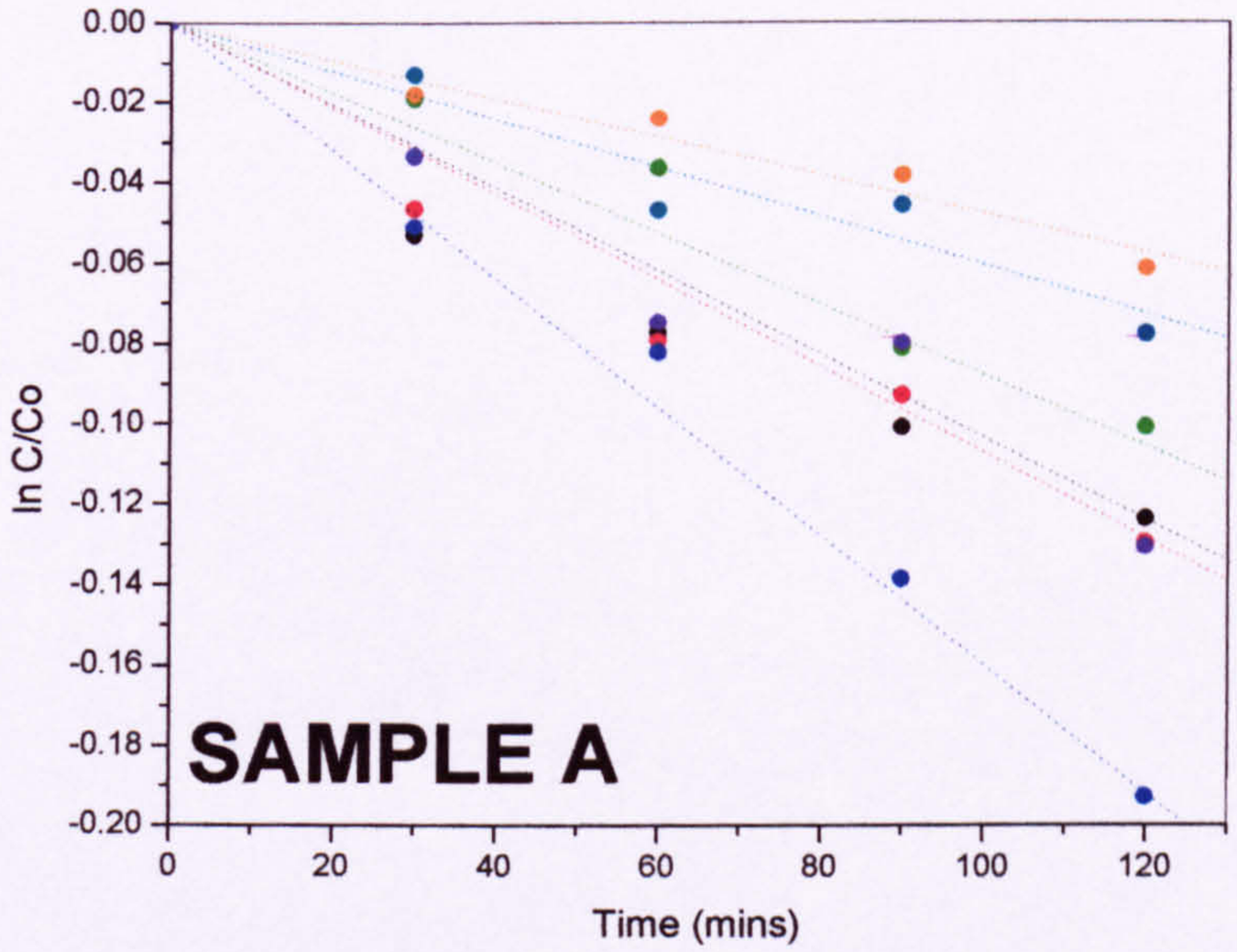

Fig 3.vi and 3.vii. ln C/Co against time for surface iron treatment by precipitation for Sample A (above) and P25 (below). --- 0.001%; --- 0.005%; --- 0.01%; --- 0.1%; --- 1%; --- 5%; --- Untreated sample.

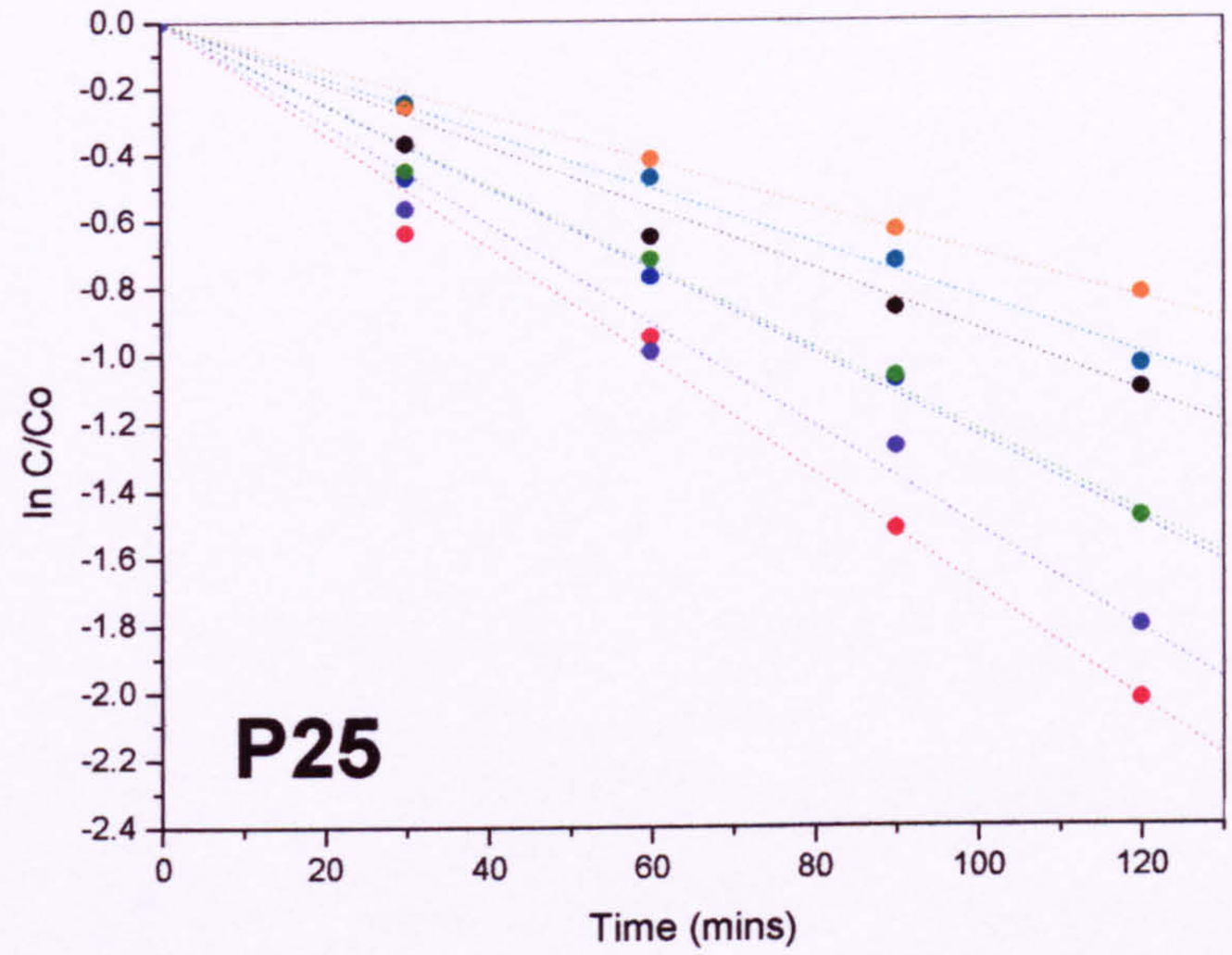

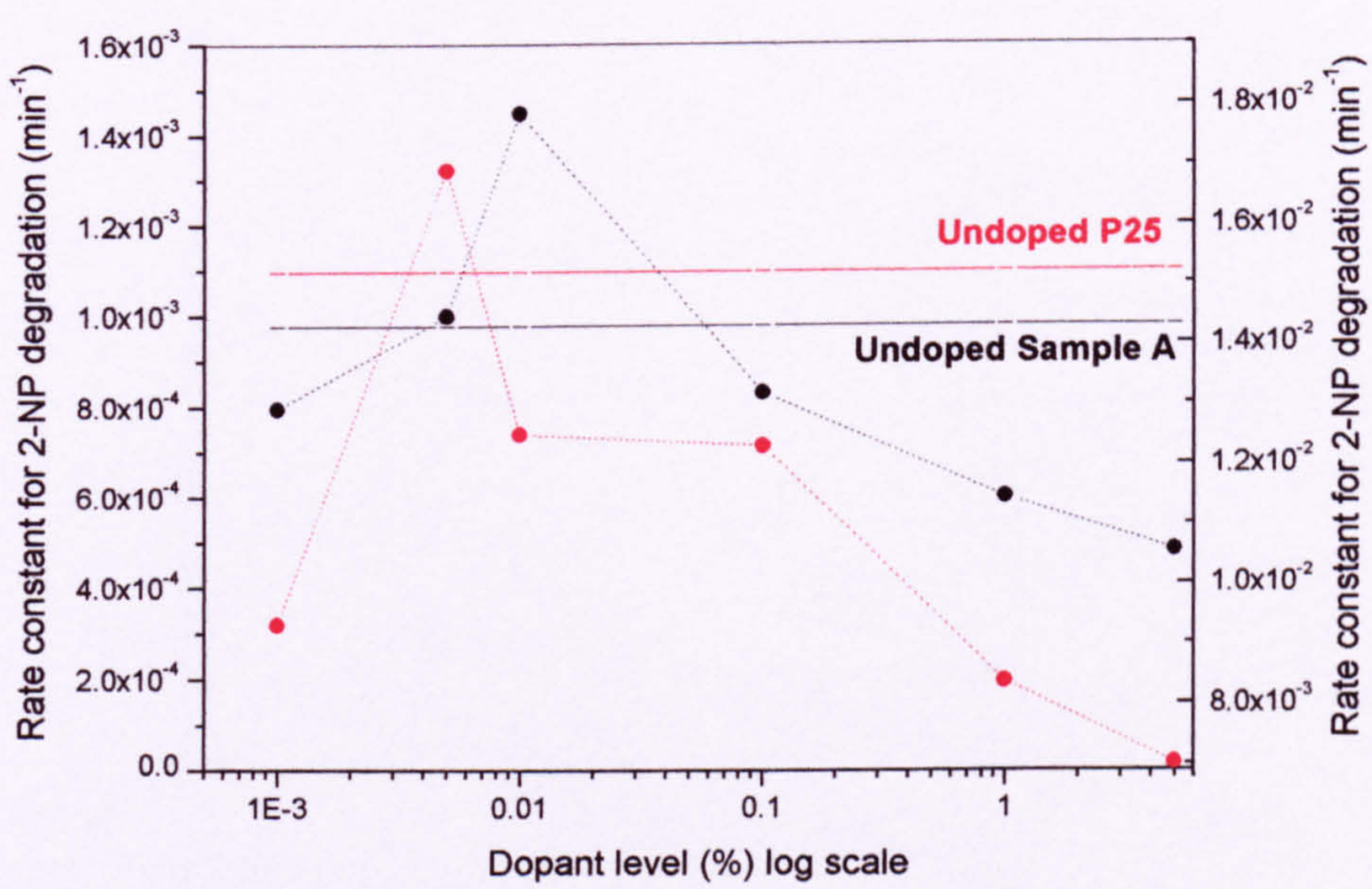

Fig 3.viii. Rate constants for nitrophenol degradation against dopant level. Sample A --- left hand scale; P25 --- right hand scale Horizontal lines represent undoped samples in both cases.

As can be seen from Fig 3.viii the effect of surface doping both Sample A and P25 was increased photoactivity at an optimum (low) level, reduced at higher levels, and either reduced or unaffected at dopant levels less than this optimum. In general, when measured by this technique, the photoactivity of doped P25 is proportionally lower than doped Sample A when compared to the undoped titania. It was not desirable to mill the samples in aqueous media to break up any agglomerates as explained in section 2.3.2.2. However, since the effect of iron doping on the photoactivity measured by NP follows similar trends to that for IPA the unmilled results for this technique can be considered to be sufficiently valid.

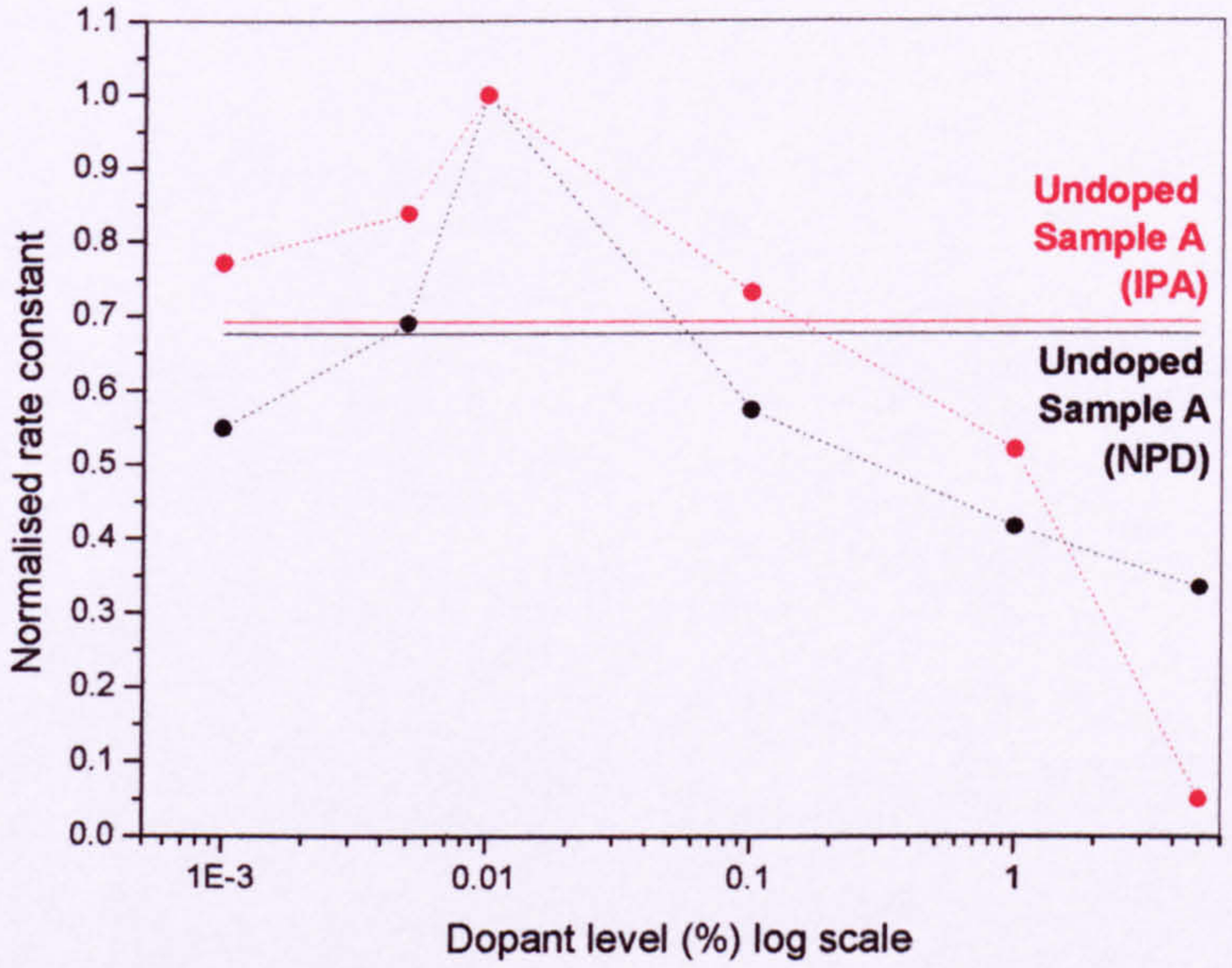

Fig 3.ix. Comparison of the rates of degradation of surface iron doped Sample A as measured by NP --- and IPA --- Rate constants are normalised to the maximum at the dopant level of 0.01%

Fig 3.ix compares the effect of surface iron doping of Sample A on the photoactivity measured by the IPA method with that for nitrophenol degradation (NP) for unmilled samples - in both cases the rate constants have been normalised to that for the common optimum level of 0.01%. There is a reasonable correlation between the two

methods, although in general the measured photoactivity was lower for the aqueous NP method. This suggests that surface iron treatment is more effective at reducing the photoactivity in aqueous solution than in isopropanol.

3.4. Effect of lattice iron doping by coprecipitation on photoactivity measured by IPA and NP.

Isopropanol oxidation (IPA) and nitrophenol degradation (NP) were then used to determine the photoactivity of lattice iron doped Sample A by coprecipitation as described in section 2.2.1 – as explained, it was not possible to lattice dope P25 in a similar manner. The typical titania concentration for these experiments of 8 g dm^{-3} and 1 g dm^{-3} respectively was used. Plots of acetone concentration against time (IPA) and ln C/Co (NP) for unmilled samples are shown in Figure 3.x and 3.xi respectively. The corresponding plots for unmilled samples are shown for comparison.

Fig 3.xii compares the effect of lattice doping of sample A on the photoactivity as measured by NP and IPA for unmilled samples, and the effect of milling for 30 mins measured by IPA. For ease of comparison, the rate constants are normalised in every case to that for the undoped Sample A, the black dotted horizontal line is the undoped rate constant for all three plots. When measured by both IPA and NP the same trends are observed in both methods of measurement - there is a maximum photoactivity at a dopant level of 0.01% and a sharp decrease at higher levels. However, the photoactivity measured by IPA is lower than the undoped Sample A at all levels, while for NP it is only lower for the higher dopant levels i.e. the iron is not as effective at lowering the photoactivity in aqueous solution as in isopropanol.

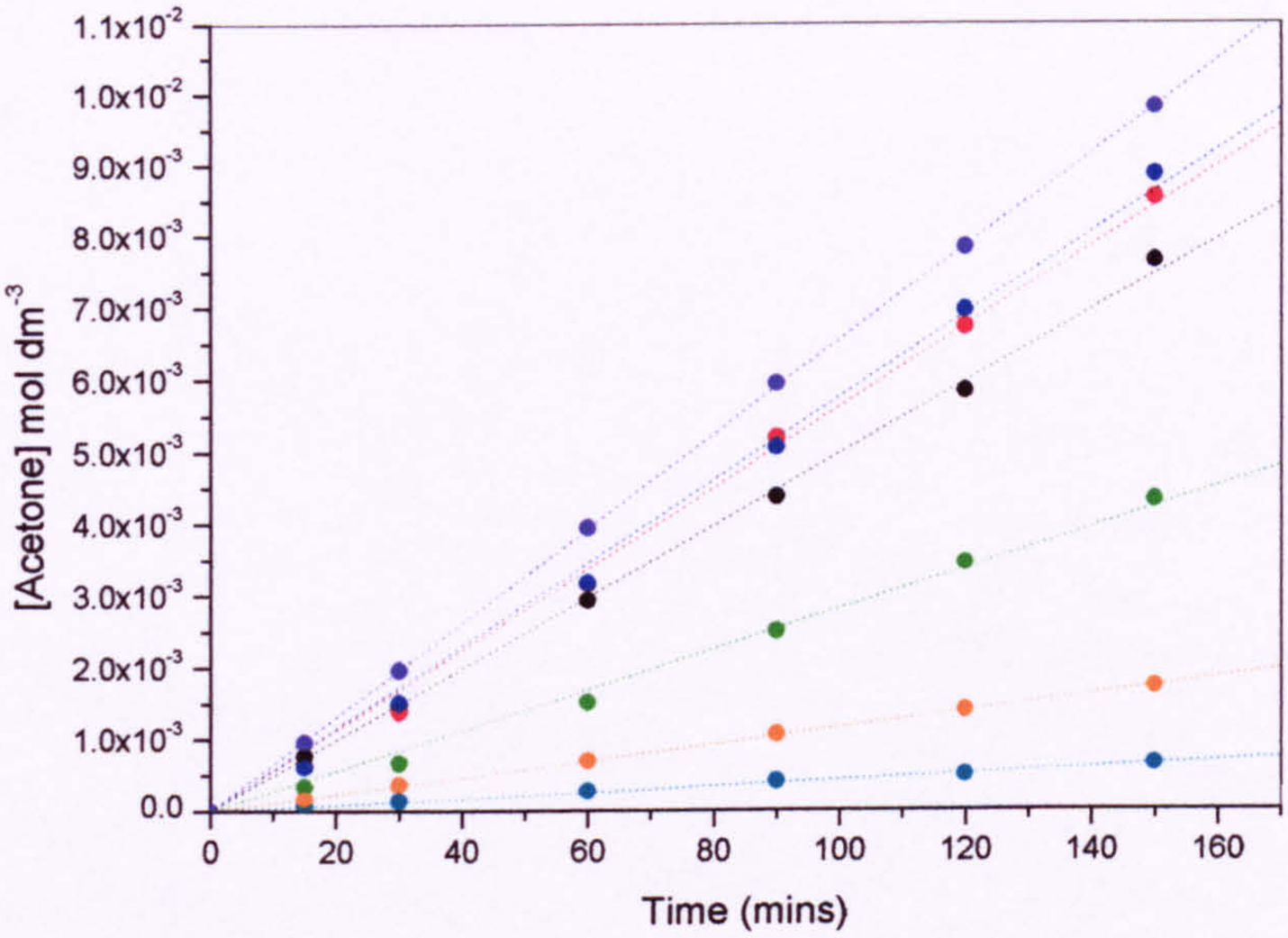

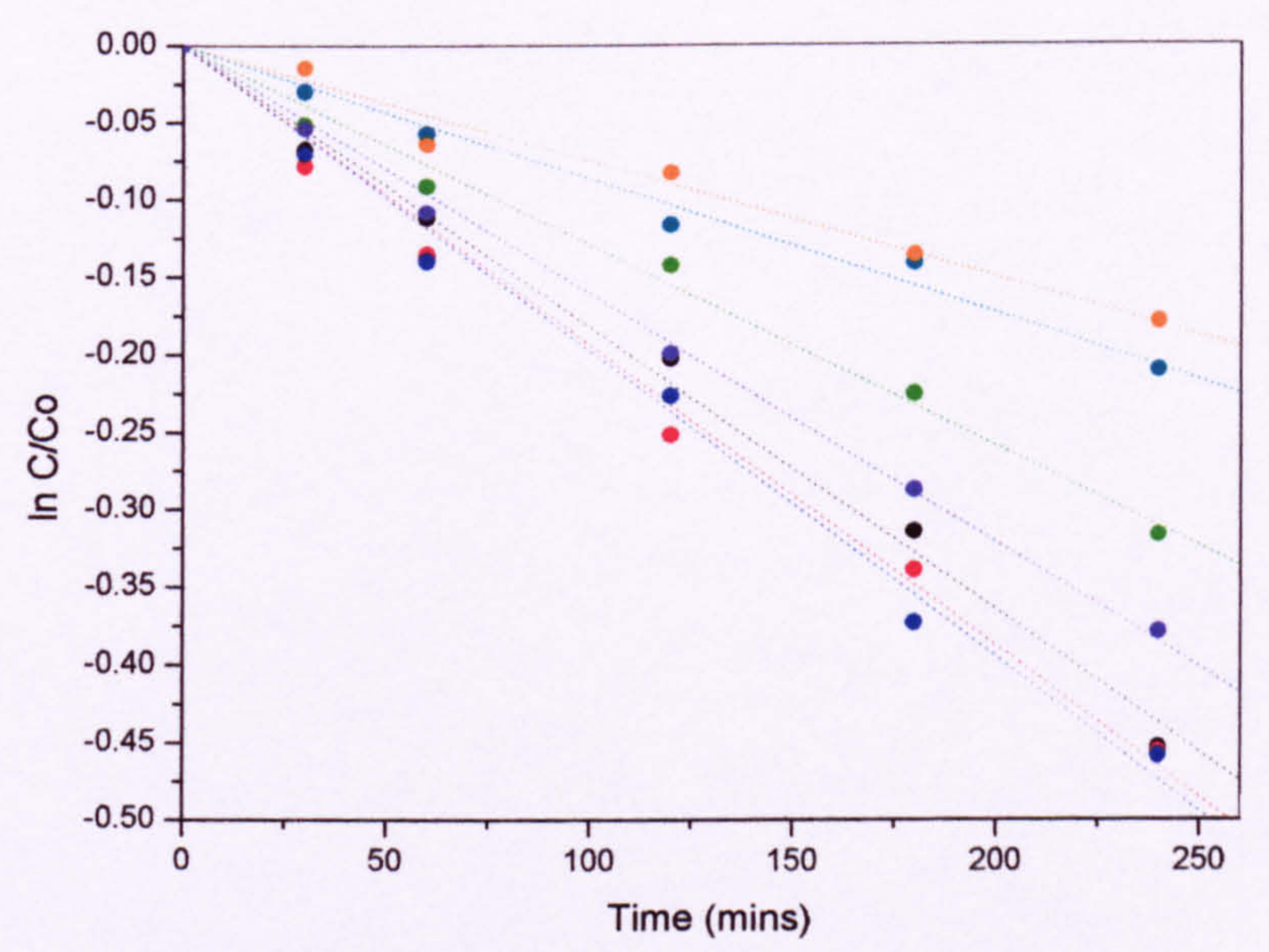

Fig 3.x and 3.xi. Plots of acetone concentration against time (top) and lnC/Co against time (bottom) for unmilled lattice doped Sample A by coprecipitation. --- 0.001%; --- 0.005%; --- 0.01%; --- 0.1%; --- 1%; --- 5%; --- Untreated sample.

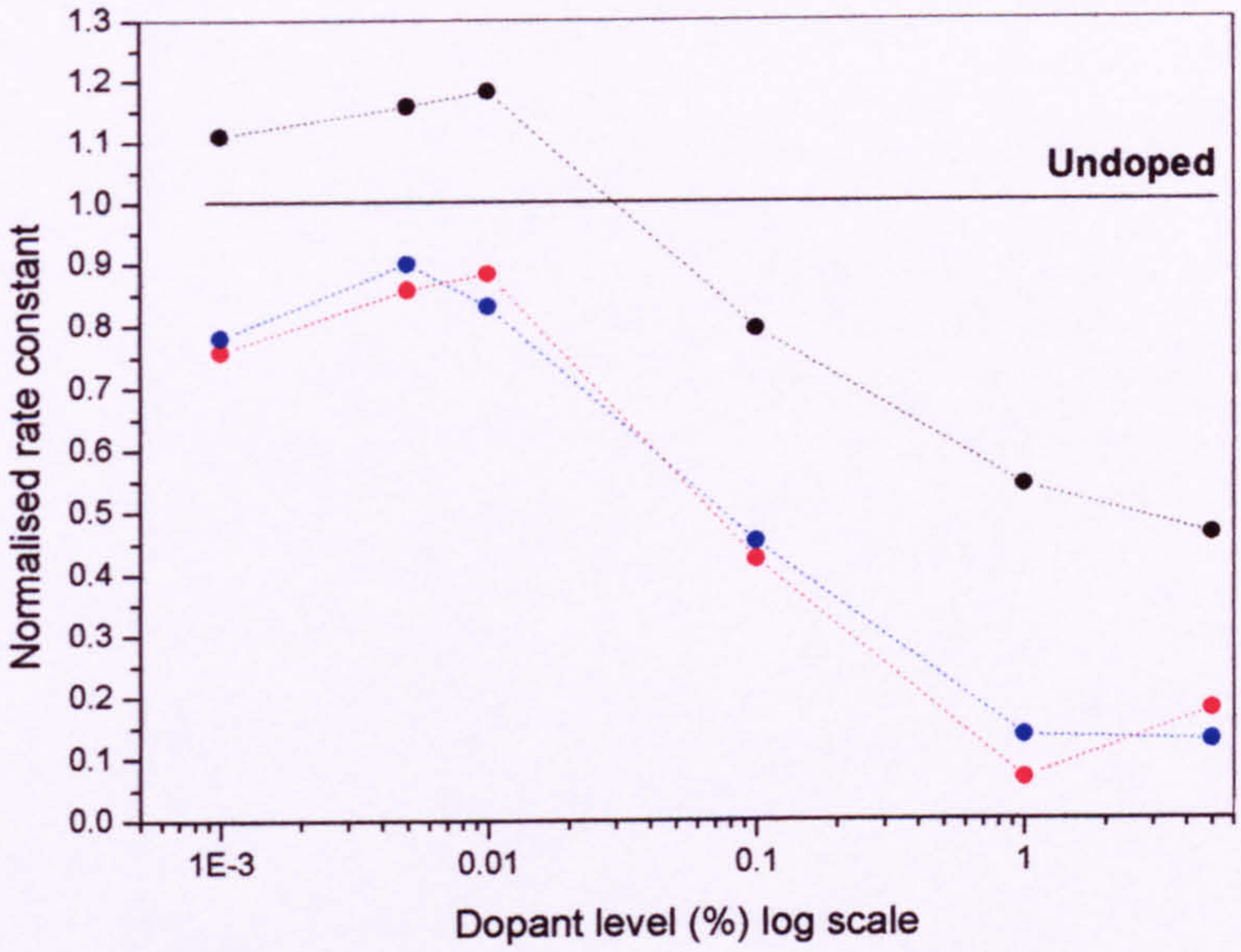

Fig 3.xii. Comparison of the photoactivity of lattice doped Sample A as measured by NP (---) and IPA (---) unmilled, and IPA (---) milled. In all three cases the rate constants are normalised to the rate constant for the undoped sample indicated by the solid black line.

As can be seen by comparison of the unmilled (red line) and milled samples (blue) for IPA, milling decreases the photoactivity by roughly the same proportion for the undoped and doped samples. This indicates that agglomeration does not significantly affect the trends in the photoactivity. Therefore, whilst it was not desirable to measure the photoactivity of milled samples using NP (as explained in section 2.3.2.2) the trend is thus unlikely to be different to that observed for the unmilled samples.

3.5. Position of the Fe^{3+} measured by Electron Paramagnetic Resonance (EPR).

Fe^{3+} doped titania has been thoroughly investigated both theoretically and experimentally [4,5,6] by EPR spectroscopy and the characteristic spectra arising from Fe^{3+} in surface rhombic sites and lattice tetragonal sites are well known. The former gives rise to a single peak at $g \sim 4.3$, and the latter five peaks at $g \sim 8.11$, 5.57, 3.36, 2.6 and 1.52 [5,6].

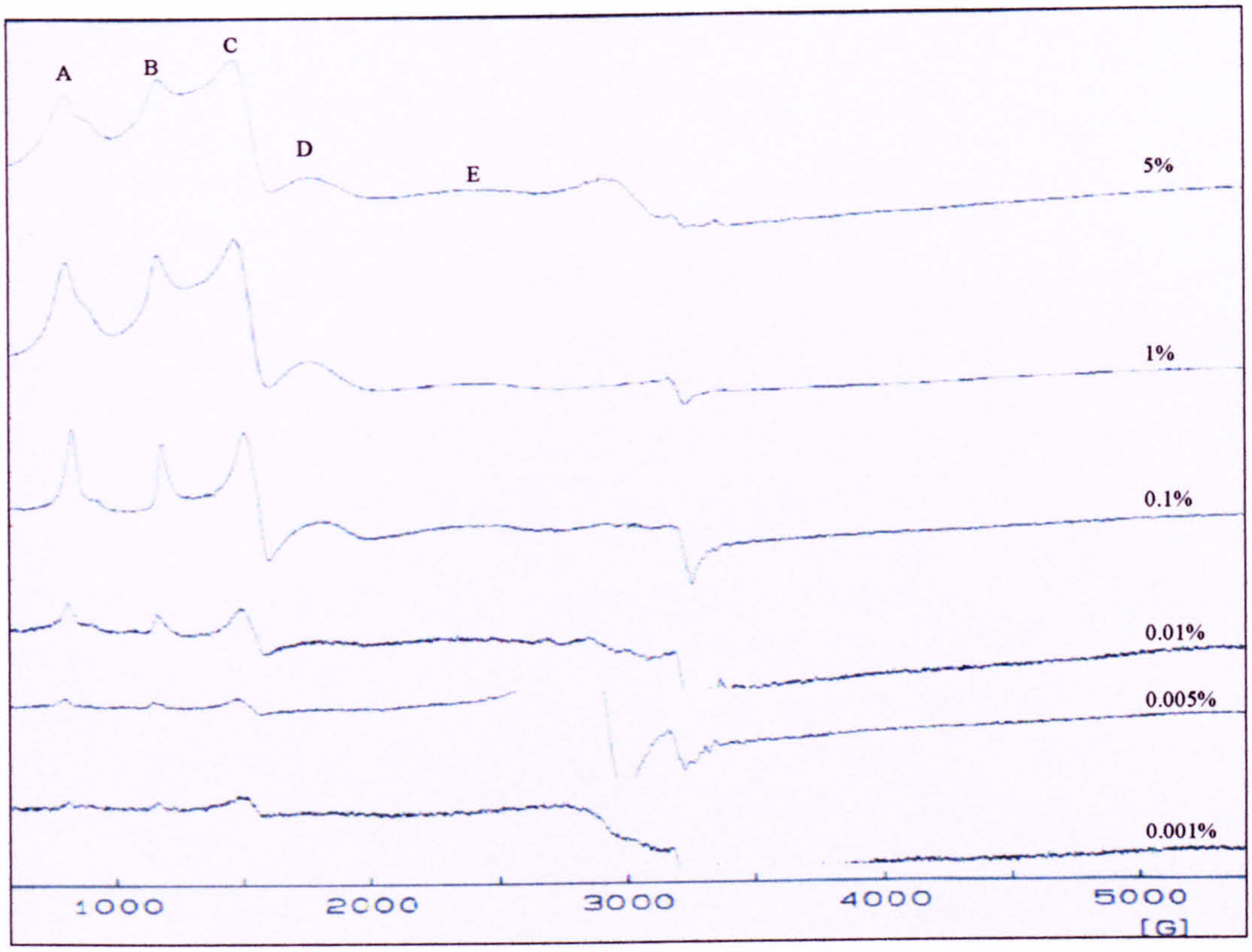

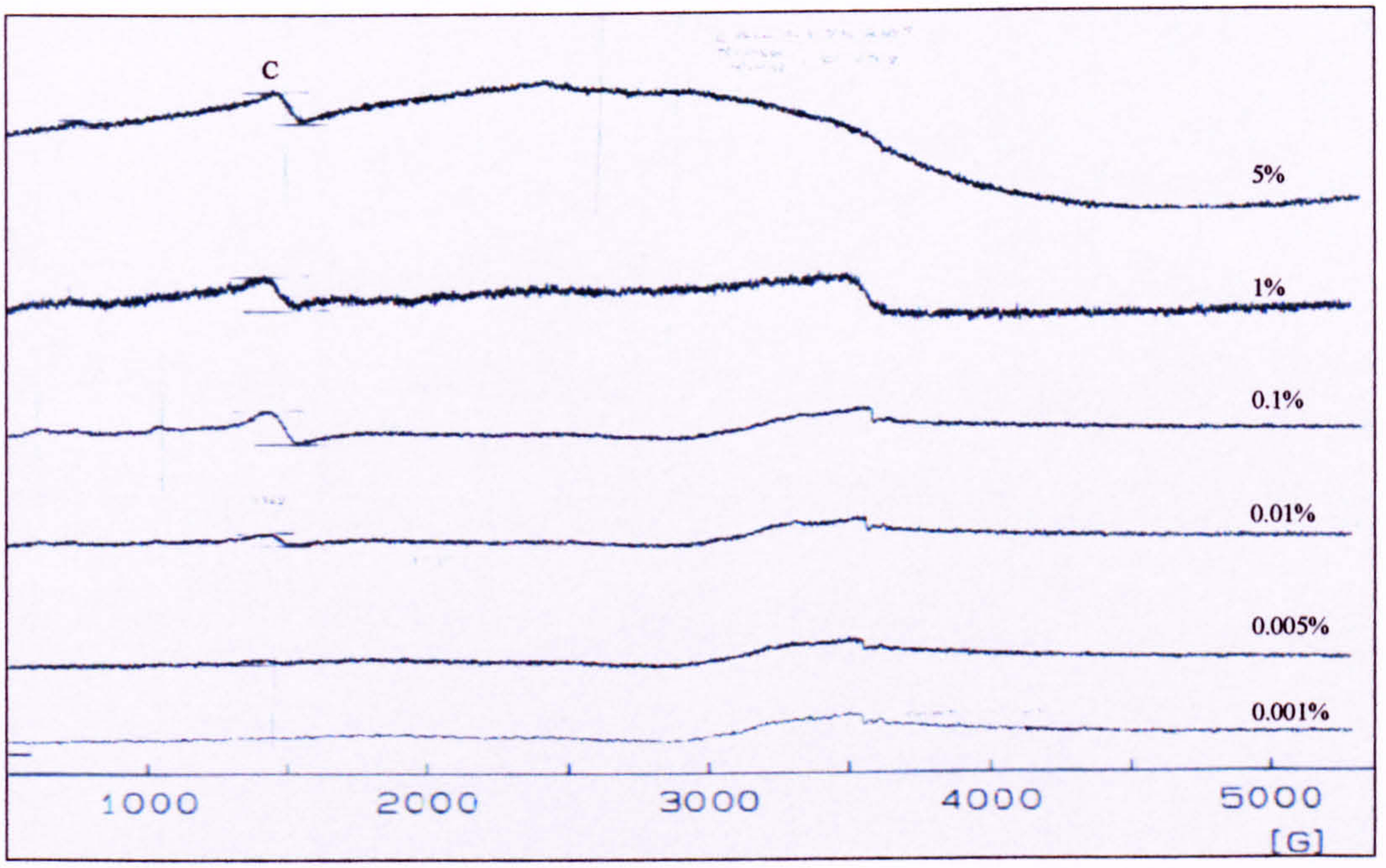

Fig 3.xiii. EPR spectra for lattice iron doped Sample A (a) - top and surface iron doped (b) - lower.

Thus, solid state EPR of iron doped titania can be used to determine whether Fe^{3+} ions are on the surface of the titania or in substitutional sites within the lattice. Fig 3.xiii (a) and (b) shows the room temperature EPR spectra of Sample A lattice iron doped (a) and surface iron doped (b) measured over the 500-5500G range; comparable spectra for P25 surface iron doped are shown in Appendix 3.1 Figure A3.i.

The spectra of surface iron doped Sample A and P25 show only the characteristic peak at g ~ 4.3 (signal C) corresponding to iron on the surface of the titania as would be expected from the preparation method. The energy barrier for diffusion of Fe^{3+} into the titania lattice has been shown to be significantly higher than the drying temperature of 110 °C of these samples. Egerton *et al* investigating iron diffusion in pigmentary rutile (~ 250 nm) reported that a temperature greater than 300 °C was required to induce migration into the lattice [6]. Similar studies using high calcination temperatures reported similar results [7]. The spectra of lattice iron doped Sample A show this peak at g ~ 4.3, and additional peaks at g ~ 8.1, 5.5, 3.2, and 2.4 (signals A, B, D, E) corresponding to Fe^{3+} substituted within the lattice i.e. iron doping by coprecipitation gives iron incorporated into the titania lattice and at the surface. As the dopant concentration is increased the peak heights increase although this increase is only semi-quantitative. Due to a defect in the EPR cavity, signals appear in the high field region, these appear for undoped samples, an empty tube, and an empty cavity and are not due to Fe^{3+} or any other species associated with the titania.

3.6. Powder X-Ray Diffraction (XRD).

The addition of metal ions to the precipitation mixture during titania preparation has been shown to affect the final morphology and crystal size [2] by acting to promote or retard the anatase-rutile transformation and alter grain growth. Whilst Fe^{3+} has been shown to act as a rutile promoter [8,9] and is therefore unlikely to have an effect on the final morphology which is 99%+ rutile in the undoped case, it is nonetheless pertinent to determine if the addition of iron acetate significantly affects the crystal size. To this end, room temperature powder X-ray diffraction was measured for lattice iron doped (C) and undoped Sample A between 15° - 60° and is shown in Figure 3.xiv

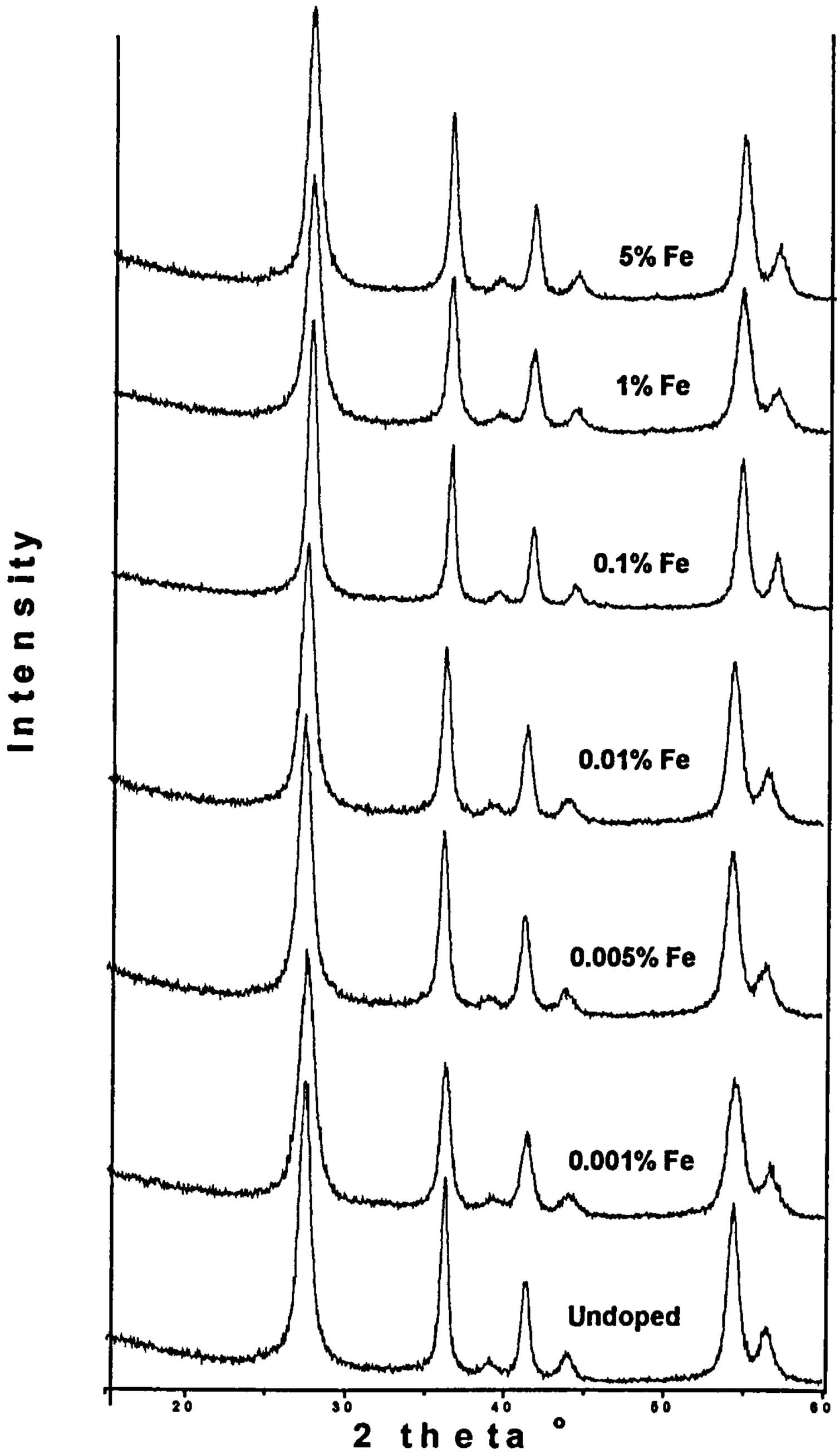

Fig 3.xiv. XRD patterns for undoped and lattice iron doped Sample A.

Seven characteristic peaks at 27°, 36°, 39°, 41°, 44°, 54° and 56° that correspond to the rutile morphology are observed for the undoped and all of the lattice doped modifications. There are no observable peaks for amorphous titania or the crystalline anatase or brookite morphology. It can therefore be concluded that all of the samples are pure rutile. Table 3.i shows the primary crystal size of the iron doped samples relative to the undoped Sample A calculated from line broadening of the (110) peak at 27° using the Scherrer calculator. It can be seen that there is some small variation in the crystal size for iron treated samples although it should be noted that that all values are within 2 nm of that for the untreated sample.

Sample	Primary crystal size (nm)
5% Fe	9.3
1% Fe	8.0
0.1% Fe	11.0
0.01% Fe	8.5
0.005% Fe	8.4
0.001% Fe	7.5
Untreated Sample A	9.5

Table 3.i. Primary crystal size for undoped and lattice iron doped Sample A

3.7. Fourier Transform Infra Red (FTIR) spectroscopy.

FTIR spectroscopy was used to investigate whether acetate was adsorbed onto the titania during the iron doping preparation process as this might reasonably be thought to affect the photoactivity. The diffuse reflectance (DRIFTS) spectrum of P25 coated with 66% acetate and the spectra of P25 doped with surface iron from iron acetate by precipitation are shown in Fig 3.xv (for clarity, the spectra are offset). Spectra were measured at room temperature between 1000 cm^{-1} and 4000 cm^{-1} although only the region between 1300-1750 cm^{-1} is shown as this contains the carbonyl stretching region. Below this region the titania lattice stretches obscure any bands, and above this region only the broad envelope hydroxyl stretch centred at approximately 3300 cm^{-1} and terminal hydroxyl

groups at 3631 cm^{-1}, 3669 cm^{-1} and 3695 cm^{-1} are present with a gradually increasing shoulder as dopant level is increased for the alkane stretches centred at ~ 2930 cm^{-1}.

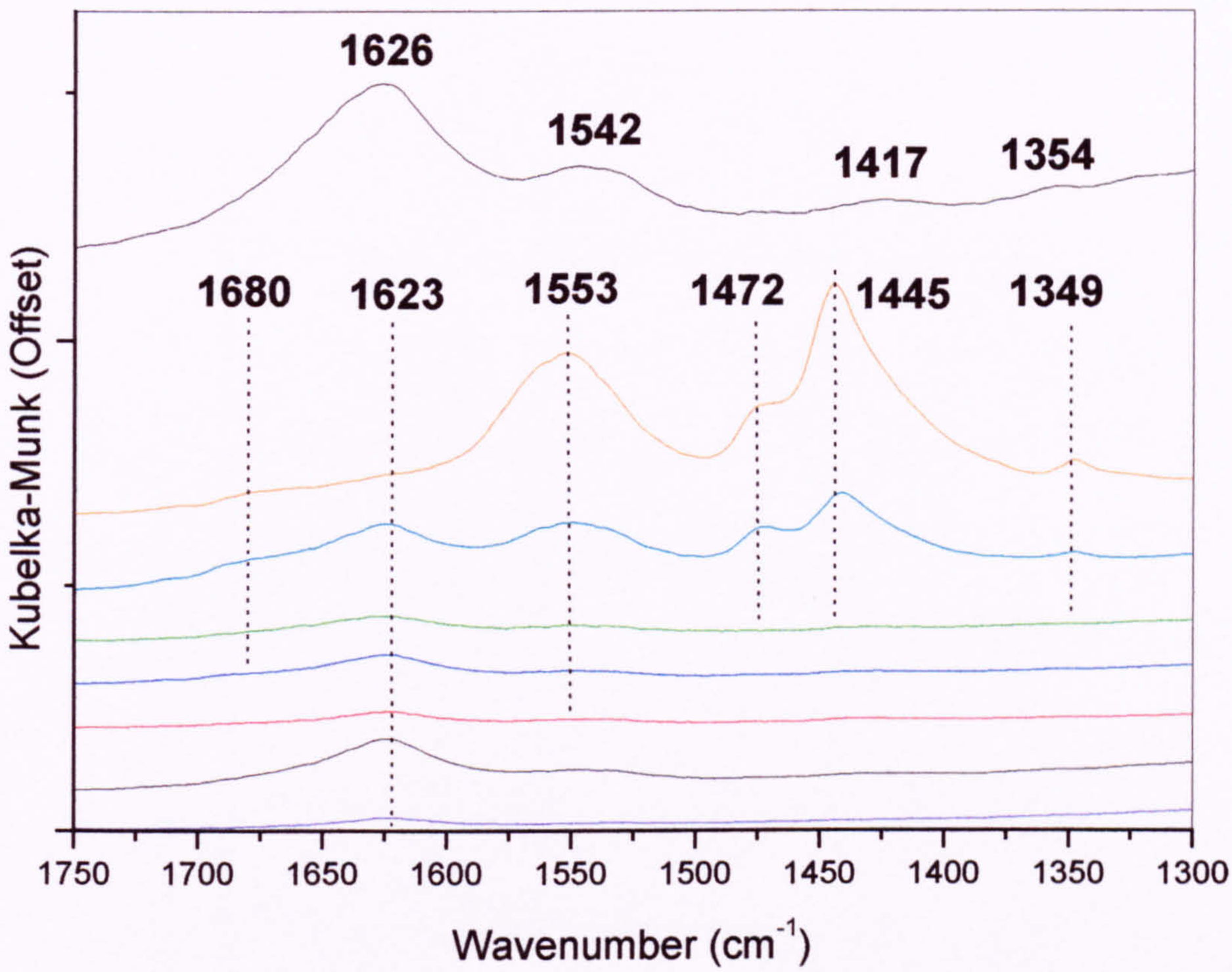

Fig 3.xv: DRIFTS spectra of untreated and iron treated P25.
--- 0.001%; --- 0.005%; ---0.01%; --- 0.1%; --- 1%; --- 5%;
--- Untreated P25. For comparison, the spectrum of P25 coated with 66% acetate is shown (top). For clarity spectra are offset.

Several papers [10-15] have reported the FTIR spectra of acetate adsorbed on an unmodified titania surface. Bridged bidentate acetate has characteristic bands at 1585 - 1570 cm^{-1} and 1420 – 1410 cm^{-1} for the asymmetric and symmetric carbonyl stretches. Chelate bidentate acetate has corresponding bands at 1550 – 1540 cm^{-1} and 1440 – 1430 cm^{-1}. The spectra of acetate coated P25 above has bands at 1546 cm^{-1} and a small shoulder at 1436 cm^{-1} that correspond to the asymmetric and symmetric stretches of the chelate

acetate, and a band at 1417 cm^{-1} that may be assigned to bridged acetate. In the latter case, the expected symmetric stretch is likely obscured by a broad band centred at 1626 cm^{-1}, assigned to the scissor vibration from adsorbed water, which is also present in the uncoated P25.

Between 1300-1750 cm^{-1}, the spectrum of untreated P25 has only a single peak (at 1623 cm^{-1}), which corresponds to the scissors vibration of adsorbed water molecules. The spectra of the iron treated samples also show this peak, but there is also a growth of five other bands at the higher loadings of 1% and 5%: approximately 1680 cm^{-1} (shoulder), 1553 cm^{-1}, 1472 cm^{-1} (shoulder), 1445 cm^{-1} and 1349 cm^{-1}. By comparison with the spectrum of P25 coated from sodium acetate it can be seen that the observed bands are not due to acetate adsorbed directly onto the P25. Further, they do not fall within the range for either bridged bidentate or chelate adsorbed acetate reported in the literature [10-15]. Therefore, it is reasonable to explore whether the acetate is adsorbed as an iron acetate species.

To the authors knowledge there are no published studies for the FTIR spectra of iron acetate adsorbed to titania and so the following band assignments are necessarily tentative. The band at 1623 cm^{-1} has already been ascribed to the titania hydroxyl group deformation. The two bands at 1445 cm^{-1} and 1349 cm˙1 can be assigned to asymmetric and symmetric alkane deformations, the former band being identified as such in the literature for the spectrum of solid sodium acetate [16,17]. The weak shoulder at approximately 1680 cm^{-1} may be indicative of carboxyl character, being somewhat beyond the normal range for adsorbed acetate carbonyl stretches. The remaining bands at 1553 cm^{-1} and 1472 cm^{-1} are thus assigned to the asymmetric and symmetric carbonyl stretches respectively and the difference of 81 cm^{-1} between the two modes indicates a chelate, rather than a bridging, conformation to a central iron atom. Arana *et al* [18] have observed that for iron modified P25 formates adsorbed on iron exhibit higher wavenumbers for both asymmetric and symmetric carbonyl stretches. The shift to higher wavenumbers for the carbonyl stretches for iron doped P25 (1553 cm^{-1} and 1472 cm^{-1}) when compared to acetate

treated P25 (1546 cm^{-1} and 1436 cm^{-1}) therefore supports the theory that the acetate is bound to the iron rather than directly to the titania.

The diffuse reflectance (DRIFTS) spectrum of sample A doped with iron from iron acetate by precipitation and coprecipitation were measured at room temperature between 1000 cm^{-1} and 4000 cm^{-1}. There is some evidence that acetate is present at high dopant levels due to an alkane deformation band at 1349 cm^{-1} which is also present in the iron doped P25 above. Unfortunately, it was not possible to determine the carboxyl band positions, and hence the bonding mode, for the adsorbed acetate as these are likely obscured by several broad and strong bands in the undoped and doped samples at 1524 cm^{-1}, 1424 cm^{-1}, 1391 cm^{-1} and 1331 cm^{-1}. These bands probably correspond to an adsorbed carbonate from the dissociative adsorption of carbon dioxide [19,20]. Therefore, it can only be concluded from these results that acetate is present at high dopant levels.

3.8. Gravimetric surface area analysis.

While it has been demonstrated that it is the number of active sites on a titania surface rather than the overall surface area that determines the photoactivity [21], it has nevertheless been shown that the surface area can influence the photoactivity [22,23]. Since there is reasonable evidence to suggest an acetate coating for surface iron doped P25, albeit most likely through the iron, the surface area was measured to determine if the surface area was significantly affected by the doping procedure. A representative adsorption isotherm (P25/0.1%/P) measured by M^{c}Bain gravimetric adsorption of nitrogen is shown in Figure 3.xvi with the corresponding BET analysis plot.

Surface areas calculated using BET analysis are shown in table 3.ii with that for undoped P25 for comparison. There is a trend for a reduction in the surface area at the lowest and highest treatment level, with a maximum area at the 0.1% level. However, the reproducibility is taken to be $^{+}_{-}7$ m^2 g^{-1} and within this error range there is little change of the surface area with iron treatment. This is consistent with reported results by Palmisano et al [24], who investigated surface impregnated anatase ($SSA_{BET} \sim 50$ m^2 g^{-1}) in the range

0.01-5 at% and found that while the level of iron affected the surface area, there was a change of only 8 m^2 g^{-1} in either direction with a maximum at 0.1-0.5 at%.

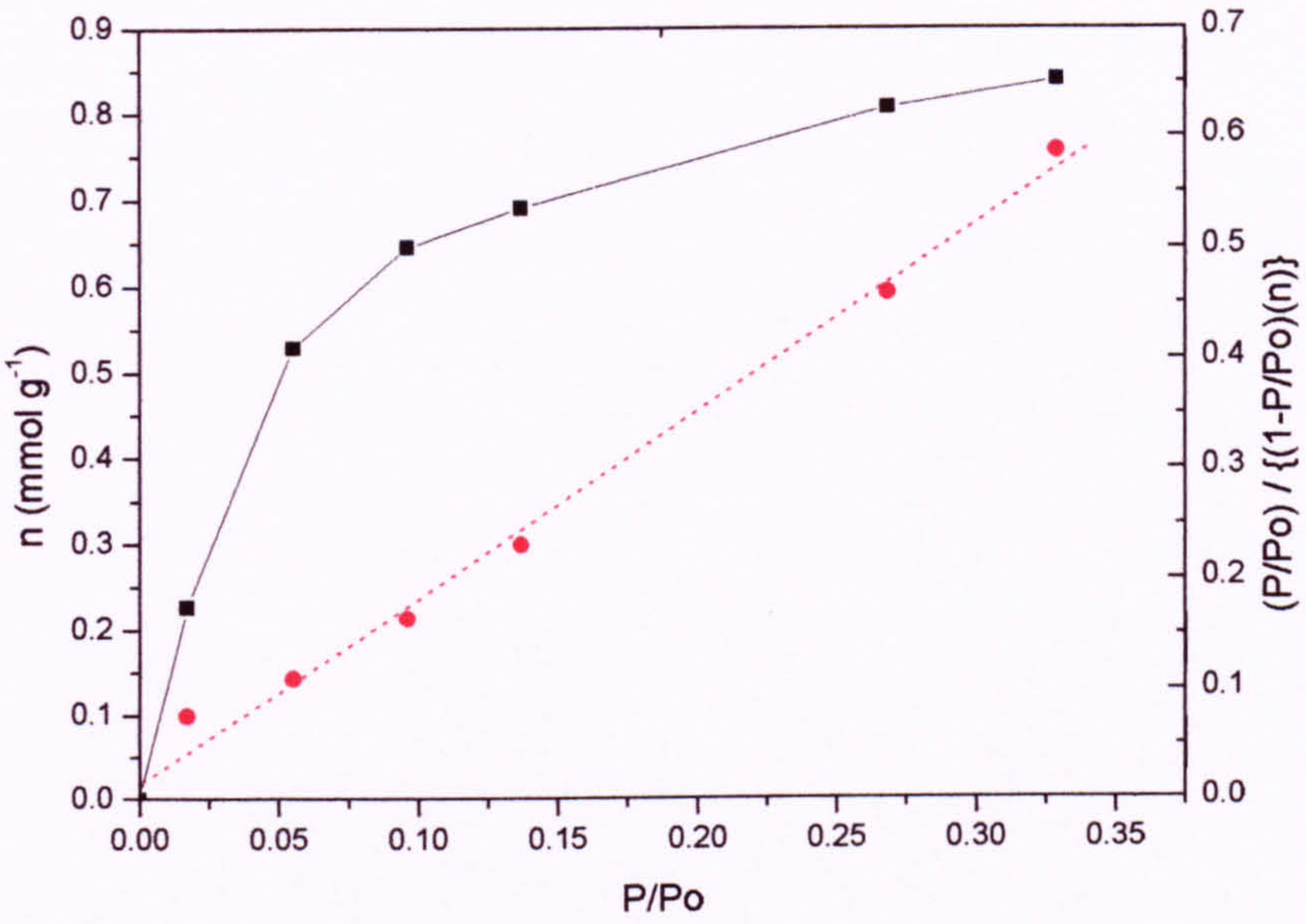

Fig 3.xvi. Nitrogen adsorption isotherm (left-hand axis) and the corresponding BET analysis plot (right-hand axis) for 0.1% surface doped P25.

Sample	Surface area $^{+}_{-}$7 (m^2 g^{-1})
5% Fe	36
1% Fe	36
0.1% Fe	57
0.01% Fe	50
0.005% Fe	45
0.001% Fe	35
Undoped P25	42

Table 3.ii. BET Surface areas of iron treated P25.

3.9 Diffuse reflectance spectroscopy (DRS) measurements and colour.

In the absence of impurities or crystal defects, titania photoactivity is only possible under ultraviolet radiation due to the band gap energy. Doping titania with transition metals may result in a red shift in the absorption edge, or the appearance of new absorption bands i.e. the doped titania may absorb visible as well as ultraviolet radiation leading to visible radiation photocatalysis [1,25]. To investigate this possibility the reflectance spectra was measured between 400 nm and 700 nm of selected samples were determined by Diffuse Reflectance Spectroscopy (DRS). DRS spectra of 0.1at% and 5at% lattice doped Sample A prepared by the coprecipitation method are shown in Figure 3.xvii. *These spectra were kindly measured and provided by Dr Liwei Wang.*

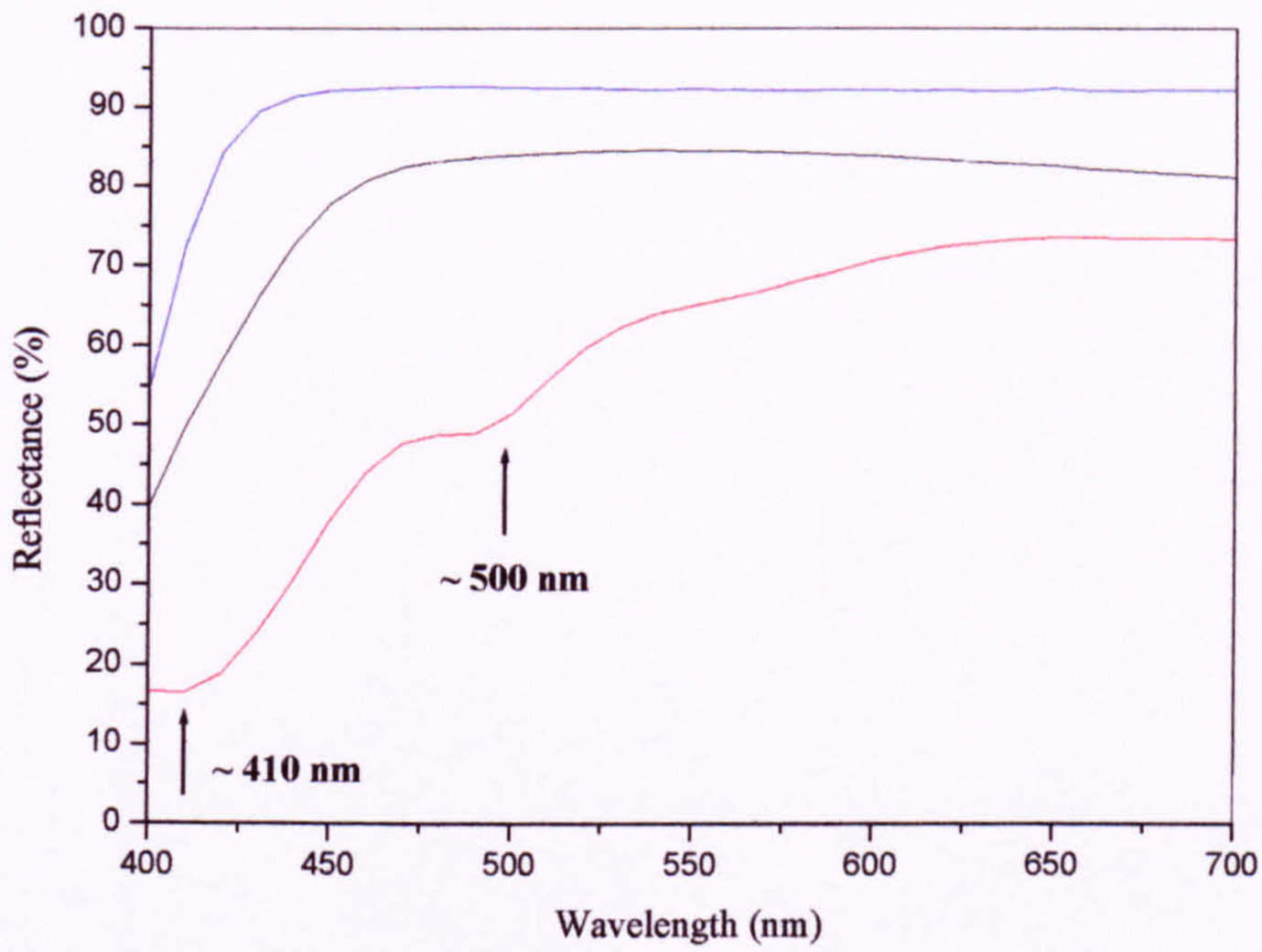

Fig 3.xvii. DRS spectra of 0.1at% (---) and 5at% (---) lattice doped Sample A and undoped (---). *Measurements by Dr L Wang.*

For A/C/0.1% is similar to that for the undoped Sample A with the exception that there is increased absorption in the visible region evidenced by a red shift in the absorption edge. For A/C/5% the spectra show two additional absorption bands centred on ~ 410nm

and 500nm. These bands suggest the appearance of segregated iron phases in the heavily loaded samples.

Unfortunately, it was not possible to measure all samples due to a lack of time and resources. However, the visible colour of the samples can give a qualitative indication of absorption and therefore pictures of all iron doped samples are shown in Figures A3.ii to A3.iv in Appendix 3.2. It can be seen that the colour of the samples changes from white for lightly doped samples through to yellow/brown for heavily loaded samples. In addition, the surface doped samples are qualitatively more coloured than the lattice doped samples, most likely due to a greater degree of surface segregated iron phases in these samples.

3.10. Salicylic acid degradation.

3.10.1. Introduction.

Tunesi and Anderson [26] concluded from their studies that at low pH (4) the oxidation of salicylic acid proceeded by direct electron transfer i.e. photogenerated holes from the titania oxidise the adsorbed salicylic acid. This was supported from experiments showing that addition of an alcohol to scavenge hydroxyl radicals did not reduce the rate of degradation.

Studies by Vione, et al [27] on this reaction supported the conclusion that salicylic acid was degraded by a direct hole transfer mechanism, unlike for example phenol which proceeded by a hydroxyl radical mediated mechanism. They suggested in a later study [28] that strategies to reduce titania photoactivity should be supported by a test to determine degradation by the direct hole mechanism and a test for the hydroxyl radical mediated mechanism.

The addition of methanol by Tunesi and Anderson [26] tested whether salicylic acid degrades by a direct electron transfer mechanism as alcohols have been shown to degrade by a hydroxyl radical mediated mechanism. In the present study, we have added 2-propanol, rather than methanol, and the literature supports the supposition that this alcohol is oxidised by a hydroxyl mechanism (see Section 1.8.1.1), and thus would scavenge

hydroxyl radicals. By adding an excess of 2-propanol to the reaction mixture and observing the effect on the rate of salicylic acid degradation we hope to show that at pH4 this molecule degrades by a direct electron transfer mechanism. This section shows the development of a test to determine degradation by the direct hole mechanism and its application for determining the efficiency of surface and lattice iron doping Sample A to reduce this type of photoactivity. Other authors have also used 2-propanol to scavenge holes [29]

3.10.2. Development of method.

Preliminary experiments using 0.36mM salicylic acid and unmilled titania with pH adjusted to 4 demonstrated that an initial time of 90 minutes was sufficient for the slurry to reach equilibrium with respect to adsorption. No degradation was observed in the absence of UV or titania over the subsequent 150 minutes experiment time. The initial salicylic acid concentration was chosen to correspond with the experiments described above [28]. In common with results shown in these references, the titania is coloured yellow upon adsorption of salicylic acid. This is ascribed to the formation of a strongly covalently adsorbed salicylate complex, (for more detail see section 1.8.1.3).

Separate oxidation experiments were performed to determine a suitable titania loading using unmilled Sample A and varying the loading between 2 and 8 g dm^{-3} (0.1 to 0.4 g in 50 ml salicylic acid solution). In all cases, the degradation of salicylic acid most closely followed first order kinetics i.e. the rate constant is equal to the gradient of straight line plots of ln C/Co against time. Plots of ln C/Co against time are shown in Figure 3.xviii, and the rate constants for degradation, taken from these plots, against titania loading for Sample A and are shown in Figure 3.xix.

A Langmuirian type relationship is followed for the effect of titania loading on the rate constant over the 0.1g to 0.4g range. Ideally, the typical loading chosen for this technique would be in the region where rate is independent of loading i.e. at higher loadings than studied here. Higher loadings were impractical, as this would leave too small a salicylic acid solution concentration to be conveniently measured, so a typical loading of 2 g dm^{-3} (0.1 g in 50 ml) was chosen to be consistent with that for the NP technique.

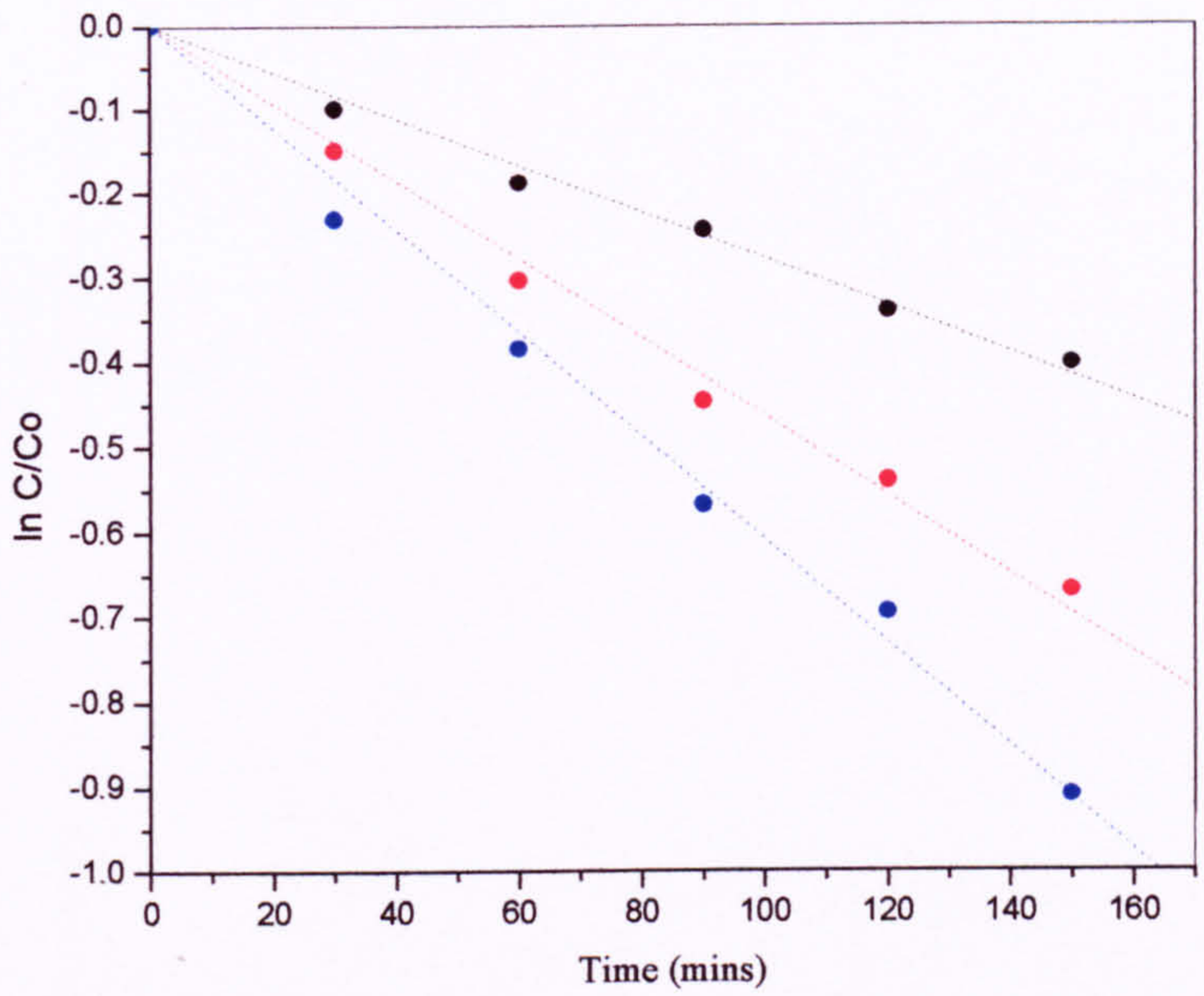

Fig 3.xviii. Plots of ln C/Co against time for unmilled Sample A for loadings of 0.1g (---); 0.2g (---); 0.4g (---).

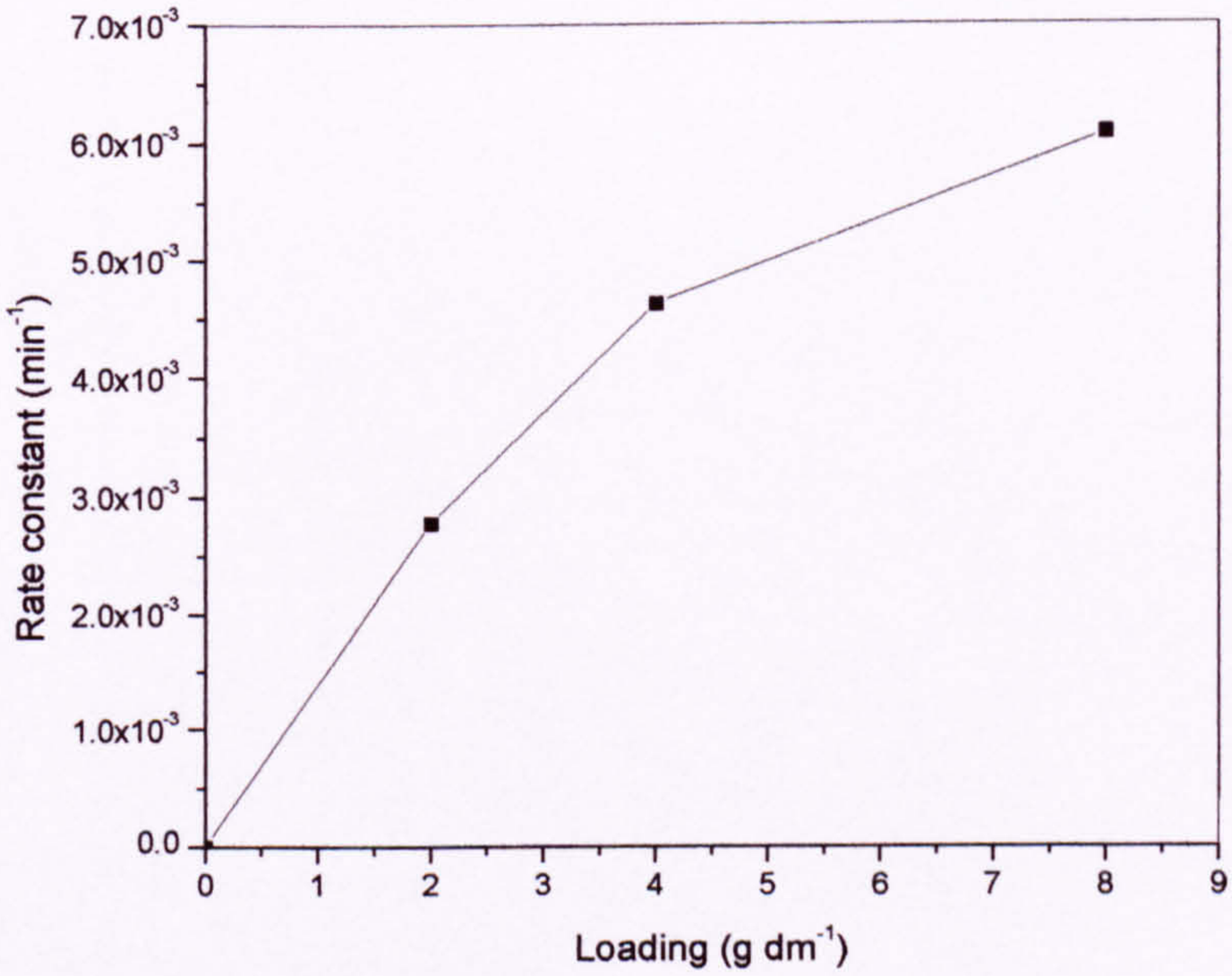

Fig 3.xix. Effect of titania loading on the rate constant for salicylic acid degradation.

To test the hypothesis that salicylic acid degradation proceeds by a direct hole (electron transfer) mechanism, the effect on the rate constant of adding an excess of isopropanol to scavenge hydroxyl radicals was determined as isopropanol oxidation has been shown to proceed by the hydroxyl radical mediated mechanism Isopropanol (35ml) was added to the initial salicylic acid slurry (titania loading of 2g dm^{-3}), all other variables remaining identical to above, giving a molar excess of isopropanol over salicylic acid of ~ 5000:1. To rule out the possibility that the rate constant was affected by changes in the titania dispersion the same reactions (one with, and one without added isopropanol) were performed with samples milled for 30 minutes. Plots of ln C/Co against time for unmilled and milled samples are shown in Figure 3.xx and the relative rate constants from these plots for unmilled samples, and samples milled for 30 minutes are shown in Table 3.iii.

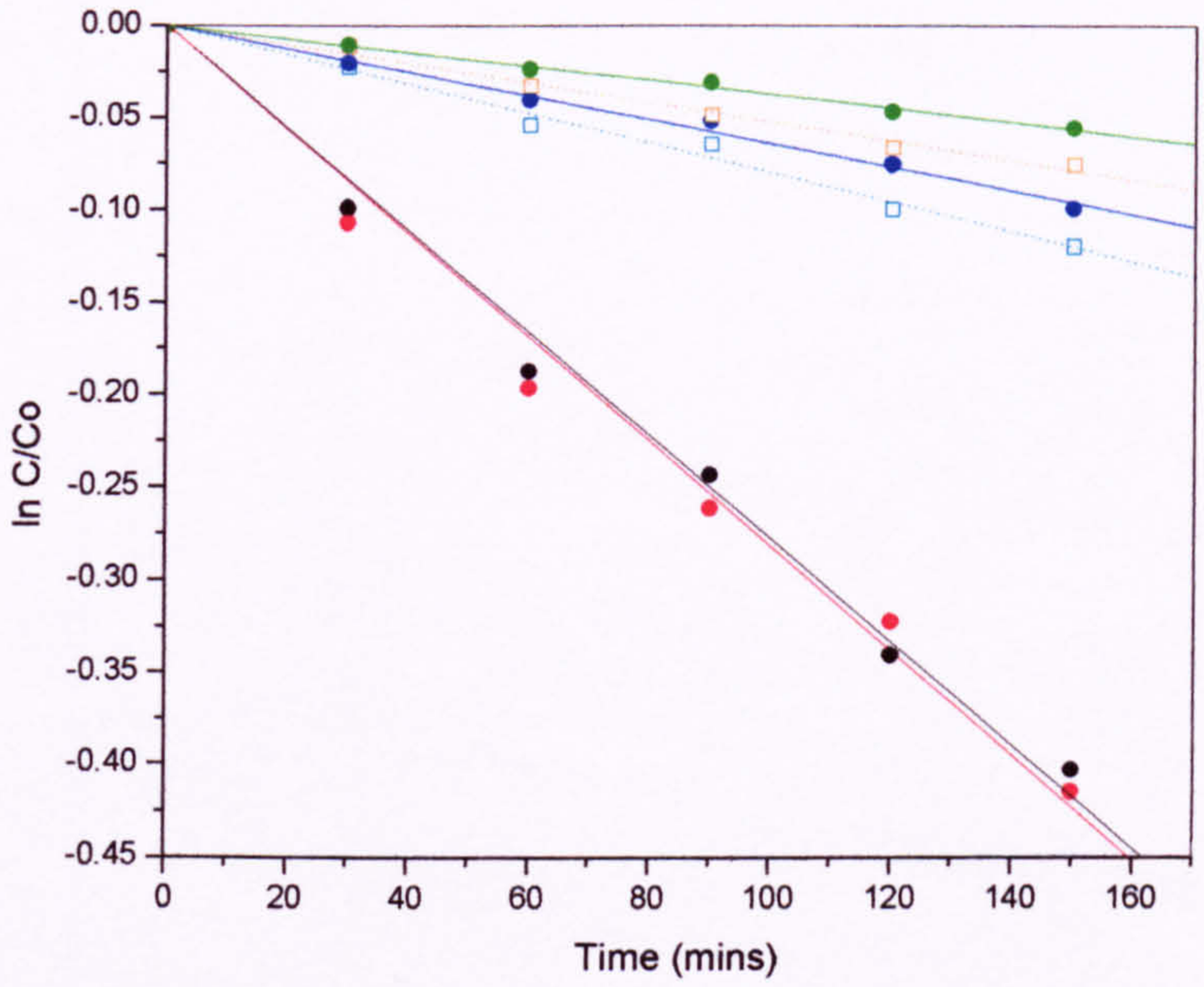

Fig 3.xx. ln C/Co against time plots for salicylic acid degradation 0.1g titania. Unmilled (---); unmilled with added alcohol (---); milled 30 mins (---); milled 30 mins with added alcohol (---); milled 15 mins (---); milled 60 mins (---).

	Unmilled	Milled 30 mins
No alcohol	1	0.232
Added alcohol	1	0.135

Table 3.iii. Rate constants for salicylic acid degradation relative to that for unmilled titania with no alcohol added.

As can be seen from table 3.iii, for unmilled titania there is no effect on the rate constant when a 5000 fold excess of isopropanol is added to the slurry to scavenge hydroxyl radicals. By comparing the rate constants for milled and unmilled samples I conclude that in both cases milling (better dispersion) lowered activity. If the salicylic acid degradation proceeded by a hydroxyl mediated mechanism then the addition of alcohol would be expected to reduce the photoactivity, and since any changes to dispersion would also be expected to reduce photoactivity, then it can be concluded that salicylic acid degradation does proceed by a direct hole mechanism.

The effect of milling the titania on the rate constant is shown in Figure 3.xxi. Rate constants are taken from linear fits of ln C/Co (salicylic acid concentration) against time in Figure 3.xx above.

Milling the titania to break up agglomerates reduces the measured photoactivity. There was a large reduction for short milling times then modest reductions beyond this, similar to the trend observed for the isopropanol oxidation technique. Despite this result, samples were not typically milled so that the measured photoactivities can be directly compared to those for the 2-nitrophenol technique, and also because the extent of the decrease (~80%) would have an adverse effect on sensitivity.

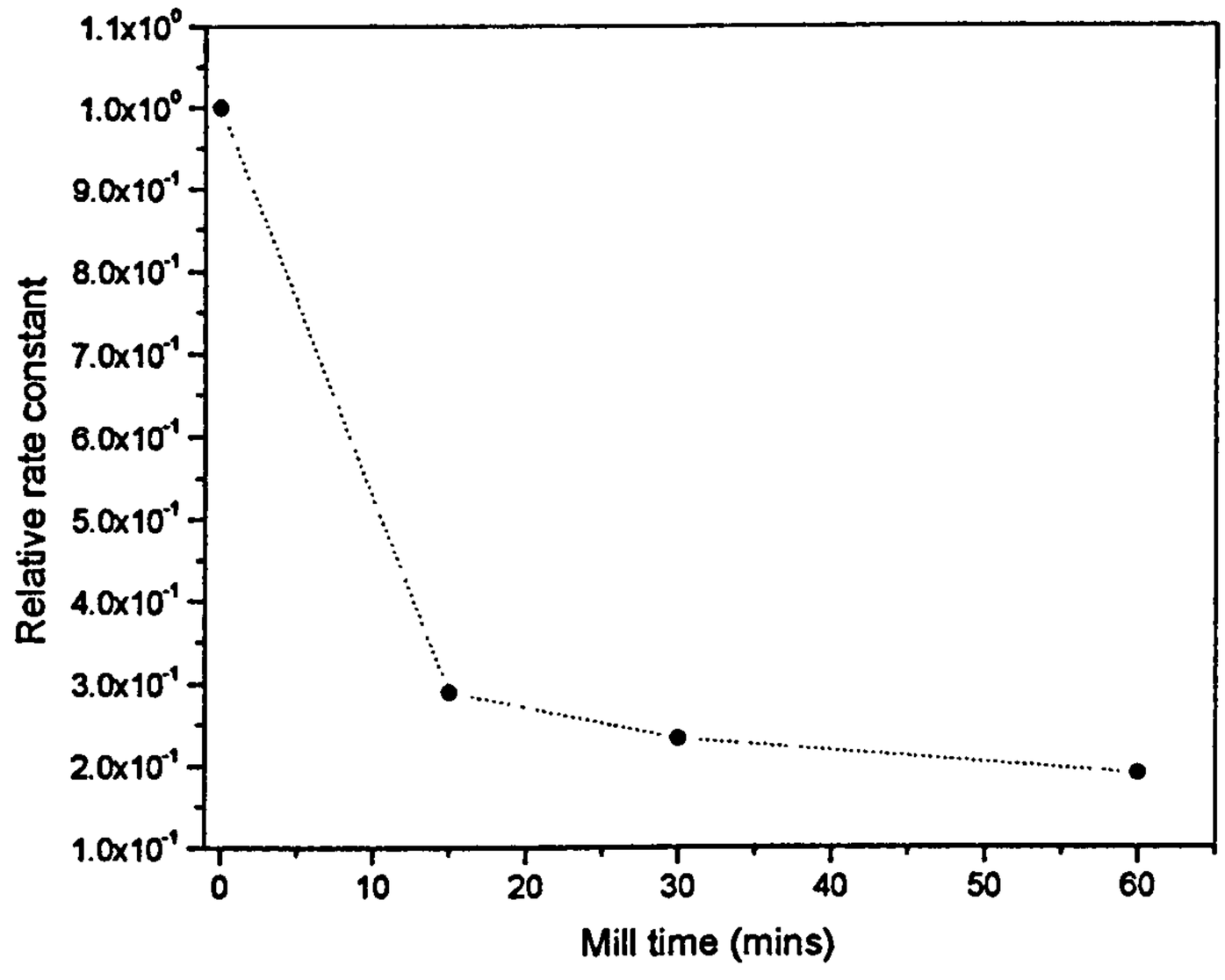

Fig 3.xxi. Normalised rate constant for salicylic acid against milling time.

3.10.3. Effect of iron doping Sample A on photoactivity measured by SA degradation.

Isopropanol oxidation and 2-ntirophenol degradation have been shown to proceed predominately by a hydroxyl radical mediated pathway (see literature reviews in Section 1.8.1.1 and 1.8.1.2 and [30]. The technique developed above can be used to determine the photoactivity by the direct hole transfer mechanism. This is especially useful for the surface and iron doped samples in this study, as a comparison of the measured photoactivity by salicylic acid degradation with that for NP should add understanding of how the treatment affects photoactivity.

Salicylic acid degradation was used to determine the effect on photoactivity (by the direct hole transfer mechanism) of surface and lattice iron doped Sample A. For these experiments samples were unmilled (for reason described above) and the typical titania loading of 2 g dm^{-3} was used. Plots of ln C/Co against time for surface iron doped and lattice iron doped samples with undoped Sample A for comparison are shown in Figures 3.xxii and 3.xxiii respectively. The rate constants for salicylic acid degradation against iron

dopant level (log scale) for surface and lattice doped Sample A are shown in Figure 3.xxiv, the horizontal line corresponds to that for the undoped sample.

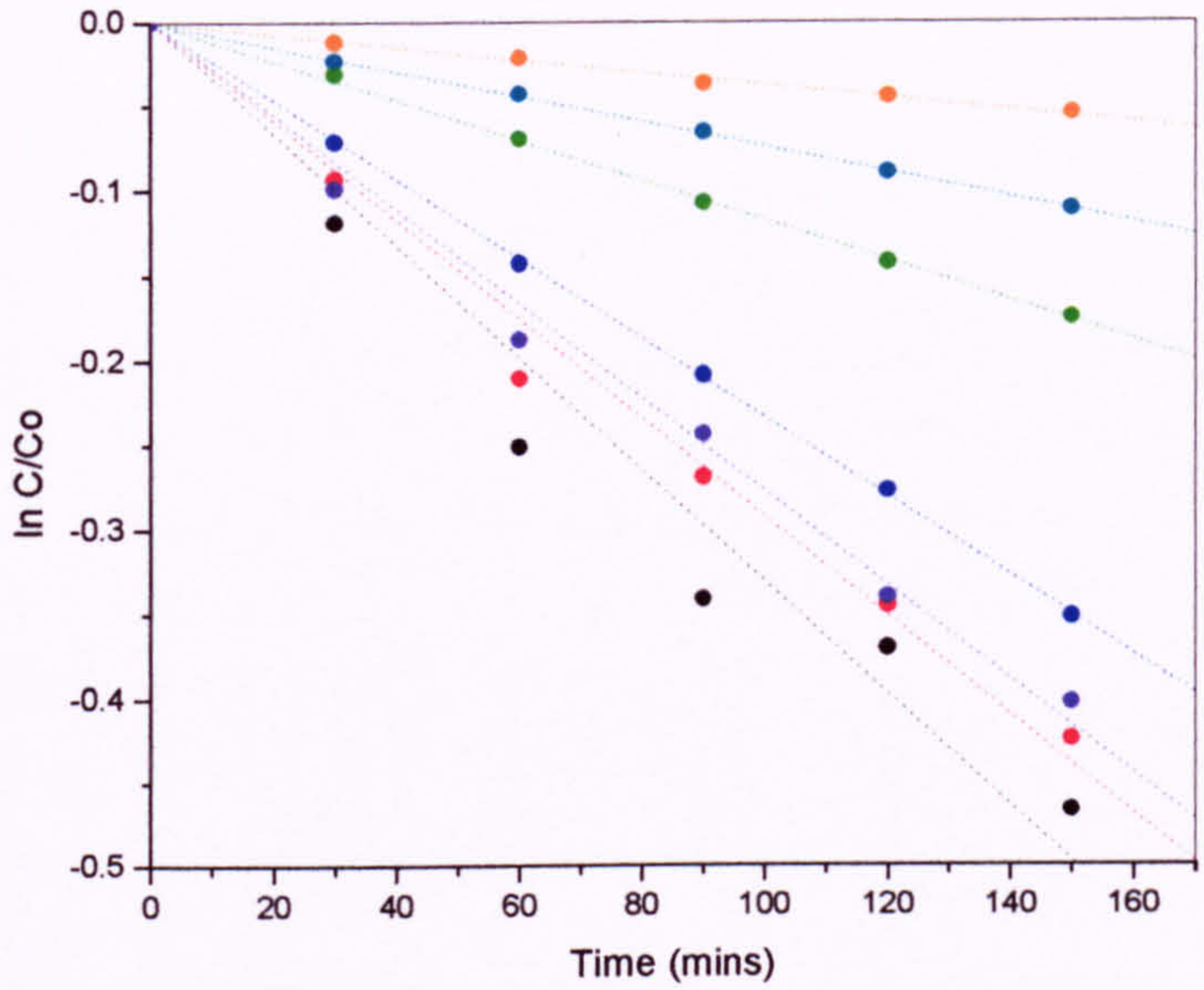

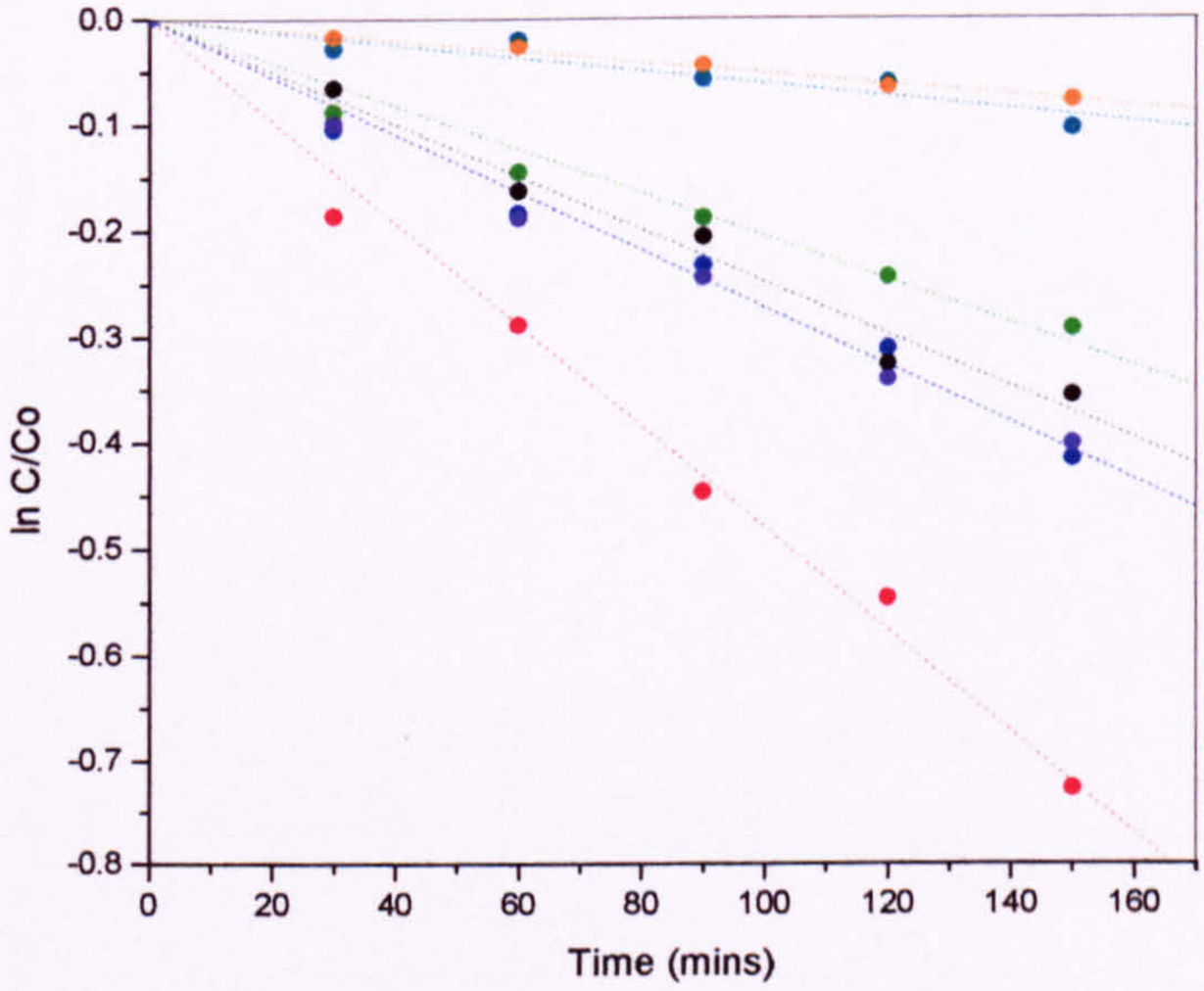

Fig 3.xxii and 3.xxiii. Plots of ln C/Co against time for surface (above) and lattice (lower) iron doped Sample A. 0.001% (---); 0.005% (---); 0.01% (---); 0.1% (---); 1% (---); 5% (---); undoped Sample A (---).

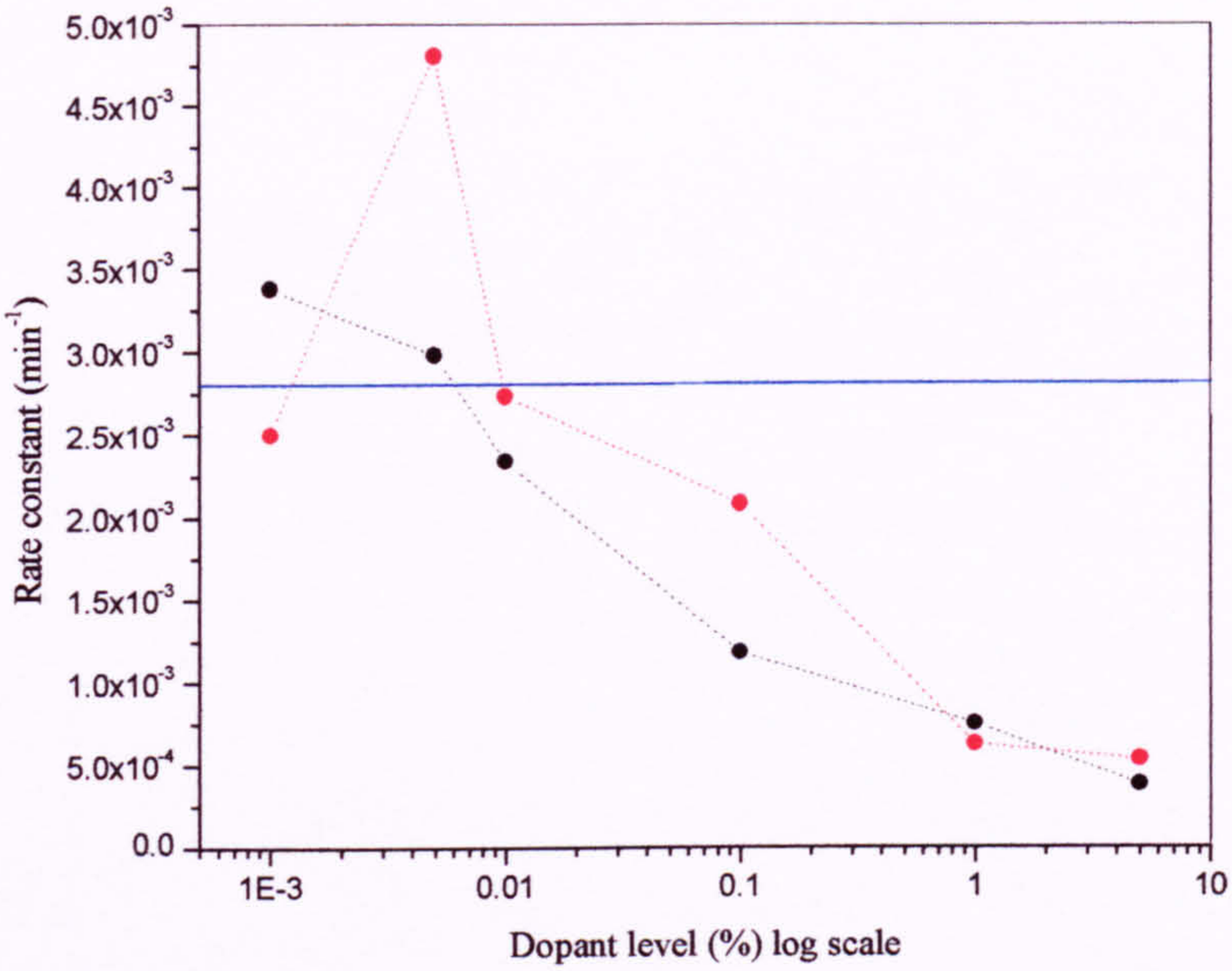

Figure 3.xxiv. Rate constants for salicylic acid degradation for surface iron (---); lattice iron (---); undoped (---) Sample A.

It is immediately obvious that the effect of surface iron doping on the photoactivity measured by this method is different from the effect of lattice doping. In the former case, the photoactivity at low levels is greater than the undoped Sample A and decreases with coating level across the range studied, whereas for lattice doping there is an increase at an optimum level of 0.005% with a decrease at higher and lower levels. Further, if the relative rate constants for surface iron doped Sample A for salicylic acid degradation are compared with those measured by NP and IPA (Figure 3.xxv) it can be seen that the trends differ. For techniques measuring photoactivity by the hydroxyl radical mediated pathway (NP and IPA), there is a broad similarity between trends with an increased photoactivity at a maximum of 0.01%, reduced at higher levels, and either reduced or unaffected at dopant levels less than this optimum. However, when measured by salicylic acid degradation, which follows a direct hole mechanism, the photoactivity follows a different trend with a moderate increase at low levels and a steady decrease as the level is increased i.e. *there is no optimum dopant level*.

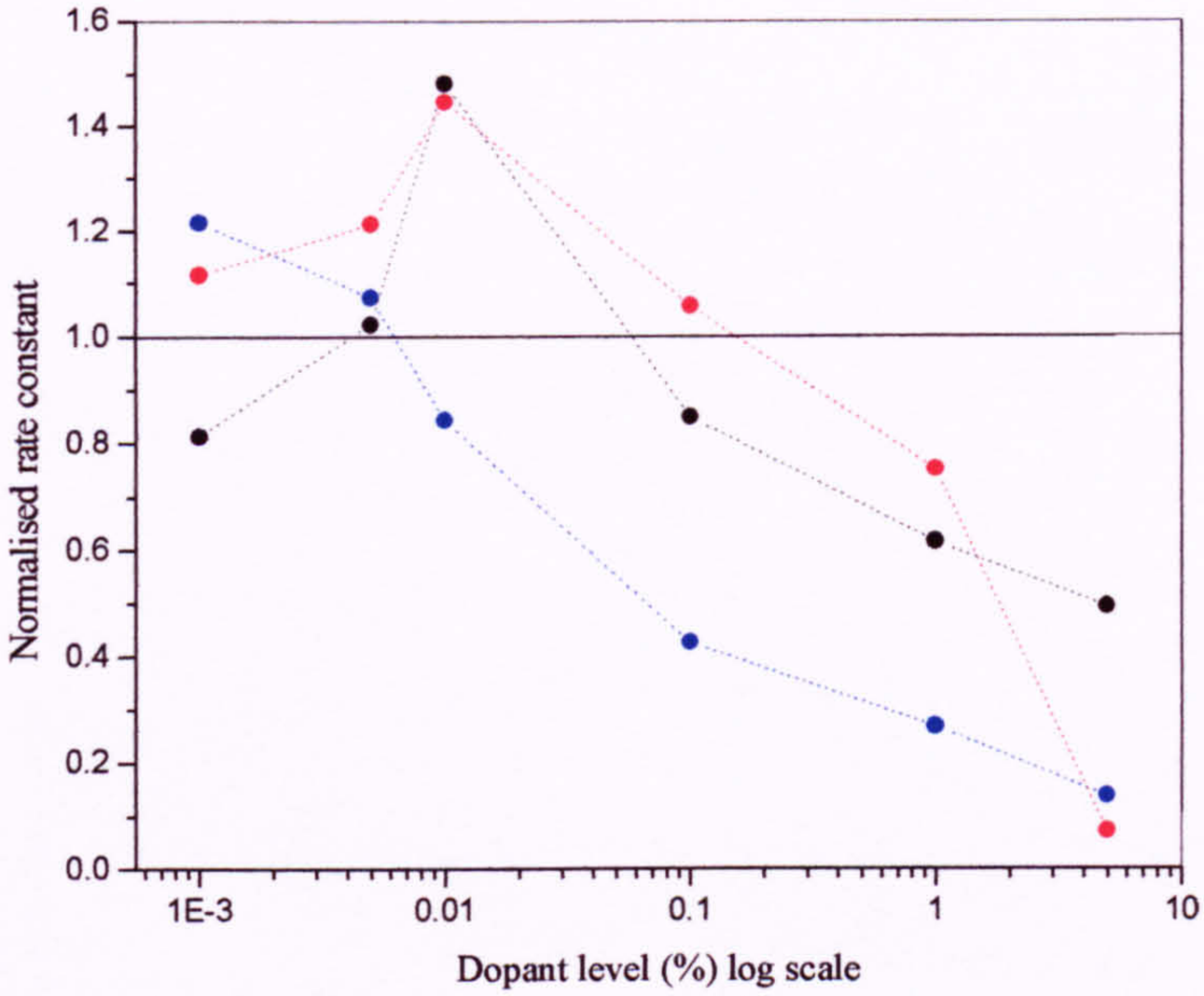

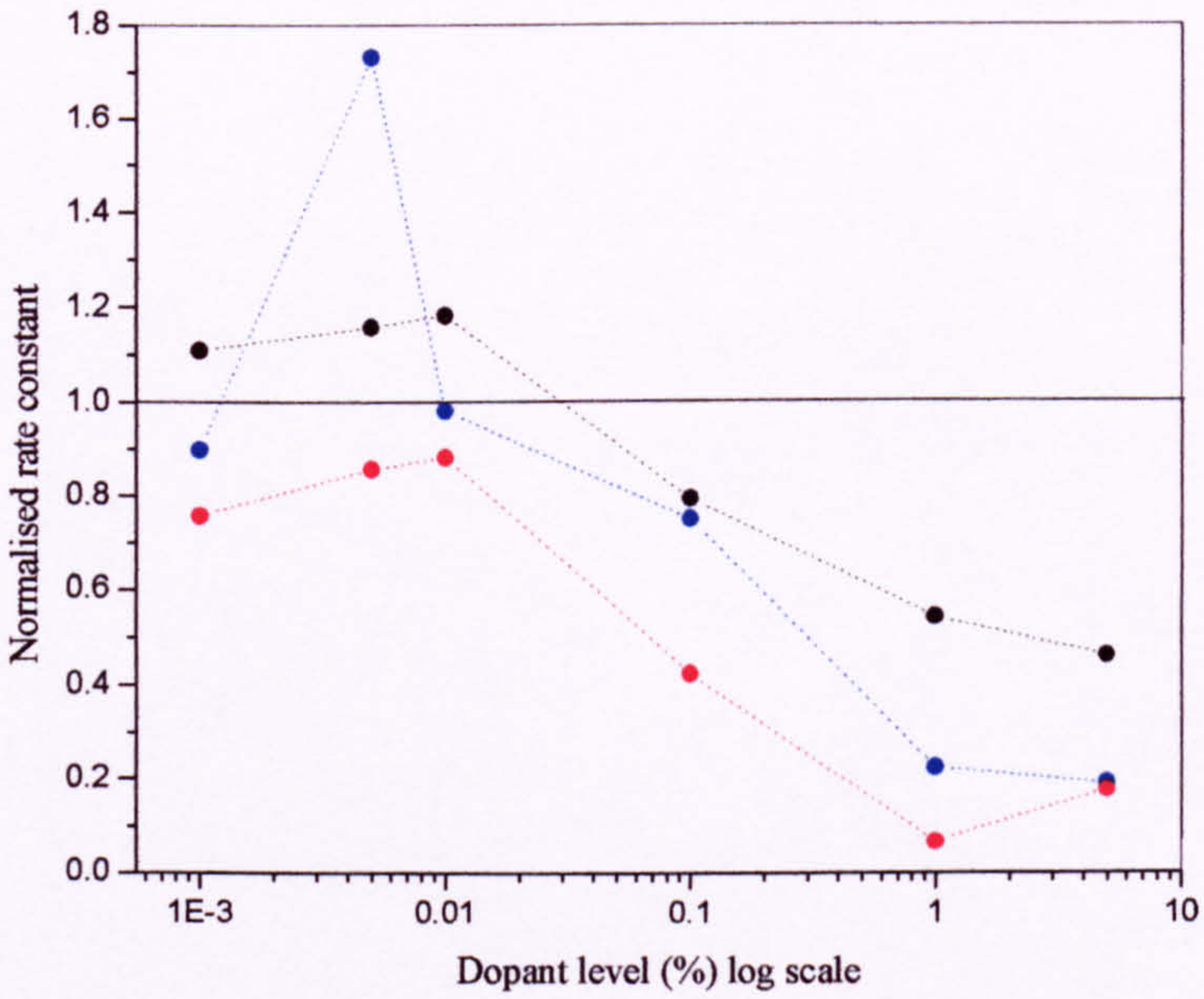

Fig 3.xxv and 3.xxvi. Comparison of the normalised rate constant for NP (---); IPA (---) and SA degradation (---) for surface (top) and lattice (lower) iron doped Sample A.

A comparison of the photoactivity of lattice doped Sample A, measured by salicylic acid degradation with that for NP and IPA (Figure 3.xxvi) showed that while there is some difference in the magnitude of the optimum value, there is a similar trend. Interestingly, omitting the optimum, the relative photoactivities measured by salicylic acid degradation are lower than those measured by the NP technique (also in aqueous solution), but are higher than those for IPA. This reinforces the result above (section 3.4) that for lattice doping the iron is not as effective at lowering the photoactivity in aqueous solution as in isopropanol.

3.11. Conclusions: the effect of iron doping on the photoactivity of titania.

The main conclusions from this chapter are as follows:

1. The effect of surface iron doping on the photoactivity as measured by IPA is similar for both Sample A and P25. At low levels of iron oxidation relative to the undoped samples is increased, whereas at high iron levels it is reduced. This trend is maintained when the samples are milled to break up agglomerates that may have been formed during the dopant process.
2. When measured by NP a similar effect is observed. For Sample A, there is good correlation between the photoactivity of samples measured by IPA and NP. For doped P25, the correlation is quantitatively not as good; the photoactivity is lower relative to the undoped sample when measured by NP than by IPA.
3. When measured by SA degradation, a technique shown to proceed by a direct hole mechanism, in contrast to the NP and IPA there is no optimum iron dopant level, there is a modest increase at low levels, but a steady decrease as the level is increased.
4. In contrast to surface doping, the effect of lattice doping is to lower the photoactivity measured by IPA relative to the undoped Sample A at all iron levels. This trend is maintained when the samples are milled suggesting that there is minimal agglomeration during the doping process. There is a profound difference in the photoactivity of these samples measured in an aqueous environment by NP. In this case, there is an increase in photoactivity at low iron levels relative to the

undoped sample, and a reduction only at the higher dopant levels. This conclusion is reinforced by the effect measured by SA degradation,

5. EPR spectra show that for lattice doped Sample A, iron is present in the lattice *and* on the titania surface. For surface doped Sample A and P25, the iron is only present on the surface.
6. The addition of iron (II) acetate during the Sample A preparation process does not alter the titania morphology as measured by powder XRD. Neither does it significantly alter the titania crystal size, a maximum variance of $\pm$ 2nm between the undoped and doped samples.
7. While the results are far from conclusive, the FTIR spectra of surface iron doped P25 indicate that acetate is present for high dopant levels and is most likely bound to the surface iron rather than directly to the titania. Similar measurements for Sample A also indicated acetate at high dopant levels but did not yield sufficient information to speculate on the binding mode.
8. Gravimetric analysis showed that surface iron doping did not significantly alter the surface area of P25. Whilst there is a trend for lower surface areas at high and low iron levels the maximum variance between the undoped and doped samples is within experimental error.
9. A new technique of SA degradation has been developed that has been shown (by addition of an alcohol in excess to scavenge hydroxyl radicals) to measure the photoactivity by a direct electron transfer mechanism rather than by a predominately hydroxyl radical mediated route.

3.12. Appendices.

Appendix 3.1. EPR spectra of surface iron doped P25.

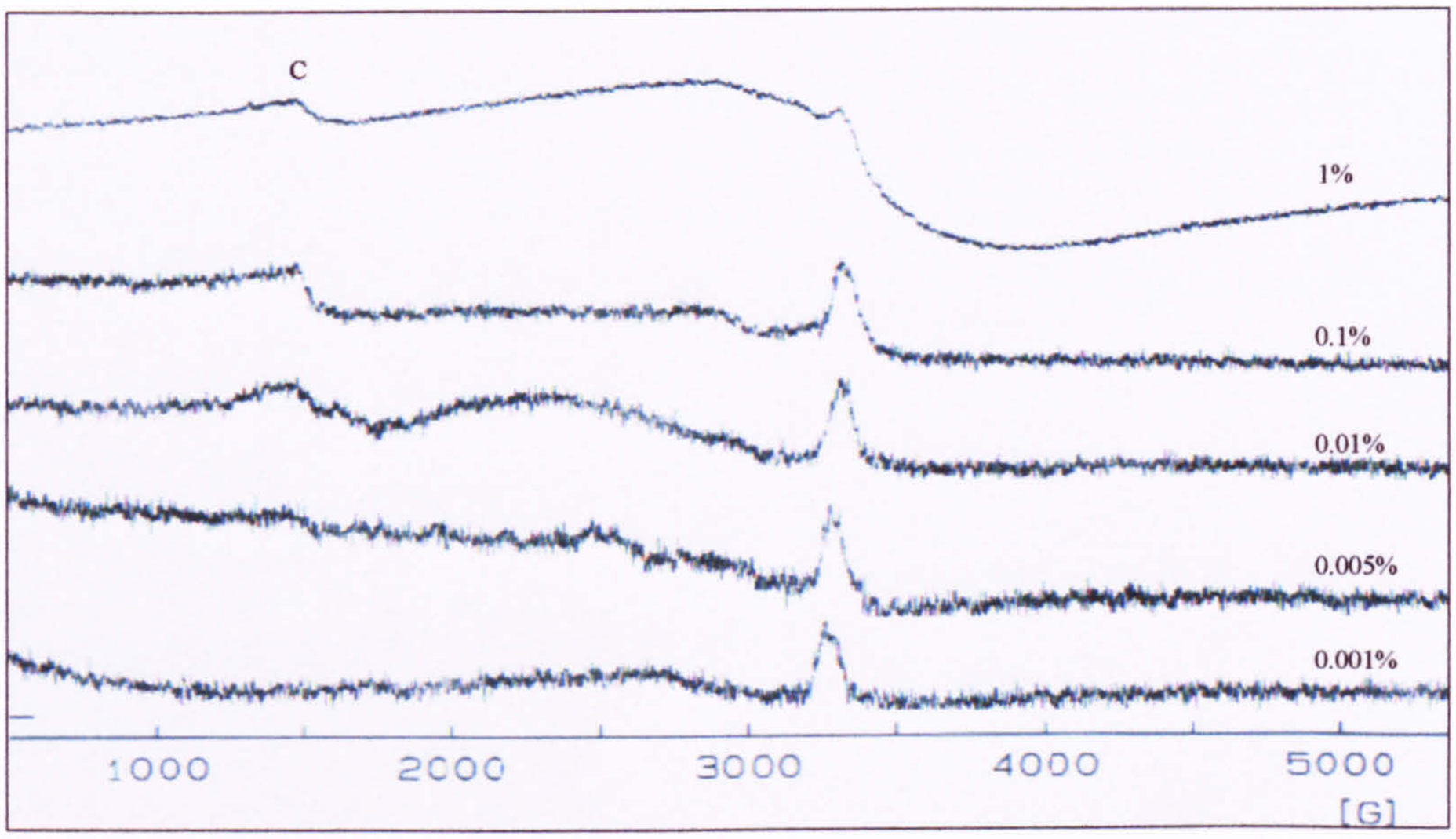

Figure A3.i. EPR spectra of surface iron doped P25.

Appendix 3.2. Colour of iron doped samples.

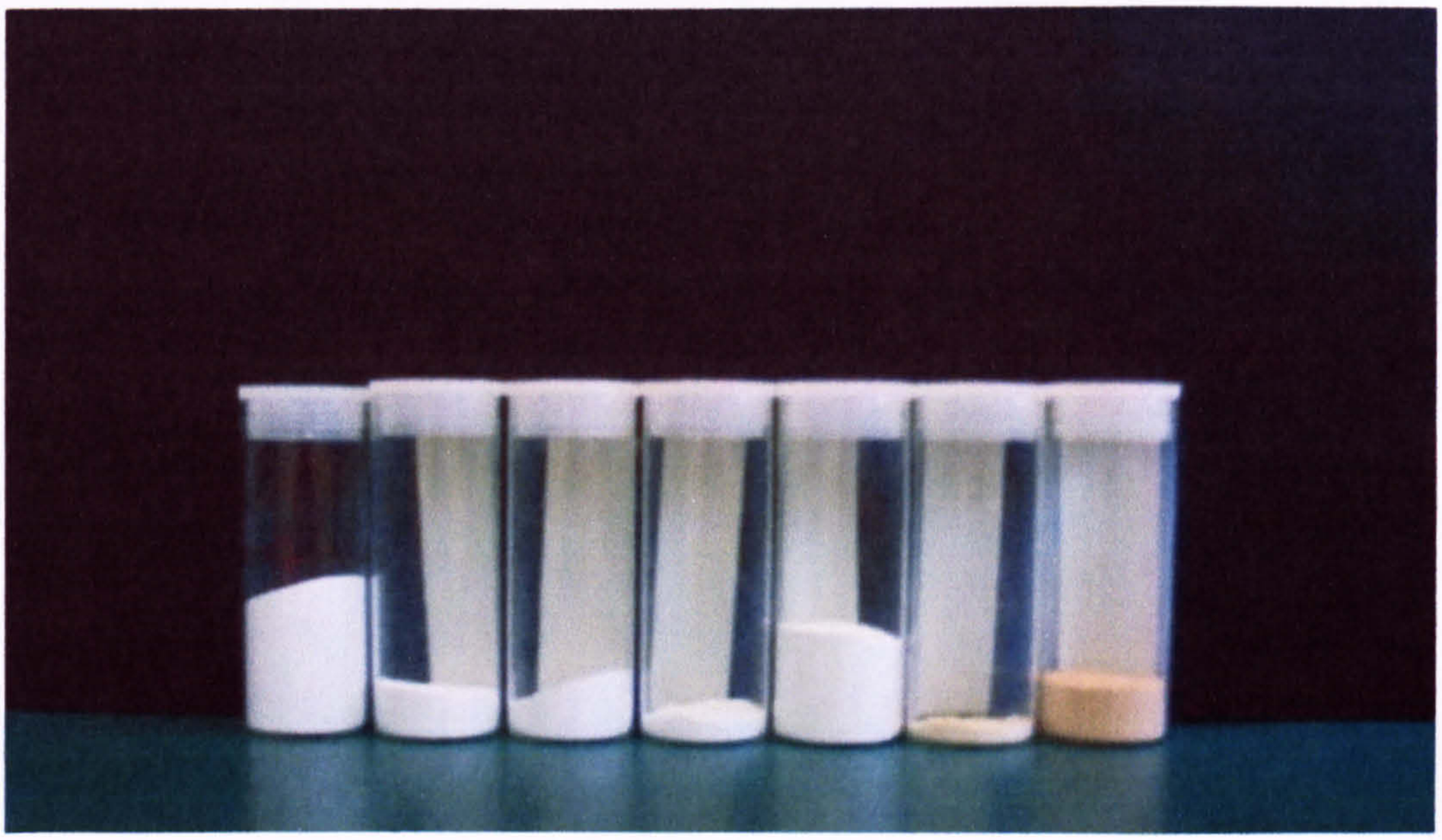

Fig 3A.ii. Surface doped P25. 0.001 at% to 5 at%.

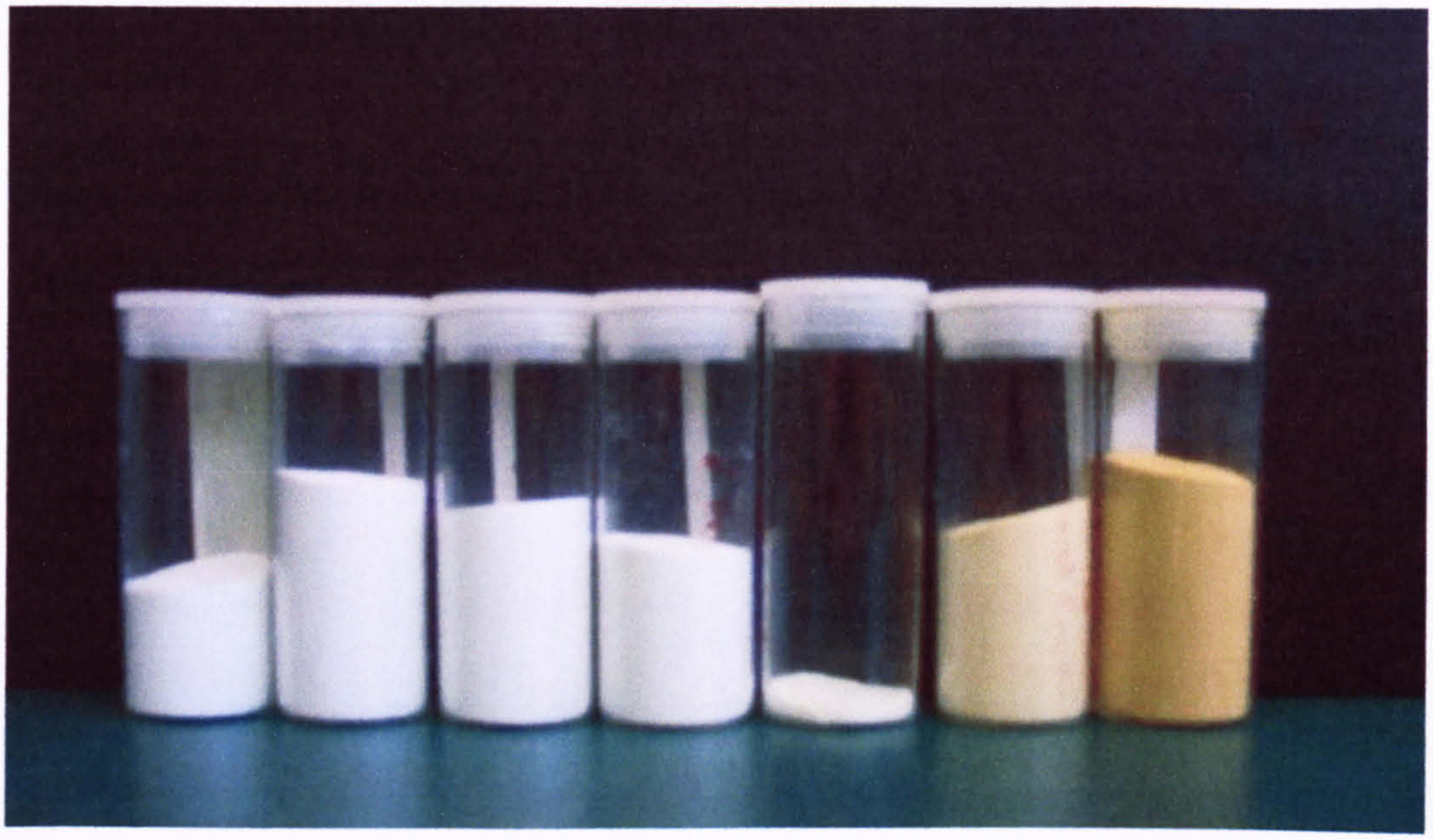

Fig 3A.iii. Surface doped Sample A. 0.001at% to 5at%

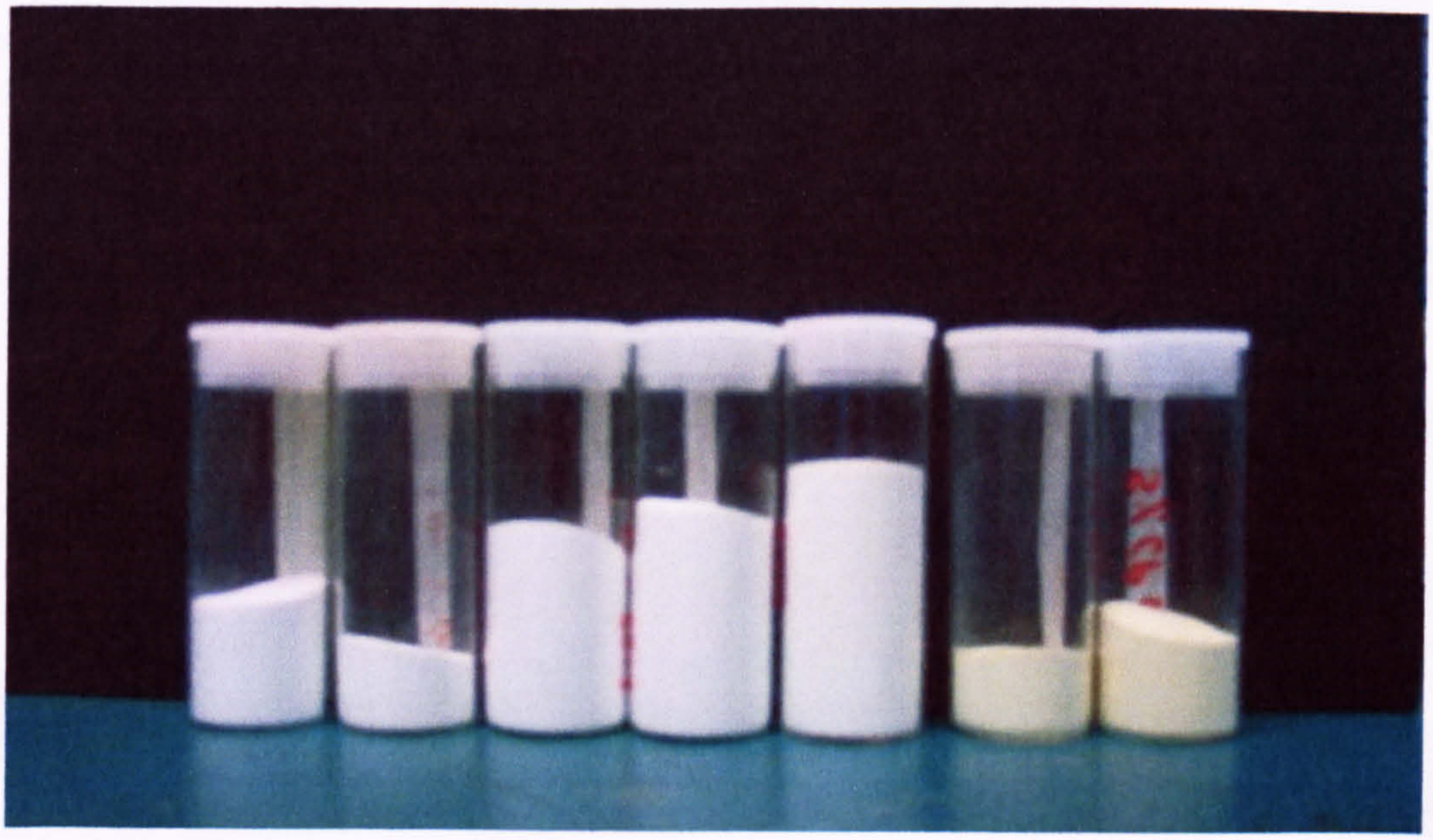

Fig 3A.iv. Lattice doped Sample A. 0.001at% to 5at%

3.13. References.

1. M. I. Litter; J. A. Navio, *J. Photochem. Photobiol. A*, **1996**, *98*, 171 and references contained within.
2. S. Karvinen, *Solid state Sci*, **2003**, *5*, 811.
3. T. A. Egerton and I. R. Tooley, *J. Phys. Chem. B*, **2004**, *98*, 5066.
4. J. R. Pilbrow, *J. Magn. Reson*, **1978**, *31*, 479.
5. S. Doeuff; M. Henry; C. Sanchez; J. Livage, *J. Non-Cryst. Solids*, **1971**, *89*, 84.
6. T. A. Egerton; E. Harris; E. J. Lawson; B. Mile; C. C. Rowlands, *Phys. Chem. Chem. Phys*, **2001**, *3*, 497.
7. J. S. Thorp; H. S. Eggleson; T. A. Egerton; A. J. Pearman, *J. At. Sci. Lett*, **1986**, *5*, 54.
8. A. Navio; M, Marcius; M. Gonzalez-Catalan; A Justo, *J. Mater. Sci*, **1992**, *27*, 3036.
9. K. MacKenzie, *Tran. Br. Ceram. Soc*, **1975**, *74*, 29.
10. J. Arana; J. M . Dona-Rodriguez; O. Gonzalez-Diaz; E. T. Rendon; J. A. H. Melian; G. Golon; J. A. Navio; J. P. Pena, *J. Mol. Cat A*, **2004**, *215*, 153.
11. J. M. Coronado; S. Kataoka; I. Tejedor-Tejedor; M. A. Anderson, *J. Catal*, **2003**, *219*, 219.
12. M. El-Maazawi; A. N. Finkin; A. B. Nair; V. H. Grassian, *J. Catal*, **2000**, *191*, 138.
13. L. Liao; W. Wu; C. Chen; J. Lin, *J. Phys. Chem B*, **2001**, *105*, 7678.
14. W. Rachmady; M. A. Vannice, *J. Catal*, **2002**, *207*, 317.
15. M. A. Hasan; M. I. Zaki; L. Pasupulety, *Applied. Cat A*, **2003**, *243*, 81.
16. M. Kaklhana; M. Kotaka; M. Okamoto, *J. Phys. Chem*, **1982**, *86*, 4385.
17. K. Ito; H. J. Bernstein, *Can. J. Chem*, **1956**, *34*, 170.
18. J. Arana; O. Gonzalez-Diaz; J. M . Dona-Rodriguez; J. A. Herrera; J. P. Pena, *Applied Cat B*, **2001**, *32*, 49.
19. J. D. Russell; E. Paterson; A. R. Fraser; U. C. Farmer, *J. Chem. Soc. Far. Trans*, **1975**, *71*, 1623.
20. C. H. Rochester; S. A. Topham, *Ibid*, **1979**, *75*, 872.
21. T. A .Egerton and I. R. Tooley, *J. Phys. Chem B*, **2004**, *98*, 5066.

22. N. Serpone; D. Lawless; R. Khairlutdinov; E. Pelizetti, *J. Phys. Chem*, **1995**, *99*, 16655.

23. A. J. Maira; K. L. Yeung; C. Y. Lee; P. L. Yue; C. K. Chan, *J. Catal*, **2000**, *192*, 185.

24. L. Palmisano; M. Sciavello; A. Sclafani; C. Martin; I. Martin; V. Rives, *Cat lett*, **1994**, *24*, 303.

25. O. Carp; C. L. Huisman; A. Reller, *Prog. Sol. State. Chem*, **2004**, *32*, 33 and references within.

26. S. Tunesi; M. Anderson, *J. Phys. Chem*, **1991**, *95*, 3399.

27. T. Picatonotto; D. Vione; M. E. Carlotti, *J. Disp. Sci. Tech*, **2002**, *23*, 845.

28. D. Vione; T. Picatonotto; M. E. Carlotti, *J. Cosm. Sci*, **2003**, *54*, 513.

29. C. Richard; P. Boule, *New. J. Chem*, **1994**, *18*, 547.

30. R. W. Harrison, MPhil Thesis, University of Newcastle Upon Tyne, Newcastle Upon Tyne, NE1 7RU, **(2001)**.

4. EFFECT OF IRON DOPING ON THE PHOTOACTIVITY.

This chapter discusses the results on the effect of iron doping on the photoactivity of titania shown in the previous chapter (3). In particular, the general effect of iron is discussed, and probable reasons for the observed effect of surface and lattice doping on the photoactivity measured by the different methods are suggested. These different techniques are indicated by the following acronyms: IPA is used to indicate 2-propanol oxidation, NP 2-nitrophenol degradation, and SA salicylic acid degradation.

4.1. Introduction

Several authors [1-5] have focused their efforts on iron doped titania of mixed morphology prepared by high calcination temperatures. Changes in crystal size, surface area, and morphology make it difficult to directly compare published works and thus to predict the precise effect of iron doping on the photoactivity except in the specific cases described. The preparation conditions appear to be very important to the final effect of iron doping on the photoactivity with contradictory results, especially for the photodegradation of different probe molecules [6].

The present work has been concerned with iron doping titania of a single morphology (Sample A) or one that is well characterised such as the commercially available Degussa P25. Conditions were carefully chosen so that iron doping did not significantly alter material characteristics that would be expected to affect photoactivity such as surface area, crystal size and morphology. In this way the precise nature of the effect of iron doping on the photoactivity can be usefully shown by isolating the effect of other variables. By studying the iron doping of Degussa P25 we can compare our results with those of other authors who have also studied this material, which is often used as a benchmark for photocatalysis studies [7]. The photoactivity was determined in several ways by the degradation of more than one type of probe molecule.

4.2. The general effect of iron doping.

Before beginning a discussion on the general theory of iron doping it is useful to first consider the processes that lead to titania photoactivity. These are summarised here - a full description is given in Section 1.5.3. Absorption of a photon of energy greater

than the titania bandgap (E_{bg}) leads to the generation of mobile charge carriers, an electron (e^-) in the conduction band and a hole in the valence band.

$$TiO_2 + hv \rightarrow TiO_2 (h^+_{vb} - e^-_{cb}) \quad [4.1]$$

These charge carriers either migrate to the surface or recombine in the lattice (Equation 4.2).

$$TiO_2 (h^+_{vb} - e^-_{cb}) \rightarrow TiO_2 + \text{Thermal energy} \quad [4.2]$$

If they reach the surface the hole is trapped by an adsorbed hydroxyl, while Ti^{IV} traps the electron.

$$h^+_{vb} + >Ti^{IV}\text{-}OH \rightarrow (>Ti^{IV}\text{-}OH^{\bullet})^+ \quad [4.3]$$

$$e^-_{cb} + >Ti^{IV}\text{-}OH \rightarrow (>Ti^{III}\text{-}OH) \quad [4.4]$$

Some authors [8,9] have also suggested that the hole may be trapped in a subsurface site.

$$h^+_{vb} + Ti^{IV}\text{-}O^{2-}\text{-}Ti^{IV} \rightarrow (Ti^{IV}\text{-}O^{\bullet-}\text{-}Ti^{IV}) \quad [4.5]$$

Once the charge carriers are trapped at the surface, interfacial charge transfer can occur with electron donors (D) and accepters (A); except in deaerated systems the acceptor is typically O_2 (leading to reactive oxygen species). Interfacial charge transfer can only occur by Equation 4.8 under certain circumstances i.e. when the electron donor molecule is strongly adsorbed [10].

$$(>Ti^{IV}\text{-}OH^{\bullet})^+ + D \rightarrow >Ti^{IV}\text{-}OH + D^{\bullet} \quad [4.6]$$

$$(>Ti^{III}\text{-}OH) + A \rightarrow >Ti^{IV}\text{-}OH + A^{\bullet-} \quad [4.7]$$

$$(Ti^{IV}\text{-}O^{\bullet-}\text{-}Ti^{IV}) + D \rightarrow Ti^{IV}\text{-}O^{2-}\text{-}Ti^{IV} + D^{\bullet} \quad [4.8]$$

Or surface recombination can occur, either by directly quantum tunnelling of the two charge carriers trapped on the surface (Equation 4.9) or by recombination with newly formed charge carriers from subsequently photoexcited electrons.

$$(>Ti^{IV}\text{-}OH^{\bullet})^+ + (>Ti^{III}\text{-}OH) \rightarrow 2\,(>Ti^{IV}\text{-}OH) \quad [4.9]$$

$$h^+_{vb} + (>Ti^{III}\text{-}OH) \rightarrow >Ti^{IV}\text{-}OH \quad [4.10]$$

$$e^-_{cb} + (>Ti^{IV}\text{-}OH^{\bullet})^+ \rightarrow >Ti^{IV}\text{-}OH \quad [4.11]$$

The characteristic times for interfacial charge transfer reactions are usually much slower than those for charge trapping and recombination processes [11]. For large particles lattice recombination is a significant process [12]. For small particles the bulk recombination rate is lower as the diffusion length of the charge carriers is typically greater than the particle size [12,13], and surface recombination becomes important due to the lack of a driving force for charge separation.

4.2.1. The energy level of iron dopants.

Mizushima et al [14,15] determined the energy levels for metal dopants in single crystal rutile by photocurrent measurements and semi-empirical calculations from optical absorption experiments – the proposed energy level diagram is shown in Figure 4.i. Depending on the energy level for the dopant ion states, charge carrier trapping may be thermodynamically allowed. Kinetic constraints may determine whether this actually takes place. As can be seen from this diagram, the Fe^{3+}/Fe^{2+} couple lies close to, or just above, the conduction band, and the Fe^{4+}/Fe^{3+} just above the valence band. Thus, the localised energy states of the iron dopants can receive electrons from the titania conduction band and donate electrons into the valence band. The introduction of iron dopants to titania therefore has implications for both photoactivity and colour.

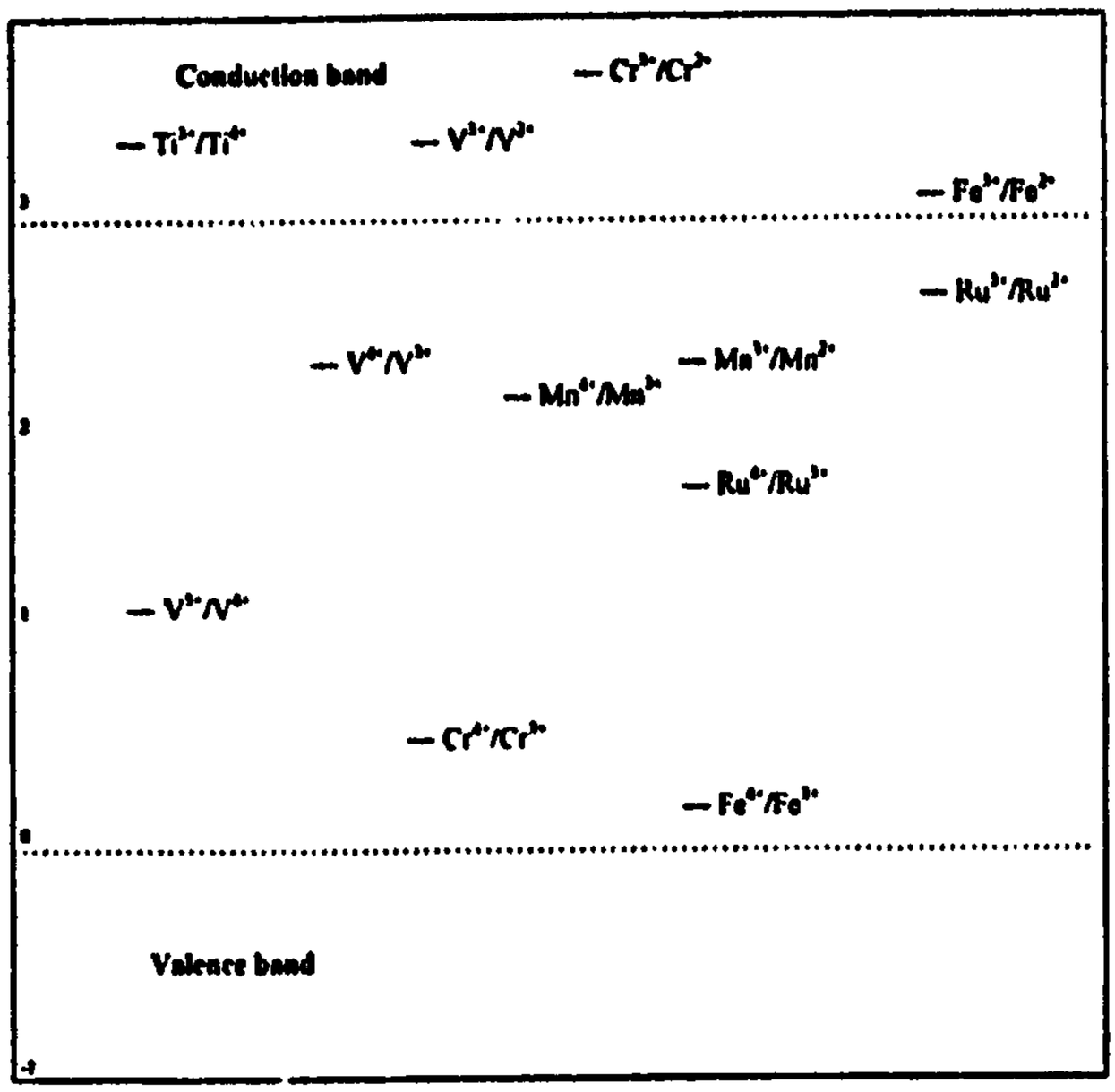

Fig 4.i. Energy level diagram for metal ions in rutile [14]

The energy level of the Fe^{3+}/Fe^{2+} couple is only just above the level of the bottom of the titania conduction band, and thus it would be expected to always return to Fe^{3+}. However, the experiments performed by Mizushima et al [14,15] used single crystal large particle size rutile and the actual levels for iron dopants in nano sized particles may be slightly shifted, and the Fe^{3+}/Fe^{2+} level may be within the band gap.

4.2.2. Colour of iron doped samples.

Iron dopants introduce localised energy states into the bandgap of the titania, resulting in a red shift and a degree of visible light absorption [16,17] due to charge transfer reactions between the localised states of the dopant and the conduction or valence band of the titania, or d-d transitions in the crystal field. Diffuse Reflectance Spectroscopy (DRS) measurements have shown that iron doped samples have higher absorption in the visible range that increases for doping level together with a change in colour from white to yellow. Navio et al [6] reported that at low dopant concentrations, there is a red shift in the shoulder, while for more heavily doped samples two absorption bands are evident at 410nm and 500nm, suggesting a segregated iron phase. The broad band at ~ 500 nm can be ascribed to the d-d transition T_{2g} to A_{2g}, or T_{1g} or charge transfer reactions between dopant ions via the conduction band. Kim et al [18] used photoluminescence spectroscopy to probe iron doped P25 and ascribed a band at 614nm to a transition between the Fe^{4+}/Fe^{3+} localised level and the titania conduction band. Bands at ~ 410 nm have been ascribed to the formation of surface peroxo species stabilised by the transition metals rather than dopant electronic transitions, as these have been observed for peroxide impregnated titania by Martin et al [19].

4.2.3. Electronic effects of iron doping on the photoactivity.

According to the energy level diagram proposed by Mizushima et al [14] above, iron dopants have suitable localised energy levels to trap both holes and electrons photogenerated by the titania through the Fe^{4+}/Fe^{3+} and Fe^{3+}/Fe^{2+} couples. However, there is some controversy over whether in practice holes *and* electrons are trapped, or whether the iron traps just the holes – the electrons being trapped at surface Ti^{4+} sites as for undoped titania (Equation 4.4 above). Spectroscopic or EPR evidence after flash photolysis or steady state irradiation has prompted some authors [20,21,22,23] to postulate that Fe (III) ions are better electron traps than surface Ti (IV). In addition, conductivity measurements on iron doped anatase electrodes prepared by hydrolysis of

titanium isopropoxide and iron acetylacetonate by Kosa et al [24] showed that iron dopants trap photogenerated electrons - as evidenced by reduced photocurrents that are coincident with increased photoactivity. EPR and absorption spectroscopy has shown that iron does shallowly trap holes at 0.12 eV above the valence band level [25,26,27]. On the basis of the studies above, the author considers that it is most likely that iron dopants can trap both holes and electrons rather than just holes. An important aspect for photoactivity is the kinetics of charge release. In the case of iron dopants it should be noted that crystal field theory dictates that Fe^{2+} (d^6) is relatively unstable due to the loss of exchange energy and tends to return to the more stable Fe^{3+} (d^5) configuration by transfer of an electron to the energetically close titania conduction band (Ti^{3+}/Ti^{4+} level) i.e. the carrier is only shallowly trapped with important implications for mobility. By trapping the charge carriers iron dopants affect the photoactivity of the titania in several ways dependant on the loading.

For samples with a low loading of iron, it has been shown that trapping can reduce recombination and consequently increase the lifetime of charge carriers [28,29] by separation and immobilisation of the photogenerated electron-hole pair [28] as the characteristic recombination rate for a trapped electron-hole pair is relatively slow. However, trapping of only one of the pair is thought to be ineffective as the trapped charge quickly recombines with its mobile counterpart [30]. An increase in the mean lifetime of charge carriers from 30 ns to minutes or longer has been reported for 0.5% Fe^{3+} doped 12 nm colloidal anatase titania [28,30]. The reduction in recombination leads to an enhanced photoactivity as has been found by several authors [30,31]. In addition, the diffusion length of the minority charge carriers for doped electrodes has been shown to increase to 2 for Fe^{3+} and decrease to 0.2 μm for Cr^{3+} from 1 μm for undoped [32]. While this has important implications for the photoactivity of large pigmentary size titania, it is not significant for the small particles used in the present study as the crystal size of ~10nm (0.01 μm) is smaller than the characteristic diffusion length.

However, for samples with a high loading of iron, the iron dopants tend to act as recombination centres and there is an increased rate of recombination. Gratzel [33] determined that the rate of recombination by tunnelling between trapped charge carriers is inversely proportional to the distance (R) separating the electron-hole pair:

$$k_{recomb} \alpha \exp(-2R/a_0) \quad [4.12]$$

(Where a_0 is the hydrogenic wave function of the trapped charge carriers)

i.e. the rate of recombination increases exponentially with dopant concentration due to the decrease in the average distance between dopant trap sites. In addition, an increase in the number of dopant trap sites within the particle leads to a reduction in charge carrier mobility [34]. Charge carriers with low mobility are likely to recombine with subsequently generated counterparts. This aspect was emphasised by Zhang et al [34] who suggested that at high dopant concentrations the charge carriers would be trapped several times during migration to the particle surface. Lastly, the solubility of iron dopants in titania is reported to be 1 at% for anatase [22] and between 1 at% and 3 at% for rutile dependant on the calcination temperature [35]. Thus at high iron dopant loadings the existence of low activity segregated phases of amorphous or crystalline iron oxides such as haematite and pseudobrookite [3] is evident, contributing to a low photoactivity.

The balance between the two extremes of high and low loadings determines the optimum iron dopant level for maximum photoactivity. At concentrations lower than the optimum, the photoactivity increases with loading as the number of trap sites increases leading to efficient trapping [30,33]. At concentrations higher than the maximum the photoactivity decreases with loading caused by an increase in the rate of recombination due to a decrease in the average distance between trap sites, lower charge carrier mobility, and the formation of inactive segregated surface iron oxide phases [3]. The appearance of an optimum iron loading has been observed for several liquid and gas phase photocatalytic systems [5, 17,30,34, 36, 38].

Choi et al [30] found an optimum iron dopant level of 0.5 at % for the oxidation of $CHCl_3$ and reduction of CCl_4 for 4nm anatase titania doped with iron in the range 0.1 at% to 3 at%. There was a quantitative correlation between the transient charge carrier recombination kinetics for these samples and the photocatalytic rates for both oxidation and reduction. On the basis of these results the authors concluded that charge carrier trapping by the metal ions was the dominant factor for metal doping with iron and

several other transition metals. They also suggested that trap sites provided by the dopants mediate interfacial charge transfer i.e. that dopant trap sites are more effective at transferring charge to surface species than intrinsic Ti^{3+} sites.

Tachikawa et al [39] studied the influence of Na, Li, Mg dopants in Degussa P25 titania and found that metal dopants may mediate interfacial charge transfer by decreasing the reverse, back electron transfer process. They found that the metals promoted desorption of the organic radical generated by hole oxidation and thus suppress charge recombination.

The role of titania particle size in determining the optimum iron dopant level for photocatalysis was examined by Zhang et al [34]. The authors studied the rate of chloroform oxidation by 6nm and 11nm anatase titania doped with iron in the range 0.02 at%-1 at% and postulated that at low iron concentrations charge separation by dopant trap sites reduces recombination, while at high concentrations charge carrier mobility is low due to multiple trapping of the carriers during migration to the surface. Particle size was important with, an optimum iron loading of 0.2at% for 6nm, and 0.05% for 11nm titania. For larger particles the average pathlength of a charge carrier to the surface is greater, and if the dopant concentration does not change then the possibility of the carrier meeting a dopant increases, and so does the chance of multiple trappings. The authors concluded that the optimum dopant concentration thus decreases with increased titania particle size; an argument supported by both examination of published work (in particular Choi et al, above [30]) and their experimental results.

Li et al [38] studied the effect of iron doping in the range 0.05-5 at% on 9-13 nm sized anatase for the selective oxidation of cyclohexane. In contrast to Degussa P25, the majority product is the cyclohexanol with iron doped samples rather than cyclohexanone, suggesting that the surface state of these samples affects the products. They reported an optimum of 1 at% with the reduction at higher levels attributed to segregated hematite that was undetectable by EPR. *In situ* EPR monitoring of the bulk and surface Fe^{3+} signals under illumination show that both decrease exponentially. The authors suggest that holes are trapped at surface Fe^{3+} trap sites and electrons in bulk Fe^{3+} sites.

4.2.4. Structural effects of iron doping on photoactivity.

In addition to the electronic effects of doping discussed above, the preparation procedure and incorporation of metal ions causes changes to the structural aspects with important implications for photoactivity. For example, iron doping affects the light absorption, charge transfer rates, lattice defects, extent of hydroxylation, properties that may contribute to the altered photoactivity of iron doped samples.

The incorporation of iron into the titania lattice causes changes to the light absorption properties necessary to initiate photocatalysis. In particular the incorporation of iron has been reported to result in a red shift in the absorption into the visible range with increased loading (see Fig 4.ii below) raising the possibility of visible light photocatalysis [16,17]. The introduction of localised iron levels within the titania bandgap (the Fe^{4+}/Fe^{3+} couple lies just above the valence band and the Fe^{3+}/Fe^{2+} close to the conduction band – see above in section 4.2.1) allows transitions of energy less than the characteristic bandgap energy either between the two iron levels or between these levels and the titania conduction band [18]. Some authors [40] have suggested that the increased light utilisation by iron doped titania contributed to an improved rate of photocatalysis. Visible light excitation has been reported although this is thought to arise in some cases by surface complexation of the organic with Fe^{3+} [41]. It is generally considered that the increased light utilisation for highly doped titania is outweighed by the increased recombination of charge carriers in these samples with a consequent overall reduction in the photoactivity [6].

Wang et al [4] determined the proportion of cationic defects in the titania structure for iron doped samples in the range 1-10 at% prepared by a sol-gel technique. For anatase samples, iron doping was found to increase the proportion of these defects from 17%-23% (although calcination at 600°C reduced all samples to a similar level) while corresponding analysis of the rutile structure showed lower defects and only a marginal increase with iron level. These defects have been suggested as likely recombination sites [42] and the increase with greater iron incorporation may contribute to lower photoactivity.

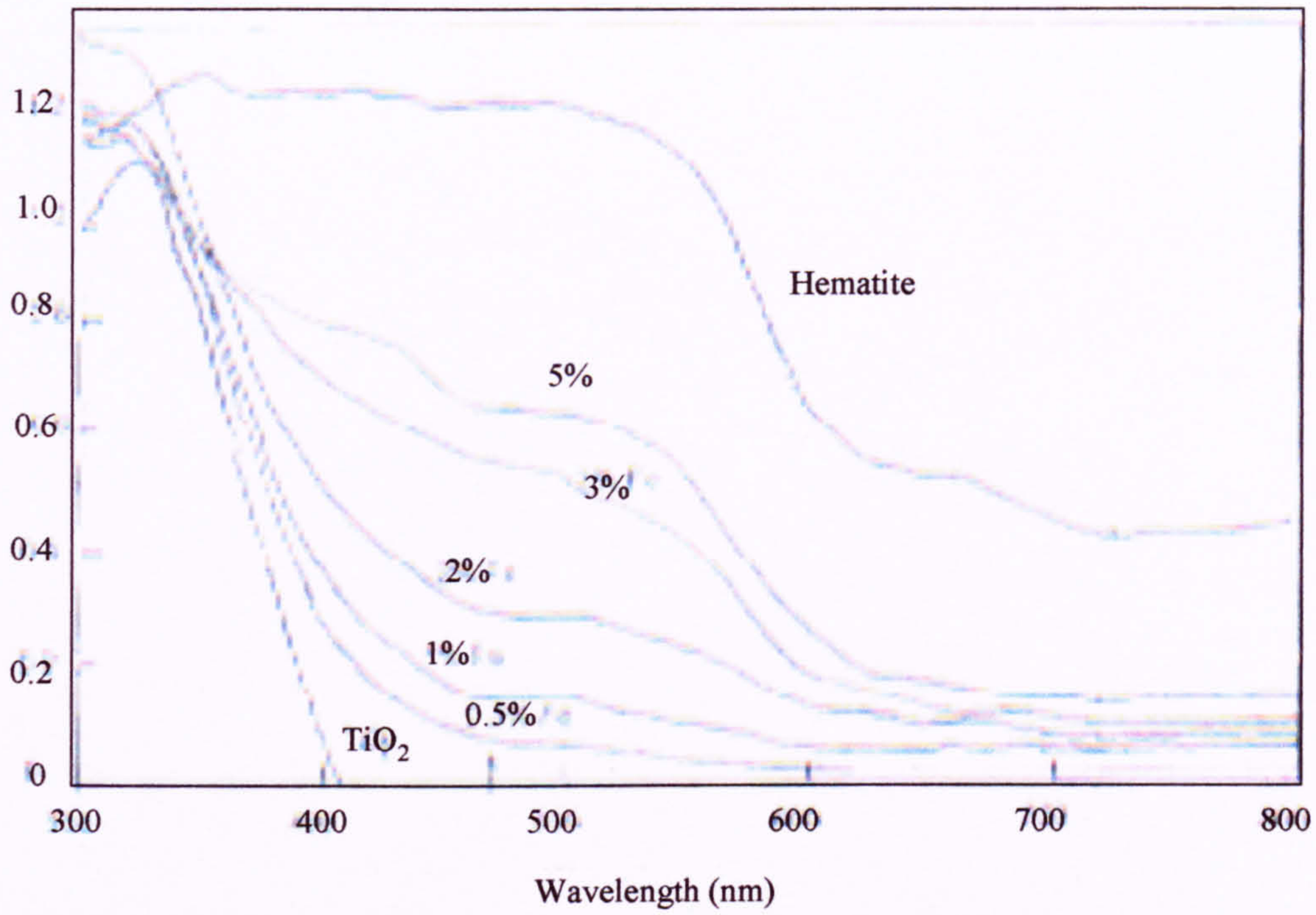

Fig 4.ii. Diffuse reflectance spectra of iron doped P25 [6].

The reduction in hydroxylation has also been suggested as a contributory factor in iron doped samples with lowered photoactivity, as the surface hydroxyl groups are trap sites for holes [40,41]. Park et al [40] investigated the effect of doping titania with different transition metals at 0.1at% and found a qualitative correlation between the rate of gaseous trichloroethylene conversion and the surface hydroxylation (measured by the XPS signal for Ti-OH) for these samples. For iron doped titania the reduction in surface hydroxylation was suggested as a contributory factor in the decreased photoactivity. Several authors have found a reduction in titania hydroxylation caused by the presence of surface iron oxide [40,41].

Palmisano et al [37] found that in the case of iron doped (0.01-5at%) anatase titania prepared by impregnation or coprecipitation that the surface acid-base properties of the doped samples are similar to those for undoped and consequently adsorption/desorption of substrates, intermediates and products should not differ significantly with iron doping. However, this is not the case for all transition metal dopants. For example, Wilke and Breuer [43] examined 0.1-10 at% Cr^{3+} and Mo^{5+} doped anatase titania with a crystal size of 10-18 nm. They found a quantitative

correlation between the lifetime of the charge carriers by time resolved photocharge measurements and the photodegradation of Rhodamine B (RB) for the chromium doped samples and lower <1at% doped Molybdenum samples. However, for heavily doped (>1at%) Mo^{5+} samples, where adsorption of the RB was significantly affected by doping, a correlation was only achieved by combining both the lifetime of the charge carriers and dark adsorption isotherm measurements. Thus, while it is likely that there are no significant changes to the surface acid-base properties by iron doping, for other dopants such as Mo^{5+} this can contribute to the photoactivity.

An important omission from many studies on iron doped titania was the lack of knowledge of the iron distribution - lattice, on the surface, or a combination of both. For example, the postulated theory by Zhang et al [34] appears to suggest that the iron is predominantly distributed in the titania lattice, but the preparation method for all of the samples (coprecipitation with crystallisation at pressure with low temperatures) does not include the high calcination temperatures that are necessary to induce diffusion of *all* of the iron dopant into the lattice [44]. The authors also note that in small particles, surface recombination is a major process rather than bulk (or volume) recombination. It appears likely that in this case, iron is present on the surface and in the lattice and thus affects the rates of surface and bulk recombination. Indeed, it has been shown that even with high temperature calcination to induce migration into the lattice, surface iron persists. Thorp et al [45] demonstrated that for pigmentary sized rutile titania prepared by gas phase hydrolysis and iron doping by calcination at 600°C for 12 hours the iron has not all migrated into the lattice and, particularly for high dopant levels, there is a significant amount of surface enrichment.

4.3. Effect of lattice iron doping on material characteristics and photoactivity.

Having reviewed the various reported results and theories on the effect of iron doping, it is now discussed whether this can be applied to explain the photoactivity results observed for iron doped Sample A prepared by coprecipitation of the precursors.

4.3.1. Material characterisation.

Before discussing the effect of iron dopants in the titania lattice and on the surface it is first useful to recap the material characteristics of the iron doped titania samples. Electron Paramagnetic Resonance (EPR) spectra of lattice iron doped Sample

A show a broad peak for all iron doped samples at g ~ 4.3 that is attributed to surface Fe^{3+} ions in a rhombic site. In addition, there are four peaks at g ~ 8.1, 5.5, 3.2, and 2.5 that are attributed to Fe^{3+} ions in the titania lattice occupying sites of tetragonal symmetry. Thus, the coprecipitation method leads to Fe^{3+} in both the lattice and on the titania surface. There is a qualitative rise in signal height with increased iron dopant concentration for both surface and dopant iron, and thus there is no suggestion from the EPR spectra that either the surface or the lattice is significantly enriched with Fe^{3+} ions as the iron concentration is increased, Thorp et al [45] found similar results. The authors of that study also noted that EPR inactive iron species were present, and this could not be dismissed for the present study. In particular, Navio et al [46] have suggested that EPR may not detect agglomerated surface iron such as α-Fe_2O_3.

Powder X-Ray Diffraction (XRD) of iron doped and undoped Sample A show that all the samples are 99+ % rutile with similar crystal sizes (9.5 $\pm$ 2nm) i.e. the addition of the iron acetate during titania sample preparation does not significantly alter either the morphology or crystal growth. Some studies [46,47] have suggested that the addition of iron affects these properties (most probably during calcination) so the preparation conditions for the present study have been specifically chosen, with success, to eliminate this effect. There is no evidence from the XRD spectra for any segregated crystalline or agglomerated iron oxide phases as have been reported in some studies [3,46].

Iron dopants introduce localised energy states into the bandgap of the titania, resulting in a red shift and a degree of visible light absorption [16,17,18,40] due to charge transfer reactions between the localised states of the dopant and the conduction or valence band of the titania, or d-d transitions in the crystal field. Diffuse Reflectance Spectroscopy (DRS) measurements have shown that for the lattice iron doped samples prepared by coprecipitation there is a higher absorption in the visible range that increases for doping level (see section 3.9) together with a change in colour from white to yellow. At low levels (0.1%), the spectra showed a red shift in the shoulder, while for the more heavily doped sample (5%), there are two absorption bands at 410nm and 500nm suggesting a segregated iron phase - similar to the spectra of iron doped P25 with the same loading prepared by impregnation reported by Navio et al [6]. The failure

of XRD to detect a segregated phase could result from non-crystallinity, or a low level of the crystalline phase.

4.3.2. Photoactivity measurements.

The photoactivity of lattice iron doped Sample A was measured by isopropanol oxidation (IPA), nitrophenol degradation (NP), and salicylic acid degradation (SA). The IPA technique measures hydroxyl radical mediated oxidation [48] in an alcohol environment while the NP technique measures the oxidation in an aqueous environment, by a predominately hydroxyl radical mediated mechanism, as shown by a reduction in rate when bicarbonate is added as a radical scavenger, [49,50]. The IPA technique has been widely used for the determination of titania photoactivity but 2-nitrophenol degradation for photoactivity testing is relatively novel and therefore in addition to determining the photoactivity of iron doped samples in aqueous media, an aim of this project was to see how this compares to the IPA technique. The SA technique measures oxidation by a direct hole mechanism in an aqueous environment as has been shown in section 3.9, confirming results reported by Tunesi and Anderson and Vione et al [51,52,53]. The oxidative rate dependence (normalised) on the iron dopant level in the range 0.001at% to 5at% as measured by these three techniques, for lattice doped Sample A is shown in Figure 4.iii.

The effect of lattice iron doping on the oxidation rate measured by all three techniques is dependant on the dopant level. There is a very similar trend for both the oxidation of isopropanol (IPA technique) and nitrophenol degradation (NP) i.e. both techniques measuring oxidation by hydroxyl radical, and the good correlation of results for these techniques confirm that NP is measuring photoactivity in a similar manner to IPA. Both show moderate rises in photoactivity at the lowest iron levels as concentration is increased, an optimum at 0.01at%, and sharp decreases above this level. This is consistent with results on anatase titania of 4nm and 11nm size reported by Choi et al [30] and Zhang et al [34] respectively - in both cases the authors attributed this behaviour to electronic effects (this is discussed in more detail above in section 4.2.3). While the coprecipitation technique of iron doping employed in the present study to incorporate iron into the lattice, and on the surface, may lead to structural changes of the kind described above, it is reasonable to conclude from these results that the changes in photoactivity with iron doping are primarily the results of electronic effects i.e. the

introduction of iron trap sites in the titania lattice and on the surface. At iron dopant concentrations lower than the 0.01at% optimum, the photoactivity rises with the number of iron dopant trap sites as this leads to more efficient charge trapping and charge mediation, while at higher concentrations the photoactivity decreases as this leads to a decrease in the average distance between trap sites and thus an increase in the rate of recombination [33]. This latter effect may be emphasised by the formation of aggregated or segregated iron phases on the titania surface for the heavily loaded samples as shown by DRS measurements which may reduce surface hydroxylation as reported by Park et al [40] or form an inactive 'barrier' to charge carriers as for other oxides such as SiO_2 [54].

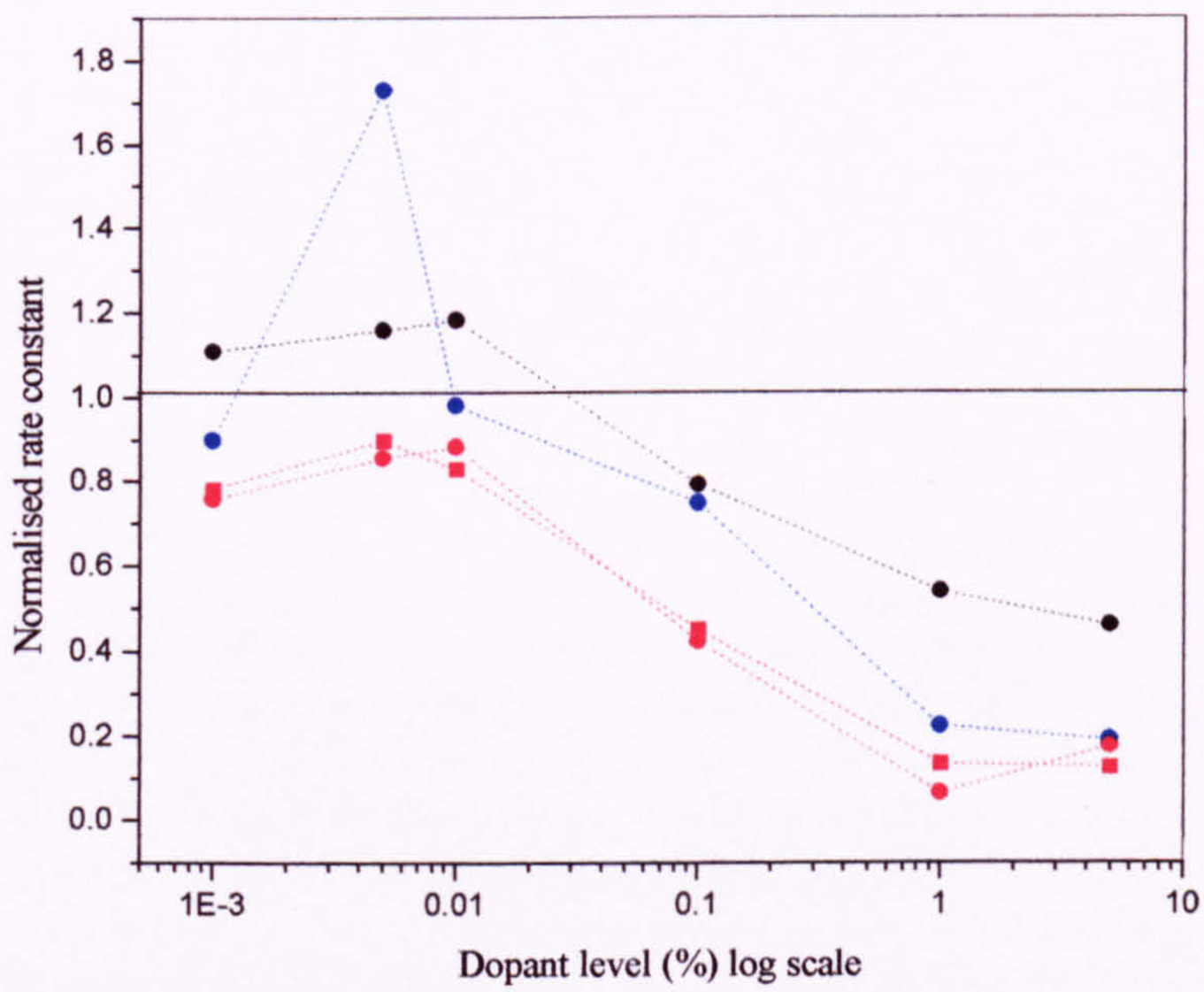

Fig 4.iii. Effect of the iron dopant level for lattice doped Sample A measured by NP (---); SA (---); and IPA (---); IPA, milled for 30 minutes (squares). Normalised to undoped Sample A.

A similar trend is observed for salicylic acid degradation (SA), where oxidation has been shown to proceed by a direct hole mediated mechanism, with a rise to an optimum then decrease with iron concentration. In this case there are slight differences when compared with the other measurement techniques - most notably, the position of

the optimum is at a lower iron dopant level of 0.005at%. The decrease beyond this point is most probably due to two separate effects. Firstly, as described in more detail above, iron has been demonstrated [30] to be a more efficient charge carrier mediator than surface Ti^{IV} sites i.e. more efficient at transferring charge to surface species, and therefore leads to an increase in rate as dopant level is increased due to a greater number of Fe^{3+} surface sites to mediate (qualitatively shown in the present study by EPR). However, salicylic acid has been shown to effectively capture the charge [51,52,53] in the absence of dopants and thus this effect is likely to have a lesser effect than for molecules such as isopropanol or 2-nitrophenol. Secondly, as shown by DRS spectra, for the higher levels of iron, segregated iron oxide phases form that may reduce photoactivity by altering the titania surface properties. The adsorption of salicylic acid has been demonstrated to be a more important factor for salicylic acid degradation than for example 2-nitrophenol (2-nitrophenol and 4-nitrophenol degradation at similar rates despite negligible adsorption by the latter) and thus surface properties would be expected to be of more importance than for IPA and NP. This is demonstrated more profoundly for surface iron doped Sample A below.

There is a similar trend in the photoactivity for the iron doped samples for both hydroxyl radical and direct hole mediated mechanisms, whether in alcohol or aqueous media, and this trend is that which would be expected from electronic effects so it therefore seems likely that if there is adsorbed acetate from the iron acetate precursor, as the FTIR results were not conclusive in determining this, then it does not play a major role in determining the photoactivity. Although not a major influence, it is possible at the higher iron dopant levels that acetate, if present, does contribute to the lower photoactivity for these samples.

A further observation from Figure 4.iii is that while the overall trend for the photoactivity of iron doped Sample A is similar whether measured by IPA, NP or SA, the absolute effect of iron doping is different depending on the media. The effect of iron doping measured in an alcohol media (IPA) is to reduce the photoactivity for all dopant levels relative to the undoped, while for measurements in aqueous media the photoactivity is enhanced for low levels and reduced for high levels (but not to the same extent as in alcohol) relative to the undoped Sample A i.e. iron doping is not as effective at reducing photoactivity in aqueous media and increases it at low dopant levels.

One explanation for this result is that, in addition to the electronic effects described above, iron doping alters the dispersion of the titania particles so that the measured photoactivity is higher relative to the undoped sample due to changes in the optics of the slurry. However, there was no change in either the trend, or relative photoactivities for the IPA technique when milled suggesting that in an alcohol medium there is no significant optical changes with doping. A second possibility is that the presence of iron dopants may increase photoactivity through the promotion of certain reaction steps in an aqueous media. Most likely this would be through the stabilisation of surface species, for example iron has been shown to stabilise surface hydrogen peroxide [19]. In either case, it was not possible to explore this result but it may be suitable for further study.

4.4. Effect of surface iron doping on the photoactivity.

Having discussed the effect of lattice and surface doping combined, these results are now compared below with those for surface doped Sample A. In addition, results are compared with the commonly used benchmark Degussa P25 that has been surface doped in a similar way, to provide a direct link with published work.

4.4.1. Material characterisation.

Firstly, it is pertinent to recap the results for the material characterisation of the surface doped samples. Electron Paramagnetic Resonance (EPR) spectra for all samples of iron doped Sample A and P25 show only a single peak at g ~ 4.3 which corresponds to iron in a surface rhombic site i.e. the precipitation method of doping results in iron on the surface and *not* in the lattice. This was expected as high calcination temperatures, much greater than the drying temperature used in the present study, are required to induce diffusion into the lattice when an impregnation method is used [44].

The surface areas of selected surface iron doped P25 samples were determined by gravimetric analysis. While there was a trend for a reduction in surface area at the lowest and highest dopant concentrations, the results are within experimental error and it can therefore be concluded that surface iron doping did not significantly alter the surface area for P25. Given the similarity in preparation procedure it would not be expected that the surface area would be altered for doping Sample A.

Surface iron doped samples are more coloured than those prepared by coprecipitation, perhaps due to a greater amount of segregated iron on the surface. The colour shifts from an off white to yellow and dark brown as the iron loading is increased.

Diffuse Reflectance Infra Red Spectroscopy (DRIFTS) was used to determine whether acetate, from the iron acetate precursor, was adsorbed to the titania during the doping process. For surface doped P25, it was concluded that acetate was most likely present at higher dopant levels as an iron acetate species rather than directly bonded to the titania. Similarly, for sample A, there was some evidence of adsorbed acetate at high doping levels but interfering species in the region of interest precluded a full determination of the bonding mode. It is discussed below whether adsorbed acetate is likely to affect the measured photoactivity.

4.4.2. Photoactivity measurements.

The photoactivity of surface iron doped Sample A and P25 was measured by propan-2-ol oxidation (IPA) and 2-Nitrophenol degradation (NP). Both these processes are known to proceed by a hydroxyl mediated mechanism (Equation 4.6 above), shown by a reduction in rate when bicarbonate is added as a radical scavenger [49,50]. By measuring the photoactivity by both methods the effect of the medium (alcohol or aqueous) was determined. The photoactivity of surface iron doped Sample A was also measured by salicylic acid degradation (SA) which has been shown in Chapter 3 to proceed by a direct hole transfer mechanism (Equation 4.5).

Figures 4.iv and 4.v compare the photoactivity measured by IPA with that measured by the NP technique for iron doped Sample A and P25, with the rate constants normalised to that for the relevant undoped samples.

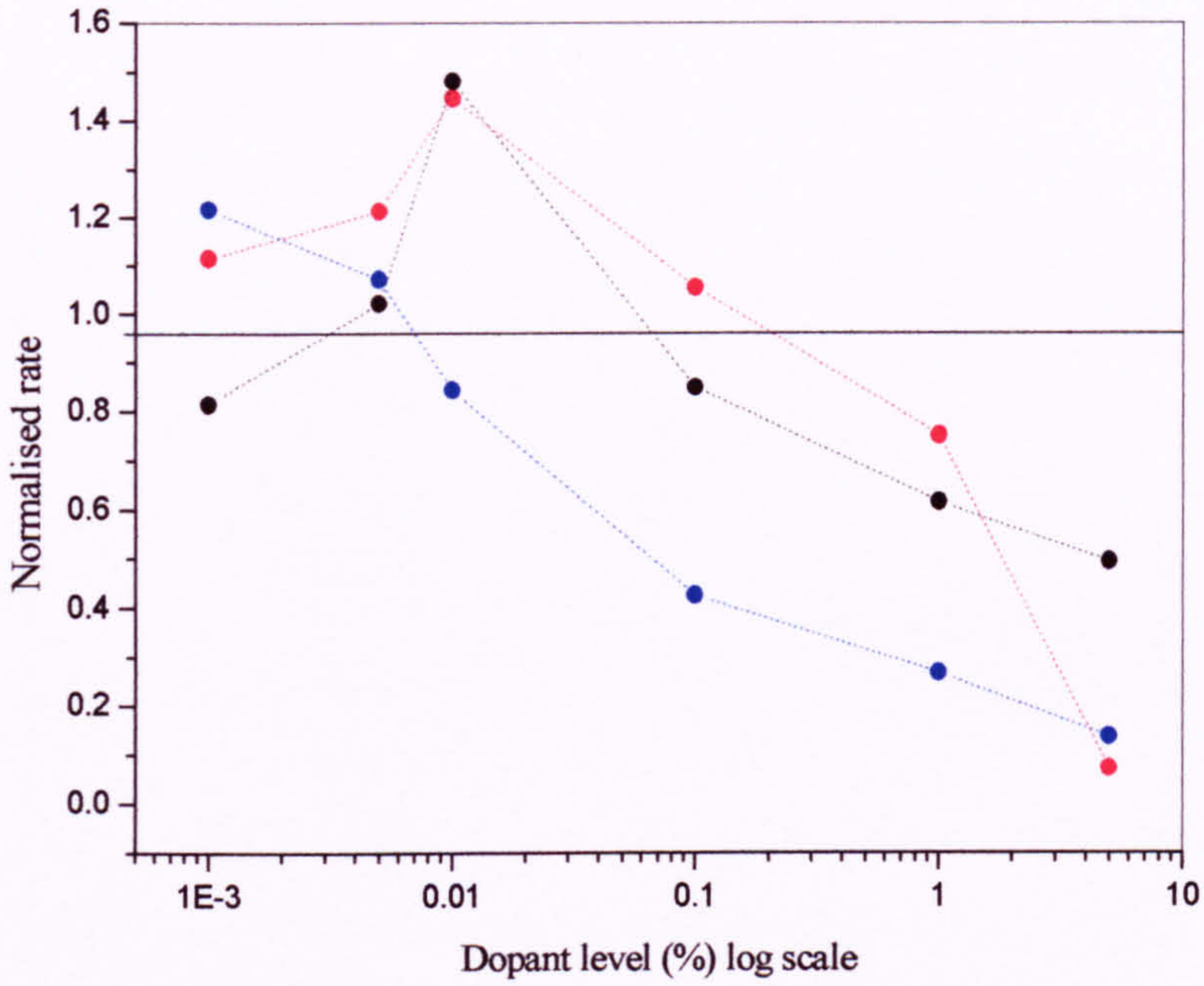

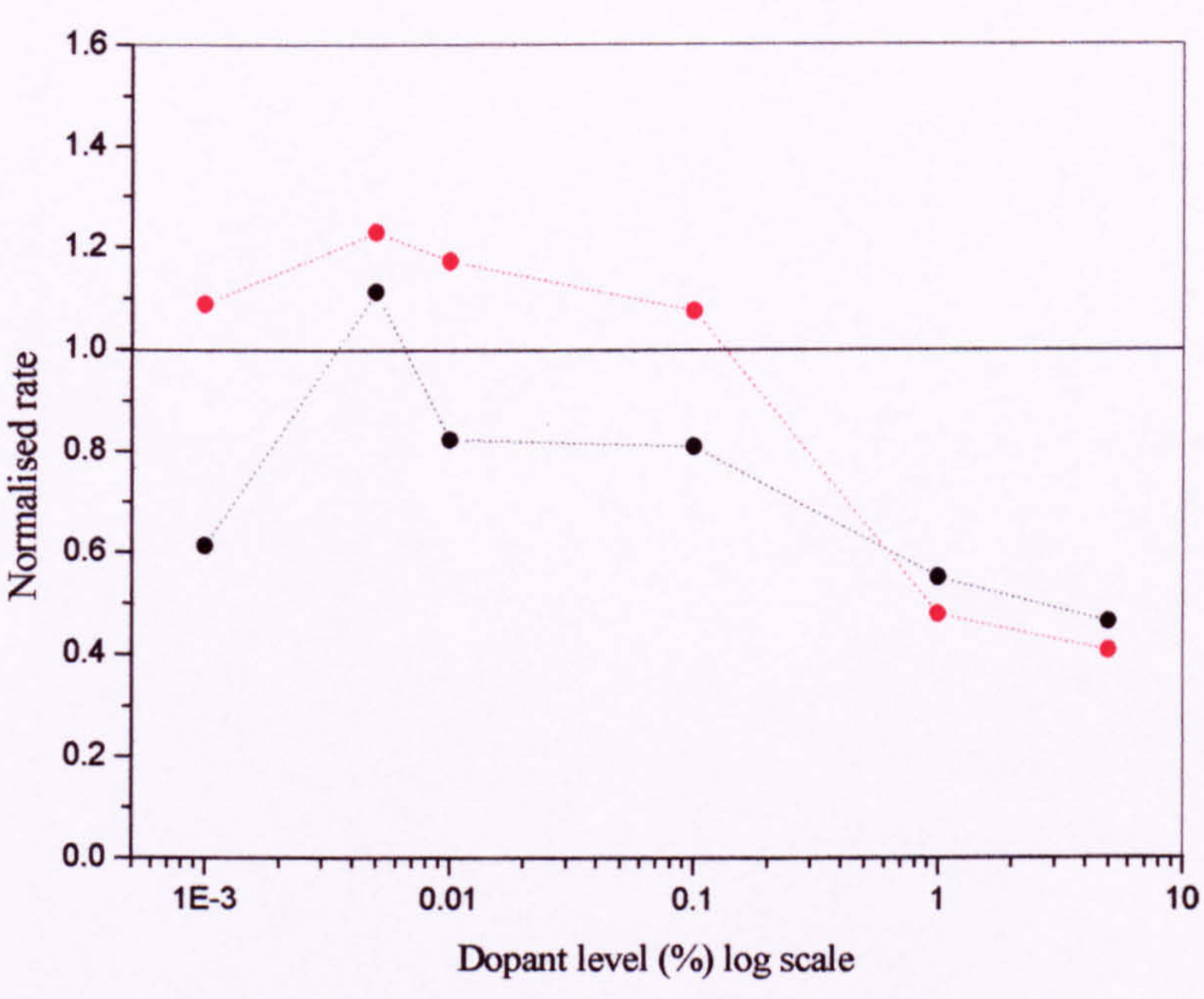

Figure 4.iv and 4.v. Normalised photoactivity for surface iron doped Sample A (above) and P25 (below) measured by NP (---) and IPA (---). Sample A also measured by SA (---).

As can be seen from a comparison of the photoactivity measured by IPA and NP, similar trends for dopant concentration are observed for both surface iron doped Sample A and P25. For both sets of titania samples, both techniques show a rise in photoactivity at the lowest iron levels as concentration is increased to an optimum, and sharp decreases above this level. The optimum is at 0.01 at% for Sample A, and at 0.005at% for P25 when measured by both IPA and NP. The observed trends are remarkably similar to those observed for lattice/surface doped Sample A, which were attributed to electronic effects in common with studies by Zhang et al [34] and Choi et al [30]. Therefore similar arguments may be made to explain the trends for surface doping, i.e. that the changes in photoactivity are primarily the result of charge trapping and mediation by the iron dopants (in this case on the surface). At iron dopant concentrations below the optimum, the photoactivity rises due to the increased number of dopants that lead to more efficient trapping and charge mediation. At concentrations above the optimum, the photoactivity decreases due to an increase in the rate of recombination caused by a decrease in the average distance between dopant trap sites [33,30]. In addition to the balance in the electronic effects, there may be a contribution towards reduced photoactivity caused by structural factors such as the formation of inactive aggregated iron phases (observed for heavily loaded lattice doped Sample A) that may reduce hydroxylation [40], or acetate coatings from the precursor may form that are evident from FTIR measurements and may act as 'sacrificial' electron donors i.e. the adsorbed acetate species are degraded [55,56].

The differences in the optimum dopant level between Sample A (0.01at%) and P25 (0.005at%) most likely arise from either differences in the morphology or the surface area of the samples. It has been hypothesised that the high photoactivity of P25 derives from efficient charge separation due to the migration of the photogenerated electrons migrating to the rutile phase, while the holes remain in the anatase [57,58] (for more detail see Section 1.5.4.1). A positive influence on the photoactivity from dopants is expected to be less, as charge separation is reasonably effective for undoped samples and a lower concentration is required for maximum benefit. Alternatively, the lower surface area for P25 (50 $m^2 g^{-1}$) than Sample A (~130 $m^2 g^{-1}$) may lead to a reduction in optimum dopant concentration as the *effective* surface concentration for P25 is higher than Sample A i.e. for a fixed dopant concentration the average number of surface dopants per m^2 will be higher for P25. Thus, for P25, the average distance between

dopant sites is lower leading to increased recombination at a lower dopant concentration. Either hypothesis may also be the cause of the lower increase in photoactivity for P25 at the optimum value. Another possibility may be that P25 has been reported to have an iron impurity of 0.012at% (120 ppm) and thus the nominal concentration of 0.005% is in fact greater [59], although this is unlikely, as Fe^{3+} was not detected by EPR in the undoped P25 batch used in the current study.

The correlation between the IPA and NP techniques confirms that the latter is a valid test and is measuring photoactivity in a similar manner to the more usual IPA technique, but in an aqueous rather than alcohol media. In common with the lattice doped samples, there are minor systematic differences between the photoactivities measured by two methods. For the surface doped case, in general the normalised photoactivity as measured by NP is slightly lower than that for IPA - most likely caused by an increase in agglomeration in aqueous solutions (NP). It was not possible to quantify this increase as the samples did not disperse sufficiently in aqueous solutions to measure optical density (OD). If the samples are heavily agglomerated in aqueous solution then the 'surface' Fe^{3+} dopants will most likely be enclosed within large aggregate particles and will be likely to act as recombination centres rather than to separate charge carriers or mediate interfacial charge transfer [6]. Choi et al [30] studied the effect of calcination at 100°C, 200°C, and 400°C on the photoactivity of iron doped anatase measured by chloroform degradation. The authors concluded that the observed decrease in photoactivity was caused by an increase in agglomerate size, measured by Transmission Electron Microscopy (TEM), as well as a larger primary particle size.

In contrast to both the IPA and NP techniques (where oxidation has been shown to proceed by a hydroxyl radical mediated mechanism), for salicylic acid degradation (SA) there is a different trend in the photoactivity with dopant concentration. For the former two techniques, the photoactivity rises to an optimum value as the greater number of dopants increases the beneficial charge separation and charge mediation and then decreases as the iron concentration is increased (due to a decrease in the average distance between dopants leading to increased recombination), with the optimum dopant level determined by a balance of these factors. However, for the SA technique there is no optimum value, rather there is a modest increase in photoactivity at the lowest dopant level, and the photoactivity decreases as the iron dopant concentration is

increased. The absence of an optimum may arise from two factors. Firstly, salicylic acid has been demonstrated both within this text and elsewhere [51,52] to efficiently trap photogenerated holes and thus the ability of iron dopants to increase the rate through charge trapping and mediation is lower than for molecules that do not efficiently trap the charge such as 2-propanol or 2-nitrophenol. Secondly, the formation of segregated inactive iron oxide phases (observed in DRS spectra for lattice doped Sample A) may reduce the photoactivity to a greater degree for this molecule as the adsorption is a more dominant factor in the degradation kinetics [51] than for example 2-nitrophenol (2-nitrophenol and 4-nitrophenol degradation at similar rates despite negligible adsorption by the latter [50]) and thus surface properties would be expected to be of more importance for SA than for IPA and NP.

That the observed trend for salicylic acid degradation is significantly different to that for both IPA and NP supports the finding that the degradation of this molecule proceeds by a different mechanism i.e. direct hole oxidation. This is especially true given that the NP technique also uses a substituted benzene (2-nitrophenol) as a probe molecule, is in similar media, and is measured at a similar pH as in the SA technique.

4.5. Comparison of the photoactivity for lattice doping and surface iron doping.

The discussion above has focused on likely reasons for observed trends in the photoactivity for lattice doped Sample A and surface doped Sample A and Degussa P25 and it is now pertinent to compare the photoactivity trends of lattice doping and surface doping measured by IPA, NP and SA. Necessarily, and for reasons previously discussed, this comparison is confined to the iron doping of Sample A. Figure 4.vi shows the rate constants for IPA and NP (normalised to the undoped samples) for lattice doped and surface doped Sample A and Figure 4.vii shows the corresponding plots for SA.

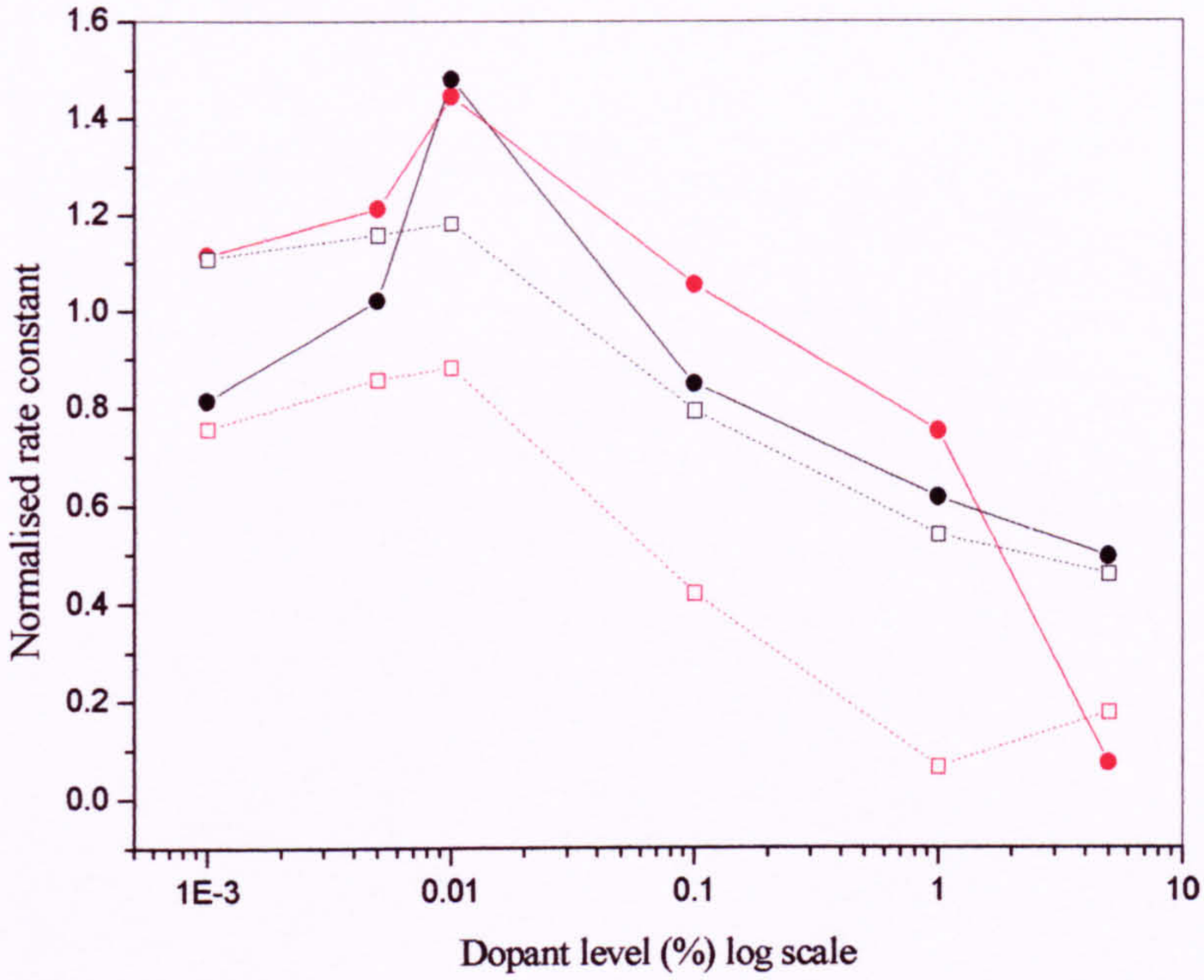

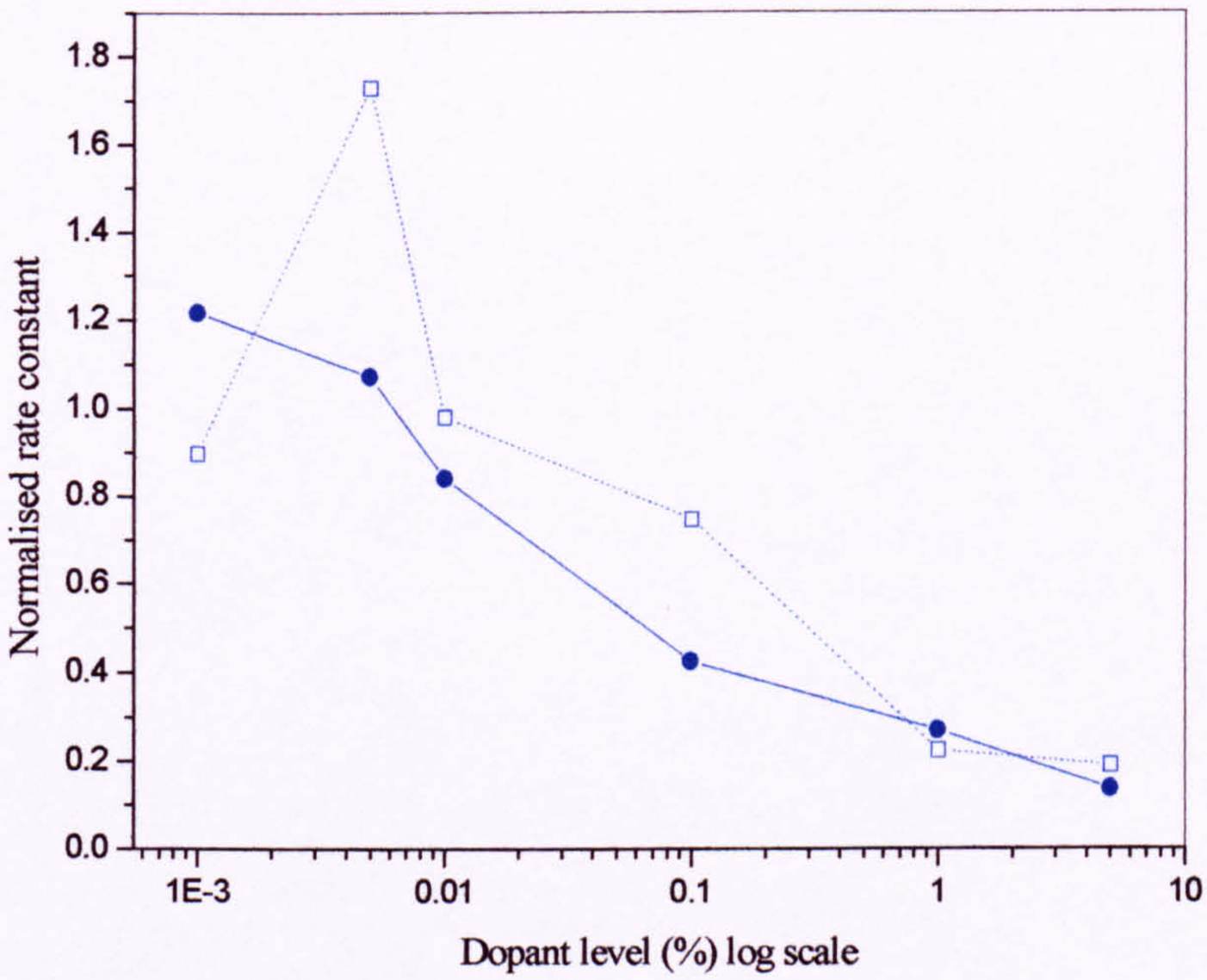

Fig 4.vi and 4.vii. Normalised photoactivity for lattice doped (□) and surface doped (●) Sample A measured by NP (---), IPA (---), and SA (---).

By comparison of the plots depicted in figures 4.vi, it is evident that there are similar photoactivity trends with dopant level for lattice doped and surface doped Sample A when measured by NP and IPA. The photoactivity rises to an optimum value and then decreases as the iron concentration is increased beyond this level with this trend mainly attributed to electronic factors. The photoactivity rises with dopant level due to increased charge separation and charge carrier mediation to surface species from a greater number of dopants, and then decreases after the optimum due to increased recombination due to a decrease in the average distance between dopants, the optimum being determined by a balance between these two factors. It is noteworthy that in all cases the optimum photoactivity is attained at the same dopant level of 0.01 at%.

In general, lattice iron doping led to lower photoactivity than surface doping for similar dopant levels whether measured by NP or IPA. Given that electronic effects determine the observed photoactivity trends for both types of doping (as discussed above) this effect is also most likely to occur from this consideration rather than from structural differences arising from the different preparation methods, which were in any case carefully chosen to limit structural changes. For lattice doped titania, a greater amount of dopant iron is located within the lattice than for surface doped samples where all the iron is located either on, or very close to, the surface. Dopant trap sites within the lattice (rather than on the surface) are more likely to act as recombination centres than sites for interfacial charge transfer. Thus it was both expected from electronic considerations, and observed from the experimental results, that iron located within the lattice is more effective at reducing titania photoactivity than surface iron.

There are minor systematic differences in the absolute photoactivity caused by iron doping relative to the undoped Sample A when measured by NP and IPA. For lattice doped Sample A, the photoactivity is greater in aqueous solution (NP) than in alcohol media (IPA), whereas for surface doping the opposite is generally the case. It is likely that these systematic differences are caused by changes in the dispersion of Sample A in the different media. For lattice doped samples, while it could not be determined experimentally, the increase in measured photoactivity in aqueous compared to alcohol media may be caused by an increase in agglomeration caused by the iron doping process. For the surface doped samples the increased agglomeration in aqueous media may be the cause of the generally lower photoactivity than when measured in

alcohol media, due to the isolation of 'surface' Fe^{3+} dopants within large aggregate particles where they will be more likely to act as recombination centres.

While the trend for NP and IPA measurements are similar for both lattice and surface doping (despite minor systematic differences affecting the absolute photoactivity) this is not the case for the photoactivity measured by the SA technique – the observed trends for photoactivity with dopant level are different for lattice doping and surface doping. For lattice doping, there is still an optimum dopant level as for photoactivity measured by IPA and NP, but at a lower value, whereas for surface iron doping there is no optimum dopant level but rather a decrease as iron level is increased. In both cases, these differences have been ascribed to two possibilities. Firstly, the ability of salicylic acid to efficiently trap photogenerated holes at the surface, thus reducing the effect of iron increasing the rate at low dopant levels through charge trapping and mediation. Secondly, the formation of segregated inactive surface iron oxide phases, that were observed in DRS spectra for selected lattice doped samples, may reduce the rate to a greater degree for molecules such as salicylic acid where adsorption, and thus surface properties, are a dominant factor.

In either the former or latter case, the effect would be expected to be more pronounced for surface rather than lattice doping and this is shown in Figure 4.vii. For lattice doping the general photoactivity trend with dopant level for SA are only mildly different to those measured by IPA and NP (the optimum is at a lower value), while for surface doping the trend is completely altered and there is no optimum dopant level as found for the IPA and NP techniques.

4.6. Conclusions.

The main conclusions from this chapter, regarding the effect of iron doping on the measured photoactivity are as follows:

1. For both Sample A and P25, the general effect on the photoactivity of lattice doping or surface iron doping, whether measured by IPA, NP, or SA are most likely caused by electronic effects i.e. charge trapping and mediation by the iron dopant. Structural considerations, and the dispersion in different media may

affect the absolute photoactivity of iron doped samples, but are not the cause of the observed trends.

2. For the photoactivity measured by NP or IPA, an optimum photoactivity was observed, at 0.01at% for Sample A and 0.005at% for P25. At dopant levels less than the optimum, photoactivity rises as there are more dopants to trap and mediate charges; whereas above the optimum, the photoactivity drops as the low average distance between dopant sites increases charge carrier recombination. This latter effect may be aggravated by the formation of inactive iron oxide layers or acetate coatings on the particle surface.

3. In general, for Sample A, lattice iron doping led to a lower photoactivity than surface doping for similar dopant levels as dopant trap sites within the lattice (rather than on the surface) are more likely to act as recombination centres than sites for interfacial charge transfer. For both lattice and surface doping, minor systematic variations in the absolute photoactivity when measured by NP or IPA are probably due to the altered dispersion in different media. The good correlation between photoactivities measured by NP and IPA i.e. both techniques measuring oxidation by hydroxyl radical confirm that NP is measuring photoactivity in a similar manner to IPA

4. For the SA technique, the doping method determined the trend of photoactivity with iron level. For lattice doped Sample A, prepared by coprecipitation, there are only minor differences to the trends observed by NP/IPA, whereas for surface doping the trend is completely altered. The clear differences between photoactivity trends measured by NP or IPA and those observed by SA reinforce the conclusion in Chapter 3 that this technique is measuring a different reaction pathway i.e. direct hole oxidation rather than a hydroxyl mediated mechanism.

4.7. References.

1. J. Soria; J. C. Conesa; V. Augugliarno; L. Palmisano; M. Schiavello; A. Sclafani, *J. Phys. Chem*, **1991**, *95*, 274.
2. R. I. Bickley; J. S. Lees; R. J. D. Tilley; L. Palmisano; M. Sciavello, *J. Chem. Soc. Faraday. Trans*, **1992**, *88*, 377.
3. R. I. Bickley; T. Gonzalez-Carreno; A. R. Gonzalez-Elipe; G. Munuera; L. Palmisano, *J. Chem. Soc. Faraday. Trans*, **1994**, *90*, 2257.
4. J. A. Wang; R. Limas-Balleseros; T. Lopez; A. Mereno; R. Gomez; O. Novaro; X. Bokhimi, *J. Phys. Chem. B*, **2001**, *105*, 9692.
5. J. Yang; D. Li; Z. Zhang; Q. Li; H. Wang, *J. Photochem. Photobiol A*, **2000**, *137*, 197.
6. M. I. Litter; J. A. Navio, *J. Photochem. Photobiol. A*, **1996**, *98*, 171 and references contained within.
7. A. Mills; S. Le-Hunte, *J. Photochem. Photobiol. A*, **1997**, *108*, 1.
8. O. Legrini; E. Oliveros; A. M. Barun, *Chem. Rev*, **1993**, *93*, 671.
9. M. R. Hoffmann; S. T. Martin; W. Choi; D. W. Bahnermann, *Chem. Rev*, **1995**, *95*, 69.
10. S. Tunesi; M. Anderson, *J. Phys. Chem*, **1991**, *95*, 3399.
11. N. Serpone; E. Pellizzetti, Photocatalysis, Fundamentals, and Applications, Wiley, New York, **(1989)**.
12. N. Serpone; D. Lawless; R. Khairlutdinov; E. Pelizetti, *J. Phys. Chem*, **1995**, *99*, 16655.
13. M. A. Hines; P. Guyot-Sionnest, *J. Phys. Chem*, **1996**, *100*, 468.
14. K. Mizushima; M. Tanaka; S. Iida, *J. Phys. Soc. Jap*, **1972**, *32*, 1519.
15. K. Mizushima; M. Tanaka; A. Asai; S. Iida; J. B. Goodenough, *J. Chem. Phys. Solids*, **1979**, *40*, 1129.
16. J. A. Navio; G. Colon; M. I. Litter; G. N. Bianco, *J. Mol. Cat A*, **1996**, *106*, 267.
17. J. Zhu; W. Zheng; B. He; J. Zhang; M. Anpo, *J. Mol. Cat A*, **2004**, *216*, 35.
18. D. H. Kim; H. S. Hong; S. J. Kim; J. S. Song; K. S. Lee, *J. Alloys. Comp*, **2004**, *375*, 259.
19. C. Martin; I. Martin; V. Rives; L. Palmisano; M. Sciavello, *J. Catal*, **1992**, *134*, 434.
20. J. Soria; j. C. Conesa; V. Augugliarno; l. Palmisano; M. Sciavello; A. Sclafani, *J. Phys. Chem*, **1991**, *95*, 274.

21. J. C. Conesa; J. Soria; V. Augugliarno; L. Palmisano, in Structure and Reactivity of Surfaces, Elsiever, Amsterdam, (1989).
22. D. Cordishi; N. Burriesci; F. D'Alba; M. Petrera; G. Polizzotti; M. Sciavello, *J. Solid. State. Chem*, **1985**, *56*, 182.
23. D. W. Bahnemann, *Isr. J. Chem*, **1993**, *33*, 115.
24. Internal correspondence, paper submitted.
25. B. W. Faughman; Z. J. Kiss, *Phys. Rev. Lett*, **1968**, *21*, 1331.
26. O. W. Johnson; W. D. Ohlsen; P. I. Kingsbury, *Phys. Rev*, **1968**, *175*, 1102.
27. M. Graztel; R. F. Howe, *J. Phys. Chem*, **1990**, *94*, 2566.
28. J. Moser; M. Gratzel; R. Gallay, *Helv. Chem. Acta*, **1987**, *70*, 1596.
29. S. T. Martin; M. Hermann; W. Choi; M. R. Hoffmann, *J. Chem. Soc. Faraday. Trans*. **1994**, *90*, 3315.
30. W. Choi; A. Termin; M. R. Hoffmann, *J. Phys. Chem*. **1994**, *98*, 13669.
31. S. Ikeda; N. Sugiyama; B. Pal; G. Marci; L. Palimsano; H. Noguchi; K. Uosaki; B. Ohtani, *Phys. Chem. Chem. Phys*, **2001**, *3*, 267.
32. H. P. Maruska; A. K. Ghosh, *Sol. Energy. Mater*, **1979**, *1*, 237.
33. M. Gratzel, in Heterogeneous Photochemical. Electron. Transfer. CRC Press Inc, Florida, (1989).
34. Z. Zhang; C. C. Wang; R. Zakaria; J. Y. Ying, *J. Phys. Chem. B*, **1998**, *102*, 10871.
35. J. P. Witke, *J. Am. Chem. Soc*, **1967**, *50*, 586.
36. J. A. Navio; F. J. Marchena; M. Rocel; M. A. De La Rosa, *J. Photochem. Photobiol A*, **1991**, *55*, 319.
37. L. Palmisano; M. Sciavello; A. Sclafani; C. Martin; I. Martin; V. Rives, *Cat lett*, **1994**, *24*, 303.
38. X. Li; P. Yue; C. Kutal, *New. J. Chem*, **2003**, *27*, 1264.
39. T. Tachikawa; S. Tojo; M. Fujitsuka; T. Majima, *J. Phys. Chem. B*, **2004**, *108*, 11054.
40. S. E. Park; H. Joo; J. W. Kang, *Sol. Energy. Mat. Sol. Cells*, **2004**, *83*, 39.
41. M. I. Litter; J. A. Navio, *J. Photochem. Photobiol A*, **1994**, *84*, 183.
42. J. A. Navio; J. J. Testa; P. Djedjeian; J. R. Padron; D. Rodrriguez; M. I. Litter, *Applied. Cat. A*, **1999**, *178*, 191
43. K. Wilke; H. D. Breuer, *J. photochem. Photobiol. A*. **1999**, *121*, 49.
44. T. A. Egerton; E. Harris; E. J. Lawson; B. Mile; C. C. Rowlands, *Phys. Chem. Chem. Phys*, **2001**, *3*, 497.

45. J. S. Thorp; H. S. Eggleson; T. A. Egerton; A. J. Pearman, *J. At. Sci. Lett*, **1986**, *5*, 54.

46. J. A. Navio; M. Macias; M. Gonzales-Catalan; A. Justo, *J. Mat. Sci.* **1992**, *27*, 3036.

47. S. Karvinen, *Solid state Sci*, **2003**, *5*, 811.

48. C. Richard; P. Boule, *New. J. Chem*, **1994**, *18*, 547.

49. R. W. Harrison, MPhil Thesis, University of Newcastle Upon Tyne, Newcastle Upon Tyne NE1 7RU, (**2001**).

50. T. A. Egerton; P. A. Christensen; R. W. Harrison; J. W. Wang, *J. Applied. Electro*, **2005**, *35*, 799.

51. S. Tunesi; M. Anderson, *J. Phys. Chem*, **1991**, *95*, 3399.

52. T. Picatonotto; D. Vione; M. E. Carlotti, *J. Disp. Sci. Tech*, **2002**, *23*, 845.

53. D. Vione; T. Picatonotto; M. E. Carlotti, *J. Cosm. Sci*, **2003**, *54*, 513.

54. T. A. Egerton and I. R. Tooley, *J. Phys. Chem B*, **2004**, *98*, 5066.

55. J. M. Coronado; S. Kataoka; I. Tejedor-Tejedor; M. A. Anderson, *J. Catal*, **2003**, *219*, 219.

56. W. Rachmady; M. A. Vannice, *J. Catal*, **2002**, *207*, 317.

57. D. C. Hurum; A. G. Agrios; K. A. Gray; T. Rajh; M. C. Thurnauer, *J. Phys. Chem*, **2003**, *107*, 4545.

58. R. I. Bickley; T. Gonzalez-Carreno; J. S. Lees; L. Palmisano; R. J. D. Tilley, *J. Solid. State. Chem.* **1991**, *92*, 178.

59. Degussa P25 data sheet.

5. NOVEL ORGANIC COATINGS.

This chapter describes the analysis of organic coated titanium dioxide. Sample A and Degussa P25 were coated using a range of organics: octadecyl-trimethoxy-silane (ODTMOS), a phosphate ester – trade name: Arlatone Map160K (AM160K), and sodium hydrogen phosphate (SHP). The procedures for these treatments are described in sections 2.1.5-2.1.7. Coating levels are expressed as a percentage of the amount of coating required to cover the entire titania surface. For example, "Sample A 50% AM160K" refers to sample A coated with a quantity of AM160K to cover half the titania surface; see Chapter 2, appendix A2.1 for a sample calculation.

5.1. Introduction.

While the previous two Chapters have dealt with iron doping, which is often studied to increase the titanium dioxide photoactivity for catalytic applications, this Chapter and Chapter 6 describe the effects of coating titanium dioxide with the intention of reducing photoactivity. In this manner the results have more application to possible cosmetic uses for the high area rutile Sample A. However, by similarly coating Degussa P25, commonly used as a standard [1] a link to the general body of published photocatalytic work is provided.

Several patents describe the coating of titanium dioxide with silanes of various types [2-7] for use in for example paper or plastics. However, these are predominately used for pigmentary grade titanium dioxide, and it is useful to examine whether their use can be extended to nanosized crystals for use in cosmetic fields. Several patents also describe the incorporation of phosphate as a constituent in coatings [8-10] as a minor component. It is useful to examine whether the use of phosphate as the sole constituent in a coating is of value; certainly, phosphate has been shown to significantly reduce photoactivity when it is present as a contaminant in aqueous mixtures [11].

5.2. Effect of surface coatings on photoactivity measured by IPA.

The effect of the various surface coatings on the photoactvity of Sample A and P25 was determined by comparison of the rates of isopropanol oxidation of the uncoated and coated modifications. This technique is described in section 2.2.1, and for these oxidation experiments the typical titania concentration of 8 g dm^{-3} was used. For selected samples, the optical density was measured as described in section 2.2.6, to determine if the photoactivity was affected by changes in dispersion.

5.2.1 Phosphate coated titania from sodium hydrogen phosphate (SHP).

A plot of acetone concentration against time for unmilled phosphate coated Sample A is shown in Figure 5.i. The corresponding plots when the samples have been milled prior to oxidation to break up agglomerates are shown in Appendix 1 (Figure A5.i and A5.ii for Sample A and P25 respectively). Uncoated samples are shown for comparison. In all cases the plots of acetone vs time were good straight lines and the reproducibility of repeat measurements was within $^{\pm}$5%. The rates of acetone formation against coating level (% of BET surface area) for SHP coated samples relative to the corresponding uncoated samples (0%) are shown in Figure 5.ii.

For unmilled Sample A, there is effectively no change in photoactivity by applying a phosphate coating. When the coated samples are milled there is a decrease in their photoactivity relative to that for the uncoated sample – although the reduction is modest for both Sample A and P25 (maximum of 10-15% in both cases). Evidently the phosphate coating causes increased agglomeration in the unmilled samples that masks the reduction in photoactivity observed when the samples are milled. An increase in particle agglomeration results in increased penetration of light into the slurry and thus a higher measured photoactivity as the UV is absorbed by a higher number of titania particles, suppressing charge recombination [12]. Milling the samples breaks up the agglomerates giving a similar state of dispersion, and thus a similar penetration of UV, for the uncoated and coated samples - this argument is explained more fully in section 1.5.4.4.

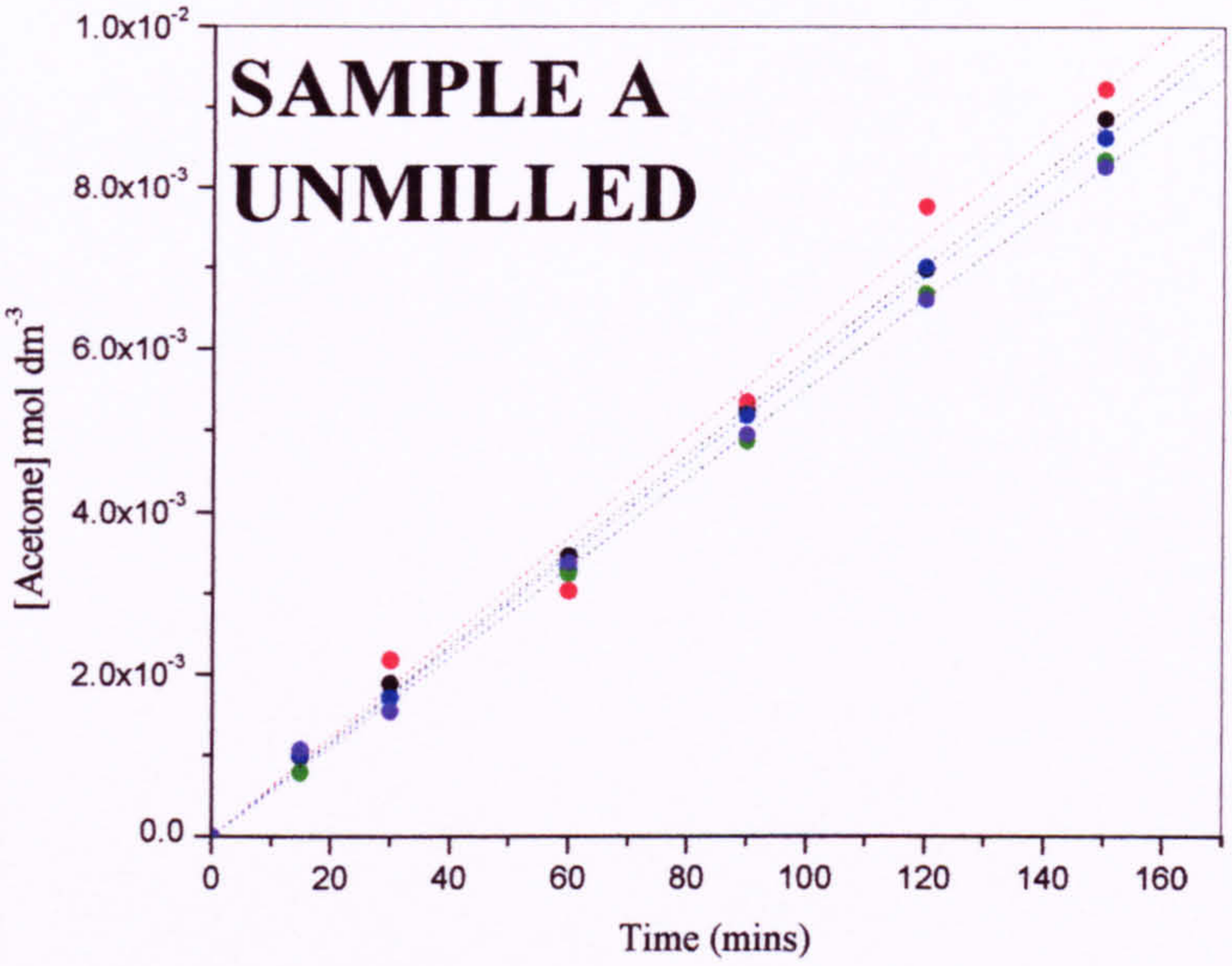

Fig 5.i. Acetone concentration against time for unmilled SHP coated Sample A --- 10%; --- 25%; --- 50%; --- 100%; --- Uncoated.

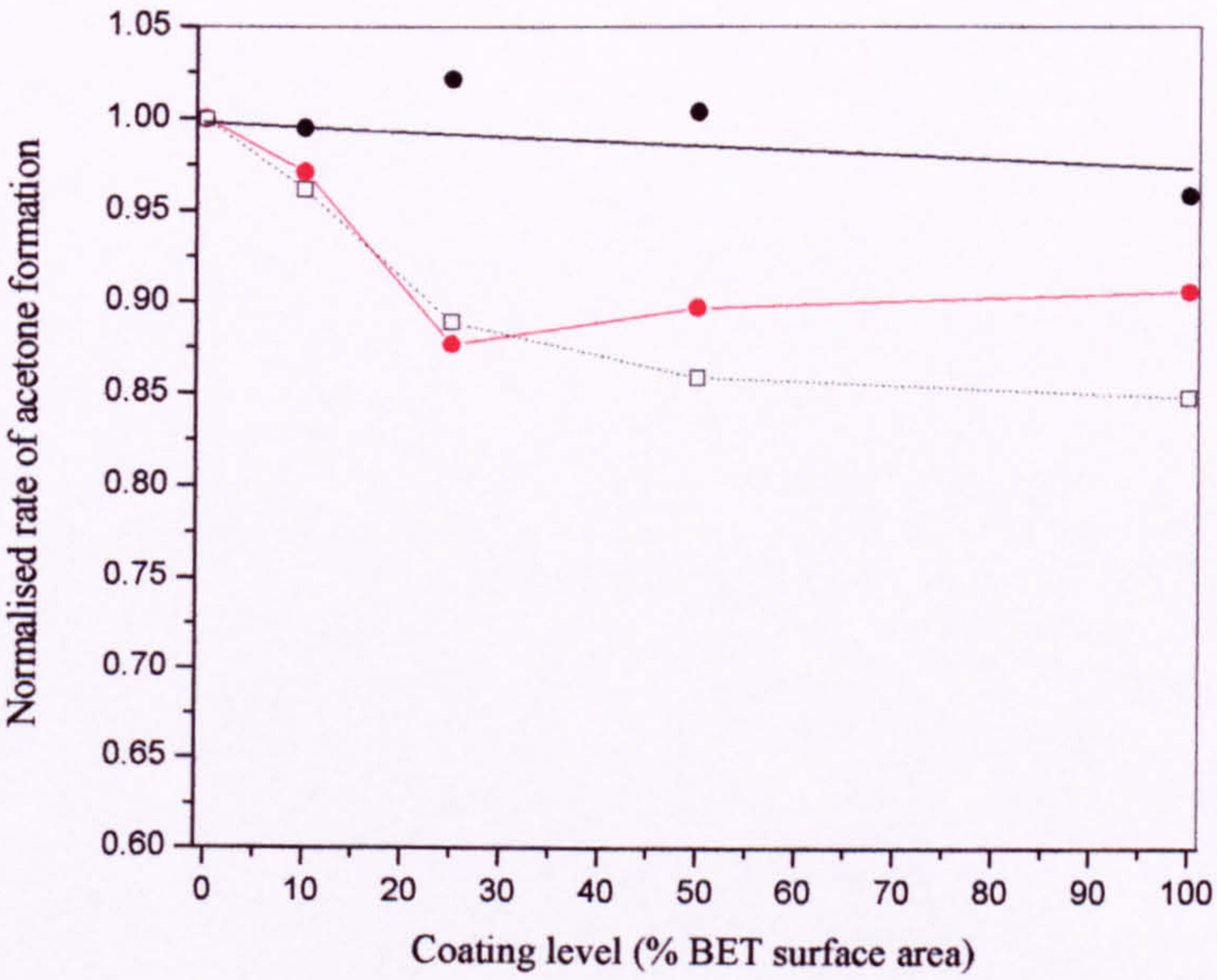

Fig 5.ii. Rates of acetone formation for unmilled (---) and milled (---) SHP coated titania. Sample A (full lines), P25 (dotted)

An important observation from these results is that low levels of coating are sufficient to cause the maximum decrease. For SHP treated samples, unlike the AM160K treated samples below, there is no rise in activity at the lowest coating levels. This emphasises that the observed decreases in activity occur at quite small coating levels.

5.2.2 Octadecyl-trimethoxy-silane (ODTMOS) coated titania.

Plots of acetone concentration against time for samples of ODTMOS coated Sample A and P25 milled for 30 minutes to break up agglomerates are shown in Figure 5.iii - uncoated samples are shown for comparison. In all cases the plots of acetone vs time were good straight lines and the reproducibility of repeat measurements was within $^{\pm}5\%$.

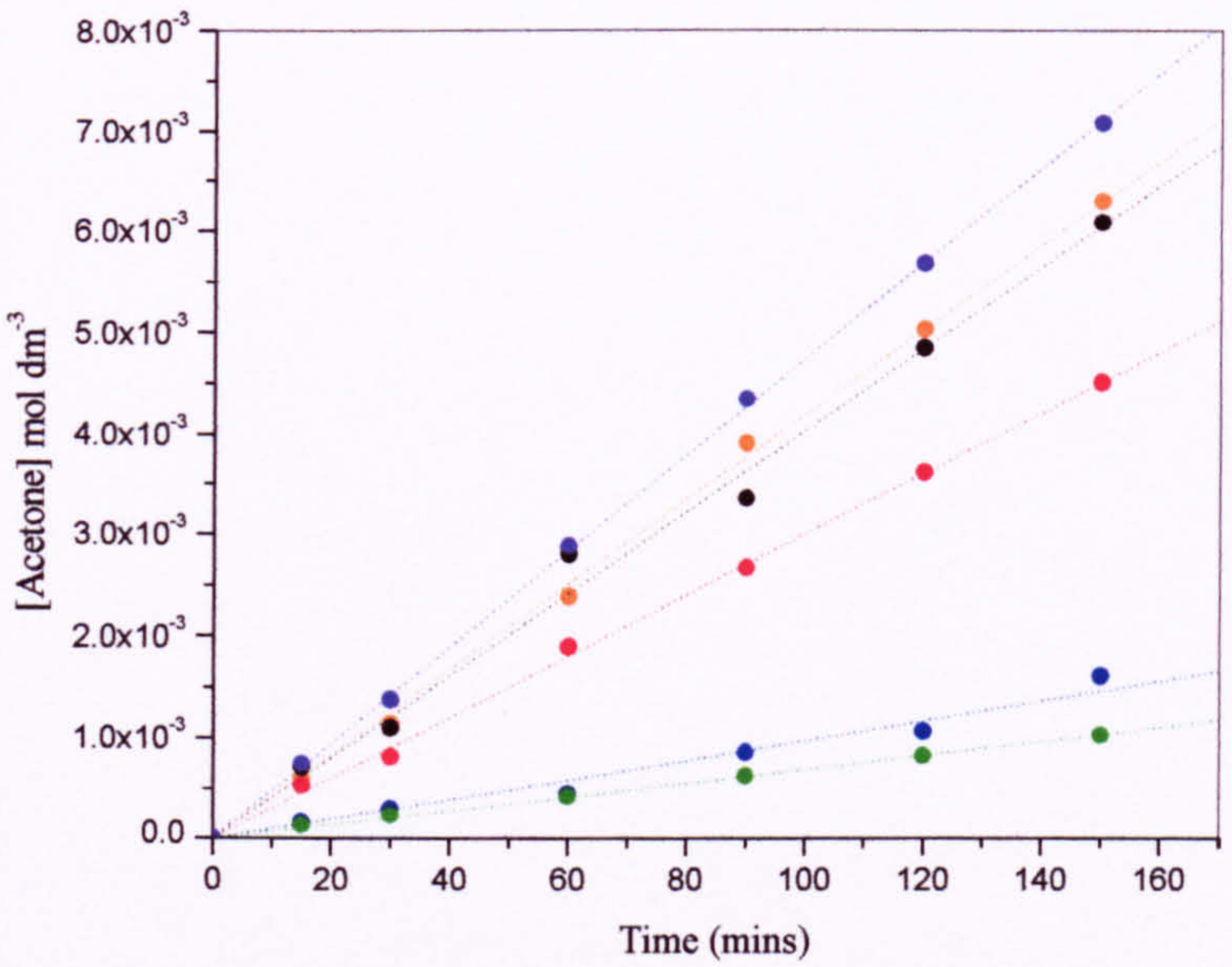

Fig 5.iii. Acetone concentration against time for milled ODTMOS coated Sample A (---) 31%; (---) 64%; (---) uncoated; and P25 (---) 40%; (---) 84%; (---) uncoated.

The rates of acetone formation against coating level for ODTMOS coated Sample A and P25 normalised to the corresponding uncoated samples are shown in Figure 5.iv.

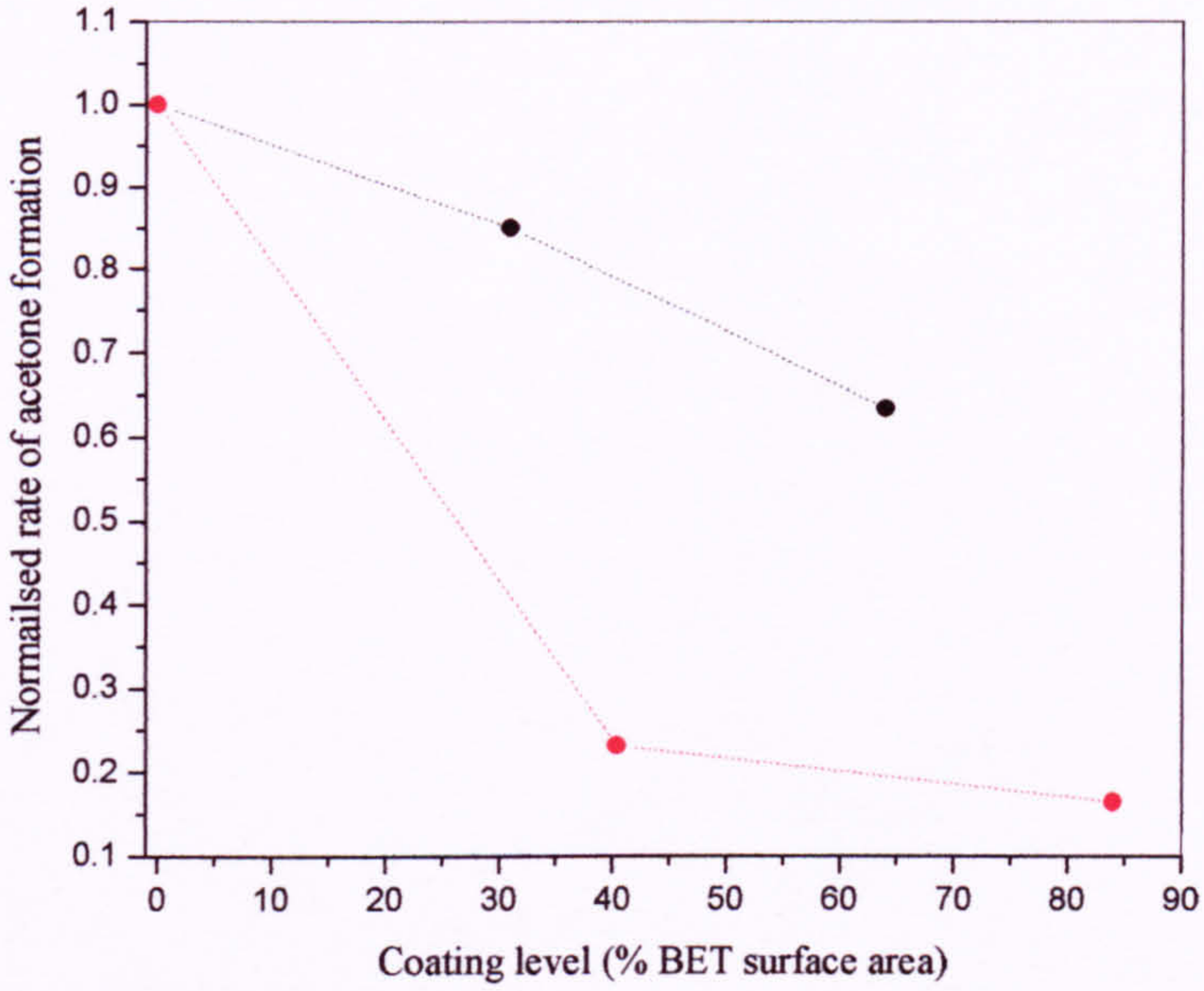

Fig 5.iv. Normalised rates of acetone formation for milled ODTMOS coated titania. Sample A (---), P25 (---).

As can be seen from Figure 5.iv, the effect of applying an ODTMOS coating is markedly different for the two types of titania. For both Sample A and P25, the coating lowers the photoactivity with the decrease for P25 much greater than for Sample A – more than twice the extent. Further, in the case of P25 there is a large decrease in photoactivity at relatively low levels of coating (40%) with only modest decreases beyond this, similar to the pattern for other coatings described in this chapter, while for Sample A there is a roughly linear decrease with coating level. An ODTMOS coating is thus significantly more effective in reducing photoactivity in P25 than in Sample A. Possible causes for the observed differences of the effect of the ODTMOS coating on the two types of titania are discussed later in section 6.4.

5.2.3. Arlatone Map 160K (AM160K) coated titania.

A plot of acetone concentration against time for unmilled AM160K coated Sample A is shown in Figure 5.v. The corresponding plot for AM160K coated P25 is shown in Appendix 1 (Figure A5.iii). Plots for uncoated samples are shown for comparison. In all

cases the plots of acetone vs time were good straight lines and the reproducibility of repeat measurements was within $\pm$ 5 %.

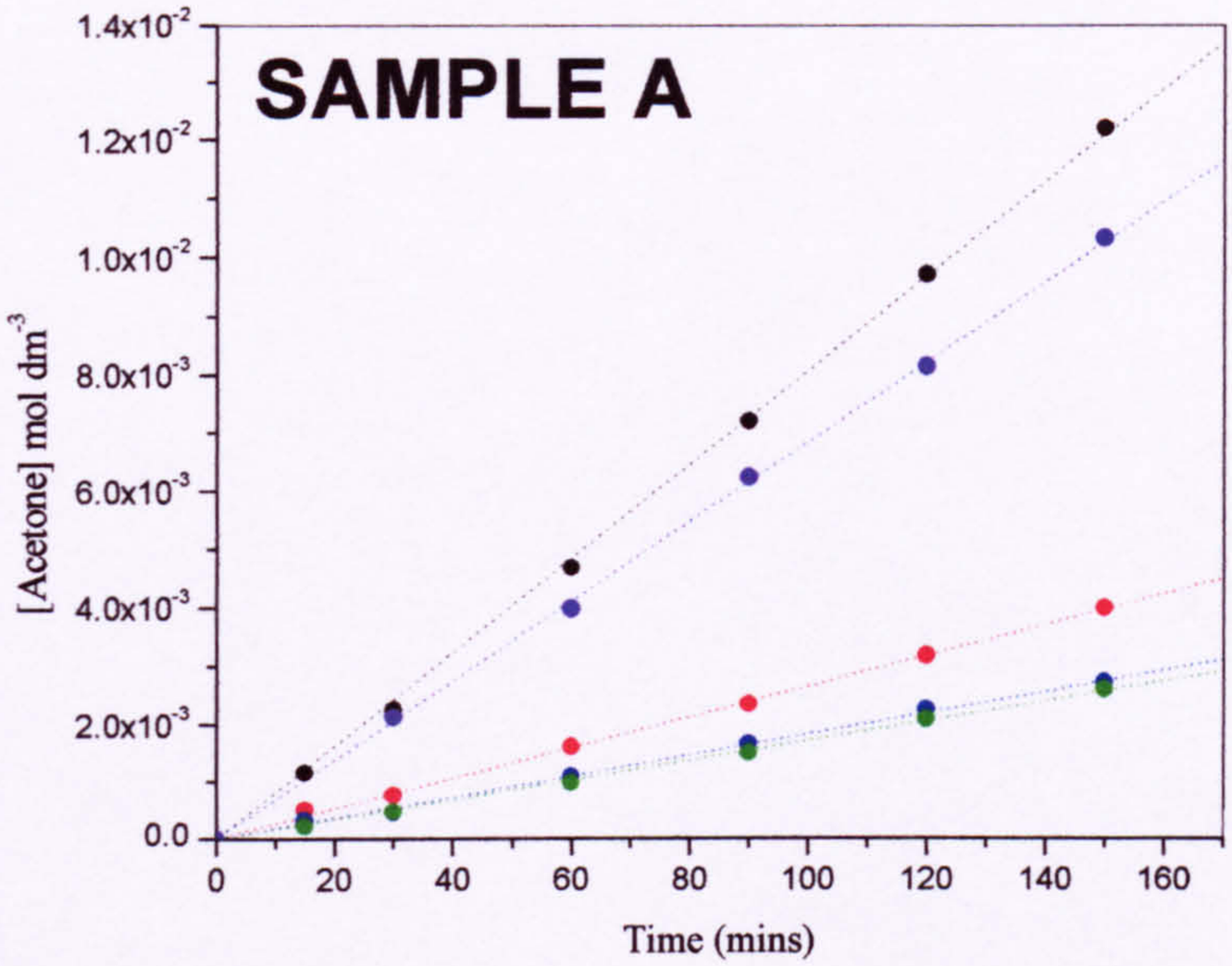

Fig 5.v. Acetone concentration against time for unmilled AM160K coated Sample A. --- 10%; --- 25%; --- 50%; --- 100%; --- Uncoated.

The rates of acetone formation against coating level (% of BET surface area) for unmilled AM160K coated samples are shown in Figure 5.vi. The rate constant for uncoated samples (0 %) is shown for comparison. As can be seen from Fig 5.vi, the general effect of applying a coating of AM160K to both Sample A and P25 is to lower the photoactivity as measured by isopropanol oxidation, with the decrease greater for Sample A. An additional observation is that even at low levels of coating the photoactivity is significantly reduced, with only moderate further reductions for higher levels. While this result is expected (Egerton and Tooley [13] - discussed in Chapter 6), the increase at a coating level of 10% for Sample A is not. This increase is above the 5% reproducibility for this oxidation experiment and thus cannot readily be attributed to experimental error. To investigate the possibility that the measured photoactivity may have been affected by agglomeration

during the coating process, the same oxidation experiments were repeated with the titania samples milled for 30 minutes prior to oxidation to break up the agglomerates. Plots of acetone concentration against time for milled AM160K coated Sample A are shown in the appendix with the corresponding plot for P25 (Figure A5.iv and A5.v). Rates of acetone formation against coating level, normalised to the uncoated sample, for milled and unmilled AM160K coated Sample A (full lines) and P25 (dotted lines) are shown in Figure 5.vii. The optical density for the coated Sample A milled for 30 minutes was measured to examine changes in dispersion and the absorbencies at regular intervals are shown in Table 5.i.

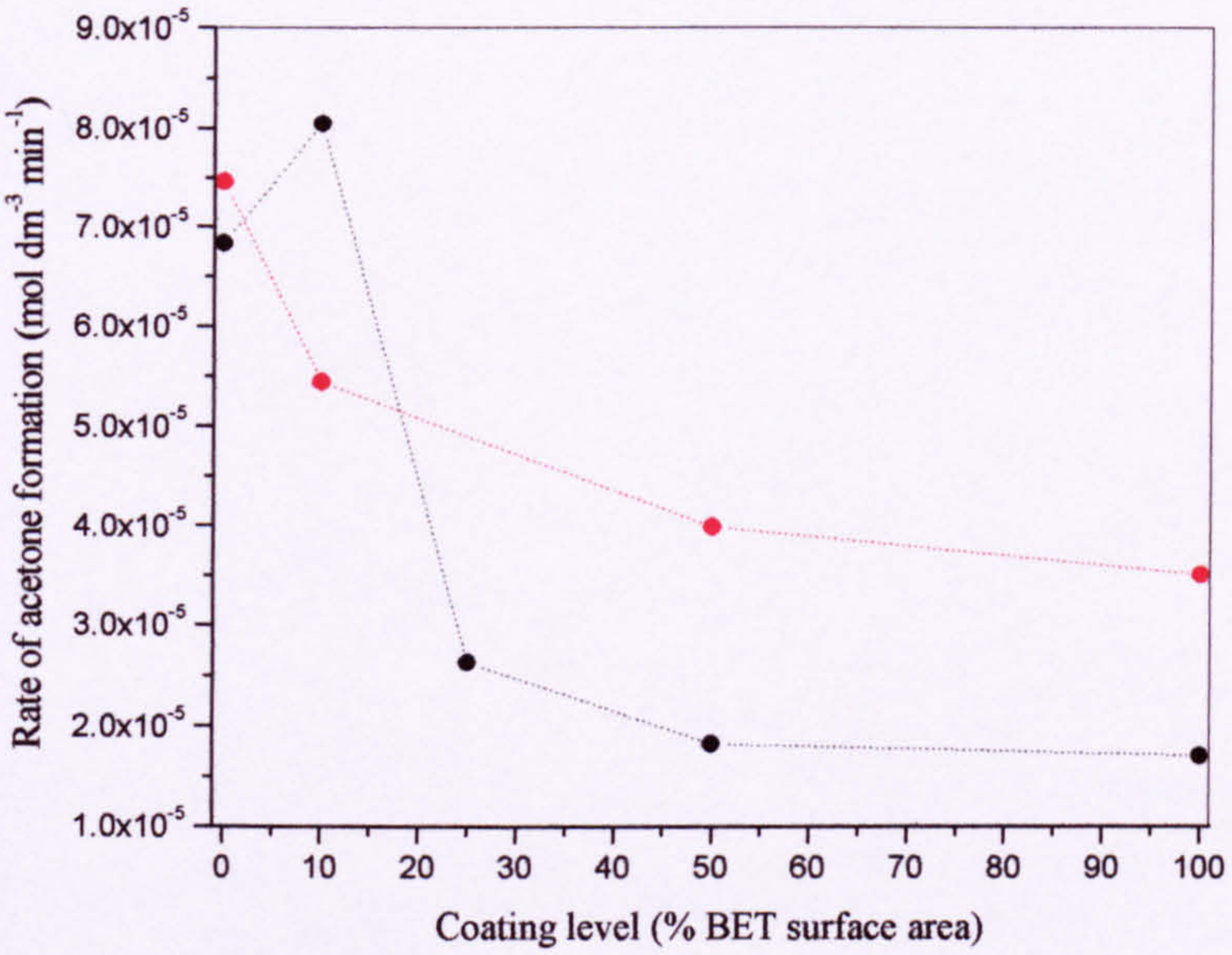

Fig 5.vi. Rates of acetone formation for unmilled AM160K coated titania. --- Sample A; --- P25.

By comparison of the milled and unmilled plots in Fig 5.v, it can be seen that milling the samples did not alter the overall trend in the photoactivity. With the exception of the 10% coating on Sample A, the effect of coating with AM160K was to reduce the photoactivity at even very low levels and then marginal further decreases beyond this. Milling the 10% coating of AM160K on Sample A reduced the relative increase in photoactivity shown for the unmilled case in Fig 5.vi.

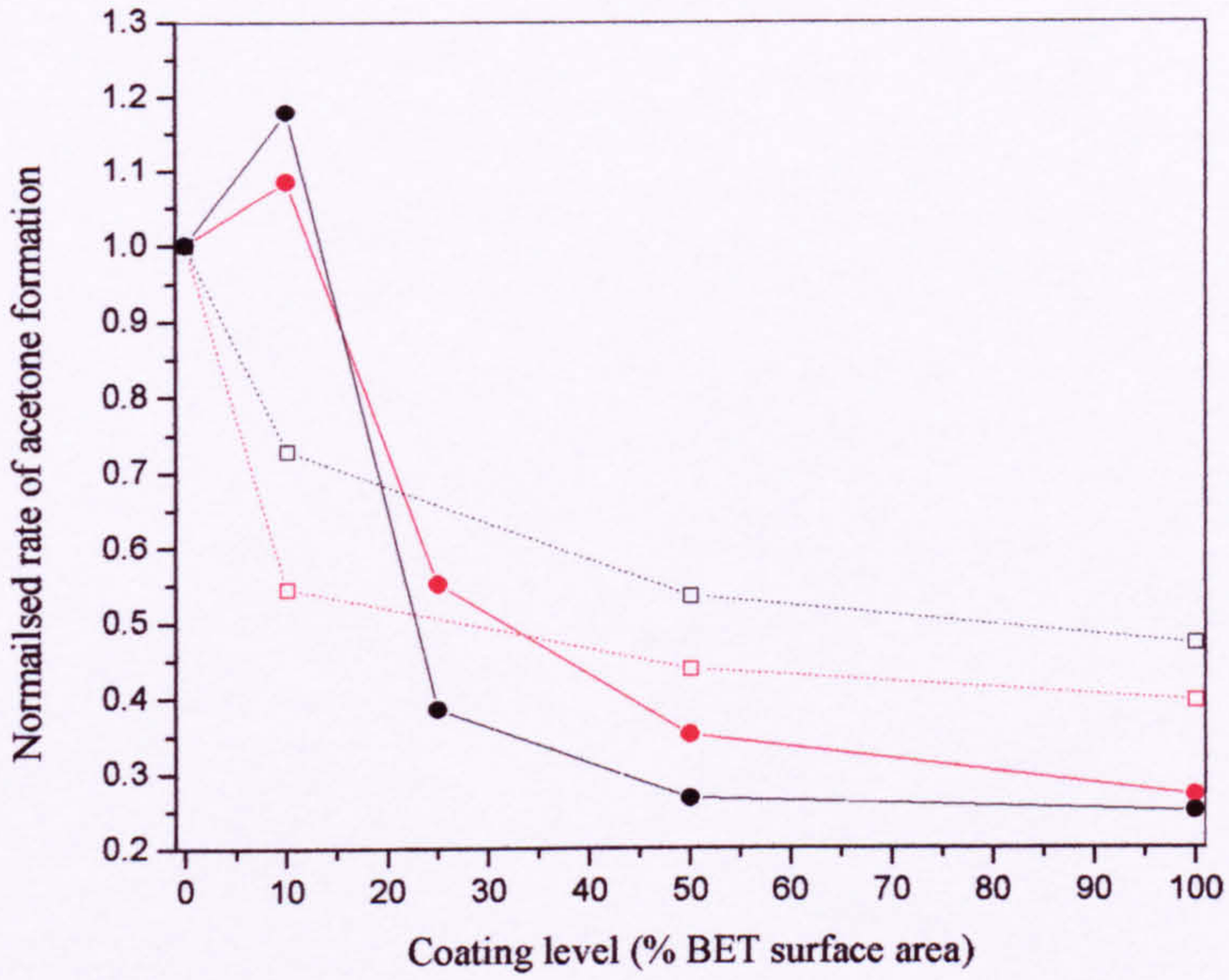

Fig 5.vii. Rates of acetone formation for unmilled (---) and milled (---) AM160K coated samples. Sample A (full lines); P25 (dotted lines).

Sample	Absorbance		
	350 nm	365 nm	370 nm
Uncoated	0.29	0.25	0.24
10%	0.32	0.28	0.26
25%	0.39	0.31	0.29
50%	0.41	0.36	0.35
100%	0.58	0.52	0.50

Table 5.i. Optical density of uncoated and AM160K coated Sample A. Absorbance at selected wavelengths.

At first glance this suggests that this increase is partly due to changes in the dispersion of the titania caused by the coating. However, this is not borne out by the optical

density results for milled Sample A which show that the absorbance increases with coating level. The role of dispersion in determining apparent photoactivity is discussed elsewhere (section 1.5.4.4), but briefly, an *increase* in absorbance such as this would be expected to decrease photoactivity and therefore changes in dispersion are not likely to be the cause of the increase at the 10% coating level. The effect of coating with AM160K on the photoactivity as measured by nitrophenol degradation in aqueous solution is explored later in section 5.3.3

5.3. Effect of surface coatings on photoactivity measured by NP.

To explore the effect of the various surface coatings on the photoactvity of Sample A and P25 in aqueous solution, the rates of nitrophenol degradation (NP) of the uncoated and coated modification were determined and compared. This technique is described in section 2.2.2, and for these oxidation experiments the typical titania concentration of 2 g dm^{-3} was used. In summary, the degradation follows first order kinetics and plots of ln C/Co against time yield straight lines with the rate constant given by (–dy/dx). The measured rate constants for nitrophenol degradation with P25 are of the order of ten times greater than with Sample A.

Unlike the case of isopropanol oxidation (IPA) described above, it was not desirable to mill the samples prior to nitrophenol degradation – the reasons for which are explained in section 2.2.2.2. However, several of the hydrophobically coated samples required milling to be dispersed in aqueous solution, and where this is the case, all samples in the series are milled for a set time to maintain comparability.

5.3.1. Phosphate coated titania from sodium hydrogen phosphate (SHP).

Plots of ln C/Co against time for SHP coated modifications of Sample A and P25 are shown in Figure 5.viii and 5.ix respectively, with the comparable plots for uncoated samples. As would be expected, the relatively hydrophilic phosphate coated samples disperse reasonably well and thus are not milled prior to the degradation experiments.

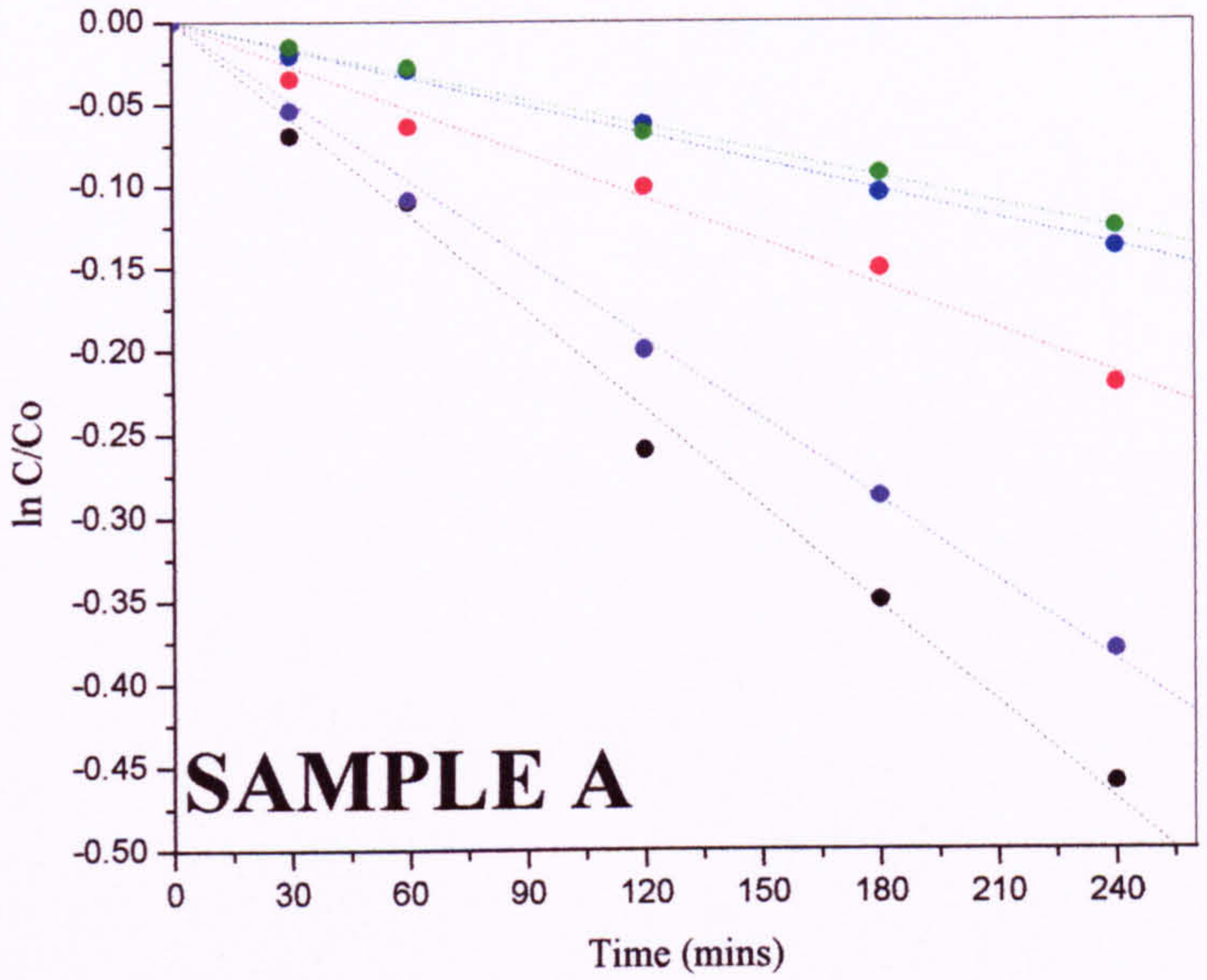

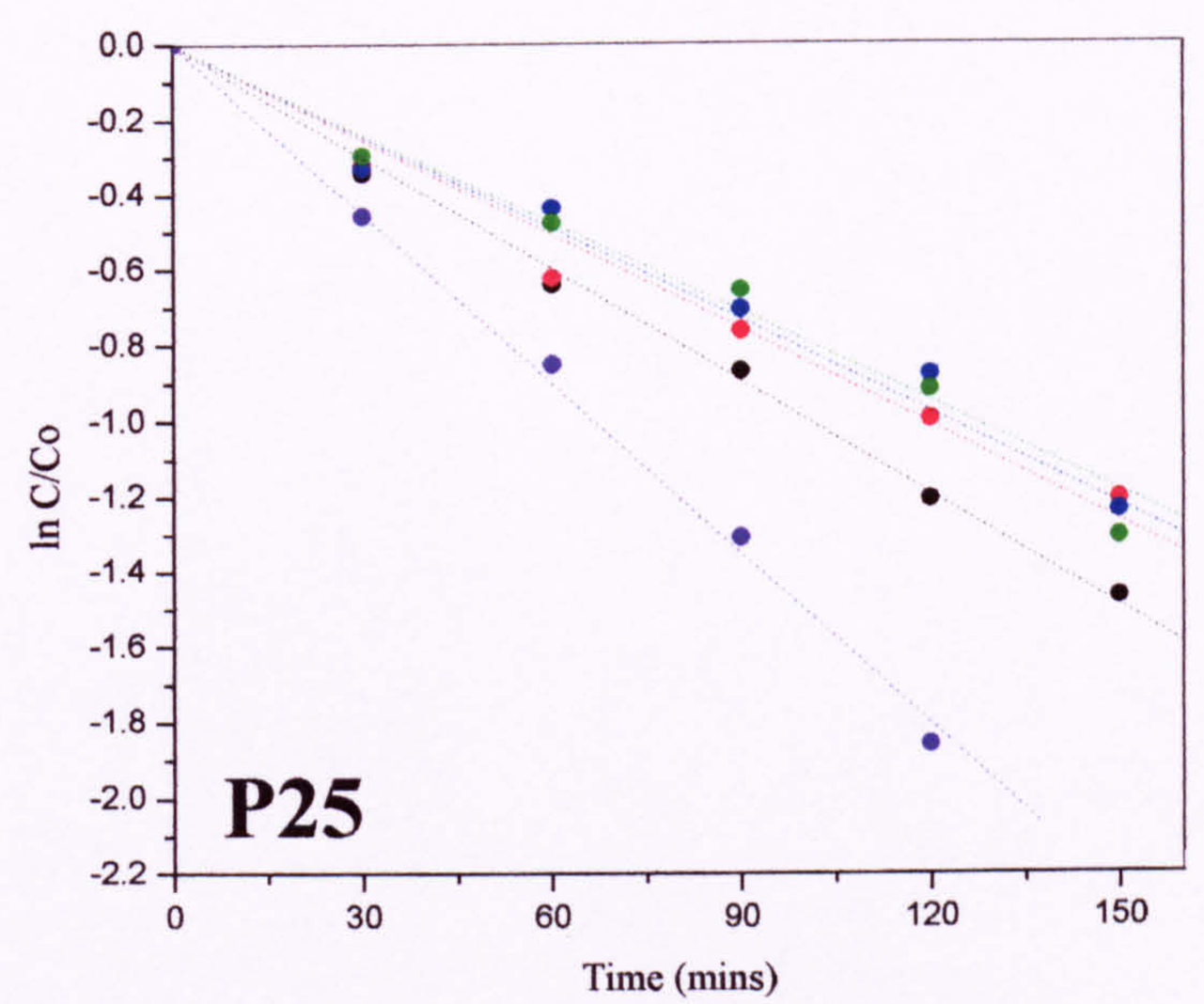

Fig 5.viii and 5.ix. ln C/Co against time for SHP coated Sample A (above) and P25 (below). --- 10%; --- 25%; --- 50%; --- 100%; --- Uncoated.

A comparison of the photoactivity of SHP coated Sample A and P25 measured by nitrophenol degradation (---) and isopropanol oxidation (---) is shown in figures 5.x. In all cases the plots are normalised to the reaction rate for the uncoated level. The error for both techniques was calculated to be less than 5% by reproducibility.

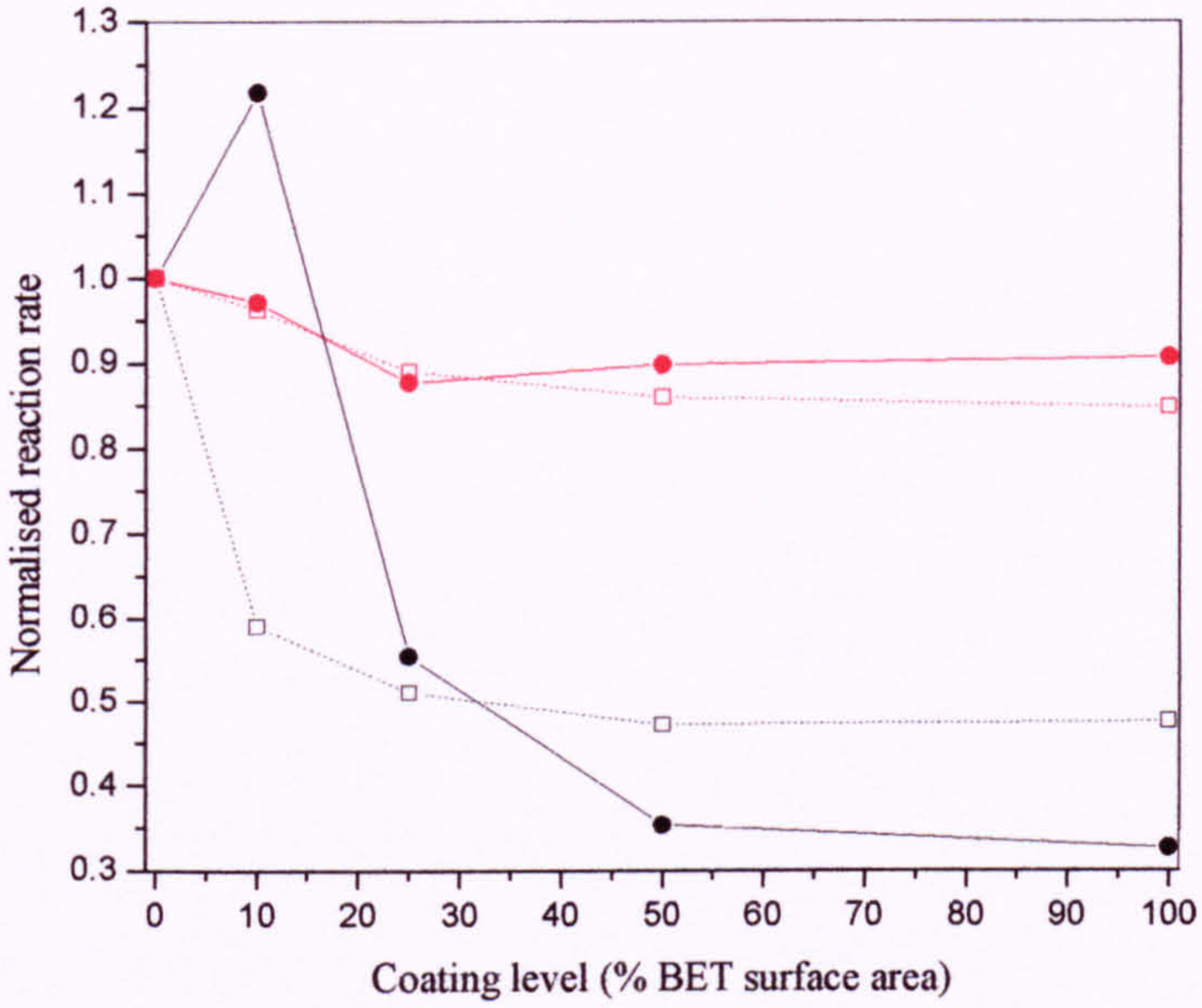

Fig 5.x. Comparison of the photoactivity of SHP coated Sample A (solid lines) and P25 (dotted lines) measured by NP (---) and IPA (---). In all cases the reaction rate has been normalised to that for the respective uncoated sample.

It is immediately obvious from Figure 5.x that for both Sample A and P25, the effect on the photoactivity of applying a phosphate coating to titania is markedly different depending on the method for assessing the photoactivity. In an aqueous environment i.e. when measured by nitrophenol degradation, the photoactivity is significantly reduced, while it is barely affected when measured by isopropanol oxidation. When measured by NP the trends for phosphate coating level are markedly similar to those observed for applying an AM160K coating (see below-section 5.3.3). If we disregard Sample A 10%AM160K, then for both types of titania low levels of coating (25%) significantly reduce the photoactivity, with only moderate further reductions beyond this level.

The increase in photoactivity for a 10% coating level on Sample A is similar to the trend observed for AM160K coatings when measured by IPA (section 5.2.3) and NP (section 5.3.3). That this should occur for a relatively hydrophilic coating such as phosphate as well as the hydrophobic AM160K coating is further evidence that changes to dispersion caused by the presence of the coating are not responsible for the increase. Instead, it is suggested that some property of phosphate/phosphate ester coatings on Sample A is responsible and this possibility is discussed later in Chapter 6.

5.3.3. Octadecyl-trimethoxy-silane (ODTMOS) coated titania.

Plots of ln C/Co against time for ODTMOS coated modifications of Sample A and P25 are shown in the appendix with the comparable plots for uncoated samples (Figure A5.vi). In order to disperse the hydrophobically coated titania in the nitrophenol solution the samples were all milled for 15 minutes prior to the degradation experiment.

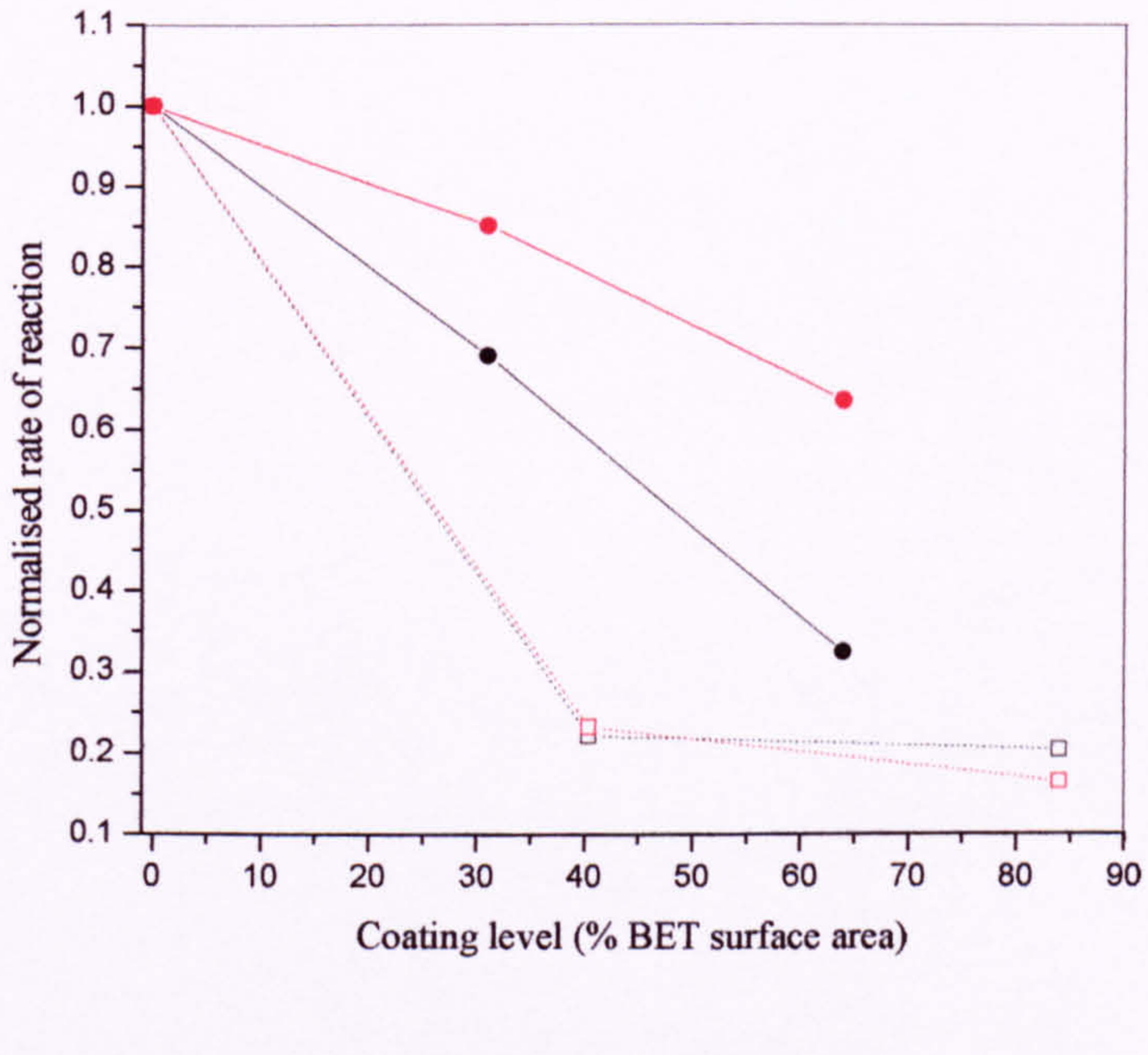

Fig 5.xi. Comparison of the photoactivity of ODTMOS coated Sample A (solid lines) and P25 (dotted lines) measured by NP (---) and IPA (---). In all cases the reaction rate has been normalised to that for the respective uncoated sample.

A comparison of the photoactivity of ODTMOS coated Sample A and P25 measured by nitrophenol degradation (---) and isopropanol oxidation (---) is shown in figures 5.xi. In all cases the plots are normalised to the reaction rate for the uncoated level. The error for both techniques was calculated to be less than 5% by reproducibility.

As can be seen from Figure 5.xi, the effect on the photoactivity from applying a coating of ODTMOS is similar whether measured by NP or IPA. For Sample A, there is a roughly linear decrease with coating level, with the decrease somewhat greater when measured by NP. For P25 there is a large decrease in photoactivity measured by either NP or IPA at relatively low levels of coating (40%) with only modest decreases beyond this, similar to the pattern for the other coatings described above. Possible causes for the observed differences of the effect of the ODTMOS coating on the two types of titania are discussed later in section 6.4

5.3.3. Arlatone Map 160K (AM160K) coated titania.

Plots of ln C/Co against time for AM160K coated modifications of Sample A and P25 are shown in the appendix with the comparable uncoated samples (Figure A5.vii and 5.viii respectively). In order to disperse the coated titania in the nitrophenol solution the samples were all milled for 15 minutes prior to the degradation experiment.

A comparison of the photoactivity of AM160K coated titania measured by nitrophenol degradation and isopropanol oxidation are shown in figures 5.xii (Sample A) and 5.xiii (P25). In both cases the plots are normalised to the reaction rate for the uncoated level. The error for both techniques was calculated to be less than 5% reproducibility.

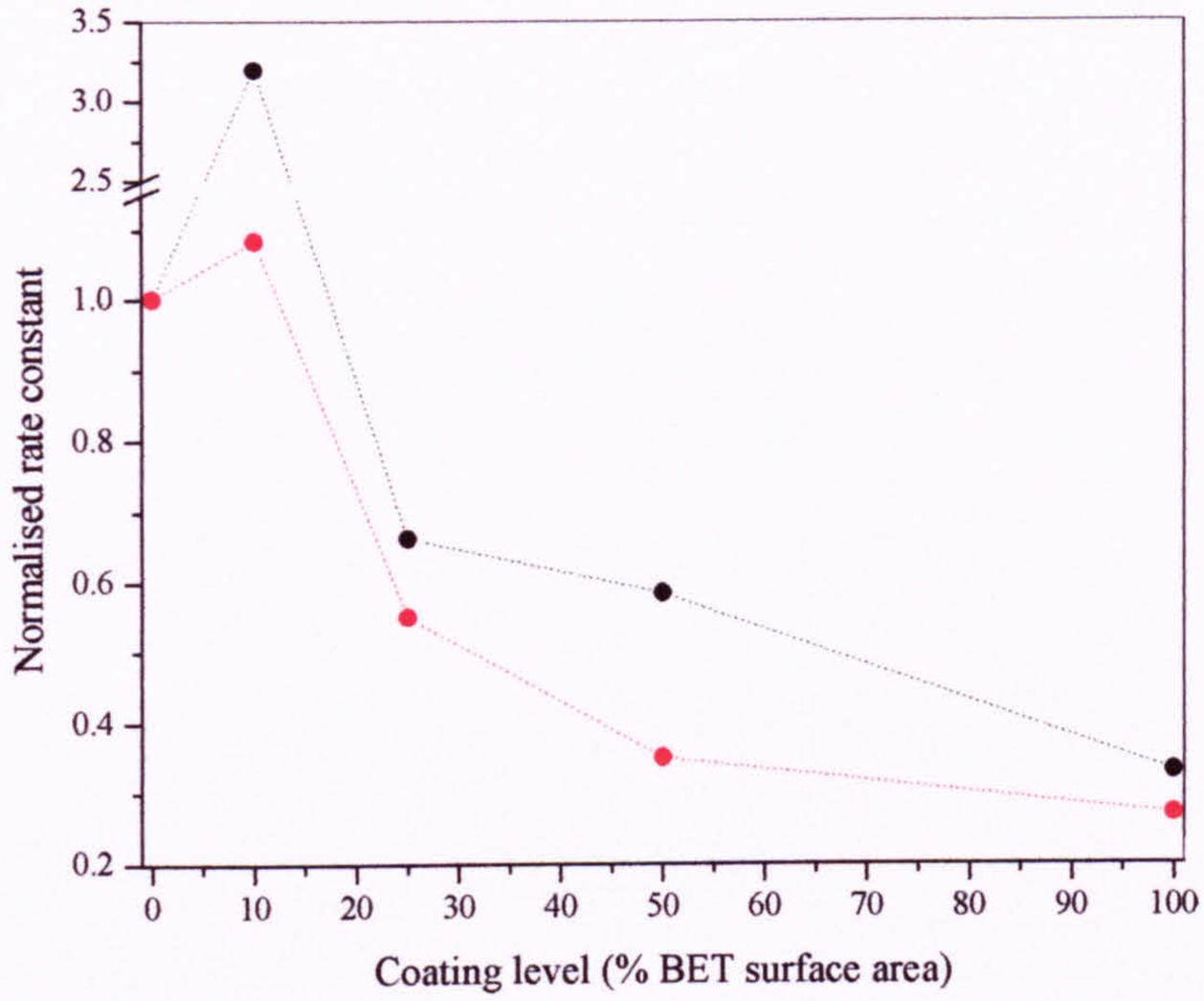

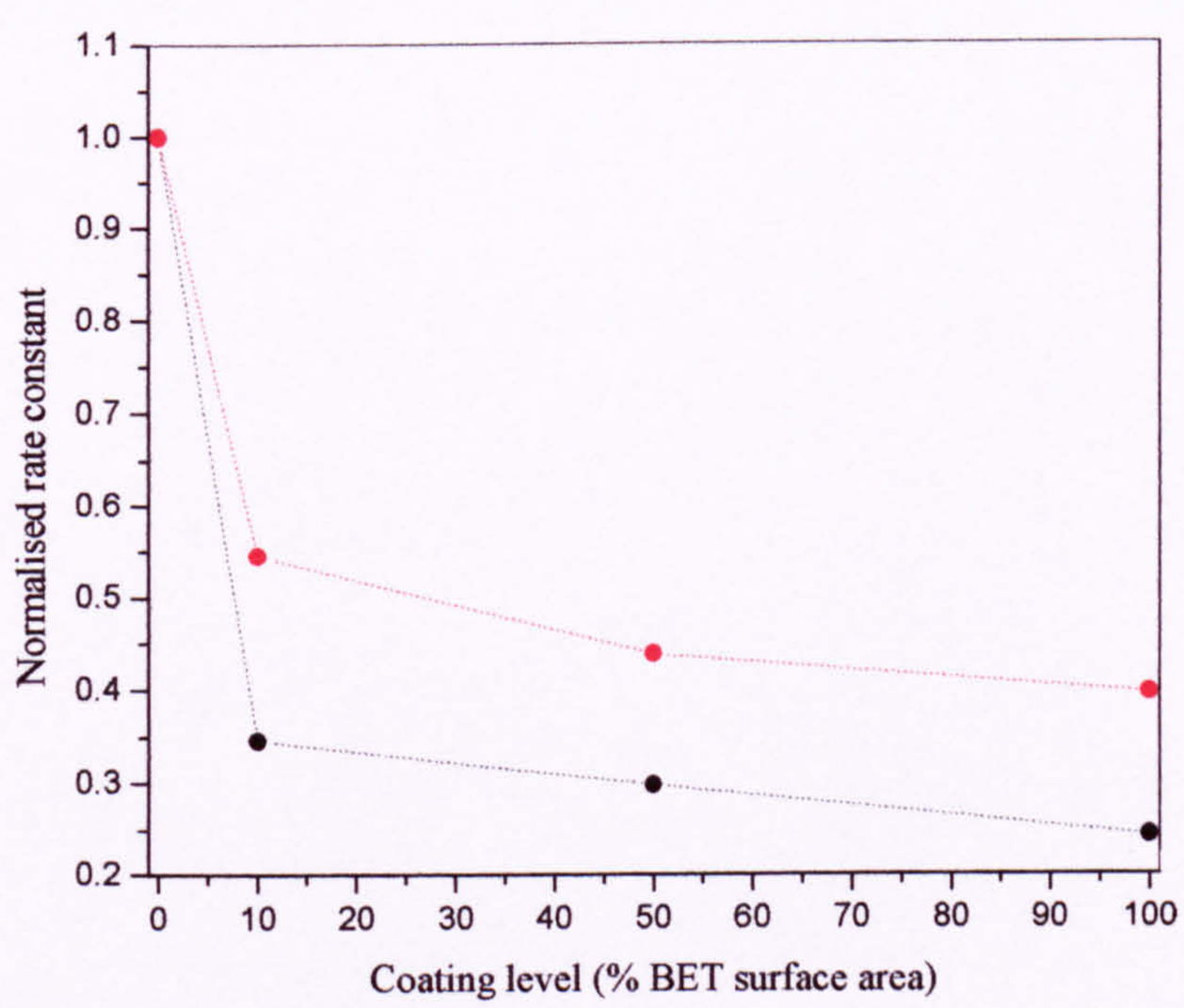

Fig 5.xii and 5.xiii. Normalised rate constants for NP (---) compared with those for IPA (---) for AM160K coated Sample A (above) and P25 (below). Note axis break.

As can be seen from figures 5.xii and 5.xiii, for both Sample A and P25 the trends in the photoactivity with coating level of AM160K are similar whether measured by nitrophenol degradation (NP) or by isopropanol oxidation (IPA). If we disregard Sample A 10%AM160K, then for both NP and IPA low levels of coating (25%) significantly reduce the photoactivity, with only moderate further reductions beyond this level. For Sample A, the increase at 10% coating level is much greater for NP than IPA. This effect is discussed further in Chapter 6.

5.4. Fourier Transfer Infra Red Spectroscopy (FTIR).

Samples were analysed by FTIR spectroscopy to determine whether a coating had been successfully formed and to analyse how the coatings are bonded to the titania surface. Spectra were taken of the bare titania, the organic material and then the coated titania. If a coating is formed rather than just a physical mixture of the constituents then alterations in the symmetry and bond strengths of the organic material will give rise to either new IR bands or shifts in the position of existing bands.

This technique is fully described in section 2.2.5. Spectra were measured at room temperature between 800 cm^{-1} and 4000 cm^{-1}, a resolution of 4 cm^{-1}, as a pressed disc of sample/KBr and referenced to a KBr disc. There were two distinct areas of interest for this study, the alkyl stretching region centred at 2900 cm^{-1} and the low frequency area between 1750 cm^{-1}- 800 cm^{-1} showing the crucial phosphate and silicate stretching region.

5.4.1. FTIR of Arlatone Map 160K (AM160K) coated titania.

The region between 1750 cm^{-1}- 800 cm^{-1} of the absorbance spectra for Sample A and P25 coated with various levels of AM160K are shown in Figure 5.xiv and Figure 5.xv with the solid state spectra of AM160K for comparison.

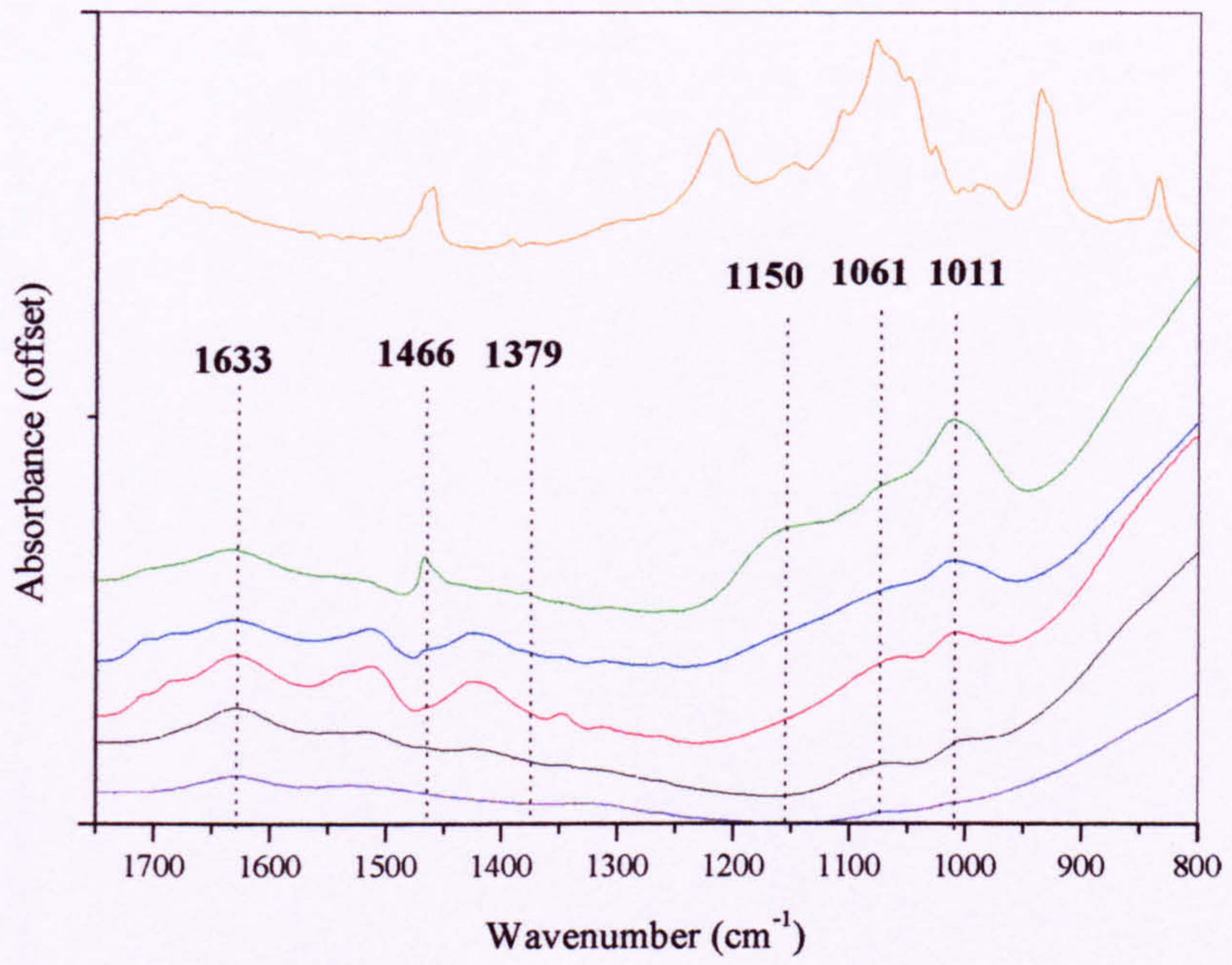

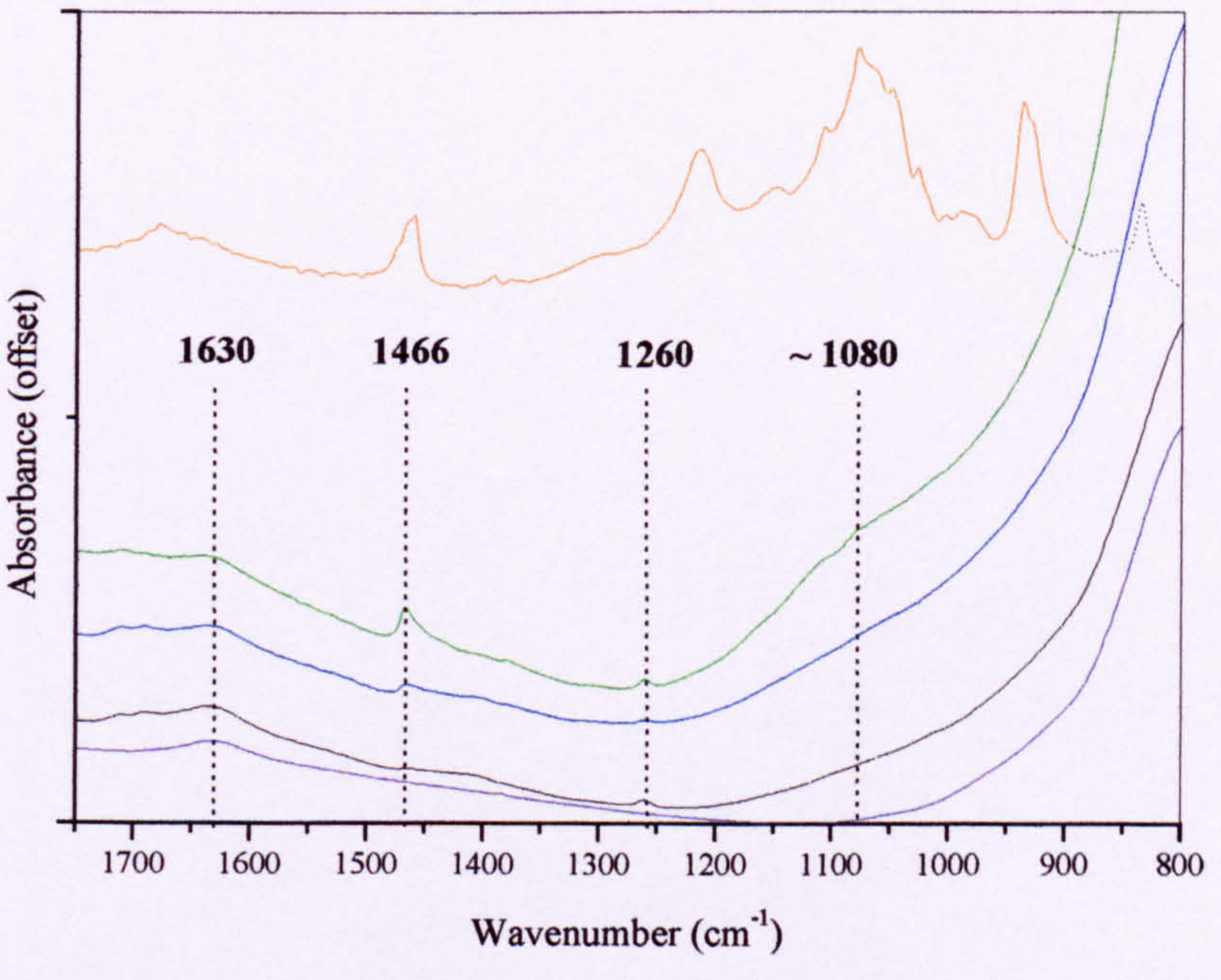

Fig 5.xiv and 5.xv. Absorbance spectra of AM160K coated Sample A (top) and P25 (lower) --- 10%; --- 25%; --- 50%; --- 100%; --- uncoated; --- AM160K

As can be seen from Figure 5.xii, the bands for P=O (1215 cm^{-1}) and P-OH (937 cm^{-1}) in the solid state spectrum of AM160K are not present in the spectra for the AM160K coated Sample A and the complex of PO_3^{2-} bands centred at 1078 cm^{-1} are broadened and shifted to approximately 1150 cm^{-1}, 1060 cm^{-1}, 1010 cm^{-1}. [14,15]

Similarly, Kim *et al* [16] observed bands at 1150, 1055 and 983 cm^{-1} for covalently adsorbed methyl phosphonate ($CH_3PO_3^{2-}$) on TiO_2 (P25) formed by reaction with surface hydroxyl groups. Comparable results were observed for this species on alumina [17-19].

Gao *et al* [20] studied the formation of self-assembled monolayers (SAM) of octadecylphosphonic acid (ODPA) on metal oxides. The FTIR results showed the loss of the P-O stretches in ODPA at 1228 (P=O) and 950 (P-OH) and the PO_3^{2-} peaks shifted to 1145 and 1090 cm^{-1} when SAM's are formed on ZrO_2. Similar results were found for adsorption of phenylphosphonic acid on ZrO_2 by Randel et al [21] and attributed to a tridentate bonding mode.

However, Connor and M^{c}Quillin [22] studied in situ adsorption of n-butyl phosphate onTiO_2 films and attributed bands at 1150, 1098, and 1004 cm^{-1} to an adsorbed bidentate phosphate species on the basis of protonation experiments. They also found that dimethyl phosphate ($Me_2P(O)O^-$) which cannot form bidentate complexes due to the alkyl groups did not adsorb and concluded from this result that monodentate attachment is not possible.

The adsorption of methacryloyloxy alkyl dihydrogen phosphates on silver films was studied by Ando *et al* [23,24] by IR reflection spectroscopy. They found that this species undergoes dissociative adsorption with bands for ν_{as} (PO_3^{2-}) at 1085 and ν_s (PO_3^{2-}) at 970 cm^{-1}. In particular they examined the ratio of these peaks to examine surface orientation.

On the basis of the results above and these studies it can be concluded that AM160K is covalently adsorbed, in either a bidentate or tridentate mode, on Sample A through the phosphate headgroup – a schematic of the two bonding modes is shown below

in Figure 5.xiv. A full study of the precise bonding mode was not possible as the lattice stretching vibrations of titania at below 1200 cm^{-1} coincide with the phosphate stretching region and thus may obscure important bands. Unfortunately there are no clear bands in this region for the analogous case of AM160K coated P25 (Figure 5.xv), these possibly being obscured by the titania lattice stretching at below 1200 cm^{-1}. A new peak at 1260 cm^{-1} may indicate a phosphate group with double bond character [14,15] but is not unambiguously assignable. Although the precise bonding of AM160K to P25 was not elucidated, it is clear from the methylene stretching frequencies for AM160K coated P25 that a coating has formed (see below).

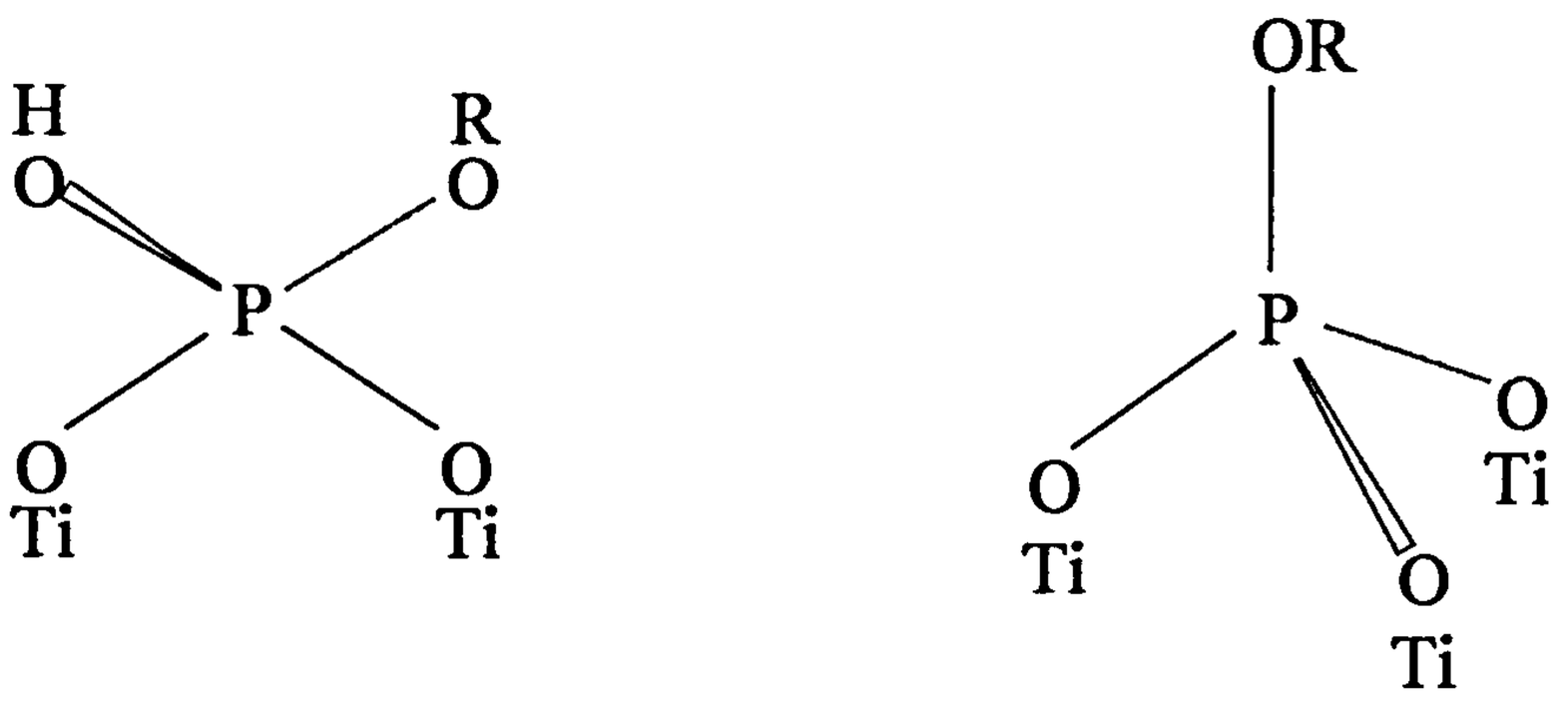

Fig 5.xvi. Possible bonding modes for adsorbed AM160K on Sample A. Bridged bidentate (left) and bridged tridentate (right)

To study the packing of the alkyl chains in AM160K coated titania and to demonstrate that a coating has been formed on P25 we examined the alkyl stretching region of Sample A and P25 coated with increasing levels of AM160K in Figure 5.xvii and Figure 5.xviii. The position of the methylene stretching bands for adsorbed long chain alkyls is indicative of the degree to which those chains are ordered [25,26]. For completely disordered chains the frequency of the methylene stretching band approaches that for the liquid alkane (ν_{as} ~2926 cm^{-1}). For well ordered structures the frequency is lowered and approaches that for a crystalline alkane (ν_{as} ~ 2915 – 2918 cm^{-1}) [25,27].

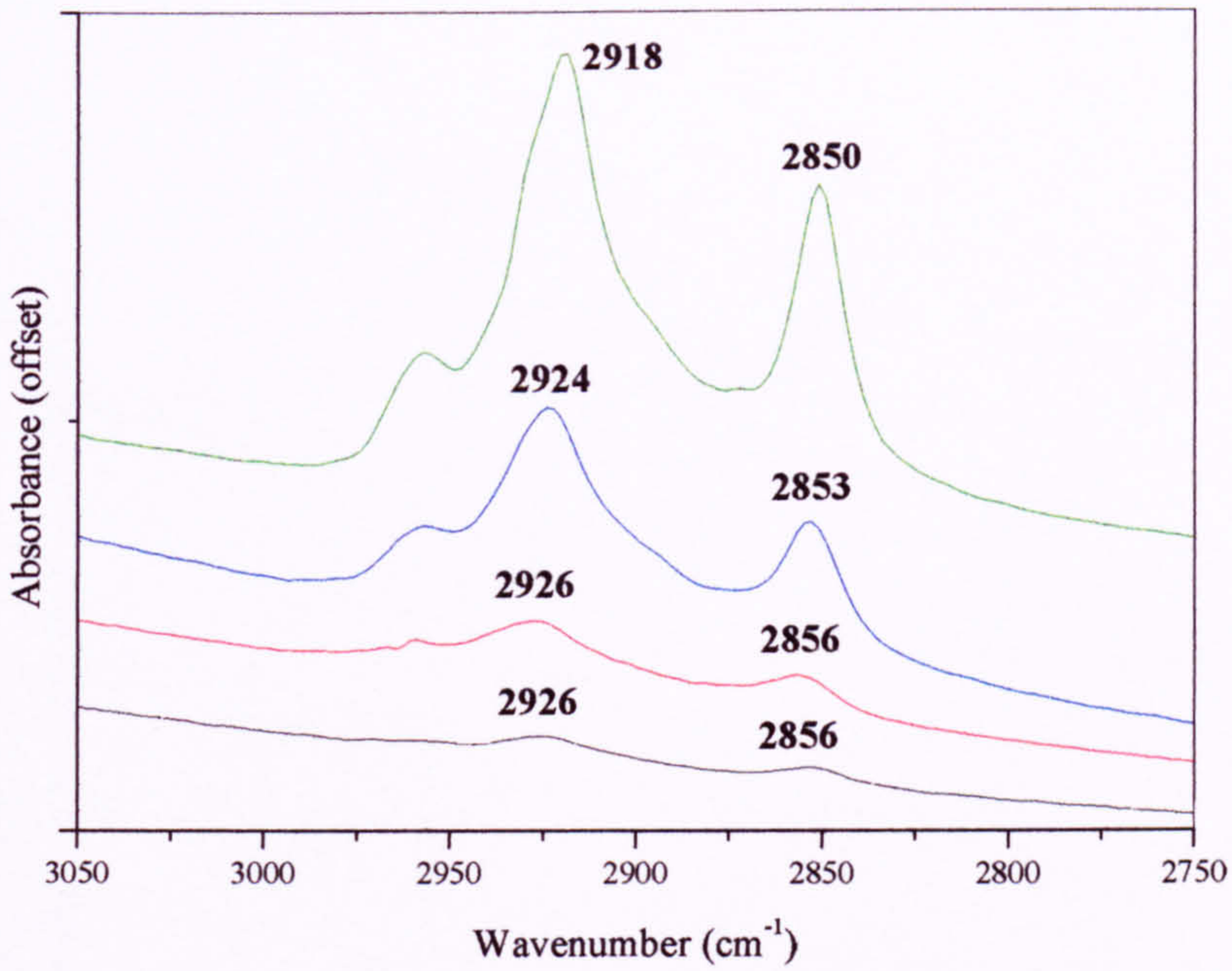

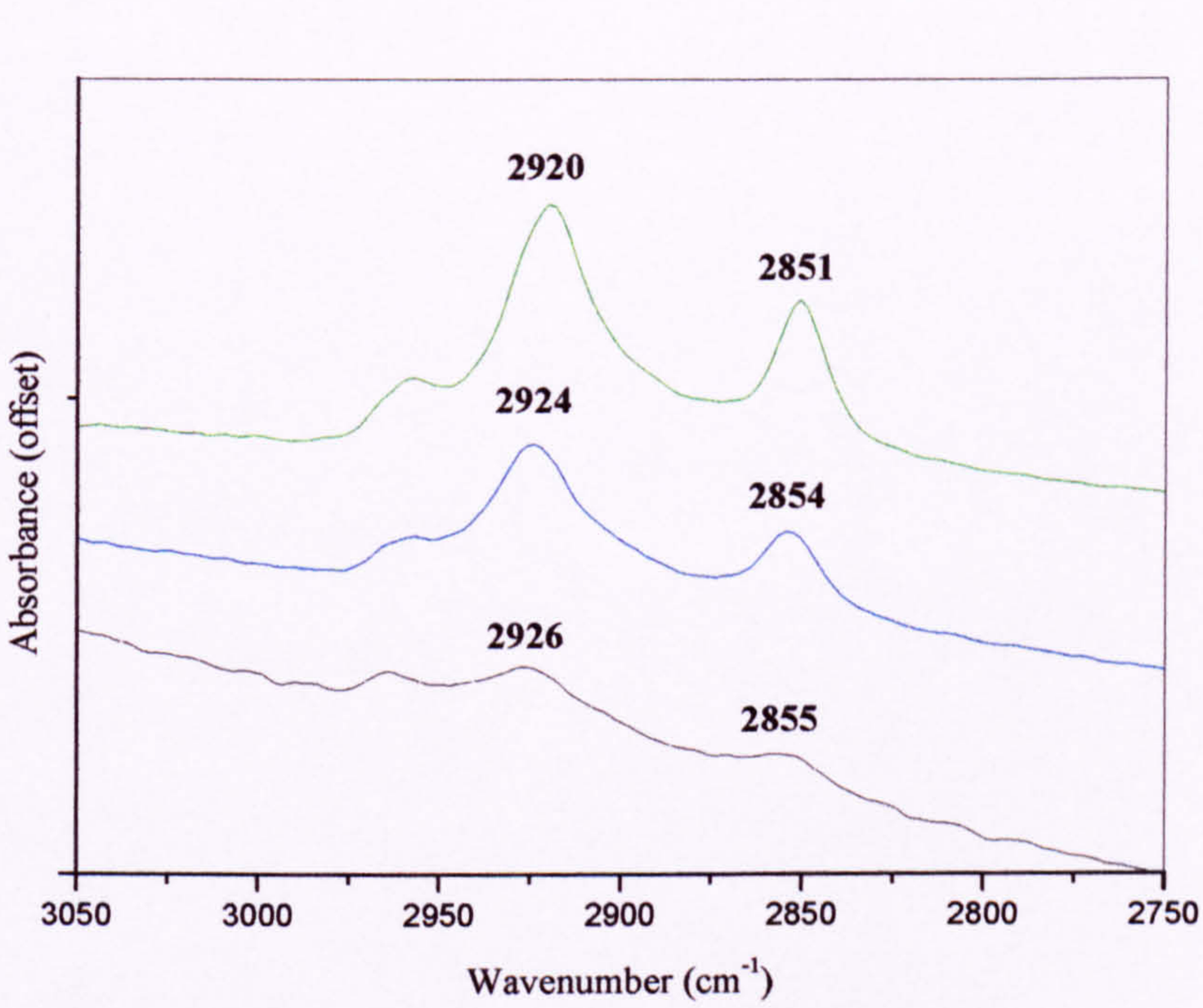

Fig 5.xvii and 5.xviii. Absorbance spectra of AM160K coated Sample A (top) and P25 (lower) --- 10%; --- 25%; --- 50%; --- 100%;

As shown by the figures above, for both Sample A and P25, as the coating level of AM160K is increased the methylene stretches progressively shift to lower wavenumbers indicating an increase in the order of the alkyl chains. In the case of Sample A, the methylene stretching peak positions for the 100% coating level even indicate chains ordered to the same degree as that reported for self assembled monolayers of octadecyl-phosphonic acid on TiO_2, ν_{as} = 2918 cm^{-1}, ν_s = 2849 cm^{-1} [28]. The methylene frequency against coverage is plotted below, and compared with that for ODTMOS coated titania, in Figure 5.xxiv.

5.4.2. FTIR of phosphate coated titania from sodium hydrogen phosphate (SHP).

The 1750 cm^{-1}- 800 cm^{-1} region of the spectra for Sample A coated with various levels of phosphate is shown in Figure 5.xix, with the solid state spectra of SHP for comparison.

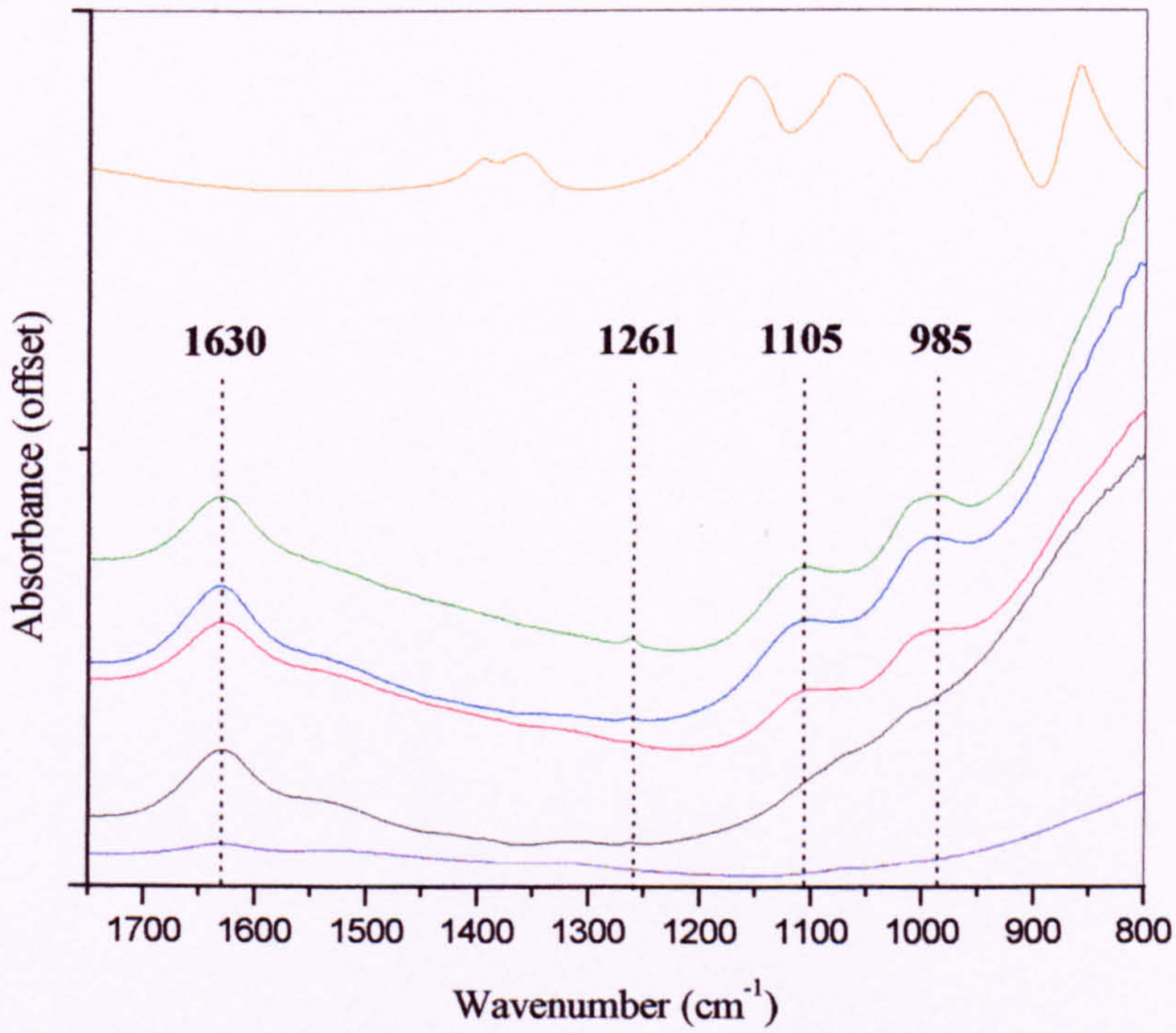

Fig 5.xix. Absorbance spectra of SHP coated Sample A. --- 10%; --- 25%; --- 50%; --- 100%; --- uncoated, --- SHP.

As can be seen from Figure 5.xix, the four strong bands corresponding to v_{as} (P-O), v_s (P-O), v_{as} (P-OH) and v_s (P-OH) at 1157, 1072, 947 and 858 cm^{-1} in the solid state spectra of SHP have been replaced by two broad bands at 1105 and 993 cm^{-1} in the spectra of SHP coated Sample A. Once more, the changes in the band positions indicates a change in the symmetry or bond strengths of the phosphate through adsorption to the titania and demonstrate that the phosphate is not present as simply a physical mix. Although there was not sufficient time to examine the corresponding spectra for SHP coated P25, the similarity in coating technique (and other results reported in this chapter) suggests that a phosphate coating has also formed for these samples.

Gong [29] studied the in-situ adsorption of phosphate to home prepared titania from titanium tetra-ethoxide at different pH by FTIR. He observed a spectra similar to that for $(HO)_2PO_2^-$ with two doublets; for the asymmetric and symmetric stretches of P-O (at 1115 and 1055 cm^{-1}), and for the P-OTi (at 972 and 915 cm^{-1}) and concluded that the most likely species was a bridging bidentate surface phosphate $(TiO)_2PO_2$. The former doublet ($\nu_{P\text{-}O}$) is at a lower frequency than for $(HO)_2PO_2^-$ as P-OTi is stronger than P-OH, and the lower doublet at higher frequencies as TiOP-O is weaker than HOP-O. A schematic of this bonding mode is shown in figure 5.xx. A single band at 1008 cm^{-1} was assigned to an electrostatically bound PO_4^{3-}.

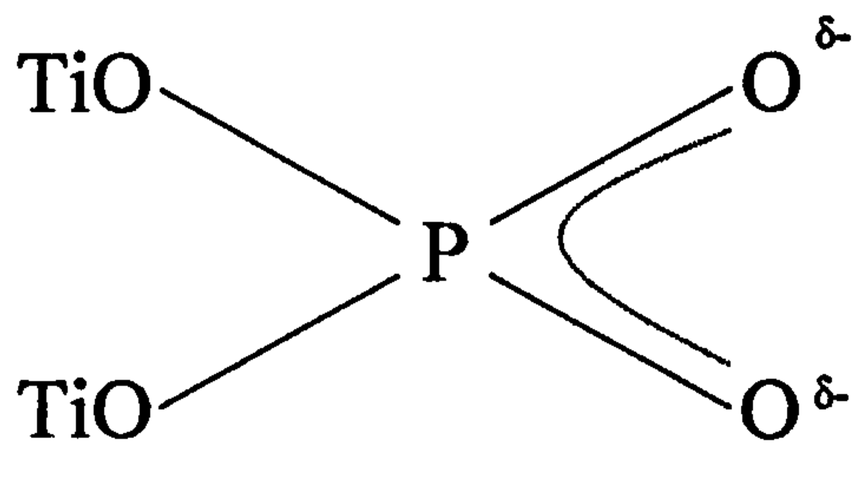

Fig 5.xx. Bridged bidentate bonding mode for titania bound phosphate proposed by Gong [29].

It is beyond the range of the present study to fully identify the adsorbed phosphate as the strong absorption of the titania lattice stretches and the broadness of the phosphate

bands prevent this. However, the presence of bands in the spectra of SHP coated Sample A at 1105 cm^{-1} and 985 cm^{-1} may be assigned to the asymmetric P-O and P-OTi stretches and indicate a bridged bidentate similar to that observed by Gong. The bands for the corresponding symmetric stretches at 1055 and 915 cm^{-1} are very weak in the deconvoluted spectra observed by Gong and may be masked by the titania lattice stretches in the present study. The weak band at 1261 cm^{-1} is assigned to the P-O-H bending mode indicating that the adsorbed phosphate is protonated, consistent with a study by Connor and M^{c}Quillin which found that adsorbed phosphates are protonated below pH 5 [22].

5.4.3. FTIR of octadecyl-trimethoxy-silane (ODTMOS) coated titania.

The region between 1750 cm^{-1}- 800 cm^{-1} of the absorbance spectra for Sample A and P25 coated with two levels of ODTMOS are shown in Figure 5.xxi and Figure 5.xxii with the liquid ODTMOS spectra for comparison.

For both ODTMOS coated Sample A and P25, the two peaks corresponding to Si-H_2R (1192 cm^{-1}) and Si-OMe (1090 cm^{-1}) are absent and have been replaced by a complex shoulder at ~1115 and 1015 cm^{-1} for Sample A and ~1177 and 1034 cm^{-1} for P25. This shoulder is assigned to a surface siloxane network formed from the cross-linking of silanols either before or after surface bonding as reported by Fadeev et al [28,30]. Similar bands have been reported for siloxane networks on silica [27]

The positions of the methylene stretching peaks again contain further information on the attachment of the silane to the titania. As discussed in section 5.4.1, in a coating with a high degree of order the alkyl chains are fully extended and the methylene peaks occur at a lower wavenumber than if they are disordered, where they approach that for a liquid alkane (v_{as} ~2926 cm^{-1}) [25-27]. Thus, the position of the v_{as} (CH_2) peak indicates the degree to which the alkyl chains are ordered in a coating. Figure 5.xxiii shows the position of the methylene asymmetric stretching peak for ODTMOS coated Sample A and P25 compared with that for the Arlatone Map 160K (AM160K) coated modifications as the coating level is increased.

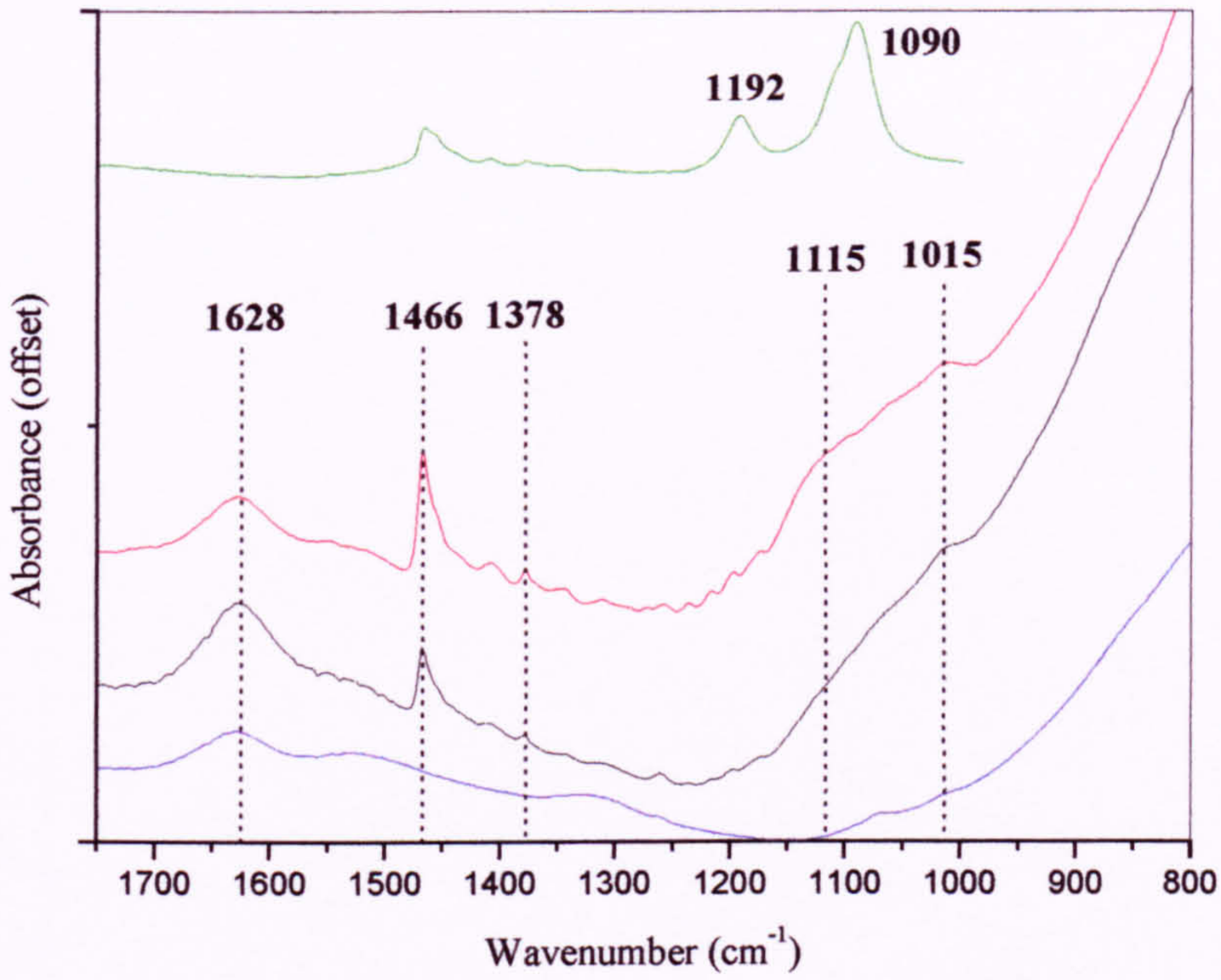

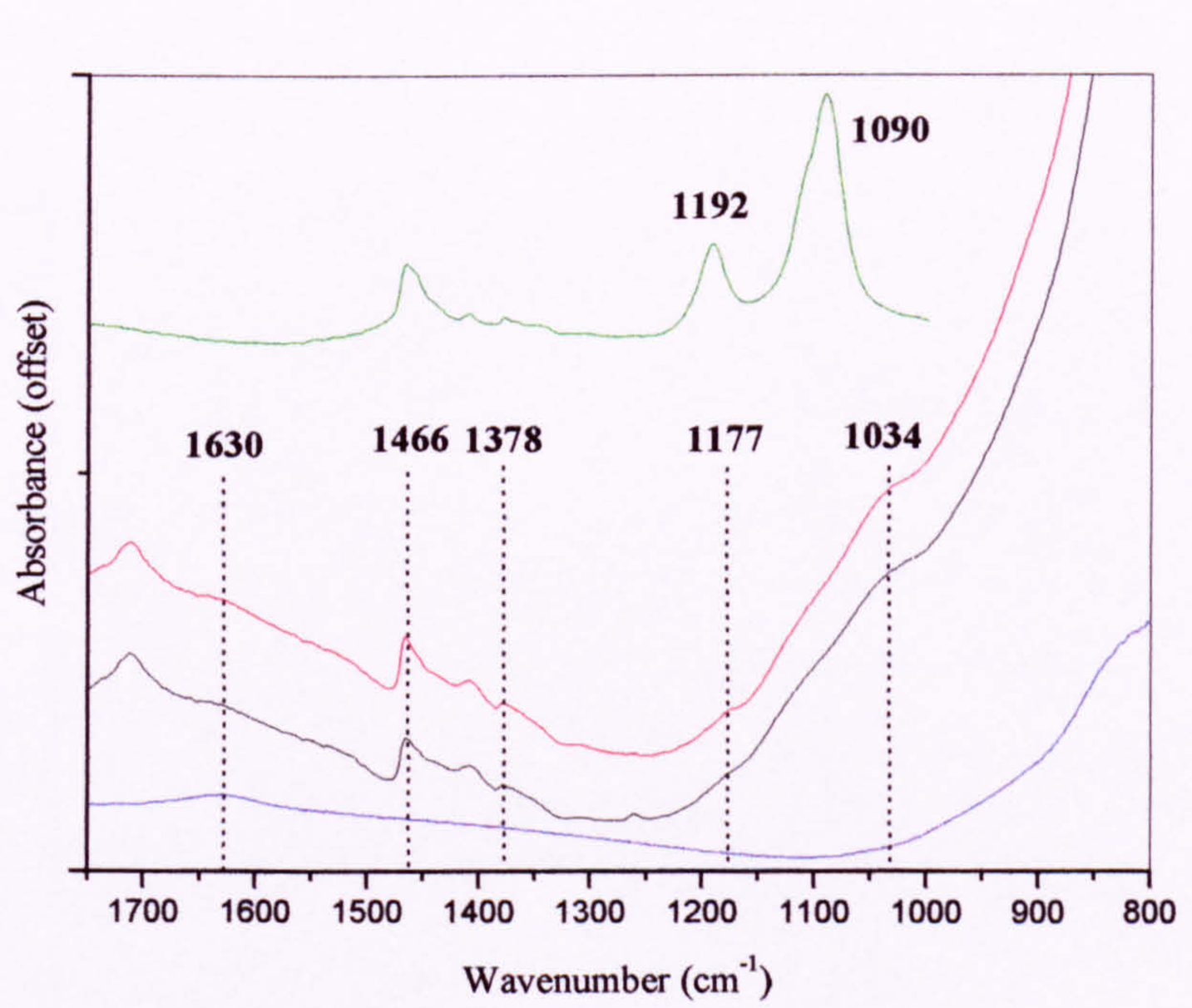

Fig 5.xxi and 5.xxii. Absorbance spectra of ODTMOS coated Sample A (top) --- 31%; --- 64%; P25 (lower) --- 40%; --- 84%; --- uncoated; --- ODTMOS.

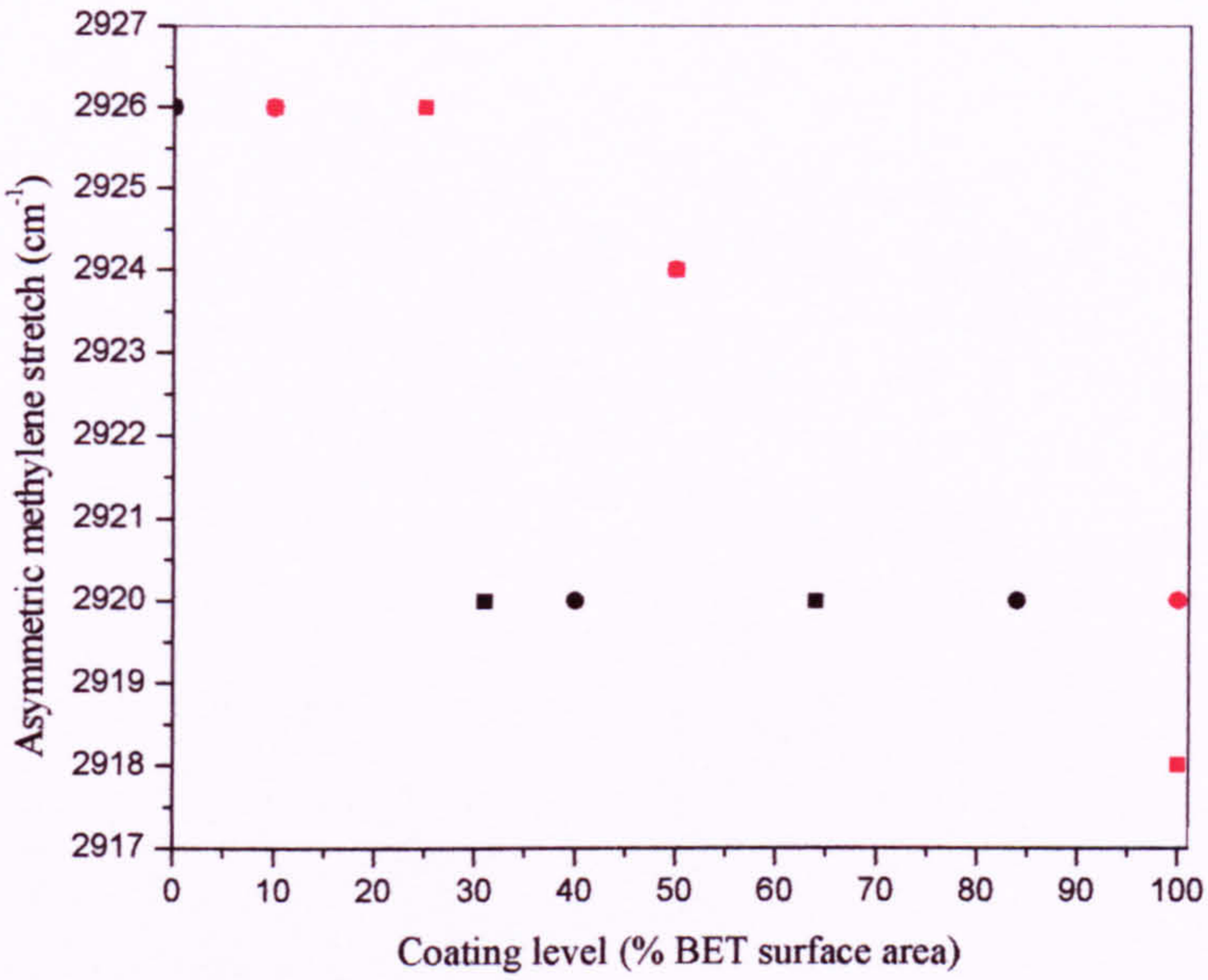

Fig 5.xxiii. Asymmetric methylene stretching peak positions for ODTMOS (---) and AM160K (---) coated Sample A (squares) and P25 (circles).

For the AM160K coated titania, the chains are disordered up to ~ 25% level with a gradual increase in chain ordering as the level of coating is increased. In contrast to this, ODTMOS coatings have a good degree of order at even the lowest (31%) level of coating, which is maintained as the coating level increases. This is in good agreement with results by Helmy and Fadeev [28] who studied the effect of the headgroup on the growth and ordering of C_{18} alkyl phosphonate and various silanes. The authors found that molecules with headgroups that could crosslink (for example ODTMOS) exhibited a good degree of chain ordering at even low levels of coating, while those that did not (e.g. octadecylphosphonic acid) were ordered only at higher levels. This was attributed to a random attachment versus islandlike growth mechanism i.e. islands of alkyl siloxane are formed from crosslinked silanes (see figure 5.xxiv). Islandlike growth of silanes through a siloxane network has been proposed for chloro- and alkoxy-silanes on silica [27, 31-37].

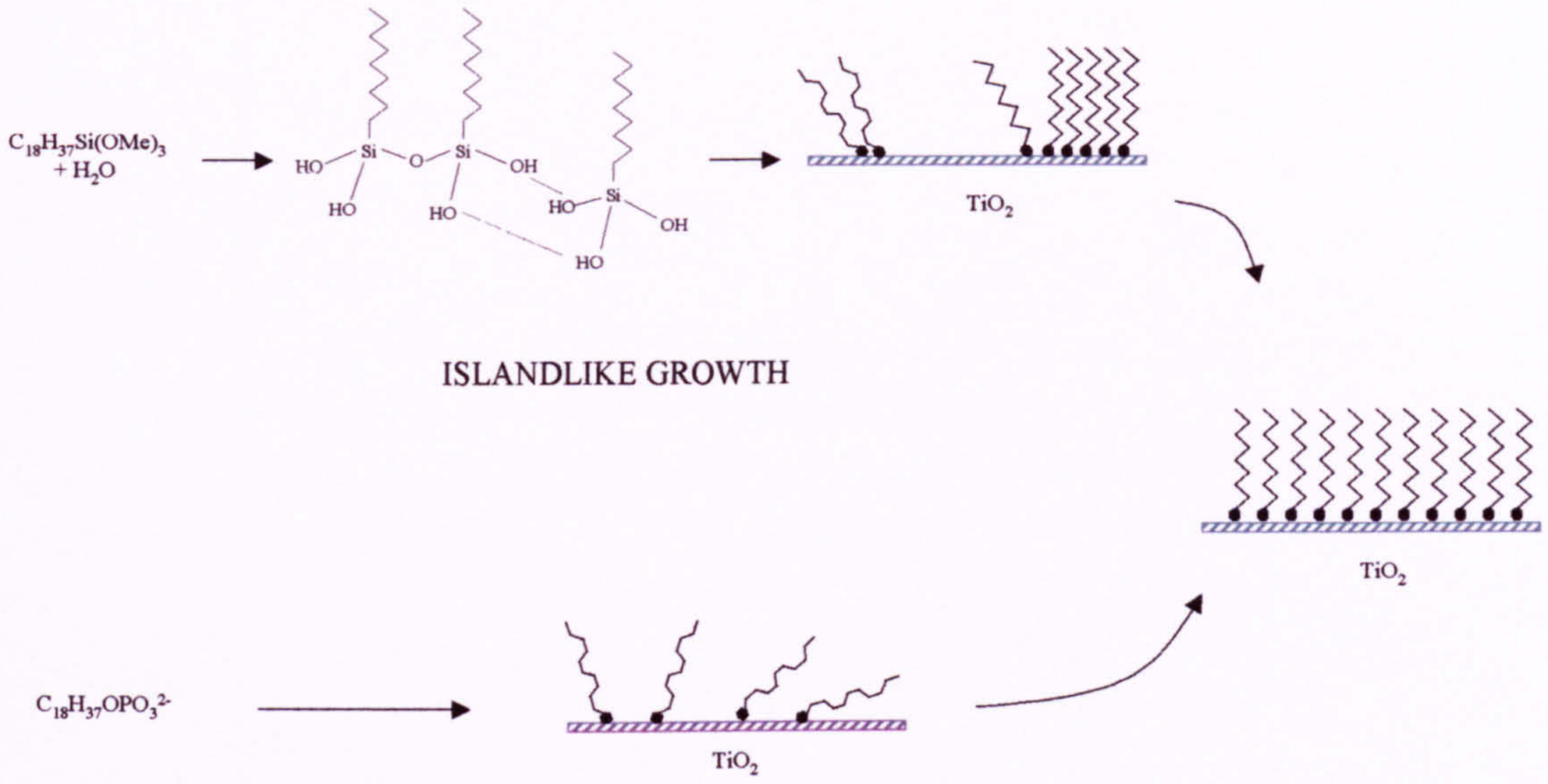

Fig 5.xxiv. Scheme showing different proposed methods of attachment for ODTMOS and AM160K – based on model by Helmy and Fadeev [28,38]

That the pattern of methylene stretching positions indicates island like growth of ODTMOS supports the assignment of the shoulder in the titania lattice region (Fig 5.xxi and 5.xxii) as a siloxane network.

5.5. Gravimetric surface area analysis.

Surface area analysis is one of the simplest techniques for the characterisation of coated powders. This technique may be used to discover important information about the underlying powder, coating formation and integrity, and how the coating 'builds up' at increasing coating levels.

For an ideal spherical particle of radius (r) and density (ρ) the specific surface area (SSA) is given by equation 5.1. Assuming that the density of the coating is equal to that of the underlying particle, the specific surface area of a particle with a coherent non-porous coating of weight percentage (x) will, to a first approximation, be given by equation 5.2 [39], sample calculations are given in Appendix 5.2:

$$(SSA)_{uncoated} = 3/(r.\rho) \qquad [5.1]$$

$$(SSA)_{coated} = \frac{3}{r.\rho.\left[1 + \frac{X}{300}\right]} \qquad [5.2]$$

Despite the idealised nature, reasonable surface areas were calculated using equation 5.1 - 140 $m^2\ g^{-1}$ for rutile ($\rho = 4.2\ g\ cm^{-2}$) with a particle size of 10.5 nm, and 50 $m^2\ g^{-1}$ for a 80% anatase/20% rutile composition ($\rho = 4.0\ g\ cm^{-2}$) with a particle size of 30 nm. These compare well with the measured surface areas of 133 $m^2\ g^{-1}$ and 43 $m^2\ g^{-1}$ for Sample A and P25 respectively.

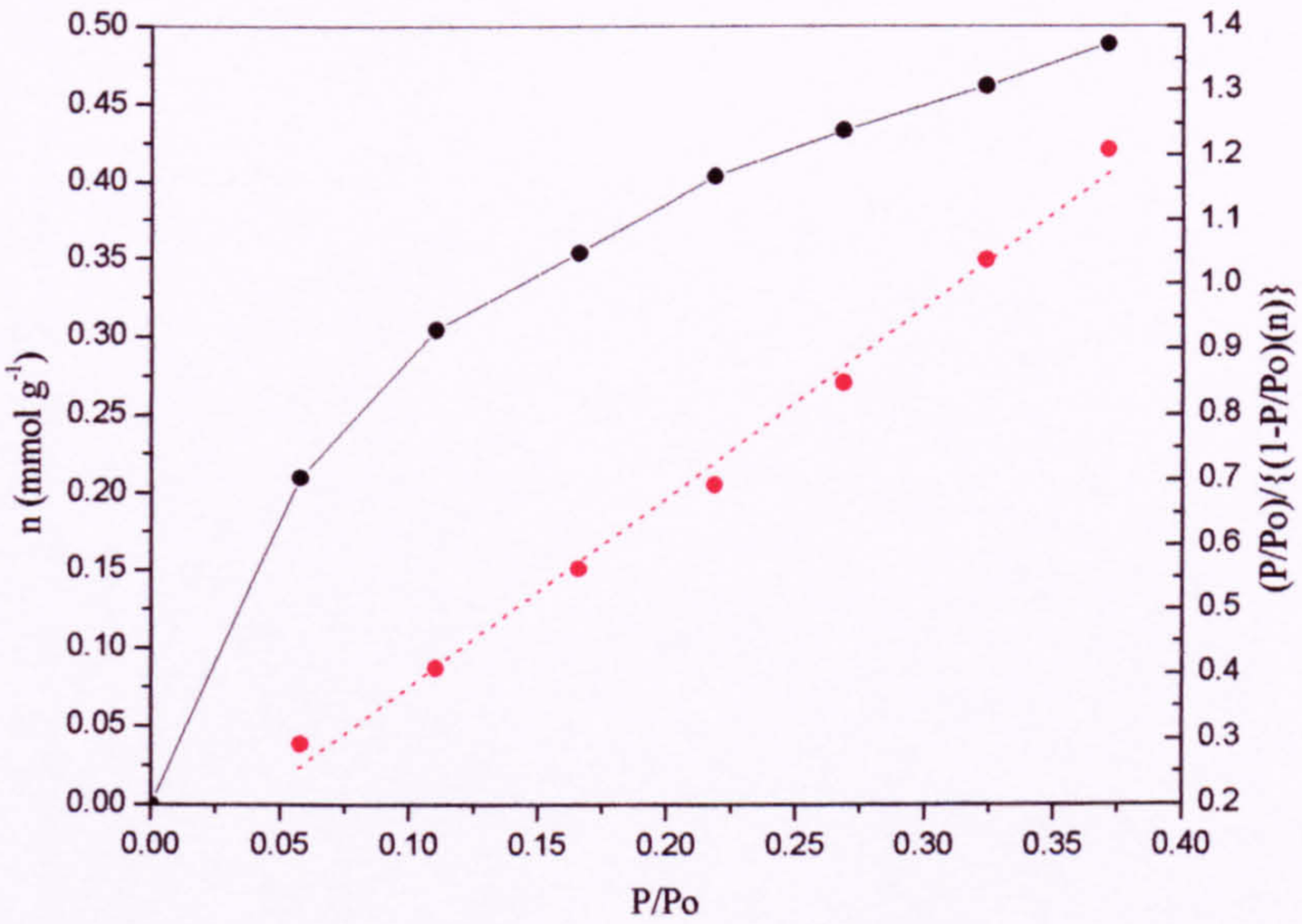

Fig 5.xxv. Adsorption isotherm (---) for nitrogen on P25 with a 10% AM160K coating and BET analysis (---).

The uptake of nitrogen on coated Sample A and P25 was measured by M^{c}Bain gravimetric adsorption of nitrogen as described in Section 2.2.4 and the surface areas

determined by BET analysis. A representative adsorption isotherm together with the corresponding BET analysis for P25/10%/AM160K is shown in Figure 5.xxv.

5.5.1. Arlatone Map 160K (AM160K) coated titania.

The variation in surface area with coating level for AM160K coated Sample A and P25 is shown in Figure 5.xxvi. The reproducibility of this technique is $\pm$ 5 m^2 g^{-1} for Sample A and $\pm$ 7 m^2 g^{-1} for P25 based on repeat measurements of the uncoated samples.

For both Sample A and P25, the trends of surface area with coating level are similar, with a large decrease in surface area not predicted by calculations using equation 5.2. This equation predicts a theoretical decrease in surface area for a 100% AM160K coating on 136 m^2 g^{-1} rutile of ~ 8%, and ~ 3% for a powder like P25 (assuming 80% anatase, 20% rutile). Most remarkable was the large reduction in surface area for the low levels of coating, which was more pronounced for Sample A.

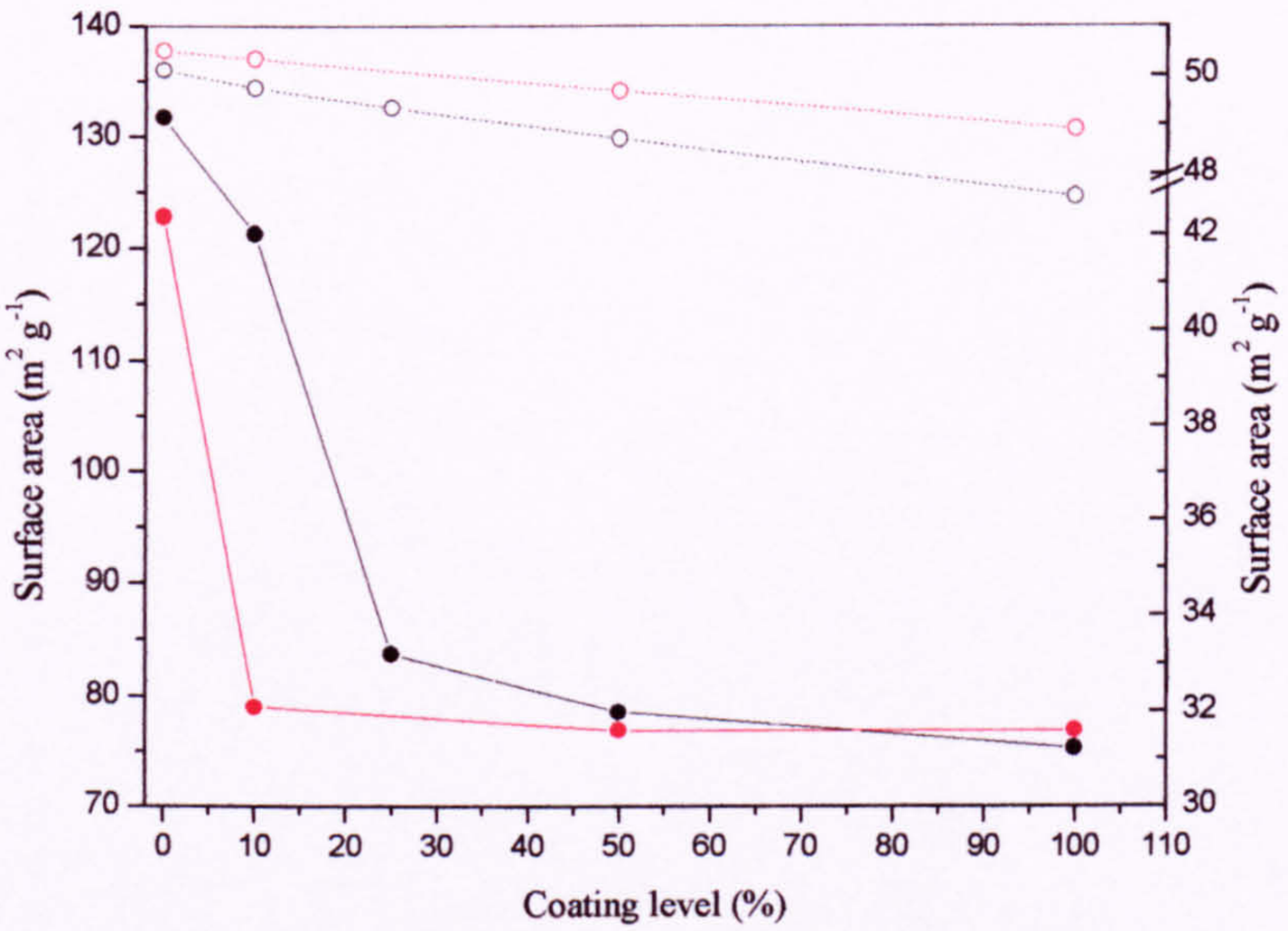

Fig 5.xxvi. Surface area of AM160K coated Sample A (---) left hand axis, and P25 (---), right hand axis. Experimentally determined surface areas (solid lines) and theoretical calculated values (dotted lines) from equation 5.2.

A similar behaviour was observed for dense silica coatings on Sample A by Tooley [40] where a 2 wt% coating reduced the surface area by ~25%. This was attributed to the blocking of pores that exist between aggregates of the individual primary crystals identified by Transition Electron Microscopy (TEM). Further, an increase in surface area at higher outgassing temperatures suggested that Sample A is microporous. It is thus reasonable to argue that the AM160K coating in the present study is unduly reducing the surface area in a similar way by blocking these pores.

The author also concluded that P25 did not have microporous structure [40], as this material did not exhibit an increase in surface area when the outgassing temperature was increased from 110°C to 300°C. This agreed with results reported by Navio et al that while P25 has a porous surface shown by Scanning Electron Microscopy (SEM) [41], the pore sizes are between 300 - 400 Å, and the average pore diameter of 315 Å (32 nm). There are however similarities between the trends observed with Sample A in the present study and this suggests the possibility that P25 may indeed have some other specific sites of high surface area or adsorption capacity that are blocked at low levels of coating. It is worth noting that at higher coating levels the surface area is only moderately reduced as predicted theoretically from equation 5.2 suggesting that the 10% coating covers these sites/areas.

5.5.2. Phosphate coated titania from sodium hydrogen phosphate (SHP).

The variation in surface area with coating level for SHP coated Sample A and P25 is shown in Figure 5.xxvii. The reproducibility of this technique is $\pm$ 5 m^2 g^{-1} for Sample A and $\pm$ 7 m^2 g^{-1} for P25 based on repeat measurements of the uncoated samples.

In common with AM160K coatings (above), the trends of surface area with coating level are similar for both Sample A and P25, with a large decrease in surface area at low coverage that is not predicted theoretically from equation 5.2. In common with the analysis for AM160K coatings, these trends may be attributed to the blocking of pores between aggregates of individual crystals for Sample A and similarly for P25 to the blocking of specific areas with high adsorption capacity.

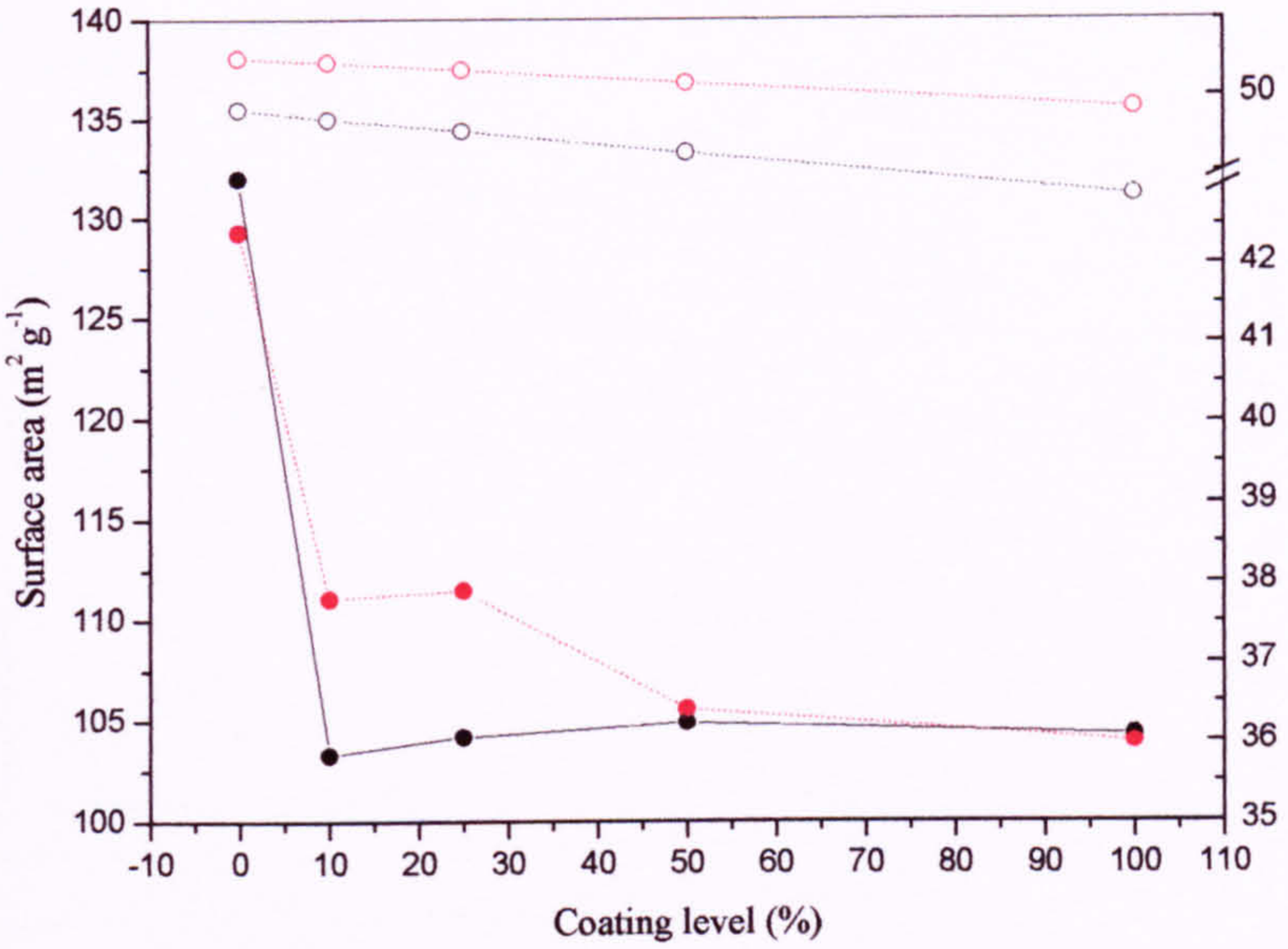

Fig 5.xxvii. Surface area of SHP coated Sample A (---), left hand axis, and P25 (---), right hand axis. Experimentally determined surface areas (solid lines) and theoretical calculated values (dotted lines) from equation 5.2.

5.5.3. Octadecyl-trimethoxy-silane (ODTMOS) coated titania.

The variation in surface area with coating level for ODTMOS coated Sample A and P25 is shown in Figure 5.xxviii. Surface areas have a reproducibility of $\pm$ 5 m^2 g^{-1} for Sample A and $\pm$ 7 m^2 g^{-1} for P25 based on repeat measurements of the uncoated samples.

In contrast to AM160K (a phosphate ester) and phosphate coatings described above, the trends in surface area with coating level is different for Sample A and P25. For Sample A, there is a large decrease in surface area at low levels of coating as for the SHP and AM160K coatings above, while for P25 there is a roughly linear decrease in surface area with coating level in contrast to the phosphate coatings. That the ODTMOS coatings reduce surface area differently to the phosphate coatings reinforces the conclusion from the FTIR evidence (Section 5.4.3) that they form on the titania surface in a different manner to the AM160K coatings i.e. the trends may be due to the island-like formation of this coating.

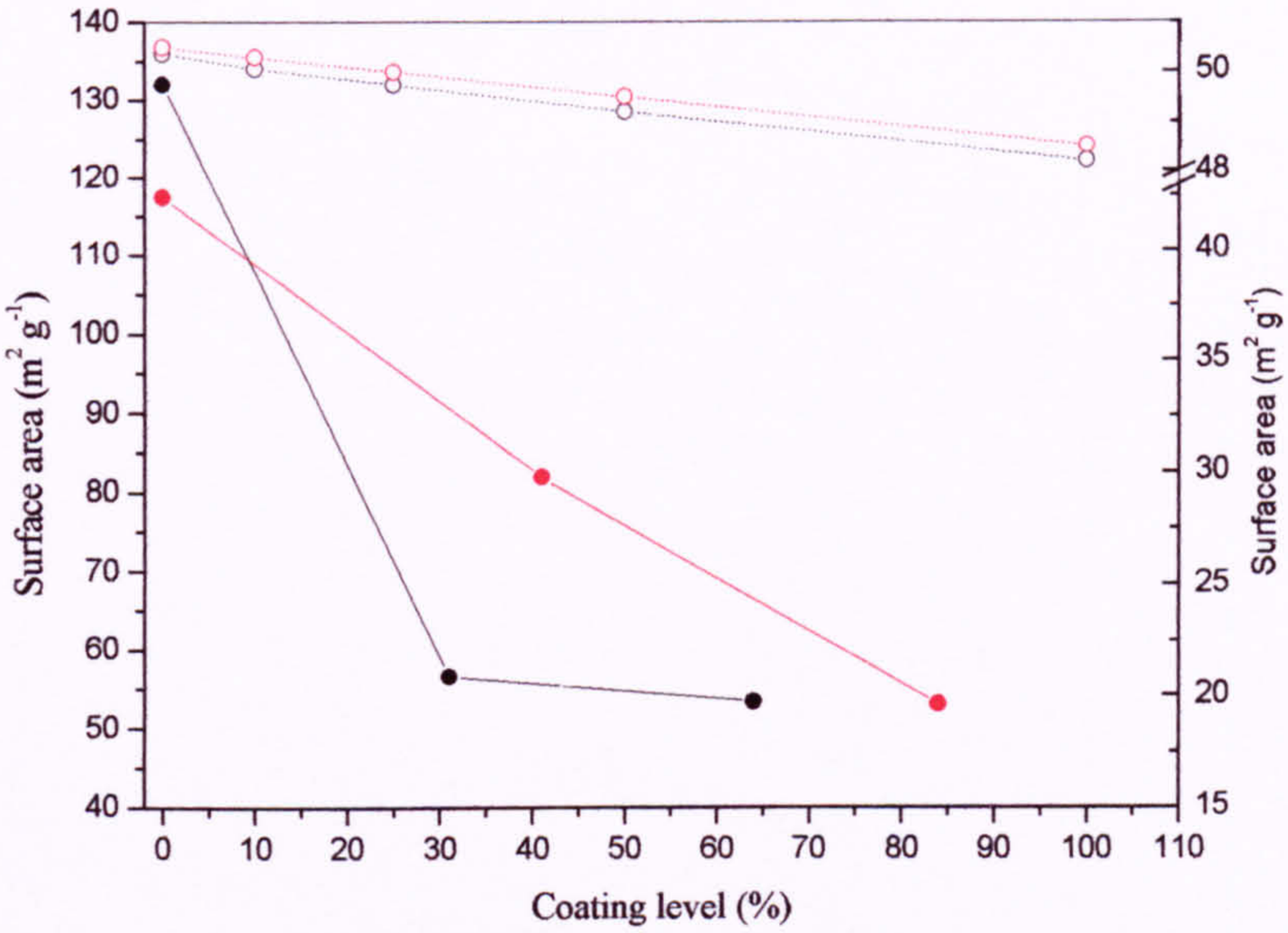

Fig 5.xviii. Surface area of ODTMOS coated Sample A (---), left hand axis, and P25 (---), right hand axis. Experimentally determined surface areas (solid lines) and theoretical calculated values (dotted lines) from equation 5.2.

This point is clarified by a comparison of the absolute reduction in surface area for the different coatings on Sample A (Figure 5.xxix) - it can be observed that ODTMOS coatings more effectively reduce surface area than either SHP or AM160K. Despite the differences in trends for the ODTMOS coating between Sample A and P25, it can be seen from 5.xxix and 5.xxx that for both these samples there is a similar order in the effectiveness of the three different coatings to reduce surface area i.e. ODTMOS > AM160K > SHP. This implies that ODTMOS and AM160K are more effective at covering the titania surface than phosphate coatings or that phosphate coatings are porous to nitrogen. Implications for the photoactivity are discussed in the following chapter.

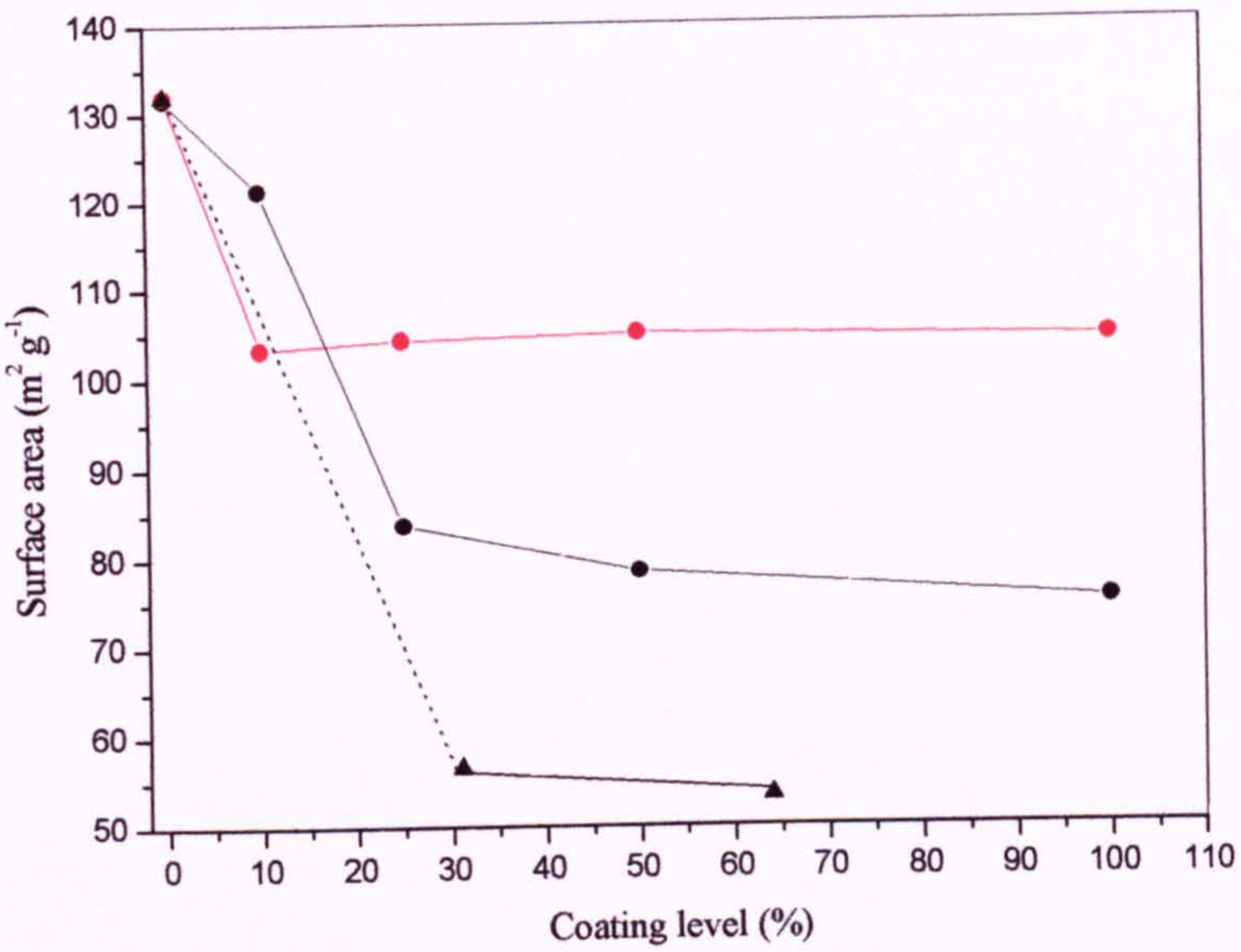

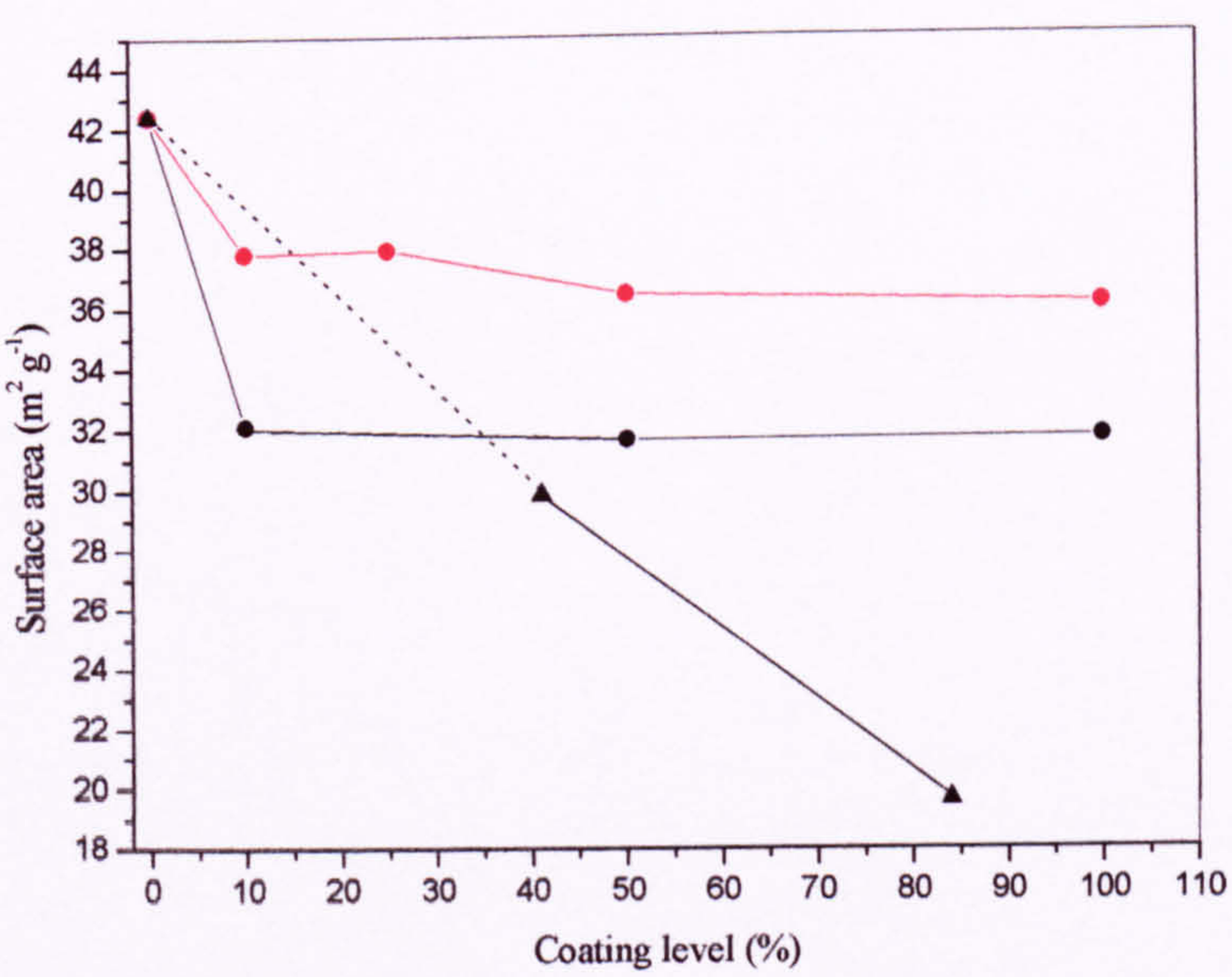

Fig xxix and xxx. Comparison of the surface area reductions by SHP (---), AM160K (●) and ODTMOS (▲) coatings on Sample A (above) and P25 (lower).

5.6. Conclusions: the effect of organic coatings on the photoactivity of titania.

The main conclusions from this chapter are as follows:

1. The effect of phosphate ester (AM160K), phosphate (SHP) and silane (ODTMOS) coatings on the photoactivity of Sample A and Degussa P25 has been determined by measurement of the rates of isopropanol oxidation (IPA) and nitrophenol degradation (NP).
2. AM160K on both Sample A and P25 reduced the photoactivity at low levels of coatings with only marginal further decreases in photoactivity with higher levels whether measured by IPA or NP. However, for a 10% coating on Sample A there is an increase in photoactvity that is greater when measured by NP.
3. A similar effect is seen for SHP coatings when the photoactvity is measured by NP. When measured by IPA, the coating barely affects the photoactvity.
4. ODTMOS coatings reduce the photoactivity for both Sample A and P25, but the effect of coating level is different for the two types of titania - a roughly linear decrease in the former case, whereas there is a sharp decrease at low levels of coating for P25 followed by marginal decreases thereafter. The effect is similar whether measured by IPA or NP.
5. FTIR spectroscopy has been used to confirm that a coating of the substrate has formed on the titania and that they do not exist as a discrete physical mixture of the two. While it was beyond the scope of the project to fully probe the nature of the surface bond formation, suggestions have been made with the available evidence, which are necessarily tentative. From comparison of the methylene stretches it was found that ODTMOS coatings form in island-like siloxane patches with high chain ordering due to the crosslinking of individual silane molecules, which is in contrast to AM160K coatings.
6. For both Sample A and P25 all the coatings reduce the surface area more than predicted by equation 5.2 (most especially at low levels) suggesting that these coatings preferentially block pores (Sample A) or other areas with a high adsorption capacity (P25). However, there is a different trend for the reduction in surface area for ODTMOS coatings between Sample A and P25. ODTMOS and AM160K coatings more effectively reduce the surface area than SHP.

5.7. Appendices.

Appendix 5.1.

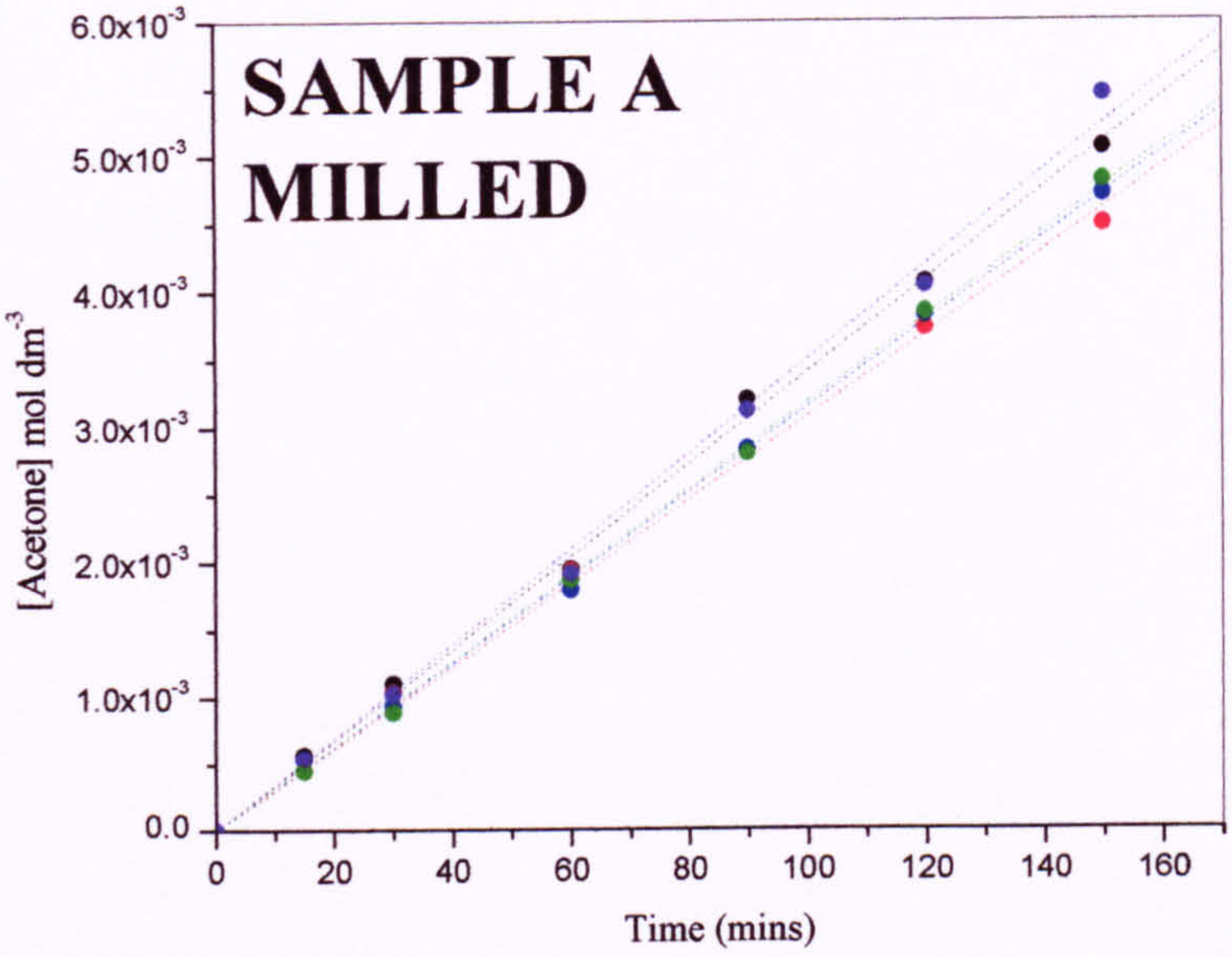

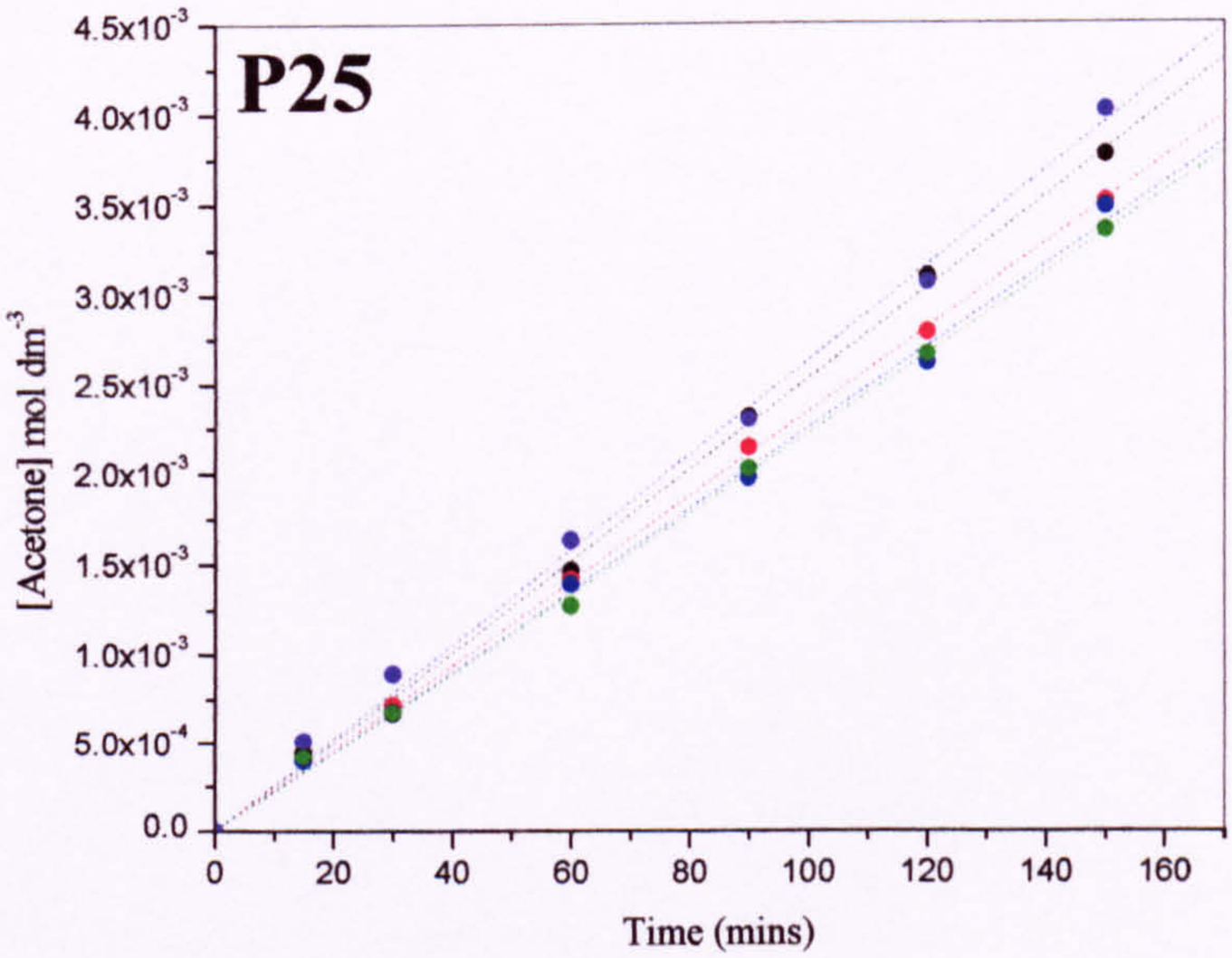

Fig A5.i and A5ii. Acetone concentration against time for milled SHP coated Sample A (upper) and P25 (lower). --- 10%; --- 25%; --- 50%; --- 100%; --- Uncoated.

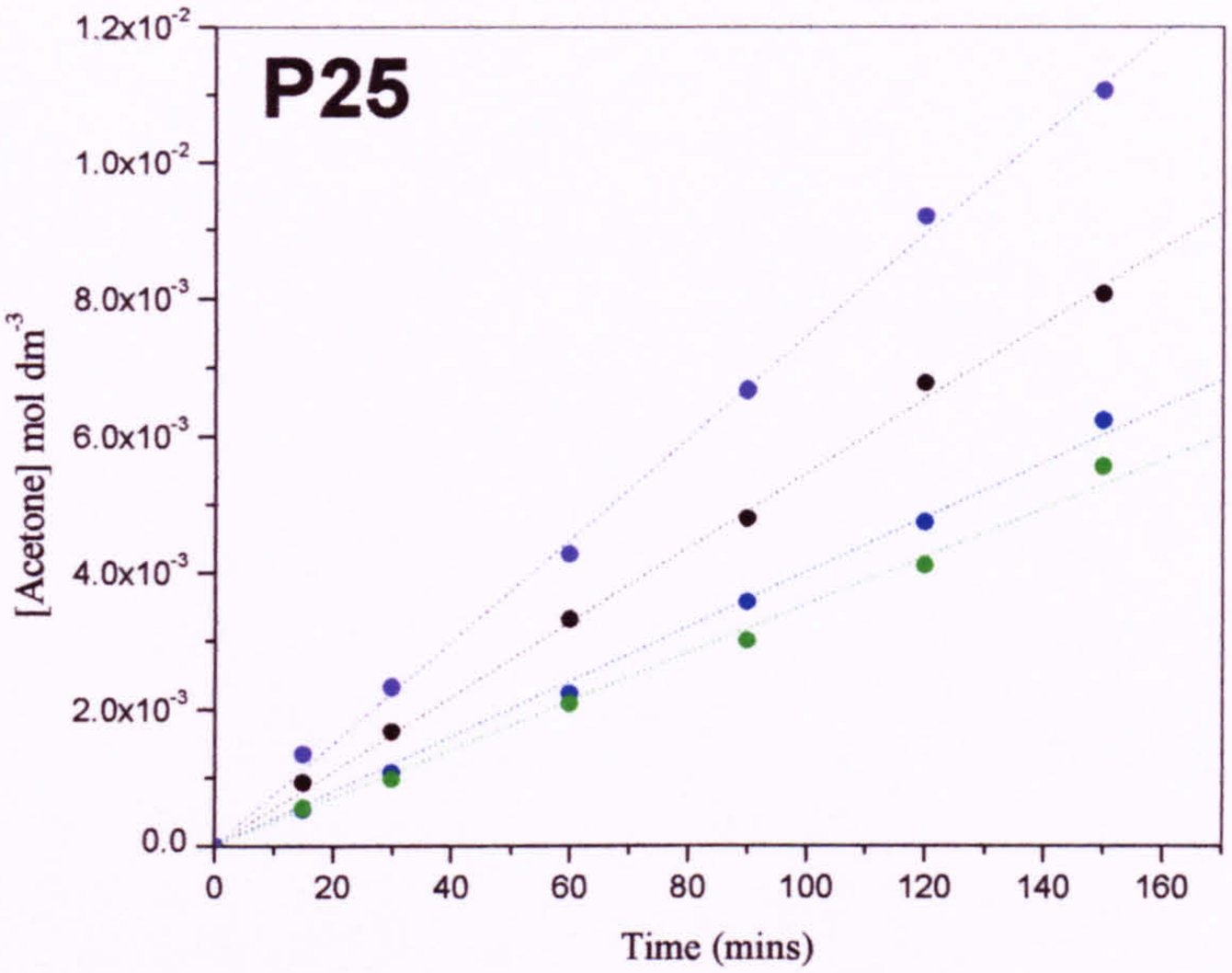

Fig A5.iii. Acetone concentration against time for unmilled AM160K coated P25. --- 10%; --- 50%; --- 100%; --- Uncoated.

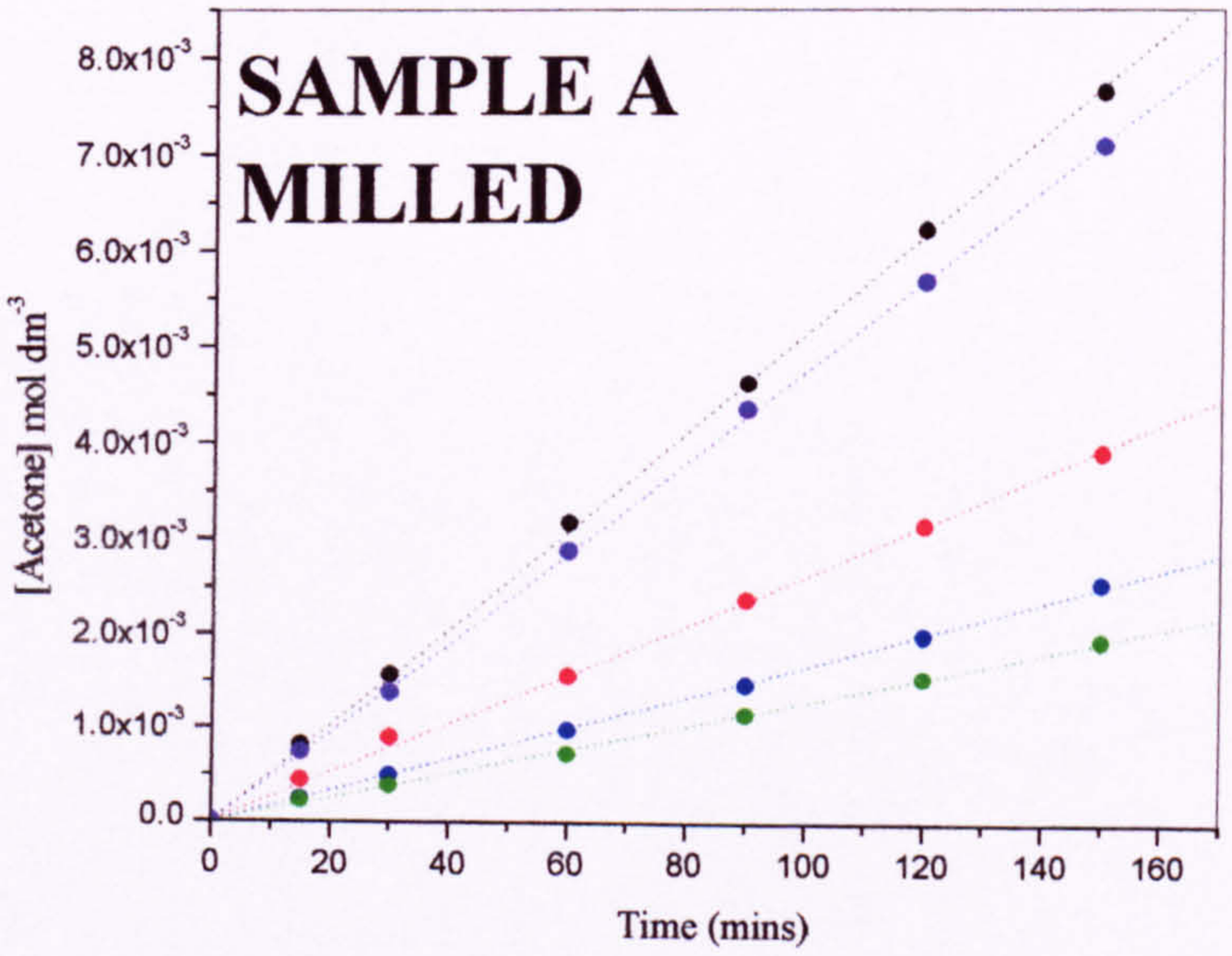

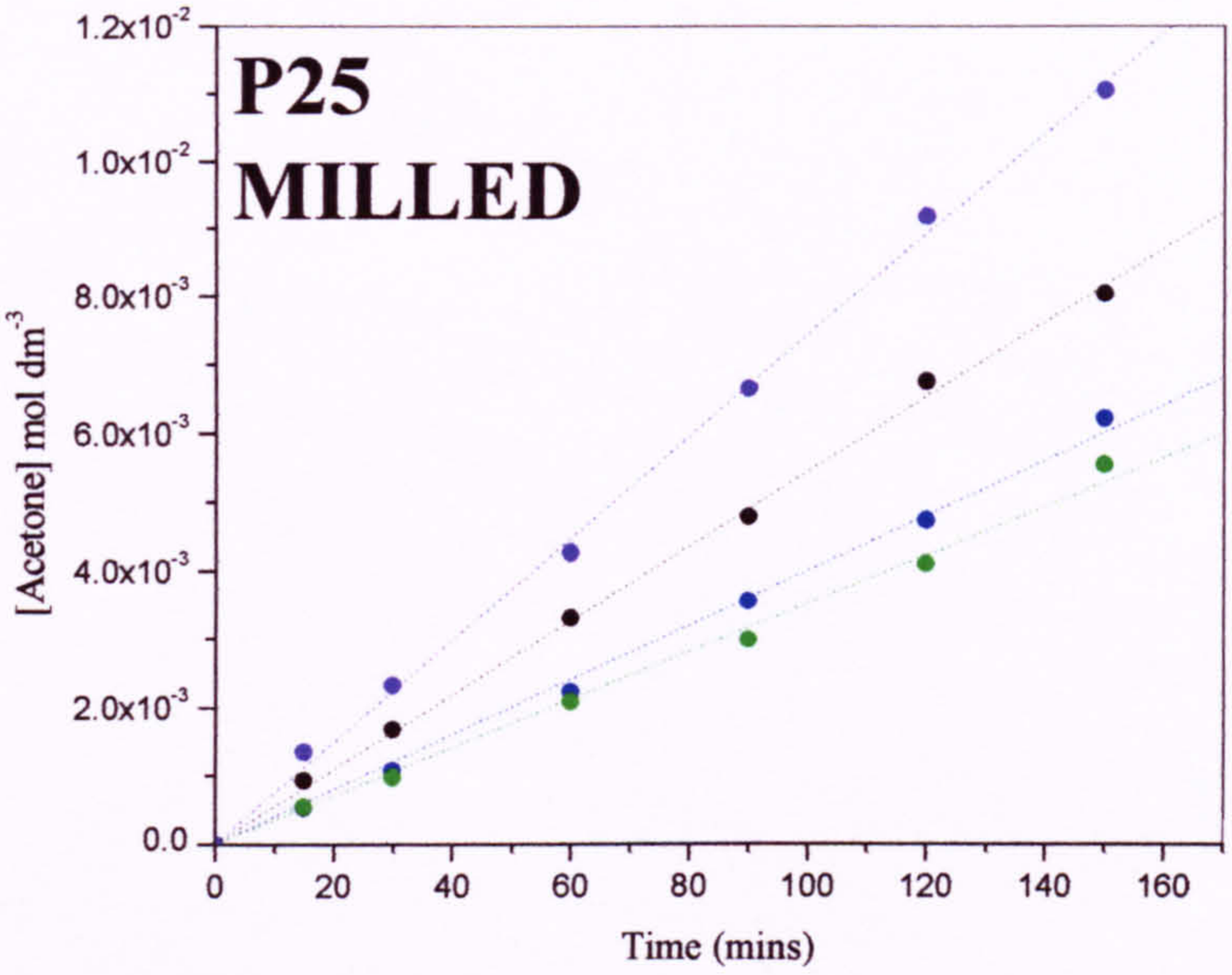

Fig A5.iv and A5.v. Acetone concentration against time for milled AM160K coated Sample A (above) and P25 (below). --- 10%; --- 25%; --- 50%; --- 100%; --- Uncoated.

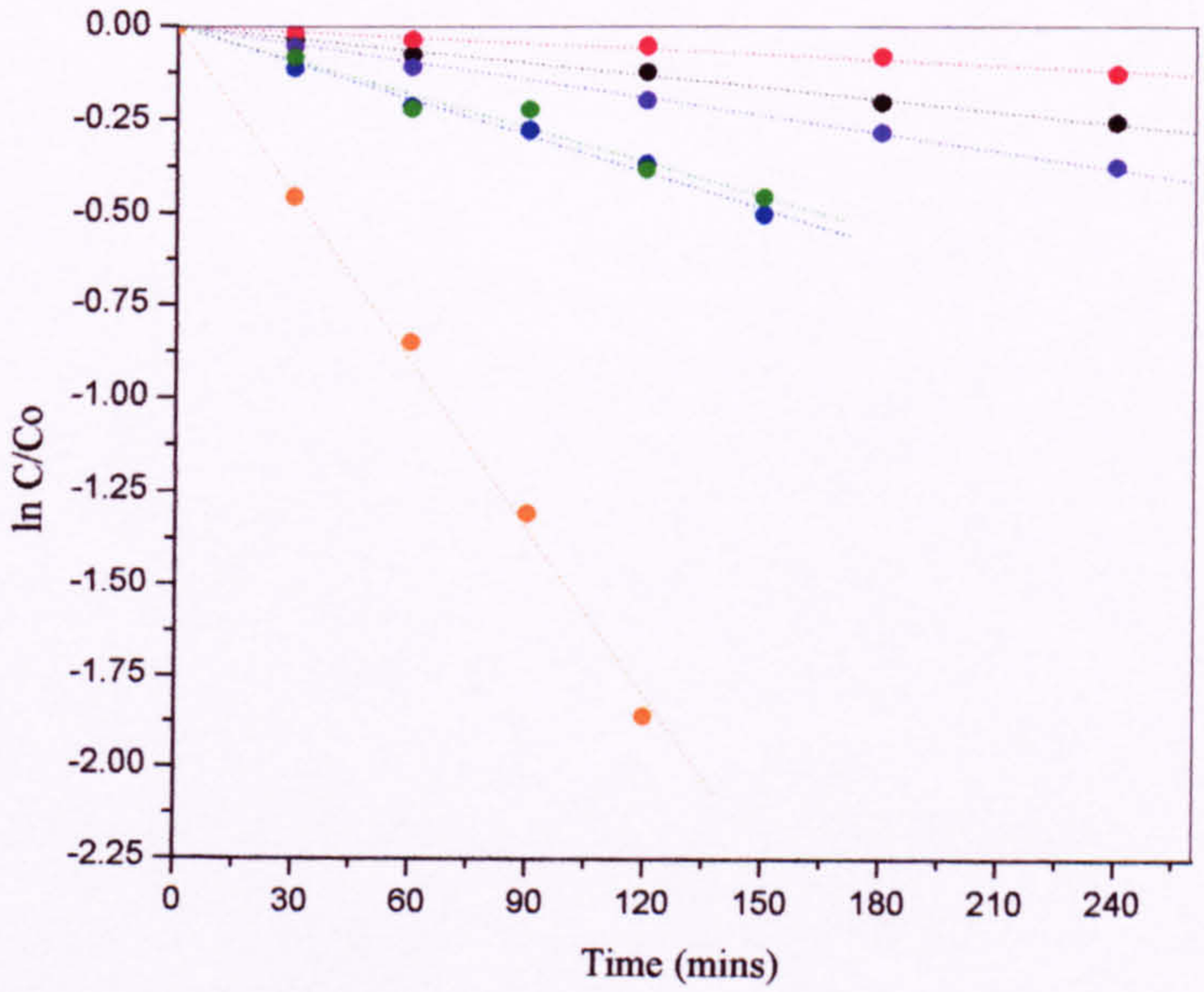

Figure A5.vi. ln C/Co against time for ODTMOS titania --- 31%; --- 64%; --- uncoated Sample A; --- 40%; --- 84%; --- uncoated P25.

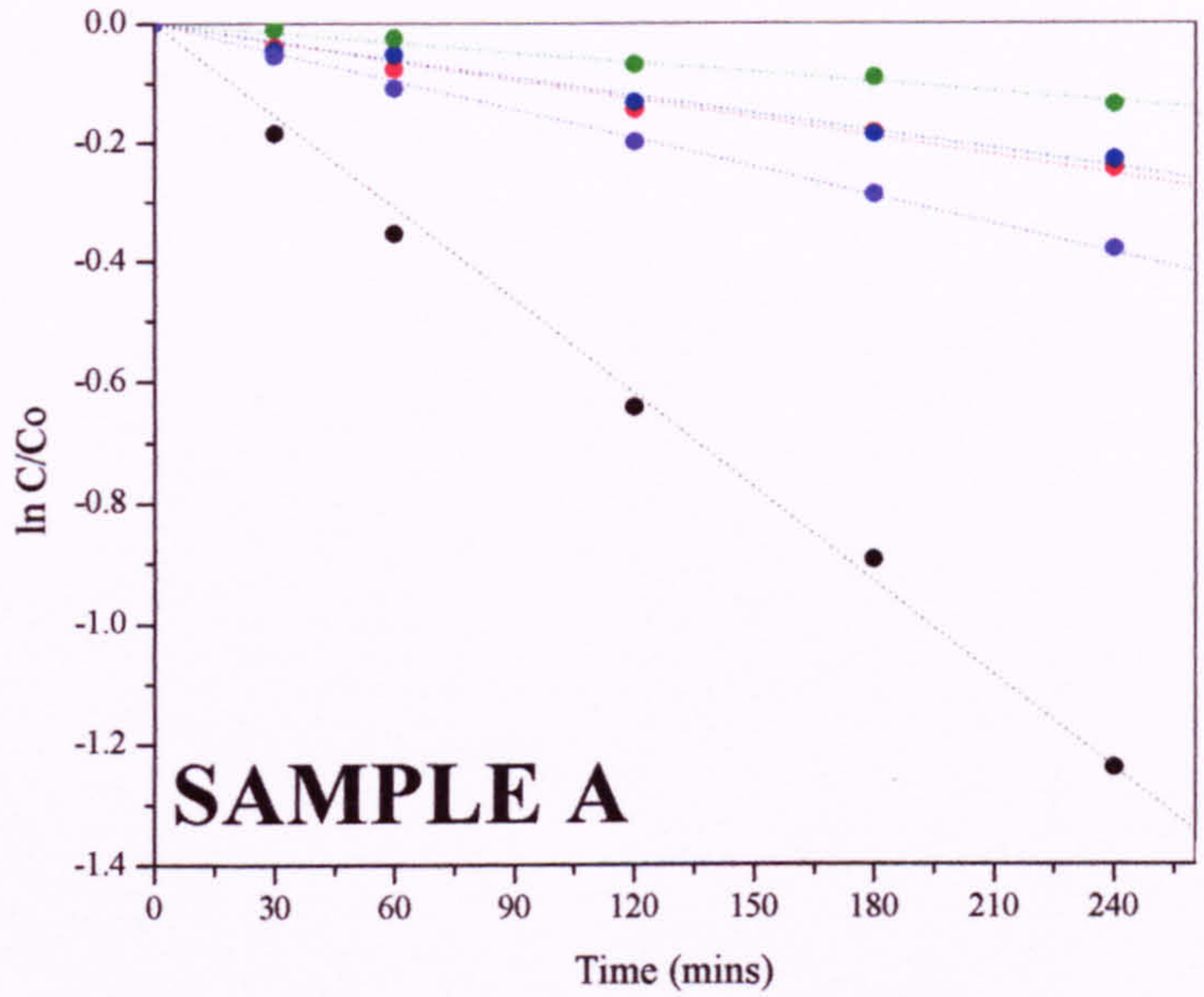

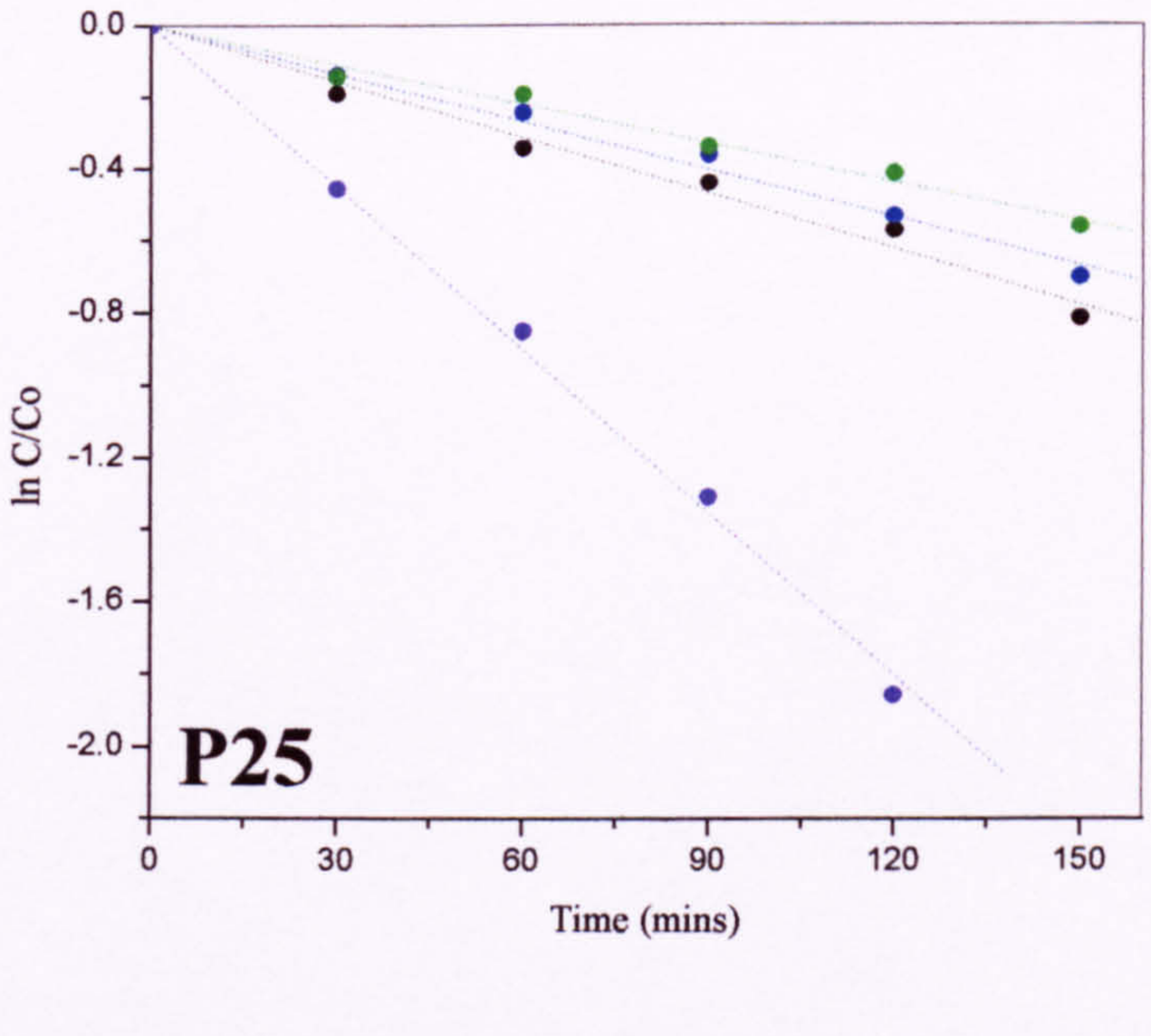

Fig A5.vii and 5.viii. ln C/Co against time for AM160K coated Sample A (above) and P25 (below). --- 10%; --- 25%; --- 50%; --- 100%; --- Uncoated.

Appendix 5.2. Sample calculations for equations 5.1 and 5.2.

For uncoated particles:

$$(SSA)_{uncoated} = 3/(r.\rho) \qquad [5.1]$$

For coated particles the value of the radius (**r**) is replaced by (**r+t**) where **t** is the coating thickness.

Weight of coating = $4.\pi.r^2.p.t$

Weight of the core = $(4.\pi.r^3.p)/3$

Weight % coating = X = $Wt_{(coating)} / Wt_{(core)}$ x 100%

$= (4.\pi.r^2.p_{(coating)}.t)/ [(4.\pi.r^3.p_{(core)})/3]$ x 100%

This cancels to:

$= (\cancel{4.\pi.r^2}.p.t)/ [(\cancel{4.\pi.r^3}.p)/3]$ x 100%

$= (300.t./r)$ x $(p_{(coating)}/p_{(core)})$

Assumption that the density of the coating is equal to that of the underlying particle core:

If we assume that the density of the coating is equal to that of the core then this reduces to:

Weight % = X = (300.t./r)

And rearranges to: t = r.X/300

Therefore the new radius (R) of the coated particle is:

R = r + t = r + (r.X/300) = r.(1+X/300)

And if we substitute this new value of r for coated particles into Equation 5.1 we find:

$$(SSA)_{coated} = \frac{3}{r.\rho.\left[1+\frac{X}{300}\right]} \qquad [5.2]$$

There are two potential sources of error in Equation 5.2. Firstly, the approximation that the coating shell is $4\pi.r^2.t$ is not exact but errors due to this are small. The second, much larger error is the assumption that the density of the coating is equal that of the core. The error due to this assumption is now discussed.

If the density of the coating is 75% that of the core:

Weight % coating = X = $Wt_{(coating)}$ / $Wt_{(core)}$ x 100%

= (300.t./r) x ($p_{(coating)}$/$p_{(core)}$)

If $p_{(coating)}$ = 0.75. $p_{(core)}$ then substituting:

Weight % coating = X = (300.t./r) x (0.75.$p_{(core)}$/$p_{(core)}$)

Which cancels to: X = 0.75. (300.t./r)

And rearranges to: t = (r.X) / (300 x 0.75)

Therefore the new radius (R) of the coated particle is:

R = r + t = r + [(r.X) / (300 x 0.75)] = r.[1+X/(300x0.75)]

And if we substitute this new value of r for coated particles into Equation 5.1 we find:

$$(SSA)_{coated} = \frac{3}{r.\rho.\left[1+\frac{X}{300 \times 0.75}\right]} \qquad [5.3]$$

Calculated surface areas using equation 5.3 will thus be lower than those calculated using equation 5.2.

For a 10% coating of AM160K on sample A the weight % is 2.9%. If we assume the density of the coating is equal that of the rutile core (i.e. using equation 5.2) we see a theoretical reduction in surface area from 136 $m^2.g^{-1}$ to 134.8 $m^2.g^{-1}$. If the coating has a density of 75% that of the underlying particle (Equation 5.3) then a theoretical surface area of 134.3 $m^2.g^{-1}$ is calculated.

In a similar manner, even if the coating has a density of only 50% that of the underlying particle then a theoretical surface area of 133.5 $m^2.g^{-1}$ is calculated. Thus it is valid, as a general approximation, to assume that there is only a relatively small difference in calculated theoretical surface areas if the density of the coating is taken to be that of the core.

5.8. References.

1. A. Mills; S. Le-Hunte, *J. Photochem. Photobiol. A*, **1997**, *108*, 1.
2. M. Kazuyuki; F. Masahiro; Y. Masaaki; Y. Akira (To Shinetsu Co JP): EU Patent number EP0902069 (**1999**).
3. G. R. Davidson; M. J. Goldsworthy; M. I. James (To Proctor and Gamble US): UK Patent number 2300629 (**1995**).
4. P. A. Tooley; P. M. Neidenzu; A. H. Reid (To EI Du Pont US): Int Patent number WO 95/23193 (**1995**).
5. J. N. Birmingham; D. A. Holtzen; J. F. Hunt; R. S. Jenkins; P.D. Spohn; J. T. Walnock (To EI Du Pont US): Int Patent number WO 95/23417 (**1995**).
6. P. M. Niedenzu; S. M. Herkimer; R. L. Chaney (To EI Du Pont US): Int Patent number WO 95/23194 (**1995**).
7. M. A. Mitchinick; A. J. O'Lenick (To Sunsmart Inc, Silatech Inc): US Patent number 5,756,788 (**1998**)
8. P. B. Howard; B. Barnard; D. Unwin, (To Tioxide Group PLC UK): UK Patent number 2115394 (**1982**).
9. B. Barnard; W. T. Laverick (To Tioxide Group LTD UK): US Patent number 4239548 (**1980**).
10. F. Takashi; Y. Kazuo; K. Tsuneo (To Toho Titanium Co LTD JP): JP Patent number 11222442 (**1999**).
11. P. A. Christensen; T. P. Curtis; T. A. Egerton; S. Kosa; J. R. Tinlin, *J. Appl. Cat B*, **2003**, *44*, 371.
12. T. A. Egerton; I. R. Tooley, *J. Phys. Chem B*, **2004**, *98*, 5066.
13. T. A. Egerton; I. R. Tooley, *J. Mater. Chem*, **2002**, *12*, 1111.
14. K. Nakamoto. Infrared and Raman Spectra of inorganic and Co-ordination compounds, Wiley New York, (**1978**).
15. G. Socrates, Infrared and Raman Characteristic Group Frequencies: Tables and Charts, Wiley New York, (**2004**).
16. C. S. Kim; R. J. Lad; C. P. Tripp, *Sensors. Actuators B*, **2001**, *76*, 442.
17. M K. Templeton; H. Weinberg, *J. Am. Chem. Soc* **1985**, *107*, 97.

18. M. B. Mitchell; V. N. Sheinker; E. A. Mintz, *J. Phys. Chem* **1997**, *101*, 11192.
19. B. Blajeni-Aurian; M. M. Boucher, *Langmuir*. **1989**, *5*, 170.
20. W. Gao; L. Dickensson; C. Grozinger; F. G. Morin; L. Reven, *Langmuir*, **1996**, *12*, 6429.
21. J. Randon; P. Blanc; R. Paterson, *J. Membrane. Sci*, **1995**, *98*, 119.
22. P. A. Connor; A. J. McQuillan, *Langmuir*, **1999**, *15*, 2916.
23. H. Ando; M. Nakahra; M. Yamamoto; K. Itoh, *Langmuir*, **1996**, *12*, 6399.
24. M. Suzuki; A. Fujishima; T. Miyazaki; H. Hiramatsu; H. Ando; M. Nakahara; M. Yamamoto; K. Itoh, *J. Biomed. Mater. Res*. **1997**, 252.
25. R. G. Snider, *J. Chem. Phys*, **1967**, *47*, 1316.
26. A. H. M. Sondag; M. C. Raas, *J. Chem. Phys*, **1989**, *91*, 4926.
27. S. R. Cohen; R. Naaman; J. Sagiv, *J. Chem. Phys*, **1986**, *90*, 3054.
28. R. Helmy; A. Y. Fadeev, *Langmuir*, **2002**, *18*, 8924.
29. W. Gong, Int. *J. Miner. Process*, **2001**, *63*, 147.
30. A. Y. Fadeev; R. Helmy; S. Marcinko, *Langmuir*, **2002**, *18*, 7521.
31. D. L. Angst; G. W. Simmons, *Langmuir*, **1991**, *7*, 2236.
32. P. Siberzan; L. Leger; D, Ausserre; J. J. Benattar, *Langmuir*, **1991**, *7*, 1649.
33. J. D. Le-Grange; J. L. Markham; C. R. Kurkjiam, *Langmuir*, **1993**, *9*, 1749.
34. J. B. Brzoska; I. B. Azouz; F. Rondelez, *Langmuir*, **1994**, *10*, 4367.
35. M. E. McGovern; K. M. R. Kallury; m. Thompson, *Langmuir*, **1994**, *10*, 3607.
36. A. N. Parikh, B. Leidburg; S. V. Atre; M. Ho; D. L. Allara, *J. Phys. Chem*, **1995**, *99*, 9996.
37. D. W. Britt; V. J. Hlady, *J. Colloid Inetrface. Sci*, **1996**, *178*, 775.
38. A. Y. Fadeev; R. Helmy; S. Marcinko, *Langmuir*, **2002**, *18*, 7521.
39. T. A. Egerton, *Kona Powder and Particle*, **1998**, *16*, 46.
40. I. R. Tooley, PhD Thesis, University of Newcastle Upon Tyne, Newcastle Upon Tyne, NE1 7RU, **(2002)**.
41. G. Colon; M. C. Hidalgo; J. A. Navio, *J. Photochem. Photobiol*. **2001**, *138*, 79.

6. EFFECT OF SURFACE TREATMENTS ON THE PHOTOACTIVITY.

This Chapter discusses the results shown in the previous chapter (5) on the effect of the different surface treatments: phosphate from sodium hydrogen phosphate (SHP), a phosphate ester – Trade name Arlatone Map 160K (AM160K), and octadecyl-trimethoxy-silane (ODTMOS). In particular, the effect of these coatings on the photoactivity, measured by the two techniques of 2-propanol oxidation (IPA) and 2-nitrophenol degradation (NP), is discussed and likely theories propounded for the observed behaviour based on the photoactivity, surface area, and infrared spectroscopic results. Coating levels are expressed as a percentage of the amount of coating required to cover the entire titania surface. For example, "Sample A 50% AM160K" refers to sample A coated with a quantity of AM160K targeted to cover half the titania surface.

6.1. Introduction.

Silica and alumina coatings are typically applied to titanium dioxide to affect the dispersive properties or to minimise the photoactivity [1]. The coating composition is usually optimised either for light scattering properties or for the minimisation of photocatalysis dependant on the end use [1]. Both silanes and phosphate esters have a high degree of functionality, and thus can potentially be used as coatings to ensure suitable light scattering properties and low photoactivity. Phosphate is often used as a dispersing agent in formulations but there may be specific advantages in areas such as processing to using this material as a permanent coating.

Egerton and Tooley [2] found that the high area rutile sample they studied, analogous to Sample A in the present study, had specific surface sites ('active sites') responsible for a disproportionate amount of the photoactivity. The dense silica coatings preferentially deposited on these sites, thus disproportionately lowering photoactivity at low coating levels, while the alumina did not. A specific aim was to examine whether the novel coatings used in the present study acted in a similar way to these dense silica coatings. A second aim was to investigate if Degussa P25 similarly has active sites, as suggested by some authors [3-5] by coating this material in an analogous manner to Sample A.

6.2. Photoactivity of Arlatone Map 160K (AM160K) coated titania.

Sample A and Degussa P25 were coated with AM160K by a heating and subsequent precipitation method as described in Section 2.1.5, and the effect of coating level investigated by varying the amount of coating between 10% and 100%. As described above, these values indicate the quantity of material required to cover the particle surface, assuming a surface area of 130 m^2 g^{-1} for Sample A and 50 m^2 g^{-1} for P25 [6], rather than the more usual weight percentage so that the effect of coating level on titania of different surface areas may be quantitatively compared. A footprint of 0.3 nm^2 was used for AM160K, similar to that for phosphate.

The photoactivity of AM160K coated titania was measured by the 2-propanol oxidation (IPA), and 2-nitrophenol degradation (NP) techniques. The IPA technique measures hydroxyl radical mediated oxidation [7] in an alcohol medium while the NP technique measures the oxidation in an aqueous medium, by a predominately hydroxyl radical mediated mechanism, as shown by a reduction in rate when bicarbonate is added as a radical scavenger, [8,9]. In Chapters 3 and 4 it was shown that, systematic changes in dispersion aside, the two techniques measure the same photocatalytic effects for a wide range of iron doped samples of Sample A and P25. The variation of photoactivity with coating level of AM160K coated Sample A and P25 measured by IPA and NP is shown in Figure 6.i. As can be seen, there is in general a good correlation between photoactivity as measured by IPA with that for NP showing that these techniques are indeed measuring the same photocatalytic effects.

With the notable exception of Sample A 10% AM160K, the effect of applying an AM160K coating to Sample A and P25 is to reduce the photoactivity, with a higher coating level leading to the greatest reduction. This being said, a higher coating level does not give a pro-rata level of reduction - low levels are significantly more effective at reducing the photoactivity, with higher levels giving only modest further decreases.

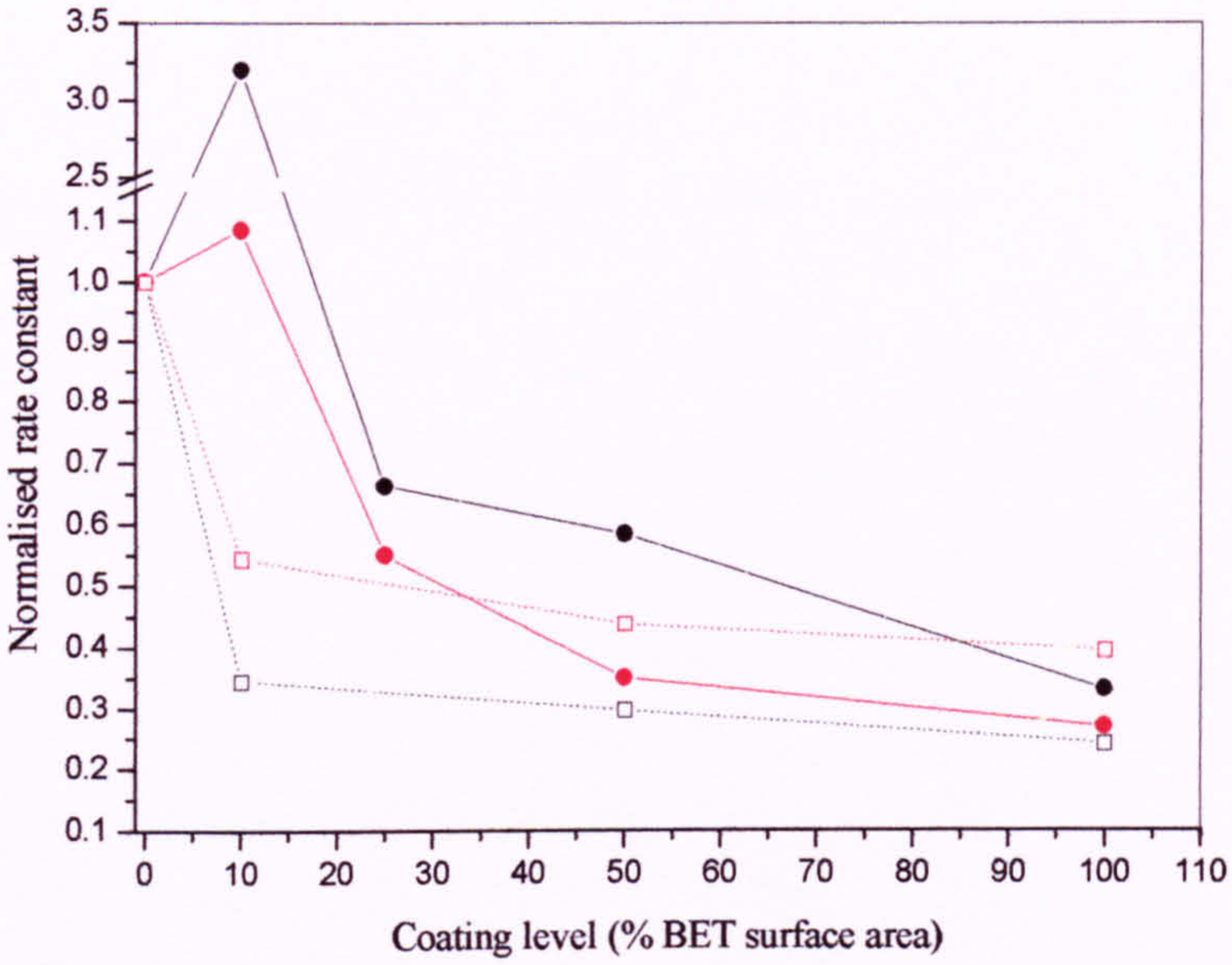

Fig 6.i. Photoactivity of AM160K coated Sample A (solid lines) and P25 (dotted lines) measured by NP (---) and IPA (---). Note: axis break.

Egerton and Tooley [2,10] found a similar pattern of results for silica coated Sample A: low levels of silica (2 wt%) reduced the photoactivity as measured by IPA by ~ 50% with almost five times this level (9 wt%) required to almost eliminate the photoactivity. They hypothesised that Sample A has specific surface sites that have a disproportionate effect on the photoactivity, and that silica preferentially deposits on these areas - these specific sites also give rise to IR active nitrogen due to high electrostatic charge. The silica coatings also disproportionately reduce the surface area by blocking micropores between aggregates of primary crystals (a TEM of Sample A is shown below in Appendix A6.i). The authors hypothesised that the silica coatings preferentially deposit at these areas, and that the active sites are thus at the microporous surface sites. They concluded that only about 10% of the rutile surface in Sample A is associated with high photocatalytic activity.

The broad pattern of results observed in the present study for Sample A can thus similarly be attributed to AM160K preferentially coating those areas of the titania that are disproportionately responsible for the photoactivity. Although the trend is somewhat

complicated by the rise in photoactivity at 10 %, discussed below, a low level of AM160K coating (25%) gives an ~ 50% decrease in photoactivity as measured by IPA (30% by NP). This level of coating also leads to a large reduction of ~ 35 % in surface area as shown by 5.xxvi in the previous section. This decrease is much greater than that predicted from the formation of a uniform coating on a spherical rutile particle, and thus from analysis of the surface area of coated samples it is likely that the AM160K is preferentially depositing in the micropores between aggregates of primary crystals identified on the surface of this material [10].

The FTIR spectra (Section 5.4.3) show that for this level of coating, the alkyl C16 chains of the AM160K are disordered (the methylene stretches are at the same position as for a liquid alkane) and thus the AM160K cannot be considered to form a coherent coating at this level. At higher levels of coating (50 % to 100 %) the methylene frequencies show that the coatings are ordered to the same degree as for self assembled monolayers of octadecyl-phosphonic acid on TiO2 [11]. The decrease in surface area from 25 % to 100 % is also consistent with the formation of a uniform coating. Thus, all the evidence supports the theory that at low levels, AM160K preferentially deposits on specific sites of high photoactivity, that these sites are in micropores (possibly between aggregates of primary crystals), and that a coherent coating is not formed until a quantity of AM160K is added that is sufficient to completely cover the surface area of the titania.

A simple model can therefore be hypothesised (Figure 6.ii) for these coatings that is similar to that suggested by Egerton and Tooley [2], above. At low coating levels the AM160K preferentially deposits in the micropores as shown by surface area results, where it also leads to a disproportionate reduction in photoactivity. At higher levels the AM160K forms a coherent coating around the titania as shown in Chapter 5 by a comparison of the FTIR spectra, and in this respect the AM160K coatings have an advantage over silica as it has been shown that a coherent coating does form at high levels:

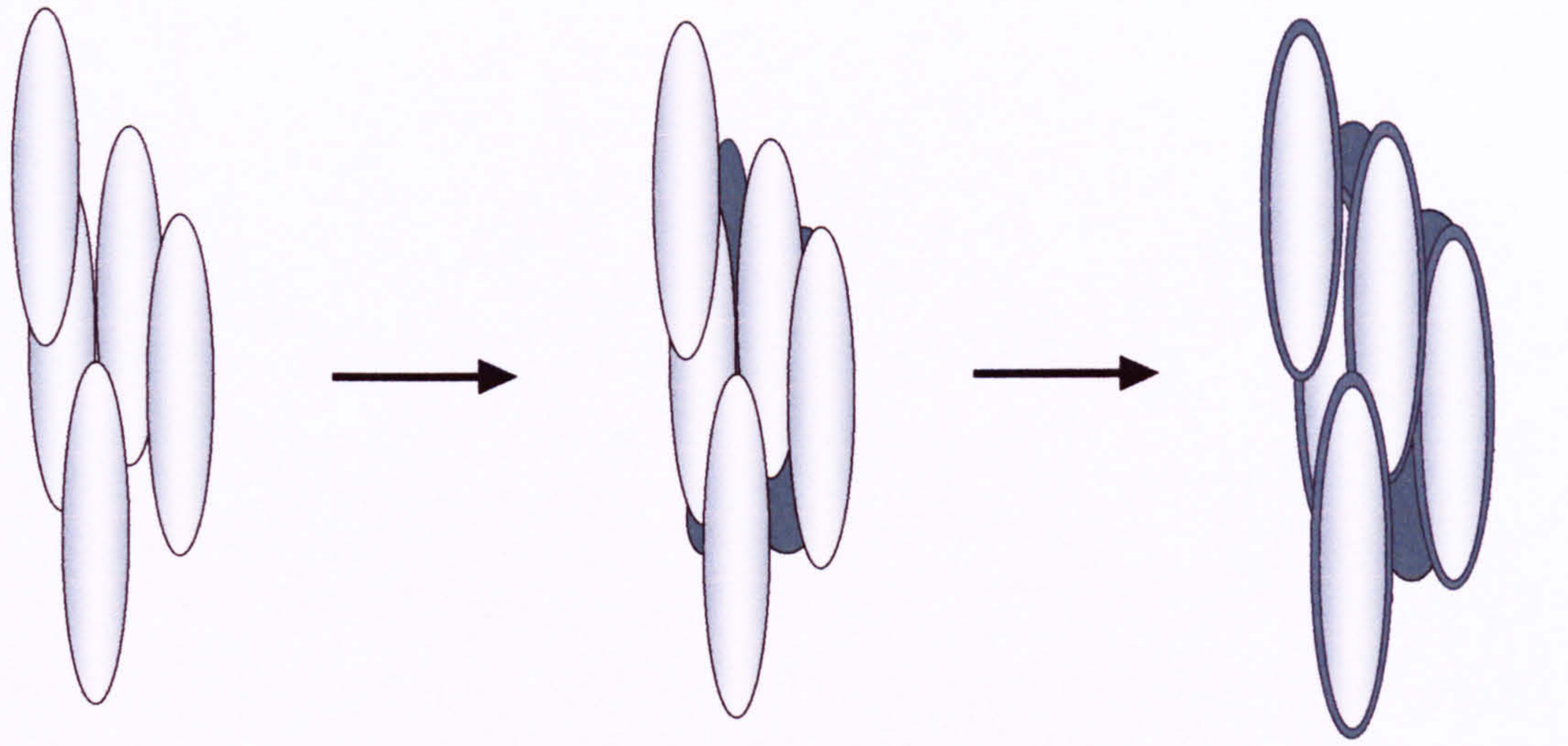

Fig 6.ii. Scheme showing coating formation for increasing levels of AM160K on Sample A. The acicular primary particles of titania are shown in pale grey, and the coating indicated by the dark grey patches.

AM160K coated P25 shows similar photoactivity trends as for Sample A i.e. sharp decreases at low levels and only moderate decreases beyond this level - a 10% coating giving ~ 50 % reduction in photoactivity measured by IPA (65 % by NP). This coating level gives a ~ 25% reduction in surface area (see Figure 5.xxvi in the previous chapter), with higher coating levels giving < 5% reduction - consistent with the formation of a uniform coating on a spherical particle. Given that it has been shown that P25 is not microporous - average pore diameter of 315 Å (32 nm) [3], this effect is unlikely to be due to the filling of micropores. Instead it is likely that the AM160K preferentially deposits at low levels on active sites that are not pores but may be other areas of high surface area, and subsequently at higher levels forms a more uniform coating on the surface.

The formation of a coherent coating at high coating levels is also supported by FTIR results. The methylene stretching frequencies from the alkyl backbone chain are disordered below a 25 % coating (Figure 5.xxiii), with the frequency shift at higher levels consistent with a degree of ordering approaching that of self assembled

monolayers of alkyl phosphonates [11]. Thus the FTIR results support the theory that a coherent surface coating is only formed at higher levels.

Given that the trend in photoactivity, surface area and methylene chain ordering for AM160K coated P25 is similar to that for Sample A, a similar model may be hypothesised for P25. At low coating levels (10 %), the AM160K preferentially deposits at surface sites with high surface area, leading to a sharp reduction in surface area, above this level (25% to 100%) the AM160K coats the remaining surface forming a coherent coating with a good degree of alkyl chain ordering. The sharp reduction in photoactivity for a 10% coating where the coating has apparently deposited on the active sites suggests that P25, in common with Sample A, has active surface sites at specific areas of the crystal – and that these sites are preferentially blocked by an AM160K coating i.e. ~ 10% of the surface is responsible for the majority of the photoactivity. A coherent coating is formed around the remaining surface once the active sites are coated with only modest further reduction in photoactivity. The finding that P25 has certain active sites or 'hotspots' has been shown by structural [3] and Electron Spin Resonance (ESR) studies [5] and it has been suggested that these are at the phase boundary between anatase and rutile. The present study suggests that these active sites may additionally be preferentially coated by the phosphate ester AM160K.

The general trends established, it is now pertinent to discuss the apparently anomalous rise in photoactivity for Sample A with a 10% AM160K coating, measured twice in case of experimental error. The simplest explanation is that this is simply a consequence of the altered optics of the system due to the application of a hydrophobic coating. It has been quantitatively shown for the IPA technique [12] that an increase in particle agglomeration for Sample A leads to an increased penetration in light into the slurry and thus a higher measured photoactivity – this argument is discussed in more detail in Section 1.5.4.4. The ~ 20% increase in photoactivity for the 10% AM160K coated Sample A measured by IPA is reduced to ~ 10% if the sample is milled to reduce the aggregation. In addition, when the sample is measured in an aqueous environment by NP then the increase is of the order of three times greater consistent with the theory that the increase is caused by optical effects as the dispersion of a hydrophobically coated sample would be significantly poorer in this environment.

However, as shown in Table 5.i in the previous chapter, this theory is not supported experimentally by the optical density results which show a rise (rather than a reduction) in UV absorption by the coated Sample A and thus a lower penetration of light into the slurry. In addition, there is an analogous rise for the hydrophilic 10% phosphate coated samples (below), and thus both qualitatively and quantitatively the argument that the rise at 10% AM160K coating level is due to the dispersion qualities of the coated samples is not supported by the experimental evidence.

There was not sufficient time to fully explore this interesting anomaly, which is counter to the general trend of AM160K coatings. However, an alternative view is that the rise in photoactivity at the lowest coating level may be caused by changes in the electronic character of the surface. The point of zero charge (pzc) for unmodified titania is ~ 6 [13], and this falls to ~ 2 for phosphate coated titania [14] which may account for the rise due to a change in the surface adsorption properties. While photocatalytic reactions may occur at short distances form the titania surface [15] the rate of reaction would be greater if it occurred on the surface i.e. if the molecule is adsorbed. For both the IPA and NP techniques used to study the photoactivity, the solution pH is mildly acidic and thus for unmodified titania the surface is roughly neutral. For phosphate coated titania, a fall in the pzc to ~ 2 would result in a negatively charged surface at mildly acidic pH values and the increased adsorption of the organic molecule (2-nitrophenol or 2-propanol) would be expected to lead to increased rates of reaction. Indeed, the lowering of the pzc due to phosphate adsorption has been shown to increase thionine adsorption on anatase titania films [14].

6.3. Photoactivity of phosphate coated titania from sodium hydrogen phosphate (SHP).

Sample A and Degussa P25 were coated with phosphate (PO_4^{2-}) by heating a solution of SHP and titania slurry as described in Section 2.1.7, and the effect of coating level investigated by varying the amount of coating between 10% and 100%. These percentages indicate the quantity of material required to cover the particle surface, assuming a surface area of 130 $m^2\ g^{-1}$ for Sample A and 50 $m^2\ g^{-1}$ for P25 [6], rather than the more usual weight percentage so that the effect of coating level on titania of different surface areas may be quantitatively compared.

The photoactivity of phosphate coated titania was measured by the 2-propanol oxidation (IPA), and 2-nitrophenol degradation (NP) techniques both of which have been shown to proceed by a predominately hydroxyl radical mediated mechanism [7-9]. The variation of photoactivity with coating level for phosphate coated Sample A and P25 is shown in Figure 6.iii.

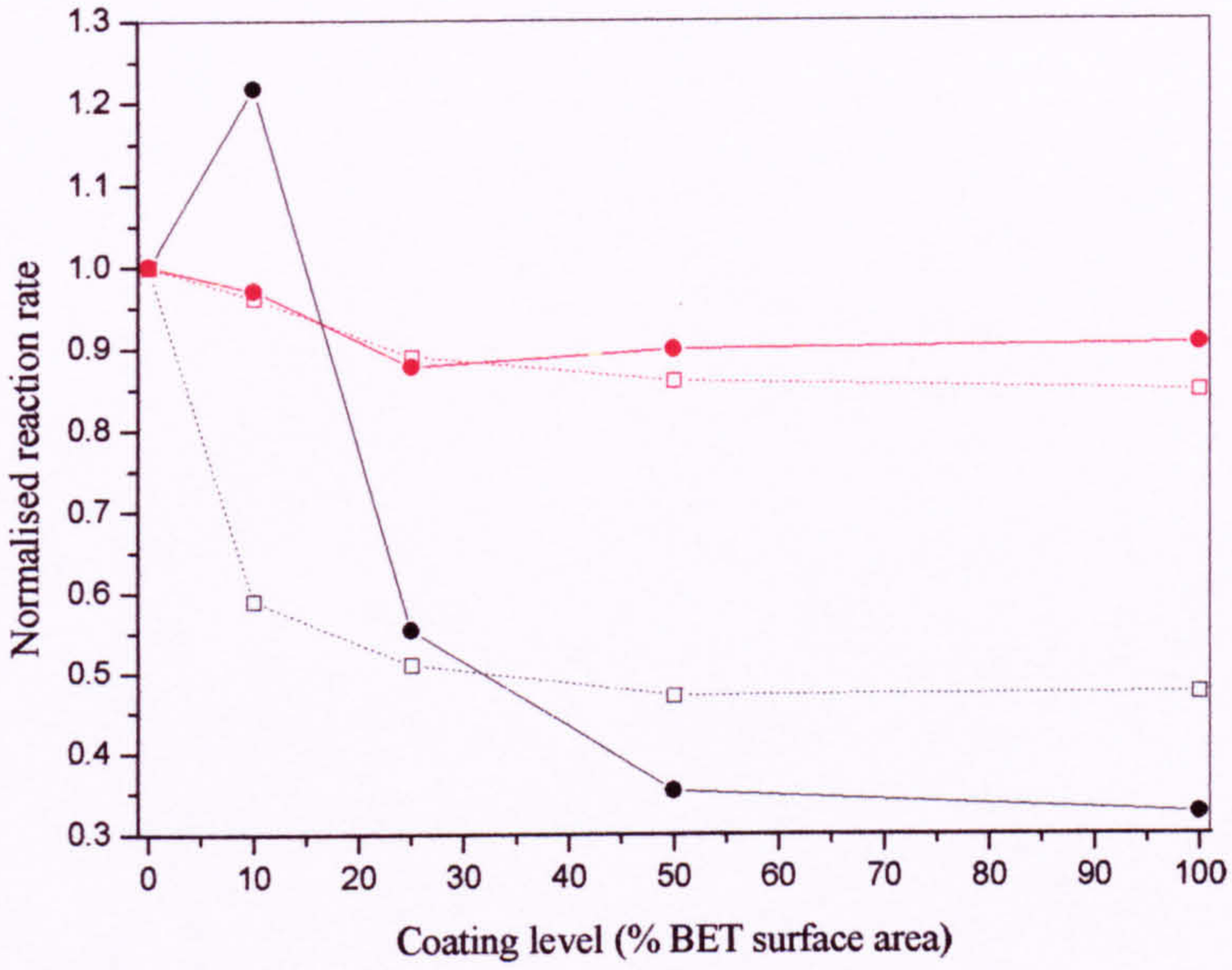

Fig 6.iii. Variation in photoactivity for phosphate coated Sample A (solid lines) and P25 (dotted lines) measured by NP (---) and IPA (---).

There are two comparisons to be made from Figure 6.iii, between the two types of base titania, and the two techniques to measure photoactivity. Firstly, with the exception of Sample A 10% SHP, the effect of applying a phosphate coating to Sample A and P25 is qualitatively similar i.e. the photoactivity is reduced with higher levels giving the greatest reduction. However, the majority of the reduction in photoactivity is at low levels of coating (25%) with higher levels giving only modest further decreases i.e. low coating levels are significantly more effective at reducing the photoactivity.

This being said, there are major differences between the qualitative extent of the reduction in photoactivity caused by phosphate coating whether measured by NP or IPA. In the former case, the reduction in photoactivity is significant (~ 50% for a 25%

coating on Sample A and P25) and the trends are similar to that for AM160K coatings above (Figure 6.i). However, when the photoactivity is measured by 2-propanol oxidation (IPA) there is a very modest decrease in photoactivity (~ 10 % for a 25% coating). That there is a difference between photoactivity as measured by the two techniques for phosphate coatings is particularly unusual given that a good correlation was achieved for the measurement of the photoactivity of iron doped samples (Chapter 3 and 4) and for the other coatings described in this Chapter (including the phosphate ester AM160K). This suggests that the poor correlation is unique for phosphate coatings (in the present study at least) and thus does not invalidate previous conclusions that the two techniques are substantially measuring the same changes in photocatalytic behaviour.

Given the similarity between the variations between the photoactivity for phosphate coated titania as measured by NP and that for AM160K coatings above it is appropriate to first examine whether the experimental results can be explained by a similar model. This is particularly suitable given that it has been shown by FTIR that, most probably, phosphate bonds to the surface in a similar manner to AM160K.

If we disregard the rise in photoactivity for Sample A 10% SHP (discussed below) then the trends for photoactivity for both Sample A and P25 are that low levels of coating significantly reduce the photoactivity (~ 50 % reduction for a 25% phosphate coating for both samples) while increasing the coating level (even adding sufficient phosphate to completely cover the titania surface) gives only modest further increases. Low levels of coating also disproportionately reduce the surface area (Figure 5.xxvii), for example a 25 % coating reduces the surface area by ~ 20 % for Sample A (10% for P25) – much greater than predicted by a coherent coating on a spherical particle. It can thus be concluded from the surface area results that, in common with the AM160K coatings described above, the phosphate is preferentially deposited in pores for Sample A and some other undefined high area site for P25. The phosphate disproportionately reduces the photoactivity, as these are the specific sites or 'hotspots' that are responsible for a disproportionate degree of the photoactivity. Despite the absence of FTIR information (as there are evidently no methylene stretches), it is likely from the negligible further decreases in surface area at higher coating levels that a coherent

coating forms. The phosphate coating formation at high and low levels is thus adequately represented by the model depicted in Figure 6.ii.

As discussed above for the analogous rise in photoactivity for a 10% AM160K coating, the increase for Sample A 10% SHP is most likely caused by increased adsorption of the organic caused by a lower pzc for phosphate coated samples rather than by changes in dispersion. While it was not possible to measure the optical density due to the generally poor dispersion of the titania in 2-nitrophenol solutions, a hydrophilic coating would not be expected to lead to significantly different dispersion properties, especially as the hydrophobic AM160K coatings were shown not to be responsible for the analogous increase. Another, albeit less likely, possibility is that due to the electronic structure of phosphate, it may act as an electron scavenger and thus reduce surface recombination by enhancing charge separation. Unfortunately there was not time to fully explore this theory, possibly by varying the amount of oxygen to determine whether phosphate is a more efficient electron trap.

It is now pertinent to discuss why there are significant differences in photoactivity when measured by the two different techniques of IPA and NP for phosphate coated Sample A and P25. The significant differences between the two methods for measuring photoactivity is apparently unique (at least in the present study) to phosphate coated titania, as there is good correlation for iron doped samples, and for other coatings - notably including AM160K (a phosphate ester). Therefore, the differences are unlikely to be caused by changes in dispersion between phosphate coated titania in aqueous and alcohol environments, as these would be more likely to occur for hydrophobic coatings such as AM160K.

One possibility may be that due to the lack of an organic alkyl chain, phosphate does not form a dense surface coating as for AM160K and ODTMOS and is either porous or patchy. This supposition is supported by a comparison of the effect of coating on the surface area (Figures 5.xxix and 5.xxx in the previous chapter) that show that, while there is still a sharp reduction in surface area at low levels (consistent with coating deposition in the pores), for a given level of coating phosphate does not reduce the surface area by the same extent as AM160K and ODTMOS i.e. phosphate does not effectively fill the pores for Sample A. A patchy, or porous phosphate coating may

allow small molecules such as 2-propanol to interact with bare uncoated titania patches, while larger molecules such as 2-nitrophenol are sterically hindered. Thus, the coating does not effectively reduce the rate of 2-propanol oxidation, but does protect against 2-nitrophenol degradation. AM160K or ODTMOS effectively reduce the rate of both reactions, as they form dense layers on the surface due to the alkyl backbone.

6.4. Photoactivity of Octadecyl-trimethoxy-silane (ODTMOS) coated titania.

Sample A and Degussa P25 were coated with ODTMOS by a mixing a pre-hydrolysed silane solution with the titania slurry to allow the coatings to precipitate onto the titania surface as described in Section 2.1.6, and the effect of coating level investigated by varying the amount of mixing time. The preparation method allowed two coating levels to be investigated, 31 % and 64 % for Sample A, and 41 % and 84 % for P25. These percentages indicate the quantity of material required to cover the particle surface, assuming a surface area of 130 m^2 g^{-1} for Sample A and 50 m^2 g^{-1} for P25 [6], rather than the more usual weight percentage, so that the effect of coating level on titania of different surface areas may be quantitatively compared.

The photoactivity of ODTMOS coated titania was measured by the 2-propanol oxidation (IPA), and 2-nitrophenol degradation (NP) techniques both of which have been shown to proceed by a predominately hydroxyl radical mediated mechanism [7-9]. The variation of photoactivity with coating level for ODTMOS coated Sample A and P25 are shown in Figure 6.iv.

The effect of applying a ODTMOS coating to Sample A and P25 was to reduce the photoactivity, with a higher coating level leading to the greatest reduction, and there is a good correlation between the photoactivity as measured by the IPA and NP techniques. The general trend of photoactivity with coating level is different for the two types of titania. For P25, in common with AM160K coatings, there is a large reduction in photoactivity at low levels of coating; in the present case the lowest level studied was 41%. An approximate doubling of the coating level only gave marginal further decreases in photoactivity. However, for Sample A there is a roughly linear decrease in photoactivity whether measured by IPA or NP, which is in sharp contrast to the trend observed for AM160K coatings.

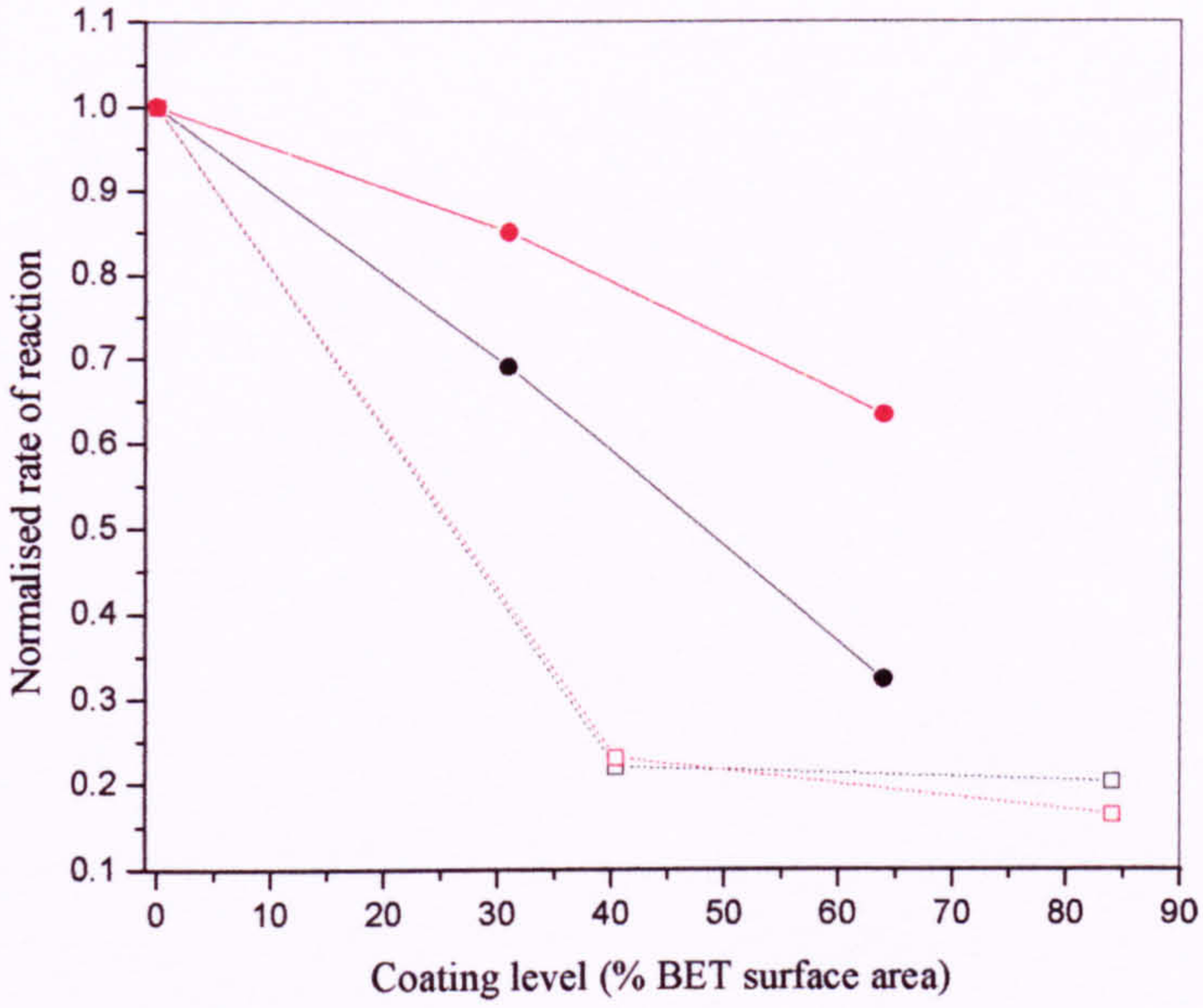

Fig 6.iv. Variation in photoactivity of ODTMOS coated Sample A (solid lines) and P25 (dotted lines) measured by NP (---) and IPA (---).

For the AM160K coatings, a model was proposed (shown schematically in Figure 6.ii) that the AM160K preferentially deposits in pores between aggregates, thus disproportionately reducing the surface area. The pores are the most photocatalytically active areas, and thus at low levels the coating disproportionately reduces the photoactivity. The difference between the trends in photoactivity with coating level for ODTMOS and AM160K (described above) modified sample A suggest that these coatings are depositing on the titania surface in different ways and thus a different model is required to explain the observed trends.

The surface area of Sample A is sharply reduced at low levels of coating (31%), as shown by Figure 5.xviii in the previous chapter, suggesting that ODTMOS preferentially deposits on specific porous sites in common with AM160K and phosphate coatings. The large reduction in surface area (>50%) suggests that ODTMOS coatings are very effective at blocking these pores, possibly due to the formation of siloxane links between individual silane molecules as found by FTIR resulting in a very dense impervious coating that completely blocks the pores.

The FTIR spectra for ODTMOS coated Sample A also show that the alkyl chains are highly ordered even at low coverages due to islandlike coating of the surface i.e. the coating deposits as a film of siloxane linked silane molecules rather than individual molecules (see Figure 5.xxiv). The islandlike growth may explain why the ODTMOS coatings do not preferentially reduce the photoactivity at low coating levels in a similar way to AM160K. Since the driving force for the reaction is determined more by lateral interactions between silane molecules to form a coherent film [16,17] rather than with disproportionately photoactive specific surface sites at several surface locations, the coating is unlikely to form in such a way as to mask all of the various pores. Rather, the ODTMOS attaches at a specific site and spreads from this area until the surface is completely covered at higher levels i.e. only a portion of the titania is coated at low levels, and this does not include all of the active sites and pores. This model would explain why the photoactivity decreases in a linear manner with coating level rather than disproportionately at low levels; a diagrammatical representation is depicted in Figure 6.v.

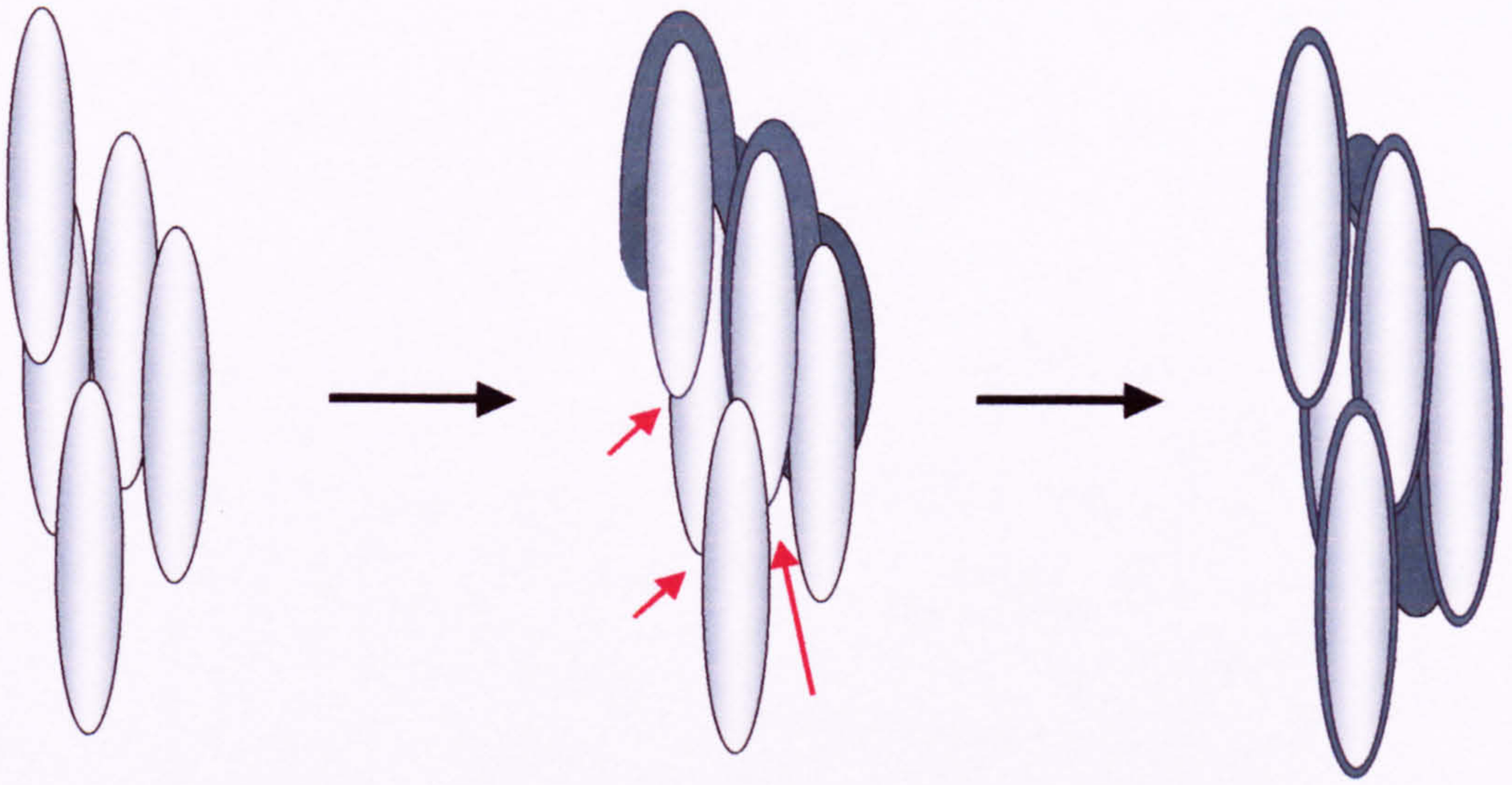

Fig 6.v. Scheme showing coating formation for increasing levels of ODTMOS on Sample A. The acicular primary particles of titania are shown in pale grey, and the coating indicated by the dark grey patches. Uncoated active sites or pores are indicated by the red arrows.

As would be expected, the ODTMOS coating is similarly ordered for P25 as shown by the frequency of the methylene stretches in the FTIR spectra, which are similar to those for self assembled monolayers of silane [16,17]. However, unlike the analogous case for Sample A, the coating disproportionately reduces the photoactivity at low levels in a similar manner to the AM160K coatings on this titania – a 41% coating reduces the photoactivity by >80 %. While further study would be required to support this hypothesis, the observed results suggest that the active sites or 'hotspots' are geographically closer than those for Sample A. Thus, an 'island' of ODTMOS sufficient to cover less than half of the P25 surface was able to reduce the photoactivity by <80 % by coating to a large amount of active sites in reasonably close vicinity to one another.

6.5. Conclusions on the effect of organic coatings on the photoactivity.

The main conclusions from this chapter, regarding the effect of surface coating on the measured photoactivity are as follows:

1. For AM160K a simple model has been proposed to explain why low levels of coating disproportionately reduce the surface area and photoactivity of Sample A as measured by IPA and NP. Previous studies by Egerton and Tooley [2,10] found that specific surface sites were unduly responsible for photoactivity and hypothesised that these were the pores between aggregates of individual particles. The present study extends this model to show that AM160K preferentially coats these areas significantly reducing photoactivity and surface area at low levels, and further shows by FTIR spectroscopy that at higher coating levels a coherent coating forms that has highly ordered alkyl chains. This model has been applied to explain the similar behaviour of AM160K coated Degussa P25 and it is hypothesised that the photoactive sites ('hotspots') proposed by several authors [3-5] are preferentially coated by the AM160K unduly reducing surface area and photoactivity at low levels. A seemingly anomalous rise in photoactivity at the 10% coating level for Sample A was shown not to be caused by the altered optics and it was suggested that this may be due to increased adsorption of the organic substrates caused by a lowering of the pzc giving a higher rate of reaction.

2. This model was also found to be valid for phosphate coated Sample A and P25, where the photoactivity as measured by NP is reduced in a similar way to AM160K coatings. The analogous rise for a 10% phosphate coating on Sample A was attributed to a lowering of the pzc, the higher adsorption of NP giving a higher rate of degradation. Interestingly, the phosphate coatings were not effective at reducing the photoactivity as measured by IPA and it was proposed that this was due to the patchy or porous nature of the coating (as shown by the higher surface area of these samples in comparison to AM160K and ODTMOS coatings). This hypothesis suggests that the 2-propanol molecule was small enough to interact with the bare patches of underlying surface despite the coating while the much larger 2-nitrophenol molecule was too sterically hindered. These results, when compared with those for AM160K, show that in addition to the surface sites coated, the composition of the coating is just as critical, and demonstrates that to adequately reduce photoactivity it is important to form dense impervious layers, and that the alkyl backbone of the molecule may thus play an important role.

3. A different model was proposed for ODTMOS, as the coatings form as an 'islandlike' siloxane film of bridged silane molecules (shown by FTIR). These siloxane films effectively reduce the surface area by blocking pores. However, at low coating levels the ODTMOS only covers a portion of the surface with coating growth dominated by lateral interactions between silane molecules rather than with active surface sites, leaving uncoated pores for Sample A and thus the photoactivity is not disproportionately reduced as was found for the AM160K coating. The ODTMOS coating forms in a similar manner on P25, but does disproportionately reduce photoactivity. It was thus tentatively hypothesised that the active sites on P25 are located sufficiently close so that even though the ODTMOS covers only a portion (~40%) of the surface, most of the active sites are coated. In addition to providing information on the nature of the photoactive sites, these results demonstrate that the composition of the coating, in particular whether there is a strong driving force for crosslinking may determine the efficiency of the final coated product.

6.6. Appendices.

Appendix 6.1. TEM of Sample A.

Figure A6.i. High magnification transmission electron micrograph (TEM) of high area rutile Sample A showing acicularity of the crystals, the bar represents 50 nm. [2]

6.7. References.

1. T. A. Egerton, *Kona Powder and Particle*, **1998**, *16*, 46 and reference therein.
2. T. A. Egerton; I. R. Tooley, *J. Mater. Chem*, **2002**, *12*, 1111.
3. R. I. Bickley; T. Gonzalez-Carreno; J. S. Less; L. Palmisano; R. J. D. Tilley, *J. Solid. State. Chem.* **1991**, *92*, 178.
4. A. G. Agrios; K. A. Gray; E. Weitz, *Langmuir*, **2003**, *19*, 1402.
5. D. C. Hurm; A. G. Agrios; K. A. Gray; R. Rajh; M. C. Thurnauer, *J. Phys. Chem B*, **2003**, *107*, 4545.
6. Degussa P25, Data sheet.
7. C. Richard; P. Boule, *New. J. Chem*, **1994**, *18*, 547.

8. R. W. Harrison, MPhil Thesis, University of Newcastle Upon Tyne, Newcastle Upon Tyne, NE1 7RU, (**2001**).
9. T. A. Egerton; P. A. Christensen; R. W. Harrison; J. W. Wang, *J. Applied. Electrochem*, **2005**, *35*, 799.
10. I. R. Tooley, PhD Thesis, University of Newcastle Upon Tyne, Newcastle Upon Tyne, NE1 7RU, **(2002).**
11. R. Helmy; A. Y. Fadeev, *Langmuir*, **2002**, *18*, 8924.
12. T. A. Egerton and I. R. Tooley, *J. Phys. Chem. B*, **2004**, *98*, 5066.
13. G. D. Parfitt, Prog. Surf. Membrane. Sci, **1976**, *11*, 181.
14. B. P. Nelson; R. Candal; R. M. Corn; M. A. Anderson, *Langmuir*, **2000**, *16*, 6094.
15. C. S. Turchi; D. F. Ollis, *J. Catalysis*, **1990**, *122*, 178.
16. R. Helmy; A. Y. Fadeev, *Langmuir*, **2002**, *18*, 8924.
17. A. Y. Fadeev; R. Helmy; S. Marcinko, *Langmuir*, **2002**, *18*, 7521.

7. EFFECT OF UV ABSORPTION ON THE PHOTOCATALYTIC OXIDATION OF 2-NITROPHENOL AND 4-NITROPHENOL.

In Chapter 3 and 5, 2-nitrophenol degradation has been used as a standard test to determine titania photoactivity. All the test measurements have been made using a single initial concentration of 0.2 mM 2-nitrophenol. However, as part of an MPhil programme [1] the effect of 2-nitrophenol concentration on the degradation rate was measured. Later, during the course of the authors PhD studies complementary measurements on 4-nitrophenol degradation were carried out under my guidance by a visiting student, J.W.Wang from the Department of Chemical Engineering, Taiyun University of Technology, Peoples Republic of China. Based on these two experimental studies the effect of UV absorption by nitrophenol on its photocatalytic oxidation has been considered. It has been suggested that the decrease in the photocatalytic degradation rate constant at higher initial nitrophenol concentration is due to UV absorption and not due to surface coverage (Langmuir-Hinshelwood) considerations. This work has been published separately; see Appendix 1 at the end of this Thesis. For clarity, it is summarised to demonstrate why, for example in Chapter 3 the nitrophenol degradation appears to increase in rate at the end of the experimental run.

As this Chapter is based on collaborative research and thus is not solely the authors own work, it has been moved to the appendices (Appendix 1).

8. CONCLUSIONS AND FURTHER WORK.

8.1. Conclusion

8.1.1. Effect of iron doping on the photoactivity.

The effect of iron doping on the photoactivity of nanosized titanium dioxide, rutile (Sample A) and the mainly anatase Degussa P25, has been determined. In addition, for Sample A, the effect of whether the dopant resides in the lattice or on the titanium dioxide surface has also been investigated. Electron Paramagnetic Resonance (EPR) spectra showed that samples doped by a coprecipitation method iron resided in the lattice and on the titania surface, whereas samples prepared by a precipitation method the iron was only on the surface. Three tests were employed to determine the photoactivity of iron doped samples; 2-propanol oxidation (IPA), 2-nitrophenol degradation (NP), and salicylic acid degradation (SA). The former is the most commonly used in the field, and the development of the latter two techniques, which measure photoactivity in an aqueous medium was an addition aim in this study.

For both Sample A and P25, the general effect on the photoactivity of lattice doping or surface iron doping, whether measured by IPA, NP, or SA are most likely caused by electronic effects i.e. charge trapping and efficient charge mediation to surface species by the iron dopant. In general photoactivity rises to a maximum at low levels of iron 0.01 % (100 ppm) for Sample A and 0.005 % (50 ppm) for P25. Above this level increased charge recombination lowers the photoactivity. Structural considerations such as degree of hydroxylation, lattice defects, differences in light absorption, and the dispersion in different media may have a minor effect on the absolute photoactivity of iron doped samples, but are not the cause of the observed trends. Iron doping did not significantly change the surface area, crystal size and morphology of the samples, as shown by X-Ray Diffraction (XRD). Infrared spectra showed some evidence of an adsorbed acetate species from the iron doping precursor, but it was concluded that any acetate species, if present, did not affect the overall trends.

In general, for Sample A, lattice iron doping led to a lower photoactivity than surface doping for similar dopant levels, as dopant trap sites within the lattice (rather than on the surface) are more likely to act as recombination centres than sites for interfacial charge transfer. For both lattice and surface doping, minor systematic

variations in the absolute photoactivity when measured by NP or IPA are probably due to the altered dispersion in different media.

During the development of the technique, salicylic acid degradation (SA) was shown to proceed by direct electron transfer with the titanium dioxide (oxidation by subsurface holes) rather than by a hydroxyl mediated mechanism as the addition of excess alcohol to the titanium dioxide/salicylic acid mixture did not reduce the rate of degradation. This hypothesis was strengthened by the observation that for *surface* iron doped samples the photoactivity trend with dopant level was different to that observed for NP and IPA. For lattice iron the trend was similar to that for NP/IPA as surface effects are less important.

Regarding the development of 2-nitrophenol degradation (NP) for measuring photoactivity, there was a good correlation with the more common IPA technique for all iron doped samples i.e. both techniques are measuring photoactivity in a similar manner. The general photoactivity trends are similar, and the optimum dopant concentration is at the same level for both techniques.

8.1.2. Effect of surface coating on the photoactivity.

The effect of coating nanosized titanium dioxide, rutile (Sample A) and the mainly anatase Degussa P25, with a phosphate ester (AM160K), octadecyl-trimethoxy-silane (ODTMOS), or a phosphate (SHP) on the photoactivity has been determined. Two techniques were employed, 2-propanol oxidation (IPA) and 2-nitrophenol degradation (NP), measuring photoactivity in an alcohol or an aqueous medium respectively. The coating formation at different levels was investigated by surface area determination and infrared spectroscopy (FTIR).

For AM160K coatings, a simple model has been proposed to explain why low levels of coating disproportionately reduce the surface area and photoactivity of Sample A as measured by IPA and NP. Previous studies by Egerton and Tooley [1,2] found that specific surface sites were unduly responsible for photoactivity and hypothesised that these were the pores between aggregates of individual particles. The present study extends this model to show that AM160K preferentially coats these areas significantly reducing photoactivity and surface area at low levels, and further shows by FTIR

spectroscopy that at higher coating levels a coherent coating forms that has highly ordered alkyl chains. This model has been applied to explain the similar behaviour of AM160K coated Degussa P25 and it was hypothesised that the photoactive sites ('hotspots') proposed by several authors [3-5] are preferentially coated by the AM160K unduly reducing photoactivity at low levels, the reduction in surface area also supports this. A seemingly anomalous rise in photoactivity at the 10% coating level for Sample A was shown not to be caused by the altered optics and it was suggested that this may be due to increased adsorption of the organic substrates caused by a lowering of the pzc giving a higher rate of reaction. The good correlation between measured photoactivity by the IPA and NP methods strengthen conclusions from the iron doping work that these two methods are measuring similar photocatalytic effects.

The model was also found to be valid for phosphate coated Sample A and P25, where the photoactivity as measured by NP is reduced in a similar way to AM160K coatings. The analogous rise for a 10% phosphate coating on Sample A was attributed to a lowering of the pzc, the higher adsorption of NP giving a higher rate of degradation. Interestingly, the phosphate coatings were not effective at reducing the photoactivity as measured by IPA and it was proposed that this was due to the patchy or porous nature of the coating (as shown by the higher surface area of these samples in comparison to AM160K and ODTMOS coatings). This hypothesis suggests that The 2-propanol molecule was small enough to interact with the bare patches of underlying surface despite the coating while the much larger 2-nitrophenol molecule was too sterically hindered. These results, when compared with those for AM160K, show that in addition to the surface sites coated, the composition of the coating is just as critical, and demonstrates that to adequately reduce photoactivity it is important to form dense impervious layers, and that the alkyl backbone of the molecule may play an important role.

A different model was proposed for ODTMOS, as the coatings form on the titanium dioxide surface as an 'islandlike' siloxane film of bridged silane molecules (shown by FTIR). These siloxane films effectively reduce the surface area by blocking pores. However, at low coating levels the ODTMOS only covers a portion of the surface with coating growth dominated by lateral interactions between silane molecules rather than with active surface sites, leaving uncoated pores for Sample A and thus the

photoactivity is not disproportionately reduced as was found for the AM160K coating. The ODTMOS coating forms in a similar manner on P25, but does disproportionately reduce photoactivity. It was thus tentatively hypothesised that the active sites on P25 are located sufficiently close so that even though the ODTMOS covers only a portion (~40%) of the surface, most of the active sites are coated. In addition to providing information on the nature of the photoactive sites, these results demonstrate that the composition of the coating, in particular whether there is a strong driving force for crosslinking may determine the efficiency of the final coated product.

The coating most effectively reducing the photoactivity has thus been shown to depend on the surface properties of the titanium dioxide, how the active sites are distributed, the measurement method, and the type of coating. The role of the alkane backbone appears to be important for reducing photoactivity.

FTIR spectroscopy was successfully used to elucidate a model for the differing bonding mechanisms of silane and phosphate esters. From the methylene stretch positions, the former tends to form in an islandlike fashion due to siloxane formation, the latter in a more evenly distributed manner across the surface. The results were more mixed for determining the phosphate bonding bond, mono- bi- or tri-dentate, although rational suggestions have been made based on the evidence. It was beyond the range of the present study to fully examine this issue but may be useful to examine in future.

8.2. Further work.

A series of different silane and phosphate/phosphate ester coatings have been shown to successfully reduce the photoactivity of titanium dioxide. It would be of interest to investigate whether more functionalised silanes or phosphate esters, perhaps with more hydrophilic alkane chains for better dispersion in aqueous media similarly reduce the photoactivity. Some exploratory experiments have been performed using phosphate esters with amide backbones with promising results and this work could be extended. In addition, the differing effects for phosphate and a phosphate ester in reducing photoactivity prompt speculation on the effect of chain length, for example how would a phosphate ester with a C_8 or C_3 chain compare with the C_{16} chain studied?

Conventional coatings have been shown to be practically ineffective at reducing the photodegradation of molecules that are oxidised by a direct electron transfer mechanism i.e. salicylic acid [6]. It would be of use to determine whether the coatings used in the current study are effective. Iron doping has however been shown to reduce this type of photoactivity.

Iron doping has been shown to reduce the photoactivity by enhancing recombination at moderate to high dopant levels especially lattice doping by a coprecipitation method. It would be useful to determine if iron doping could be combined with either a conventional silica/alumina coating, or a novel coating such as those developed in the present study, to determine whether this would provide more effective reduction of photoactivity.

The areas of examination in the current study continue to be of both commercial and academic interest and studies will undoubtedly shed light on some if not all of these areas in the future.

8.3. References.

1. T. A. Egerton; I. R. Tooley, *J. Mater. Chem*, **2002**, *12*, 1111.
2. I. R. Tooley, PhD Thesis, University of Newcastle Upon Tyne, Newcastle Upon Tyne, NE1 7RU, (**2002**).
3. R. I. Bickley; T. Gonzalez-Carreno; J. S. Less; L. Palmisano; R. J. D. Tilley, *J. Solid. State. Chem.* **1991**, *92*, 178.
4. A. G. Agrios; K. A. Gray; E. Weitz, *Langmuir*, **2003**, *19*, 1402.
5. D. C. Hurm; A. G. Agrios; K. A. Gray; R. Rajh; M. C. Thurnauer, *J. Phys. Chem B*, **2003**, *107*, 4545.
6. D. Vione; T. Picatonotto; M. E. Carlotti, *J. Cosm. Sci*, **2003**, *54*, 513.

APPENDIX 1.

Overview and full text 'The effect of UV absorption on the photocatalytic oxidation of 2-nitrophenol and 4-nitrophenol' T. A. Egerton; P. A. Christensen; R. W. Harrison; J. W. Wang, *J. Applied. Electro*, **2005**, *35*, 799.

APPENDIX 1 (FORMERLY CHAPTER 7). OVERVIEW: EFFECT OF UV ABSORPTION ON THE PHOTOCATALYTIC OXIDATION OF 2-NITROPHENOL AND 4-NITROPHENOL.

In Chapter 3 and 5, 2-nitrophenol degradation has been used as a standard test to determine titania photoactivity. All the test measurements have been made using a single initial concentration of 0.2 mM 2-nitrophenol. However, as part of an MPhil programme [1] the effect of 2-nitrophenol concentration on the degradation rate was measured. Later, during the course of the authors PhD studies complementary measurements on 4-nitrophenol degradation were carried out under my guidance by a visiting student, J.W.Wang from the Department of Chemical Engineering, Taiyun University of Technology, Peoples Republic of China. Based on these two experimental studies the effect of UV absorption by nitrophenol on its photocatalytic oxidation has been considered. It has been suggested that the decrease in the photocatalytic degradation rate constant at higher initial nitrophenol concentration is due to UV absorption and not due to surface coverage (Langmuir-Hinshelwood) considerations. This work has been published separately; Part 2 of this Appendix. For clarity, it is summarised here to demonstrate why, for example in Chapter 3 the nitrophenol degradation appears to increase in rate at the end of the experimental run.

7.1. Dependence of the rate constant on nitrophenol concentration.

The degradation of 2- and 4- nitrophenol under UV illumination and an oxygen sparge was followed using HPLC to detect the decreasing concentration over time. First order plots, Figure 7.i, are linear within experimental error and suggest that the system may be described by pseudo first order kinetics, with the rate constant (k) equal to – dy/dx. However, as shown in Table 7.i, increasing initial concentration of nitrophenol results in decreasing rate constants and therefore the degradation does not increase proportionally to the concentration as would be expected for a true first order reaction. A 16 fold increase in 4-nitrophenol concentration decreased the pseudo first order rate constant but doubled the absolute amount of 4-nitrophenol degraded - a pattern mirrored for 2-nitrophenol in the previous MPhil programme [1]. Several authors have reported similar results for photocatalytic degradation of nitrophenols [2-5].

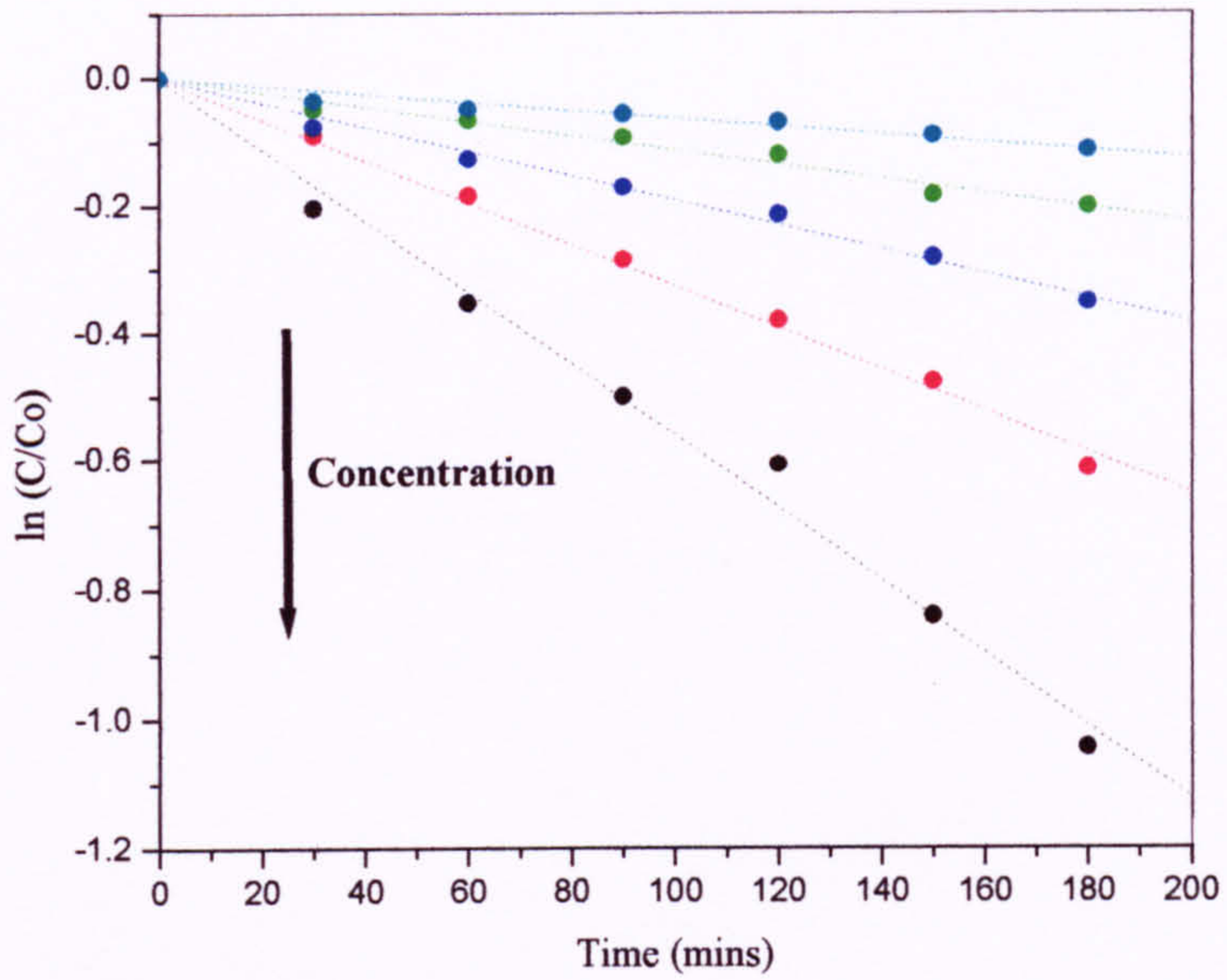

Fig 7.i. First order plot for 4-nitrophenol degradation. C_i = 0.25mM (---); 0.5mM (---); 1mM (---); 2mM (---); 4mM (---).

Initial 4-NP concentration C_0 (mmol dm^{-3})	10^4 x Rate constant (s^{-1})	10^4 x Rate (mmol dm^{-3} s^{-1})
0.25	0.935	0.234
0.5	0.545	0.273
1	0.318	0.318
2	0.188	0.377
4	0.105	0.418

Table 7.i. Rates and derived rate constants, for photocatalytic removal of 4-nitrophenol in aqueous solution.

The simplest explanation for this is that, because the photon flux limits the *number* of molecules which react, the *fraction* of molecules which react necessarily decreases as nitrophenol concentration increases. This argument is too simple for three reasons. First, only a minority, <5%, of incident photons lead to oxidation [6-8] – i.e., not all of the incident photons are used. Second, our results and those of others [5] show that the absolute amount of degradation increases despite the decrease of pseudo first order rate constant. For example, in our system, a 16-fold increase in 4-NP

concentration doubled the number of 4-NP molecules removed (see table 7.i) whilst a 20-fold increase in 2-NP concentration increased, by six, the number of 2-NP molecules removed. This confirms that not all photons are being used. Thirdly, the variation in the apparent rate constant caused by fixed changes in concentration is not constant, but depends on other factors such as pH; see, e.g. [5].

7.2. The Langmuir-Hinshelwood model.

Despite differences in the detailed application, most authors [2-5] consider that nitrophenol oxidation is (with certain necessary simplifications) consistent with a Langmuir-Hinshelwood type model such as equation 7.1. Decreases in the rate constant, k, with concentration are attributable to competition for specific surface sites by the initially formed products of reaction i.e. different forms of P.

$$\text{Oxidation Rate} = \frac{-dc}{dt} = -kc_s = -k_{surf}\left(\frac{K_a c_s [OH^{\cdot}]_s}{1 + K_a c_s + \sum_p K_p P}\right) \qquad [7.1]$$

However, while this has been used with success to model changes in the rate of nitrophenol oxidation with concentration, we consider that it does not adequately account for the changes in the rate constant for several reasons. Firstly, the conditions were deliberately chosen to minimise the intermediates. The concentration of intermediates was monitored by comparative analysis of total organic carbon (TOC) and HPLC in preliminary studies and restricted the kinetic analyses to times less than 180 minutes where the total solution concentration of intermediates as a percentage of organic carbon was less than 5% for 2-nitrophenol and 15% for 4-nitrophenol.

Another finding from these initial studies was that for very long reaction times (<360 minutes) the intermediates constitute a large percentage of the organic carbon in solution and could therefore be expected to affect the measured kinetics. The first order rate plot showed no decrease in rate at these longer reaction times, as would be expected if the surface was blocked by intermediates, the deviation instead being in the direction of increased rate. This suggests that the decrease in rate constant for higher initial nitrophenol concentrations is not caused by competition with intermediates.

Separate adsorption results performed in the dark demonstrated that $K_{4\text{-NP}}$ (0.02 $mmol^{-1}$ dm^3) << $K_{2\text{-NP}}$ (0.4 $mmol^{-1}$ dm^3) and therefore a Langmuir-Hinshelwood model would predict that the plot of oxidation rate against nitrophenol concentration would saturate less rapidly for 4-NP than for 2-NP. Figure 7.ii shows that the reverse is the case. Although the conventional test of Langmuir-Hinshelwood behaviour – a plot (Figure 7.ii inset) of $1/k_{obs}$ against c_0 gives acceptable straight lines – leading to values of $K_{2\text{-NP}} = 1.1$ $mmol^{-1}$ dm^3 ($k_{s\ 2\text{-NP}} = 0.018 \times 10^{-3}$ s^{-1}) and $K_{4\text{-NP}} = 3.1$ $mmol^{-1}$ dm^3 ($k_{s\ 4\text{-NP}} = 0.052 \times 10^{-3}$ s^{-1}) these values of K are inconsistent with those derived from direct measurements. Therefore, quantitative analysis does not support the Langmuir-Hinshelwood model, in common with results reported by other authors [1,9]. Results for 2-nitrophenol are taken from the MPhil programme [1].

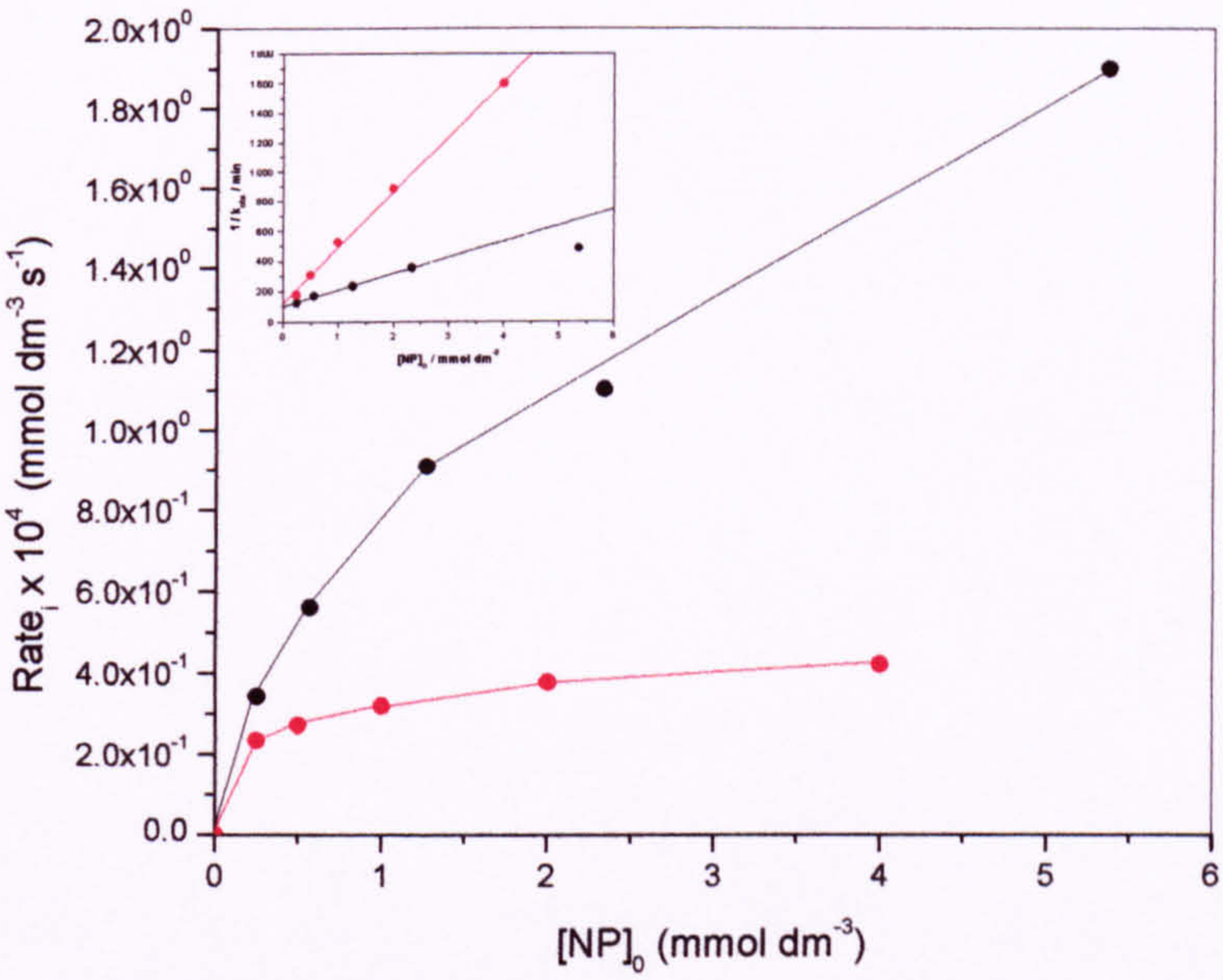

Fig 7.ii. Initial rate of disappearance of nitrophenol as a function of equilibrium concentration. Inset: Test for L-H behaviour. 2-nitrophenol (---); 4-nitrophenol (---).

7.3. The effect of UV absorption by nitrophenol on the measured oxidation rates.

As shown in Fig 7.iii, 4-nitrophenol absorbs UV radiation < 400nm coincident with the titania bandgap energy and the lamp output. Previous results for 2-nitropehnol and new results for 4-nitrophenol have shown that the oxidation rate varies with incident intensity according to an I^1 dependency (except for 0.25mM solutions of the

more weakly absorbing 2-NP at high incident UV intensity), which is consistent with a low light intensity system where charge carrier recombination is not rate limiting. However, if the same lamps, catalyst and reactor, as used for the nitrophenol oxidation, are used for isopropanol oxidation, n =0.5 [10], demonstrating that the UV flux is sufficiently large for charge-carrier recombination to dominate. I.e. A sufficient amount of UV is absorbed by the nitrophenol solution so as to affect the oxidation kinetics.

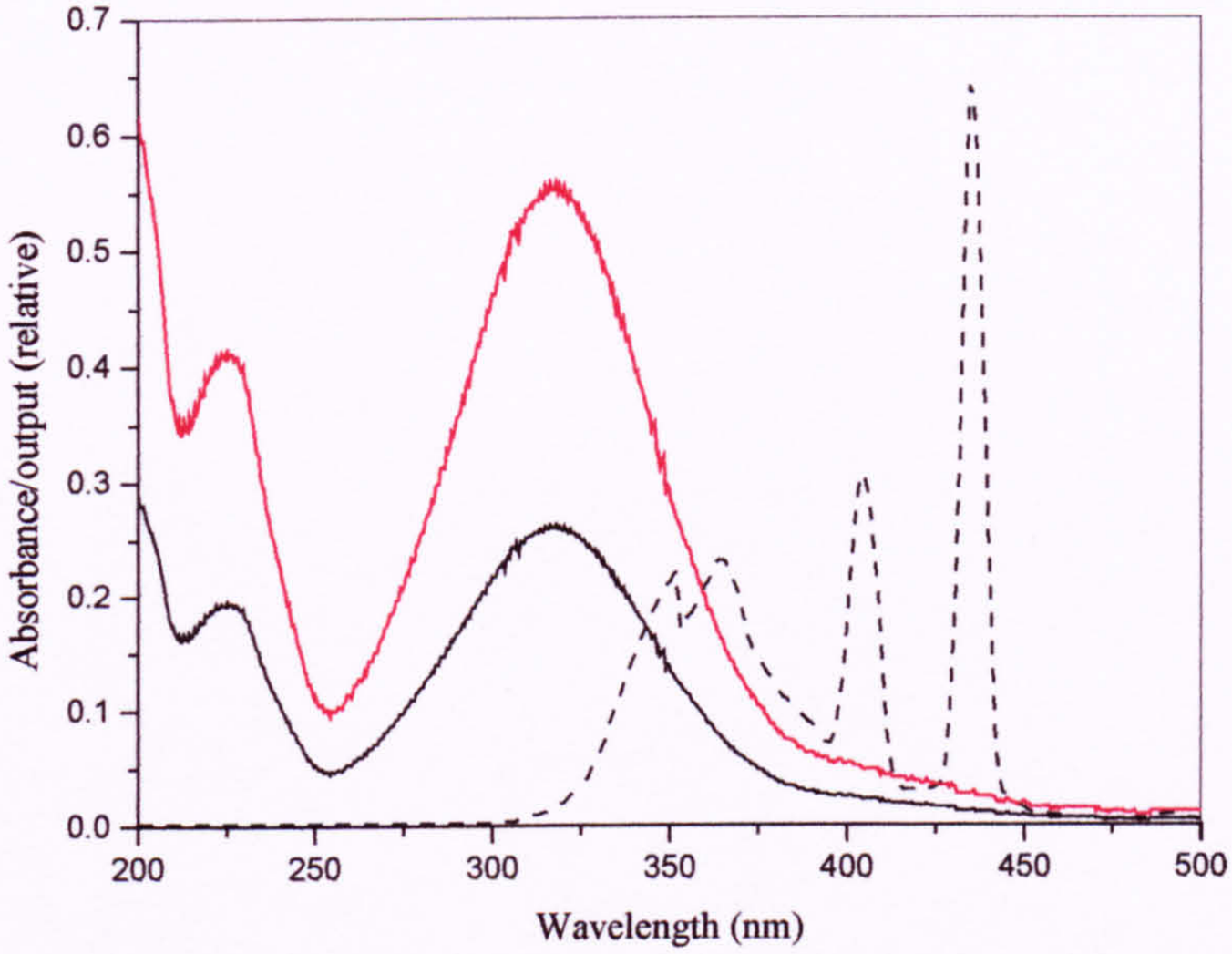

Fig 7.iii. Lamp output and absorption spectra of 4-nitrophenol; 0.25mM (---) and 0.5mM (---).

The authors consider the same UV attenuation by nitrophenol to be the main factor responsible for decreasing pseudo first order rate constant with increasing nitrophenol concentrations; i.e. in Equation 7.1 the main cause of the decrease in k_{obs} is the resultant decrease in $[OH^{\bullet}]_s$ rather than the increase in the denominator suggested by the Langmuir Hinshelwood model. A semi-quantitative analysis, ignoring UV attenuation by TiO_2, to test whether this is the case was constructed based on these considerations, such that a plot of k_A/k_B against c_B/c_A (Fig 7.iv) will be a straight line (k is the rate constant, c_A and c_B two different nitrophenol concentrations). The agreement is as good as can realistically be expected for a model which ignores scattering and absorption by the titania particles, and supports the conclusion of the 'rate vs. intensity study' that UV absorption by the nitrophenol is the major cause of the observed decrease in pseudo first order rate constant with increasing concentration of nitrophenol.

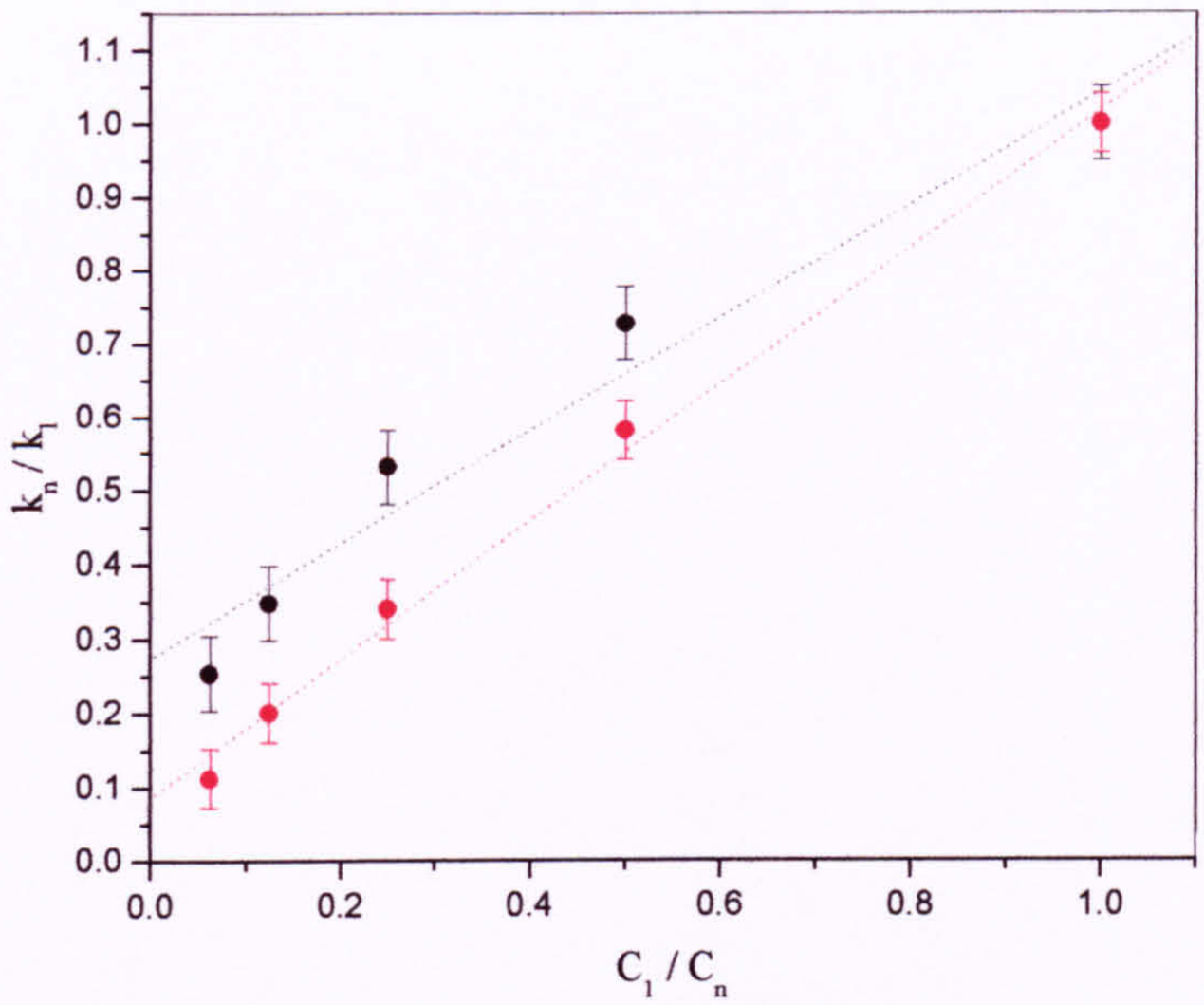

Fig 7.iv. Test for correlation of observed rate constants with proposed model for 2-nitrophenol (---) and 4-nitrophenol (---).

7.4. Conclusions.

We have analysed nitrophenol oxidation kinetics under conditions which were demonstrated to give a low concentration of intermediates. We therefore consider that the decreases in the measured pseudo first order kinetic rate constants are not primarily controlled by adsorption of reaction intermediates. Further, the adsorption constants derived from a Langmuir Hinshelwood analysis of the rates of degradation of 2 and 4-NP are not only quantitatively different from those determined by direct adsorption measurements but their relative magnitude is reversed. We propose that the major cause of the reduction in measured rate constants is UV absorption by nitrophenol. This absorption reduces the photon flux available at the surface of catalyst particles in suspension.

While we have only examined in detail the hypothesis that light absorption by the nitrophenol solutions affects the oxidation rate, it is also reasonable to assert that differing absorption may affect other aspects, for example relative rates between different isomers, or the dependence of pH on the oxidation rate.

7.5. References.

1. R. W. Harrison, MPhil Thesis, University of Newcastle Upon Tyne, Newcastle Upon Tyne, NE1 7RU, (**2001**).
2. K. H. Wang, Y.H. Hsieh and L.J. Chen, *J. Haz. Mater.* **1998**, *59*, 251.
3. D. Chen and A.K. Ray, *Wat. Res.* **1998**, *32*, 3223.
4. V. Augugliarno, L. Palmisano, M. Schiavello and A. Sclafani, *Appl. Catal.* **1991**, *69*, 323.
5. V. Augugliarno, M..J. Lopez-Munoz, L. Palmisano and J. Soria, *Appl. Catal* **1993**, *101*, 7.
6. C. E Homecroft and E.C. Constable, 'Chemistry' 2nd Edition, Pearson Education Ltd, Harlow, (**2002**).
7. P. A. Christensen, T. A. Egerton, S. Kosa, J. R. Tinlin and K. Scott, submitted to *J. Appl. Electrochem.*
8. T. A. Egerton and C. J. King, *J. Oil Col. Chem. Assoc.* **1979**, *62*, 386.
9. A. Mills and J. Wang, *J. Photochem. Photobiol. A:Chem.* **1998**, *118*, 53.
10. T. A. Egerton and I. R. Tooley, *J. Phys. Chem. B.* **2004**, *108*, 5066.

Journal of Applied Electrochemistry (2005) 35:799–813
DOI 10.1007/s10800-005-5168-9

The effect of UV absorption on the photocatalytic oxidation of 2-nitrophenol and 4-nitrophenol

T.A. EGERTON*, P.A. CHRISTENSEN, R.W. HARRISON and J.W. WANG
School of Chemical Engineering and Advanced Materials, University of Newcastle on Tyne, Newcastle on Tyne, NE1 7RU, UK
*(*author for correspondence, e-mail: T.A.Egerton@ncl.ac.uk)*

Received 13 December 2004; accepted 5 February 2005

Key words: Langmuir–Hinshelwood, nitrophenol, photocatalysis, titanium dioxide, UV

Abstract

Adsorption of 2-nitrophenol and 4-nitrophenol by titanium dioxide was measured and their photocatalytic oxidation was followed by both HPLC analysis and measurement of the total organic carbon content of the solution. The oxidation follows pseudo-first order kinetics with rate constants that decrease as the nitrophenol concentration increases. However the adsorption constants inferred from the reaction kinetics are inconsistent with those measured in the adsorption experiments, even though the relative amounts of reaction intermediates remain low. We conclude that the decrease in rate constant cannot be explained by a Langmuir–Hinshelwood model. Instead we suggest that the strong, but differing, UV absorption by nitrophenols lowers the effective UV flux at the catalyst surface and that the greater absorption of more concentrated solutions is primarily responsible for the apparent decrease in rate constant. A simple treatment of this absorption adequately describes the observed changes in rate. The quantitative effect of UV absorption depends on the lamp and on the reactor optics. It his suggested that variations are responsible both for differences in the reported relative oxidation rates of the two isomers, and for the different conclusions reported with respect to the effect of pH on oxidation rate.

1. Introduction

1.1. *Mechanism*

This paper describes the photocatalytic oxidation of nitrophenol by titanium dioxide. Photocatalytic oxidation by semi-conductors has been widely reviewed [11, 22]. It can occur either by direct transfer of a photo-generated positive hole to an organic molecule – direct hole transfer – or by reaction of the positive holes with hydroxyl ions, or surface hydroxyl groups, to form highly active hydroxyl radicals. Hydroxyl radical formation is believed to control the photocatalytic oxidation of nitrophenols, and during oxidation hydroxylated intermediates have been identified [33–55].

Nitrophenol by-products are representative of the substituted aromatics which may be present in a range of industrial effluents. In nitrophenols, hydroxyl substituents donate electrons to the aromatic ring whilst NO_2 withdraws electrons. Electron donating substituents increase the rate of the electrophilic bromination of benzene whilst electron-withdrawing–NO_2 groups reduce the rate [66, 77]. The effect of the nitro substituent on the hydroxyl group is reflected in the dissociation constants of the three isomers. K_a for 2-nitrophenol (2-NP) and 4-nirophenol (4-NP) are similar (6.8×10^{-8} and 7×10^{-8} respectively) but both are greater than that for 3-nitrophenol (3-P), (5.3×10^{-9}); i.e. the ionization of the OH is much greater in the 2- and 4-isomers [88].

1.2. *Apparent oxidation kinetics*

The decrease in the concentration of nitrophenol during photocatalytic oxidation by TiO_2 generally follows pseudo-first order kinetics [33–55, 88–1212], despite the wide range of experimental conditions used in these studies (Table 1). However, an increase in the initial concentration of nitrophenol is reported [88, 99, 1111] to decrease the measured rate constant, k, even though the amount of nitrophenol oxidized either increases or goes through a maximum as the concentration is increased. Most authors [44, 55, 88, 99] consider the kinetics of nitrophenol oxidation to be represented adequately by an expression of the form

Table 1. A summary of previous work photocatalytic oxidation of nitrophenol

Reference & overall kinetics	TiO_2 type, Surface Area/$m^2\ g^{-1}$ & Catalyst loading/g dm^3	pH range	NP Conc./mM	Lamp type & analytical measurement method	Pseudo-first order rate constant $k_{obs} \times 10^4/s^{-1}$ & Langmuir adsorption constants, K
Tanaka et al. [33]	Fujititan (Anatase) 17, Loading of 3/g dm^{-3}	Natural	1	500 W Hg (HP), HPLC + TOC	1.2
Wang et al. [44] Langmuir–Hinshelwood	Degussa P25 55, Loading of 2/g dm^{-3}	3–11	0.1	125 W Hg (High P), HPLC + TOC	4.2–1.0
Cinar et al. [1212]	Degussa P25 55, Loading of 3/g dm^{-3}	5.1	0.035–0.093	5 × 8 W, Black light fluorescent lamps. 3.1×10^{-7} einstein s^{-1} UV spectra	0.7×10^{-4} at 0.1 mM
Chen et al. [55] Langmuir–Hinshelwood	Degussa P25 55, Hombikat > 250, 0.2–4/g dm^{-3}, normally 2 /g dm^{-3}	2–10	0.14–1.7	125 W Hg (High P) UV/VIS + TOC	K_i(Intensity)$^{0.84}$ = 1.54 k_r(Intensity)$^{0.84}$ = 0.6 5.8–0.84; $K_{4NP=10,400}\ M^{-1}$
Palmisano et al. [88] Langmuir–Hinshelwood assuming O_2 and NP adsorb on different sites	Merck (Anatase) 11, Tioxide -(Anatase) 14, Tioxide (Rutile) 20, BDH (Anatase), 11 Montedison B5, Anatase 22, Normally 0.6/g dm^{-3}	pH 3 (b) Natural	0.7–7 Or (b) 0.22–2.2	1500 W Xe, 6.8×10^{-4} einstein s^{-1} Or 500 W Hg (HP), 1.5×10^{-4} $einsteins^{-1}$, UV/VIS. absorption	0.28; $K_{2NP=7650}\ M^{-1}$ $K_{4NP=8915}\ M^{-1}$
Augugliarno et al. [99], Langmuir–Hinshelwood	Merck (Anatase) 11, Loading of 0.8/g dm^{-3}	3–11	0.2–1.4	500 W Hg (Med P), UV/VIS + TOC	2.77–0.21
Andreozzi et al [1010], Langmuir–Hinshelwood or Rideal Eley	Eurotitania 100, Loading of 0.2–6/g dm^{-3}	3 & 8.5 Phosphate-Buffer	0.25 to ~0.7	125 W Hg (High P) 0.88 kW dm^{-3} HPLC	8, K_{4NP} 1000 M^{-1} at pH 3
Adesina et al. [1111]	Aldrich (>99% anatase), 0.5–1.5, normally 1/g dm^{-3}		0.1–0.7	200, 300 or 400 W with a significant 250–310 nm component	

$$\text{Oxidation rate} = \frac{-dc}{dt} = -\mathrm{k}c_s = -\mathrm{k}_{surf}\left(\frac{K_a c_s [OH^\bullet]_s}{1 + K_a c_s + \sum_p K_p P}\right) \quad (1)$$

where c_s is the solution concentration of nitrophenol at time t and the observed rate constant k depends on the surface rate constant k_{surf}, the surface concentration of hydroxyl radicals $[OH]_s$ and the surface concentration of nitrophenol. The nitrophenol surface concentration depends not only on its equilibrium solution concentration, c_s, and adsorption constant K_a, but also on adsorption of different intermediates and products–here represented as P. The detailed interpretation of Equation (1) varies. It may be derived for the Langmuir–Hinshelwood mechanism–i.e. a bimolecular surface reaction of two adsorbed reactants whose adsorption may be affected by the adsorption of one or more products species. However, Turchi and Ollis [1313] derived this form of equation from four different hypotheses, including the postulate that the hydroxyl radical may migrate from the TiO_2 surface and thus the two reactants need not be surface bound. By contrast Palmisano et al. [88] suggest that nitrophenol and oxygen adsorption occur independently on different sites. Despite differences in the detailed application of Equation (1), most authors consider that nitrophenol oxidation is consistent with the Langmuir–Hinshelwood (LH) model and that the decrease in the rate constant, k, with concentration is attributable to competition for specific surface sites by the initially formed products of reaction, i.e. different forms of P. It is usually assumed that the adsorption constants for P are similar to that of the nitrophenol isomer i.e. that $K_a c_s + \Sigma K_p P = K_a c_0$. In turn this approximation implies that the adsorption of substituted aromatics is relatively insensitive to the nature of the substituents. Although it is usually impractical to measure the concentration of either the many different adsorbed species or the hydroxyl radical concentration on the surface of working catalysts, the Langmuir–Hinshelwood concept, of a reaction rate controlled by reaction between adsorbed species whose concentration is modified by competition for limited sites, remains useful. The term, 'Langmuir–Hinshelwood model' is widely used in studies of photocatalysis [88, 1111, 1414] and is therefore adopted in this paper.

Andreozzi et al. [1010] applied the model to oxidation of 4-NP. They measured the adsorption of 4-NP, and evaluated K_{NP}, at pH 3, but at higher pH, 8.5, adsorption was undetected. This difference was attributed to the fact that, at pH 8.5, 4-NP (pK_a 7) exists in the anionic form which cannot adsorb on the negatively charged (assuming pzc 6) TiO_2 surface. However, their measurements were made in the presence of a phosphate buffer and the effect of phosphate adsorption was not considered. Chen and Ray [55, 1515] fitted parameters for the adsorption constants of 4-NP and O_2, and the effect of light intensity and temperature to a more complete expression stated to be predict the concentration profiles throughout a photocatalytic oxidation. The maximum rate was found at pH ~5, but had fallen to ~1/3 of this maximum by pH 8. The reaction rate also decreased at low pH. Adesina and Lea [1111] reported a much smaller decrease, ~10%, in rate constant as the pH increases from 5.5 to 11. Chen and Ray [1515] later derived an expression, using the UV absorption coefficient of the TiO_2, to predict the optimum catalyst loading. They concluded that the design of effective slurry reactors must take into account the dependence of UV penetration on catalyst loading. Cinar and co workers [1212] demonstrated that the enhanced photo-oxidation of 4-NP in the presence of H_2O_2 and the reduced photo-oxidation following addition of Cu^{2+} in solution both followed pseudo-first order kinetics. (They interpreted the reduced rate as due to the Cu^{2+}/Cu^{+} acting as an additional recombination route).

1.3. *Comparison of different isomers*

Previous reports agree that the mononitrophenols are more reactive than the dinitrophenols [33] and that 2-NP and 4-NP are more reactive than the 3-NP [33, 44, 88, 99], but there is less agreement on the relative oxidation rates of 4-NP and 2-NP. Two studies [33, 88] suggest that the reactivities of the two isomers are similar. A third [44] reports that 2-NP is oxidized more rapidly than the 4-isomer. A fourth [99] reports the opposite. These discrepancies suggest that the measured rates are influenced by other experimental parameters, some of which are listed in Table 1.

Most authors consider different adsorption strengths, K_a, to be responsible for the differences in oxidation rate of the various isomers. However, Tanaka and co-workers [33] considered that degradation rate was controlled by the relative rates of electrophilic addition of the hydroxyl radical to the nitrophenol and demonstrate reasonable correlation between the activities of the nitrophenols and their respective Hammett constants.

1.4. *The objectives of this study*

UV attenuation caused by changes in the TiO_2 concentration is often invoked to explain changes in degradation rates with changes in catalyst loading [88, 1010–1212]. However, although the strong TN absorption of nitrophenol has been used to monitor its solution concentration [88, 1212], little attention has been paid to the effect of this absorption on the effective UV intensity at the surface TiO_2 particles in suspension.

UV attenuation is important because a reduction in the UV intensity incident on any one catalyst particle decreases the rate of hydroxyl radicals formation, their equilibrium concentration, $[OH^\bullet]_s$, and consequently the rate constant, k, in Equation (1). Therefore, kinetic analyses should allow for the reduction of $[OH^\bullet]_s$,

caused by increases in nitrophenol concentration. UV attenuation is expected to be especially significant for reactors using immobilized photocatalyst. It is recognized that photocatalyst immobilization may lead to increased mass transfer problems [1414, 1616], but less attention has been paid to the problems associated with UV penetration of the water to be treated. This paper reports measurements of adsorption on, and photocatalytic oxidation by, Degussa P25 TiO_2, of 2-NP and 4-NP over a range of concentration. The photo-oxidation measurements have been made at relatively low light intensities – as would be used in practical photo-reactors or photoelectrocatalytic reactors – and this has allowed the effect of UV attenuation by nitrophenol to be explicitly considered.

2. Experimental details

A commercial TiO_2 (Degussa P25, ~80% anatase; 20% rutile) was used for all the experiments. The surface area, determined by gravimetric adsorption of N_2 (σ_{N2} = 0.162 nm^2), after outgassing at 110 °C for 2 h, was 45 ± 5 $m^2\ g^{-1}$ consistent with a primary particle size of 30 nm. Nitrophenol solutions were prepared by sonication of nitrophenol crystals (Aldrich; purity of 99 + % and used without further purification) in deionized water.

UV/visible spectra were recorded, on Shimadzu UV-160A single beam spectrometer, using a 1 mm far-UV quartz cell. Solution pH was altered by addition of 1 M HCl or 0.5 M NaOH. Nitrophenol concentration was followed by high-pressure liquid chromatography (Dionex model UVD170S HPLC fitted with a C_{18} reverse phase column). Sample of 50 μl in a 40:60 v/v methanol/millipore water carrier solution were manually injected at a flow rate of 1 ml min^{-1}. Total carbon content was determined using a Dohrmann Phoenix, model 8000, UV persulphate TOC analyser. Organic carbon content was calculated by subtraction of the inorganic carbon from the total carbon content.

For measurements of nitrophenol adsorption on TiO_2, nitrophenol solutions, 50 ml, of concentrations 1, 2, 4, 5, 6, 8 and 10 mM were placed in 100 ml conical flasks, sealed and equilibrated for 18 h. A 5 ml sample of the nitrophenol was first taken for TOC analysis. 1.5 g P25 was then added to the solution. The flask was resealed and the stirred slurry was equilibrated in the dark for 18 h. After equilibration, samples (2 ml) were taken and centrifuged at 3200 rpm for an initial 30 min. The supernatant suspension was then decanted and centrifuged at 3200 rpm for a further 30 min. This removed the TiO_2 powder, 5 ml aliquots of the centrifugate were diluted with millipore water to 25 ml for injection into the TOC for analysis. This was taken to be the equilibrium concentration. The adsorption constant (K_{NP}) and the monolayer volume (V_m) were calculated using Langmuir analysis.

Nitrophenol oxidation was measured using 8 g dm^{-3} TiO_2 dispersions prepared by mixing 0.4 g P25 in 50 ml nitrophenol solution for 30 min prior to illumination. (Preliminary experiments had indicated that this was sufficient equilibration time). During this period the vessel was equilibrated at 303 K and sparged with a constant flow of oxygen. Subsequently, irradiation was begun whilst a flow of oxygen was slowly bled across the top of the continuously stirred suspension. Measurements were made for initial concentrations from 0.5 to 8 mM, for 2-NP, and 0.25 to 4 mM, for 4-NP. When appropriate, pH alteration or sodium bicarbonate additions were made prior to equilibration.

The reaction was carried out in a cylindrical pyrex vessel [1717] illuminated, from the base, by two Philips PL-L 36W 09 lamps placed horizontally in a light box from which radiation was emitted through a circular port, whose aperture matched the reactor diameter, and heat filter. The relative wavelength distribution of the lamp immediately above the heat filters was measured at him intervals with a Spex 740A Radiometer and is shown in Figure 1b. Where appropriate, neutral density filters were fitted between the heat filter and the bottom of the reactor. Two sizes of reactor were used, one of 45 mm diameter and 130 mm height, and one (used if oxidation was to be followed by TOC measurement) of 60 mm diameter and 200 mm height. The reactor temperature was controlled at 303 K by a closely fitting cylindrical heater. Samples of the reaction mixture were withdrawn by a hypodermic syringe through a sampling port fitted with a septum cap both before illumination and typically at 30 min intervals. They were then centrifuged, to remove TiO_2, prior to analysis by HPLC or TOC as described above.

3. Results

3.1. *UV absorption spectra*

The absorption spectra of solutions of 2-NP (1 mM) and 4-NP (0.25 mM) are shown in Figure 1a and lb. At their natural pH (~5.8), both compounds absorb to a similar extent at 36 nm the wavelength of maximum UV output. However, from 300 to 350 nm and at wavelength above 375 nm, the 4-NP absorbs more strongly than 2-NP. The figures also show the dependence of absorption on pH which results from the change in nitrophenol ionization with pH. For 2-NP a peak at 415 nm replaces the peak at 350 nm as pH increases. A similar effect is observed for 4-NP – a peak at 400 nm gradually replaces that as 317 nm. At 365 nm, the wavelength of maximum UV emission from the PL-L 09 lamps, the absorption of 2-NP gradually decreases, by ~20%, as pH is raised, but the absorption of 4-NP increases by a factor of 4 as the pH is raised from 5 to 9.

3.2. *Adsorption of nitrophenols by TiO_2*

Adsorption of nitrophenols on the TiO_2 at the natural pH (~5) of the nitrophenol/TiO_2 slurries is shown in Figure 2. It is immediately obvious that 2-NP adsorbs

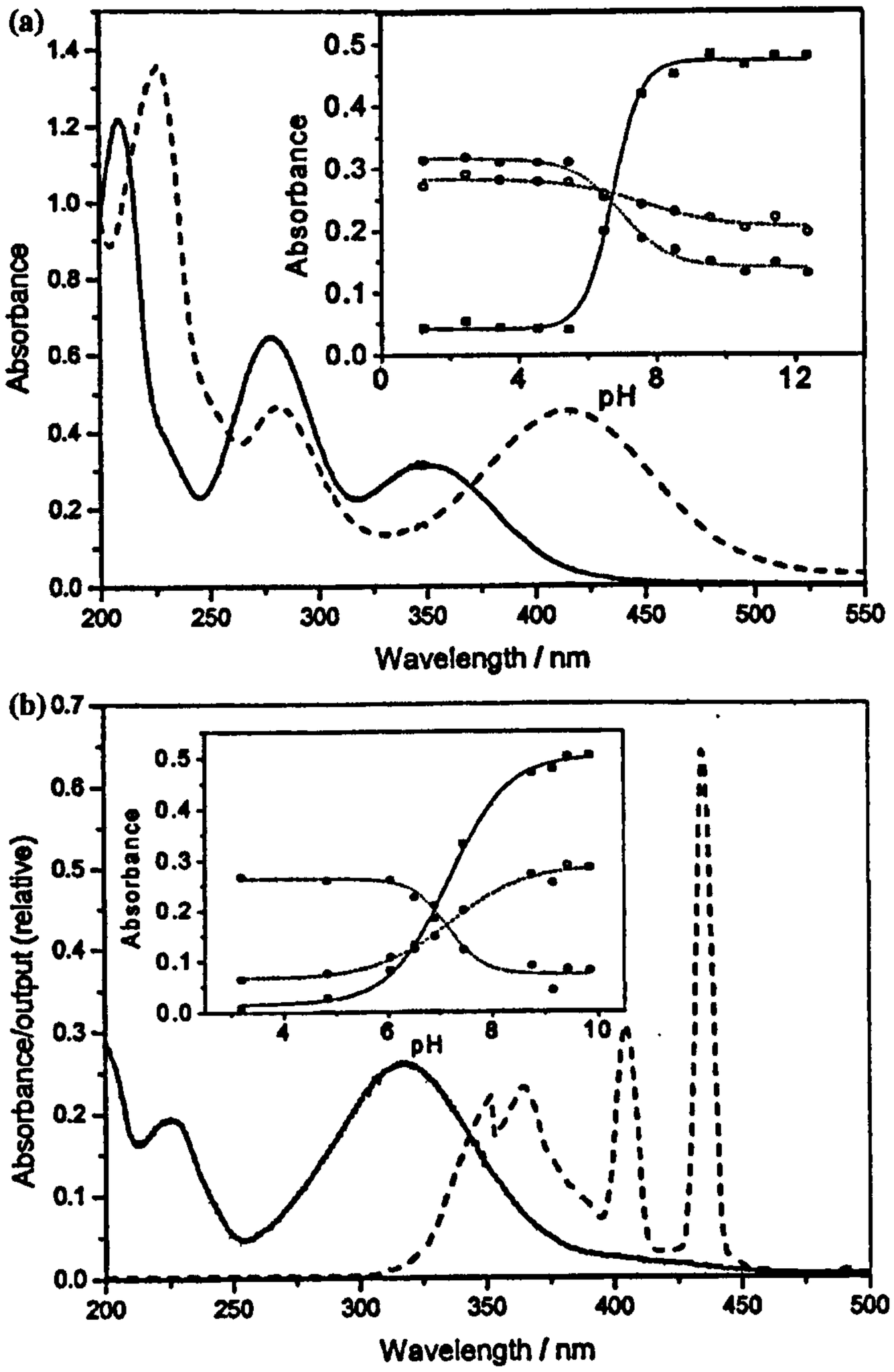

Fig. 1. (a) Absorption spectra of 2-Nitrophenol (1 mM) at the natural pH of 5.2 (solid line) and pH 8.5 (dotted line). The inset shows the absorbance at 415 nm (solid line), 365 (empty symbols, dotted line) and 350 nm (full symbols, dotted line) as a function of pH. (b) Absorption spectra of 4-Nitrophenol (0.25 mM) at the natural pH of 5.4 (solid line) and spectral output of the UV lamps (dotted line). The inset shows the absorbance at 400 nm (solid line), 365 nm (empty symbols dotted line) and 317 nm (full symbols, dotted line) as a function of pH.

much more strongly than 4-NP. In the range 0 to 3.5 mM, adsorption of 2-NP can be fitted to a Langmuir model and leads to $K_{2\text{-NP}} \sim 0.4$ mmol^{-1} dm^3. The corresponding value for 4-NP is too small to measure but is less than 5% of 2-NP value. Andreozzi et al. [1010] inferred that $K_{4\text{-NP}} = 1.4\times10^{-3}$ mmol^{-1} dm^3 at pH 3 but detected no measurable adsorption at pH 8.5

3.3. *Oxidation of 2-nitrophenol*

Most oxidations were monitored by HPLC to follow the decrease in nitrophenol concentration. During the reaction small changes in the form of the UV absorption spectrum suggested the presence of intermediate oxidation products. Correspondingly, the HPLC output indicated the presence of three possible intermediates. None corresponded to catechol and it is probable that the most important is nitrohydroquinone. The relative amounts of these intermediates were assessed from comparative analyses by TOC and HPLC. The result of such an experiment, Figure 3a, shows that, at any given time, the total organic carbon is close to, but slightly higher than the nitrophenol. The small difference represents the total amount of intermediate oxidation products. By contrast, Figure 3b shows the total amount of the intermediate products as a fraction of the total amount of organic carbon and demonstrates that for reaction times below 180 min, the intermediates were less than 5% of the total organic molecules in solution. Hence, most measurements of 2-NP oxidation were followed by HPLC only and, to minimize the effects of possible reaction intermediates,

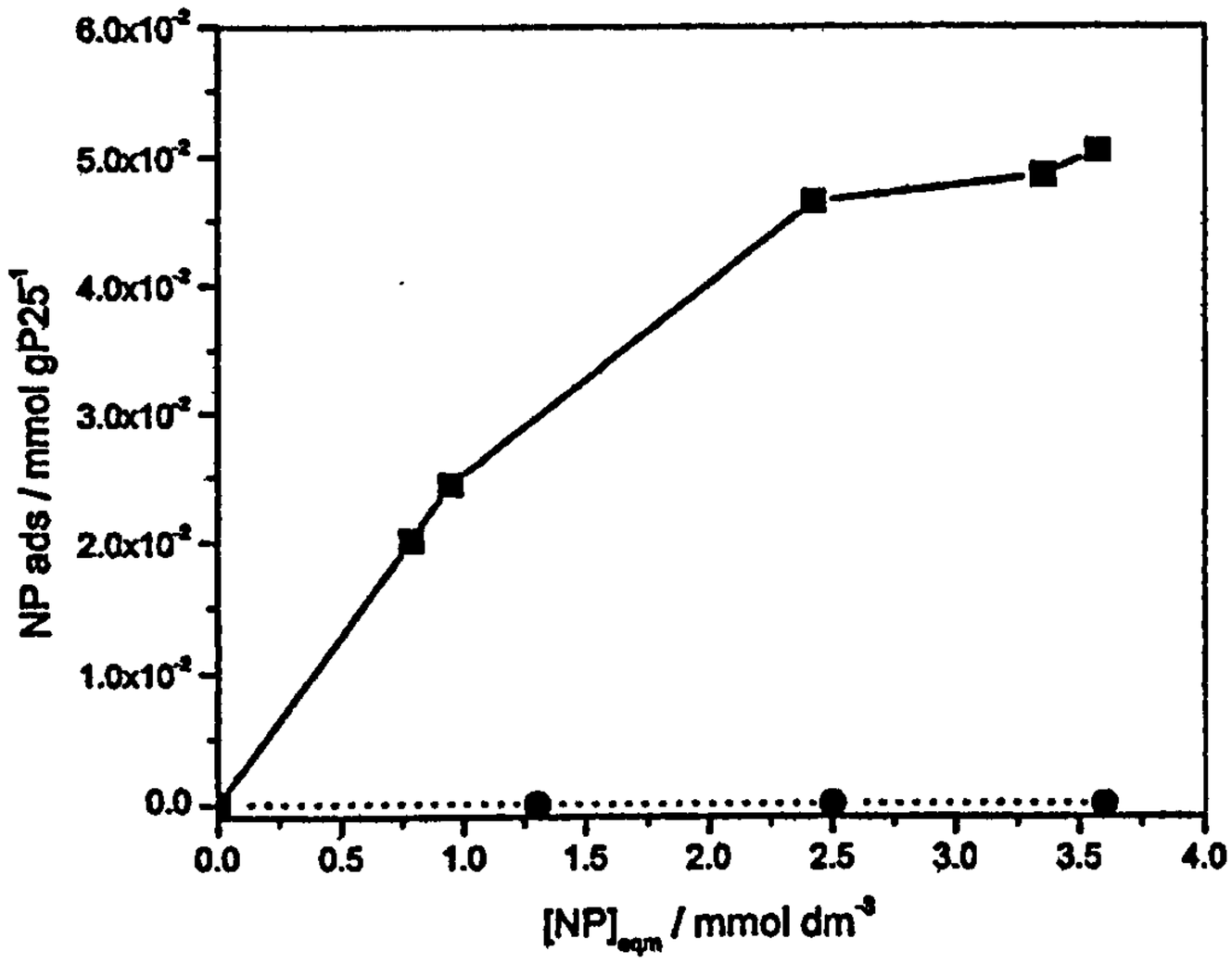

Fig. 2. Adsorption of 2-nitrophenol (■) and 4-nitrophenol (●) on TiO_2 (Degussa P25) from aqueous solution at natural pH.

kinetic analysis was restricted to times less than 180 min.

The results of a series of photo-oxidations of 2-NP are shown in Figures 4a. As adsorption on the TiO_2 led to significant reductions in (c_i) the nominal initial concentration of 0.5 to 8 mM, sufficient time was allowed, prior to starting a photocatalyzed degradation, for the solution concentration to reach an equilibrium value (c_0). It is this value that is plotted at $t=0$ used to derive rate constants. The corresponding first order plots, Figure 4b, are linear within experimental error (Triplicate measurements for selected runs indicated a reproducibility of ±5% in the derived slopes) and suggest that the system may be described by pseudo-first order kinetics, However, as shown in Table 2, increasing initial concentration of 2-NP results in decreasing rate constants and therefore the degradation rate of 2-NP does not increase proportionally to the concentration as would be expected for a true first order reaction. A 20-fold increase in 2-NP concentration leads to a 6 fold increase in the number of 2-NP molecules removed.

3.4. *Oxidation of 4-nitrophenol*

The results of an initial study to follow the 4-NP oxidation by both HPLC and TOC are shown in Figure 5a. From 30 to 150 min reaction the total amount of intermediate-products, shown as a fraction of the total amount of organic carbon were approximately constant at 15% of the total organic molecules in solution. This figure, though higher than the corresponding result for 2-NP oxidation still represents a relatively small fraction of the solution molecules. Hence, as for 2-NP, 4-NP oxidation was followed by HPLC only, with kinetic analysis based on results obtained within, the first 150 min.

Results of 4-NP photo-oxidation are shown in Figure 5b and in Table 3 showing similar trends to 2-NP oxidation. E.g. a 16 fold-increase in 4-NP concentration decreased the pseudo-first order rate constant but doubled the absolute amount of 4-NP degraded. These results were measured some time later than those for 2-NP, and, because of possible variations in the lamp output, are not strictly comparable with the, earlier, 2-NP results.

3.5. *The effect of pH on nitrophenol oxidation*

All the above results were measured on nitrophenol solutions at their natural pH, This was typically ~5, but the precise value depended on the nitrophenol concentration and type, and on the reaction extent. Good first order plots were obtained despite the slight downward pH drift during oxidation (e.g. from 4.8 after equilibration to 4.2 during the first 1.50 min of oxidation of 1 mM 2-NP) and, to avoid possible effects of buffer adsorption, no attempt was made to use buffers to hold the pH constant. However, in order to investigate the dependence of oxidation rate on concentration of sodium bicarbonate, which increases the pH, the effect on oxidation rate of deliberately increasing pH with NaOH was measured. Figure 6 shows that a pH increase from 5.2 to 5.8 increases the degradation rate of 1 mM 2-NP by ~70% but from 5.84 to 7.7 any further increase was marginal (~10%). Correspondingly, results for 0.25 mM 4-NP showed a ~10% increase as the pH was increased from 5.0 to 5.8, a plateau until 8.0 and then a similar increase the pH was increased to 9.1. The results are reasonably consistent with the conclusion of Wang et al. [44], that pH 7 is the optimum for oxidation of both isomers, but contrary to the general decrease in

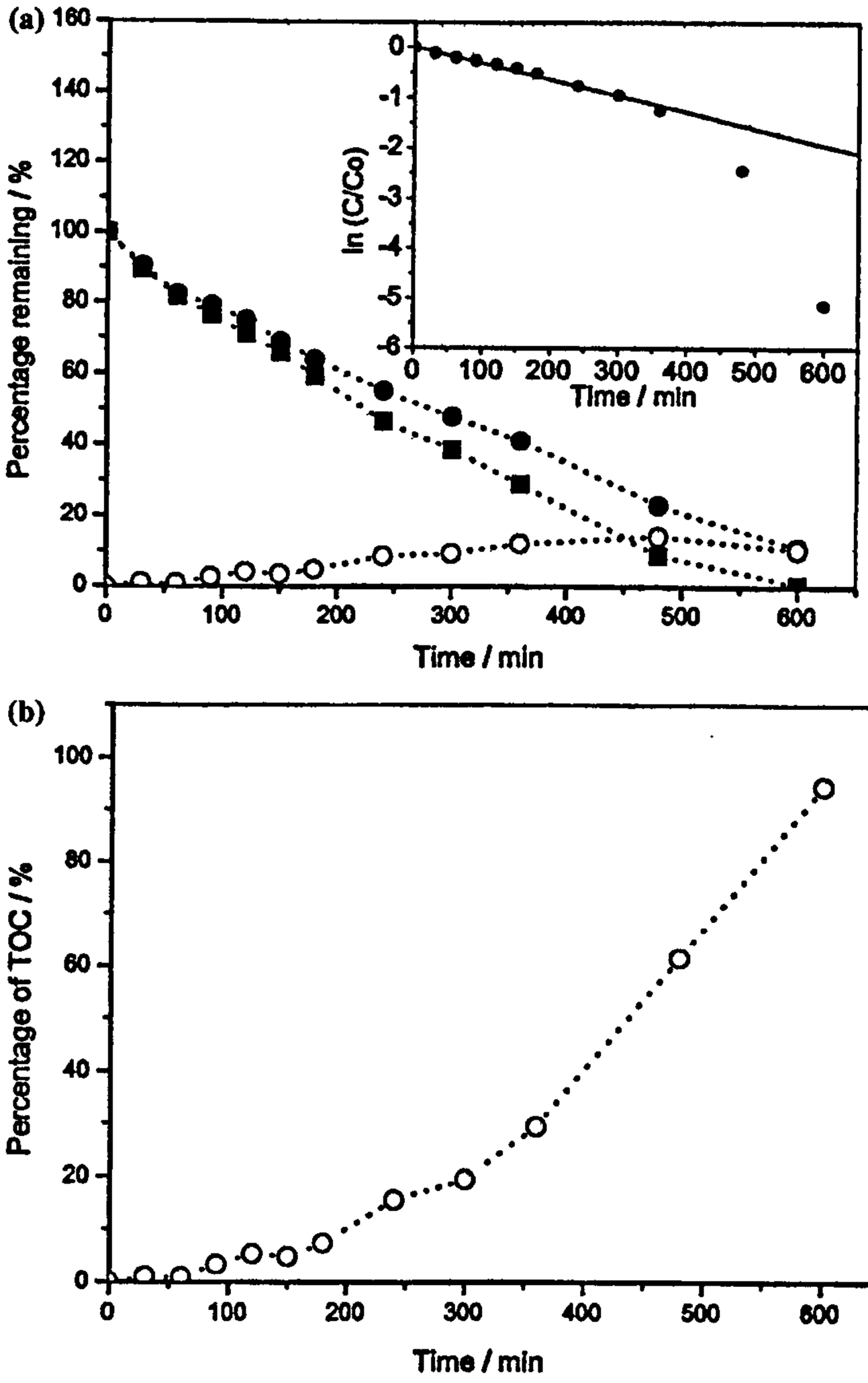

Fig. 3. (a) A comparison of the removal of 2-nitrophenol (initial concentration $c_i = 1$ mM), measured by HPLC (■), and the removal of organic carbon, measured by TOC (●). The total amount of intermediate oxidation products (○) corresponds to the difference between the curves. The inset shows the first order kinetic rate plot as measured by HPLC. (b) The increase with time of the total amount of intermediate products, expressed as a fraction of the total organic carbon.

rate with increasing pH reported by Augugliarno et al. [99]. The differences may be due to the different TiO_2 used, Degussa P25, as here, and Merck Anatase, respectively.

Table 2. Rates, and derived rate constants, for photocatalytic removal of 2-nitrophenol in aqueous solution

C_0, 2-NP Initial concentration/m mol dm^{-3}	$10^4 \times$ (Rate constant derived from the slope of Figure 4b)/s^{-1}	$10^4 \times$ Rate/m mol $dm^{-3}s^{-1}$
0.25	1.35	0.34
0.57	0.98	0.56
1.27	0.72	0.91
2.3	0.47	1.1
5.4	0.34	1.9

3.6. *The effect of sodium carbonate addition on nitrophenol oxidation*

If oxidation of nitrophenol is via catalytically active hydroxyl radicals the addition of sodium bicarbonate, which trap hydroxyl radicals by

$$OH + HCO_3^- \rightarrow H_2O + CO_3^- \quad (1)$$

should decrease the rate of nitrophenol oxidation. The results in Table 4 show that, although increasing pH increased the nitrophenol degradation rate, bicarbonate addition decrease the rate *relative to solutions at the same pH* by an amount that is proportional to log [$NaHCO_3$], Figure 7. However a 35 mM solution of $NaHCO_3$ decreases the rate by only 40% and extraction of Figure 7 suggest that >10 M $NaHCO_3$ would be

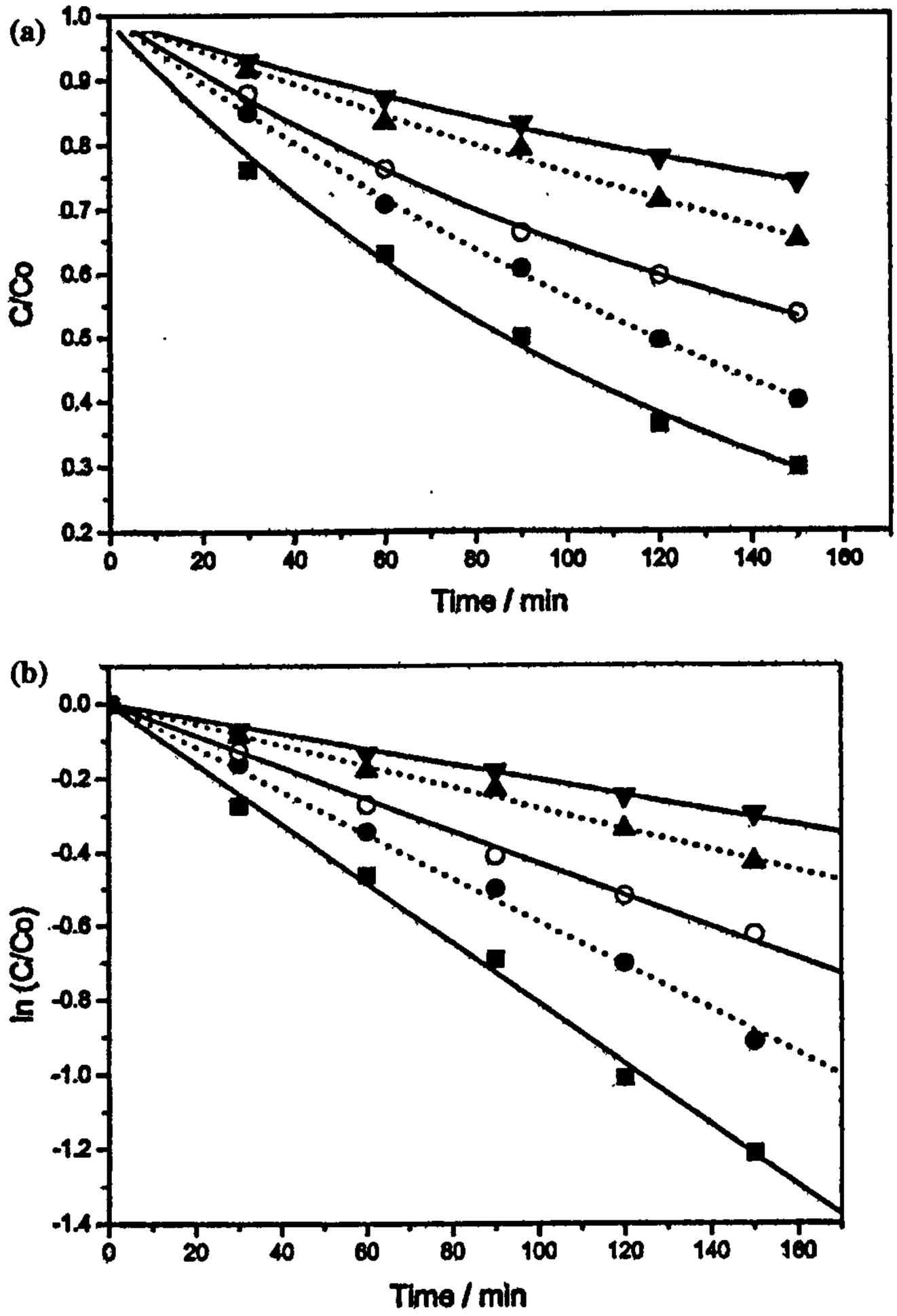

Fig. 4. (a) Photo oxidation of 2-nitrophenol expressed as C/C_0 C_i=0.5 mM (■), 1 mM (●), 2 mM(○),4 mM (▲), 8 mM (▼). (b) Corresponding first order kinetic rate plots for photo-oxidation of 2-nitrophenol C_i=0.5 mM (■),1 mM (●), 2 mM (○), 4 mM (▲), 8 mM (▼).

necessary to completely eliminate photocatalytic oxidation. Possibly, nitrophenol is oxidized not only by hydroxyl radicals but also by a direct hole transfer. In the accompanying paper [1818] methanol enhancement of photocurrent – attributed to direct hole transfer – is reported for sol gel electrodes which were more active for nitrophenol oxidation than were thermal electrodes for which methanol did not cause an increase in photocurrent.

3.7. *Variation of oxidation rate with UV intensity*

Photocatalytic oxidation rate varies with I, the incident UV intensity, according to I^n where the value of n depends on the details of the charge-carrier recombination [1919]. Figure 8 shows the effect of changes in light intensity on the degradation rate of 2-NP and 4-NP. For 1 mM 2-NP the rate is proportional to I^1. For 0.25 mM 2-NP the dependence is more consistent with I^1 dependence at low intensities and $I^{0.5}$ at high light intensity, For 0.25 mM 4-NP the rate is proportional to I^1 over the whole range of intensitics.

4. Discussion

This study of nitrophenol oxidation has confirmed the decrease in the apparent first order rate constant with increasing nitrophenol concentration reported by others [33–55, 88–1212].

The simplest explanation is that, because tile photon flux limits the *number* of molecules which react, the *fraction* of molecules which react necessarily decreases as nitrophenol concentration increases. This argument is too simple for three reasons. First, only a minority, <5%, of incident photons lead to oxidation [11, 1919, 2020] – i.e., not all of the incident photons are used. Second, our results and those of others [99] show that the absolute amount of degradation increases despite the decrease of pseudo-first order rate constant. In our

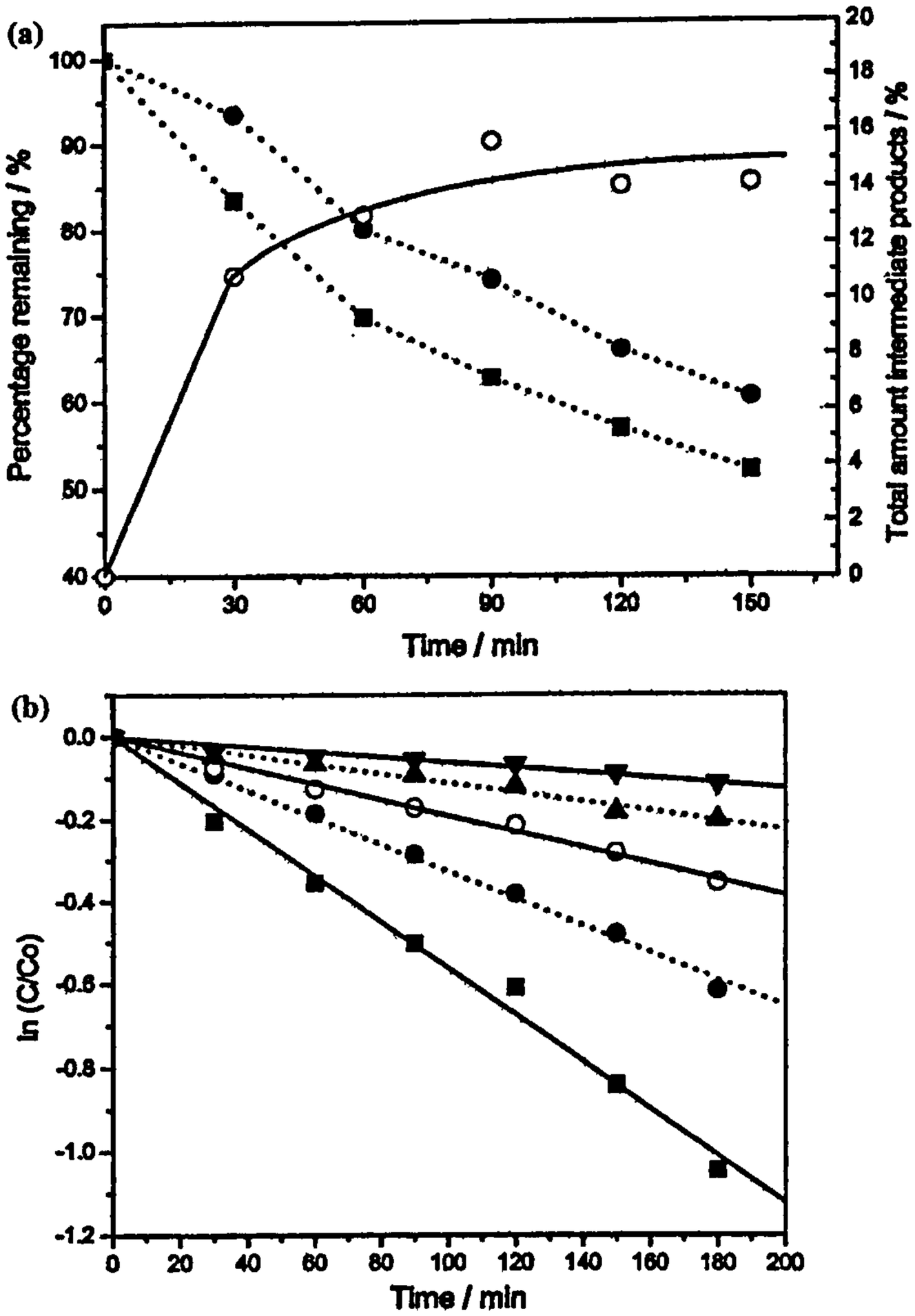

Fig. 5. (a) A comparison of the removal of 4-nitrophenol (C_i=0.25 mM), followed by HPLC (■), and by TOC (●), monitored over 2 h 30 min (left hand scale). The total amount of intermediate oxidation products (○) corresponds to the difference between the two curves (right hand scale). (b) First order kinetic rate plots for photo-oxidation of 4-nitrophenol. C_i=0.25 mM (■), 0.5 mM (●), 1 mM(○), 2 mM (▲), 4 mM (▼).

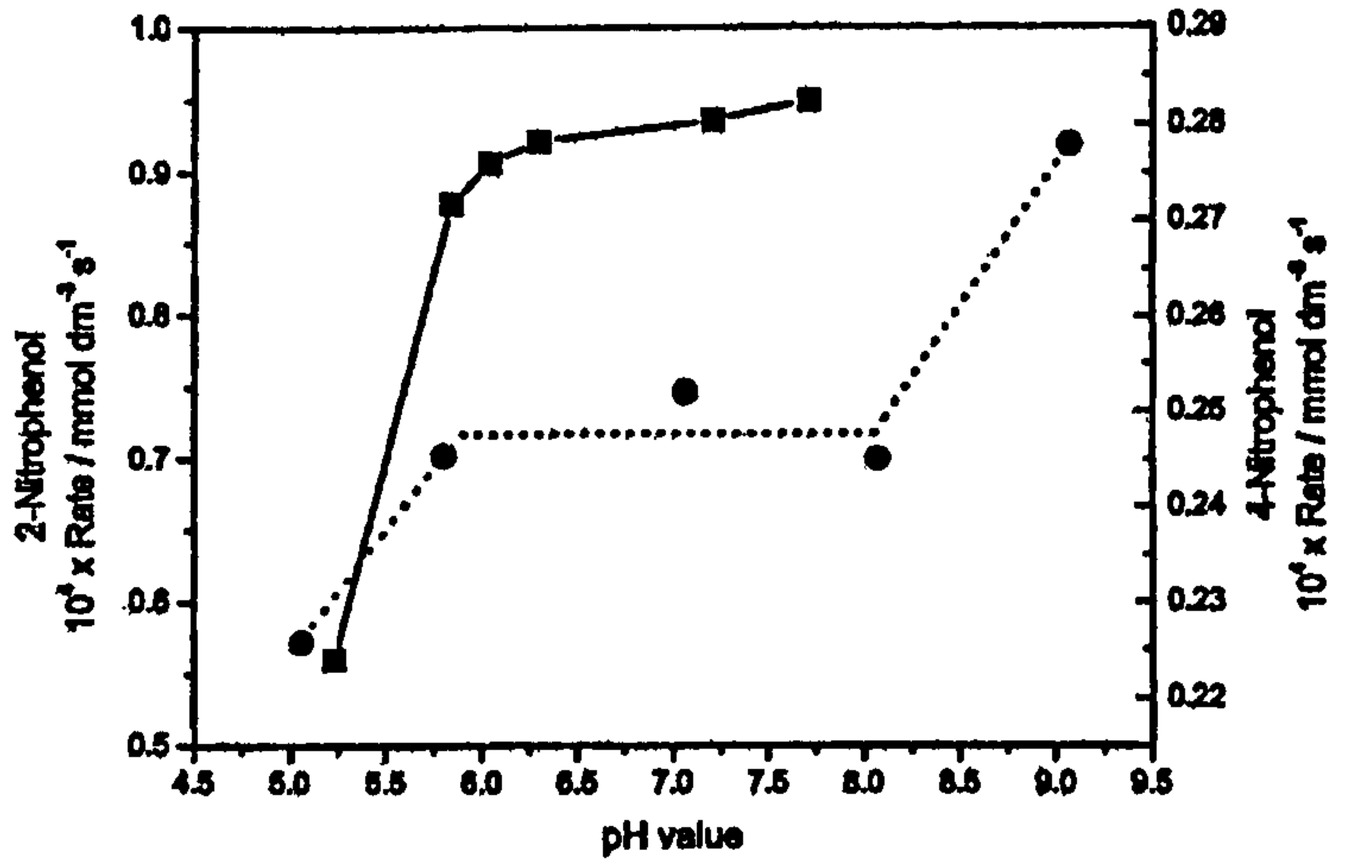

Fig. 6. The effect of pH on the initial degradation rate of 2-nitrophenol (■), left hand axis and 4-nitrophenol (●), right hand axis (1 mM initial concentration).

Table 3. Rates and derived rate constants, for photocatalytic removal of 4-nitrophenol in aqueous solution

C_0 4-NP Initial concentration/m mol dm^{-3}	10^4 × (Rate constant derived from the slope of Figure 5b)/s^{-1}	10^4 × Rate/m mol $dm^{-3}s^{-1}$
0.25	0.935	0.234
0.5	0.545	0.273
1	0.318	0.318
2	0.188	0.377
4	0.105	0.418

Table 4. Rates of degradation in the presence of bicarbonate relative to the rate at the same pH but in the absence of bicarbonate

10^3 × $[HCO_3^-]$/M	pH	10^4 × Rate/ mM s^{-1} in the presence of bicarbonate	10^4 × Rate/ mM s^{-1} at indicated pH, no bicarbonate	Bicarbonate induced Rate decrease%
0	5.2	0.560	0.560	0
2.2	5.8	0.785	0.878	11
4.4	6.0	0.743	0.907	18
8.8	6.3	0.693	0.922	25
17.6	7.2	0.645	0.937	31
35.2	7.7	0.578	0.950	39

system, a 16-fold increase in 4-NP concentration doubled the number of 4-NP molecules removed (Table 3) whilst a 20-fold increase in 2-NP concentration increased, by six, the number of 2-NP molecules removed (Table 2). This confirms that not all photons are being used. Thirdly, the variation in the apparent rate constant caused by fixed changes in concentration is not constant, but depends on other factors such as pH, see, e.g. [99].

Others have proposed that decreases in pseudo-first order rate constant with increased reactant concentration are caused by adsorption of intermediates or products. However, we emphasize the reduction of the effective UV flux at the surface of to catalyst particles.

4.1. *Nitrophenol adsorption*

The unexpected difference in adsorption of the two isomers mirrors a pattern in which the physical properties of 2-NP differ significantly from those of 3 and 4-NP. Thus 2-NP melts at a lower temperature, 45 °C, than 3-NP,97 °C or 4-NP, 144 °C. These differences are attributed to the strong intramolecular hydrogen bonds between the nitro-and ON groups in 2-NP which suppress intermolecular hydrogen bonding. No intramolecular bonds occur in the other isomers and hence intermolecular association loads, e.g., to the increased melting points of 3-NP and 4-NP. We suggest that the hydrogen bonding between. 4-NP molecules and H_2O and between and other 4-NP molecules reduces the adsorption of 4-NP at the solid surface. (The similar degree of adsorption of 2-NP and 2-6 dinitrophenol (DNP) [2121] on TiO_2 is consistent with this argument) 2-NP adsorption appears to reach an equilibrium value of $\sim 5 \times 10^{-2}$ mmol g^{-1} of TiO_2. If this corresponds to a monolayer, the calculated footprint of 0.98 nm^2 would agree reasonably well with 0.84 nm^2 estimated from bond lengths for a 2-NP flat on the surface. At higher solution concentrations of nitrophenol there is upturn in the isotherm (0.12 mmol g^{-1} at 7 mmol dm^{-3}) possibly caused by a change to a more vertical orientation of the adsorbed molecules.

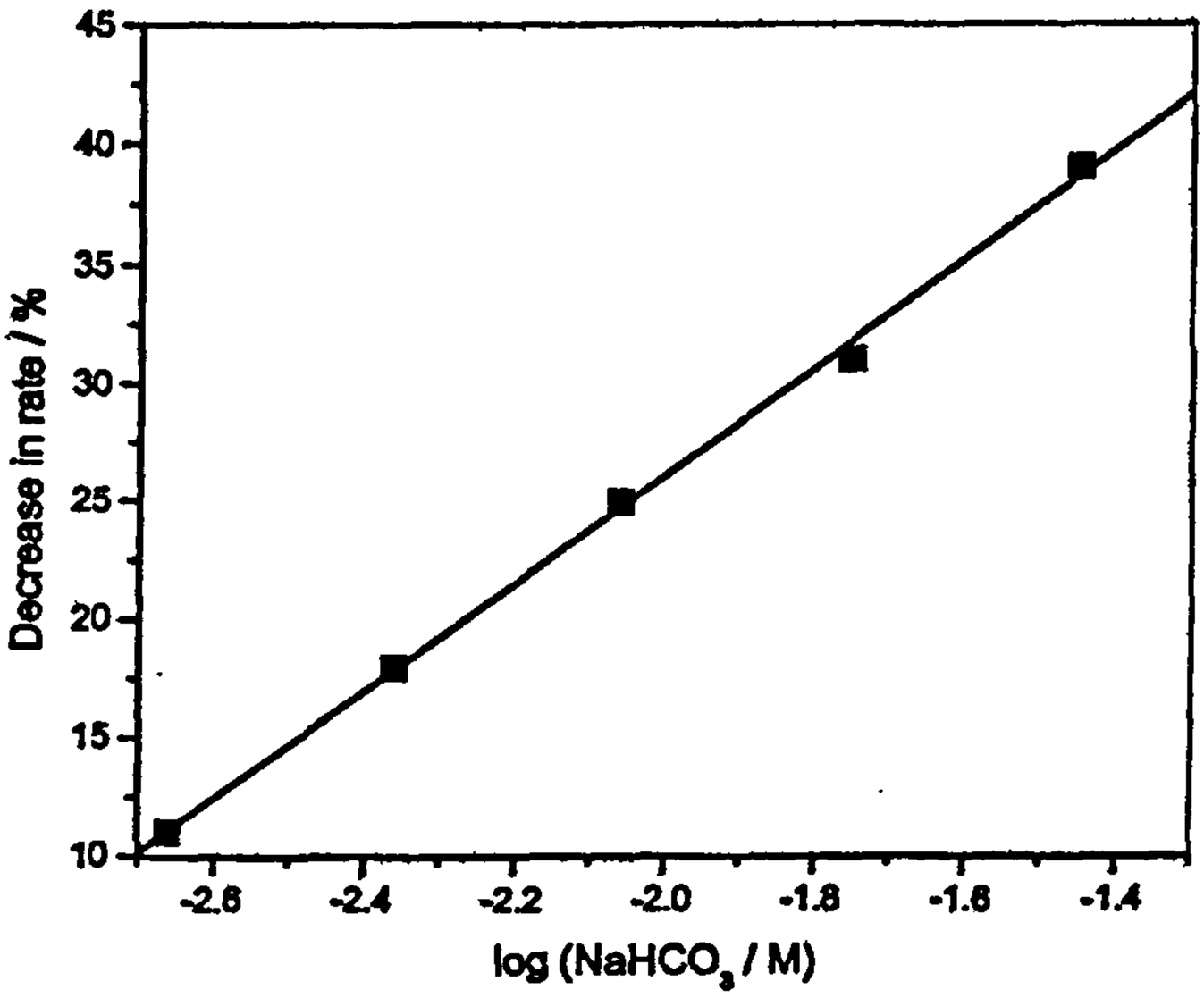

Fig. 7. The dependence of the % decrease in the rate of photocatalytic oxidation of 2-nitrophenol on the log of the concentration of sodium bicarbonate in solution.

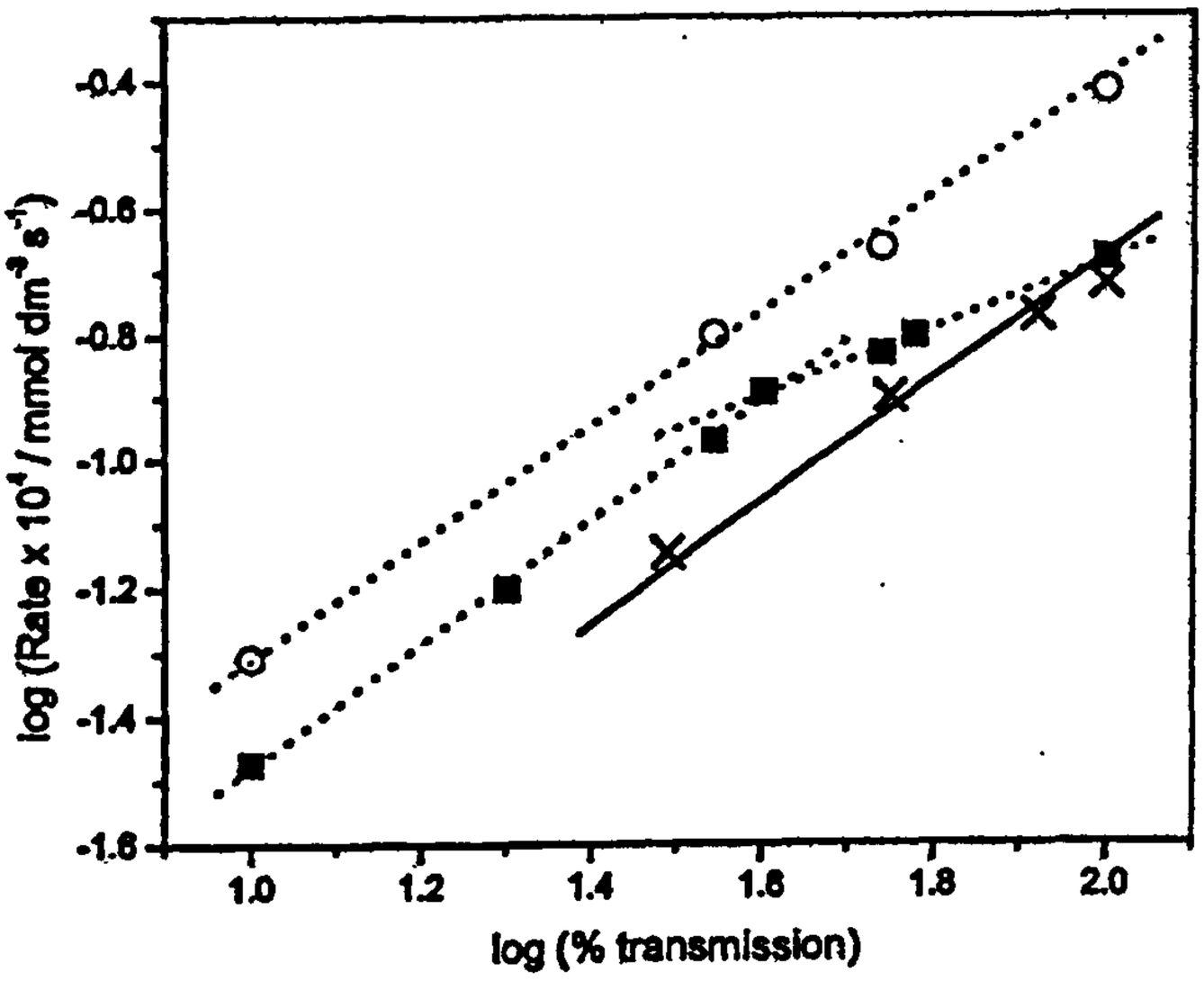

Fig. 8. Dependence of the rate of oxidation on the incident UV intensity for a (■) 0.25 mM; O 1 mM, 2-nitrophenol and × 0.25 mM 4-nitrophenol (solid line) solutions.

4.2. *The effect of nitrophenol concentration on the measured rates of oxidation*

The measured rates of 2-NP and 4- NP oxidation are shown in Figure 9. The measured first order rate constants, enumerated in Tables 2 and 3, decrease with increasing 2-NP or 4-NP concentration, as first reported by Augugliarno et al. [88] and confirmed by others [55, 99, 1212]. This decrease is generally attributed to competitive adsorption by degradation–intermediates but this seems improbable, in our case, because our results were derived using conditions that minimized the presence of reaction intermediates. The resulting simplified form of Equation (1)

$$\text{Oxidation Rate} = \frac{-dc}{dt} = -\text{kc} = \frac{-k_{\text{surf}} K_a c_s [\text{OH}^\bullet]_s}{1 + K_a c_s} \quad (2)$$

leads to a plateau value of the rate constant, k, but does not explain decrease.

Since the previous argument *assumes* that OH and adsorbed nitrophenol do not compete for the same sites, 1 mM 2-NP solution was oxidized for 10 h, to test the kinetics in an alternative way (To provide sufficient sample for analysis, this experiment was carried out in

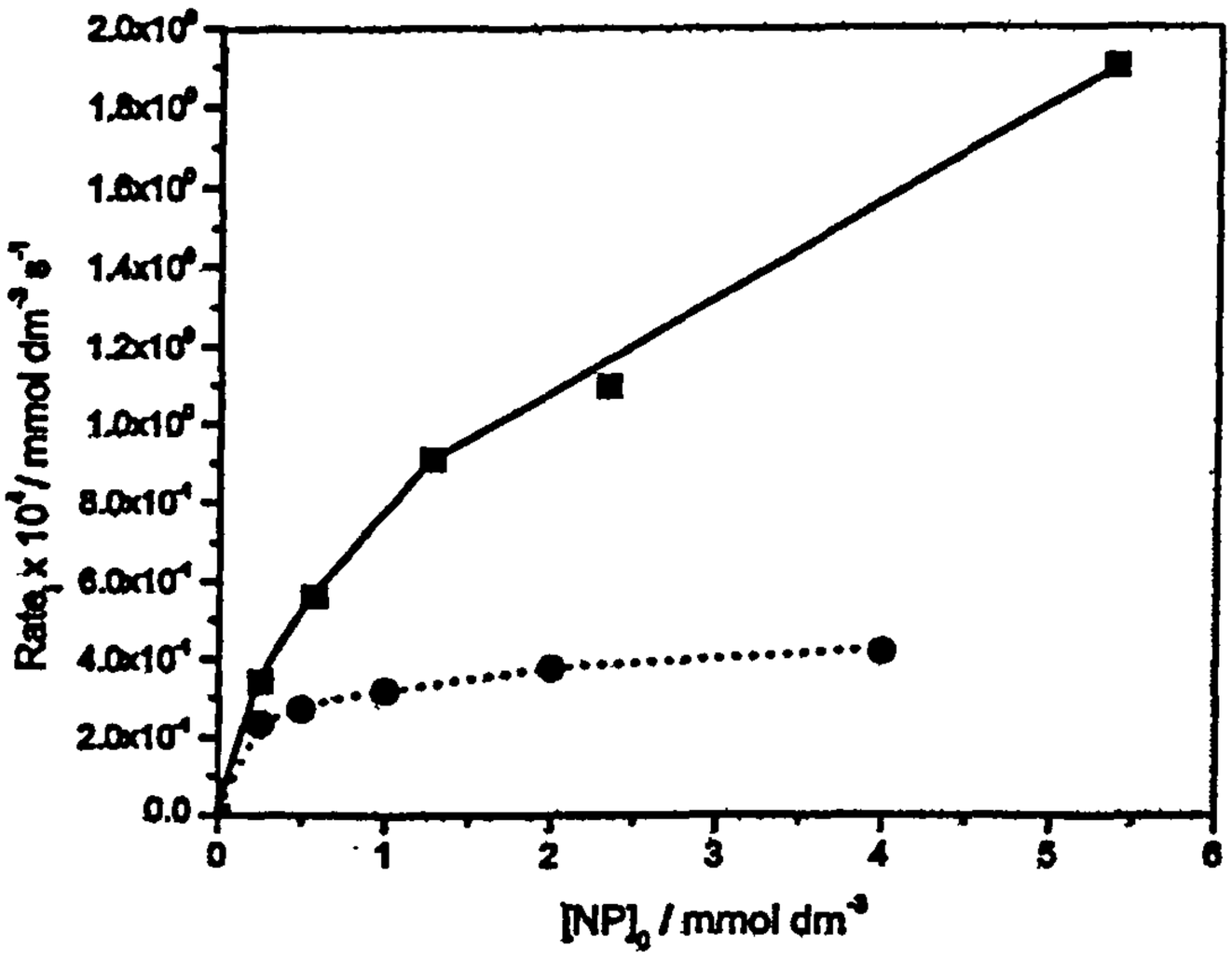

Fig. 9. Initial rate of disappearance of 2-nitrophenol and 4-nitrophenol and as a function of equilibrium concentration. (■) 2-nitrophenol; (●) 4-nitrophenol.

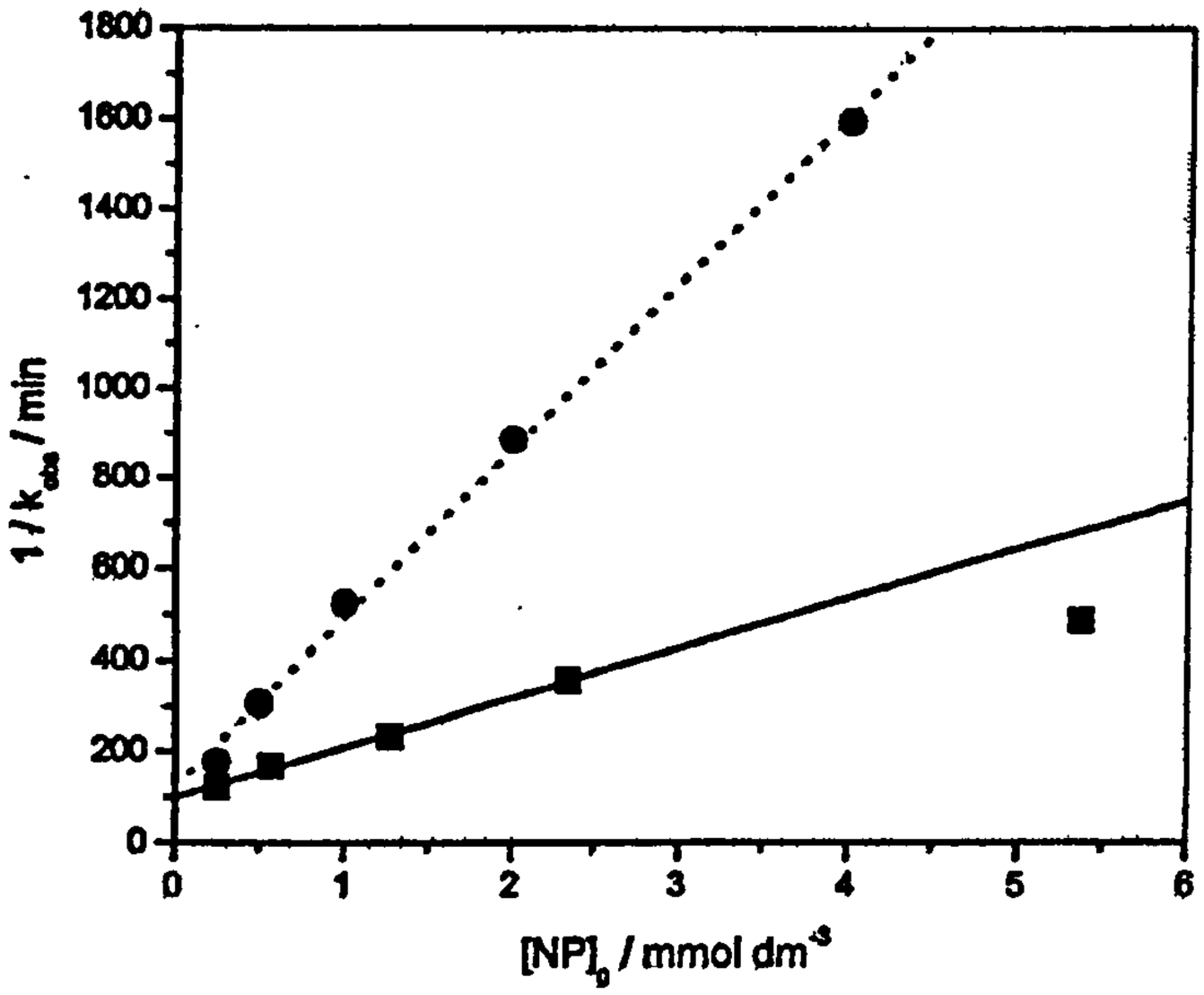

Fig. 10. Conventional test of Langmuir–Hinshelwood behaviour for 2-nitrophenol (■) and 4-nitrophenol (●).

the larger of the two reactors and because of slight differences in the optics the derived rate constants are not directly comparable with those in Table 2). At these long times the proportion of intermediates exceeds 20% of the total number of organic molecules, and could therefore be expected to affect the measured kinetics. The first order rate plot (see inset Figure 3a) showed no decrease in rate at reaction times greater than 360 min, as would have been expected if the surface was blocked by intermediates. Instead the deviation from the straight line is in the direction of *increased* degradation. Therefore, we again conclude that the decrease in measured rate constant with increased 2-NP concentration is unlikely to be caused by increasing competition by intermediate oxidation products.

The pattern of results found. for 2-NP is repeated for 4-NP. The adsorption results demonstrated that $K_{4\text{-NP}}$ (0.02 m mol^{-1} dm^3) $\ll$ $K_{2\text{-NP}}$ (0.4 m mol^{-1} dm^3) and therefore a Langmuir–Hinshelwood model would predict that the plot of oxidation rate vs. nitrophenol concentration would saturate less rapidly for than for Figure 9 shows that the reverse is the case. Although the conventional test of Langmuir–Hinshelwood behaviour – a plot (Figure 10) of $1/k_{obs}$ vs. c_0 gives acceptable straight lines – leading to values of $K_{2\text{-NP}} = 1.1$ $mmol^{-1}$ dm^3 ($k_{s\ 2\text{-NP}} = 0.018\times10^{-3}$ s^{-1}) and $K_{4\text{-NP}} = 3.1$ $mmol^{-1}$ dm^3 ($k_{s\ \ 4\text{-NP}} = 0.052\times10^{-3}$ s^{-1}) these values of K are inconsistent with those derived from direct measurements (Note also that the, often used, assumption that the adsorption constant K, for intermediate products equals the adsorptions coefficient of nitrophenol [55,99] does not fit well with the large differences in K found for the two nitrophenol isomers). Quantitative analysis does not support the LH model.

Thus, all three different approaches to analysis of the measured rate constants have indicated the inadequacy of a simple Langmuir–Hinshelwood model. Similar analyses, comparing adsorption constants inferred from oxidation kinetics of benzoic acids with those derived from direct adsorption measurements, led Cunningham and Al-Sayyed [2222] to conclude that for substituted benzoic acids, as for nitrophenol, the Langmuir–Hinshelwood model cannot fully explain the experimental results. Mills and Wang [1414] found that the values of K derived from kinetic of chlorophenol oxidation by photocatalyst slurries are much larger than that previously measured [2323] in the dark – i.e. the variation of oxidation rate with concentration is larger than would be predicted from adsorption measurements made in the dark. Surprisingly, values of K derived from measurements on immobilized films were smaller than those found for dispersions of the same TiO_2, even thought the rate of oxidation was higher on the immobilized film.

Table 5. Average pathlength corresponding to 90% absorption of the incident intensity between 300 and 400 nm

Nitrophenol solution Concentration/mM	Path length/corresponding to 90% attenuation for 2-NP solution	Path length/mm corresponding to 90% attenuation for 4-NP solution
0.25	–	7.64
0.5	8.2	5.02
1	4.6	2.37
2	2.6	2.62
4	1.4	1.32
8	0.8	–

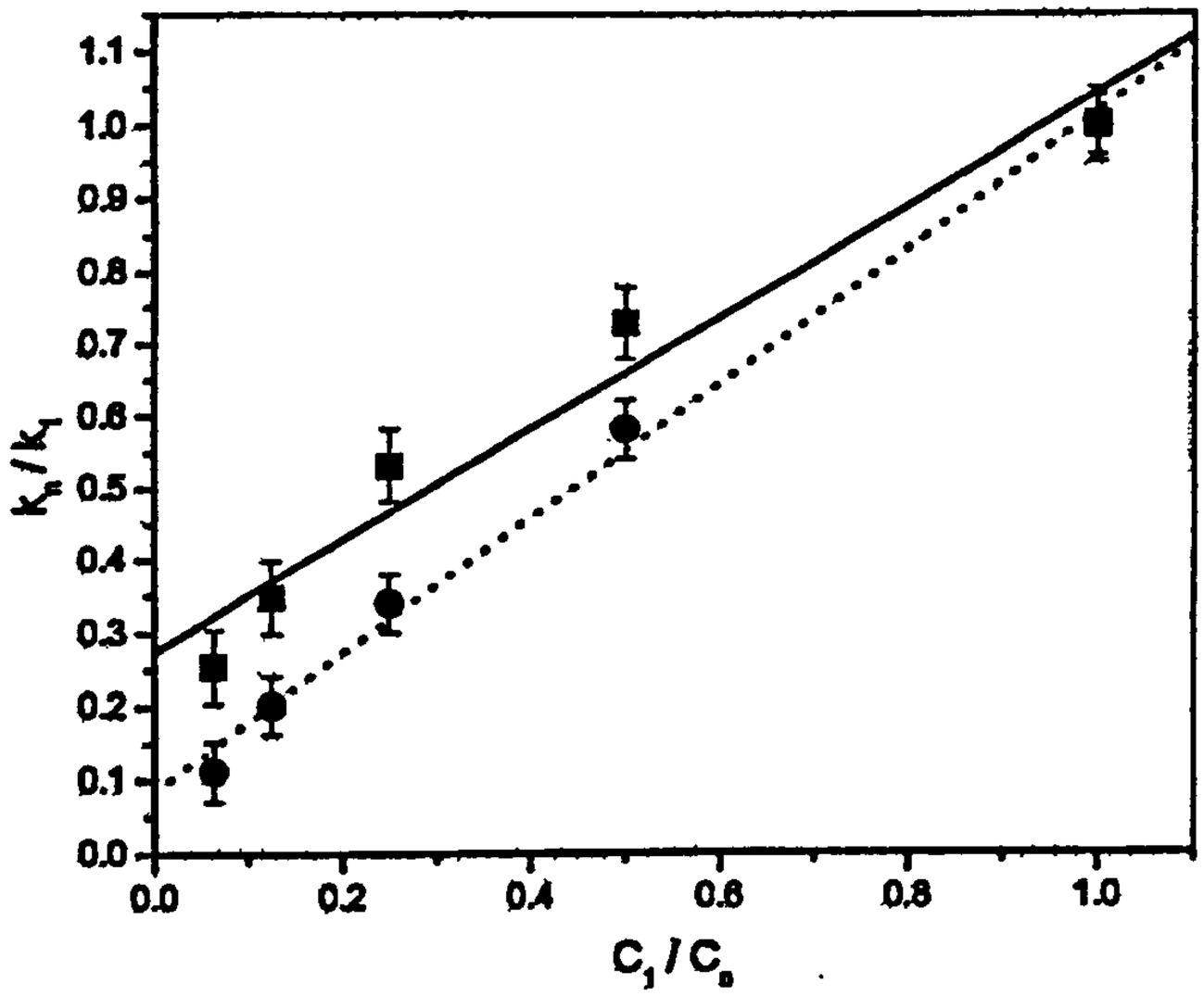

Fig. 11. Test for correlation of observed rate constants with proposed model for 2-nitrophenol (■) and 4-nitrophenol (●).

4.3. *UV absorption*

There is significant UV attenuation by nitrophenol solutions, even in the absence of TiO_2. For 2-NP, the mean path-length corresponding to an absorbance of 1, i.e. to absorption of 90% of the incident UV, was estimated at 20 nm intervals from 300 to 400 nm. Mean pathlengths, Table 5, decrease from 2 to 0.8 mm as the concentration increases from 0.5 to 8 mM. Not only is all of the incident UV absorbed within the reactor, but, in addition, the UV flux experienced by most TiO_2 particles is significantly less than that at the reactor window. We therefore propose that the most probable cause of the inconsistencies in the LH analysis of nitrophenol oxidation is a failure to account for changes in the hydroxyl radical concentration that result from the strong absorption of 300–400 nm radiation in solutions of aromatic compounds such as nitrophenol.

4.4. *The effect of UV absorption by nitrophenol on the measured oxidation rates*

The rate of many simple photocatalytic oxidations has been demonstrated to be proportional to I^n, where the value of n depends on the details of the charge-carrier recombination. At very low light intensities $n=1$ but at higher light intensities, when charge carrier recombination dominates, n falls to 0.5 [1919, 2020, 2424, 2525]. If the same lamps, catalyst and reactor, as used for the nitrophenol oxidation, are used for isopropanol oxidation, $n=0.5$ [2626], demonstrating that the UV flux is sufficiently large for charge-carrier recombination to dominate. However the corresponding results for nitrophenol oxidation show an I^1 dependence (except for 0.25 mM solutions of the more weakly absorbing 2-NP at high incident UV-intensity), The difference is attributed to strong UV attenuation, by the nitrophenol, which causes the effective UV flux at the catalyst particles to be much less that in a corresponding propan-2-ol/TiO_2 slurry. Consequently, the rate of charge carrier generation is lowered below the level at which recombination is rate-determining.

We consider the same UV attenuation by nitrophenol to be the main factor responsible for decreasing pseudo-first order rate constant with increasing nitrophenol concentrations; i.e. in Equation (1) the main cause of the decrease in k_{obs}, is the resultant decrease in $[OH]_s$ rather than the increase in the denominator suggested by the Langmuir–Hinshelwood model. A semi-quantitative analysis, ignoring UV attenuation by TiO_2, assumes that the useful intensity, I, at a catalyst particle is the amount not absorbed by the nitrophenol, If I_0 is the UV intensity incident on the reactor, the pseudo-first order rate constant, k, at a catalyst particle at a distance x from the reactor window is,

$$k = \kappa I = \kappa I_0 \, e^{-\alpha x c} \tag{3}$$

where, α is the absorption coefficient of the nitrophenol of concentration c and κ is a constant. Integrating over all distances from 0 to leads to the expression

$$k = \frac{\kappa I_0}{\alpha c} \tag{4}$$

and for two different concentrations (A and B) of nitrophenol

$$\frac{k_A}{k_B} = \frac{c_B}{c_A}$$

A plot of k_A/k_B vs. c_B/c_A should therefore be a straight line. In Figure 11, the predicted behaviour is compared with the experimental results by normalising the results to B = 1 mM. The agreement is as good as can realistically be expected for a model which ignores scattering and absorption by the titania particles, and supports the conclusion of the 'rate vs. intensity study' that UV absorption by the nitrophenol is the major cause of the observed decrease in pseudo-first order rate constant with increasing concentration of nitrophenol.

4.5. *The effect of pH on the rate of nitrophenol oxidation*

Although the measurement of pH dependence of oxidation rate was carried out only to provide a reference for the bicarbonate addition, studies, we note that the increase in oxidation rate of 2-NP as pH is increased from 5 to 10 is qualitatively predicted by the corresponding decrease in both 350 and 365 nm absorption (Figure 1a inset). Quantitatively, this increase will depend not only on the nitrophenol concentration but also on the reactor geometry and wavelength distribution of the lamp This may explain why different studies reported diverging conclusions with respect to the dependence of oxidation rate on pH.

4.6. *The comparative oxidation rates of 2 and 4-nitrophenol*

Light absorption would affect comparisons of the relative rates of photocatalytic oxidation of different nitrophenols. Our direct comparison gave relative rates for 1 mM 2-NP and 4-NP of 1:0.61. However, these relative rates depend on concentration and Figure 9 shows that the rates of 2N and 4-NP converge at low concentrations (though these 4-NP oxidations were measured some time after the 2-NP photo-oxidations.) Again, the comparative rates will also depend on the reactor geometry and wavelength distribution of the lamp. For example, measurements made with an immersed lamp reactor are likely to decrease the importance of 4-NP's greater absorption at 365 nm. Palmisano et al. [88] report that, using 50 ml flasks placed in a (Xe lamp) Solarbox the oxidation rate of 24 was 1.25 times that of 4 NP. However, when an immersed lamp (500 W Hg lamp) reactor was the two rates were similar.

5. Conclusions

We have analyzed nitrophenol oxidation kinetics under conditions which were demonstrated to give a low concentration of intermediates. We therefore consider that the decreases in the measured pseudo-first order kinetic rate constants are not primarily controlled by adsorption of reaction intermediates. Further, the adsorption constants derived from a Langmuir–Hinshelwood analysis of the rates of degradation of 2 and 4-NP are not only quantitatively different from those determined by direct adsorption measurements but their relative magnitude is reversed. We propose that the major cause of the reduction in measured rate constants is UV absorption by nitrophenol. This absorption reduces the photon flux available at the surface of catalyst particles in suspension.

Although there is substantial agreement that first order rate constants decrease with increasing nitrophenol concentration, there is much less agreement concerning the relative rates of oxidation of the different isomers. We suggest that this is because changes in optical conditions affect the various isomers differently because they absorb differently. Similarly the practical effects of changed UV absorption associated with pH changes will depend on both the reactor geometry and the wavelength distribution of the UV.

The most general conclusion of this paper is that UV absorption by reactants must be taken into account when designing practical reactors for photocatalytic or photocatalytic degradation of strongly absorbing solutions. This is particularly important when designing either photocatalytic or photo-electrocatalytic reactors employing immobilized catalyst [1818].

References

1. A. Mills and S.L. Hunte, *J. Photochem. Photobial. A: Chem.* **108** (1997) 1.
2. A. Fujishima, T.N. Rao and A. Donald, *J. Photochem. Photobiol. C: Rev.* **108**(1) (2000) 1.
3. K. Tanaka, W. Luesaiwong and T. Hisanaga, *J. Mol. Catal.* **122** (1997) 67.
4. K.H. Wang, Y.H. Hsieh and L.J. Chen, *J. Hazard. Mater.* **59** (1998) 251.
5. D. Chen and A.K. Ray, *Water Res.* **32** (1998) 3223.
6. C. E Homecroft and E.C. Constable, *Chemistry* 2nd ed., (Pearson Education Ltd, Harlow, 2002) p. 970.
7. A. Reingold, 'Organic Chemistry' (Houghton Miflin, New York, 2002), pp. 756.
8. V. Augugliarno, L. Palmisano, M. Schiavello and A. Sclafani, *Appl. Catal.* **69** (1991) 323.
9. V. Augugliarno, M.J. Lopez-Munoz, L. Palmisano and J. Soria, *Appl. Catal.* **101** (1993) 7.
10. R. Andreozzi, V. Caprio, A. Insola, G. Longo and V. Tufano, *J. Chem. Tech. Biotechnol.* **75** (2000) 131.
11. J. Lea and A.A. Adesina, *J. Chem. Tech. Biotechnol.* **76** (2001) 803.
12. N. San, A. Hatipoglu, G. Kocturk and Z. Cinar, *J. Photochem. Photobiol. A:Chem.* **146** (2002) 189.
13. C.S. Turchi and D.F. Ollis, *J. Catal.* **122** (1990) 178.
14. A. Mills and J. Wang, *J. Photochem. Photobiol. A:Chem.* **118** (1998) 53.
15. D. Chen and A. K. Ray, *Appl. Catal. B: Environ.* **23** (1999) 143.
16. J.C. Harper, P.A. Christensen, T.A. Egerton and K. Scott, *J. Appl. Electrochem.* **31** (2001) 267.
17. T.A. Egerton and I.R Tooley, *J. Mater. Chem.* **12** (2002) 1111.
18. P.A. Christensen, T.A. Egerton, S. Kosa, J.R. Tinlin and K. Scott, *J. Appl. Electrochem.* **35** (2005) 581–590.

19. T.A. Egerton and P. A. Christensen, *in* S. Parsons (ed.), 'Advanced Oxidation Processes for Water and Wastewater Treatment', (IWA Publishing, London, 2004) p. 167.
20. T.A. Egerton and C.J. King, *J. Oil. Col. Chem. Assoc.* **62** (1979) 386.
21. R.W. Harrison, Photocatalytic Degradation of Nitrophenols by Titanium Dioxide, M.Phil. Thesis (University of Newcastle Upon Tyne, Newcastle Upon Tyne, 2001).
22. J. Cunningham and G. Al-Sayyed, *J. Chem. Soc. Faraday. Trans.* **86** (1990) 3935.
23. A. Mills and S. Morris, *J. Photochem. Photobiol. A: Chem.* **71** (1993) 75.
24. J.C.D. Ollveira, G. Al-Sayyed and P. Pichat, *Environ. Sci. Technol.* **24** (1990) 990.
25. G. Al-Sayed, J.C.D. Ollveira and P. Pichat, *J. Photochem. Photobiol. A: Chem.* **58** (1991) 99.
26. T.A. Egerton and I.R. Tooley, *J. Phys. Chem. B.* **108** (2004) 5066.

APPENDIX 2

'An EPR study of thermally and photochemically generated radicals on hydrated and dehydrated titania surfaces' A. L. Attwood; D. M. Murphy; J. L. Edwards; T. A. Egerton; R. W. Harrison, *Res. Chem. Intermed*, **2003**, *29*, 449.

VSP 2001/04/20 Prn:16/05/2003; 9:43 {RA} F:rc12208.tex; VTeX/lina p. 1 (47-123)

Res. Chem. Intermed., Vol. 00, No. 0, pp. 1–17 (2003)

Also available online - www.vsppub.com

An EPR study of thermally and photochemically generated oxygen radicals on hydrated and dehydrated titania surfaces

A. L. ATTWOOD [1], D. M. MURPHY [1,*], J. L. EDWARDS [2], T. A. EGERTON [3] and R. W. HARRISON

[1] *Department of Chemistry, Cardiff University, P.O. Box 912, Cardiff CF10 3TB, UK*
[2] *Huntsman Tioxide, Haverton Hill Road, Billingham TS23 IPS, UK*
[3] *School of Chemical Engineering and Advanced Materials, University of Newcastle, Newcastle NE1 7RU, UK*

Received 21 April 2003; accepted 25 April 2003

Abstract—The formation of a series of oxygen-centred radicals on different TiO_2 samples (P25 and two different rutile materials) under various conditions was investigated using X-band c.w. Electron Paramagnetic Resonance (EPR) spectroscopy. The radicals were formed either on thermally-reduced TiO_2, or by UV irradiation of the oxide under an oxygen atmosphere. The nature and stability of the radicals was also explored as a function of surface hydration. On thermally reduced TiO_2, containing surface and bulk Ti^{3+} centres, oxygen adsorption at 300 K results in the preferential formation and stabilisation of O_2^- anions on the P25 surface, but O^- and O_3^- anions are generated on the rutile surfaces. Superoxide anions (O_2^-) and trapped holes (O^-) were also identified after photo-irradiation of the thoroughly dehydrated TiO_2 samples under oxygen. The O^- anions were only visible at low temperatures under continuous irradiation, while the O_2^- anions were stable for days at 300 K. By comparison, on fully hydrated surfaces, no stable oxygen centred radicals could be detected on P25, while O_2^- anions were easily observed on the rutile surfaces. On partially hydrated P25, the O^-, O_2^- and HO_2^- anions were detected after UV irradiation at 77 K; all radicals decayed upon warming to 298 K. On partially hydrated rutile, the O^- and O_2^- anions were detected and, unlike the case for P25, were found to be stable for days under the same conditions. The results illustrate the varied formation and stability of the oxygen centred radicals on TiO_2 surfaces depending on the pretreatment conditions.

Keywords: EPR; titanium dioxide; oxygen radicals; hydrated surface

*To whom correspondence should be addressed. E-mail: murphydm@cardiff.ac.uk

VSP 2001/04/20 Prn:16/05/2003; 9:43 {RA} F:rc12208.tex; VTeX/lina p. 2(123-190)

INTRODUCTION

Photocatalytic reactions involving semiconductor metal oxides, such as titanium dioxide (TiO_2), have attracted significant attention in the past 10 years, because of their wide ranging applications from solar energy conversion and environmental clean-up to the transformation of chemical feedstocks [1–5]. In many cases, the successful applications of these materials relies on the photocatalytic reactions which occur at the oxide surface. An understanding of the interfacial photochemistry at the molecular level, particularly the fundamental chemistry of electron and hole transfer to the adsorbed substrate, is therefore considered central to the design of more improved photocatalysts with high quantum yields.

It is well recognised that upon band-gap irradiation of TiO_2, the photogenerated electrons and holes are ultimately responsible for the photocatalytic redox reactions. While the mechanistic details remain uncertain, it is clear that the presence of oxygen and water is crucial in controlling the reaction pathways often *via* the intermediacy of active oxygen species [6–8]. Since these active oxygen species can be trapped and stabilised at the TiO_2 surface, the Electron Paramagnetic Resonance (EPR) spectroscopy technique is ideally suited to studying these systems [9–11]. Several types of active oxygen species have been characterised and proposed as reaction intermediates in the photocatalytic process, including the mononuclear oxygen anion (O^-), superoxide (O_2^-), ozonide (O_3^-), hydroxy ($HO^\cdot$), hydroperoxy ($HO_2^\cdot$), alklyperoxy ($ROO^\cdot$) or other precursor states such as hydrogen peroxide (H_2O_2) or singlet oxygen ($^1O_2$) [12–25]. These radicals are formed by interfacial charge transfer at the gas–solid interface, and provided the lifetime of the radicals are sufficiently long, many can be unambiguously detected by EPR. For example, superoxide anions are easily formed by interfacial electron transfer from trapped electron sites to adsorbed dioxygen ($Ti^{3+}_{surf} + O_2 \rightarrow Ti^{4+} \cdots O_2^-$), and the anions can then react with protons on the hydrated surface producing hydroperoxy radicals ($O_2^- + H^+ \rightarrow HO_2^\cdot$). Both radicals produce very characteristic spin Hamiltonian EPR parameters. On the other hand the positive holes can be trapped by lattice oxide ions ($Ti^{4+} - O^{2-} + h^+ \rightarrow Ti^{4+} - O^-$) and at surface hydroxyl groups forming hydroxy radicals ($OH^- + h^+ \rightarrow OH^\cdot$). The formation of ozonide radicals by reaction of molecular oxygen with a trapped hole has also been reported ($Ti^{4+} - O^- + O_2 \rightarrow Ti^{4+} \cdots O_3^-$) [20]. Other competing surface reactions may also occur, leading to a decrease in surface radical concentration, such as the recombination of surface hydroxy radicals producing additional radical species ($2OH^\cdot \rightarrow H_2O_2$, and $H_2O_2 + OH^\cdot \rightarrow O_2H^\cdot + H_2O$), or continued capture of photogenerated electrons producing diamagnetic species ($O_2^- + e \rightarrow O_2^{2-}$) not visible by EPR.

The complexity of the interfacial reactions, coupled with the variabilities in the abundance, nature and indeed lifetime of the radicals as a function of surface treatment or morphology, suggests that the nature of the active oxygen species may change depending on the reaction conditions. While EPR can provide clear evidence

for the existence of stable surface oxygen radicals, it may not readily detect transient unstable species ($ROO^{\cdot}$) which may be more reactive and participate more extensively in the photocatalytic process, at the expense of the long-lived EPR-visible species. In the this paper we will demonstrate that the nature of the paramagnetic oxygen species can change depending on the pretreatment conditions and nature of the surface, and thereby illustrate the importance of studying these surface radicals under various conditions to fully understand the initial electron-transfer reaction processes.

EXPERIMENTAL

The P25 titanium dioxide used throughout this work was supplied by Degussa (surface area 49 $m^2\,g^{-1}$). The high surface area rutile material (surface area approx. 135 $m^2\,g^{-1}$, hereafter labelled Rutile A sample) was synthesised by hydrolysis of an aqueous solution (about 5 M) of $TiCl_4$. The medium surface area rutile TiO_2 material (hereafter called Rutile B sample) used throughout this work was supplied by the Solaveil business of ICI, Uniqema when owned by Tioxide (surface area 97 $m^2\,g^{-1}$). The polycrystalline TiO_2 powders (*ca.* 5 mg) were slowly heated (over a 5-h period) under vacuum (10^{-4} torr) up to a maximum temperature of 823 K, and held at this temperature for a further hour. The reduced powder (blue in colour due to the excess number of Ti^{3+} centres [16]) was then cooled to 300 K and exposed to oxygen (10 torr) at this temperature for 5 min. The excess oxygen was subsequently evacuated at room temperature, and the EPR spectra were recorded at 100 K. In order to prepare a clean dehydrated sample, the TiO_2 powder was reduced at 823 K (as described above) and subsequently exposed to oxygen (50 torr) at this temperature for 30 min. The sample was then cooled to room temperature under the oxygen atmosphere, producing a clean activated surface free from contaminants. The excess oxygen was subsequently evacuated at room temperature. The activated material was then exposed to the probe gases (10 torr) at 298 K.

The high purity O_2 gas was supplied by BOC Ltd. Triply-distilled water was used in the hydration experiments, and was subjected to repeated freeze–pump–thaw steps prior to use. A 1000 W Oriel Instruments UV lamp, incorporating a Hg/Xe arc lamp (250 nm to >2500 nm), was used for all irradiations in the presence of a water filter. The UV output below 280 nm accounts for only 4 to 5% of the total lamp output. The EPR spectra were recorded on a Varian E-109 spectrometer and a Bruker ESP-300e series spectrometer. All spectra were recorded at X-band frequencies (≈9 GHz), 100 kHz field modulation and 10 mW microwave power. The g values were obtained using a DPPH standard. EPR computer simulations were performed using the SIM14S programme (QCPE 265).

VSP 2001/04/20 Prn:16/05/2003; 9:43 {RA} F:rc12208.tex; VTeX/lina p. 4 (246-325)

RESULTS AND DISCUSSION

Oxygen adsorption of thermally reduced TiO_2

The response of anatase (P25) and rutile TiO_2 to reduction *in vacuo* at various temperatures was measured in order to determine the optimum temperature of reduction for solid–gas interface studies. In all cases, the thermally reduced materials produced an intense blue colour as expected. The EPR spectra, measured at 100 K, for thermally reduced P25, rutile A and rutile B are shown in Figs 1a, 2a and 3a, respectively. The samples were reduced under vacuum (10^{-4} torr) at varying temperatures from 573 K to 873 K, and qualitatively the spectra are similar in all cases. The P25 sample reduced at 573K contains an extra sharp feature at $g = 1.99$ due to traces of interstitial Ti^{3+} centres.

The appearance of these spectra arises from the thermovacuum reduction of the materials. The bulk and surface reduction of the samples is clearly evidenced by the increase in intensity of the Ti^{3+} resonance at $g = 1.962$. This signal has been reported previously [18, 22, 23] and has been assigned to a composite resonance arising from both surface and bulk Ti^{3+} centres formed *via* O_2 loss from the oxide surface during thermal reduction under vacuum;

$$2O^{2-}_{(latt)} \rightarrow O_{2(g)} + 4e^-, \tag{1}$$

$$4Ti^{4+} + 4e^- \rightarrow 4Ti^{3+} \tag{2}$$

As the reduction temperature is increased, the signal due to the medium polarised conduction electrons at $g = 2.0023$ also increases. Simultaneously, the Ti^{3+} signal broadens considerably due to extensive spin–spin interactions occurring at the higher Ti^{3+} concentrations. As a result accurate integrations of the spectra are not possible. At temperatures higher than 873 K extensive bulk reduction occurs, as the proportion of Ti^{3+} centres formed in the oxide bulk increases as a fraction of the total Ti^{3+} signal at $g = 1.962$ [18].

After addition of 10 torr of oxygen at 298 K, the blue colour of each sample was immediately bleached, and the EPR spectra of the trapped electron centres in the TiO_2 lattice (i.e. Ti^{3+} and medium polarised conduction electrons) were immediately replaced by the spectra shown in Figs 1b, 2b and 3c for P25, rutile A and rutile B, respectively. In the case of P25, the new spectra can easily be assigned to adsorbed superoxide (O_2^-) anions. This assignment has been unambiguously confirmed using ^{17}O-enriched O_2 (spectra not shown) where the observed hyperfine pattern is identical to that expected for the side-on bonded ionic superoxide species [9, 10, 26]. After reduction of P25 at 573 K, the g components $g_{xx} = 2.002$, $g_{yy} = 2.008$ and $g_{zz} = 2.018$ can be seen, indicating the presence of a single adsorption site for the anion on the TiO_2 surface after reduction at this temperature. However, at higher reduction temperatures, the complexity of the g_{zz} region increases; new features are observed at $g_{zz} = 2.022$ and 2.025. This indicates the presence of additional adsorption sites for the anion, possibly arising from the

VSP 2001/04/20 Prn:16/05/2003; 9:43 {RA} F:rci2208.tex; VTeX/lina p. 5 (325-325)

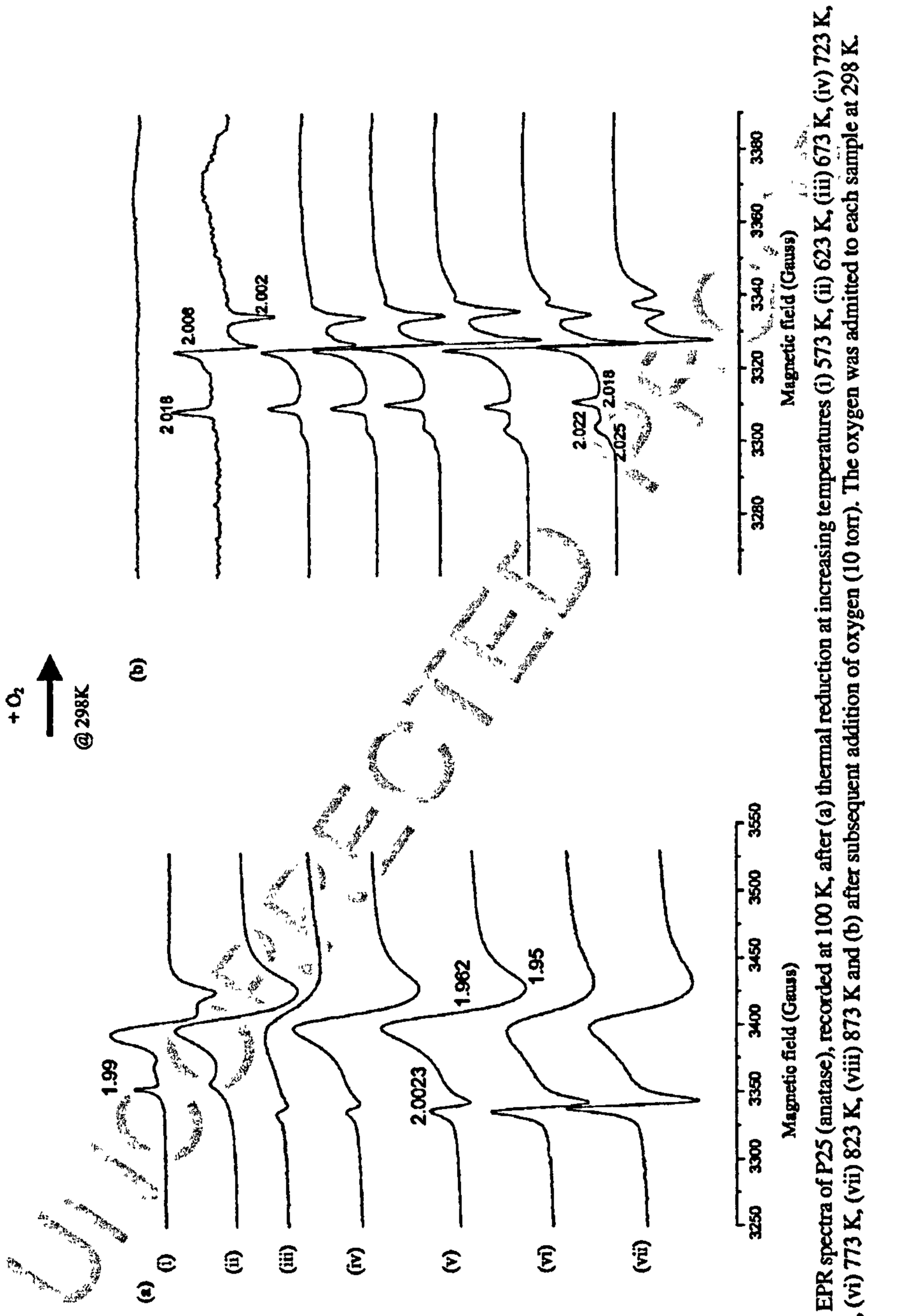

Figure 1. EPR spectra of P25 (anatase), recorded at 100 K, after (a) thermal reduction at increasing temperatures (i) 573 K, (ii) 623 K, (iii) 673 K, (iv) 723 K, (v) 723 K, (vi) 773 K, (vii) 823 K, (viii) 873 K and (b) after subsequent addition of oxygen (10 torr). The oxygen was admitted to each sample at 298 K.

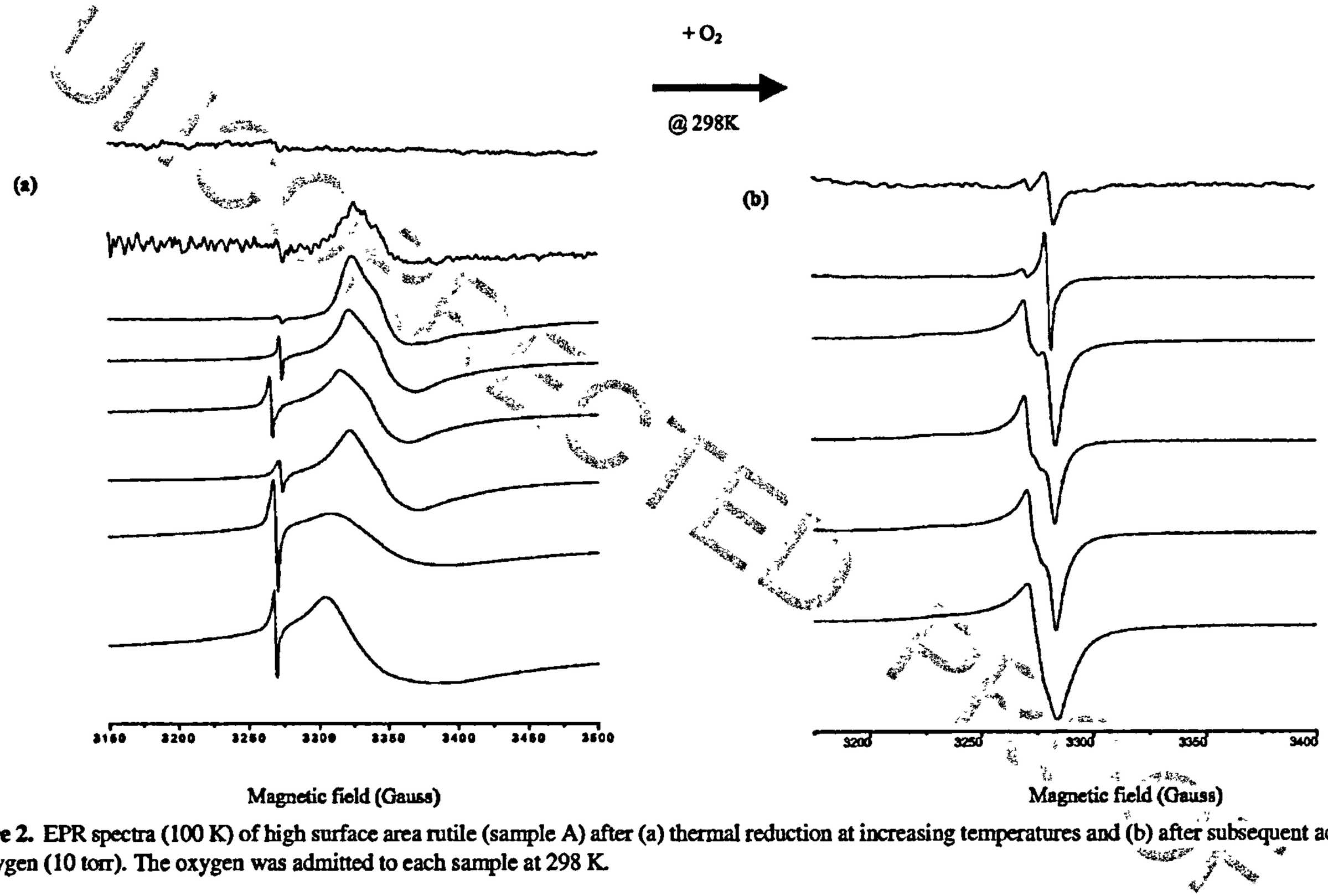

Figure 2. EPR spectra (100 K) of high surface area rutile (sample A) after (a) thermal reduction at increasing temperatures and (b) after subsequent addition of oxygen (10 torr). The oxygen was admitted to each sample at 298 K.

VSP 2001/04/20 Prn:16/05/2003; 9:43 {RA} F:rci2208.tex; VTeX/lina p. 6 (325-325)

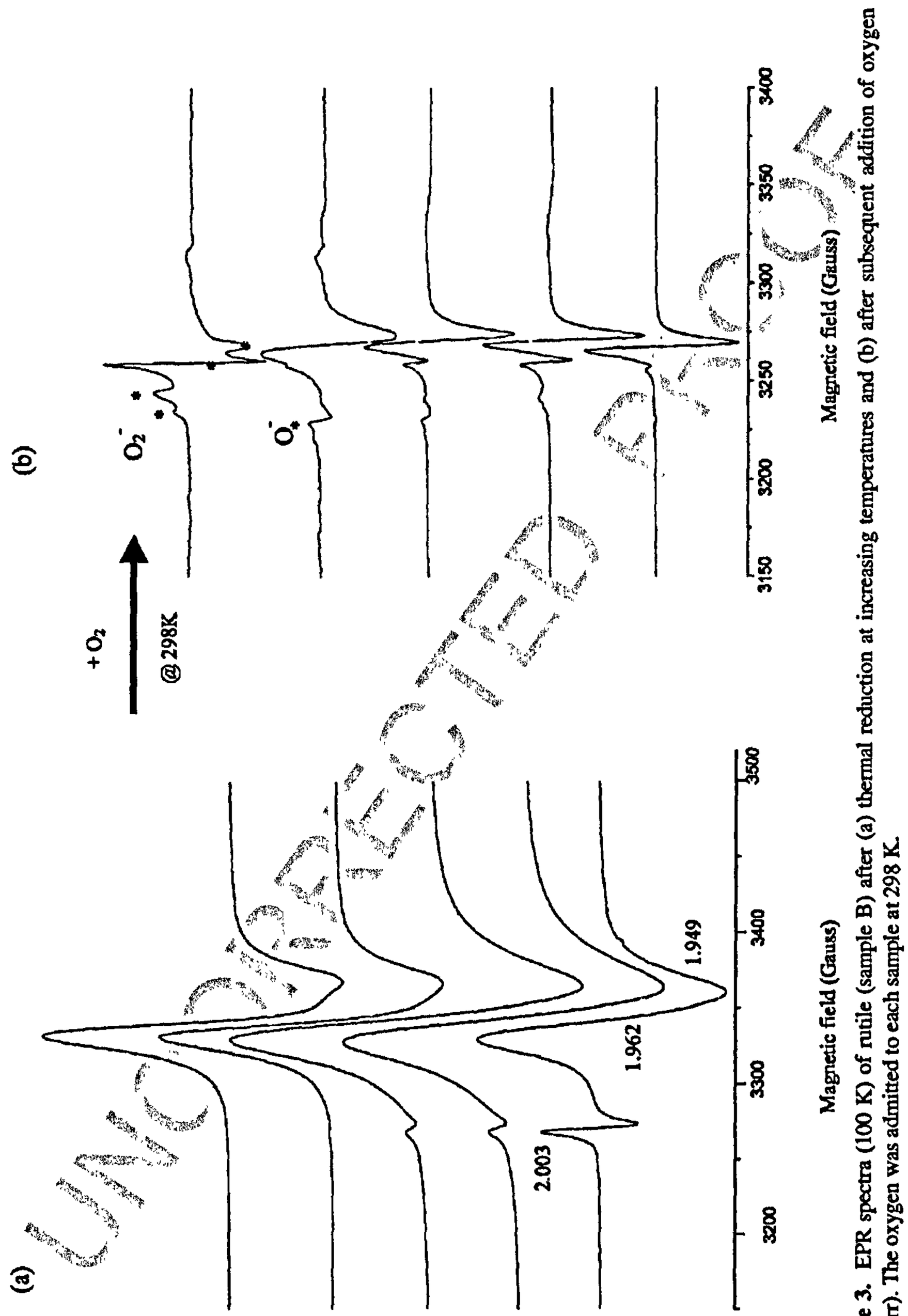

Figure 3. EPR spectra (100 K) of rutile (sample B) after (a) thermal reduction at increasing temperatures and (b) after subsequent addition of oxygen (10 torr). The oxygen was admitted to each sample at 298 K.

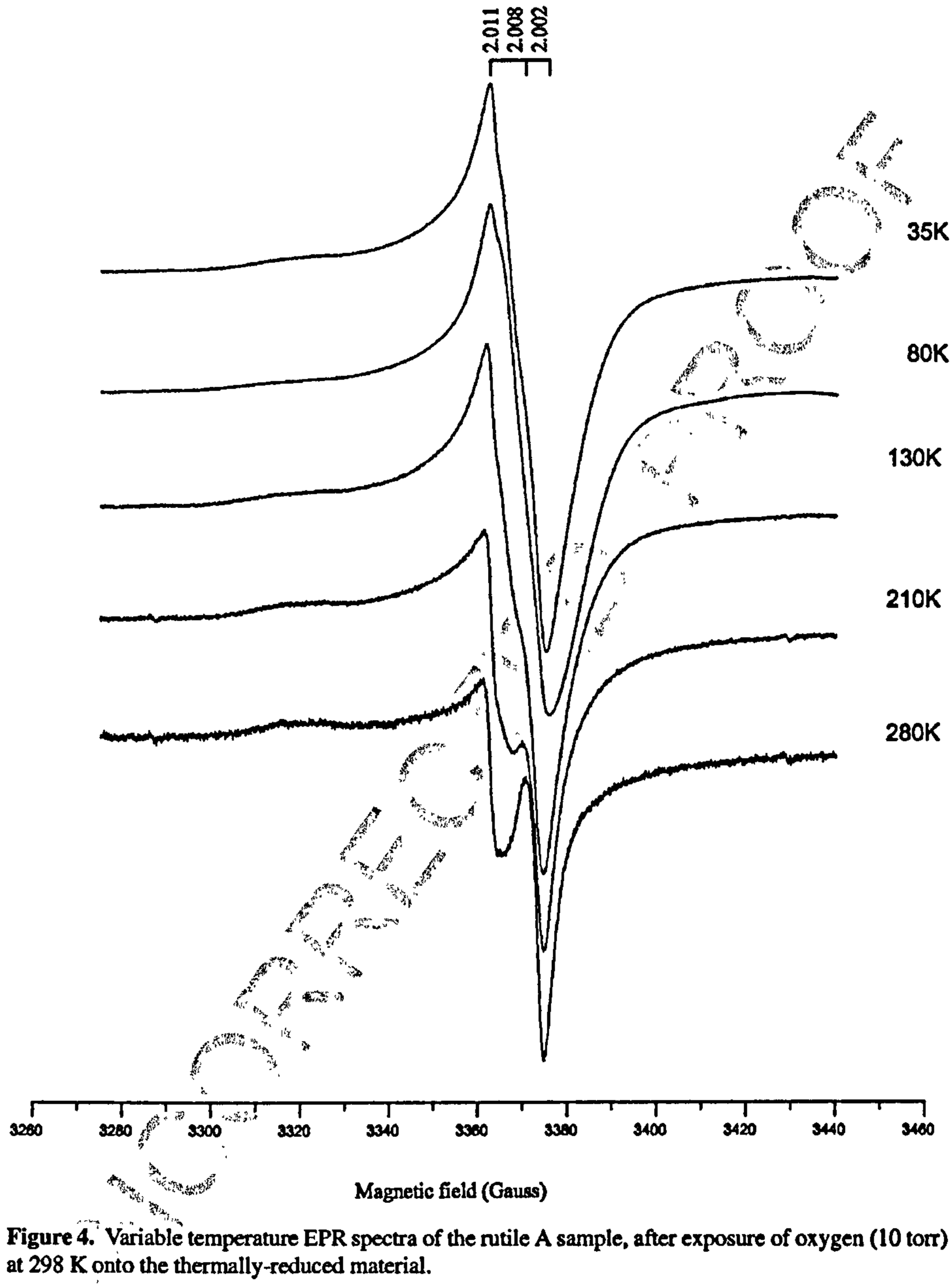

Figure 4. Variable temperature EPR spectra of the rutile A sample, after exposure of oxygen (10 torr) at 298 K onto the thermally-reduced material.

increased heterogeneity of defect sites which trap the anions on the increasingly more reduced and therefore more non-stoichiometric surface.

In the case of rutile A and B, the resulting EPR spectra of the bleached samples display far smaller amounts of adsorbed superoxide, i.e. the characteristic O_2^- peaks

are virtually absent. On the contrary, for the high surface area rutile (sample A) the EPR spectra shown in Fig. 2b can be easily assigned to the adsorbed ozonide anion (O_3^-) with the g components $g_{xx} = 2.003$, $g_{yy} = 2.008$ and $g_{zz} = 2.011$. This assignment is also confirmed by the variable temperature study (Fig. 4) which indicates the dynamic rotational characteristics of the anion at elevated temperatures. The EPR spectra of oxygen adsorbed on rutile sample B are more complex and reveal an apparent intermediate trend where O^- and O_2^- anions are simultaneously visible at different temperatures (Fig. 3b). Furthermore, the intensity of the spectra in Fig. 3b are far less intense compared to the initial Ti^{3+} signal, suggesting that the majority of the reduced oxygen species following electron transfer from the rutile surface produce diamagnetic centres.

It is clear from the results presented above that surperoxide formation and stabilisation is the main process occurring on the predominantly anatase surface of P25 according to equation (3). This is an exothermic reaction (−42 kJ/mol) facilitated by the additional Coulombic stabilisation from the lattice, and is not unexpected. On the other hand, the formation of ozonide radicals on the rutile surface implies that oxygen dissociation must first occur; i.e. O^- anions must be generated upon oxygen adsorption on the reduced surface, as a precursor to ozonide formation. The likely source of O^- anions originates from dissociation of the peroxide anion O_2^{2-} formed in a simultaneous or sequential reduction of O_2 according to equations (4) and (5). While these two equations are highly endothermic processes in the gas phase (*ca.*, 650 kJ/mol) [9, 10], dissociation of O_2^{2-} (equation 6) is highly exothermic (*ca.* −435 kJ/mol) and this may compensate for the formation of the peroxide. It should be recalled that thermovacuum reduction of TiO_2 follows the concerted four-electron transfer from $2O^{2-}$ to adjacent Ti^{4+} ions. These thermally-generated defective surfaces would contain coupled Ti^{3+}/O vacancy centres. In this non-stoichiometric state there will be a large driving force for O^{2-} formation, so that reactions (4–6) could conceivably occur on the rutile surface. In the presence of excess oxygen the surface O^- anions will react with O_2 to form O_3^- (equation 7) as commonly observed on other oxide surfaces [9, 10, 27, 28];

$$Ti^{3+} + O_2 \rightarrow Ti^{4+} + O_2^-, \tag{3}$$

$$2Ti^{3+} + O_2 \rightarrow 2Ti^{4+} + O_2^{2-}, \tag{4}$$

$$Ti^{3+} + O_2^- \rightarrow Ti^{4+} + O_2^{2-}, \tag{5}$$

$$O_2^{2-} \rightarrow 2O^-, \tag{6}$$

$$O^- + O_2 \rightarrow O_3^- \tag{7}$$

While it is possible for O^- to form directly *via* alternative pathways as illustrated in equations (8)–(10);

$$O_2 + e^- \rightarrow O^- + O, \tag{8}$$

$$O_2 + 2e^- \rightarrow 2O^-, \tag{9}$$

$$O_2^- + e^- \rightarrow 2O^-, \tag{10}$$

all of these processes are endothermic and are not accompanied by a negative enthalpy process shown in equation (6). Whatever the precise mechanism of surface re-oxidation, the above results clearly demonstrate that the pathways are different on the two thermally reduced titania polymorphs, since O_2^- is clearly preferred on anatase while O_3^- (*via* O^-) is preferred on rutile.

Photogeneration of oxygen radicals on dehydrated TiO_2

Following thermovacuum reduction at elevated temperature (823 K), the samples were exposed to 50 torr of oxygen at this temperature for 1 h, then cooled to 298 K under the oxygen atmosphere. The oxygen gas was finally evacuated at this

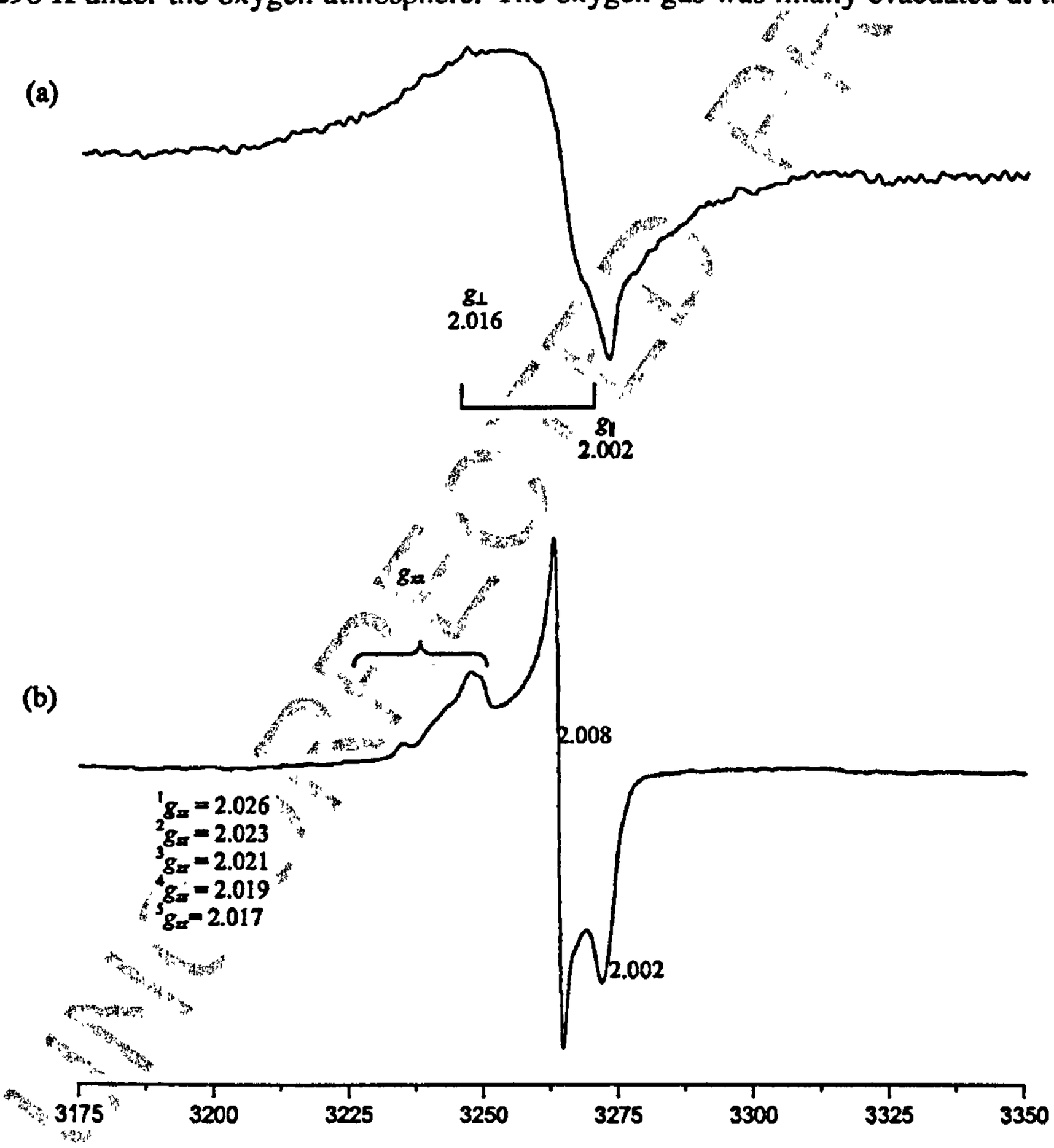

Figure 5. EPR spectra (100 K) of fully-dehydrated P25 after (a) UV irradition under 10 torr of oxygen at 100 K and (b) after subsequent evacuation of the excess oxygen at 298 K.

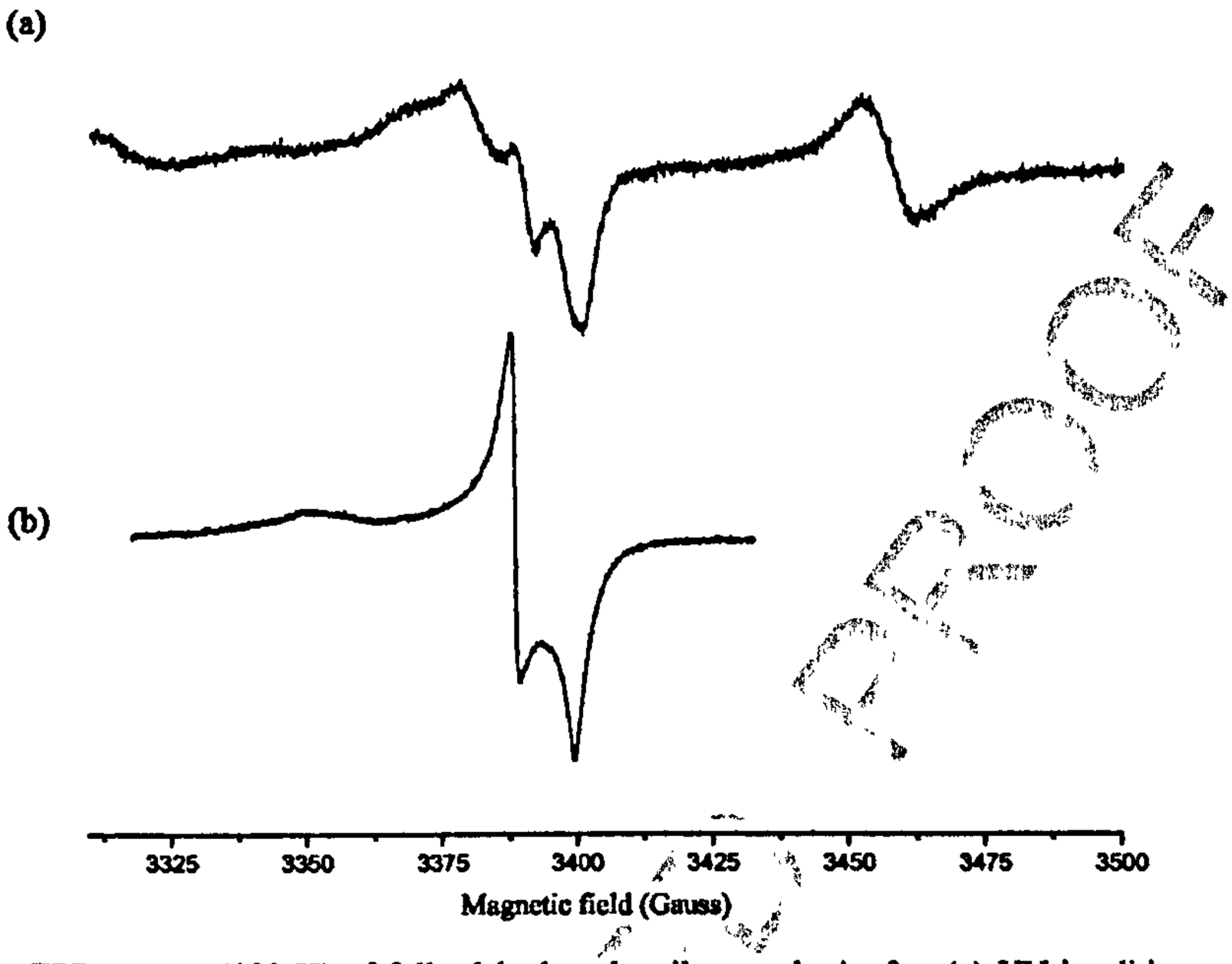

Figure 6. EPR spectra (100 K) of fully-dehydrated rutile sample A after (a) UV irradition under 10 torr of oxygen at 100 K and (b) after subsequent evacuation of the excess oxygen at 298 K.

temperature producing a clean, activated TiO_2 surface free of surface contaminants or bound water. A small quantity of oxygen (*ca.* 5 torr) was subsequently admitted to this clean dehydroxylated sample in the EPR tube, and UV irradiated at 100 K for 30 min. The resulting (100 K) EPR spectra are shown in Figs 5 and 6 for P25 and the high surface area rutile (sample A), respectively.

After UV irradiation at 100 K, the presence of photogenerated trapped holes (O^-) are clearly visible (Figs 5a and 6a) in both samples (Table 1). These active oxygen species are short lived, and decay quickly in the dark or upon warming the sample to room temperature. The long-lived photogenerated O_2^- anions are not visible under these conditions due to the excess pressure of dioxygen (resulting in line broadening) but can be observed following evacuation. No photogenerated trapped electron centres (Ti^{3+}) are visible in P25, while traces of a bulk reduced Ti^{3+} centre can be seen in the rutile sample (Fig. 6a). After evacuation of oxygen at 298 K, the EPR spectra were again recorded at 100 K, and the results are shown in Figs 5b and 6b. As expected the observed spectra can be easily assigned to the adsorbed superoxide anion, with no traces of the trapped holes. The difference in g_{zz} heterogeneity of O_2^- reflects the different surface morphologies, creating slightly different adsorption sites for the anion. At least 5 sites are visible in P25 whereas only 2 dominant adsorption sites exist on the stable surface (Table 1). The anion is stable for several days on the fully dehydrated anatase and rutile surfaces. The large electrostatic attraction between the charged oxygen species and the ionic surface is

Table 1.
Spin Hamiltonian parameters for the paramagnetic centres observed by EPR on P25 (anatase) and the two rutile samples used

Species	P25 (Anatase)			Rutile A			Rutile B		
Ti^{3+}	$g\perp$ 1.962	$g\parallel$ 1.95		$g\perp$ 1.967	$g\parallel$ 1.941		$g\perp$ 1.962	$g\parallel$ 1.949	
LCE	g_{iso} 2.003			g_{iso} 2.003			g_{iso} 2.003		
O^-	$g\perp$ 2.016	$g\parallel$ 2.002		$g\perp$ 2.016	$g\parallel$ 2.002		$g\perp$ 2.016	$g\parallel$ 2.002	
O_2^-	g_{xx} 2.002	g_{yy} 2.008	g_{zz} 2.019 2.022 2.025	g_{xx} 2.002	g_{yy} 2.008	g_{zz} 2.022 2.026	g_{xx} 2.002	g_{yy} 2.009	g_{zz} 2.019 2.023 2.027
O_3^-				g_1 2.002	g_2 2.008	g_3 2.011	g_1 2.002	g_2 2.008	g_3 2.001
$HO_2^{\cdot}$	g_1 2.002	g_2 2.008	g_3 2.034				g_1 2.002	g_2 2.008	g_3 2.032

See experimental section for a description of the samples.

likely responsible for the long lifetime of the species. Deactivation of O_2^- *via* release of an electron to TiO_2 [29] is not observed on these dehydrated surfaces.

Photogeneration of oxygen radicals on hydrated TiO_2

Following activation of the TiO_2 surface (as described above), the sample was subsequently exposed to water in two different ways in order to study the effects of surface hydration on the nature of the photogenerated oxygen radicals. In the first case, the sample was exposed to 10 torr of water vapour at 673 K for 1 h, and subsequently evacuated at 298 K to remove the excess physisorbed water molecules. This will hereafter be referred to as a fully-hydrated surface. Oxygen (10 torr) was then added to the sample and UV irradiated at low temperature. In the second case, a mixture of oxygen and water (5 : 1 ratio; 10 torr total pressure) were co-adsorbed at 298 K on the activated surface and UV irradiated at low temperature. This sample will hereafter be referred to as a partially-hydrated surface.

In the case of oxygen adsorption and subsequent UV irradiation on the fully-hydrated P25 surface, no signals were observed in the EPR spectrum. In other words, there was no evidence for any radical species existing within the lifetime of the EPR measurement at low temperatures. By comparison, when oxygen was adsorbed on the partially-hydrated P25 surface, and subsequently UV irradiated at 77 K, an intense EPR spectrum was observed (Fig. 7). The spectrum is dominated by the presence of O^- radicals; traces of O_2^- and photogenerated bulk Ti^{3+} centre can also be seen. While the characteristic features of adsorbed O^- can be easily

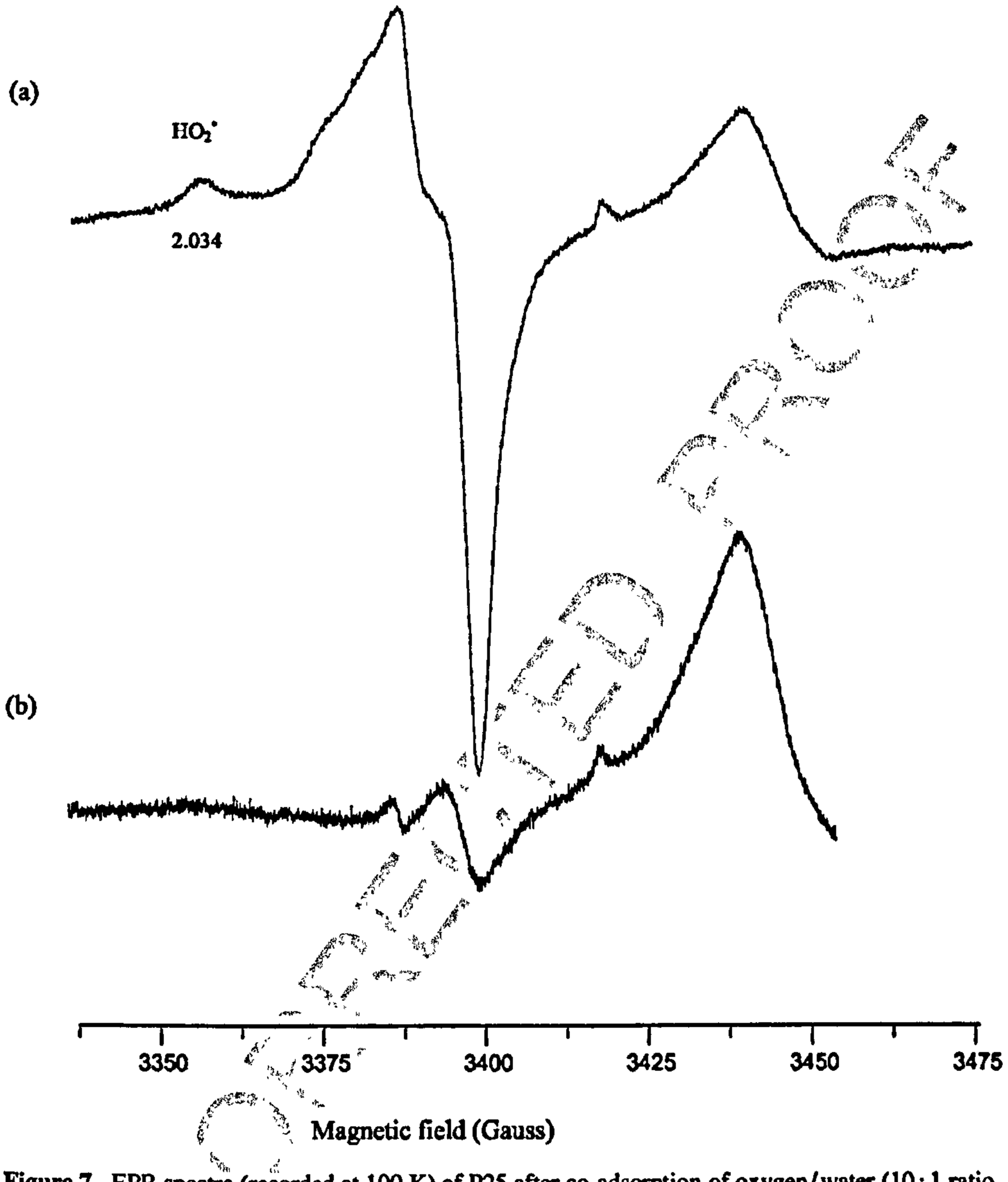

Figure 7. EPR spectra (recorded at 100 K) of P25 after co-adsorption of oxygen/water (10 : 1 ratio, 10 torr total pressure) following (a) UV irradiation at 77 K and (b) after warming to 298 K for 1 min followed by re-cooling to 100 K.

identified, the g_{zz} component at 2.034 signifies the presence of the hydroperoxy radical ($HO_2^{\cdot}$). The g_{zz} component of peroxy radicals is always *ca.* 2.034, and is often used as a fingerprint to identify the species [19, 24, 30, 31]. This radical is likely formed *via* the reaction with surface hydroxy groups

$$O_2^- + H^+ \rightarrow HO_2^{\cdot} \tag{11}$$

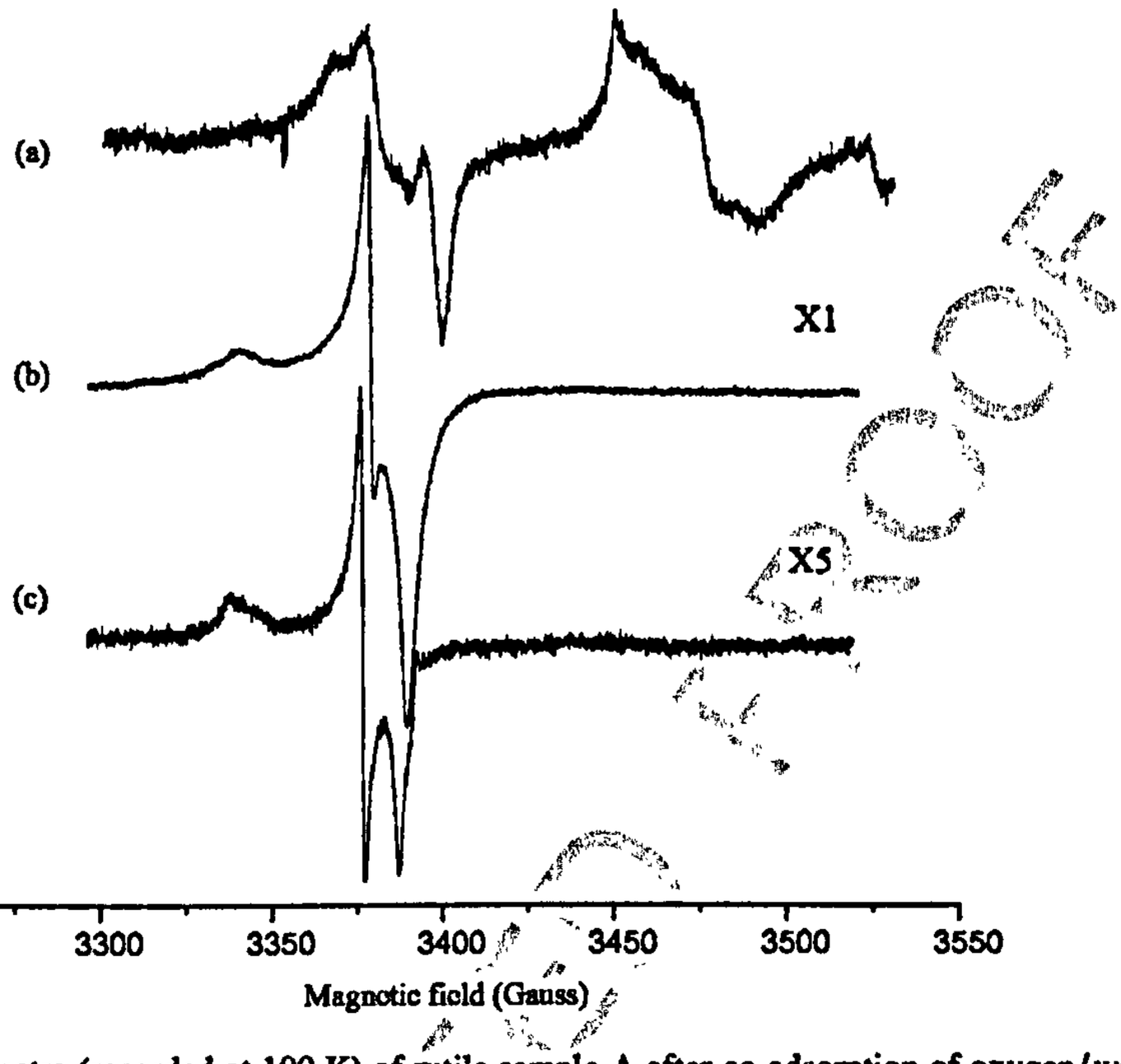

Figure 8. EPR spectra (recorded at 100 K) of rutile sample A after co-adsorption of oxygen/water (10 : 1 ratio, 10 torr total pressure) following (a) UV irradiation at 77 K and (b) after warming to 298 K for 24 h followed by re-cooling to 100 K.

since exposure of a TiO_2 surface containing pre-adsorbed O_2^- to 5 torr of water vapour resulted in a 5-fold decrease in O_2^- signal intensity, but no new signals arising from $HO_2^{\cdot}$ were observed. When the sample was warmed to 298 K and re-cooled to 100 K, the signals dissappeared completely (Fig. 7b). They could be re-generated by a further irradiation of the sample at 100 K. Therefore, by comparison to the nature of the radicals formed of fully dehydrated P25, on the partially-hydrated sample, hydroperoxy radicals are formed in addition to superoxide radicals, and both radicals were found to be thermally unstable. On the fully-hydrated surface, the radicals (O_2^- and $HO_2^{\cdot}$) could not be observed even after prolonged UV irradiation at 100 K.

When the analogous experiments was performed on the fully and partially hydrated rutile surfaces, the photogenerated superoxide radical was again observed, but with smaller levels of the associated hydroperoxy radicals. The EPR spectra of the partially hydrated rutile A and B samples arfter UV irradiation under oxygen at 100 K are shown in Figs 8 and 9, respectively. The most striking difference between the anatase (Fig. 7) and rutile samples (Figs 8 and 9) relates to the stability of the radicals. Warming the rutile sample to room temperature followed by cooling to 77 K produced no visible change in the EPR spectra. The intensity of the spectra was found to decrease (by a factor of 5) only after standing for 24 h at 300 K. In addition,

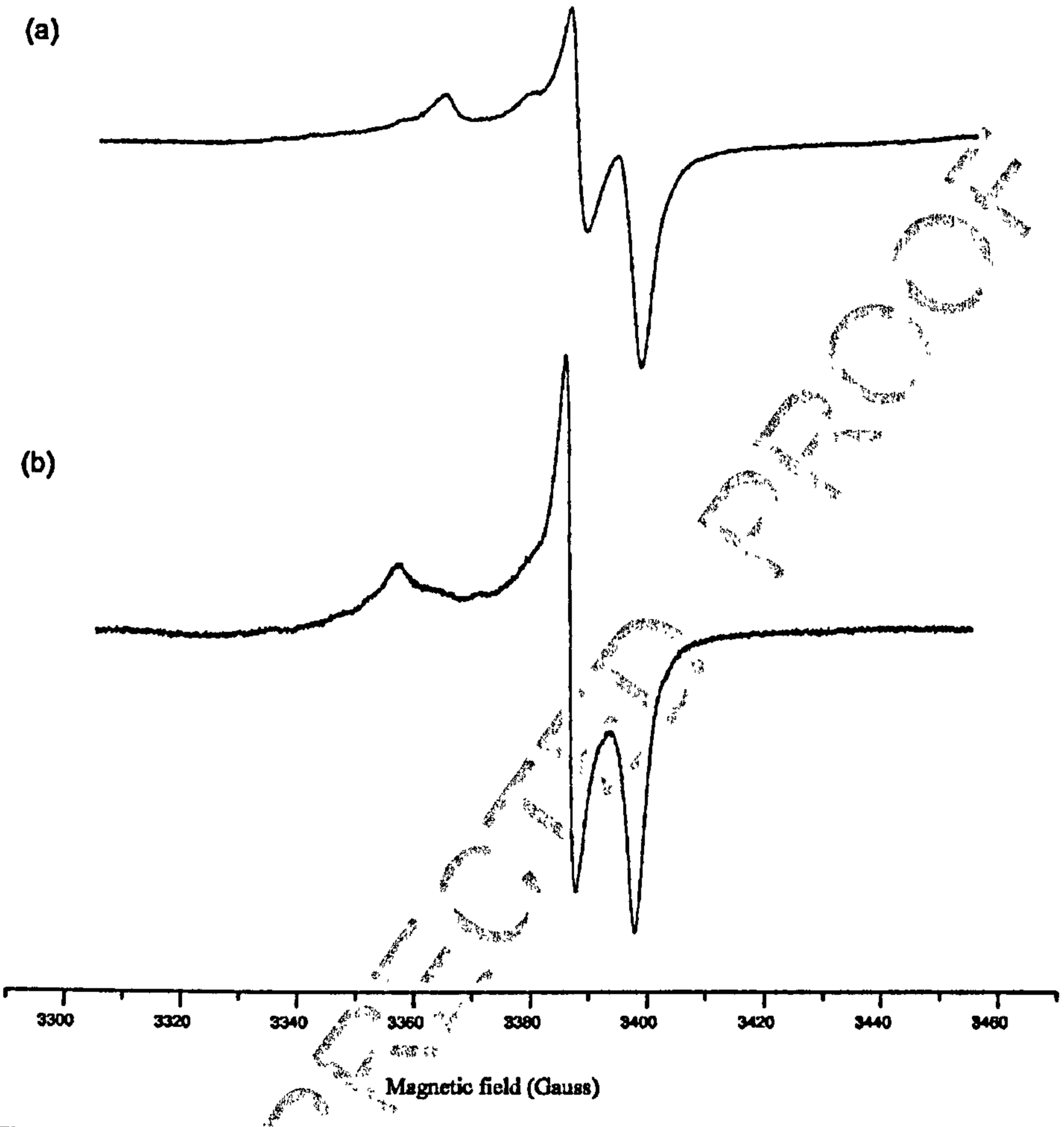

Figure 9. EPR spectra (recorded at 100 K) of rutile sample B after co-adsorption of oxygen/water (10 : 1 ratio, 10 torr total pressure) following (a) UV irradiation at 77 K and (b) after warming to 298 K for 24 h followed by re-cooling to 100 K.

traces of the O_2^- signal were even observed on the fully-hydrated rutile surface, albeit with lower stability compared to the partially-hydrated sample. This contrasts significantly with the fully-hydrated P25 sample, where no photogenerated oxygen-centred radicals were observed. These results indicate the inherent differences in the lifetimes of the radicals on the anatase and rutile surface depending on the extent of surface hydration.

In aqueous systems O_2^- radicals readily interact with protons forming the hydroperoxy radicals (according to equation 11 above). Deactivation of the radical can subsequently occur according to the disproportionation reactions;

$$HO_2^{\cdot} + O_2^- + H^+ \rightarrow H_2O_2 + O_2, \qquad (12)$$

$$HO_2^{\cdot} + HO_2^{\cdot} \rightarrow H_2O_2 + O_2, \tag{13}$$

$$O_2^- + O_2^- + 2H^+ \rightarrow H_2O_2 + O_2 \tag{14}$$

While it has been reported that O_2^- deactivation on TiO_2 proceeds *via* first-order kinetics, suggesting a reaction with species present in large excess [29], the presence of the hydroxyl groups on the hydrated surface remove any adsorption sites for O_2^- anions. The O_2^- anions are very stable on dehydrated surfaces, and are often stabilised at the site of initial electron transfer. However, they can be sufficiently mobile on fully and partially hydrated surfaces such that reactions (12)–(14) may occur. The reason for the different lifetimes observed on rutile compared to anatase, is proposed as due to the different morphologies, whereby some surface sites capable of O_2^- stabilisation remain on hydrated rutile surfaces. This may also explain the difference in $HO_2^{\cdot}$ abundance on the two surfaces. On P25 $HO_2^{\cdot}$ formation occurs easily (signified by the $g = 2.034$ component), indicating a facile interaction between O_2^- and an adsorbed OH group, while on rutile the levels of $HO_2^{\cdot}$ formation is far smaller. This indicates preferential adsorption of the charged anion as O_2^-.

CONCLUSIONS

It is well known that a variety of oxygen radicals, including O^-, O_2^-, O_3^- and $HO_2^{\cdot}$, can be stabilised on the TiO_2 surface. These radicals have been extensively studied by many authors using EPR spectroscopy. The current results however have demonstrated how differences in sample pretreatment conditions or type of titania sample, can lead to appreciable differences in the nature, stability and lifetimes of the observed radicals.

On thermally-reduced anatase (P25), superoxide formation is the preferred route for re-oxidation of the Ti^{3+} sites at temperatures in the range 300–400 K. The chemistry is apparently more complex on the rutile surface, since O^-, O_2^- and O_3^- anions can be formed within the same temperature region. The presence of O_3^- demonstrates the strong preference of the rutile material for oxygen dissociation leading to O^- formation.

On dehydrated surfaces, the photogenerated O_2^- anion is stable for extended periods of time. In the absence of any surface hydroxyl groups no hydroperoxy radicals are observed. However, on the partially-hydrated surface both O_2 and $HO_2^{\cdot}$ are simultaneously formed. On the anatase surface, these radicals were found to be thermally unstable, and quickly decayed to diamagnetic species upon warming to 300 K. By comparsion, the same radicals are stable for at least 24 h on the partially-hydrated rutile surface, and could even be observed at low temperatures on the same fully-hydrated surfaces. These results show the inherent differences in radical formation and stability on anatase *vs.* rutile surfaces, and may have implications in explaining the different photoreactivties of the two (anatase and rutile) materials.

VSP 2001/04/20 Prn:16/05/2003; 9:43 {RA} F:rc12208.tex; VTeX/lina p. 17 (686-786)

Among these oxygen-centred radicals the O_2^- anion is undoubtely the most stable surface species. However, as these results demonstrate, the fate of the radicals will vary depending on the experimental conditions, and this must always be taken into consideration when suggesting possible reaction pathways in photocatalysis.

REFERENCES

1. E. E. Ollis and H. Al-Ekabi (Eds), *Photocatalytic Purification and Treatment of Water*. Elsevier, Amsterdam (1993).
2. A. Fujishima, K. Hashimoto and T. Watanabe, *TiO_2 Photocatalysis; Fundamentals and Applications*. BKC, Tokyo (1999).
3. M. A. Fox and M. T. Dulay, *Chem. Rev.* **93**, 341 (1993).
4. A. L. Linsebigler, G. Q. Lu and J. T. Yates, *Chem. Rev.* **95**, 735 (1995).
5. M. R. Hoffmann, S. T. Martin, W. Choi and D. W. Bahnemann, *Chem. Rev.* **95**, 69 (1995).
6. T. Tatsuma, S. Tachibana and A. Fujishima, *J. Phys. Chem. B* **105**, 6987 (2001).
7. R. Nakamura and S. Sato, *J. Phys. Chem. B* **106**, 5893 (2002).
8. S. H. Szczepankiewicz, A. J. Colussi and M. R. Hoffmann, *J. Phys. Chem. B* **104**, 9842 (2000).
9. M. Che and A. J. Tench, *Adv. Catal.* **31**, 77 (1982).
10. M. Che and A. J. Tench, *Adv. Catal.* **32**, 1 (1983).
11. M. Anpo, M. Che, B. Fubini, E. Garrone, E. Giamello and M. C. Paganini, *Top. Catal.* **8**, 189 (1999).
12. J. M. Coronado, A. J. Maira, J. C. Conesa, K. L. Yeung, V. Augugliaro and J. Soria, *Langmuir* **17**, 5368 (2001).
13. A. J. Maira, K. L. Yeung, J. Soria, J. M. Coronado, C. Belver, C. Y. Lee and V. Augugliaro, *Appl. Catal. B* **29**, 327 (2001).
14. D. R. Park, B. J. Ahn, H. S. Park, H. Yamashita and M. Anpo, *Kor. J. Chem. Eng.* **18**, 930 (2001).
15. D. R. Park, J. Zhang, K. Ikeue, H. Yamashita and M. Anpo, *J. Catal.* **185**, 114 (1999).
16. P. Claus, A. Brückner, C. Mohr and H. Hofmeister, *J. Am. Chem. Soc.* **122**, 11430 (2000).
17. M. Okumura, J. M. Coroando, J. Soria, M. Haruta and J. C. Conesa, *J. Catal.* **203**, 168 (2001).
18. C. A. Jenkins and D. M. Murphy, *J. Phys. Chem. B* **103**, 1019 (1999).
19. A. L. Attwood, J. Edwards, C. C. Rowlands and D. M. Murphy, *J. Phys. Chem. B* **107**, 1779 (2003).
20. H. Einaga, A. Ogata, S. Futamura and T. Ibusuki, *Chem. Phys. Lett.* **338**, 303 (2001).
21. H. Liu, A. I. Kozlov, A. P. Kozlova, T. Shido, K. Asakura and Y. Iwasawa, *J. Catal.* **185**, 252 (1999).
22. R. F. Howe and M. Gratzel, *J. Phys. Chem.* **89**, 4495 (1985).
23. R. F. Howe and M. Gratzel, *J. Phys. Chem.* **91**, 3906 (1987).
24. A. R. Gonzalez-Elipe and M. Che, *J. Chim. Phys.* **79**, 355 (1982).
25. M. Anpo, T. Shima and Y. Kubokawa, *Chem. Lett.*, 1799 (1985).
26. M. Chiesa, E. Giamello, M. C. Paganini, Z. Sojka and D. M. Murphy, *J. Chem. Phys.* **116**, 4266 (2002).
27. E. Giamello and D. M. Murphy, *Top. Mol. Org. Eng.* **13**, 147 (1995).
28. D. M. Murphy and E. Giamello, in: *Electron Paramagnetic Resonance*, B. C. Gilbert, M. J. Davies and D. M. Murphy (Eds), Vol. 13, p. 183. Royal Society of Chemistry, Cambridge (2002).
29. K. Ishibashi, Y. Nosaka, K. Hashimoto and A. Fujishima, *J. Phys. Chem. B* **102**, 2117 (1998).
30. M. D. Sevilla, D. Becker and M. Yao, *J. Chem. Soc., Faraday Trans.* **86**, 3279 (1990).
31. D. C. McCain and W. E. Palke, *J. Magn. Reson.* **20**, 52 (1975).

APPENDIX 3.

T. A. Egerton; Paul A. Christensen; Keith Scott; Rob Harrison; and James R Tinlin. '*UV absorption by nitrophenol: implications for design of photocatalytic and photoelectrocatalytic reactors*' in '*Proceedings of TiO_2-9 and AOT-10*' San-Diego, USA, 2004

UV ABSORPTION BY NITROPHENOLS: IMPLICATIONS FOR DESIGN OF PHOTOCATALYTIC AND PHOTOELECTROCATALYTIC REACTORS

Terry A. Egerton*, Paul A. Christensen, Keith Scott, Rob Harrison, and James R Tinlin
School of Chemical Engineering and Advanced Materials, Bedson Building
University of Newcastle, Newcastle on Tyne, NE1 7RU, UK

*Author to whom communications should be addressed; E-mail: T.A.Egerton@ncl.ac.uk

Abstract

This paper reports, as have previous authors, that, although the linear $\ln(C_0/C)$ vs time plots for nitrophenol photo-oxidation suggest first order kinetics, the derived first-order rate constants decrease with increasing nitrophenol concentration. However, we consider that the widely proposed explanation that the rates decrease because the surface is progressively blocked by adsorbed intermediates is improbable because the fraction of partially oxidized products is small. Instead, we propose that the major contribution to decreased oxidation rates, as the nitrophenol concentration increases from 0.25 to 8 mM, is increased UV absorption by the nitrophenol itself. The UV attenuation causes reduced photocurrents to be generated at TiO_2 electrodes and this reduced activity is expected for all applications involving an immobilized catalyst. Even for dispersed and agitated catalyst, such as that used in a slurry reactor, attenuation of UV is significant. The significance is demonstrated by the dependence of nitrophenol oxidation on I^1, where I is the UV intensity, for conditions which lead to an $I^{0.5}$ dependence for oxidation of isopropanol – which does not absorb UV.

Introduction

This paper explores the effect of UV absorption by a reactant upon the measured rate of its photocatalytic oxidation by investigating the photocatalytic oxidation of nitrophenol. Both 2-Nitrophenol (2-NP) and 4-nitrophenol (4-NP) absorb strongly in the UV and initial studies of their photocatalytic oxidation (1) used this absorption to monitor the change in reactant concentration. We suggest that this UV absorption –shown in Figs.1a and 1b - limits the number of photons incident on the surface of suspended catalyst particles and hence limits the extent of oxidation. Limitations caused by UV attenuation in slurry reactors are likely to be even more significant when an immobilized catalyst is used and we have explored this aspect of the problem by focusing on photoelectrocatalysis (PEC). In PEC the TiO_2 is in the form of a thin layer on a conducting substrate (a photo-anode) and, as illustrated in Fig. 2a, the UV excited electrons are monitored as a photocurrent when they move to the counter-electrode under the influence of an applied potential.

Experimental

In this study of nitrophenol photocatalytic oxidation (PCO) the decrease in the initial concentration of NP (after first allowing adsorption in the dark to reach equilibrium) has been followed by HPLC. The HPLC measurements have been supplemented by measurements of total organic carbon concentration (TOC). The difference between the HPLC and TOC measurements represents the concentration of partially oxidized products. For 2-NP, during the first 180 minutes of reaction, these intermediates account for less than 10% of the organic species in

solution; for 4-NP they account for less than 20%. Details of these measurements and of the reactors used have been reported more fully in a separate paper (2).

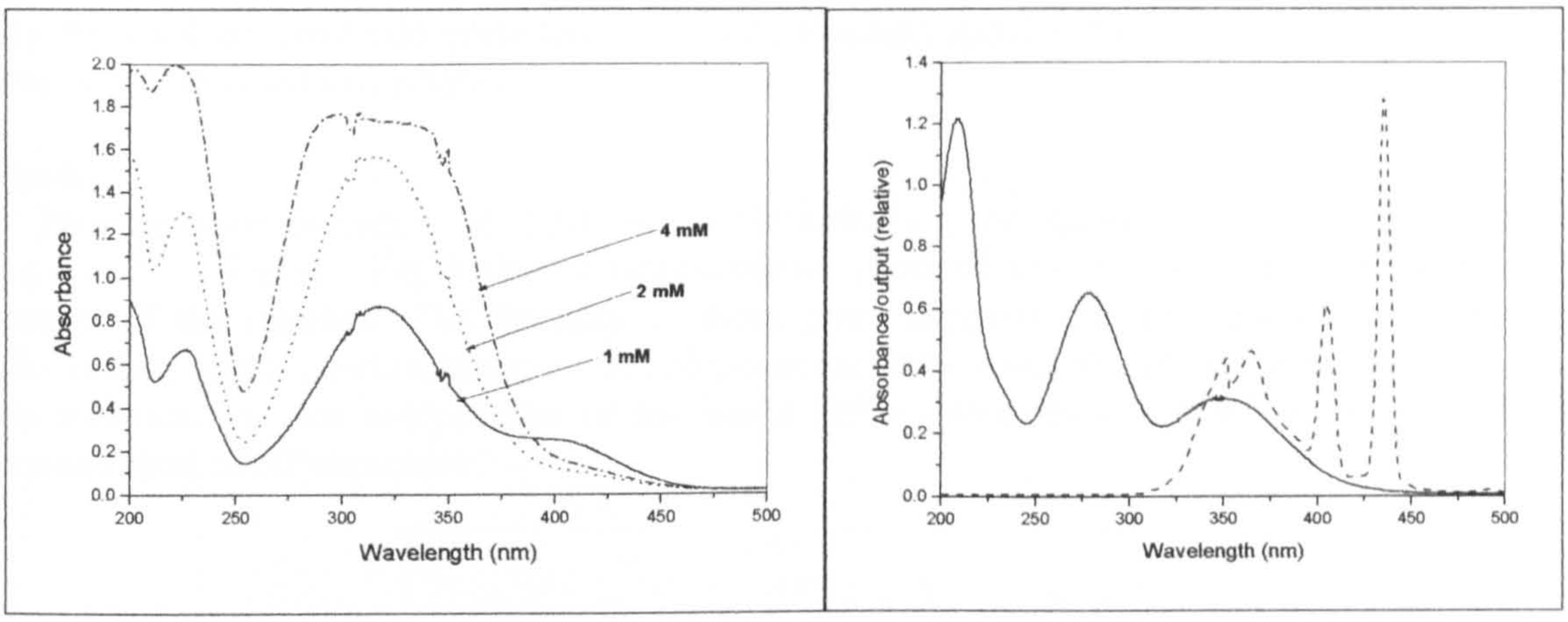

(a) **(b)**

Figure 1. (a) UV/VIS absorption spectra of 4-nitrophenol. C = 1 mM (—), 2mM (·····), 4 mM (- - - - - - - - - -). **(b)** Absorption spectra of 2-Nitrophenol (1mM) (solid line) and spectral output of the Phillips PL-9 UV lamps (dotted line). Aqueous solutions of nitrophenol (a weak acid) naturally attain a pH of ~ 5.2 .

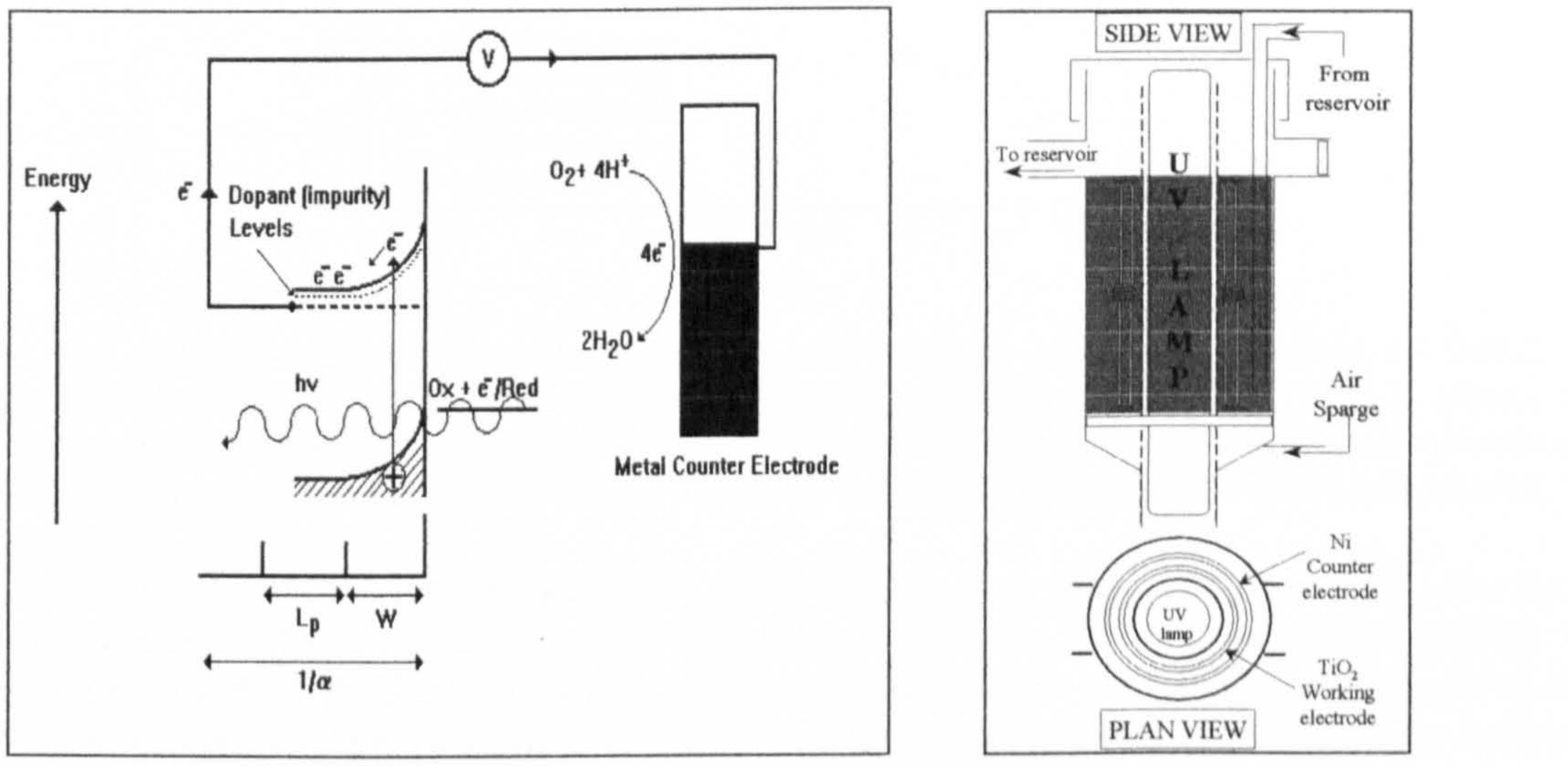

(a) **(b)**

Figure 2. (a) A diagrammatic representation of the photo-electrocatalytic (PEC) experiment in which the electrons excited by UV incident on a TiO_2 photo-anode are transported via the external circuit to a metal counter electrode. **(b)** The PEC reactor used for the nitrophenol oxidation experiments showing the concentric arrangement of the nickel counter electrode and TiO_2 photo-anode around a UV source placed in an axial well.

The PEC measurements were made using a reactor of the type shown in Fig. 2b. In this reactor the distance between the pyrex-glass wall of the central well and the TiO_2 mesh anode is nominally ~ 1mm. The anode may either be heated-treated titanium metal – a thermal anode, or may be a sol-gel electrode prepared by coating titanium metal with a titania gel. Further details have been published elsewhere (3).

Results

Photocatalytic oxidation of 2-NP and 4-NP solutions was measured over the concentration range 0.25 – 8 mM. Fig 3 shows representative plots of $\ln(C/C_0)$ vs. time for the first 160 minutes of the reaction. The linearity of these plots suggests that the removal of nitrophenol follows first order kinetics, however, the slope of the plots – and therefore the derived first order rate constant - is not independent of the initial NP concentration. Instead it decreases as the concentration of NP increases.

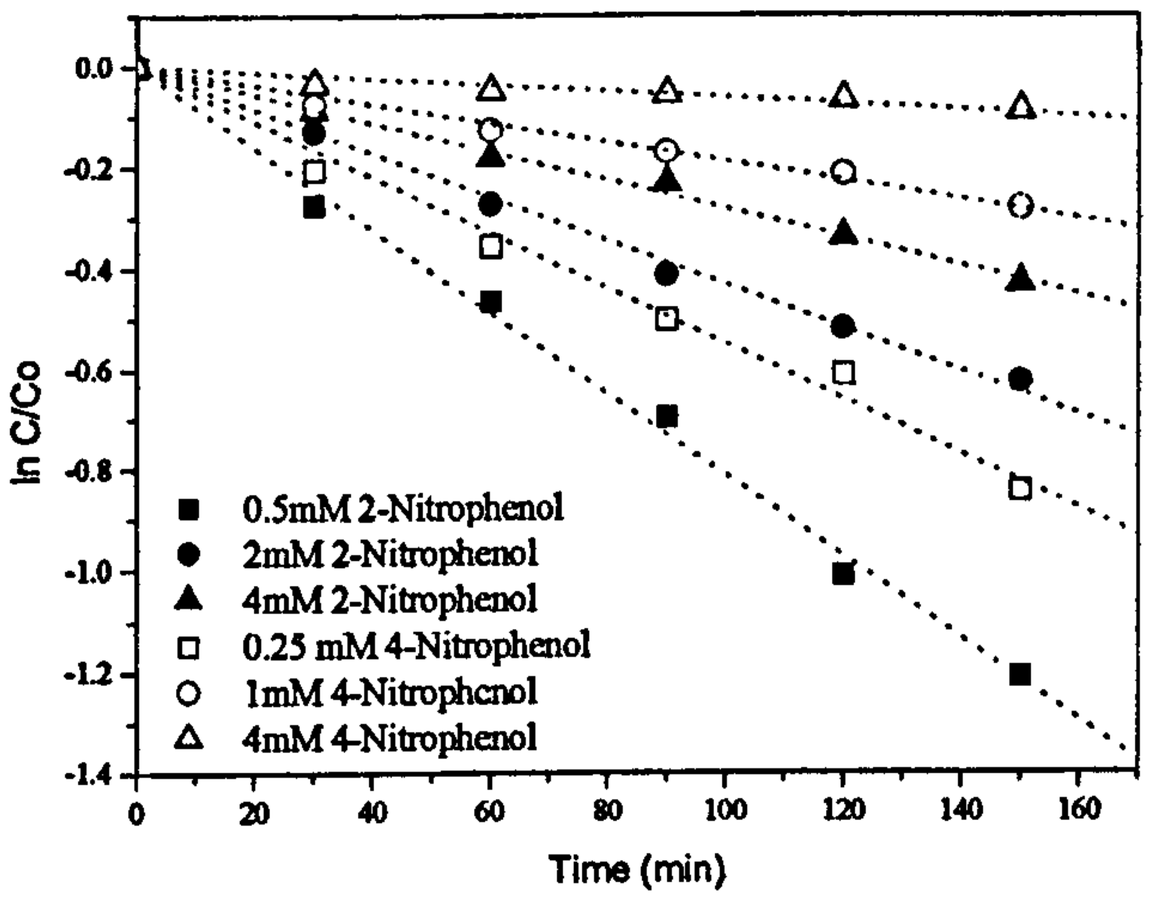

Figure 3(a). Representative 'first-order' plots for photocatalytic oxidation, measured by HPLC, of nitrophenol solutions. The concentration decrease during oxidation by 4 g dm^3 TiO_2 is shown for different values of C_0, the concentration after adsorption equilibrium has been reached, for nitrophenol solutions of initial concentration C_i (see insert). Results are shown for 2-nitrophenol and 4-nitrophenol.

Similar results have been reported by many others, e.g. Chen and Ray (4), who have generally attributed the decrease in measured rate constant to inactivation of the surface by intermediate oxidation products. However, this explanation does not seem consistent with the relatively low concentration of intermediate products deduced from the small difference between TOC and HPLC results (Fig. 3b). Further, we have shown elsewhere (2) that the adsorption coefficients derived from a Langmuir Hinshelwood analysis of the dependence of rate on concentration are not consistent with adsorption constants derived from (dark) measurements of adsorption isotherms. Hence we seek an alternative explanation of the trends found by us and others.

The UV transmittances at 365 nm of 2-NP and 4-NP solutions were calculated from measured absorption spectra and are listed in Table 1. They show that, in TiO_2-free nitrophenol solutions, the UV attenuation is significant and suggest that the UV attenuation could be a significant contribution to the observed decrease in apparent rate constant of photocatalytic oxidation with increasing NP concentration.

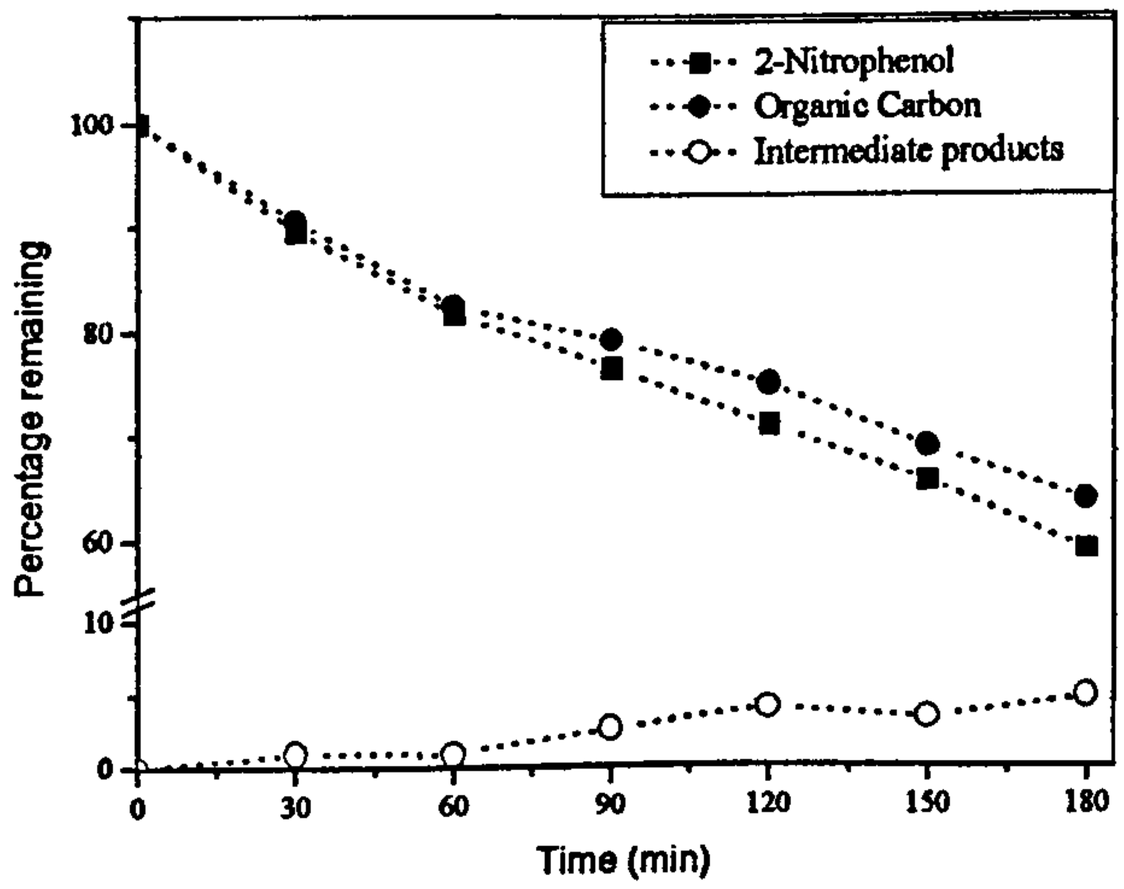

Figure 3(b). A comparison of the removal of 2-Nitrophenol (Initial concentration, C_i=1 mM), measured by HPLC, and the removal of organic carbon. The total amount of intermediate oxidation products corresponds to the difference between the two curves – note the break in the y-axis scale.

Table 1. The transmittance of 2- nitrophenol and 4-nitrophenol for a 1 mm path length.

Concentration of nitrophenol solution (mM)	Transmittance at a pathlength of 1mm (%)	
	2-Nitrophenol	4-Nitrophenol
0.25	-	82
0.5	68	67
1	51	45
2	26	30
4	9	11
8	<1	<1

The concept that attenuation of incident radiation by a UV-absorbing reactant may reduce the measured rate of oxidation finds its simplest application in the case of oxidation by a layer of immobilized catalyst. If this immobilized TiO_2 forms the photoanode of a reactor of the type shown in Fig.2b the photocurrent generated at a fixed potential by a constant incident UV flux may be used to monitor indirectly the effective UV flux reaching the electrode. For a reactant that does not absorb in the UV the measured photocurrent may be expected to increase with increasing solute concentration as has been demonstrated by John and co-workers in the case of glucose solutions (5). They report that that increasing the concentration of glucose from 0.2 mM to 50 mM increased the measured photocurrent by a factor of 5. Fig. 4 shows this increase over the range 0 to 1.6 mM. Similarly a decrease in photocurrent as a 10 mM oxalate solution was progressively degraded was found in our own work (6) as is shown in Fig 4b.

By contrast to the results shown in Fig 4a and 4b, the photocurrent generated at a thermal TiO_2 electrode, i.e. one made by heat treatment of titanium metal decreases with increasing concentration of nitrophenol. These thermal electrodes are relatively inactive for the PEC oxidation of nitrophenol and, in contrast to the sol–gel electrodes, direct charge transfer from the electrode to the nitrophenol is small. We assume that the photocurrent, i, is related to I, the incident UV intensity incident on the electrode, after passing through the nitrophenol solution, by a relation of the form

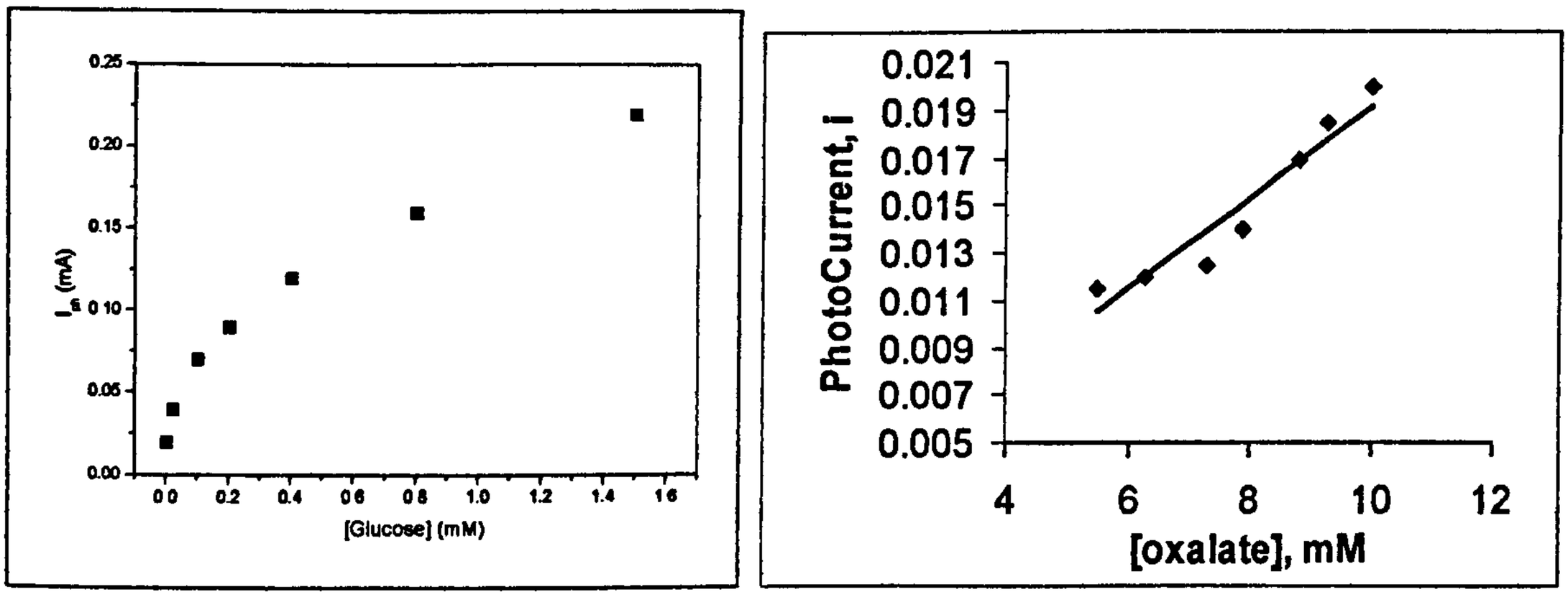

(a) **(b)**

Figure 4. **(a)** The increase in photocurrent at -0.2 volts vs Ag/AgCl with increasing concentration of glucose as derived from the results reported by R. John and co-workers (5). **(b)** The decrease in photocurrent measured during the photooxidation of 10 mM oxalate at pH 7 using sol gel electrodes at 1.2V (6).

$$i = k I^n$$

or

$$\log i = \log k + n \log I$$

(where n is 1 at very low light intensity and 0.5 at moderate intensity, when recombination dominates (9)). Combining this with the Beer Lambert law,

gives

$$\log i = \log k + n \log I_0 - \varepsilon n l.c$$

where I_0 is the UV intensity at the point at which UV enters the solution (i.e. at the glass/solution interface, and predicts that a plot of log i vs. concentration should be a straight line with gradient (- εnl). The results shown in Fig. 5 conform to this predicted trend. The contrast between the increase of photocurrent with solute concentration for non-absorbing glucose and oxalate and the decrease for UV-absorbing nitrophenol demonstrates the importance of UV absorption in determining the performance of a photolectrocatalytic reactor – even when the reactor has been specifically designed with a short UV path length in order to minimize UV attenuation.

The significance of these results is that, although it has generally been considered that, for both photocatalysis and photoelectrocatalysis using immobilized TiO_2, the biggest challenge is to achieve good mass transfer, UV-penetration may be equally, or more important. Thus, it may be beneficial to use falling film (7) or spinning disc (8) reactors to minimize the path length of strongly absorbing pollutants. Alternatively, the radiation source should be selected to minimize UV absorption.

It is now appropriate to consider whether UV absorption by the reactant is of similar significance for slurry reactors. In these reactors the catalyst dispersion is normally agitated to stop the particles from settling and consequently individual particles are intermittently swept close to the reactor windows. It is not, *a priori*, clear that the constraints of UV attenuation apply to reactors of this type in which the individual catalyst particles are mobile. To answer this question we have measured, in the same equipment, the dependence of oxidation rate on light intensity of nitrophenols – which absorb strongly in the 300 – 400 nm region of the spectrum –

with isopropanol which does not. It has been demonstrated previously that for propan-2-ol the exponent n in the relationship

$$\text{Rate} = k I^n$$

is 0.5 at moderate intensities, when recombination controls oxidation rate, and 1 at low intensities, when the rate of charge carrier generation is so low that surface reaction dominates (9). Hence the exponent n (which can be determined from the gradient of a plot of log(rate) vs. log (I)) is a sensitive monitor of the effective light intensity incident on the catalysts particles.

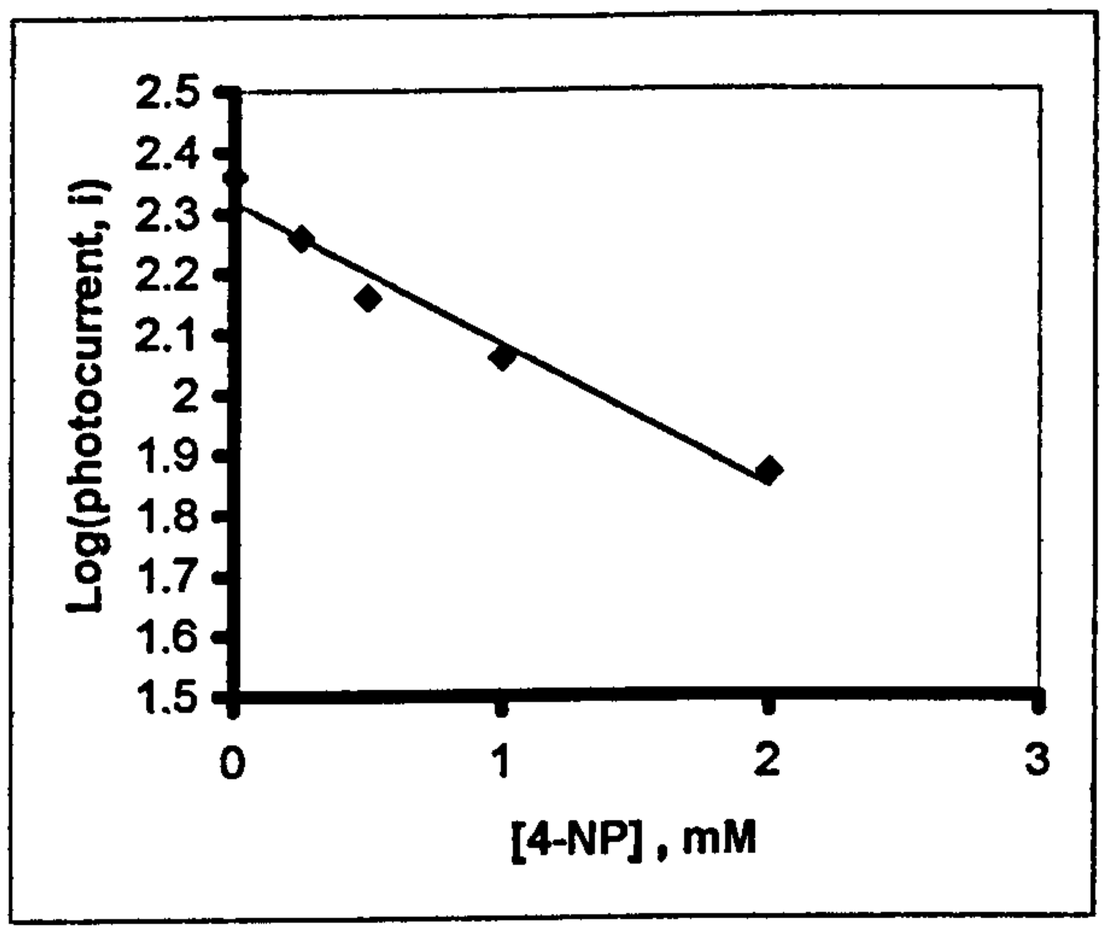

Figure 5. The decrease in photocurrent with increasing concentration of nitrophenol. Photocurrents were measured at a potential of 3 V in the reactor shown in Fig 2b.

Fig 6a demonstrates that for isopropanol oxidation the gradient of the log-log plot is 0.5, i.e. the UV intensity is sufficiently large that recombination dominates. However, for 1mM 2-NP the slope is ~1 demonstrating that the UV incident on the reactor windows has been attenuated to such an extent that by the time it reaches the catalyst particles the effective intensity is insufficiently high for recombination of excited charge carriers to control the oxidation rate. Fig. 6b shows corresponding results for 0.25 mM 4-NP and 0.25 mM 2-NP for which UV attenuation by the nitrophenol will be reduced. [The scale of this graph is not the same as for Fig. 6a.]. For 4-nitrophenol the gradient of 0.9 is close to 1 and to Chen and Ray's (4) reported value of 0.84. However for 2-NP although the gradient of the 'best fit' straight line through all points is 0.8 there is, as implied by the dashed line, some evidence at the highest intensities of a transition from a linear to a square root dependence of rate on intensity. Overall the results indicate that even for a mobile catalyst UV attenuation may significantly reduce the photocatalytic oxidation of strongly UV-absorbing molecules.

In the light of these conclusions it is unsurprising that in both photoelectrocatalytic and photocatalytic oxidations over extended times significant deviations from the initial good first order plots were observed – as shown in Fig. 7 for the photoelectrocatalytic oxidation of 1 mM 4-NP. Under these circumstances UV attenuation is reduced as reaction proceeds and therefore the rate of photo-degradation accelerates.

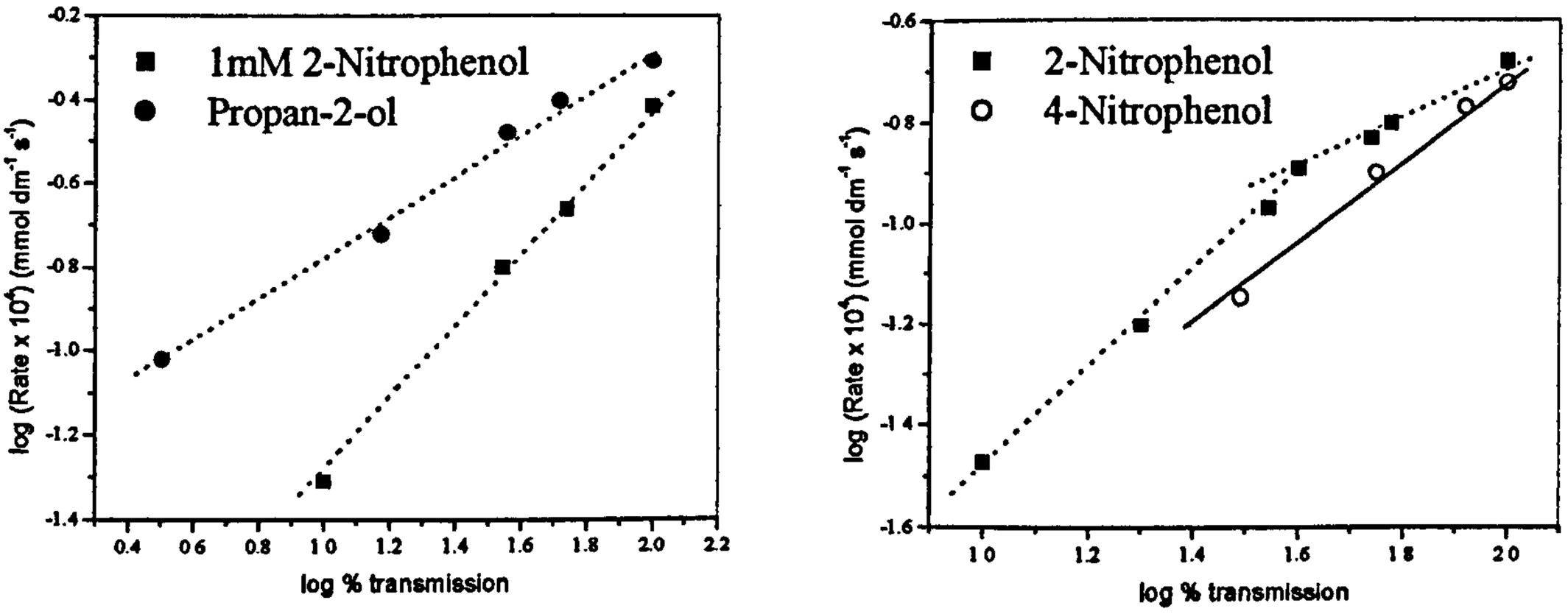

Figure 6. **(a)** Dependence of the rate of oxidation on the incident UV intensity for 1 mM 2-nitrophenol and Propan-2-ol. **(b)** Dependence of the rate of oxidation on the incident UV intensity for 0.25 mM solutions of 2-nitrophenol and 4-nitrophenol.

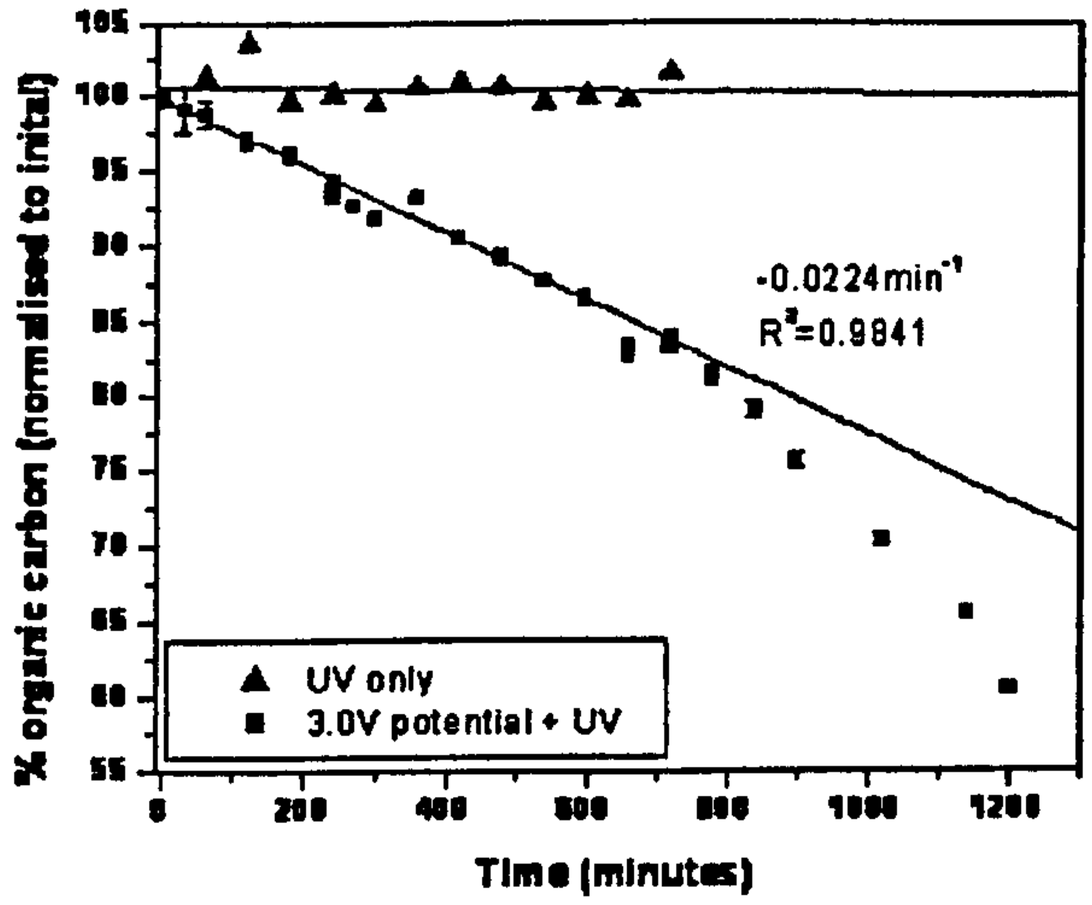

Figure 7. The extended oxidation of 1 mM 4-Nitrophenol solution by sol-gel electrodes at a potential of 1V. The total oxidation was measured by TOC.

Finally, we note that changes in the absorption spectrum of nitrophenols, such as those that occur when the pH is altered, must be taken into account when comparing the rates of photocatalytic oxidation under different conditions. Failure to account for the changes in UV absorption with pH may contribute to the inconsistent effects reported by different research groups. Similarly overall rate equations which take into account adsorption constants for nitrophenol and O_2, and the effect of light intensity and temperature to give an expression capable of predicting the concentration profiles throughout a photocatalytic oxidation (4) may be of limited generality because they will be sensitive to the detailed optics of the reactor for which they are derived.

Acknowledgments

We thank the EPSRC for financial support of Rob Harrison and James Tinlin and Dr. John Harper, Dr Ian Tooley and Mr. J.W. Wang for their contributions to the experimental work.

References

(1) Augugliarno, V.; Palmisano, L.; Schiavello, M.; Sclafani, A. *Appl. Catal.*, **1991,** *69*, 323-340.
(2) Egerton, T.A.; Christensen, P.A.; Harrison R.W. & Wang J.W. *J.Appl. Electrochem.* In press.
(3) Christensen, P.A.; Egerton, T.A.; Kosa, S.A.M.; Scott K.; Tinlin, J.R., *J.Appl. Electrochem.* In press.
(4) Chen D.; Ray, A.K. *Appl. Cat. B: Environmental*, **1999,** *23*, 143-157.
(5) Jiang, D.L.; Zhao, H.J.; Zhang, S.Q.; John, R. J Phys. Chem. B., **2003** 107 (46): 12774-12780.
(6) Tinlin, J.R. Ph. D. Thesis, University of Newcastle, UK 2002.
(7) Hamnett A.; Shaw, K.E.; Walker, G.M.; Walker, S.A.; Howarth, C.R.; Butterfield I.M.; Christensen P.A, *J. Appl. Electrochem.* **1997,** *27 (4)*, 385-395.
(8) Yatmaz, H.C, Wallis, C.; Howarth, C.R., Chemosphere **2001,** 42 (4): 397-403.
(9) Egerton,T.A.; King, C.J.; *J. Oil Col Chem Assoc.* **1979,** *26*, 386-391.